Low-order wavefront control and calibration for phase mask coronagraphs

Garima Singh

École Doctorale d'Astronomie & Astrophysique
d'Île-de-France

LESIA — Laboratoire d'Études Spatiales et d'Instrumentation en Astrophysique
Subaru Telescope — National Astronomical Observatory of Japan

THÈSE DE DOCTORAT

présentée pour obtenir le grade de

DOCTEUR DE L'OBSERVATOIRE DE PARIS

Spécialité Astronomie et Astrophysique, Mention Instrumentation

par

Garima Singh

Analyse et correction des aberrations de bas ordre pour les coronographes à masque de phase

Low-order wavefront control and calibration for phase mask coronagraphs

soutenue le 21 Septembre 2015

Composition du jury

Président	Didier Pelat	LUTH, Observatoire de Paris
Rapporteurs	Anand Sivaramakrishnan	STScI Baltimore
	M. Dimitri Mawet	California Institute of Technology
Examinateurs	David Mouillet	OSUG/IPAG Grenoble
	Maud Langlois-Moretto	Centre de recherche astrophysique de Lyon
Directeur de thèse	Olivier Guyon	Subaru Telescope
	Daniel Rouan	LESIA, Observatoire de Paris
	Pierre Baudoz	LESIA, Observatoire de Paris

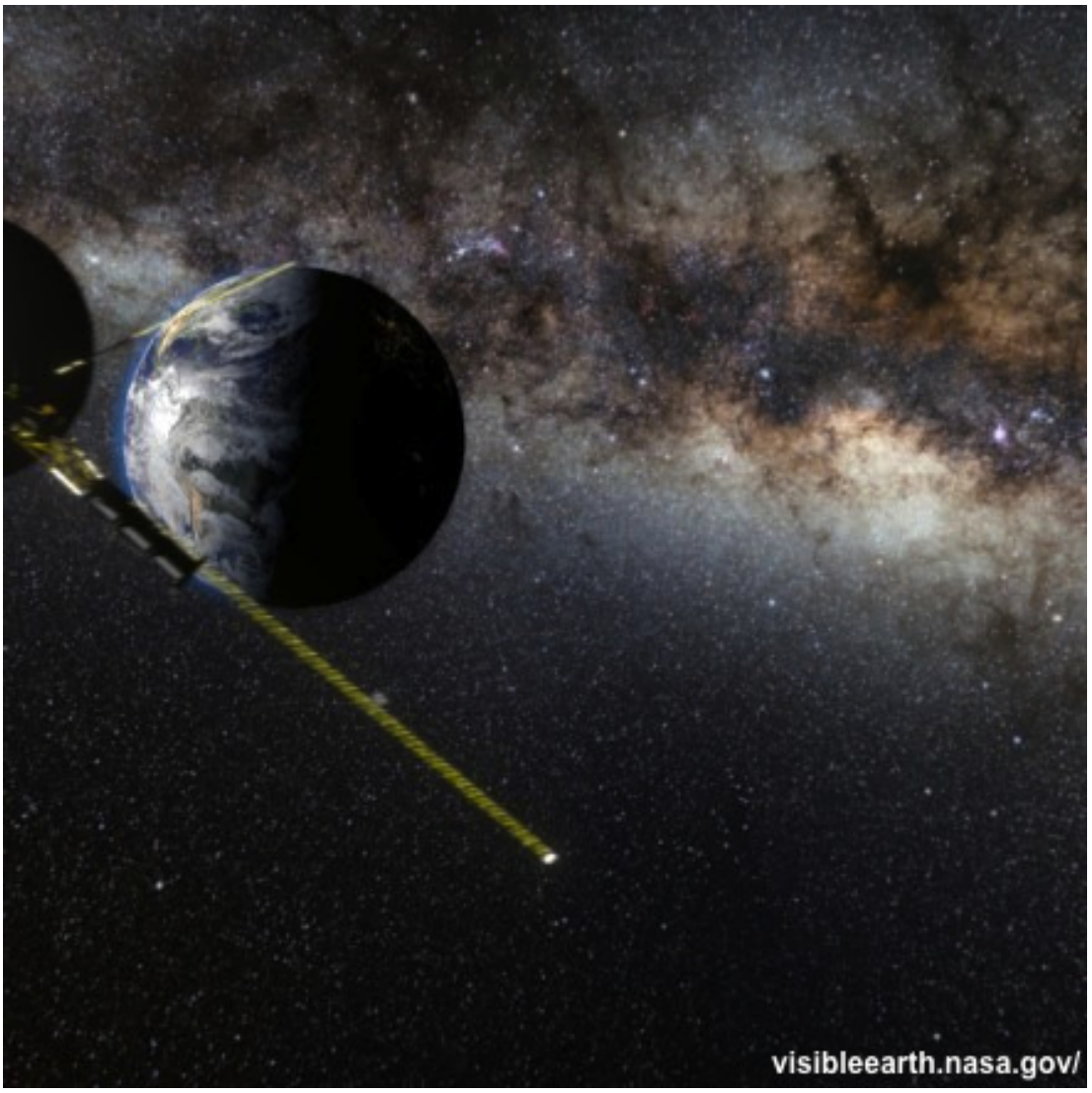

“When you look at the stars and the galaxy, you feel that you are not just from any particular piece of land, but from the solar system."

- Late Dr Kalpana Chawla
NASA Astronaut
STS-87, STS-107

Acknowledgement

My inspiration, source of strength and greatest support is my mother *Indu* (means *"Moon"*). Without her, I would not have been able to rise from a small town in India and reach the heights of Mauna Kea to accomplish my dream of studying the heaven. Without her perseverance, I would not have convinced my family to let me go out of course and follow my dreams passionately. Without her zest, I would not have found the courage to face the odds in the field. Without her constant push and motivation, I would not have finished my research on time. My father *Jeet* (means *"Victory"*), despite of being the negative force for the first few years of my academic career became the source of positivity and patience after my Masters. Without him, I would not have learnt to welcome the obstacles with a calm smile on my face. My younger brother *Rohit* (means *"first rays of the sun"*) always stood by my side in my tough times. He always made sure that I didn't feel weak and unconfident when I faced major obstacles in my journey. My parents and brother are the driving force of my life and I happily dedicate all of my life accomplishments to them.

I would like to thank *Claude Catala*, the *President* of the *Observatoire de Paris* for understanding my VISA issues and permitting me to defend outside of France, which was uncustomary for the Doctoral school in Paris. I admire the help of *Anand Sivaramakrishnan* for allowing me to use the facility of the *Space Telescope Science Institute* in *Baltimore* for my defense. Above all, I highly appreciate the efforts of all the Jury members of my PhD defense to make adjustments with their schedule and manage to fly to Baltimore to participate to my defense.

For the successful completion of my research, I would like to wholeheartedly thank the *Subaru Telescope* and staff to welcome me in the community and provide this wonderful opportunity of working at one of the best telescopes in the world. I am equally thankful to the telescope operators and the adaptive optics scientists and engineers including *Yutaka Hayano-san, Yosuke Minowa-san* and *Tomoyuki Kudo-san* for operating Subaru's AO system during SCExAO's observation nights, which has not only helped me to run my sensor on-sky but also taught me the functioning of a typical AO system.

I would like to convey my regards to my PhD advisors *Olivier Guyon* and *Pierre Baudoz* who have helped me to develop a thorough understanding of the high contrast imaging field. With them, I have learnt to work the problem in a rational way. *Pierre* made sure that we had two meetings every month and I was not stuck due to their absence. I am thankful to him for pushing me for the deadlines, managing all of the issues with French administration throughout my research and selecting/arranging Jury committee for my defense. *Olivier*, on the other hand, despite of traveling almost every month, taught me not only the basics of Exoplanets, coronagraphs and wavefront sensing but also helped me built my software skills. I admire his commitment and contribution in the field, calm-

ness and positivity under stressful situations and balanced approach with political issues. I would like to thank him for his support, motivation and encouragement in pushing me forward to achieve my long-term goals.

Frantz Martinache stayed with SCExAO till the end of first year of my research but he remained a great source of knowledge. He not only helped me built my skills in Python but also helped me to develop the theoretical understanding of the coronagraphic low-order wavefront sensing, which built the basic foundation of the concept I worked on. I would also like to thank *Christophe Clergeon*, a former student of SCExAO, who stayed in the team during first two years of my research. He helped me to understand the first few versions of the SCExAO bench. With him, I also had the opportunity to attend adaptive optics courses and spend hours discussing the problems in tutorials.

Nemanja Jovanovic or *Nemo*, self-proclaimed as *Captain Awesome* is SCExAO's lead Psotdoc, who really taught me *'How to get shit done in time! :)'*. On a serious note, I have always looked up to his managerial skills, actively taking lead and solving problems logically. I would like to thank him for eagerly teaching me these skills. Throughout my thesis, he has been a constant source of motivation and positive push towards setting shorter goals and achieving them in weekly/monthly basis. Under his supervision, I have learnt a lot about optics and astronomical instrumentation in general. He helped me built the skeleton of the sensor I worked on. Working with him at the summit was quite an experience sometimes but most of it has taught me how to remain calm and focused during the observation nights at the telescope. Be it a problem with work, tensions within team mates or with visitors, health problems and personal matters, I have always found him ready for help and advice.

Special thanks goes to *Julien Lozi*, friend and a mentor, who is a Senior Scientist of SCExAO *(ahmm ahmm . . . just a bad cough)*. Though he put me into troubles several times, but I am very much grateful to his endless efforts in making sure that my research paper, postdoc applications and thesis manuscript is well written and truly reflects the amount of exciting work I have performed. I can't thank him enough for his time in going through my documents several times and correcting all the grammatical mistakes. He has not only made me understand the relevant ways of processing the sensor telemetry but also helped me to get hold of vibration issues on the instrument. The results I present in chapter 4 & 5 are performed under his continuous supervision. His guidance has truly helped me to wrap up my work neatly during the third and last year of my PhD research.

My Hawaiian/American surrogate family *Uncle Dan Taylor* and *Toshi Aunty* deserve a very special praise. Homemade cookies and brownies, hours of discussion on different cultures and religions, celebrations during birthdays and christmas, outings on cultural events, wonderful homely meals and daring excursions to Halema'uma'u crater rim to get the glimpse of lava lake has hardly gave me a chance to miss my family in India. I was honored to have them around me during these past three years.

Last but not the least, I would like to thank all of my friends especially *Varsha, Sharmad, Abhijith, Anmol, Ankit, Madhav, Vinita, Pooja, Suman, Amit, Aniruddha, Manu, Gurpreet, Dipanjan, Danielle* and *Rieko* for always believing in me and motivating me to keep moving forward against all odds. The confidence I carry is the reflection of the proudness in the eyes of my friends and family.

Abstract

The direct detection of young and warm extrasolar giant planets in the habitable zone of nearby cool stars is one of the major goals of current ground-based high contrast imaging (HCI) instruments. To characterize such exoplanets by spectroscopy of their atmospheres requires isolating the planet light from the brighter stellar light, which is challenging due to high contrast at small angular separation. Using high performance small inner working angle (IWA) coronagraphs, it is possible to detect faint companions in the proximity of the stellar source. However, the uncontrolled pointing errors and other low-order wavefront aberrations degrade the rejection capability of these coronagraphs by leaking starlight around the coronagraphic focal plane mask. This additional unwanted light can prevent detection of a companion at small angular separation. How well these wavefront aberrations upstream of various coronagraphs can be controlled and calibrated is the focus of my thesis.

To prevent coronagraphic leaks at small IWA, I worked on a concept where within a coronagraph, the low-order wavefront aberrations are sensed at the Lyot plane. The starlight diffracted by the focal plane mask is reflected by the Lyot stop towards a detector, which reliably estimates low-order aberrations present in the wavefront. I called this new sensor a Lyot-based low-order wavefront sensor (LLOWFS). During the course of my thesis, I have designed, developed and programmed this sensor and implemented it on the Subaru Coronagraphic Extreme Adaptive Optics instrument at the Subaru Telescope. In this thesis, I present the principle of the LLOWFS and the very first simulation with a Four Quadrant Phase Mask (FQPM) coronagraph. I study the sensitivity of the Phase-Induced Amplitude Apodization (PIAA) coronagraph, the Vector Vortex Coronagraph (VVC), the FQPM and the Eight Octant Phase Mask coronagraphs to low-order wavefront aberrations. I present the measurement of low-order errors up to 35 Zernike modes for all the coronagraphs and using a 2000-actuator Deformable Mirror, I demonstrate a closed-loop pointing accuracy between $10^{-3}\lambda/D$ and $10^{-4}\lambda/D$ in H-band in the laboratory. On-sky, I demonstrate the low-order control of 10 Zernike modes for the PIAA and the VVC and demonstrated a closed-loop accuracy of $10^{-4}\lambda/D$ under good seeing and $10^{-3}\lambda/D$ under moderate seeing on a routine basis.

I present in this thesis the versatility of this new coronagraphic wavefront sensor by demonstrating its compatibility with different coronagraphs. Due to its simplicity in the design, the existing/planned ground-based HCI instruments can easily implement LLOWFS and control the low-order aberrations beyond pointing errors near the IWA of their coronagraphs. The next generation of space coronagraphs with a dedicated LLOWFS-like technology can also address the telescope pointing errors caused by the reaction wheels and thermal variations.

Résumé

La détection directe de jeunes et chaudes planètes extrasolaires géantes dans la zone habitable de naines rouges est l'un des principaux objectifs des instruments d'imagerie à haut contraste pour les télescopes au sol actuels. Pour caractériser l'atmosphère de ces exoplanètes par spectroscopie, il est nécessaire d'isoler la lumière planétaire de celle de son étoile, ce qui est difficile en raison du contraste élevé entre leurs luminosités ainsi que leur faible séparation angulaire. En utilisant un coronographe de haute performance pouvant observer très près de l'étoile, il est possible de détecter des compagnons de faible intensité près de la source stellaire. Cependant, les erreurs de pointage non contrôlées ainsi que les autres aberrations de bas ordre dégradent le contraste de ces coronographes causant des fuites stellaires autour du masque coronographique. Cette lumière indésirable peut empêcher la détection d'un compagnon à faible séparation angulaire. L'étalonnage et le contrôle de ces aberrations de front d'onde en amont de divers coronographes est l'objet de ma thèse.

Pour éviter les fuites stellaires à faible séparation angulaire, j'ai travaillé sur un concept où les aberrations de bas ordre sont détectées au niveau du plan de Lyot du coronographe. La lumière stellaire, diffractée par le masque en plan focal, est réfléchie par le masque de Lyot vers un détecteur, qui mesure précisément ces aberrations. J'ai appelé ce nouveau senseur un senseur d'aberrations de bas ordre dans le plan de Lyot (Lyot-based Low-Order Wavefront sensor ou LLOWFS en anglais). Au cours de ma thèse, j'ai mis en place et programmé ce senseur sur l'instrument d'optique adaptative extrême du télescope Subaru. Dans cette thèse, je présente le principe du LLOWFS et une première simulation avec un coronographe â quatre quadrants. J'ai ensuite étudié la sensibilité de différents coronographes aux aberrations de bas ordre : le Phase Induced Amplitude Apodization (PIAA) coronagraph, le Vector Vortex coronagraph (VVC), ainsi que les coronographes à quatre quadrants et à huit octants. Je présente la mesure des bas ordres en laboratoire jusqu'à 35 modes de Zernike pour ces coronographes, et l'aide d'un miroir dèformable muni de 2000 actionneurs, je démontre un résidu de pointage en boucle fermée entre $10^{-3}\lambda/D$ et $10^{-4}\lambda/D$ en bande H. Sur ciel derrière le télescope, je démontre la mesure de 10 modes de Zernike pour le coronographe PIAA et le VVC, ainsi qu'un résidu de pointage en boucle fermée de $10^{-4}\lambda/D$ dans de bonnes conditions de visibilité, et de $10^{-3}\lambda/D$ lorsque les conditions sont dégradées. Enfin, je présente dans cette thèse la polyvalence de ce nouveau senseur de front d'onde en démontrant sa compatibilité avec différents coronographes. En raison de sa simplicité dans sa mise en œuvre, les instruments à haut contraste existants ainsi que leurs successeurs peuvent facilement utiliser le LLOWFS pour mesurer et contrôller les aberrations de bas ordre au plus près de l'étoile. La prochaine génération de coronographes spatiaux peuvent également utiliser cette technologie pour contrôler les erreurs de pointage causées par la vibration des roues à réaction ainsi que par les variations thermiques du télescope.

Preface

"There are infinite worlds both like and unlike this world of ours . . . We must believe that in all worlds there are living creatures and planet and other things we see in this world."

- Epicurus (ca. 300 BCE)

"There are countless suns and countless earths all rotating round their suns in exactly the same way as the seven planets of our system . . . The countless worlds in the universe are no worse and no less inhabited than our earth."

- Giordano Bruno, 1584

"What a wonderful and amazing Scheme have we here of the magnificent Vastness of the Universe! So many Suns, so many Earths . . . !"

". . . I have often wonder'd that when I have view'd Venus . . . she always appeared to me all over equally lucid, that I can't say I observed so much as one Spot in her . . . is not all that Light we see reflected from an Atmosphere surrounding Venus?"

- Christianus Huygens, New Conjectures Concerning the Planetary Worlds, Their Inhabitants and Productions (c. 1670)

The beauty of new discoveries always lie in posing the right question. One of the most captivating question since centuries is still the same: *"Are we the only civilization existing in the immenseness of this Universe?"* The night sky full of billions and billions of stars has always made us wondered if God did play dice and made our existence as unique as it looks like? Does the pale blue dot as spotted by the famous *Voyager I* is the only blue spec of life in the vastness of the nothingness? Was it merely a coincidence that everything has fallen together at the right time at the right place and led to the creation of species that could breathe, feel and wonder? Are there other forms of civilization somewhere asking the same questions to themselves?

The two of the most influential figures in 20th century science fiction have stated:

"Two possibilities exist: either we are alone in the Universe or we are not. Both are equally terrifying."

- Arthur C. Clarke, 1966

"Extraterrestrial life is truly an idea whose time has come."

- Carl Sagan, in The Cosmic Connection (1973)

These most fascinating all-time quests have always guided the human beings to keep exploring the edge of the unknown. We are at a unique time in the history where we have giant telescopes equipped with advanced cutting edge technologies, which gives us the opportunity to search for other worlds like ours and possibly image them directly.

Scientists and researchers have always speculated that other planetary systems would be similar to our solar system, with inner rocky planets and outer gas giants. This conception was broken soon after the detection of the first planet around a main sequence star outside of our solar system. In 1995, *Mayor & Quéloz* discovered an exoplanet with a 0.5 Jupiter mass, which orbit its Sun-like star 51 Peg in a 4.2-day period! *This planet was seven times closer to its star than Mercury is to the Sun!* This breakthrough, together with 100 more has not only given rise to a new category of planets: *the Hot-Jupiters,* but also shaped our knowledge in understanding the formation and evolution of planetary worlds. This led to the birth of a new field, which is widely known as *"Exoplanet Detection"*. 20 years after the discovery of the first hot world, we know of more than 5000 exoplanets as of August 2015, out of which ~ 1800 are confirmed[1].

In modern Astronomical sciences, there are several techniques through which the discovery of exoplanets can be conducted, which are broadly classified into "Indirect" and "Direct" methods. Indirect methods rely on the planet's effect on measured starlight while the direct methods image the exoplanets directly in the vicinity of the parent star. Both methods complements each other: Indirect methods give information about the mass, radius and the orbital parameters of the exoplanets such as its semi-major axis, period and eccentricity whereas direct methods can reveal the temperature, chemical and biological activities of its atmosphere.

The direct detection methods are of great interest to me as the ability to directly image and obtain spectra of the atmosphere lying trillions of trillions miles away from Earth is very appealing. However, the process of obtaining direct images of another world poses two challenges: – (1) The star-planet angular separation requires giant telescopes to have high angular resolution and – (2) The high contrast between the star and its planet requires sophisticated technologies to suppress the bright halo of the star, to make the signal from the planet detectable..

Both problems are well acknowledged and solutions are developed or are under development. From the ground, 8 to 10-m telescopes with monolithic/segmented primary mirror are capable of resolving exoplanets lying at a distance from their star as close as Saturn is to the Sun (looking in infrared for stars at about 10 pc). To block the starlight inside the instrument, coronagraphs are being developed, allowing to reveal the surroundings of the star. However, the biggest problem from the ground is the earth atmosphere, which scatters some of the bright starlight into a wide halo within which exoplanet are searched. Thanks to adaptive optics, even the distortion of the starlight due to atmospheric turbulence is curable to some extent. But even after counteracting the effects of the atmospheric turbulence on the images, the leftover uncorrected residual light prevents detection of exoplanets, especially the ones that are close to their star. This not only requires even higher angular resolution telescopes but also newer technologies to compensate what adaptive optics cannot.

[1] http://exoplanets.org/

There is yet another solution to avoid the atmospheric turbulence. Equipping telescopes with direct detection technologies and launching them into space. However, this is not as easy as it sounds. First, the telescope diameter is limited by the current launching technologies, that does not allow to easily carry big telescopes (~3.5-m without deployment and ~10-m if optics can be unfold). Second, maintaining the steadiness of the telescope in space is very challenging, due to errors of the telescope pointing system and reaction wheels. The stability at the sub-nanometer level is required for direct imaging of reflected light by planets in the habitable zone.

Directly imaging an Earth-like exoplanet with 8 to 10-m class ground-based telescopes is currently not possible due to the limited angular resolution and the lack in the technology to fully compensate image distortions due to Earth atmosphere. However, with the development of newer technologies or the refinement of the existing one, it is possible to directly image young Jupiters and gas giants at a similar distance from their host star as Jupiter and other inward planets are to the Sun. There are two merits behind this study: – (1) gain in the understanding of what drives the evolution of planetary systems and – (2) gain in the maturity of the newer technologies. The experience of these technologies being tested and deployed on current telescopes will provide the foundation for future ground- and space-based telescopes.

"The only way to discover the limits of the possible is to go beyond them into the impossible".

- Arthur C. Clarke, "Technology and the Future"

The era of extremely large telescopes has already begun. The construction of the European Extremely Large Telescope (40 m) in the Atacama Desert of northern Chile and the Thirty Meter Telescope on the Big Island of Hawaii has already started. The time is not far when we will actually be able to point these giant eyes in the sky and directly image Earth-like planets in the habitable zone of cool stars.

With a similar goal in mind, I present a new technology that helps to control in real-time the residual that is left uncorrected by adaptive optics. This body of work has laid the groundwork of a new coronagraphic low-order wavefront sensor that is envisioned to provide a capability to the current/future ground and space-based observatories to help their coronagraphic technologies meet their full potential.

In the first chapter of this manuscript, I will briefly introduce different methods used to detect and characterize exoplanets, problems faced during their observation and techniques used frequently to counteract those problems. I will also explain the theory of coronagraphs and the advancement in their technology to gain access to the immediate surrounding of the stars. I will then introduce the problem I solved to improve the coronagraphic image quality. First, I will compare the existing solutions that are adapted by the current exoplanet imaging instruments. Then, I will focus on the limitations of these existing solution and finally I will propose a solution that will address these limitations.

In the second chapter, I will introduce the principle of this new coronagraphic sensor, the numerical simulations and results together with the first laboratory experiment I performed at *Laboratoire d'études spatiales et d'instrumentation en astrophysique* at

Observatoire de Paris-Meudon in June 2013.

In the same year, I had the opportunity to deploy my sensor on one of the most advanced exoplanet imaging instrument, the *Subaru Coronagraphic Extreme Adaptive Optics system (SCExAO)* installed on the *8-m Subaru Telescope*, situated at the summit of Mauna Kea on the Big Island of Hawaii. In chapter 3, I will describe the SCExAO instrument, its capabilities and its current status. I will also describe in detail the implementation of the new sensor on SCExAO. This chapter will also provide a glimpse of the simplicity and the flexibility of this sensor.

From August 2013 till April 2015, I had several opportunities to test the sensor in the laboratory and on sky. In chapter 4 & 5, I will explain the experiments I performed with different coronagraphs and the results I obtained under the simulated as well as the real atmospheric turbulence. These results have allowed me to characterize the behavior of each coronagraph I studied under realistic conditions. During the on-sky operations, I achieved the high level of stability in the coronagraphic images.

Table of Contents

List of Figures

List of Tables

Table 1: Acronyms of the institutions and the observatories.

CalTech	California Institute of Technology
ESA	European Space Agency
ESO	European Southern Observatory
GEPI	Galaxie — Étoile — Physique — Instrumentation
IAS	Institut d'Astrophysique Spatiale
JPL	Jet Propulsion Laboratory
LBTO	Large Binocular Telescope Observatory
LESIA	Laboratoire d'Études Spatiales et d'Instrumentation en Astrophysique
NAOJ	National Astronomical Observatory of Japan
NASA	National Aeronautics and Space Administration
OBSPM	Observatoire de Paris-Meudon
ONERA	Office National d'Études et de Recherches Aérospatiales

Table 2: Acronyms of the testbeds, instruments and projects.

EXCEDE	Exoplanetary Circumstellar Environments and Disk Explorer
FLAO	First Light Adaptive Optics
GPI	Gemini Planet Finder
HCIT	High-Contrast Imaging Testbed
HiCIAO	High Contrast Instrument for the Subaru Next Generation Adaptive Optics
KI	Keck Interferometer
KIN	Keck Interferometer Nuller
LBTI	Large Binocular Telescope Interferometer
MagAO	Magellan Adaptive Optics
Palomar WCS	Palomar Well-Corrected Subaperture
PHARO	Palomar High Angular Resolution Observer
NAOS	Nasmyth Adaptive Optics System
SAXO	SPHERE Adaptive optics for eXoplanet Observation
SCExAO	Subaru Coronagraphic Extreme Adaptive Optics
SPHERE	Spectro-Polarimetric High-contrast Exoplanet REsearch
VLTI	Very Large Telescope Interferometer

Table 3: Acronyms of the ground and space-based telescopes.

ACESat	Alpha Centauri Exoplanet Satellite
ELT	Extremely Large Telescope
E-ELT	European Extremely Large Telescope
Exo-C	Exoplanet direct imaging - Coronagraph probe mission
GMT	Giant Magellan Telescope
GTC	Gran Telescopio Canarias
HST	Hubble Space Telescope
JWST	James Webb Space Telescope
LBT	Large Binocular Telescope
TMT	Thirty Meter Telescope
VLT	Very Large Telescope
WFIRST-AFTA	Wide-Field Infrared Survey Telescope - Astrophysics Focused Telescope Assets

Table 4: Acronyms of the stellar coronagraphs.

AIC	Achromatic Interferometric Coronagraph
DPM	Disk Phase Mask
DZPM	Dual-Zone Phase Mask
EOPM	Eight Octant Phase Mask
FQPM	Four Quadrant Phase Mask
OVC	Optical Vortex Coronagraph
PIAA	Phase-Induced Amplitude Apodization
RAVC	Ring-Apodized Vortex Coronagraph
VVC	Vector Vortex Coronagraph

Table 5: Acronyms of the wavefront sensors.

CLOWFS	Coronagraphic Low-Order Wavefront Sensor
DTTS	Differential Tip-Tilt Sensor
LLOWFS	Lyot-based Low-Order Wavefront Sensor
PyWFS	Pyramid Wavefront Sensor
SHWFS	Shack Hartmann Wavefront Sensor

Table 6: Technical abbreviations.

ADI	Angular Differential Imaging
ADU	Analog to Digital Unit
APD	Avalanche PhotoDiode
AO	Adaptive Optics
ASM	Adaptive Secondary Mirror
AU	Astronomical Unit
AZ	Azimuth
CCD	Charge-Coupled Device
CHARIS	Coronagraphic High Angular Resolution Imaging Spectrograph
CPA	Classical Pupil Apodization
DM	Deformable Mirror
DPS	Differential Pointing System
EFC	Electric Field Conjugation
EL	Elevation
EMCCD	Electron-Multiplying CCD
EOPM	Eight Octant Phase Mask
ExAO	Extreme Adaptive Optics
FOV	Field Of View
FPM	Focal Plane Mask
FT	Fourier Transformation
FWHM	Full Width at Half Maximum
GUI	Graphical User Interface
H/W	Hardware
HCI	High Contrast Imaging
HgCdTe	Mercury Cadmium Telluride
HZ	Habitable Zone
IR	InfraRed
IWA	Inner Working Angle
LGS	Laser Guide Star
LOCI	Locally Optimized Combination of Images
LQG	Linear Quadratic Gaussian
MEMS	MicroElectroMechanical Systems
MKID	Microwave Kinetic Inductance Detector
MSVC	Multi-Stage Vortex Coronagraph
NGS	Natural Guide Star
NIR	Near InfraRed

NCPA	Non-Common Path Aberrations
NCP	Non-Common Path
OAP	Off-Axis Parabola
OPD	Optical Path Difference
PDI	Polarization Differential Imaging
PMC	Phase Mask Coronagraph
PSD	Power Spectral Density
PSF	Point Spread Function
RLS	Reflective Lyot Stop
RMS	Root Mean Square
SCC	Self Coherent Camera
SPS	Speckle Phase Sensing
SDC	Stellar Double Coronagraph
SDI	Spectral Differential Imaging
SN	Speckle Nulling
SNR	Signal to Noise Ratio
S/W	Software
SVD	Singular Value Decomposition
TCP/IP	Transmission Control Protocol/Internet Protocol
TRL	Technology Readiness Level
TTM	Tip-Tilt Modulator
ULTIMATE-SUBARU	Ultra-wide Laser Tomographic Imager and MOS with AO for Transcendent Exploration at SUBARU Telescope
WFS	WaveFront Sensor

Chapter 1

Exoplanets and their direct imaging techniques

"Nature is not unique to the visible world; we must have faith that in other regions of space there exist other earths, inhabited by other peoples and other animals."

On the Nature of Things (around 60 BCE),
Roman Philosopher, Titus Lucretius Carus

Contents

1.1 Exoplanets

The concept of life somewhere other than the Earth has amazed the human race since antiquity. Exoplanet (or extrasolar planet), by definition, is a planet that orbits a star other than our sun. A plain reason to find another possible world is because we live on one! Why not search other worlds like ours, study them and revolutionize our knowledge in understanding our place in the Universe?

When the discovery of a Jupiter-mass companion orbiting around a solar-type star by Mayor & Queloz (1995) hit the headlines in 1995, astronomers have immediately turned their telescopes towards the sky to search for more extrasolar worlds. Soon after that the speculations on the possibilities of the existence of another world took a shape of reality. Today, the field of *Exoplanet Detection* is one of the most dynamic research field of astronomy. As of August 2015, we know of ~ 1800 confirmed planets in a total of 1228 planetary systems and 486 multiple planet systems[1]

1.1.1 Overview of the discoveries

The first exoplanet discovered, 51 Pegasi b, has a mass of 0.5 times the mass of the Jupiter (M_{Jup}) and a 4.2 days orbit around the Sun-like star 51 Pegasi. This detection has not only introduced a new category of exoplanets, the *hot Jupiters*, but also has changed forever the straightforward theory of planets evolution we believed in, based on the standard models on the origin of our solar system. This detection was followed by many others since 1995 using various methods.

In Fig. 1.1, I present a collective census of the exoplanets discovered as of August 2015 by all the known detection techniques. Radial Velocity (RV) and transit methods are at the forefront of all the discoveries.

The RV method is based on the principle of the Doppler effect where the movement in the star's position provoked by a surrounding planet is measured using the shifts of the star's spectral features. The parameters that can be directly determined with the RV method are the period, eccentricity, longitude of periastron of the planetary orbit, and the velocity amplitude of the star. However, due to the unknown inclination of the planet's orbit, only a lower limit of the mass can be derived.

The first exoplanet 51 Pegasi b was discovered by the RV method using the spectrometer ELODIE (Baranne *et al.*, 1996) at the *Observatoire de Haute Provence, France.* ELODIE was the result of the first few efforts made in 1980s for the detection of exoplanets that could measure radial-velocity shifts as low as 7 m/s. Nowadays, with modern spectrometer, such as the HARPS (High Accuracy Radial Velocity Planet Searcher, Mayor *et al.*, 2003) spectrometer at the ESO 3.6-m telescope in La Silla Observatory, Chile, or the HIRES (Vogt *et al.*, 1994) spectrometer at the Keck telescope, RV variations down to 0.97 m/s can be detected.

After first few years of mostly RV detections, more and more planets were discovered using the transit method. It relies on the drop of the stellar flux when a planet passes in

[1] http://exoplanet.eu/

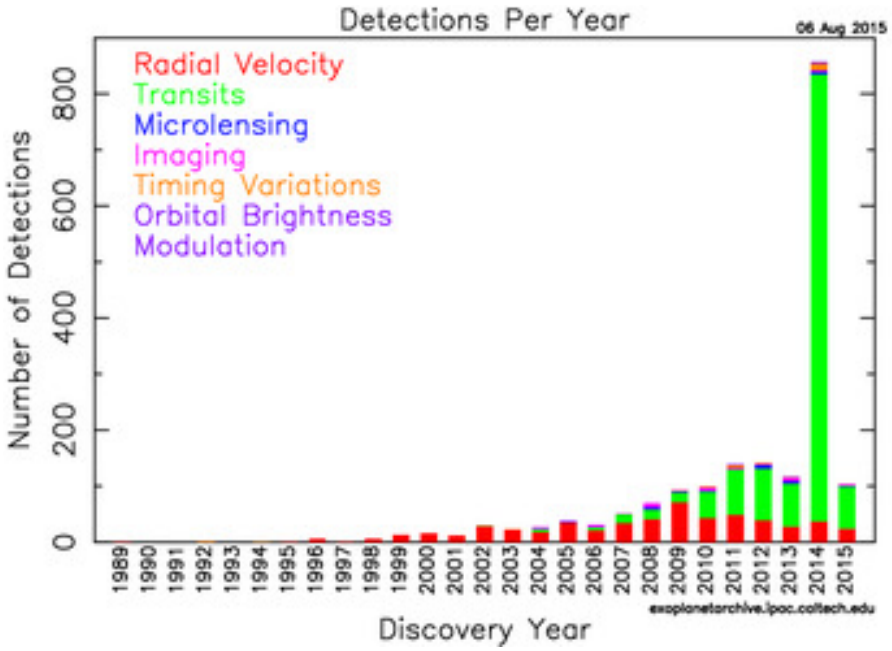

Figure 1.1: Total number of exoplanet discoveries made as of August 2015 by the different detection methods. Courtesy of http://exoplanetarchive.ipac.caltech.edu/exoplanetplots/

front of its host star. This happens only if the inclination of an extrasolar planet's orbit is very close to edge-on as viewed from Earth. With this method, in principle one can determine the radius, density, temperature, and even atmospheric composition of the planet (Cooper & Showman, 2006; Burrows *et al.*, 2008b,a; Showman, 2008). The first planet (called HD 209458 b) through transit photometry was observed in 1999 by Charbonneau *et al.* (2000). Satellites in space such as CoRoT (Appourchaux *et al.*, 2008) and Kepler (Borucki *et al.*, 2010) dedicated for transit surveys have performed the most successful discoveries of the transiting planets till today. Kepler is at the origin of a large percentage of the discoveries with 1030 exoplanets confirmed in July 2015 and 4696 planet candidates awaiting confirmations.

RV and transit methods are indirect methods to observe exoplanets. Other indirect methods also discovered a small number of planets over the years as can be seen in fig. 1.1. The only direct method called direct imaging, which looks for the photons from the planet instead of looking at its influence on the host star, has only discovered a handful of planets since 2004.

Figure 1.2 presents mass versus period of the exoplanets discovered by the different techniques. This figure shows that the exoplanets are abundant, of various masses and spread in orbits as small as < 0.01 AU to as large as 100 AU.

We also observe that each method explores a different part of the parameter space. The RV method found a majority of massive planets at large orbital periods, but also a few very close to their star like 51 Pegasi b. Complementing this, the transit method found exoplanets relatively closer to their host star. Both methods revealed small planets with small orbital periods. Direct imaging is exploring even further with very large orbital

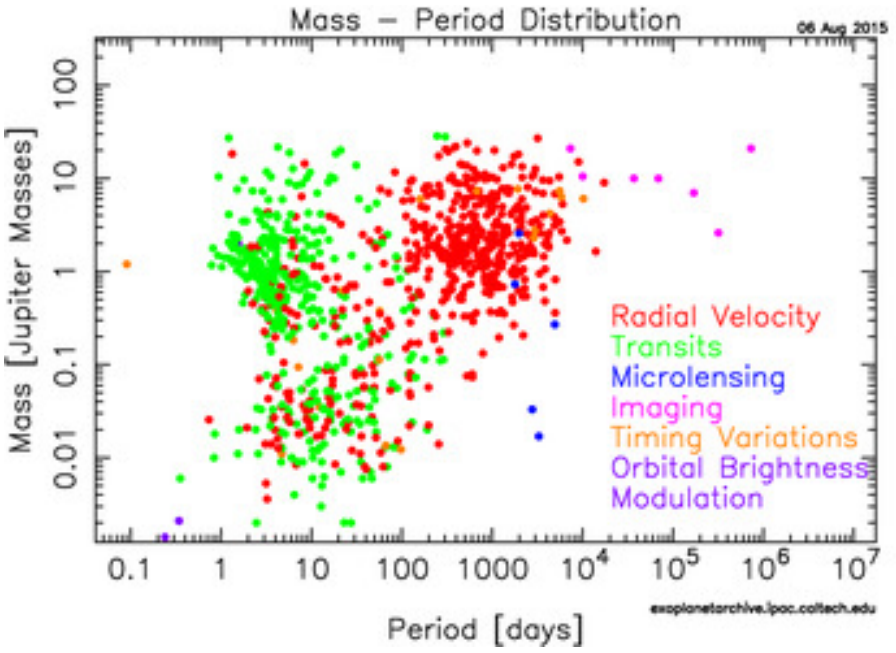

Figure 1.2: Mass versus period of the known exoplanets by detection method. Courtesy of http://exoplanetarchive.ipac.caltech.edu/exoplanetplots/

period but only observing Extrasolar Giant Planets (EGPs) and sometimes brown dwarfs Beuzit *et al.* (2007).

We also notice that, Fig. 1.2 does not show detections of planets similar to the Earth (0.3% M_{Jup} and orbital period of 365 days). This is not because these planets do not exist but because the current instruments are barely reaching that region. The different detections have an instrumental bias.

1.1.1.1 Variety of Exoplanets

Figure 1.2 shows a large variety of planets in mass and orbital period, but other parameters are also influencing the different types of planets, for ex. the planet diameter, the age of the extrasolar system, etc.

If we consider the radius, then the exoplanets smaller than 1.5 Earth radii are most likely rocky planets while exoplanets bigger than 2 Earth radii are probably all gaseous planets (Rogers, 2015). Planets with radii between 1.5 and 2 Earth radii are called Super-Earths, although most of them are probably small Neptunes. Also planets with masses one order of magnitude higher than M_{Jup} are susceptible to be brown dwarfs.

Planets that are very close to the star are extremely hot and tends to be rocky. The few giant planets discovered in that region are called hot Jupiters.

The planets detected by direct imaging are warmer than what is expected because of their large separation, indicating that these planets are young and still warm from their formation.

Another category is the free-floating planets, which are either failed stars, or planets ejected from their system by another body.

Merely finding exoplanets is not sufficient, the goal of their study is to answer fundamental questions:

- Are all exoplanets similar to the planets in our solar system?
- How common are exoplanets depending on the type of star?
- How do they form and evolve?
- What is the chemical composition of their atmospheres?
- Can they sustain liquid water on their surface?
- What is the morphology of the circumstellar disk and how is it linked with planet formation?
- Did life evolve on those planets? Can we find biological activities on these worlds?

Figure 1.3 shows a schematic diagram of the characterization of exoplanets (Madhusudhan *et al.*, 2014) indicating the principle parameters that are essential to interpret the atmospheric processes and internal structures of exoplanets. The study of all the parameters described in the figure is essential to answer these fundamental questions.

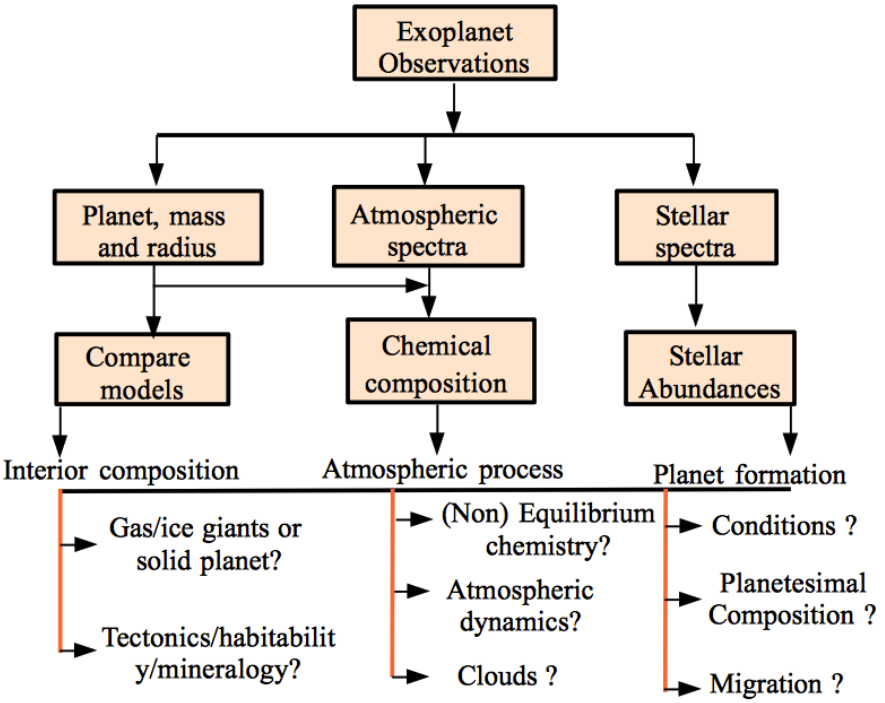

Figure 1.3: Possible parametric study of the exoplanets. The top two rows are the observables, which depends on the detection method. The remaining rows depends on the detection of the observable parameters.

The first few questions are already addressed by the RV and the transit surveys but to answer the rest of them, direct imaging is required. So the direct imaging techniques need improvement to search the parameter space explored by the indirect methods.

1.1.2 Towards the Habitable Zone

One of the ultimate goal of imaging exoplanets is to search for habitable planets and characterize them by spectroscopy of their atmospheres. This requires imaging companions in the Habitable Zone (HZ). The HZ is the region around the star where liquid water could be present on the planetary surface. As liquid water is essential to all life on Earth, we believe that it is the rule of thumb for any life to exist elsewhere. However, for a planet, apart from being at a right distance from the star, other factors such as atmospheric greenhouse gasses, oceanic circulation, internal energy sources (tidal heating etc.) are equally important to be considered. So based on these hypothesis, several definitions of the HZ are proposed by Kasting *et al.* (1993); Seager (2013); Kopparapu *et al.* (2013) .

Venus and Mars are planets similar to Earth in size and composition, so considering the last time Venus and Mars appeared to have liquid water on their surfaces, the empirical estimates on the limits of HZ for a Solar-type star is defined as:

- Inner Edge (recent-Venus): 0.75 AU
- Outer Edge (early-Mars): 1.77 AU, taking into account the evolution of solar luminosity with time (Kasting *et al.*, 1993).

Apart from the above assumptions, Kopparapu *et al.* (2013) also included Earth's climate and geological processes in the model of their HZ. To define the inner edge, they considered the photodissociation of water with subsequent hydrogen escape and for the outer edge, they took into account the maximum distance where the CO_2 greenhouse effect could maintain surface temperatures. Based on this, they defined:

- Inner edge (H_2O loss): 0.99 AU
- Outer edge (maximum greenhouse): 1.70 AU

These values depend on the spectral type of the host star. Note that the understanding of the HZ is an on-going research and these values are subjected to change depending on the new findings. For detailed discussions on the HZ, reader may refer to the literature – Hart (1978); Stevenson (1999); Meadows & Seager (2010); Zsom *et al.* (2013).

Kane & Gelino (2012) analyzed the census of confirmed giant planets within several ranges of circumstellar distances from their star that falls under the boundaries of the HZ, which they calculated using the methodology of Kopparapu *et al.* (2013, 2014). One such analysis is presented in Fig. 1.4. The planetary data they gathered is from various radial velocity surveys, the sources of which can be found in the same publication. Figure 1.4 (dark green) shows the optimistic population of inner/outer boundaries by using the "Recent Venus" and "Early Mars" criteria. These exciting findings indicates a good amount of planets currently believed to orbit their stars within the HZ.

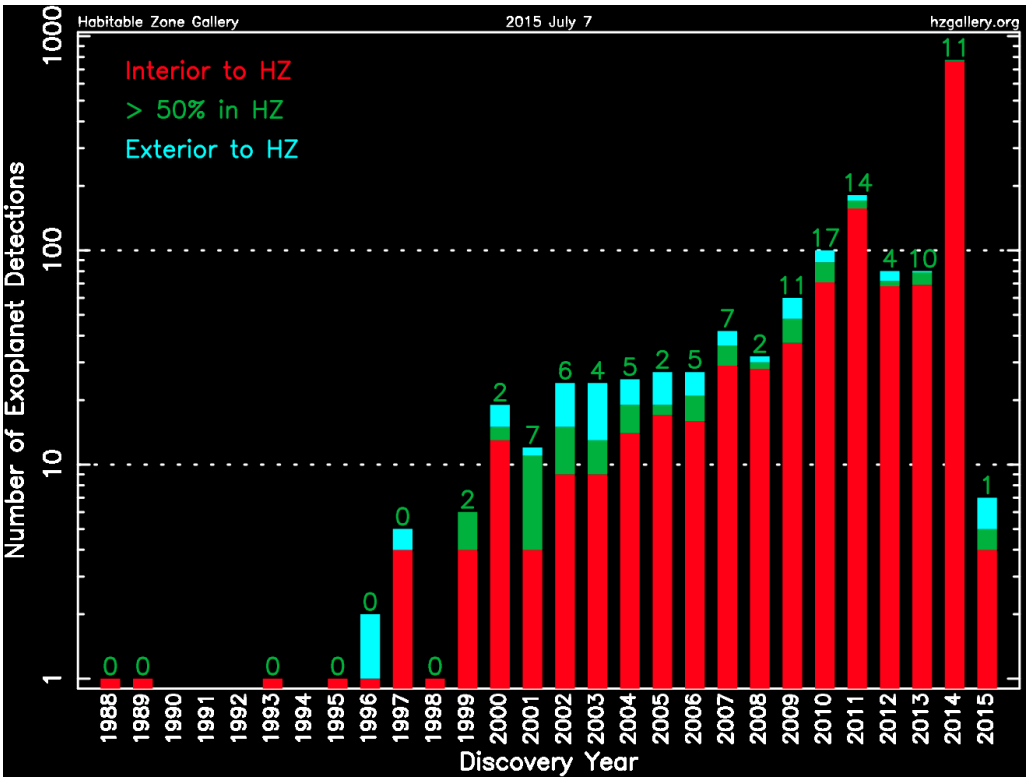

Figure 1.4: Histogram representing the census of confirmed giant planets via radial velocity method, showing the planets interior and exterior of the HZ. The calculation of the HZ is based on the models of Kopparapu *et al.* (2013, 2014). *Courtesy of* `http://www.hzgallery.org/`

Once again, a major contributor that provided evidences of planets in the HZ of their host stars is the *Kepler mission*. It is one of the most successful mission that gave us a vision on the possibility of Earth-like planets around Sun-like stars or even M-type stars beyond our solar system. The discovery of the first earth-radius planet orbiting within the HZ of a main sequence star (M1 dwarf), Kepler-186f (Quintana *et al.*, 2014) has changed our perspective. Other discoveries of Earth-like planets and Super-Earths with temperatures compatible with liquid water are summarized in Fig. 1.5 (green points).

With other findings, we also learnt that the occurrence rate of planets is higher around cooler stars (Howard *et al.*, 2012), with short period planets being roughly twice as common around M dwarfs as around G stars (Mulders *et al.*, 2015).

The most recent press release on 23rd July[2], the first near-Earth-size planet (60% larger than the Earth) in the HZ around a sun-like star has broaden our horizon. The new exoplanet *Kepler-452b* is the smallest planet discovered up to date that has found to be orbiting within the HZ of a G2-type star. This discovery has been confirmed with ground observations at the University of Texas at Austin's McDonald Observatory, the Fred Lawrence Whipple Observatory on Mt. Hopkins, Arizona, and the W. M. Keck Observatory atop Mauna Kea in Hawaii.

[2] `http://www.jpl.nasa.gov/news/news.php?feature=4665`

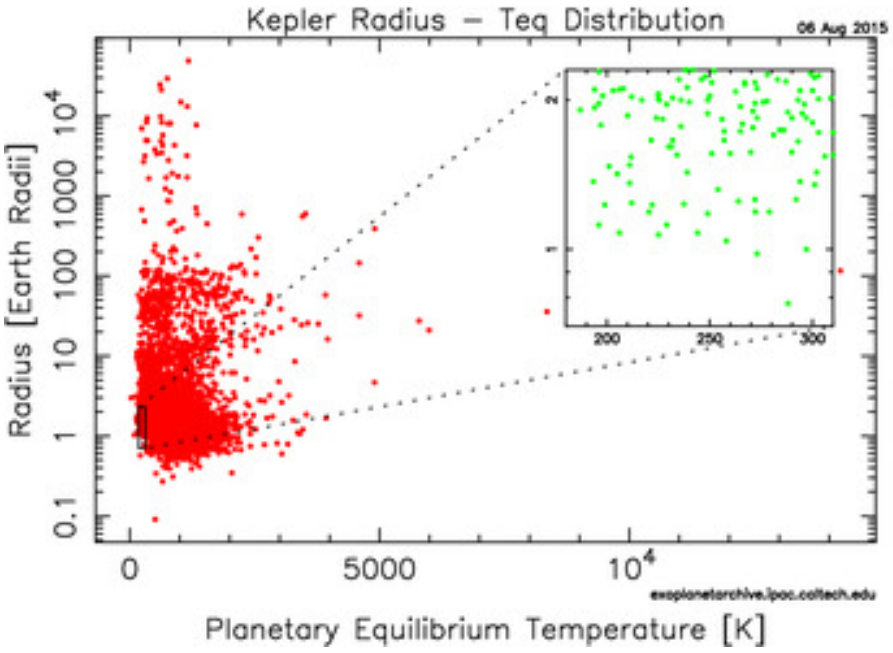

Figure 1.5: Radius versus planetary equilibrium temperature of Kepler's planet candidates. The green points are Earth-size planets and Super-Earths in the HZ. Courtesy of http://exoplanetarchive.ipac.caltech.edu/exoplanetplots/

Without a doubt, the success of the Kepler mission is a very positive result for direct imaging. Now that we know that planets are common in our galaxy, we have more chance to study them around nearby stars (10 - 25 pc). These explorations are helping us to better understand the technologies required from ground in order to directly capture the DNA of Earth-size planets, Super-Earths and EGPs in their HZ.

1.2 High Contrast Imaging

The discoveries of the different surveys presented in Fig. 1.2 show that the indirect methods are sensitive to exoplanets with relatively small orbital period, that typical corresponds to objects at a distance a few AUs from their star, especially around old, solar mass-type (G-K) stars. The results in Fig. 1.5 provide immense motivation for direct imaging because now we know that planets in the HZ exist and they are abundant. The ultimate goal is to spectrophotometrically characterize the terrestrial-like exoplanets in the HZ.

This extremely exciting goal, however, brings a lot of challenges for both current/planned ground and space-based telescopes. There are two main obstacles:

- The star-planet angular separation requiring high spatial resolution,
- The star-planet high contrast requiring capabilities to disentangle planet signal from seemingly bright stellar background.

Both issues have different implications for ground and space-based technologies.

Star-planet angular separation

For direct imaging, the angular separation between the star and its planet depends on factors such as orbital parameters and the stellar distance. Thanks to Kepler, we know that a large part of M-type stars have planets in their HZ. Directly imaging such planets from the ground requires giant telescopes of the order of 30-m or more (starting with an angular resolution of $\sim$ 10 mas in the near-Infrared). At present, we do not have enough angular resolution to look at the immediate surroundings of the stars because the current ground-based telescopes are of the order of 8 to 10-m only. However, the era of Extremely Large Telescopes (ELTs) has already started. The construction of European ELT (39 m, de Zeeuw *et al.*, 2014) in the Atacama Desert of northern Chile and the Thirty Meter Telescope (TMT, Schöck *et al.*, 2009) on the Big island of Hawaii has already begun. Guyon *et al.* (2012) and Crossfield (2013) show that imaging Super-Earths in short orbit around cooler star (M-type) will be possible with the ELTs.

On the contrary, to image a terrestrial-like exoplanet around Solar-type star from space, we need telescope diameters of only 2 to 4-m. The limit on the size of the space telescope is actually constrained (4-m diameter for non-deployable telescopes) by the current launching capabilities. The prospective of direct imaging of Earth-like planets from space are currently unclear but few ambitious direct imaging space missions are already planned for the near-future. I will briefly introduce these missions and their goals in §1.3.2.

Star-planet high contrast

Another obstacle is the overwhelming contrast between the star and its planet. For the detection of an Earth-like planet around a Sun-like star at a distance of 10 pc, the contrast requirement is 10^{-10} in the visible and for a Jupiter-Sun analog, the contrast required in the visible is of the order of 10^{-9} (Traub & Oppenheimer, 2010). Photons from planets can either be detected in the reflected light from the parent star (in the visible) or through its own thermal emission (in the infrared). The invention of coronagraphs addressed this problem by physically suppressing the starlight inside the instrument but this technology is still in its early stage. Achieving a raw contrast of the order of 10^{-7} to 10^{-8} at the 0.1 arcsec separation from the ground is still an unachievable feat. How efficiently a coronagraph suppresses the starlight in real-time is a function of several other external factors that affects its performance and are discussed in the next section.

The current ground instruments are not mature enough so they cannot overcome the listed obstacles. Therefore, direct imaging of Super-Earths in the HZ with the current capabilities is not possible. Figure 1.2 shows that direct imaging was used only to detect a handful of young and warm EGPs at angular separation > 10 AU. However, with careful selection of targets such as cooler star (M dwarfs) at 10-25 pc, detection of young EGPs in the HZ in the infrared is possible with new emerging high performance instruments discussed in §1.3.1. Beuzit *et al.* (2007) state some key scientific requirements driving the design of instruments which are as follows:

- Direct imaging instrument should be sensitive to wavelengths 0.6 to 2.5 μm. EGPs are dominated by CH_4 (below 1300 K) features in the J and H bands (Burrows *et al.*, 1997; Marley *et al.*, 1996).

- EGPs are believed to be roughly 15 magnitudes (10^6 ×) fainter than their host stars in the infrared. Instruments should be able to achieve the detection[3] contrast up to this level.
- Very high angular resolution: Access to angular separations as close as 40 mas in infrared is needed to resolve the region < 5 AU at a distance of 25 pc.
- Total field of view (FOV) extending to 2" to 4" in diameter: A FOV of 4" covers a region similar to the scale of our own solar system at a distance of around 10 pc.

Based on these goals, my research comprised of understanding the challenges faced during observations from the ground, analyzing the limitations of the current ground-based instruments and proposing a new technique that will increase the probability for current imaging instruments to directly image the EGPs at distances < 10 AU from their host star. First I will describe the theory of image formation in the telescope and then I will focus on describing the modules of HCI in the context of direct imaging with ground-based instruments only.

1.2.1 Image formation in a telescope

An astronomical object is studied from the ground by observing its two-dimensional projection on the celestial sphere. The light waves emitted or reflected by a stellar source propagates as an oscillating electric field. The emitted wavefronts are spherical in nature with the source at the center of the sphere. These spherical waves, when they reach the Earth, are treated as plane waves. The wavefront is defined as the surface over which the phase of the electric field is identical.

The telescope, which is an optical system, collects the part of the wavefront on the ground and changes its curvature to produce an image of the observed object on the detector at the focal plane. The intensity received by the detector is actually the integral of the energy emitted by the source along the line of sight. In this thesis, the light is considered as a dimensionless scalar quantity and hence the polarization phenomenon is not considered.

Now lets consider a telescope of diameter D pointing towards a monochromatic on-axis unresolved point source at infinity. Under the ideal case of no phase aberrations, the complex amplitude $\psi'_{E,\lambda}$ of the electromagnetic field E in the first pupil plane, which is being observed at wavelength λ can be written as

$$\psi'_{E,\lambda}(\vec{\xi}, t) = P(\vec{\xi})\, \psi_{0,\lambda}\ , \tag{1.1}$$

where P is the function that defines the shape of the telescope pupil, $\vec{\xi}$ is the vectorial coordinate inside the pupil plane at instant t and $\psi_{0,\lambda}$ is the mean amplitude of the field observed at wavelength λ over the pupil P. I will not consider the dependence of the flux $\psi_{0,\lambda}$ on λ (no absorption or emission lines in the spectra of the observed object), therefore in my simulations I will consider the average flux ψ_0 integrated on the detector within the

[3] contrast obtained after post-processing.

spectral band studied. The shape of the telescope pupil is considered as circular in this first description and its function P is defined as

$$P(\vec{\xi}) = \begin{cases} 1 & \text{if } \rho < D/2 \\ 0 & \text{otherwise .} \end{cases}$$

I will denote the vectorial coordinates in the image plane by $\vec{x}$. To simplify the equations, I will drop the vectorial symbol and $\vec{\xi}$, $\vec{x}$ should be read as ξ, x.

Light rays when passing through the pupil P gets (dispersed) diffracted around its edge. At the focal plane, the light waves interfere and produce a diffraction pattern with peak intensities where the amplitude of the light waves add. In the absence of aberrations, a pattern of energy distribution consisting of the bright central disc surrounded by rapidly fainting concentric rings is formed. The 2-D diffraction pattern is known as the "Airy disk" whereas the mathematical description of this focused cone of energy is known as the Point Spread Function (PSF). The PSF, also called as the impulse response of the system, is actually the shape of a point source as imaged by the telescope, which finally sets the limit to image contrast and resolution. Its form depends on the function of the pupil and the wavelength at which the source is observed. For an unobstructed pupil, the first zero of this Airy Function from its center occurs at $1.22\ \lambda/D$.

The image of a point source can be written as the square modulus of the Fourier transform of the pupil function

$$PSF(x, \lambda) = |\mathcal{F}[P(\xi)]|^2 \ . \tag{1.2}$$

For each wavelength, the image $I_*(x)$ of a point source on the detector is the convolution $(*)$ of the incident intensity of an object O_* with the PSF of the telescope

$$I_*(x, \lambda) = O_* * PSF(x, \lambda) \ . \tag{1.3}$$

If there is an off-axis companion O_C at a distance of $x^{'}$ from the object O_*, then the total intensity will be

$$I = (O_* + O_C) * PSF = I_* + I_C \ , \tag{1.4}$$

where I_C is the intensity of the companion.

Imaging under the effects of Earth's atmosphere

In realistic conditions, the wavefront from a point source is deformed by the Earth's atmosphere. The wavefront is subject to absorption, scattering and refractive index fluctuations of the air due to variations in temperature, pressure and humidity in the different layers of the atmosphere. These inhomogeneities are generally caused by convection cells, wind shear, and other hydrodynamics instabilities in the air above the telescope.

The effect of the turbulence on the wavefront are generally described by a Kolmogorov model (Kolmogorov, 1991). Variations in the optical refractive index induce phase fluctuations, or delay, across the parallel-plane wavefront that passes through the atmosphere. Figure 1.6 (a) represents phase delays of the plane wavefront. Each highlighted circle represents a region with a higher (blue) or lower (red) index of refraction than the average air at that layer. The diameter corresponds to the size of the inhomogeneity.

When the wavefront of the astronomical source crosses the atmosphere and encounters these inhomogeneities, three main distortion occurs (Fig. 1.6 (b)) – (1) Scintillation: variations in brightness, which corresponds to the spreading or concentration of the wavefront energy. (2) Agitation: variation in the angle of the mean tangent plane to the wavefront. (3) Smearing: broadening of the image due to loss of spatial coherence at the pupil.

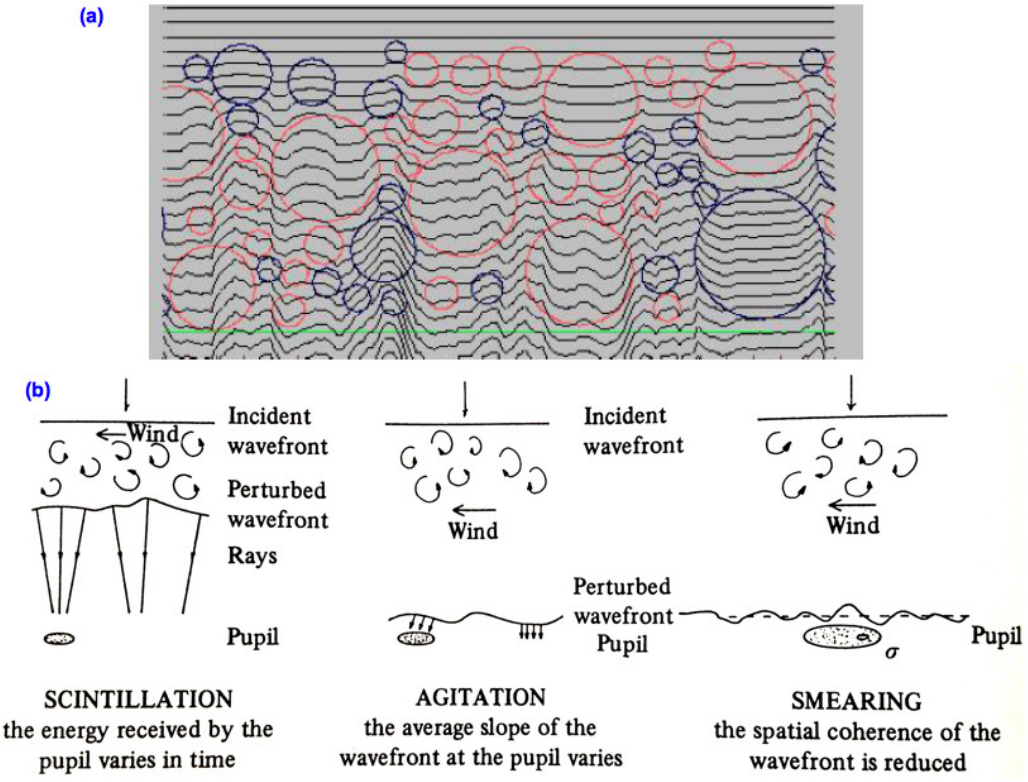

Figure 1.6: Effects of atmospheric turbulence on the images. (a) Incident plane waves when enters the turbulent region of the atmosphere get perturbed. *Courtesy of Roddier (2004)* (b) Three type of distortions encountered by the wavefront while crossing the turbulent atmosphere *(Lena, 1988)*

Considering $a(\xi, t)$ as the amplitude variations and $\phi(\xi, t)$ as the phase aberrations induced at the position ξ in the entrance pupil plane at instant t respectively, the complex amplitude in equation 1.1 of the monochromatic electromagnetic field at the telescope pupil under the turbulence can then be written as

$$\psi'_{E,\lambda}(\xi, t) = \psi_{0,\lambda}\, P(\xi)\, a(\xi, t)\, exp(i\phi(\xi, t)) \,. \tag{1.5}$$

To estimate the turbulence level, the Fried parameter (Fried, 1978), r_0 (usually expressed in centimeters) is used which represents the typical size of these turbulent cells, and corresponds to the strength of the turbulence. r_0, also called the coherence length of the turbulence, scales as $\lambda^{\frac{6}{5}}$ and represents the strength of the atmospheric turbulence. For most astronomical sites, its typical values lies between 10 and 20 cm in the visible.

Figure 1.7 (a) shows an ideal PSF of the circular aperture under no aberration. A core of diameter at 2.44 λ/D is visible as well as diffraction rings around it. If small aberrations

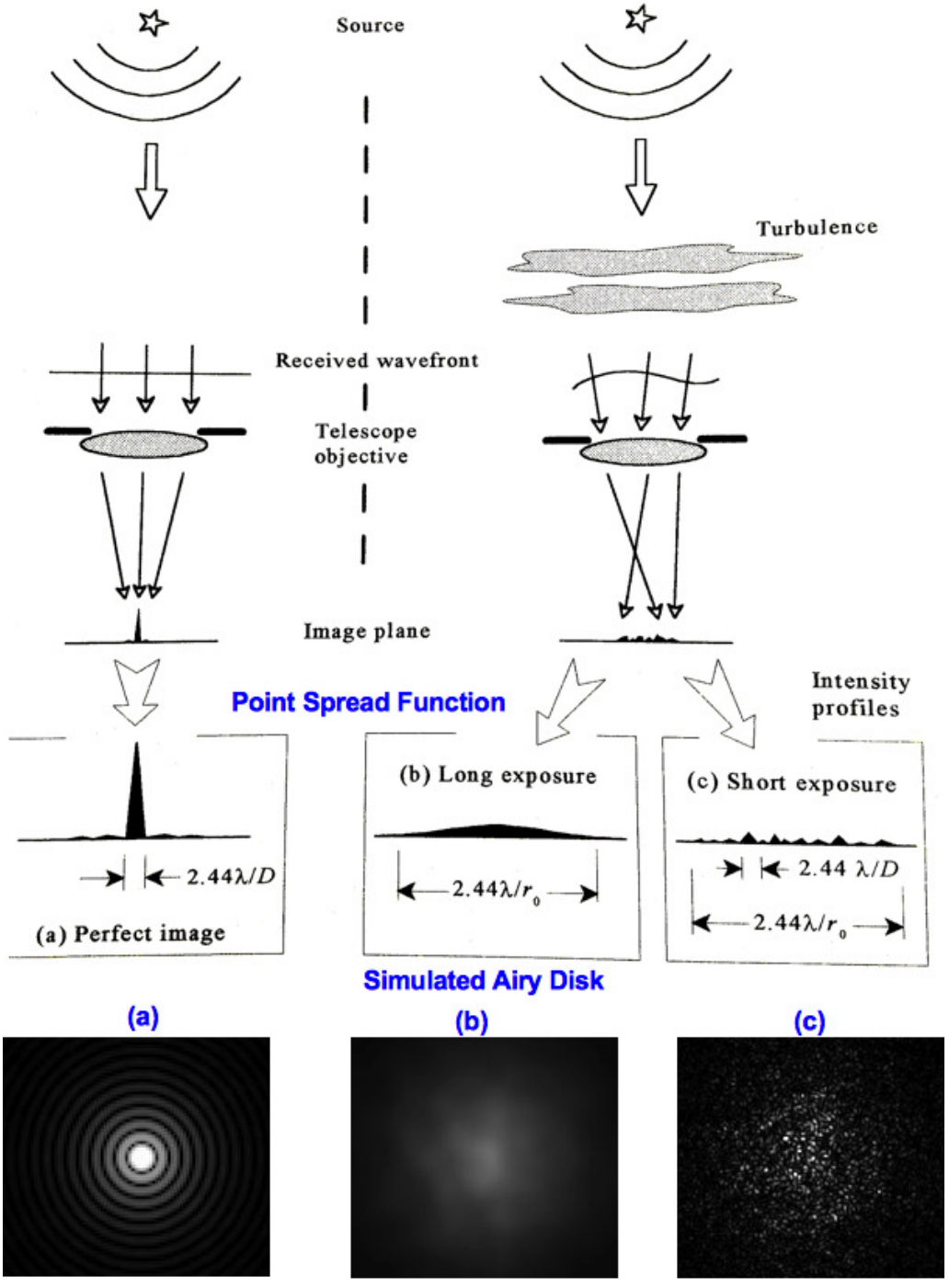

Figure 1.7: (a) Diffraction-limited and, (b)(c) Seeing-limited point spread functions of a circular pupil (Hardy, 1998). I also show the corresponding intensities I simulated after introducing an aberration of ~ 0.8 radian RMS at the entrance pupil to mimic the realistic condition of turbulence. (b) is the average of 100 frames to simulate the long-exposure.

are introduced in the wavefront, the core can still be visible but instead of the rings, it is surrounded by a speckle pattern. As long as the core stays above the speckle noise, the PSF is said to be diffraction-limited.

In the case of turbulence, for any diameter D above r_0, the phase perturbation due to atmosphere (usually over 2 radian RMS) will limit the image resolution of the telescope Hardy (1998). If the exposure time of the sensor is short, the image is just composed of speckles as shown in Fig. 1.7 (c). Those speckles are evolving very fast on the order of a milli-arcsecond, so when the sensor is using a long exposure as shown in Fig. 1.7 (b), the speckles are averaged and the image is just large patch of light. So, for $D > r_0$, the diameter of this patch is now 2.44 λ/r_0 and the PSF is called "seeing-limited". The astronomical seeing for a fixed λ, is the dominating parameter that finally sets the quality of the image during observations. At Maunakea, the average seeing in visible is 0.7 arcsec.

Criteria of a good image

I will now briefly emphasize on the factors characterizing the quality of a PSF. These metrics are used to define how much the degraded PSF differs from its theoretical shape. I will adapt these qualities in characterizing the performance of the imaging system throughout the thesis.

- **Full Width at Half Maximum (FWHM)**

  As the name suggests, FWHM is the width of an imaged object between two points where the surface brightness of the PSF is half of its maximum. FWHM characterize then the spatial resolution of the imaging system. Under ideal condition, the spread of star's light on an image is the diffraction-limited airy disk, the FWHM of which is approximately equal to λ/D.

- **Strehl ratio**

  Let us compare Fig. 1.7 (a), which represents a diffraction-limited core in the absence of the atmospheric turbulence with Fig. 1.7 (b), which is a seeing limited core under the simulated turbulence of ~ 0.8 radian RMS. It can be seen clearly in Fig. 1.7 (b) that the wavefront aberration diffracts the starlight away from the center, thereby reducing the peak intensity at its core. A widely used metric known as Strehl ratio (SR) is used frequently to account for the reduction in the peak surface brightness of the PSF. SR is the ratio of the actual peak intensity to the theoretical intensity expected from an optical imaging system

$$SR = \frac{max\,(PSF_{aberrated})}{max\,(PSF_{theoritical})}\,. \tag{1.6}$$

  Another way to evaluate the performance of the system is to express the SR statistically. According to the Marechal approximation, in the presence of small aberration (< 2 radian RMS), the SR can be expressed as

$$SR = exp(-\sigma^2)\,, \tag{1.7}$$

  where σ^2 is the variance of the wavefront error.

- **Encircled energy** This characteristic is used to study the distribution of the light in the PSF halo for the photometry. It is the measure of the flux integrated inside a disk of radius r normalized by the total flux in the image. This method of studying the radial distribution of the energy quantifies how much light is in the halo.

  I will use these metrics frequently in order to evaluate the performance of the optical imaging system I have worked on.

1.2.2 High Contrast Imaging theory in a nutshell

I have defined how an image of an astronomical object is formed in a telescope and also demonstrated in Fig. 1.7 how the quality of this image is affected by the Earth's atmosphere. So in the context of imaging exoplanets, the HCI plays a very important role. From ground, HCI has three golden rules: Correct, Cancel and Calibrate. Figure 1.8 illustrates this concept in a sequential manner.

Considering a star-planet system, when the combined light enters the Earth, it gets perturbed by the atmosphere and the optics of the telescope. When this distorted wavefront reaches the final focal plane on the detector of the telescope, we actually see a big blur of light, which is spread all over the FOV. I will refer to this tangled intensity of star and planet as $I_{Aberrated}$.

To separate the planet light from the starlight is a challenging process, that requires the following steps presented in Fig. 1.8. Below I describe the state of the art in HCI:

Wavefront correction by Adaptive Optics (AO): The AO system is the backbone of all the existing HCI instruments on the ground. This technology removes most of the wavefront errors induced by the atmospheric turbulence. It corrects in real-time the dynamic aberrations of the wavefront that limit the angular resolution of the telescope and dramatically improves the quality of the image. With a perfect AO correction, the image confine the stellar and planet light in to two separate coherent patterns, where all the light is concentrated at the core of the respective PSFs. However in reality, it is difficult to obtain a sharp image as the correction is not perfect. There is always uncorrected residual speckle field left behind in the image.

Speckle noise arises from random intensity pattern which are not only generated due to rapid atmospheric fluctuations evolving on time scales of the order of 1 to 10 ms but also due to instrumental imperfections, which on the contrary evolves at comparatively longer time scales.

I will refer to the AO corrected image as $I_{Corrected}$. The principle of AO is described in §1.2.3.

Cancellation of stellar light by Coronagraphs: The $I_{Corrected}$ is a combined image of the stellar PSF core, some speckle residuals, and the planet PSF invisible in the speckle halo. To reveal the surroundings of the star, the next step is to physically block the coherent stellar light inside the instrument, which is done by placing an opaque/phase mask at the first focal plane. Some coronagraphs also suppresses the static effects of the diffraction

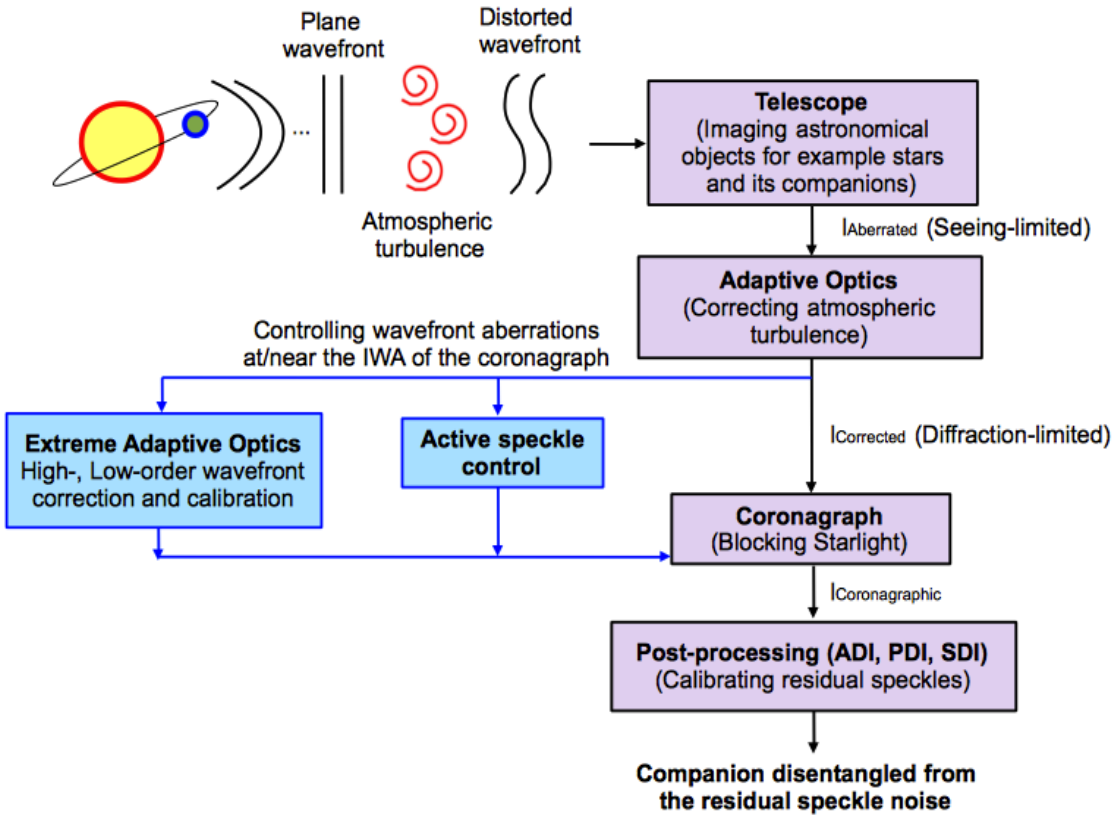

Figure 1.8: Block diagram representing different modules of High Contrast Imaging performed from the ground.

before blocking the starlight through an apodization of the pupil..

However, even after rejecting the starlight, it is hard to detect the faint signal from the planet. Ultimately, it gets buried beneath the speckle noise left by an imperfect correction. How efficiently the starlight is nulled depends on the quality of the correction provided by an upstream AO system. I will call the final intensity after starlight null as $I_{Coronagraphic}$, which contain photons from planet hidden behind the speckle noise.

The concept of coronagraphy is discussed in detail in §1.2.5.

Nowadays, most lot of astronomical imaging is performed with the help of an AO system. However, for exoplanet imaging, it is very crucial to have a very efficient AO sysetm. We will see in §1.3.1 (Fig. 1.19) that some AO systems are capable of providing the finest correction (achieving $\sim$ 90% of Strehl in H-band) and does not necessarily require a second level of correction. However, for other AO systems (that performs partial correction and provides a typical Strehl between 30-40% in H-band (§1.3.1.3)), additional correction of the high- and low-order residuals is mandatory. *Typically, an AO system that provides Strehl > 90% is called an Extreme Adaptive Optics (ExAO) system, which is capable of performing direct imaging at/near the inner working angle (IWA, defined in §1.2.5.2)) of the coronagraph.*

In addition, to achieve high contrast in the surroundings of the nulled PSF of the star,

HCI instrument can add an active speckle suppression algorithm to clear off the halo in the region of interest.

The wavefront control techniques are briefly discussed in §1.2.4.

Calibrating speckles: Correction, cancellation and speckle suppression steps of the HCI are performed in real-time, however, calibration of speckles is a post-processing method.

Speckle calibration can be an alternative solution to speckle suppression, which aims to disentangle the stellar speckles from the planet signal in the final corrected star nulled image ($I_{Coronagraphic}$). This procedure includes various methods to distinguish an artifact from a planetary signal. Based on a priori information for example spectral, polarization signal and incoherence between speckle halo and planet signal, the residual speckle field can be calibrated out.

The speckle calibration techniques are introduced in §1.2.6.

1.2.3 Adaptive Optics

In early 1950s, *Horace Babcock* (Babcock, 1953) proposed a concept of compensating the astronomical seeing. His idea was researched by the U.S. military to track satellites, and was used by astronomers to counteract the effects of the turbulnece starting in the mid-80s (Rousset *et al.*, 1990; Golimowski *et al.*, 1992; Angel, 1994; Hardy, 1998).

Figure 1.9 presents the principle of an AO system in the context of Astronomy. There are four essential elements in an AO system that works in conjunction in real-time: (1) A Wave Front Sensor (WFS) to measure the aberrations in the wavefront (temporally and spatially), (2) A control system to calculate the correction corresponding to the aberration measured by the WFS and then compute the control commands to send to the wavefront corrector, (3) A Deformable Mirror (DM, a wavefront corrector), to apply corrections in to the system to compensate the wavefront aberrations and (4) a high resolution camera to track the quality of the PSF.

The beam from an astronomical source is usually separated by a beamsplitter and directed towards the two dedicated path. One is towards the wavefront sensor for sensing and another one is towards the science detector for imaging. Because the sensing and imaging paths are different, the optics in the science path are not seen by the WFS, which causes Non-Common-Path (NCP) errors in the system. Also in AO systems, sensing and imaging wavelength are usually different, which creates chromaticity problems as wavefront errors are slightly wavelength dependent.

AO systems aim to compensate for phase fluctuations across the telescope pupil to achieve diffraction-limited resolution. In Fig. 1.9, an example of PSFs of a binary system is presented. With AO off, the light from the star and its companion is mingled and looks like a fuzzy blob of light. However, when the AO loop is on, the light corresponding to both objects are concentrated at the core of their respective PSFs and both objects are distinguishable. The quality of the AO correction is then evaluated on the basis of the SR.

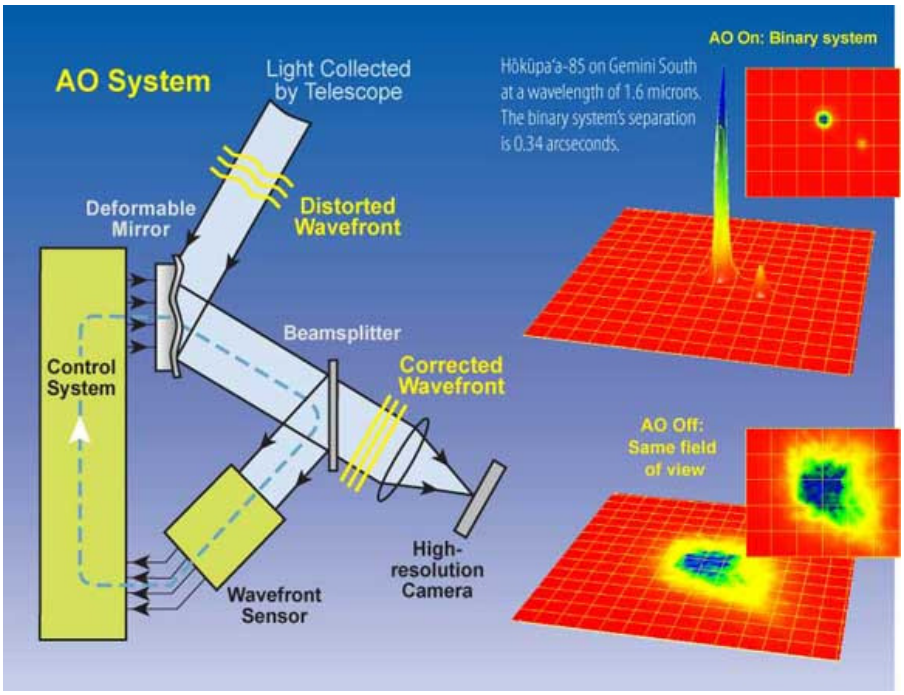

Figure 1.9: Principle of an adaptive optics system with a realistic observation of a binary system.

1.2.4 Wavefront control techniques for HCI

There are several WFSs that are used by the AO/ExAO systems. I will introduce the concept of two such sensors briefly and will discuss the importance for their selection in HCI.

- Shack-Hartmann WFS (SHWFS, Shack, 1971)

  SHWFS is a commonly used WFS in AO because of its simplicity. It consists of a microlens array (Fig. 1.10 (a)) in a re-imaged pupil plane, optically conjugated with the entrance pupil of the telescope. Each of these lenslet forms an image of the star onto a position sensitive detector, for example multiple quad cells or a single CCD. The position of each spot on the detector varies as the function of deformations in the wavefront. A local tilt in the wavefront will produce a shift in the star image. So based on the pupil plane measurement of local wavefront slopes (the first derivative of the wavefront) within a subaperture defined by the lenslet array, SHWFS patches together the slopes information and reconstructs the wavefront.

  SHWFS performance is limited by:

  - The aliasing effect because it uses a finite number of spatial sensing cells in the pupil plane. To deal with this effect, an increase of spatial sampling in the pupil plane (small subapertures) is possible but increases the measurement errors on the low-order modes due to photon-noise.
  - The size of subapertures. If the subapertures are seeing-limited, the contrast at small angular separation is independent of the number of subapertures and

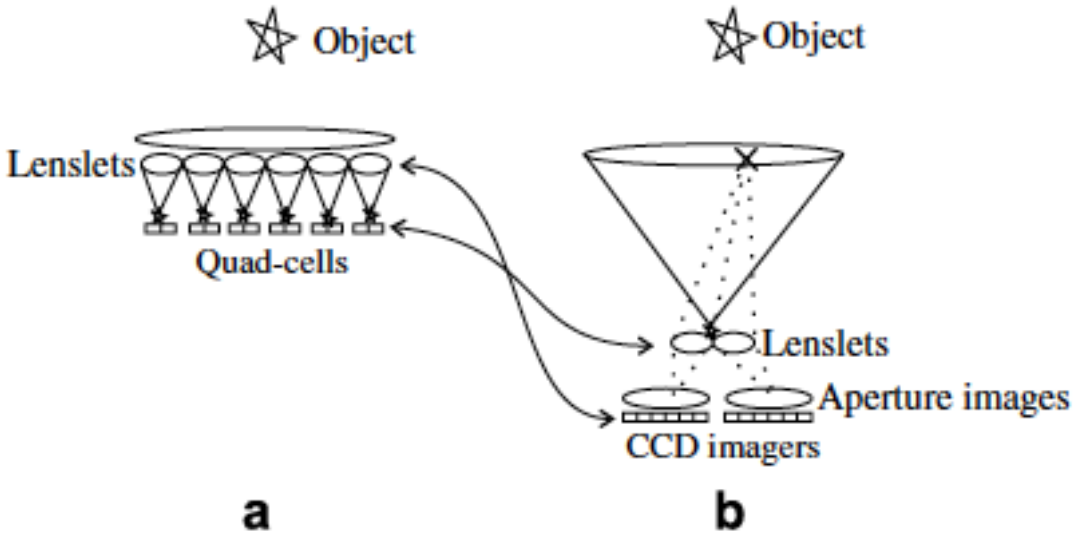

Figure 1.10: Principle of (a) the SHWFS and (b) the PyWFS (Chew *et al.*, 2006).

is limited by the quality of the wavefront correction. Whereas if the subapertures are diffraction-limited, then diffraction by each subaperture increases the subaperture's focal plane spot size and therefore reduces the sensitivity of the wavefront sensor. It is difficult to optimize contrast over wide range of separations for SHWFS (Guyon, 2005).

Nonetheless, the SHWFS is a widely used WFS in several observatories such as the Very Large Telescope (§1.3.1.1), the Palomar (§1.3.1.2) and the Gemini South (§1.3.1.1).

- Pyramid wavefront sensor (PyWFS, Ragazzoni, 1996; Esposito & Riccardi, 2001)

  The PyWFS splits the focal plane in four quadrants, which are imaged by a relay optics onto the pupil plane, producing four images of the pupil. At the focal plane, either a lenslet array (Fig. 1.10 (b)) or a pyramid optics is used to divide its plane. The wavefront aberrations are then analyzed at the pupil plane. The intensity distribution in the images of the aperture are used for estimating the phase of the wavefront.

  The PyWFS can be operated in two ways: – (1) Fixed pyramid position, where the core of the PSF is fixed at the apex of the pyramid optics and – (2) A modulated version of the fixed PyWFS, in which the focal plane point is deliberately moved in a circle (with modulation radius r) at the apex of the pyramid optics so that all the four pupil are more or less illuminated. Thus, the intensity distribution integrated over a couple of modulations also measures wavefront slopes in the pupil. r determines the sensitivity and the dynamic range of the PyWFS, which therefore offers the flexibility to adjust the modulation amplitude and hence the sensitivity of the sensor to the observing conditions. Modulating PyWFS provides better range than the non-modulated (fixed) PyWFS.

The PyWFS is used routinely at the Large Binocular Telescope (LBT, §1.3.1.4) and the Magellan Adaptive Optics (MagAO, §1.3.1.5).

The SHWFS is a slope-based WFS while the PyWFS is a phase-type sensor. The PyWFS holds the advantage of providing better sensitivity to the overall wavefront. The experimental performance comparison between the two sensors can be found in the articles Vérinaud *et al.* (2005); Chew *et al.* (2006).

Other widely used sensors include: – (1) The Curvature WFS (Roddier, 1988) , which introduces a spherical phase aberration into the focal plane and then transforms phase aberrations into light intensity modulations in the pupil plane. – (2) The Focal plane WFS (FPWFS), which is a non-linear reconstruction algorithm that allows good sensitivity and large range. In FPWFS, the amplitude and phase of focal plane speckles are measured directly by inducing interferences between the focal plane complex amplitude and a set of known references (Angel, 2003).

For direct imaging purposes, it is desirable to choose a coronagraph which can provide access to the surroundings of the star as close as a few λ/D. I will explain in §1.4 that these types of coronagraphs are extremely sensitive to errors uncorrected by the AO/ExAO systems, especially tip-tilt and other low-order wavefront aberrations and often requires a separate dedicated sensor situated close to the coronagraphs to avoid static NCP errors and chromatic errors.

SHWFS, Curvature WFS and modulated PyWFS provides a large linear and dynamical range but at the cost of sensitivity. However, fixed PyWFS provides good sensitivity but over a smaller range (limited to < 1 radian error). The FPWFS is free of NCP errors and aliasing errors since it is working directly in the focal plane. However, FPWFS, placed after the coronagraph, suffers from chromaticity and reduced throughput that eventually decreases the signal to noise ratio (Guyon, 2005).

So the choice of the WFS for ExAO is even more critical. SHWFS and Curvature WFS provides poor sensitivity to the low-order aberrations, hence are less preferable over the fixed PyWFS and the FPWFS.

Deformable Mirror

The heart of a DM is its flexible reflective membrane deposited on the array of actuators. The wavefront in Fig. 1.9 first strikes the surface of the DM before splitting between the WFS and the imaging channel. Once we have the measurements of the wavefront aberrations from the WFS, the next step is to compute the control commands[4] and send it to the DM. After receiving the commands, the actuator of the DM are controlled to create phase delays in specific areas compensating the aberrations. A DM is characterized by the following parameters:

- Number of actuators: This is a very critical variable. Few 100 actuators are sufficient to achieve a diffraction-limited PSF in an AO system. However, for the HCI, a larger number of actuators (range of 1000's) are desirable to correct higher frequency components of the wavefront and gain in the reduction of the total residual.

[4]One such procedure of computing the control commands is presented in §2.3.4

Though increasing the number of actuators increases the computational cost and the complexity in reconstruction algorithms for phase retrieval.

- Actuator stroke: defines the vertical displacement motion when the maximum rated voltage is applied. High stroke DMs are usually used to correct low spatial frequency component of the aberration whereas low stroke DMs are usually used to address high spatial frequencies.

- Influence function: characteristic shape of the DM's response corresponding to the movement of a single actuator.

In classical AO systems, choosing the number of actuators is actually a function of r_0. The number of actuators required is defined by the turbulence characteristics for a given site and is of the order of $(\frac{D}{r_0})^2$ and the inter-actuator spacing corresponds to the diameter of r_0. AO systems cannot correct for aberrations on the spatial scale smaller than the inter actuator spacing in the pupil plane. However, for ExAO systems, another parameter to take into account is the size of the dark hole, i.e. the region in the image where speckles are corrected. This region has a typical size of $N_{act}\ \lambda/D$ where N_{act} is the number of actuators across the pupil. If the ExAO system only has one DM, then it has to fit both requirements but if it is composed of two different DMs, then one can be used for correcting most of the turbulence while the other can be used to reduce the speckle pattern inside the dark hole.

There are several types of DM used in astronomy such as: Segmented, Continuous face-sheet, Piezoelectric, Bimorph, Membrane mirrors, Magnetically actuated mirrors, Micro-Electro-Mechanical Systems (MEMS). For direct imaging purpose, MEMS (Fig. 1.11 (a)) and Adaptive Secondary Mirror ((ASM, Biasi *et al.*, 2010), Fig. 1.11 (b)) are mostly popular due to high number of actuators.

MEMS DMs (Blain, 2013) are composed of a thin silicon membrane with a highly reflective metallic coating, supported by an array of electrostatic micro-actuators. Each actuator top plate is attached to the membrane through a rigid post, which is controlled to create the local deformation of the membrane. MEMS has several advantages: sub-nanometre repeatability, high stability, negligible hysteresis (below 5%), low weight, compact size, high speed, and large number of actuators with a proportionately large stroke.

On the other hand, an ASM is composed of 3 basic elements: a cold plate, holding voice-coil force actuators, a reference body and the thin shell. Each voice coil applies a force to a corresponding magnet glued onto the back face of the thin shell. A ring of conductive material (chrome, aluminum, gold) is deposited around each magnet and is mirrored on the reference body. These two opposite coatings constitute a capacitance used as space sensor. The reference backplate being a calibrated optical surface, an equal spacing for all capacitive sensors insures a basic optical quality on the shell [5].

ASM was first implemented for the LBT. ASM has several advantages: lower emissivity (ideal for thermal infrared), higher reflectivity (more photons reach science camera), common to all imaging paths (except prime focus), and have high stroke (no need for

[5] http://www.eso.org/sci/facilities/develop/ao/sys/dsm.html

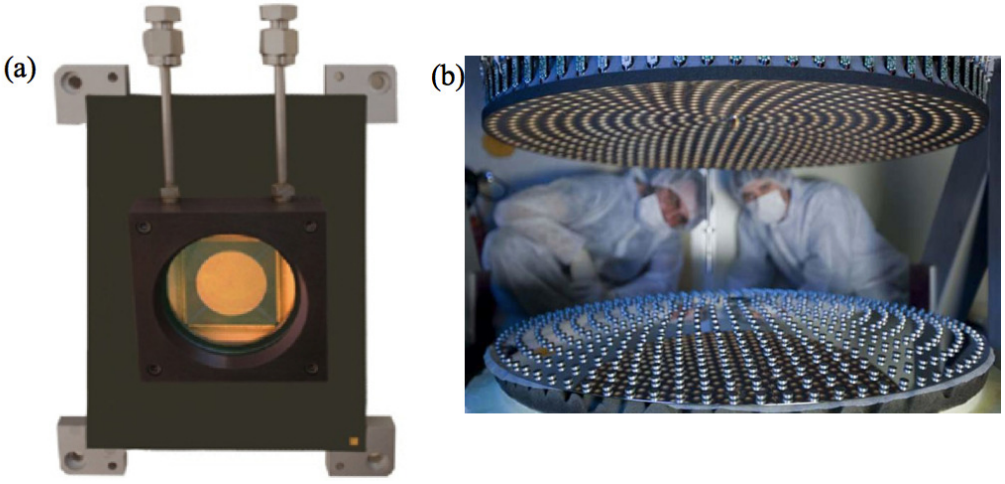

Figure 1.11: High performance deformable mirrors. (a) 2000-actuator MEMS from *Boston Micromachines* and (b) Adaptive secondary of Large Binocular Telescope showing the 672 tiny magnets spread over the back of the mirror (the reflecting face of the mirror is face down). The cold plate (upper portion) contains the electro-mechanical devices that control the magnets.

separate tip-tilt mirror). Due to these advantages, Subaru telescope observatory is also considering to replace their secondary mirror with an ASM (Guyon *et al.*, 2014).

So far I provided a glimpse of WFSs and DMs used by the current AO/ExAO systems to address the aberrations. A way to determine how well an AO system performs is to evaluate the residual errors of each subsystem.

- Fitting error, $\sigma^2_{fitting}$: DM cannot exactly match the shape of the turbulence model described by Kolmogorov. This error arises due to a finite spatial sampling of the wavefront with a finite number of correcting elements of the DM.

- Temporal error, $\sigma^2_{temporal}$: the control system that computes the correction cannot respond instantaneously to the disturbance. It is basically the time lag error, which is based on the control loop's update frequency and the wind speed during observations.

- Wavefront sensor measurement error, σ^2_{WFS}

- Alignment error, $\sigma^2_{alignment}$: residual alignment error between DM and the WFS. It is difficult to establish the set of control parameters used to drive the control loop to produce a perfect PSF.

Assuming that these values are uncorrelated, their variances can be added to determine total system error

$$\sigma^2_{system} = \sigma^2_{fitting} + \sigma^2_{temporal} + \sigma^2_{WFS} + \sigma^2_{alignment} \, .$$

Basically, the SR and the total residual value are the two parameters that differentiate between an AO and an ExAO system. For an AO system, a typical SR of $\sim$ 30% with 200 nm RMS of the total phase residuals is sufficient to obtain diffraction-limited PSF in the near infrared. However, for an ExAO system, SR > 90% and total phase residuals of < 50 nm RMS is generally desirable for coronagraphs to perform better.

As quoted by Sivaramakrishnan *et al.* (2001), *"the improvement in image quality that AO provides makes it possible to study the region within a few times the diffraction width of the image of a bright star, with dynamic range limited by the presence of the halo and bright Airy rings rather than by atmospheric seeing. Systems delivering 50-95% Strehl ratio are suitable for coronagraphic instrument to suppress maximum of the on-axis starlight and gain sensitivity to faint structure surrounding a bright source."*

Focal plane speckle suppression

The ExAO provides a stable PSF in the focal plane. Since it senses the wavefront in the pupil plane, it can leave uncorrected speckle in the focal plane. Even a perfect PSF can have diffraction rings and speckles created by the spider arms in the pupil. Based on interferometric subtraction technique, those speckles can be probed and removed, usually only on one side of the PSF. This idea make use of the fact that the speckle arising from the residual starlight are coherent with it unlike the light from the nearby companion. With the knowledge of the speckle characteristics (amplitude and phase), anti-speckles are generated artificially, which are then superimposed on the artifact speckles to remove them from the field.

Several methods exist that have the same theoretical background, but different technique to obtain the speckle characteristics. Speckle nulling (Martinache *et al.*, 2014) and Electric Field Conjugation (EFC, Give'on *et al.*, 2007) rely on additional probe images to deduce speckle's amplitude and phase. Both of these techniques are being tested for space applications at NASA Ames and have demonstrated a contrast of 5.2×10^{-8} in monochromatic and $3 \times 10^{-7}$with 10% band-width between 2-12 λ/D. On High-Contrast Imaging Testbed (HCIT, Kern *et al.*, 2013) at JPL, a contrast of 10^{-8} with 10% bandwidth between 2 - 4 λ/D has been demonstrated when combined with a Phase Induced Amplitude Apodization coronagraph (PIAA, Guyon, 2003, §1.2.5.3)

Another technique called Self Coherent Camera (SCC, Mazoyer *et al.*, 2014) codes speckle phases directly in the image by using interferences of the focal plane speckles with a sample of the residual starlight falling outside of the geometrical pupil. SCC has successfully demonstrated a contrast better than 3.10^{-8} (RMS) for monochromatic light and 4.10^{-8} in narrow band (1.5%) between 5 - 12 λ/D in the laboratory at LESIA, Observatory of Paris-Meudon.

Good quality of the AO correction for PSF, contributes to the efficient starlight null by the coronagraph as well as the accurate measurement of the residual PSF halo for speckle suppression. In the next section, first I will present a brief introduction to the historical background behind the origin of the coronagraphy. I will then describe the concept of stellar coronagraphy and the types of coronagraphs that are widely used in current ExAO systems. At the entrance pupil, I assume that the image is corrected by the AO ($I_{Corrected}$)

and the SR is > 90%.

1.2.5 Stellar Coronagraphy

A stellar coronagraph is an optical element that physically blocks the light from an on-axis source i.e. a star while allowing the light from an off-axis source i.e. a companion to pass through the optical system. The field of stellar coronagraphy was inspired from the invention of the first coronagraph Lyot (1939), a solar coronagraph by Bernard Lyot (Fig. 1.12[6]) who was the French astronomer at Observatoire de Meudon. He invented this neat and clever method to study the corona of the sun, the access to which was limited only during the total eclipse.

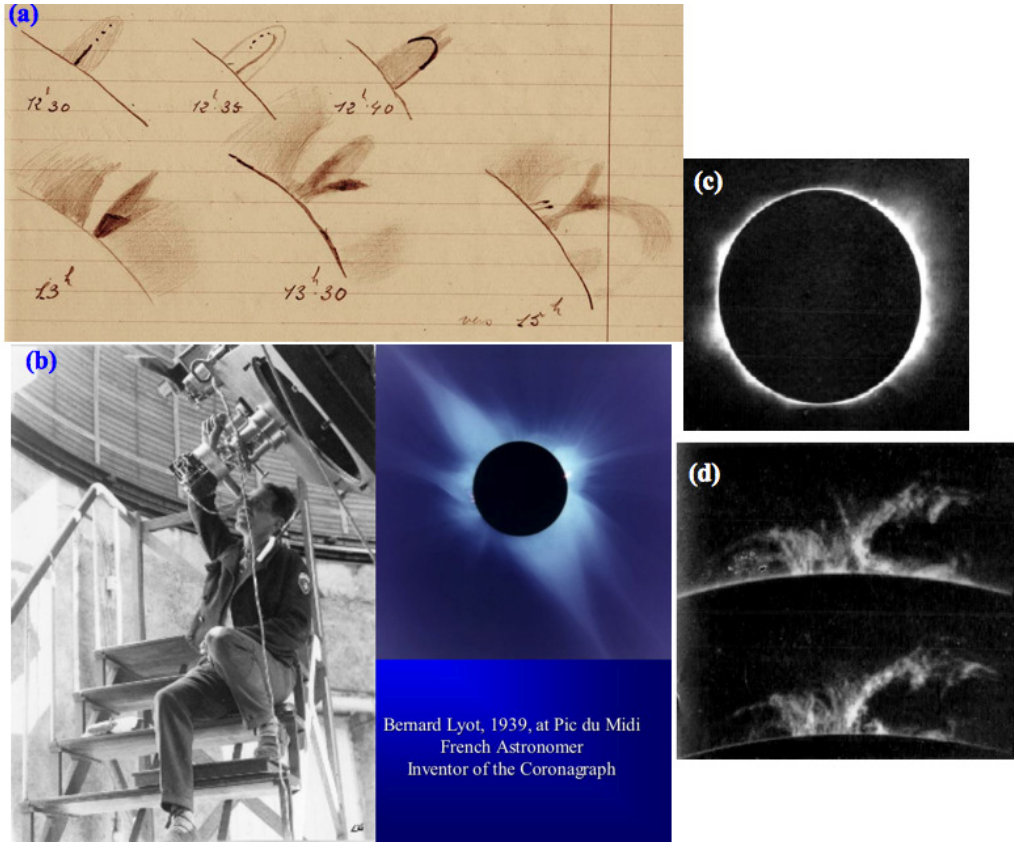

Figure 1.12: (a) Drawing of the turbulence noticed in the solar corona by Bernard Lyot during one of the observations in August 1935 (b) Bernard Lyot observing at Observatoire au Pic du midi in 1939. (c) Lyot's image of the solar corona. (d) Frames from Lyot's Prominence film in September 1935.

The first coronagraphic observations were made at Observatoire au Pic du midi in 1930. At the focal plane of a solar telescope, an opaque disk of angular size exactly that of the sun is used to block its on-axis luminosity. The residual sunlight, which is diffracted around the edge of this opaque disk is then blocked in the re-imaged pupil plane

[6]The movie of the Prominence can be found in http://www.dailymotion.com/video/x5zrz6_protus-eruptives2-bernard-lyot-pic_tech

by a diaphragm called as a Lyot stop (named in the honor of the father of coronagraphy, *Bernard Lyot*). This allowed the spectroscopic study of the Prominences (Fig. 1.12 (b and c)) and the faintest details in the solar corona in different spectral bands.

The invention of a solar coronagraph initiated the field of stellar coronagraphy to study the immediate surrounding of the stars other than our sun. The motivation is to detect faint circumstellar material around a bright stellar source. A Lyot-type coronagraph can reduce the diffracted light away from the star and can be used to study the stellar environment, however, it becomes inefficient in the close proximity of a star (Roddier & Roddier, 1997).

Nevertheless, the Lyot coronagraphs have been proposed for the analysis of the circumstellar debris disk, brown dwarfs and the extrasolar planets (Bonneau *et al.*, 1975; Kenknight, 1977; Nakajima *et al.*, 1994; Watson *et al.*, 1991). The α, β Pictoris and R Aquarii's circumstellar disk have been imaged by Paresce & Burrows (1986), Paresce & Burrows (1987). Brown dwarfs were imaged by Macintosh *et al.* (1992), Nakajima *et al.* (1994). Even from space, the Hubble Space Telescope (HST, see §1.3.2) has confirmed the detection of disks and companions around several other stars (Mouillet *et al.*, 2001; Kalas *et al.*, 2008; Hagan *et al.*, 2010).

However, the quest to study the stellar surroundings in its own vicinity (< 10 AU) has led to the discovery of several other effective coronagraphic techniques using phase and amplitude focal plane mask instead of an opaque disk, as discussed later in this section. I will now describe a general analytical study of a coronagraph and will explain briefly how the stellar coronagraphs discovered so far were branched out from a classical Lyot coronagraph.

1.2.5.1 Image formation through a Lyot-type coronagraph

Figure 1.13 represents a general optical system of a coronagraph. The equations described below are applicable to any type of coronagraph, but will depend on the pupil function and the focal plane mask. To describe the effects of the diffraction between the pupil and the focal planes, the Fraunhofer approximation (perfect lenses) is considered. Also, the Fourier transform ($\mathcal{F}$) is used to analyze the complex amplitude of the field from focal plane to the pupil plane and the inverse Fourier transform ($\mathcal{F}^{-1}$) from pupil to the focal plane.

Consider a planet orbiting a star at large angular separation. As defined in Fig. 1.13, the electromagnetic field of the on-axis star at the entrance pupil plane P (circular pupil with no central obscuration) of an imaging system is called $\psi_E^{'}(\xi)$. According to the Fraunhofer approximation, the complex amplitude at the focal plane is the Fourier transform of $\psi_E^{'}(\xi)$.

To block the luminosity of the on-axis starlight, an occulting mask M is placed at the focal plane. This mask is optically conjugated to the final detector plane and filters out the starlight at low spatial frequency. The transmission function of the mask depends on the type of coronagraph and will be discussed later briefly in this section. The complex amplitude $A_E^{'}$ in the focal plane is then

$$A_E^{'}(x, \lambda) = \mathcal{F}[\psi_E^{'}]M \, . \tag{1.8}$$

The core intensity of the star PSF (red rays) with couple of Airy rings are now blocked

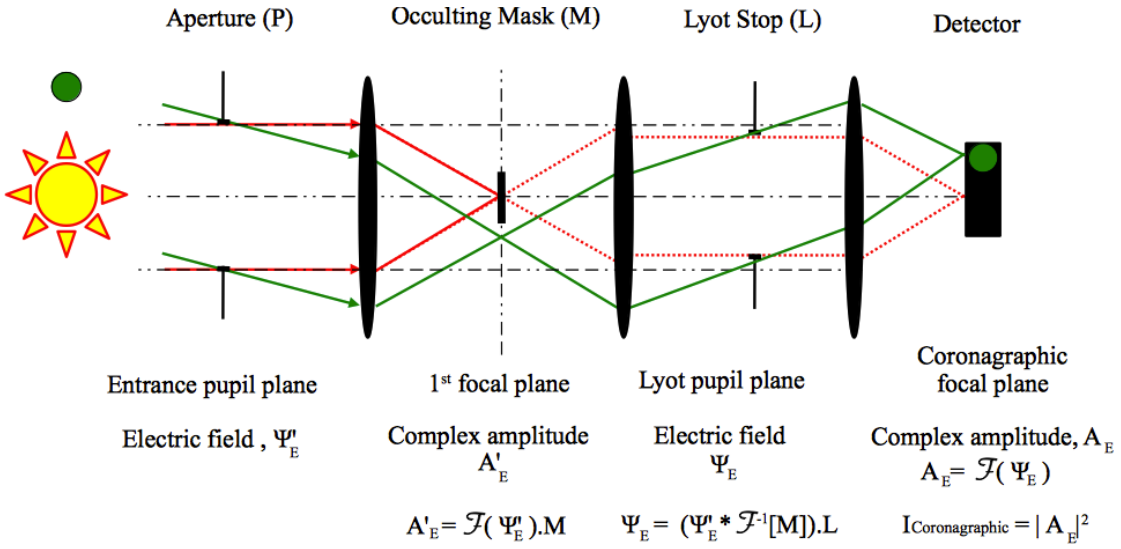

Figure 1.13: General formalism of a stellar coronagraph. Fourier transformation is used to study the complex amplitude of the field at different focal and pupil planes.

depending on the size of the mask, leaving untouched the signal from the companion (green rays, Fig. 1.13). In the re-imaged pupil plane, there lies a diaphragm called the Lyot stop (L), which is optically conjugated with the entrance pupil and is used to filter out the diffracted starlight on the edge of the pupil at high spatial frequency downstream the mask M. The field at the Lyot stop is then the inverse Fourier transform of the complex amplitude $A_E^{'}(x, \lambda)$ (in eq 1.8) at the first focal plane.

The diameter of the Lyot stop is generally a few percent undersized version of the entrance pupil plane, in order to stop the residual diffracted starlight from contaminating the planet signal at the final focal plane. The function of the Lyot stop is defined as

$$L(\vec{\xi}) = \begin{cases} 1 & \text{if } \vec{\xi} < D_L/2 \\ 0 & \text{otherwise} , \end{cases}$$

where D_L is the diameter of the Lyot stop. The field $\psi_E(\xi, \lambda)$ downstream of the Lyot stop can then be written as

$$\psi_E(\xi, \lambda) = (\psi_E^{'} * \mathcal{F}^{-1}[M])L , \tag{1.9}$$

where $*$ represents a convolution.

Using the definition of $\psi_E^{'}$ in Eq. 1.5, if we consider that there is no amplitude error, that $a(\xi) = P(\xi)$ (i.e. the errors are only defined in the pupil) and that $\phi(\xi)$ is small, then the first order expansion of Eq. 1.5 can be written as

$$\psi_E^{'}(\xi) = \psi_0 \, [P(\xi) + i\phi(\xi)] . \tag{1.10}$$

Now replacing $\psi_E^{'}$ by its expression in equation 1.10, equation 1.9 becomes

$$\psi_E(\xi, \lambda) = \psi_0 \, (P * \mathcal{F}^{-1}[M])L + i \, (\phi * \mathcal{F}^{-1}[M])L . \tag{1.11}$$

The complex amplitude in the final focal plane is $A_E(x,\lambda) = \mathcal{F}[\psi_E]$. The equation 1.11 becomes

$$\frac{A_E(x,\lambda)}{\psi_0} = (\mathcal{F}[P].M) * \mathcal{F}[L] + i\,(\mathcal{F}[\phi].M) * \mathcal{F}[L]\,. \tag{1.12}$$

Integrating the complex amplitude at wavelength λ, chromatic over the spectral range of R_λ

$$\int_\lambda \frac{A_E(x,\lambda)}{\psi_0} d\lambda = \int_\lambda (\mathcal{F}[P].M) * \mathcal{F}[L] d\lambda + i \int_\lambda (\mathcal{F}[\phi].M) * \mathcal{F}[L] d\lambda\,. \tag{1.13}$$

The final coronagraphic intensity of the star integrated on the detector can be written as

$$I_* = |A_E|^2\ . \tag{1.14}$$

Note that the resulting intensity I_* is not the convolution of the incident intensity of the on-axis object with the PSF of an imaging system as shown in equation 1.3 for a conventional non-coronagraphic invariant systems. Instead, it is the convolution of the intensity distribution before the mask multiplied by the mask function and convoluted by the Lyot PSF [7]. However, the intensity of the planet I_C is the convolution of the off-axis incident intensity from the planet O_C with the Lyot PSF (Malbet, 1996). The total intensity integrated on the detector is $I_{coronagraphic} = I_* + I_C$.

The aim of a stellar coronagraph is to cancel the on-axis star intensity I_* and reduce the off-axis residual diffracted starlight without altering the intensity of an off-axis companion.

1.2.5.2 Factors characterizing the performance of a coronagraph

Before describing the different types of stellar coronagraphs discovered so far, I will emphasize on the parameters used frequently in characterizing the coronagraphic performance.

- **Attenuation factor**

  The attenuation factor (A) is the ratio of the maximum of the star intensity $I_{coronagraphic}$ in the final focal plane of the detector downstream a coronagraph by the maximum of the image without a coronagraph

  $$A = \frac{max(I_{coronagraphic})}{|\psi_0|^2}\,. \tag{1.15}$$

  It depends on the sizes of the mask and the Lyot stop as well as on the angular separation between the on-axis star and the off-axis source.

- **Contrast**

  The raw contrast between a stellar source and its companion is the ratio between the azimuthal average profile (E) of the intensity $I_{coronagraphic}$ at an angular distance

[7] The Lyot PSF is obtained by considering that the entrance pupil is the diaphragm of Lyot.

r (in λ/D) from the center of the image by the intensity of the star obtained without a coronagraph

$$C(r) = \frac{E(I_{coronagraphic}(r))}{|\psi_0|^2} \,. \tag{1.16}$$

Equation 1.16 is also used to obtain the detection contrast from the post-processed images. The post-processing techniques are generally employed to remove the residual stray light to make the faint source emerge above the stellar noise (see §1.2.6).

This is an important metric for quantifying the performance of a coronagraph as the function of the radial distance r in the image plane.

- **Inner Working Angle**

  The minimal angular distance from the star at which a companion can be detected (in the unit of λ/D). It is defined as a point where the off-axis source throughput is 50% of the maximum throughput (the maximum throughput = 1 - non-aberrated non-coronagraphic PSF of the telescope). To obtain high contrast at small angular separation, small IWA coronagraphs are required in order to provide the search area within a few couple of Airy disk of the star.

- **Null-order**

  Describes the coronagraph (stellar) throughput as a function of angular separation (r) close to the optical axis. The higher the null order, the wider is the region for on-axis starlight suppression and the better is the immunity to pointing errors at the cost of the IWA.

A high performance coronagraph is expected to provide high throughput, high contrast at small IWA and high immunity to wavefront aberrations near the diffraction limit. The challenge in designing a stellar coronagraph is to figure out not only the best tradeoffs among the parameters listed above but also its compatibility with the pupil of any shape (including central obscuration and spider arms).

1.2.5.3 Existing stellar coronagraphs

In case of a Lyot coronagraph used for the stellar coronagraphy, the mask M is simply an opaque disk. If size of M > the size of the PSF (by a couple of Airy rings), the residual diffracted intensity at the Lyot plane is sharp and can be masked out easily by undersizing it by a few percentage of the entrance pupil diameter. However, to study the close neighborhood of the star, the mask size should be of the same order of magnitude as the PSF of the star. The problem in the later case is that the residual intensity in the Lyot plane is of the same order of magnitude as the pupil diameter, hence the size of the Lyot stop should be decreased significantly at the cost of the angular resolution Malbet (1996).

For a classical Lyot coronagraph, the Lyot stop must be sized to the mask diameter in order to block the area that has a width equal to the mask impulse response in the Lyot plane. The smaller the focal plane mask, the more constrained is the size of the

Lyot stop, hence the more is the starlight leakage. To perform high angular resolution coronagraphy near the diffraction limit of the star, several modifications to the classical Lyot coronagraph have been proposed and developed.

In Fig. 1.14, I summarize the types of stellar coronagraphs invented so far. They are broadly divided into four categories: – (1) Interferometric coronagraphs, – (2) Phase mask coronagraphs (PMCs), – (3) Amplitude coronagraphs, – (4) Apodization coronagraphs. PMCs and amplitude coronagraphs are actually the improved Lyot-type coronagraphs. Few of the coronagraphs share properties from these different categories, which I summarized in a separate group of phase/amplitude pupil apodization coronagraphs. Guyon *et al.* (2006) presents an exhaustive study of all the types of coronagraphs together with their characteristics.

The first few coronagraphs that provided a better extinction at small angles as compared with the classical Lyot coronagraph includes: an Achromatic Interferometric Coronagraph (AIC, Gay & Rabbia, 1996; Baudoz *et al.*, 2000a,b), a circular Disk Phase Mask (DPM, Roddier & Roddier, 1997), a nulling coronagraph (Guyon & Roddier, 2000) and a Prolate Apodized Lyot Coronagraph (PALC, Aime *et al.*, 2002; Soummer *et al.*, 2003b).

AIC provided a starlight null at the focus by π phase shifting of the on-axis star using a modified Michelson's interferometer. This coronagraph symmetrizes the images and is therefore not adapted to produce images of protoplanetary disks. A circular DPM, typically half the diameter of the Airy peak, introduced a π-phase shift to create the destructive interference of the PSF at the focal plane. Though DPM suffered from size and phase chromaticity. Adapted to centrally obscured pupil, an achromatic version of the apodized DPM phase mask, the Dual-Zone Phase Mask (DZPM, Soummer *et al.*, 2003a), has been introduced to compensate for phase and size chromaticity of the DPM. Multistep Apodized Pupil Lyot Coronagraph (APLC, Soummer, 2005; Aime & Soummer, 2004) improved the contrast at a reduced IWA. Vanderbei *et al.* (2004) apodized (amplitude) the pupil after the hard edge focal plane mask. 4^{th} and 8^{th} order Band-limited coronagraphs (Kuchner & Traub, 2002; Kuchner *et al.*, 2005) are developed to modify the focal plane mask to match its impulse response with the entrance pupil. For further studies on the comparison of their focal plane mask transmission function, reader may refer Ferrari *et al.* (2007).

For my thesis, I worked closely with the Phase-Induced Amplitude Apodized coronagraph (PIAA, Guyon, 2003) and the PMCs, therefore I will limit my study to these high performance coronagraphs only.

- **Phase mask Coronagraphs (PMCs)**

  The theory of these coronagraphs are somewhat based on the concept of the DPM. These phase masks generally induce self-destructive interference by retarding the phase of the on-axis source by π, which leads to the cancellation of the on-axis starlight. These kind of coronagraphs provide small IWA and are extremely sensitive to tip-tilt errors (Guyon *et al.*, 2006). They are not achromatic and generally operates with a spectral bandpass of $\sim$ 10%. Below, I will introduce few of the PMCs I have used for my research.

  The Four Quadrant Phase Mask (FQPM, Rouan *et al.*, 2000; Riaud *et al.*, 2001,

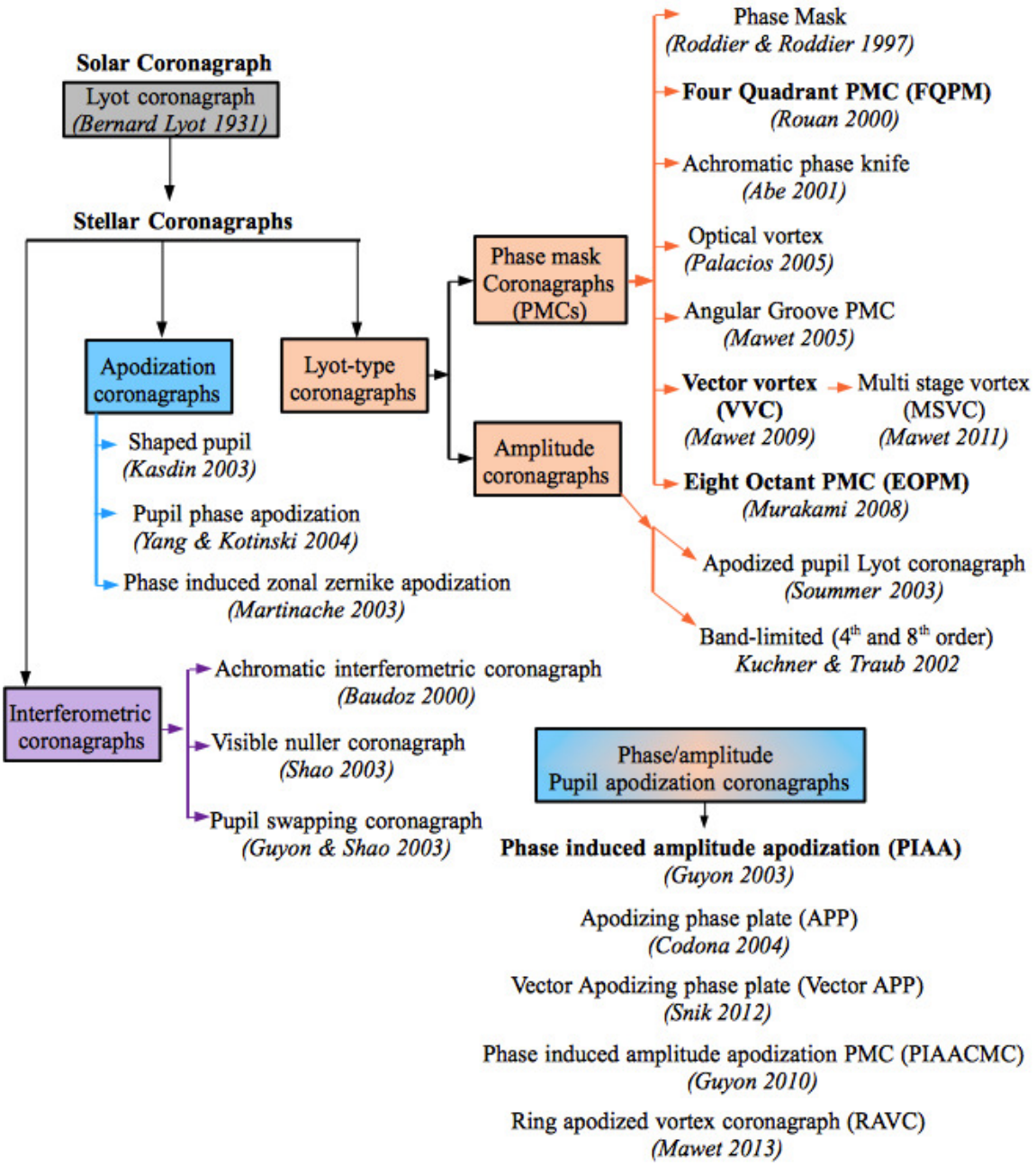

Figure 1.14: The technological tree of the stellar coronagraphs with solar coronagraph as a root. In this thesis, I have studied four coronagraphs that are highlighted in bold in this figure. *Note: The presentation of the coronagraphs is not in a chronological order.*

2003; Boccaletti *et al.*, 2004) modified the design of the DPM by dividing the PSF in 4 quadrants and introducing a π phase shift in the adjacent quadrants to produce a self destructive interference. This technique addressed the chromaticity issue with the mask dimension by introducing the azimuthal phase modulation instead of the radial modulation of the DPM. However, FQPM is highly sensitive to pupil shape and can be optimized for pupils with central obstruction and spider arms with some

pupil remodeling optics.

The transmission function of mask M for the FQPM coronagraph constitute of π phase shifted adjacent quadrants only and can be written as

$$M = exp(i\epsilon\pi) \; with \; \epsilon \; = \begin{cases} 1 & \text{in two diagonal quadrants} \\ 0 & \text{otherwise .} \end{cases}$$

To obtain a π phase shift between quadrants, the thickness e of the step is given by

$$e_\pi(\lambda) = \frac{\lambda}{2(n_\lambda - 1)} \, , \tag{1.17}$$

where n_λ is the index of refraction of the material at λ. The FQPM is generally developed for an optimal wavelength λ_{opt} for which a π phase shift produces a perfect null. The performance of the mask at any λ other than its optimized wavelength λ_{opt} is then degraded, the phase shift in that case is $\frac{\lambda_{opt}}{\lambda}\pi$.

Several solutions have been proposed to make the FQPM achromatic using for ex. birefringence (Mawet *et al.*, 2003), the concept of sub wavelength gratings (Mawet *et al.*, 2005b, 2006) and a multi-FQPM, each optimized for different wavelengths (Baudoz *et al.*, 2008).

The Eight Octant Phase Mask (EOPM, Murakami *et al.*, 2008) coronagraph is similar to the FQPM. The EOPM is put on a focal plane to divide a stellar image into eight-octant regions, and provides a π-phase difference between the adjacent octants.

The advantage of the EOPM coronagraph is that it can effectively suppress partially resolved stars and it has the fourth-order response to the tip-tilt error, which is better than for the FQPM [8]. However, both the FQPM and the EOPM have regions called the "dead zones", which are the transitions between the quadrants that attenuates signal from a potential companion (suppresses signal by up to 4 mag in case of the FQPM Riaud *et al.* (2001)). Figure 1.15 shows the manufacturing of the FQPM (Fig. 1.15 (a)) and the EOPM (Fig. 1.15 (b)) coronagraphs.

Optical Vortex Coronagraph: The (OVC, Palacios, 2005; Foo *et al.*, 2005; Swartzlander, 2006; Jenkins, 2008) and the Angular Groove Phase Mask Coronagraph (AGPM, Mawet *et al.*, 2005a) are derived from the FQPM. They used a focal plane vortex phase mask, thus addressed the problem of "dead zones" in the FQPM/EOPM. Such optical vortex devices are characterized by its topological charge l, i.e., the number of times the phase accumulates 2π radians along a closed path surrounding the singularity. If (r, θ) are the polar coordinates, the mask phase is equal to $l\theta$.

Among the family of OVCs, I have worked closely with a vector vortex coronagraph (VVC, Mawet *et al.*, 2009a, 2010a), which is based on a 360°-rotating half-waveplate, inducing a continuous helicoidal optical delay (a "vortex" phase profile)

[8] http://sciencetalks.jpl.nasa.gov/meetings/2011/xs/031401/Seminar_Murakami_v01.pdf

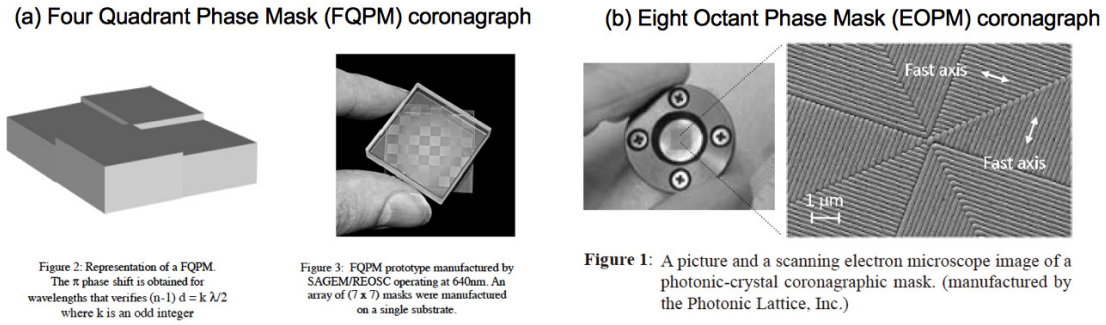

Figure 1.15: Presenting manufacturing of the FQPM (extracted from (Lemarquis *et al.*, 2004)) and the EOPM (extracted from (Murakami *et al.*, 2010)) coronagraphs.

at the focal plane of the telescope. Figure 1.16 shows the principle of a VVC. In this mask, the polarization is rotated locally (Fig. 1.16 (a) and (b)) so that a rotation around the mask creates a phase shift of 4π (Fig. 1.16 (c)).

The electric field at the Lyot plane is the Fourier transformation of the PSF of the telescope multiplied by the phase ramp $e^{i2\theta}$. The residual starlight intensity downstream a vector vortex mask is diffracted outside the geometrical pupil at the Lyot plane as can be seen in Fig. 1.16 (d) (unobstructed pupil without a Lyot stop).

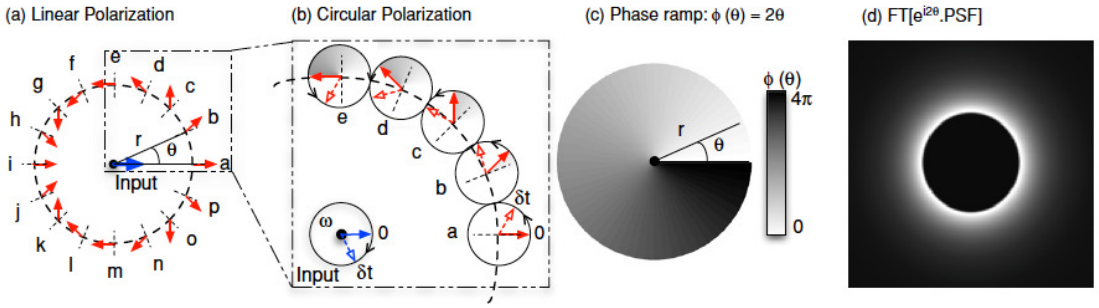

Figure 1.16: Vector Vortex Coronagraph principle. a) Effects of the rotating half-waveplate on linearly polarized light. b) for circularly polarized light. c) helix phase delay in the focal plane and d) Light distribution for an on-axis source at the Lyot plane (without a Lyot stop). *Courtesy of Mawet* et al. *(2010a).*

The optical vortex coronagraph attenuation sensitivity to low-order aberrations (especially pointing errors) is proportional to the l^{th} power of the tip-tilt errors upstream of the focal plane mask.

The performance of the PMCs mentioned above depends on the shape of the telescope pupil. For circular apertures, a null close to zero can be produced. However, for pupils with a central obscuration and spider arms, these coronagraphs are no longer optimal because the light is partially diffracted inside the pupil by the phase masks. Nevertheless, the PMCs enable high contrast imaging at small angular separation by offering a search area near the diffraction limit of the telescope.

- **Phase/amplitude apodization coronagraphs**

These high performance coronagraphs combine the property (phase or amplitude) of a modified Lyot coronagraphs and the apodization coronagraphs. The apodization is usually induced to get rid of the effects of the static diffraction by modifing the Airy pattern. I will describe only the PIAA coronagraph. For more details, reader may refer to Guyon *et al.* (2006).

The PIAA coronagraph is an alternative solution to a classical pupil apodization that preserves most of the light from an off-axis source without reducing the angular resolution of the telescope. Instead of using an amplitude mask to apodize the beam, PIAA uses two aspheric mirrors to geometrically redistribute the on-axis starlight, thereby reducing the intensity of the PSF wings without loosing any light.

The apodized beam is blocked by a focal plane occulter (a binary mask) to block the excessive starlight. A set of correcting optics, which is called the Inverse PIAA optics is then placed downstream of the focal plane mask to restore the off-axis PSF (if any). This lossless amplitude apodization provides maximum throughput at small IWA ($< 2\lambda/D$).

Figure 1.17 represents the concept of the PIAA coronagraph. Figure 1.17 a) represents PIAA architecture. The labels (1) is the telescope entrance pupil, (2) pupil after apodization, (3) focal plane before introduction of the focal plane mask, (4) focal plane after the focal plane mask, and (5) exit pupil plane before truncation by the Lyot mask (Guyon *et al.*, 2010b). Figure 1.17 b) and c) presents the pair of aspheric optics that reshapes the beam geometrically. Figure 1.17 d) shows the laboratory images of sources observed on and off-axis for different λ/D values. The shown PSFs are obtained under the following configurations. Top row: no apodization, Middle row: PIAA + binary mask and Bottom row: PIAA + binary mask + inverse PIAA. After the binary mask, a pineapple shape aberration is introduced by the PIAA optics, which is perfectly compensated by the inverse PIAA optics. These results are obtained on the Subaru Coronagraphic Extreme Adaptive Optics instrument at Subaru telescope (Lozi *et al.*, 2009) .

Using a partially transmissive phase shifting focal plane mask, the performance of PIAA has been greatly improved (50% throughput at 0.64 λ/D) by the next generation PIAA Complex Mask Coronagraph (PIAACMC, Guyon *et al.*, 2010b). For further details on PIAACMC, refer to Guyon *et al.* (2012) and (Newman *et al.*, 2015b, to achieve deep contrast over a wide spectral band).

In this section, I have introduced the concept of coronagraphy and summarized the principle of stellar coronagraphs used for the purpose of HCI. However, as I mentioned earlier, the expected performance of these coronagraphs during the astronomical observations is limited by the atmospheric turbulence and the AO systems does not always offer a perfect diffraction-limited PSF as an input to them. As a result, coronagraphs cannot null the starlight efficiently and the residual starlight scatters all over the FOV. Post-processing techniques then play a major role in calibrating these residuals, which I will introduce briefly in the next section.

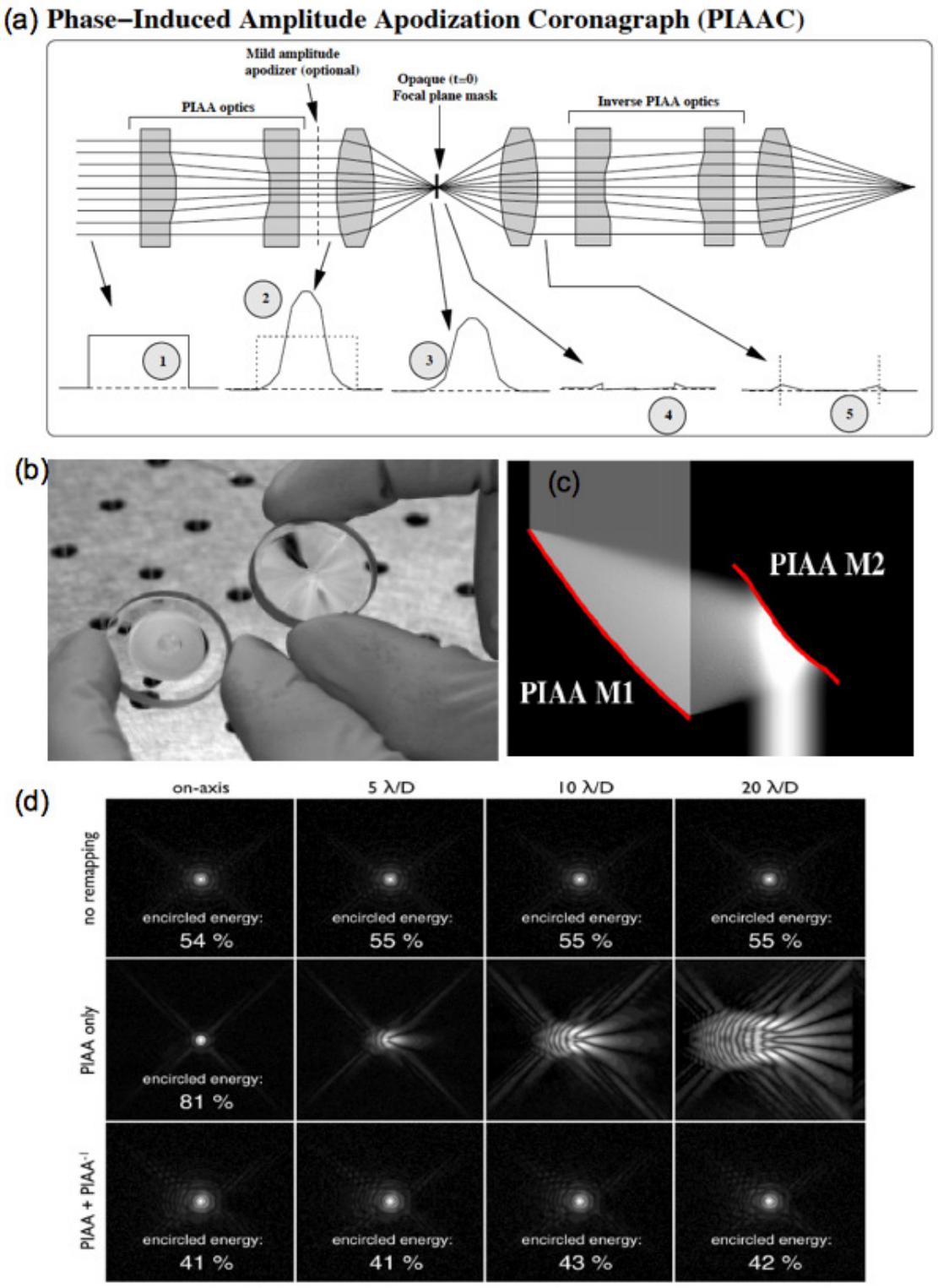

Figure 1.17: Concept of the PIAA coronagraph (Guyon *et al.*, 2010b; Lozi *et al.*, 2009). See text for detailed description of the figure.

1.2.6 Post-processing techniques

Even after the correction of the dynamic speckles by techniques presented in §1.2.4, there exist some residual static speckles. When the sensing and imaging channels are different, there often remain static deformations in the science plane, which are induced by the imperfect optics in the non common path, unseen by the WFS. These errors evolve slowly due to variations in the temperature and the weather conditions. As a result, these speckle can either mimic a planet signal or can overwhelm the signal of a faint companion. Differential imaging techniques are used frequently to find a criteria that distinguish the image of the planet from the residual speckles.

1.2.6.1 Differential Imaging

Angular differential imaging

This technique takes advantage of the intrinsic FOV rotation of altitude/azimuth telescopes. By keeping the telescope pupil fixed on the science camera, it allows the FOV to rotate slowly with time around the star, hence keeping the non common path speckles fixed on the detector (Marois *et al.*, 2006; Lafrenière *et al.*, 2007). Subtracting a rotated image with a non-rotated one eliminates the patterns associated with optical aberrations that were fixed while the image of the planet was rotating.

Spectral differential imaging (Racine *et al.*, 1999) and polarization differential imaging (Baba & Murakami, 2003) are other similar techniques used to disentangle planet signal from the speckle noise.

1.2.6.2 PSF calibration

There is yet another technique which is different from conventional differential imaging techniques. Vogt *et al.* (2011) suggested to use the wavefront sensor telemetry of the uncorrected residuals left in the image in order to calibrate the amount of scattered starlight at small angular separations. The detection of a faint companion around the occulter at $\sim 1\lambda/D$ is very challenging as leaks due to low-order wavefront aberration around the FPM can create a false positive signal. Synchronized WFS measurements and science camera frames can be used to build a library of response of the residuals on the starlight leakage. During the observation of the science target, WFS residuals can be fitted with the best match in the library. The corresponding science equivalents can then be subtracted from the science image to reconstruct the PSF.

Vogt *et al.* (2011) has used the low-order telemetry alone to study the consequences on the science images due to low-orders, and demonstrated with a Lyot coronagraph in the laboratory a forty-time improvement in the sensitivity at 4.75 λ/D, as shown in Fig. 1.18. Unlike ADI, this technique has the advantage of efficiently removing starlight leakages even in the post processing of circumstellar disks images. This technique is still new and has not been tested on-sky or explored further in detail with small IWA coronagraphs.

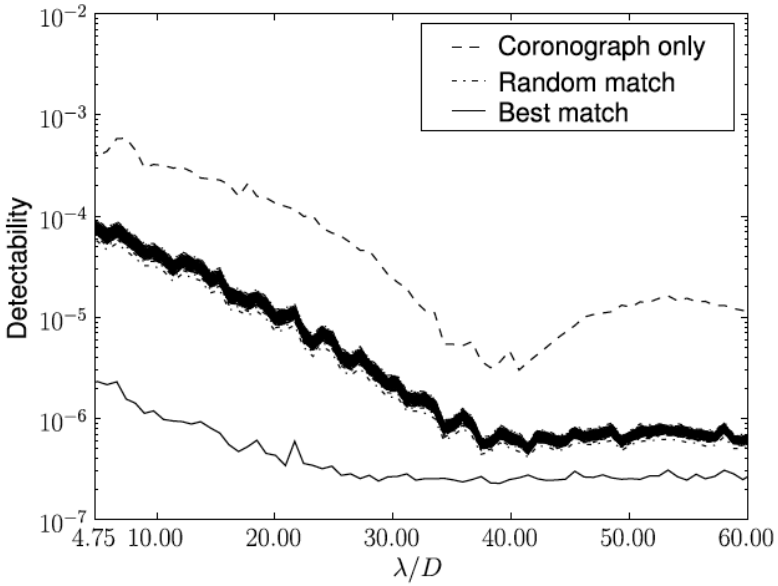

Figure 1.18: Shown are the three PSF contrast profiles: the raw science image (dashed line), standard PSF subtraction (dot-dashed lines) and the best-fit science image using proposed post-processing (solid line). The proposed post processing technique improved the calibration by two orders of magnitude at 4.75 λ/D (Vogt *et al.*, 2011).

1.3 Dedicated HCI instruments

Untill now, I introduced the – (1) scientific motivation for exoplanet imaging (§1.1.2), – (2) the field of HCI, problems faced in direct imaging (§1.2), – (3) concept of AO and wavefront sensing for coronagraphs (§1.2.2). Now, I will present the technologies with which the current ExAO instruments on ground are equipped with to tackle with the problems in HCI. I will provide a glimpse of their subsystems and the motivating results obtained with them. I will also present future HCI space telescopes (§1.3.2) whose one of the primary goal is to search faint structures (circumstellar disks/companions) around a bright stellar source.

1.3.1 Ground-based Extreme Adaptive Optics systems

1.3.1.1 SPHERE & GPI

The Spectro-Polarimetric High-contrast Exoplanet REsearch (SPHERE, Beuzit *et al.*, 2006) and the Gemini Planet Imager (GPI, Macintosh *et al.*, 2006) are currently two leading ExAO instruments on the ground that have started offering science return.

SPHERE

SPHERE is installed at the Very Large Telescope (VLT) at Paranal Observatory in Chile and is designed to perform low-resolution spectroscopic and polarimetric study of extrasolar disks and giant gaseous planets in the near-infrared (NIR). SPHERE saw its first light in May 2014. It includes SAXO (SPHERE adaptive optics module), various coronagraphs such as the classical Lyot coronagraph, FQPM and the APLC, an infrared differential imaging camera (IRDIS), an infrared integral field spectrograph (IFS) and a visible differential polarimeter (ZIMPOL).

SAXO uses a 40×40 lenslet SHWFS equipped with an EMCCD to measure the wavefront aberration and a high spatial 41×41 actuators DM to correct for the atmospheric turbulence at high frequency (1.2 kHz). In addition, it also has a tip-tilt mirror (1.2 kHz) for image motion correction and a Differential Tip-Tilt Sensor (DTTS, Baudoz *et al.*, 2010) to correct for differential tip-tilt between the imaging and the visible WFS paths.

Some of the latest science results with SPHERE includes: 0.95 - 1.80 μm spectroscopy of the $\sim$ 12 - 27 M_{Jup} companion orbiting a faint (R$\sim$13.6) young ($\sim$ 120 Myr) M-dwarf at 1.5" separation (50 AU) (Hinkley *et al.*, 2015), disproving the predicted Brown Dwarf Around V471 Tau (Hardy *et al.*, 2015), confirmation of a circumstellar dust disk around a bright southern star L_2 Pup (located at 64 pc) at visible wavelengths using SPHERE/ZIMPOL and first optical (590 - 890 *nm*) imaging polarimetry observations of the pre-transitional protoplanetary disk around the young solar analog LkCa 15 (Thalmann *et al.*, 2015).

GPI

GPI, aiming for directly imaging and spectroscopically characterizing the extrasolar

planets, is a dedicated facility instrument on the Gemini South telescope in Chile. It is designed to image and provide low-resolution spectra of Jupiter-sized, self-luminous planetary companions around young nearby stars, as well as protoplanetary disks. GPI has seen its first light in November 2013 (Macintosh *et al.*, 2014).

The AO system of GPI includes: – a SHWFS consisting of a visible light CCD behind a 43×43 lenslet array to sense the atmospheric turbulence, – a high-stroke low-actuator count piezo DM ("woofer") and a small-stroke 4096-actuator MEMS DM (with a 45-actuator-diameter region illuminated) referred to as "tweeter" to correct for the aberrations. It has an APLC, combining a classical Lyot coronagraph with a moderate apodizer. The size of the hard-edge FPM is 5.6 λ/D in diameter. The only science instrument is a cryogenic Integral Field Spectrograph (IFS).

Since its first light, GPI has performed many scientific observations and discoveries such as: (Galicher *et al.*, 2014) shows the near-infrared detection and characterization of the exoplanet HD 95086 b, Chilcote *et al.* (2015) has obtained first H-band spectra of the Giant Planet beta Pictoris b, Perrin *et al.* (2015) shows the first results from GPI's polarimetry mode, (Currie *et al.*, 2015) presents the discovery of a bright, young Kuiper belt-like debris disk around HD 115600.

Both SPHERE (Petit et al.*, 2009) and GPI (Poyneer* et al.*, 2014) use an optimal control law to correct for low-order aberrations. This controller, called Linear Quadratic Gaussian (LQG) is based on a Kalman filter that uses the knowledge of the Power Spectrum Density (PSD) of the disturbances to correct efficiently the low-order aberration, especially vibrations induced by the telescope and the instrument itself.*

1.3.1.2 Palomar-WCS, P1640, PALM-3000 + SDC

Palomar-Well-Corrected Sub-aperture

Instead of correcting the full telescope pupil using an AO system, Serabyn *et al.* (2007) introduced the concept of correcting a clear 1.5-m off-axis sub-aperture, called the well-corrected sub-aperture (WCS) that enabled the use of coronagraphs in high-Strehl (of the order of 90%) regime at a cost of loss of angular resolution. This technique provides a possible optimal solution for the small IWA coronagraphs as the unvignetted sub-aperture is free of the diffraction effects from the secondary and the spider arms.

Using the WCS in conjunction with the 241-actuator Palomar AO (PALAO) at the 5-m diameter Hale telescope, three known planets of HR8799 were detected (Strehl ratio of $\sim 90\%$) including the innermost planet 'd' located at about 2 λ/D with a VVC (Serabyn *et al.*, 2010) using the locally optimized combination of images (LOCI) algorithm.

Project-1640 & PALM-3000 + SDC

P1640 is a high contrast imaging instrumentation installed at Palomar's 5-m Hale Telescope, whose objective is to obtain images and low-resolution spectra of substellar and planetary mass companions across the Y, J, and H-bands. It has an APLC coupled with a microlens based IFS (1.1-1.65 μm for a 10" field) and a post-coronagraph wavefront calibration system (CAL).

In mid-2010, the PALAO system was upgraded to a much higher-order corrective system called PALM-3000 (Dekany *et al.*, 2011, 2013, §1.3.1.2), which provides ExAO correction in the near-IR and diffraction limited imaging in the visible upstream P1640. The ExAO system includes two DMs, one with 3388-actuator for high-order wavefront correction (the "tweeter", which runs at 2 kHz) and the second one is the original PALAO 241-actuator DM for the low-order wavefront correction (the "woofer", which runs at 1 kHz). It also has a separate fast steering tip-tilt mirror, which is used to align image and pupil on the SHWFS (with three user-selectable pupil sampling modes: 64×64, 32×32 and 8×8 sub-aperture). P1640 is used in conjunction with PALM-3000 as a specialized speckle suppression instrument (Crepp *et al.*, 2011). PALM-3000 saw its first light in June 2011.

The recently commissioned Stellar Double Coronagraph (SDC), an advanced coronagraphic relay bench between Palm-3000 and the near-infrared (NIR) imager and spectrograph PHARO (Hayward *et al.*, 2001) has recently validated in the laboratory the concept of (1) the multi-stage vortex coronagraph (MSVC) to improve the attenuation capability of the VVC and (2) the ring-apodized vortex coronagraph (RAVC) to remain insensitive to the center obscuration. SDC has demonstrated an initial contrast of $\sim 10^{-3}$ at $\sim 2\,\lambda/D$ with a MSVC during its first light in 2014 (without using any additional low-order wavefront sensor inside the SDC, Mawet *et al.*, 2014a).

Dekany *et al.* (2013) presents the first exoplanet and disk results with PALM-3000.

1.3.1.3 SCExAO & SEEDS

Subaru coronagraphic extreme adaptive optics system (SCExAO, Jovanovic *et al.*, 2015) is a high contrast imaging instrument of the Subaru Telescope. It compliments SPHERE & GPI scientifically due its location at the summit of Mauna Kea in the Northern Hemisphere. It feeds on the AO of Subaru which is known as AO188 (with a 188-element curvature WFS and DM, Minowa *et al.*, 2010; Guyon *et al.*, 2014) and use Subaru's PI instrument HiCIAO (High Contrast Instrument for the Subaru Next Generation Adaptive Optics, Hodapp *et al.*, 2008) as a science detector.

SCExAO has – a visible PyWFS that measures the high-order wavefront aberrations up to ~ 1600 modes at 3.6 kHz, – a dedicated coronagraphic low-order wavefront sensor to measure low-order aberrations at 1.6 μm and – a 2000-actuator DM to compensate for the measured errors. It also has an active speckle control loop to suppress the residual speckle field. SCExAO is under commissioning stage and currently provides diffraction-limited PSF in the visible and a SR of > 70% in H-band on the post-AO188 wavefront residuals.

SCExAO is equipped with several high performance small IWA coronagraphs ($\sim 1\,\lambda/D$) such as the PIAA, VVC, FQPM, EOPM, Shaped pupil and the PIAACMC (to be delivered in July 2015). It is one of its own kind of an instrument that is very flexible and provides a platform to easily adapt with the cutting edge technologies. I have got the opportunity to perform my thesis research by exploiting the accessibility to several small IWA coronagraphs armed with 2000-actuator DM as a wavefront corrector of this instrument. SCExAO is described in great details in Chapter 3.

SEEDS (Subaru Strategic Exploration of Exoplanets and Disks Survey, Tamura, 2009),

on the other hand, is a survey (120 Subaru nights in 5 years, began in fall 2009) of exoplanets (in wide orbits > 10 AU) and disks with a combination of Subaru-AO188-HiCIAO. The major goals are to search for giant planets (1 M_J < mass <~13 M_J) and protoplanetary debris/disks around ~ 500 nearby massive young stars. SEEDS has made several major discoveries: GJ 758, detection of a companion around sun-like star (Thalmann *et al.*, 2009), a transiting planet on a retrograde orbit around HAT-P-7 (Narita *et al.*, 2009), extended debris disk around a young star HR 4796 A (Thalmann *et al.*, 2011), just to name a few.

1.3.1.4 LBTI & LEECH

The LBT (Large Binocular Telescope, Esposito *et al.*, 2010), located on Mount Graham in Arizona is equipped with two monolithic 8.4 meter primary mirrors, which provides a combined collecting area of a single 11.8 m telescope. LBT is the first system to have corresponding secondary mirrors as the DM itself (672 actuators each), which corrects the atmospheric turbulence at 1 kHz.

The IR light from both sides of the primary mirror is redirected by flat tertiary mirrors to the LBT Interferometer (LBTI), while the optical light goes to two PyWFS on both sides to measure the aberrations (~ 400 modes). LBTAO system is itself an ExAO system capable of providing 80% SR at 1.6 μm. The science light is directed towards a 1 - 5 μm camera, a L/M-band Infrared imager/spectrograph (LMIRcam, Skrutskie *et al.*, 2010). Some of the scientific observations with LBT includes: the first light LBT AO imaging of HR 8799bcde at 1.6 and 3.3 μm (Skemer *et al.*, 2012), the first H-band detection of HR 8799e (Esposito *et al.*, 2013), the discovery of a yellow supergiant eclipsing binary in the dwarf galaxy Holmberg IX (Prieto *et al.*, 2008).

LEECH (LBT Exozodi Exoplanet Common Hunt, Skemer *et al.*, 2014) began in Spring 2013, is LBT's imaging survey to search for and characterize young exoplanets and exozodiacal disks, which compliments other HCI instruments/surveys by observing stars in L'-band (3.8 μm). The uniqueness of this survey is its operating wavelength where the brightness of the gas giant exoplanets are at their peaks and their spectra offers deeper mass sensitivity for intermediate age extrasolar systems. Maire *et al.* (2015) presents the first few results with LEECH/LMIRcam. Recently, a L'-band AGPM vortex coronagraph has been installed on LBTI/LMIRCam and a young A5V star HR8799 has been observed in the context of the LEECH survey (Defrère *et al.*, 2014).

1.3.1.5 MagAO

Magellan Adaptive Optics (MagAO, Morzinski *et al.*, 2014) system is situated at the Las Campanas Observatory on the 6.5m Clay telescope that saw its first light in November 2012. Just like LBT, it uses a modulating PyWFS to measure the wavefront aberrations and a 585-actuator adaptive secondary mirror (controlling up to 378 modes) to provide wavefront correction at 1 kHz to its two science cameras: VisAO, operating from 0.5 - 1 μm and Clio2, operating from 1 - 5 μm.

MagAO, at the verge of becoming a full-fledged ExAO instrument has already started

producing science results, which includes: the high-resolution visible light images of HD 142527 with MagAO's VisAO science camera (Close *et al.*, 2014), discovery of a planetary-mass companion, HD 106906 b (Bailey *et al.*, 2014) and the first-light observations of the Exoplanet beta Pic B (Males *et al.*, 2014).

Recently (May 2015) a vector-APP coronagraph has been installed on MagAO[9].

I present in Fig. 1.19, a summary of the specifications of the ExAO instruments I discussed so far in this section.

1.3.2 Space-based coronagraphs

One of the goal identified in Astro2010/New Worlds (the Astronomy and Astrophysics Decadal Survey, Blandford, 2009) roadmap is the spectroscopic characterization of a habitable planet through direct imaging which is essential to understand the composition and chemistry of the planetary atmosphere. Driven by the success of the Kepler mission, several space missions for the HCI are envisioned and planned. I introduce in Fig. 1.20, four such near future space missions, which will revolutionize our understanding of the exoplanets and evolution of extrasolar planetary systems in coming decades.

These missions include James Webb Space Telescope (JWST, Sabelhaus & Decker, 2004), WFIRST-AFTA (Wide-Field Infrared Survey Telescope-Astrophysics Focused Telescope Assets, Spergel *et al.*, 2013), Exo-C (Stapelfeldt *et al.*, 2014) and ACESat (Alpha Centauri Exoplanet Satellite, Bendek, 2014). These missions aims to look at the exoplanets and the extrasolar environments at different scales.

[9] https://visao.as.arizona.edu/category/press/.

ExAO Instruments	Telescope	Number of actuators in the pupil	WFS	Detector	Maximum loop frequency (kHz)	Coronagraphs	Seeing Wavelength (μm)	Strehl ratio
SPHERE	VLT (8 m)	1400 (17 dead)	Shark-Hartmann	EMCCD	1.3	Classical Lyot, FQPM, APLC	0.45 – 0.95	> 75% in H-band, seeing < 0.8", R = 0 - 9 mag
GPI	Gemini South (8 m)	2000 (4 dead)	Shark-Hartmann	CCD	1	APLC	0.7 – 0.9	89% in H-band
PALM-3K	Palomar (5 m)	3388 (1 dead)	Shark-Hartmann	CCD	2	APLC, MSVC, RAVC	0.4 – 0.9	87% in K-band, median seeing, V mag of 5
LBTAO	LBT (2 x 8 m)	600 each	Modulated Pyramid (400 modes correction)	CCD	1.5	AGPM vector vortex	0.6 – 0.9	Up to 80% in H-band
MagAO	Magellan "Clay" telescope (6.5 m)	585- adaptive secondary mirror	Modulated Pyramid (200 – 400 modes corrected)	CCD	1	Vector APP	0.63 - 1.05	>30% at 0.6 μm 0.5" seeing, R < 8 mag
SCExAO	Subaru (8 m)	1600 (2 dead)	(Non-) Modulated Pyramid (1600 modes corrected)	EMCCD	3.6	PIAA, Shaped pupil, VVC, FQPM, EOPM PIAACMC (soon)	0.6 - 0. 95	> 70% in H-band, moderate seeing, R < 10 mag

Figure 1.19: Comparing the specifications of current extreme adaptive optics system equipped on 5 - 8 meter class ground-based telescope.

Space Missions	Telescope diameter	Coronagraph	IWA	OWA	Bandpass (μm)	Required contrast	Goals	Mission lifetime (years)	Launch
JWST	6.5 m	Band-limited	4 - 6 λ/D	34 λ/D	2.1- 4.6	10^{-6}	Imaging and Spectroscopy of Transiting Exoplanets, EGPs direct imaging around young low mass star	Between 5-1/2 and 10	2018
		3 FQPM	~ 1 λ/D	14, 13.8, 10 λ/D	10.65, 11.4, 15.5				
		Lyot coronagraph	2.9 λ/D	6.9 λ/D	23				
WFIRST-AFTA	2.4 m	Under review	~ 3 λ/D	~ 21 λ/D	0.4 - 1	10^{-9}	Survey of 200 nearby stars, characterize spectra of RV planets, imaging ice, gas giant and Neptune-type exoplanets, imaging debris disk	6	2020 (uncertain)
Exo-C	1.5 m	Hybrid Lyot or PIAACMC or Vortex (under consideration)	~ 2 λ/D	~ 22 λ/D	0.45 - 1	10^{-9}	optical spectra of nearest RV planets, Imaging of Neptunes, super and exo-earths, image circumstellar disks	3 to 5	2024 (uncertain)
ACESat	45 cm	PIAA or PIAACMC	~ 1.6 λ/D	~ 3.8 λ/D	0.4 – 0.7	10^{-8}	Imaging Exo-earths in the HZ of Alpha Centauri system and also characterize circumstellar debris disks	2	2020 (uncertain)

Figure 1.20: Profile of the future space missions envisioned for performing the direct imaging of the exoplanets and circumstellar disks within a few decades.

1.4 Low-order wavefront aberration: an Introduction

In §1.3.1, I have presented several leading ExAO instruments that perform HCI of exoplanets. One of the major obstacle that they face is the lack of efficient control of the wavefront aberrations near the IWA of the coronagraph. These instruments are capable of directly imaging young ($\lesssim$ 100 Myr) substellar companions only at large separations ($\sim$ 10 – 330 AU) (Bowler *et al.*, 2010). Even from space, the Hubble Space Telescope (HST[10]) has imaged only the brightest of the self luminous young gas giants at large angular separations (> 10 AU), previously discovered by 5-10 meters class ground-based telescopes.

The number of IWA-accessible exoplanets that can be imaged goes as IWA^{-3} (volume around the observer within which a certain type of planet is IWA-accessible, Guyon (2011)). To take advantage of the small IWA coronagraphs in order to probe the extrasolar planetary region at < 10 AU, the foremost requirement is to seek an optimal solution to control and calibrate the wavefront aberrations at/near the diffraction limit. The low-order wavefront aberrations are the time dependent wavefront changes that pose problems in HCI for detection near the coronagraphic IWA (Green & Shaklan, 2003; Lloyd & Sivaramakrishnan, 2005; Shaklan & Green, 2005; Sivaramakrishnan *et al.*, 2005; Belikov *et al.*, 2006). This is a challenge even foreseen for future space-based coronagraphs (Krist *et al.*, 2012). In order to directly image a planet in the HZ, it is crucial to gain access to the region around the first couple of Airy rings of the telescope PSF for terrestrial-like exoplanet science (Guyon *et al.*, 2006).

On ground, fast varying phase errors are induced in the wavefront due to the atmospheric fluctuations, optical/mechanical vibrations and telescope pointing motors. However, in space, wavefront errors are caused by thermal distortion, pointing errors and vibrations due to reaction wheels. Not only this, drifts due to temperature variations and the alignment errors also lead to aberrations, which evolve during the exposure time used for making planet detections. As a result, these phase errors introduce low-order aberrations upstream of a coronagraph which leaks starlight around the coronagraphic mask and create a false positive signal. This residual scattered light produces intensity fluctuations, which create slow-varying speckle noise in the final focal plane. If these speckles are not calibrated, potential signal from planet can easily get confused with a speckle (Guyon *et al.*, 2006).

PSF calibration techniques relying on field rotation can calibrate to some extent residual wavefront aberrations, especially static and quasi-static features of the PSF (Marois *et al.*, 2006; Lagrange *et al.*, 2009) but becomes less effective at angular separation smaller than 0.5", where residual speckles are created by low-order aberrations. Due to minimum rotation angle allowable for small angular separations, there is a high probability of compromising the planet signal over the speckle noise.

So it is crucial to – (1) quantify the trade-off between the IWA of a coronagraph and its sensitivity towards the low-order aberrations, and – (2) optimize the post-processing techniques to calibrate the residual of the low-order errors at/near the IWA of the corona-

[10] http://hubblesite.org/newscenter/archive/releases/star/extrasolar-planets/results/100/

graph. However apart from that, one important aspect is to reliably control and calibrate the low-order wavefront aberrations, which is the major reason of the starlight leakage.

In this section, I will focus on how the low-order aberrations degrade the expected performance of small IWA coronagraphs. I will also briefly emphasize on the effects of the high-order wavefront aberrations. Note that the speckle problem is not considered here. In §1.4.1, I will study the effects of low-order errors in a coronagraph by simulating a FQPM. I will then emphasize on the low-order wavefront correction techniques adapted by the existing ExAO instruments and testbeds in §1.4.3. Continuing the efforts of addressing the tip-tilt and other low-order aberrations for the high performance small IWA coronagraphs, I will explain briefly the motivation of this thesis in the context of the HCI in §1.4.4.

1.4.1 Effect of low-order aberrations on coronagraphic PSF

In a post-AO corrected scenario, we consider that the residual phase error ϕ is $\ll 1$ radian of RMS wavefront error. Recalling Eq. 1.11, which represents the electric field $\psi_E(\xi, \lambda)$ at the Lyot plane in a coronagraphic imaging system

$$\frac{\psi_E(\xi, \lambda)}{\psi_0} = (P * \mathcal{F}^{-1}[M])L + i\,(\phi * \mathcal{F}^{-1}[M])L\,, \tag{1.18}$$

where ψ_0 represents the star flux upstream of the coronagraph. Consider a perfect coronagraph without any manufacturing defects. For a perfectly aligned on-axis star at the center of a FPM, the residual diffracted starlight downstream the FPM is rejected completely outside of the geometrical pupil and the electric field is zero inside the Lyot pupil plane. One can then analytically equate the complex amplitude of the first term in equation 1.18, which is independent of ϕ, as $\mathcal{F}[(P * \mathcal{F}^{-1}[M])L] = 0$. The complex amplitude of the electric field of the residual starlight downstream of the Lyot plane can be written as

$$\frac{\psi_E(\xi, \lambda)}{\psi_0} = i\,(\phi * \mathcal{F}^{-1}[M])L\,. \tag{1.19}$$

Equation 1.19 is a linear function of ϕ for small phase errors. Under aberrations, the starlight is mostly scattered inside the pupil and the complex amplitude of its electric field in the interior of the Lyot pupil plane is no more zero. I have studied numerically how phase errors degrade the rejection capability of a coronagraph by simulating their effects on a FQPM coronagraph. I have chosen a FQPM because it is a small IWA phase mask coronagraph which is highly sensitive to phase errors (Lloyd *et al.*, 2003) and makes a good case for studying the effects of the low-order aberrations on such type of coronagraphs. Moreover, FQPM is one of the PMCs that I have studied throughout my thesis.

In Eq. 1.19, I express the phase ϕ over the aperture P using the Noll-ordered Zernike aberrations (Noll, 1976) i.e. increasing radial power order (the n index). Zernike polynomials are a set of orthogonal polynomials (their values change independently of each other) over the unit radius two-dimensional disk. They are widely used to describe the shape of an aberrated wavefront in the pupil of an optical system. And that is why, I expanded the phase error ϕ in terms of Zernike modes as follows

$$\phi = \sum_{i=1}^{\infty} \alpha_i Z_i(x_i, y_i) \,, \tag{1.20}$$

where Z_i's are the Zernike Polynomials defined over the pupil area and α_i is a constant coefficient (RMS amplitude of the Zernike mode Z_i). Below I will present my formulations to evaluate and demonstrate the known problem of low-order aberrations.

1.4.2 Numerical simulation

I have considered the pupil of the Subaru Telesope with central obscuration and spider arms at the entrance of a coronagraphic system shown in Fig. 1.13. At the first focal plane, I assumed a perfect FQPM whose mask function is defined in §1.2.5.3. Compared to the pupil of the telescope, the Lyot stop I simulated has a 8% undersized outer diameter, and a 40% and 20% oversized secondary and spider arms respectively. I have chosen this aggressive design at the cost of reducing the throughput and angular resolution of an off-axis companion in order to mask the scattered starlight diffracted around the edges of the secondary and spider arms. A more detailed simulation of the FQPM (with manufacturing defects) and the corresponding Lyot stop is presented in §2.3.

Figure 1.21 (a) present the non-coronagraphic PSF. The starlight diffracted around the spider arms is very significant. In all the PSF figures, the green circle is at 4 λ/D. Then, I considered a FQPM at the first focal plane in Fig. 1.13. Downstream the FPM, in a re-imaged pupil plane (Fig. 1.21 (b)), the intensity is redistributed due to the FQPM as it diffracts all the starlight outside of the geometrical pupil. Because of the central obscuration and spider arms, the intensity can be seen diffracting around their edges as well. A square pattern in the redistribution of light is noticed due to the geometry of the phase mask (Fig. 1.21 (b)). The obscuration of the Lyot stop also has a square shape to match the pattern of the diffraction. Next, I placed an undersized Lyot stop (Fig. 1.21 (c)) in the beam that masked most of the residual diffracted starlight. The residual coronagraphic field at the final focal plane is shown in Fig. 1.21 (d).

I will now state and illustrate two key facts about the effect of wavefront aberrations on the coronagraph image.

1.4.2.1 Diffracted light at and near the coronagraph IWA

Fact 1. *Low-order aberrations especially pointing errors leak starlight and put the residual near the IWA, which create fake companions/structures (Lloyd & Sivaramakrishnan, 2005). Symmetric aberrations such as focus, spherical create starlight leakage that can imitate putative circumstellar disk whereas asymmetric leakage due to tip and tilt produce decentering of the central source that can mimic an off-axis companion (Mawet et al., 2012).*

Simulation 1

At the entrance of the pupil, I considered $\phi = \alpha_1 Z_1$ (pure tip mode). I created a phasemap of tip mode with an error of 0.5 λ/D and deliberately applied it upstream of

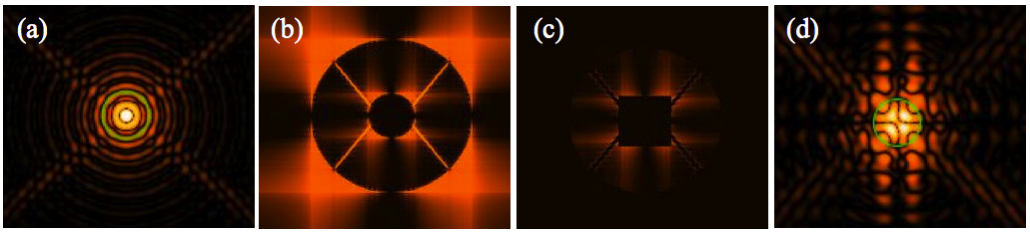

Figure 1.21: Simulated intensity distribution of the FQPM for a realistic pupil with central obscuration and spider arms. (a) Non coronagraphic field with visible diffraction features from spider arms of the entrance pupil. (b) In a re-imaged pupil plane downstream the FQPM, shown is the diffracted intensity outside of the geometrical pupil. Square intensity pattern can be noticed around the secondary and the primary pupil due to the geometry of a FQPM. (c) Coronagraphic pupil plane with a Lyot stop, (d) the final coronagraphic PSF with the phase mask downstream the Lyot pupil plane.

a FQPM. In the re-imaged pupil plane, a significant part of the starlight can be seen diffracted inside the edge of the pupil in Fig. 1.22 (a) and Fig. 1.22 (b), without and with the Lyot stop respectively, contaminating its interior with residual starlight. A shift in the final coronagraphic field downstream the Lyot pupil plane (Fig. 1.22 (c)) can be noticed as compared with the one in Fig. 1.21 (d). The PSF shifts sideways inside the green circle and starlight can be seen scattered over several Airy rings in the vertical direction, illuminating more the right side of the Airy pattern, which is giving an impression of a fake companion.

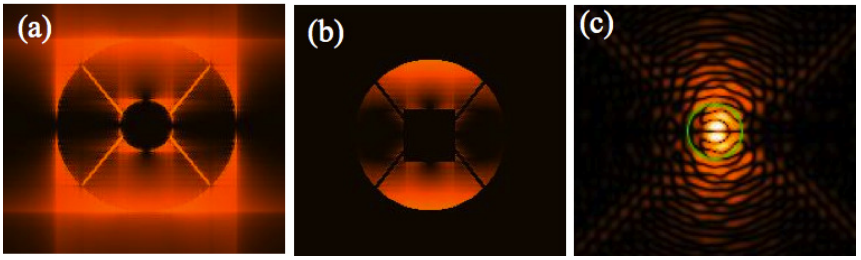

Figure 1.22: Visualization of the intensity distribution in a FQPM coronagraph (following Fig. 1.21), showing the starlight leakage in the presence of tip aberration of 0.5 λ/D. (a), (b), (c) Starlight leak after applying a tip of 0.5 λ/D at the entrance pupil. The leakage is shown downstream the the re-imaged pupil plane without and with Lyot stop and at the final coronagraphic focal plane respectively. A fake companion starts to appear in (c) due to tip aberration.

Simulation 2

I also simulated the attenuation capability of the FQPM for the tip aberration with amplitude values varying between ± 1 λ/D (± 1.58 radian RMS). I considered that at the

entrance of the pupil, the wavefront aberrations are

$$\phi = \sum_{i=1}^{100} \alpha_i Z_1 \ . \tag{1.21}$$

I created 100 Zernike phasemaps with tip mode, such that the first, middle and last phasemap had a tip error of -1 λ/D, 0 λ/D and 1 λ/D respectively. I applied these phasemaps upstream of the FQPM in the simulated optical system shown in Fig. 1.13. For each phasemap, I recorded the corresponding total intensity in the final focal plane. For each error applied, I calculated the attenuation in the intensity of the on-axis source using Eq. 1.15 defined in §1.2.5.2. Then, I calculate the attenuation factor for each tip error applied in the system, which is shown in Fig. 1.23. It is clear from this figure that even for small angles, the attenuation drops quickly and as the pointing error increases, the FQPM performs poorly in attenuating the on-axis starlight. The attenuation with no tip error is 7 times better than the attenuation with a tip error of 1 λ/D upstream the FQPM. This simulation demonstrates that the nulling performance of a coronagraph degrades under the effects of large tip/tilt errors.

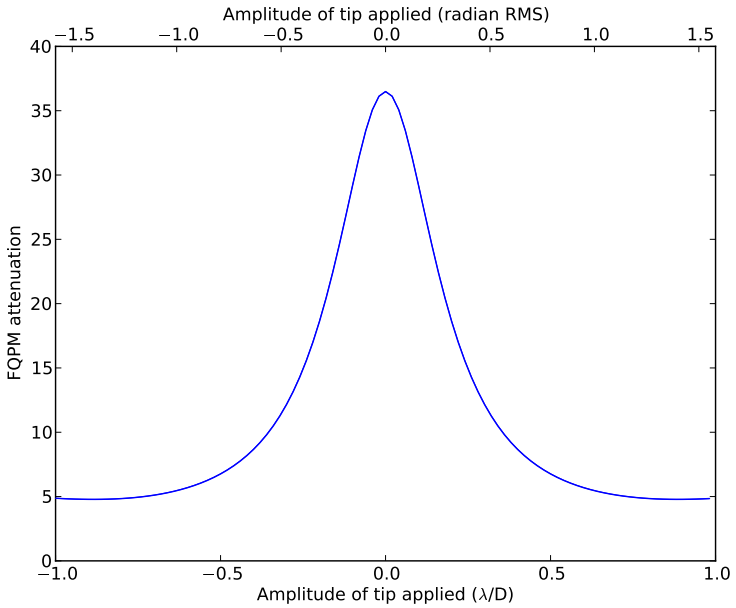

Figure 1.23: On-axis attenuation in the intensity of a simulated FQPM versus applied tip aberrations. Tip phasemap with amplitude varying between ±1 λ/D (± 1.58 radian RMS) is applied in a simulated coronagraphic system shown in Fig. 1.13.

Simulation 3

Next, I studied, $\phi = \alpha_4 Z_4$ (pure focus mode) and $\phi = \alpha_3 Z_3$ (pure oblique astigmatism) individually in the system presented in Fig. 1.13. First, I purposely introduced a Zernike phasemap of focus aberration with an amplitude of 0.4 radian RMS. I show its effect in the final coronagraphic field downstream the FQPM in Fig. 1.24 (a). Similarly the effect of

oblique astigmatism of amplitude 0.4 radian RMS on the coronagraphic PSF can be seen Fig. 1.24 (b). These symmetric aberrations expand the PSF over a large area of pixels and obscure the area around the first couple of Airy rings, thereby limiting the imaging at/near the IWA of a coronagraph.

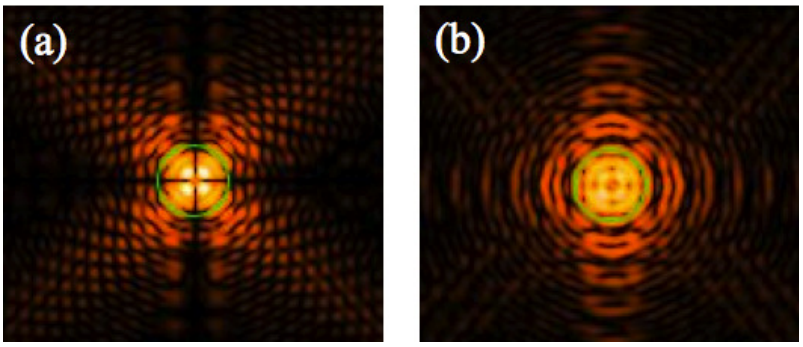

Figure 1.24: Study of FQPM response to (a) the focus and (b) the oblique astigmatism aberrations, after applying them with an amplitude of 0.4 radian RMS individually in to the system in Fig. 1.13 (simulation following Fig. 1.21).

Conclusion

I presented the consequences of the low-order aberrations in the simulations above. I showed that the tip-tilt errors de-centers the PSF behind the crosshair of the FQPM, which can easily mimic a companion (Fig. 1.22) while focus and astigmatism aberrations broaden the PSF core, which can be misinterpreted as a circumstellar feature (Fig. 1.24).

This is actually a fundamental problem because the coronagraphic image corresponding to an off-axis source at a small off-axis separation is similar to the coronagraphic leak produced by low-order wavefront errors. Every signal – either genuine photons from the planet – or leak from the star is transmitted to the final detector plane. That is why small IWA coronagraphs are very sensitive to the low-order aberrations especially pointing errors. Under these effects, starlight leakage problem and the appearance of the fake exoplanetary sources and disks are prone to happen.

1.4.2.2 Diffracted light outside the coronagraph IWA

Fact 2. *High-order aberrations (high Zernike modes) scatters the residual starlight and spread it over a large area around the PSF core, which adds up with the speckle noise (Riaud* et al.*, 2001). The scattered starlight does not only affects the nulling performance of a coronagraph but also hides the signal of a potential planet at large angular separation (multiple IWAs) under speckles. Large amplitude low-order aberrations also contribute to diffracted light at large angular separation (Guyon* et al.*, 2006).*

Simulation 4

To illustrate and quantify fact 2, I simulated the response of the FQPM in a scenario

where the wavefront aberration ϕ is a combination of unknown amplitude of low- and high-order phase residuals in a post-AO corrected wavefront. I performed this test to study how the errors other than just tip-tilt affects the performance of the FQPM. I considered that $\phi = \sum_{i=1}^{200} \alpha_i Z_i$, and simulated a series of 200 phase residuals such that the total phase RMS over the pupil for all the phasemaps is in between 0.5 - 0.7 radian RMS.

I show one of these phasemaps in Fig. 1.25 (a). With this phasemap at the entrance of the optical system in Fig. 1.13, the starlight tends to scatter everywhere inside the re-imaged pupil plane downstream the phase mask as shown in Fig. 1.25 (b).

I also show the coronagrahic field at the final focal plane in the presence of such a phasemap with random low- and high-order errors. Figure 1.25 (c) shows the final coronagraphic PSF when the total phase RMS in Fig. 1.25 (a) is 0.2 radian RMS. The crosshair of the FQPM is still partially visible. However, when the wavefront error is higher as in Fig. 1.25 (d) (0.58 radian RMS here), the crosshair is no more visible due to extra light in the FPM and the starlight scatters in the whole field of view.

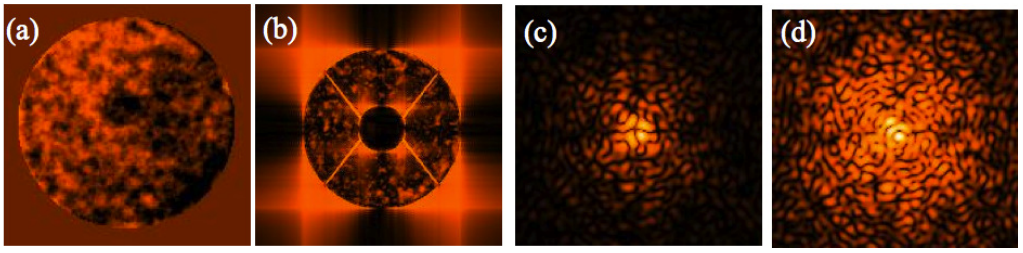

Figure 1.25: Behavior of the FQPM coronagraph under the random high- and low-order phase defects. Here, I studied a post-AO wavefront correction scenario. (a) A phasemap with a random low- and high-order errors. (b) the coronagraphic pupil plane after the phase mask. Residual intensity can be seen distributed inside the pupil. (c), (d) are the final coronagraphic focal plane PSFs (with Lyot stop at the pupil plane), obtained when the phase RMS in image (a) is 0.2 radian RMS and 0.58 radian RMS respectively.

All the residual starlight is scattered everywhere in Fig. 1.25 (d) due to high amplitude of the low- and high-order phase errors. These residuals are spread farther than the IWA, thereby masking the signal from a potential planet by hiding it beneath the speckle noise.

Simulation 5

In this simulation, I studied why the correction of low-order aberrations for more than just tip-tilt is important. To perform this study, I simulated 35 Zernike phasemaps. I applied these phasemaps at the entrance pupil each with an amplitude of 0.1 radian RMS. For each error applied, I recorded the corresponding intensities and measured the starlight leakage by integrating the light scattered within 4 λ/D region around the coronagraphic PSF. I show in Fig. 1.26 (a) that each Zernike mode contributes somewhat equally in the starlight leakage and correcting higher Zernike modes is also important as correcting tip-tilt errors.

Note: I have considered same amplitude for all the Zernike modes. However, in realistic cases, the contribution of tip-tilt in post-AO corrected phase residuals is generally

more than the other modes, where a usual case show lower amplitude for higher number of modes comparatively to the amplitude of the low-order modes.

Correcting higher modes are important because they contribute more in scattering of the starlight at large IWAs. To study this fact, I show in Fig. 1.26 (b), the difference in the intensity of the coronagraphic field with no aberration with that of the field under Zernike aberration. I present the difference only for few Zernike modes. It is clear that the intensity is smeared in a large area around the PSF core and the phase mask performs lower attenuation.

To summarize the simulations, I present the radial azimuthal average profile of the final coronagraphic field under the effects of the phase errors studied in this section. In Fig. 1.27, I present the profile of: – (1) the non-coronagraphic PSF without the FQPM (in black), – (2) the coronagraphic PSF with the FQPM and the Lyot stop (in green). A contrast of more than 5 orders of magnitude is obtained between $1 - 2\,\lambda/D$ with the FQPM. – (3) the coronagraphic PSF (in red) under the effect of the tip aberration studied in Simulation 1. The contrast degraded almost by a factor of 10 at around $1.5\,\lambda/D$ and between a factor of 10 to 15 for region beyond $5\,\lambda/D$ and, – (4) the non-coronagraphic PSF (in cyan) simulated in Fig. 1.24 (d) under the low- and high-order phase defects of a post-AO wavefront scenario studied in Simulation 4. Due to high-order errors, the starlight is scattered farther out and the contrast degrades by almost 2 order of magnitude beyond $5\,\lambda/D$. This figure also shows that not only high-order errors, but the large amplitude of tip aberration (in cyan) contaminates the region beyond the IWA ($\sim 1.5\,\lambda/D$) of the FQPM.

I showed in my simulations that the FQPM coronagraph is highly sensitive to low-order aberrations. *Riaud* et al. *(2001) states that for the FQPM, the nulling performance decreases as the square of the amplitude of the guiding errors.* For further analytical and numerical studies of the leakage problems in FQPM with different pupil shapes and for factors which affects the intensity of a companion, reader may refer to Lloyd *et al.* (2003); Riaud *et al.* (2001).

The assertions stated in Fact 1 & 2 are fundamental limits to the performance of small IWA coronagraphs. Not only the FQPM, but all high performance small IWA PMCs are affected by the tip-tilt and other low-order aberrations. Lyot-type coronagraph is also sensitive to this, but less so, especially if the opaque focal plane mask is much larger than the telescope diffraction limit. The detailed analytical study of tip-tilt errors in a Lyot-type, the Band-limited and the PIAA coronagraphs can be found in Green & Shaklan (2003); Lloyd & Sivaramakrishnan (2005) and Belikov *et al.* (2006); Pueyo *et al.* (2011) respectively. For other coronagraphs, reader may refer to Guyon *et al.* (2006).

Vector Vortex Coronagraph (VVC)

I show an experimental example of tip-tilt problem for another high performance small IWA coronagraph, the VVC. Figure 1.28 shows the effect of tilt aberration on the final coronagraphic field of a VVC. The images shown are the laboratory data I have processed (see Chapter 4): I present in Fig. 1.28 (a), a properly aligned coronagraphic PSF of the VVC at the final focal plane under no external aberration applied. This image is obtained

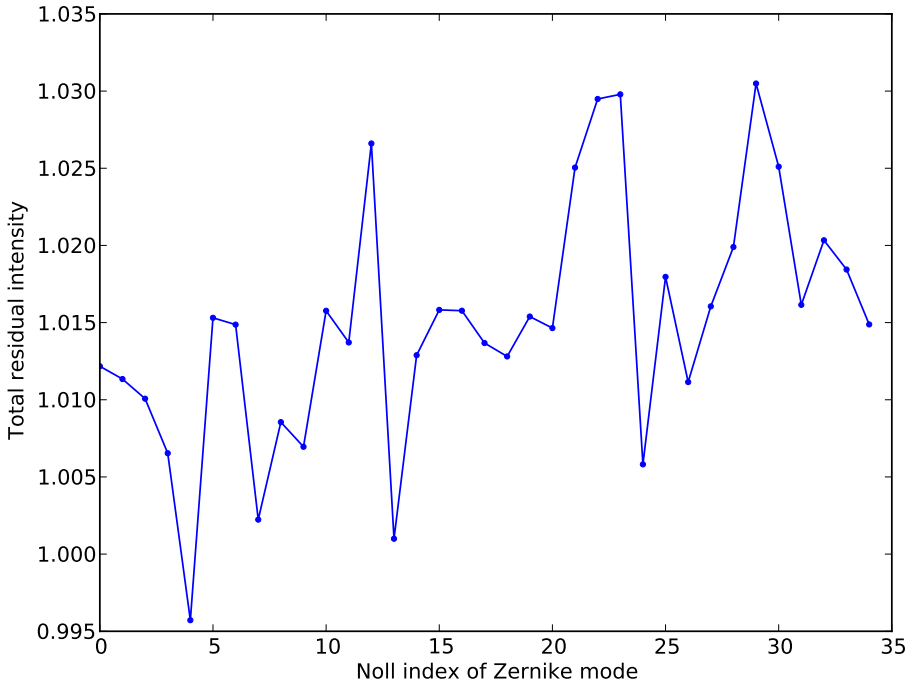

(a)

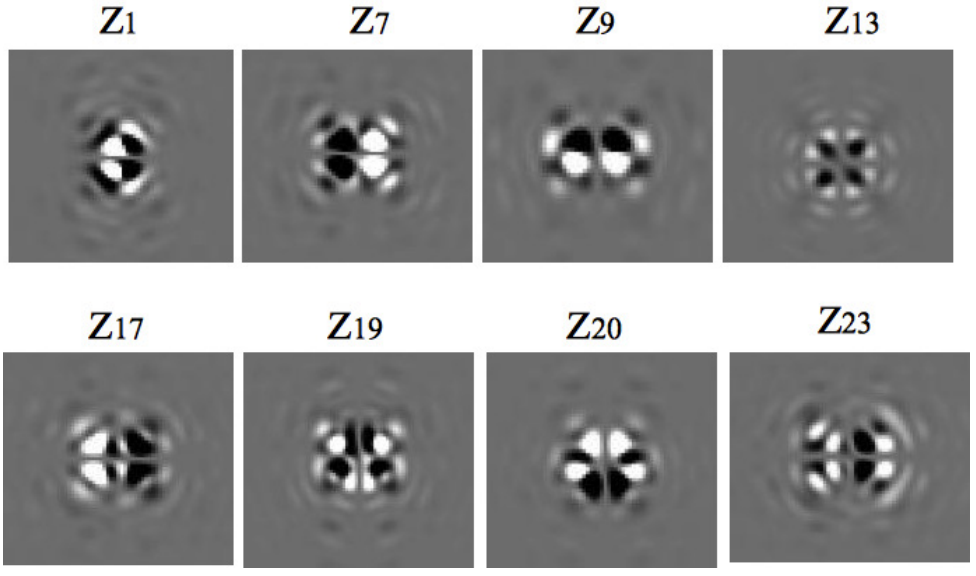

(b)

Figure 1.26: (a) Residual intensity integrated within 4 λ/D region at the final coronagraphic focal plane of the FQPM showing equal contribution of the Zernike polynomials to the leakage of starlight. Note that the Zernike phasemap with an amplitude of 0.1 radian RMS is applied individually into the system in Fig. 1.13. (b) Presents the difference between the coronagraphic field with no aberration and the field in presence of the Zernike aberration studied individually. These images show the fact that higher number of Zernike modes contributes more in the scattering of the starlight well outside the coronagraph IWA. *These images are at the same brightness scale.*

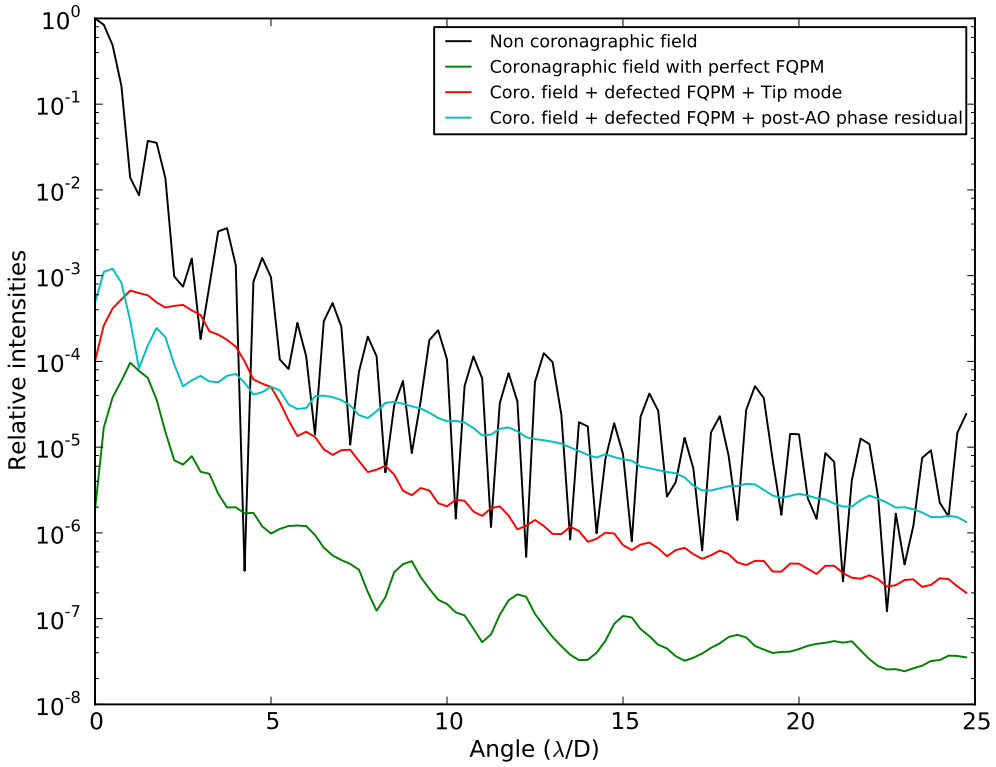

Figure 1.27: Radial azimuthal average profile of a FQPM in a simulated coronagraphic system presented in Fig. 1.13. The profile of a non-coronagraphic field is presented in black. The rest of the profiles are with a simulated FQPM coronagraph. The one in green is with no phase defects. I compare the nulling performance of the FQPM under a tip mode of 0.5 λ/D (in red) and under a realistic phase residual of a post-AO corrected wavefront (in cyan). Significant contrast degradation with a FQPM occurs under the low- and high-order phase errors.

with vector vortex at the first focal plane and the corresponding Lyot stop in the re-imaged pupil plane. In §3.5.2 of Chapter 3, I explain in detail how I obtained aligned images with a VVC like the one shown in Fig. 1.28 (a).

In the next step, I, applied a tilt of 150 nm RMS (0.1 λ/D at 1.6 μm) upstream of the vector vortex mask and show in Fig. 1.28 (b), the aberrated final field at the focal plane. Due to the injection of a deliberate tilt error at the entrance pupil, the PSF is no longer aligned with the FPM and starlight leak is quite prominent, illuminating the right side of the Airy disk. The intensity illumination at the coronagraphic pupil plane is also presented in Fig. 1.28 (c). Uneven intensity illumination can be seen around the primary and the secondary of the pupil due to starlight leakage. A circular intensity pattern can be noticed under the secondary. This is the diffracted starlight due to the VVC around a dead actuator. Significant part of the scattered starlight is fairly visible inside the geometrical pupil.

Just like the FQPM coronagraph, VVC is also very sensitive to the low-order aberra-

tions. A small error in the alignment of the on-axis source with these masks at the focal plane can create large variations of the residual starlight inside the geometrical pupil.

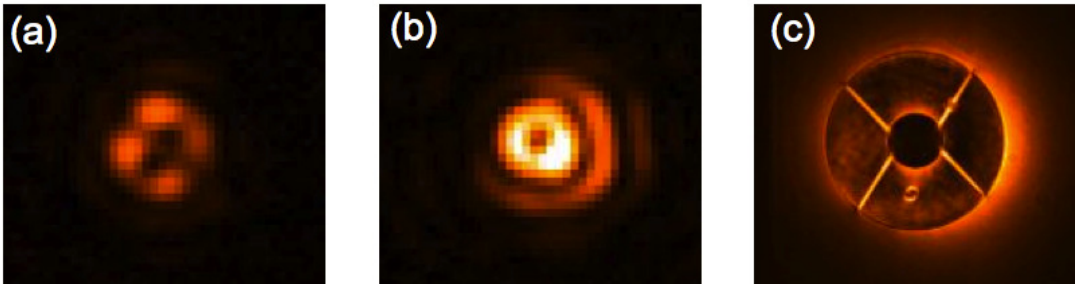

Figure 1.28: Effect of tilt aberration on the coronagraphic PSF of a VVC in the laboratory. a) Final PSF downstream of a VVC at the focal plane under no external aberration applied. b) A tilt of 150 nm RMS is applied upstream of the FPM, which spills the starlight over first few Airy rings. c) Uneven intensity distribution at the coronagraphic pupil plane of a VVC under tilt aberration.

Fact 3. *Sensitivity to low-order aberrations goes opposite to the IWA of a coronagraph. Guyon* et al. *(2006) demonstrated in their linear algebra based coronagraphic model that the small IWA coronagraphs (such as the FQPM and the VVC) are highly sensitive to the pointing errors and other low-order modes.*

This is true for some small IWA PMCs such as the VVC. Mawet *et al.* (2005a); Guyon *et al.* (2006); Jenkins (2008) show that the attenuation sensitivity of the VVC towards the pointing errors and other low-order aberrations (t) is proportional to t^l, where l is the topological charge. The VVC with high topological charge is less sensitive towards the low-order aberrations. However, while the sensitivity is reduced, the IWA is increased.

Figure 1.29 shows simulated contrast sensitivity versus applied aberrations (tilt, focus, astigmatism, coma, trefoil and spherical with amplitude between 3 λ/D to 4 λ/D) for the topological charge l of 2 (Fig. 1.29 a)) and 8 (Fig. 1.29 b)). These graphs are presented to give an idea about convincing contrast enhancement (for low amplitude of aberrations) with a high topological charged VVC as compared with the low charged one (Mawet *et al.*, 2010b). For $10^{-3}\lambda/D$ tip aberration, the raw contrast of charge 8 vortex is 10 orders of magnitude smaller than the charge 2 vortex, which means it provides more immunity towards the aberration than the charge 2 vortex.

The decreased sensitivity to the low-order aberrations at the cost of IWA also applies to classical Lyot-type and PIAA-type coronagraphs. The size of the FPM plays an important role. For small occulting mask (same order of magnitude as the FWHM), which is equivalent of small IWA amplitude coronagraphs, the pointing errors affect their performance because of increased coronagraphic leaks. An aggressively undersized Lyot stop can be used to mask the scattering of starlight due to leaks but at the cost of a loss in angular resolution and throughput. For larger masks (few widths of the Airy disk), the coronagraphs is less sensitive to tip-tilt aberrations because the leaks are blocked in the focal plane. However, the occultation of the star and its immediate surroundings by a larger

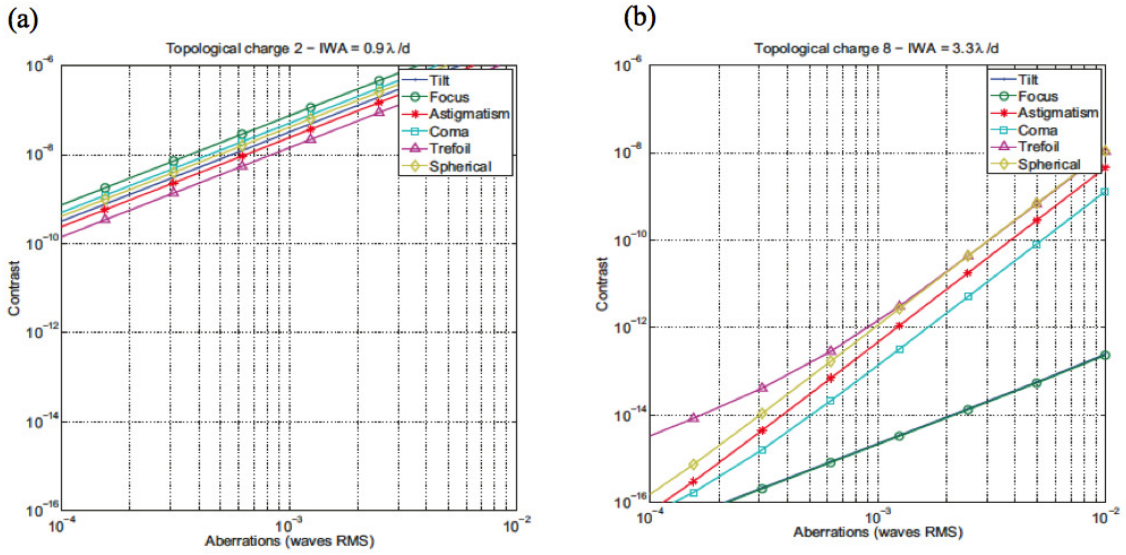

Figure 1.29: Low-order aberrations versus the contrast degradation of the VVC for two topological charges a) 2 and b) 8. The higher the charge, the more immune the VVC is towards the pointing errors (Mawet *et al.*, 2010b).

mask limits the detection probability of a potential candidate at small angular separations.

1.4.2.3 Conclusion

In my simulations, I assumed $\phi \ll 1$ radian RMS, which is generally the level of phase residuals left uncorrected in the wavefront by ground-based AO systems. I showed how the starlight attenuation capability of a small IWA coronagraph degrades for phase errors of 0.2 radian RMS presented from Fig. 1.21 to 1.27. Low-order phase errors are the dominating aberrations with most jitter, as vibrations and telescope pointing can easily induce large tip-tilt errors, which spills most of the residual starlight at small IWAs. However, I also presented in Fig. 1.26 that for the Zernike errors other than tip, tilt, focus and astigmatisms, the correction of these higher number of modes is equally important in order to prevent scattering of starlight over regions near or beyond the IWA.

So, even after the correction of the atmospheric turbulence by the AO system, the uncorrected residuals of low-order wavefront aberrations scatter the starlight in the region of science interest, particularly at small IWA where there is more probability of finding a planet at small angular separation. Also, the astrometry with coronagraphs become difficult as the leaked starlight becomes brighter than the signal from a faint source surrounding it, directly inducing errors in the astrometry of a detected companion (Digby *et al.*, 2006). Therefore, a second stage optimal control of low-order errors is required especially for high performance coronagraphs behind the AO system. This second stage control ensures that during long observations, the starlight can be positioned to within sub milliarcsecond precision of the phase mask center to avoid false interpretation of fake sources as the possible companions.

Likewise, this problem will pose challenges on the nulling performance of the coro-

nagraphs on-board next generation future space-based telescopes. Although, there is no atmospheric turbulence problem in space, their performance will depend on the level of pointing accuracy that can be achieved in order to counteract the effects of low-order aberrations on the final images on the detector. Also, low-order wavefront drifts in space are caused by the rigid body drift of individual optical elements due to thermal settling and vibrations due to reaction wheels (1 - 100 Hz) in a space telescope (Krist *et al.*, 2012).

So far, I have discussed that low-order wavefront aberrations are a major problem for HCI. However, what is the tolerable amount of tip-tilt residuals for a particular system? What is the criteria for the tip-tilt jitter to not be the limiting factor in the raw contrast performance?

Guyon *et al.* (2006) states that for small IWA coronagraphs, the final coronagraphic performance is fundamentally set by the angular size of the star. The requirement for control of tip-tilt is equal to the stellar angular size. If the stellar angular diameter is assumed to be 1 mas (Sun-like star at 10 parsec) then the level of residual tip-tilt jitter should be reduced down to its angular radius (0.5 mas) in order to avoid being dominated by tip-tilt jitter errors. If the residual tip-tilt jitter is larger than the stellar angular size, then the artifacts created by the starlight leakage can be misinterpreted as a planet.

Guyon *et al.* (2006) further states[11] that the allowable amount of tip-tilt jitter is a function of telescope diameter and is different for ground- and space-based telescopes. For the system to be limited by the stellar angular size, the jitter is set by the required level of scattered light in the coronagraphic image. To detect a planet, if present at the same raw contrast level as the coronagraphic leaks (for SNR=10), the tip-tilt contribution needs to be calibrated to $\sim \frac{1}{10}$ of the level of scattered light (intensity).

Assuming that the complex amplitude of the coronagraphic leaks at the final focal plane scales linearly with small tip-tilt errors occurring upstream of the FPM then the *leaked intensity* $\propto$ *(small) tip-tilt error*^{2}. With this assumed quadratic law between coronagraphic leaks and small pointing errors, the calibration in the image to $\frac{1}{10^{th}}$ of the coronagraphic leaks due to stellar angular diameter requires tip-tilt calibration to at most $\frac{1}{\sqrt{10}}$ of the stellar angular radius.

So for a stellar angular radius of 0.5 mas (Sun-like star at 10 parsec), the tip-tilt must be calibrated to 0.17 mas. This case is applicable for observations only from space.

From ground, assuming $\sim$ 0.15 mas as the stellar angular radius of a M spectral type star at 10 parsec, the tip-tilt error for ground-based coronagraphs then must be calibrated to 0.05 mas level provided that the tip-tilt variations are the only source of errors. Based on this assumption, tab. 1.1 summarizes the level of pointing jitter and calibration required as a function of diameter of the ground- and space-telescopes so that detection of a companion around a M-like and sun-like star at 10 parsec respectively is limited only by the stellar angular size.

For my research, I have worked on controlling the low-order aberrations (in Near Infrared) for the SCExAO instrument, which is installed on the 8.2-meter class ground-based Subaru telescope. Therefore, on the basis of the assumption presented in the third

[11] https://exep.jpl.nasa.gov/files/exep/Guyon%20Milestone%20WP%202%20Final%20Signed%20CR%202011.pdf

Table 1.1: Assuming the detection of a planet is limited by stellar angular size, this table summarizes the allowable pointing jitter and calibration requirement as a function of telescope diameter.

Telescope diameter (meters)	**Allowable tip-tilt jitter (RMS)**	**Tip-tilt calibration**
2 (Space at λ = 0.5 μm, G-type)	0.5 mas = 0.0097 λ/D	0.17 mas = 0.0032 λ/D
4 (Space at λ = 0.5 μm, G-type))	0.5 mas = 0.0194 λ/D	0.17 mas = 0.0065 λ/D
8 (Ground at λ = **1.6 μm**, M-type))	0.15 mas = **0.0036** λ/D	0.05 mas = **0.001** λ/D
30 (Ground at λ = **1.6 μm**, M-type))	0.15 mas = **0.014** λ/D	0.05 mas = **0.004** λ/D

case of Tab. 1.1, I will characterize the performance of the solution implemented on SCExAO to deal efficiently with the low-order wavefront aberrations. I will show that achieving a pointing accuracy of 0.0036 λ/D for a 8 m class telescope on ground is extremely difficult as the other factors such as fast varying components of the uncorrected turbulence and the excitation of vibrations due to telescope motors constantly degrades the expected performance of the low-order control system.

1.4.3 State of the art at small IWA

In the previous section, I have presented a brief summary on why and how the low-order wavefront aberrations pose a hurdle and degrade the expected performance of coronagraphs. Before describing my contribution in the vastness of the field, I will first summarize the efforts of various testbeds and instruments on the ground that have dealt (or are dealing) efficiently with the problem of pointing errors and other low-order wavefront aberrations.

Note: I will highlight the development and the implementation of low-order wavefront sensing and correction techniques dedicated only for a coronagraphic purpose. So, I will only focus on the control of the low-order aberrations on the AO corrected wavefront. For more information on the ExAO capabilities of the testbeds/instruments for example the high-order wavefront control and speckle suppression techniques, reader may refer to the publications mentioned in §1.3.1.

Before the era of AO systems, the very first instrument that stabilized the stellar light at the center of a FPM was the coronagraph of Bernard Lyot (Lyot, 1932). The father of coronagraphy, *Bernard Lyot*, used a reflective FPM in his instrument (label "JB" in the schematic diagram of Fig. 1.30) to reflect the unused solar light completely outside of the telescope tube "*G*". Though, he used a reflective mask mostly to guide the solar light out of the tube in order to avoid heating the air inside of the tube. This way he prevented the images to get affected by the local turbulence inside the telescope. The first coarse alignment of the solar light falling on the reflective FPM was probably done manually by looking at the symmetry of the image of the sun on the FPM.

Today, almost all the coronagraphic instruments/testbed use the starlight rejected by the coronagraph to provide the control of the tip-tilt and other low-order aberrations. Below

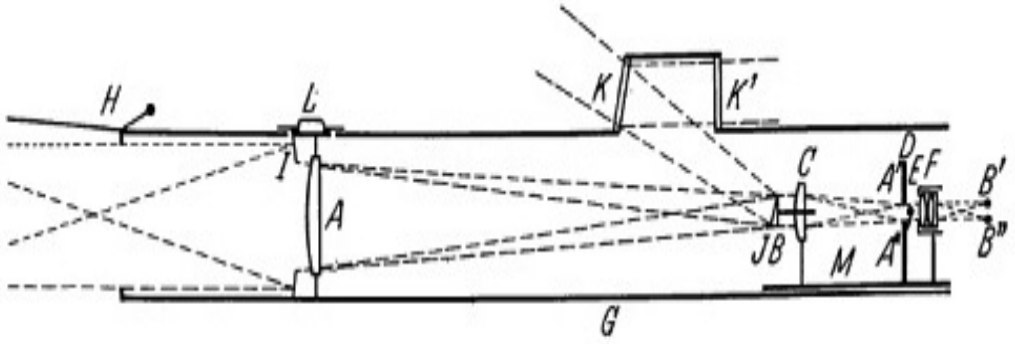

Figure 1.30: Schematic optical diagram of the coronagraph of Bernard Lyot in 1931 (Lyot, 1932) showing a reflective FPM (labelled as "*JB*").

I grouped the techniques implemented by the instruments by the number of modes that they addressed/address in their systems.

1.4.3.1 Correction of tip-tilt errors only

Lyot Project

The Lyot project (Oppenheimer *et al.*, 2004) was the first ExAO and coronagraphy combined project, which was developed not only to survey nearby stars but also to test advanced concepts in extremely high contrast imaging. The Lyot project coronagraph fed on the output of the US Air Force 3.63-m Advanced Electro-Optical System (AEOS, Roberts & Neyman, 2002) telescope in Maui, with an AO system equipped with a 941 actuator DM. They used an optimized Lyot coronagraph with an occulting FPM of diameter 4 λ/D (0.35"in H band). The system included an active pupil alignment and a high speed tip-tilt control loop (Fig. 1.31 (a)) that compensated the image motion.

The FPM they used was a diamond turned flat mirror (2 inches) with a hole of diameter 334 μm at its center. The starlight that transmitted through the hole was used to close the tip-tilt control loop. At the telescope conjugate plane, a Lyot stop was situated. This Lyot stop was a reflective metal mirror, which was placed at an angle of 6° that reflected the starlight from the regions obscured by the Lyot stop. This starlight was reflected into a Pupil Cam, which monitored the alignment of the Lyot stop relative to the telescope pupil. The Lyot stop was also mounted on a rotation stage in order to precisely match the angle of the spider arms with that of the telescope. Figure 1.31 (b) shows the reflective Lyot stops.

As shown in Fig. 1.31 a), the first stage of the tip-tilt loop was a fast steering mirror (FSM) that ensured the alignment of the star with respect to the occulting stop. Four lenslets situated on a fiber head behind the FPM fed the star light that passed through the mask's hole to photon counting devices (avalanche photodiodes). The position of the star relative to the occulting mask was determined from the centroid of the counts. The alignment of the star was then adjusted accordingly by altering the angle of the FSM at a rate of 1 kHz. The position of the occulted star with respect to the mask hole was inferred by moving the lenslets, which was mounted on an xy motorized stage parallel to the mask

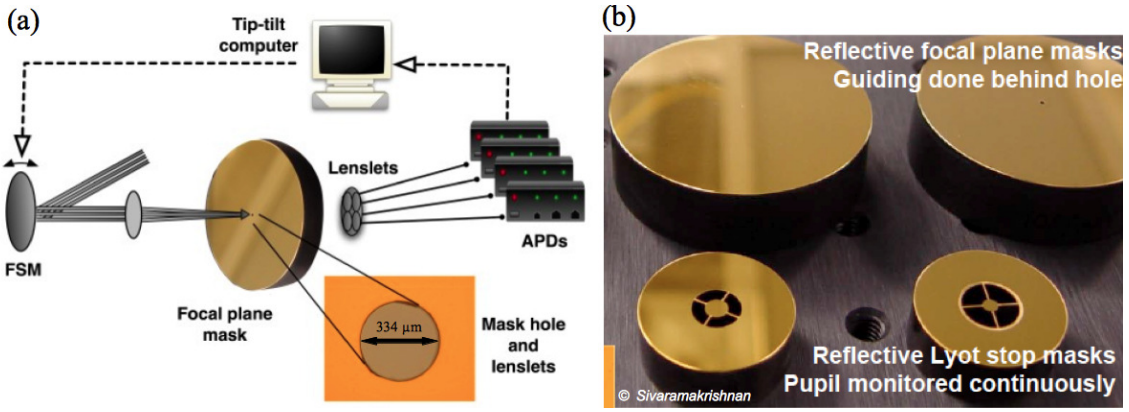

Figure 1.31: a) Tip-tilt control loop diagram on the Lyot Project. Image centroid method is used to infer the star position with respect to the occulting mask. b) Reflective Lyot stops. The starlight blocked by the Lyot stop is reflected toward a Pupil camera for the stop-to-telescope pupil alignment (Digby *et al.*, 2006).

plane. The FSM provided a precision alignment with 3 mas resolution with no significant jitter from the star (Digby *et al.*, 2006).

For recent results[12] on the survey of 86 stars from 2004 to 2007, refer Leconte *et al.* (2010). The Lyot project was one of the initial efforts to perform coronagraphy on an AO corrected beam (apart from Beuzit *et al.* (1991, 1997)) and the first instrument to demonstrate tip-tilt control on-sky. However, the instrument lacked an active alignment of the star with better accuracy and refinement. The project was used between years 2003 and 2007 at the AEOS Telescope and later it was decommissioned and several of its parts were recycled to build the instrumentation for Project 1640, which is described below.

Project-1640 (§1.3.1.2)

The P1640 setup is similar to the Lyot project. A reflective occulting mask of diameter 370 mas (5.37 λ/D at 1.65 μm) is placed at the focal plane. The star light that passes through the hole (reference beam) enters the CAL unit, which is then re-imaged onto a quad-cell sensor. The rest of the blocked starlight reflected off the FPM is split, of which 20% of the light passes again to the CAL unit and the rest is allowed to form a pupil image at the Lyot stop. CAL is designed to measure wavefronts with a precision of 1 nm which actually consists of a small Mach-Zehnder phase-shifting interferometer that measures the wavefront aberrations (at 1.65 μm, same as the science wavelength) by interfering the starlight passing through the hole of the FPM (reference beam) and 20% of the star light rejected off the FPM.

The stellar image is aligned on the quad-cell sensor using a centroiding algorithm in conjunction with a proportional-integral-derivative (PID) control loop which drives the fast-steering mirror (FSM) to compensate for the pointing errors. FSM is updated at a 1 kHz frequency to maintain the position of the star at the center of the FPM. A residual image motion of less than 5 mas per minute can be achieved on the stars with magnitude of 6 and 7 (Hinkley *et al.*, 2011).

[12] http://www.lyot.org/results/

1.4.3.2 Correction of low-order modes more than just tip-tilt errors

Woofer of GPI (§1.3.1.1)

GPI uses a reflective hard-edge FPM ($\sim 5\ \lambda/D$) that also has a hole at its center. The starlight that passes through the hole, enters a CAL unit[13], which has two WFSs: – a near-infrared low-order 7×7 SHWFS low-order wavefront sensor (LOWFS) that maintains the star at the center of the FPM hole and – a high-order Mach-Zehnder interferometer for mid-order spatial frequencies correction. The starlight which is reflected off the FPM enters the science path. The CAL unit is actually an interferometer system which interferes on-axis light passing through the FPM with a portion of the reflected off-axis light in order to reconstruct the post-coronagraph wavefront and generate reference centroid offsets that are sent to the AO control loop.

GPI's LOWFS measured 14 Zernike coefficients (7 subapertures are sampled across the pupil) using the wavefront reconstruction algorithm based on a standard vector matrix multiplier approach in the laboratory. The wavefront slopes measured are 72 in total. The 14 Zernike coefficients representing the wavefront as measured by the LOWFS are converted into a 48x48 phase grid and then applied to the high-stroke 11-actuator diameter piezo DM ("woofer") to compensate for measured aberration at 0.1 Hz. Active optical area of LOWFS DM is 9 actuators across the pupil. For GPI's observations in coronagraphic mode, LOWFS is one of the component that sets the limit on allowed brightness in H-band (maximum and minimum brightness is $m_H = 1.0$ and 9.0 respectively). The major limitation with GPI LOWFS is the use of the SHWFS itself as the sensor has low sensitivity towards the low-order aberrations.

Hartung *et al.* (2014) demonstrates the correction of the NCPAs down to < 5 nm RMS for spatial frequencies < 3 cycles/pupil under simulated turbulence. With their on-sky commissioning test, a residual wavefront error of 120 nm RMS is obtained due to the impact of the dominating vibrations. However, by implementing a LQG algorithm in the AO system, they have demonstrated on-sky corrections of common-path pointing vibrations at 60, 120 and 180 Hz to under 1 mas per axis for tip-tilt residuals and a reduction of focus aberration down to 3 nm RMS wavefront error at the 60 Hz peak (Poyneer *et al.*, 2014).

Coronagraphic low-order wavefront sensor (CLOWFS)

Guyon *et al.* (2006) has introduced the idea of re-imaging the unused starlight which is blocked by the FPM and use it to infer the amplitude of the low-order aberrations from the coronagraphic leaked intensities. Guyon *et al.* (2009) presents the principle of a coronagraphic low-order wavefront sensor (CLOWFS), which uses this concept of reusing the blocked starlight for the sensing of the low-order wavefront aberrations. Figure 1.32 presents the optical layout of the CLOWFS with a PIAA coronagraph.

As shown in Fig. 1.32, CLOWFS light is extracted by a dual-zone FPM placed after the PIAA optics. The central part of radius $r1$ of the FPM (total radius of $r2$, fixed by the IWA of the coronagraph) is opaque, surrounded by a reflective annulus of $r1 < r < r2$. As PIAA strongly apodize the beam, most of the starlight is blocked by the opaque region, al-

[13]The Calibration systems for Project-1640 and GPI were developed in parallel and share the same fundamental design.

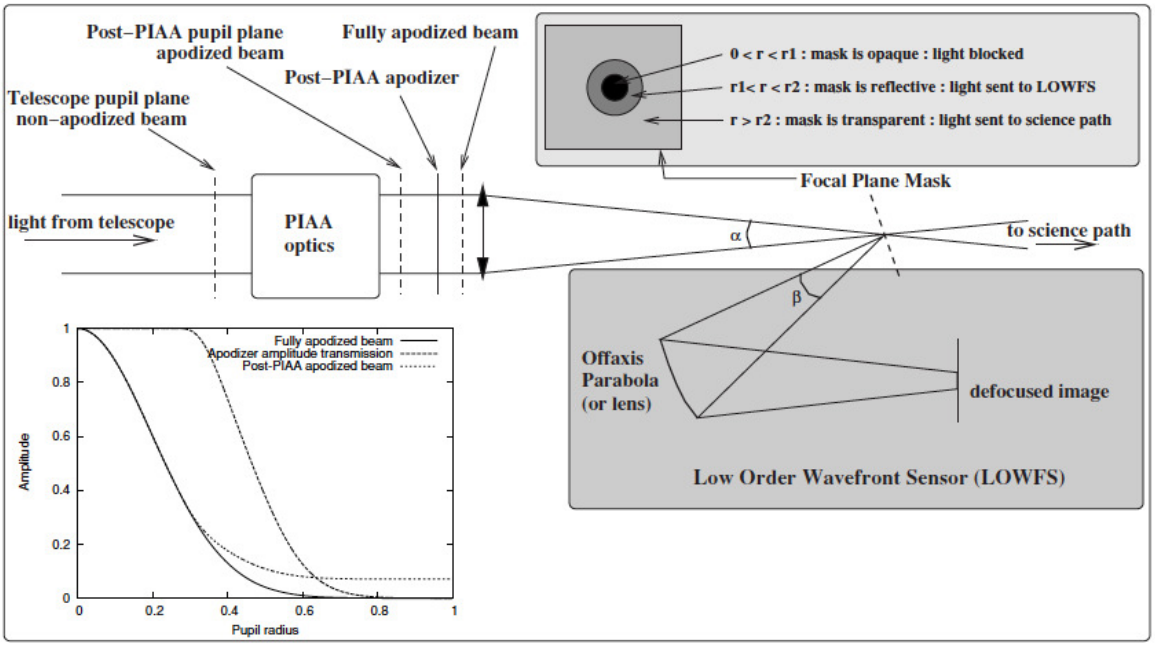

Figure 1.32: Optical layout of CLOWFS system shown with a PIAA coronagraph. Figure courtesy of Guyon *et al.* (2009).

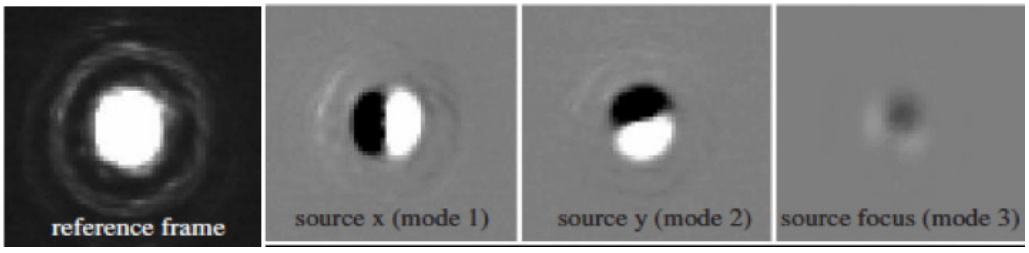

Figure 1.33: (Left to Right) Measured CLOWFS reference image and influence function for the tip, tilt and focus mode. Figure courtesy of Guyon *et al.* (2009).

lowing only a fraction of the total light to be reflected by the reflective annulus. For small wave front aberrations ($\ll 1$ rad), this reflected CLOWFS image produces large intensity signals, which can then be decomposed into the linear combination of low-order wavefront modes to be measured without requiring accurate calibration of either the detector or optical elements. This technique is free of NCPAs.

CLOWFS can measure modes more than just tip-tilt. However, for centro-symmetric aberrations such as focus and spherical aberration, a single CLOWFS image can recover the amplitude of these modes but not their sign. That is why a defocus (should be $<$ 40 radian peak to valley to avoid crosstalk) is introduced at the CLOWFS focal plane, which removes this sign ambiguity. The importance of defocus in CLOWFS image is discussed in detail in §2.3.1.2.

Figure 1.33 (left) image shows a defocused reference image of CLOWFS which is reflected off the dual-zone FPM. Prior of decomposing this reference image on a linear basis of modes, first step is to measure the linear response of the sensor by deliberately

introducing aberrations in the coronagraphic system and then using these responses to decompose CLOWFS reference image in a linear sum of aberrations. Such responses of the sensor to tip, tilt and focus mode is shown in Fig. 1.33. The procedure to acquire the response of the sensor prior of measuring the modes is explained in §2.3.2 in the context of the Lyot-based low-order wavefront sensor (LLOWFS) which uses similar principle to measure low-order wavefront aberrations.

CLOWFS technique allows high sensitive measurement of low-order aberrations as plenty of star light is made available by the FPM for sensing. Guyon *et al.* (2008, 2009) demonstrated the measurement of 5 Zernike modes with a pointing stability of $10^{-3}\lambda/D$ for a PIAA coronagraph. CLOWFS technique was also implemented on SCExAO, Guyon *et al.* (2010a) demonstrated 2×10^{-7} raw contrast in monochromatic light at 1.65 λ/D separation with a $10^{-3}\lambda/D$ closed-loop pointing control.

The Exoplanetary Circumstellar Environments and Disk Explorer (EXCEDE, Belikov *et al.*, 2014; Lozi *et al.*, 2014) testbed at NASA Ames and the HCIT at JPL have also implemented the CLOWFS to sense pointing errors using the rejected starlight reflected by the FPM. With the use of PIAA coronagraph, residuals of 10^{-3} λ/D in air and 10^{-4} λ/D in vacuum for the tip and tilt modes have been demonstrated in closed-loop in the laboratory operation at NASA AMES and JPL respectively.

The disadvantage of CLOWFS is that it can not be implemented with PMCs due to diffractive nature of the phase masks. Moreover, the performance of CLOWFS depends on the stability of the reference image and the calibration frames that CLOWFS has to acquire in advance to measure the response of the sensor to low-order modes before estimating the unknown errors in the wavefront.

Zernike wavefront sensor (ZWFS)

It is a sensor that is based on the concept of imposing a phase-shift to the core of the PSF by means of placing a static $\pi/2$ phase plate at the center of the opaque FPM. This allows the measurement of the wavefront errors from interference between the abberated wavefront and the reference wavefront generated by a phase plate (Dicke, 1975). ZWFS directly measures the phase of the electric field as it converts each phase error into measurable amplitude error.

The disadvantage is that any noise source that generates intensity measurement error will lead to the erroneous estimation of the phase in the input pupil. To avoid inaccuracy in the measurements, the static phase shift in the PSF was replaced by a dynamic and variable phase shift in (Wallace *et al.*, 2011) that allowed the intensity images to be demodulated in such a way that the phase and amplitude of the electric field were determined independently. This technique has been analyzed both with Fourier and Zernike modal base decomposition of the aberrated wavefront. In the laboratory at the Caltech Submillimeter Observatory, sensitivity up to 25 Zernike terms has been confirmed. Wallace *et al.* (2011) states that though the sensitivity analysis for both the Zernike aberrations and Fourier modes indicates some insensitivity to low-order modes but their knowledge can be used in post-processing to recover the low-order signals.

Static ZWFS is currently envisioned as a dedicated LOWFS for the future space telescope WFIRST-AFTA.

1.4.3.3 Other techniques

Differential tip-tilt sensor (DTTS) §1.3.1.1

SAXO is the ExAO system of the SPHERE instrument. A schematic description of its ExAO loops is shown in Fig. 1.34 (Petit *et al.*, 2014), which comprises of four main loops. The main AO loop (1.2 kHz) has a 41×41 actuators DM to compensate for the high-order modes and an Image Tip-Tilt Mirror (ITTM, at pupil plane) to correct for the low-order modes of the atmospheric turbulence and common path defects. It has a 40×40 visible SHWFS to measure the atmosphere and the common path phase perturbations. A slow 1 Hz Pupil TT Mirror (PTTM) is used to correct for the pupil shifts (telescope and instrument).

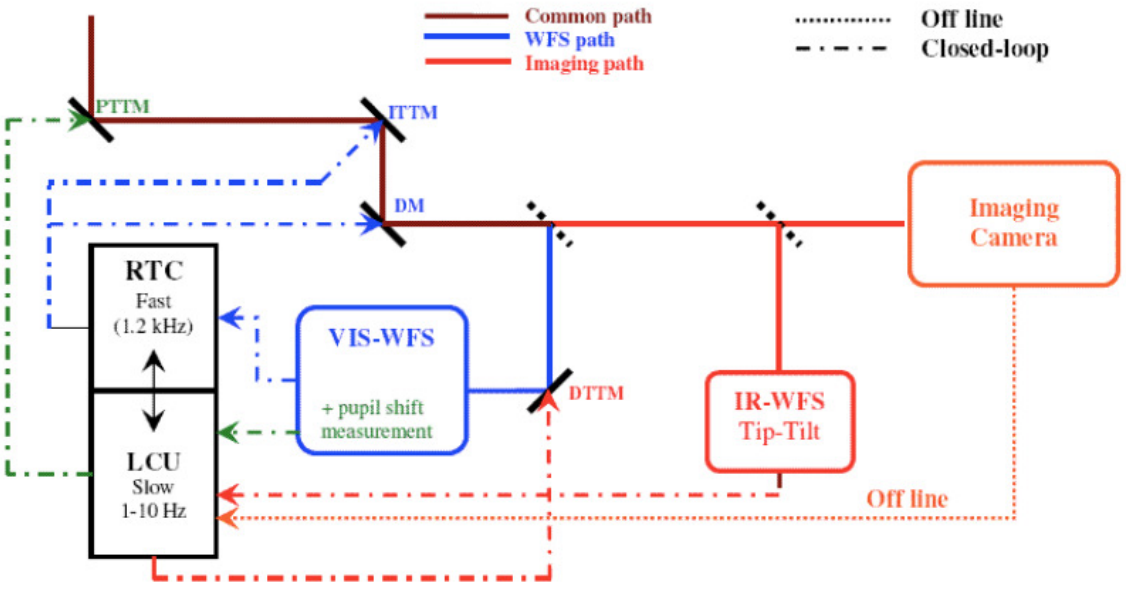

Figure 1.34: Representation of the SPHERE's extreme adaptive optics loop (Petit *et al.*, 2014). The Differential Tip-Tilt Sensor (DTTS) is used to measure the position of the star at the same wavelength as the science wavelength.

DTTS (Baudoz *et al.*, 2010) compensate the differential tip-tilt between visible and infrared channel, which includes the correction of the residual uncorrected tip-tilt fluctuations, differential refraction effect and differential thermal or mechanical effects at 1 Hz. DTTS make sure that the starlight is always centered on the coronagraphic mask.

The DTTS unit is located as close to the coronagraphic focal plane mask as possible to minimize differential movement between elements. A beamsplitter which is located a few tens of centimeters upstream of the FPM reflects only 1% of the total light towards the DTTS. It measures the centroid to estimate the exact position of the beam on the coronagraph. The measurements are then sent to the the Differential Tip-Tilt Plate, which sits inside the visible SHWFS arm. This plate is a refractive element which can be oriented to introduce small displacements of the optical beam in front of the visible WFS.

However, DTTS requires calibration to the coronagraph centering and is prone to the amplitude errors generated by the dichroic. Nevertheless, in the laboratory, DTTS has

demonstrated a RMS value of 0.14 mas/hour/axis when the room temperature variation were kept below 0.5°C/hour, which proved well within the specification of keeping the starlight centered at better than 0.5 mas over an hour.

Recently Petit *et al.* (2014) has demonstrated an on-sky residual jitter of 11 mas with an integrator controller and 9 mas with a LQG algorithm for the AO tip-tilt loop upstream the DTTS.

Sensing using science image

Très Haute Dynamique (THD) bench at Meudon is a high contrast optical imaging bench located at *LESIA, Observatoire de Paris-Meudon* with an operational speckle suppression technique, the self-coherent camera (Mazoyer *et al.*, 2013).

Mas *et al.* (2012b,a) has proposed the measurement of the tip-tilt errors directly in the coronagraphic image with no additional channel. Numerical simulations and laboratory experiments with a FQPM are presented in their paper. The estimation of the tip-tilt errors occurring upstream the mask is performed using the intensity differences in x and y directions, splitting the central part of the coronagraphic image in the FQPM. A numerical model is developed to deduce the dependency of the difference in the intensity and the pointing errors. Their simulations estimated and compensated the tip-tilt errors with an accuracy of 2.5×10^{-2} λ/D under the wavefront error of 40 nm rms. Also the errors occurring downstream the FPM due to shift of the PSF on the detector array (temperature variations) can bias the upstream error estimations. These downstream errors were measured with an accuracy of $10^{-2}\lambda/D$ using the correlation of the speckles in a ring around the center of the coronagraphic image of the FQPM.

Experimentally, on the THD bench, an accuracy of better than $6.5\times10^{-2}\lambda/D$ has been achieved in the stabilization of beam on the FPM at 2 Hz.

The advantage of sensing tip-tilt errors with the coronagraphic image is that – (1) no additional hardware is required and – (2) the final focal plane is the best location to sense for NCPAs. However, there are several disadvantages: – 1) the focal plane measurements are prone to confuse the leak due to tip-tilt error with photons from planet , – 2) requires a fast detector in order to be compatible with long exposures science observations (such as with an IFU), – 3) high amplitude higher order aberrations induce asymmetric speckle patterns in focal plane, which directly affects the tip-tilt measurement and – 4) not sensitive enough for high contrast images as there is less light for sensing.

All the techniques presented so far stabilized the starlight at the center of their respective FPMs and provided efficient control of the pointing errors. I compare in table 1.35, a summary of the solutions implemented by the current ExAO instruments illustrated in this section. I focused more on the limitations that these solutions have, because there is a need of a global sensor that should be sensitive enough to measure low-order wavefront aberrations more than just tip-tilt and can easily be implemented/adapted with any type of coronagraph.

1.4.4 Motivation of this thesis: Introduction of a reflective Lyot-based sensor

To maximize the discovery of terrestrial-like exoplanets at small angular separation (< 10 AU) from their host stars, current/future ExAO instruments are getting equipped/ planning to be equipped with high performance small IWA coronagraphs, most of which includes phase masks such as PIAACMC, VVC and FQPM. It is a well-known fact that these small IWA PMCs are extremely sensitive to the low-order wavefront aberrations and requires exquisite control of the pointing errors and other low-order phase errors. I have presented examples with the FQPM coronagraph that demonstrated this fact in §2.4. Not only from ground but for future space coronagraphs as well, one of the essential requirement is to be armed with a kind of technology that can provide a durable and stable control of the low-order aberrations more than just tip-tilt. This is required to gain access to the regions around first few wings of the diffraction-limited PSF where there is more probability of finding the rocky-type exoplanets in the habitable zone.

None of the solution that is presented in table 1.35 can correct high number of low-order wavefront aberrations for high performance PMCs. To remind the definition of a PMC: at the first focal plane of a coronagraphic system, a non-reflective phase mask is used to introduce a π phase shift that creates a self-destructive interference of the on-axis starlight, rejecting all the light outside of the geometrical pupil, thereby creating a starlight null inside of the pupil (§1.2.5.3). Hence, a reflective FPM used in the Lyot Project/Project-1640/GPI/CLOWFS can not be used to address the pointing errors in a PMC. Though, the DTTS has controlled differential tip-tilt errors for the FQPM on SPHERE but it suffered from the NCPAs and moreover could not correct more number of modes.

The paramount requirement of efficiently dealing with these low-order aberrations at small IWA has led to the development of a new kind of a coronagraphic sensor, which I called a *Lyot-based Low-Order Wavefront Sensor (LLOWFS)*. The idea is actually to sense the starlight reflected by the Lyot stop, hence justifying its name. This concept was actually proposed by a researcher at *Observatory of Paris* several years back. When *Dr. Olivier Guyon*, introduced CLOWFS technology, he mentioned to use the principle of CLOWFS to address the low-order aberrations for PMCs by using the light reflected by the Lyot stop. During three years of my research, I got the privilege to not only work on this new concept but also develop it, implement it on one of the most advanced ExAO instrument and ultimately test it on-sky on one of the world class 8-m telescope.

This thesis from now onwards is comprised of total four chapters. I will present the concept of LLOWFS and its very first simulations with a FQPM coronagraph in Chapter 2. I performed the first laboratory experiment of LLOWFS at the *LESIA, Observatoire de Paris-Meudon* under the supervision of *Dr. Pierre Baudoz*. The results I obtained led to the publication Singh *et al.* (2014). After proving LLOWFS concept, the next step was to build LLOWFS for SCExAO under the supervision of *Dr. Olivier Guyon* and demonstrate the measurement and correction of low-order aberrations with several coronagraphs. SCExAO is a HCI instrument of the Subaru Telescope that relies on the correction of Subaru's AO system. I will present the AO system, SCExAO instrument and Subaru's prime science detector in Chapter 3. I will also explain in detail the implementation of the

Techniques/Instruments	Coronagraph/ IWA	Location of starlight sensing	Number of modes	Maximum loop frequency (Hz)	Pointing residuals	Technique can be implemented with PMCs?	Disadvantages
Lyot Project/ Project-1640	Classical Lyot (4 λ/D)/ APLC (5 λ/D)	Downstream FPM (light falling through FPM)	Pointing error	1000	0.03 λ/D / 0.075 λ/D	No	Limited number of low-order modes correction
GPI	APLC (5.6 λ/D)	Downstream FPM (light falling through FPM)	Up to 14 Zernike modes	0.1	3.1×10^{-3} λ/D RMS	No	SHWFS less sensitive to low-order modes
Zernike WFS	Currently being considered for space telescope WFIRST-AFTA (IWA ~ 3 λ/D), sensitive up to 25 Zernike modes					No	Prone to NCPAs, sensitive to systematical errors, amplitude fluctuation cause spurious signals
DTTS/ SPHERE	Classical Lyot/ APLC/FQPM (4 - 5.2 λ/D)	Uses 2% of total starlight upstream FPM	Differential tip-tilt	1	3.4×10^{-3} λ/D	yes	Calibration to the coronagraph centering, prone to NCPAs, addresses only pointing errors
CLOWFS/ SCExAO, EPICS, EXCEDE, HCIT	PIAA (~ 1 - 2 λ/D)	Reflected by FPM	Up to 5 Zernike modes	1000 on EXCEDE, ~170 Hz on SCExAO/HCIT	10^{-3} and 10^{-4} λ/D in air and vacuum respectively	Not directly but can be adapted with PMCs with an improved version	Performance depends on the quality of Response matrix, need enough starlight for sensing
THD	FQPM (~ 1 - 4 λ/D)	Final focal plane	Pointing errors	2	10^{-2} λ/D	yes	Prone to confuse signal with tip-tilt, less sensitive, require fast detector

Figure 1.35: Comparison of the low-order wavefront sensing techniques implemented by the ExAO instruments/testbeds for HCI purpose.

LLOWFS on SCExAO, emphasizing especially on the LLOWFS software and hardware architecture adapted on the instrument.

Then, in the next Chapter 4, I will present the versatility of LLOWFS. I will show the results I obtained with LLOWFS in a non-ExAO regime in H-band. The laboratory results will include the linearity range analysis and the open- and closed-loop measurements of up to 35 Zernike modes with the LLOWFS for several PMCs such as the FQPM, the EOPM, the VVC and even with the PIAA coronagraph. On-sky results during several engineering and science nights will be presented with the VVC and the PIAA coronagraphs. The results I obtained in this chapter has led to the publication Singh *et al.* (2015).

SCExAO's uses a visible PyWFS for the correction of the high-order wavefront aberrations whose operation is independent of the LLOWFS. During the high-order correction i.e in the ExAO regime, LLOWFS is integrated inside the PyWFS to address the non-common path and chromatic errors in the infrared. I will present the hardware and software architecture of this integration, together with the results in the laboratory and on-sky is Chapter 5. This integration has demonstrated one of the most stable and durable correction I obtained with LLOWFS during the three years of rigorous testing in the laboratory and on-sky.

During the course of my research, SCExAO has gone through a constant phase of actively testing its capabilities on-sky, which has always set time constraints and required exhaustive testing of the LLOWFS in the laboratory to prepare for the observations in advance. The challenge I faced was to find a trade-off between either to spend time on thorough simulations or keep building and optimizing LLOWFS control loop to make it ready for on-sky operations. Therefore, a significant part of my thesis will reflect more experimental studies and comparatively less analytical study of the LLOWFS. Nevertheless, performing research on SCExAO has rewarded me with opportunities to actively participate in more than 25 engineering nights, 15 Science nights and provided me a glimpse of endless weeks of preparations for the on-sky observations on a 8-m world class observatory.

Chapter 2

Lyot-based Low-Order Wavefront Sensor

" The new and the old methods complete one another on numerous points, and their simultaneous use will increase our knowledge of the outer atmosphere of the Star much more rapidly."

– Bernard Lyot

Contents

2.1 Introduction

The idea of using the starlight itself for the control of the low-order aberration is not a novelty. §1.4.3 present various solutions developed by the current ExAO testbeds and instruments to address the pointing errors. *Lyot Project's* concept of using a reflective amplitude FPM with a hole at the center to sense the starlight for pointing control has been adapted by the *Project-1640* and *GPI* instruments. In contrast, the *CLOWFS* used the principle of a dual-zone FPM, which blocks the center of the PSF, partially reflecting its first few Airy disks with a reflective annulus, and allowing off-axis sources to be transmitted.

These solutions, in spite of providing a high-level of low-order control for the occulting coronagraphs are however, not suitable for *PMCs* due to their diffractive nature. A phase mask at the focal plane rejects the on-axis starlight and diffracts it outside of the geometrical pupil instead of blocking it in the focal plane. In a re-imaged pupil plane, a Lyot stop is then used to block the scattered starlight (§1.2.5.3). Since the FPM of a PMC cannot be made reflective, a natural solution is to make the Lyot stop reflective and use it to sense the starlight that falls on it.

To address pointing errors and other low-order wavefront aberrations for small IWA PMCs, I have worked on a concept of sensor based on the same idea as the CLOWFS, but using the starlight reflected from the Lyot stop. I named it a *Lyot-based low-order wavefront sensor (LLOWFS)*. The notion of using a reflective Lyot stop (RLS) is not unfamiliar. In the *Lyot Project*, a RLS is used to re-image the starlight in to a pupil camera to align the Lyot pupil plane with the telescope pupil. However, this reflected starlight via a RLS was not used to sense the low-order aberrations.

This chapter is an extension of the publication Singh *et al.* (2014) (§2.2), therefore I will refer the relevant sections of the publication to describe the concept, figures and results. In §2.3, I will recall LLOWFS theory by introducing the concept in the context of a FQPM. I will present the numerical simulations of the LLOWFS with a FQPM in §2.4 with and without considering phase aberrations at the entrance pupil. These simulations (§2.4.3) will also show the measurement of five Zernike modes (tip, tilt, focus, oblique and right astigmatisms) in the post-AO188[1] corrected phasemaps. §2.5 will demonstrate the first laboratory experiment of the LLOWFS measurement of the tip and tilt errors with a FQPM.

[1] AO188 is the adaptive optics facility of the Subaru Telescope and is described in Chapter 3, §

2.2 Singh et al. 2014a

PUBLICATIONS OF THE ASTRONOMICAL SOCIETY OF THE PACIFIC, **126**:586–594, 2014 June

Lyot-based Low Order Wavefront Sensor for Phase-mask Coronagraphs: Principle, Simulations and Laboratory Experiments

GARIMA SINGH,[1,2] FRANTZ MARTINACHE,[3] PIERRE BAUDOZ,[2] OLIVIER GUYON,[1] TARO MATSUO,[4] NEMANJA JOVANOVIC,[1] AND CHRISTOPHE CLERGEON[1,2]

Received 2014 January 18; accepted 2014 April 28; published 2014 May 29

ABSTRACT. High performance coronagraphic imaging of faint structures around bright stars at small angular separations requires fine control of tip, tilt, and other low order aberrations. When such errors occur upstream of a coronagraph they result in starlight leakage, which reduces the dynamic range of the instrument. This issue has been previously addressed for occulting coronagraphs by sensing the starlight before or at the coronagraphic focal plane. One such solution, the coronagraphic low order wave-front sensor (CLOWFS), uses a partially reflective focal plane mask to measure pointing errors for Lyot-type coronagraphs. To deal with pointing errors in low inner working angle phase mask coronagraphs which do not have a reflective focal plane mask, we have adapted the CLOWFS technique. This new concept relies on starlight diffracted by the focal plane phase mask being reflected by the Lyot stop towards a sensor which reliably measures low order aberrations such as tip and tilt. This reflective Lyot-based wavefront sensor is a linear reconstructor which provides high sensitivity tip-tilt error measurements with phase mask coronagraphs. Simulations show that the measurement accuracy of pointing errors with realistic post adaptive optics residuals are $\approx 10^{-2}\lambda/D$ per mode at $\lambda = 1.6$ μm for a four quadrant phase mask. In addition, we demonstrate the open loop measurement pointing accuracy of $10^{-2}\lambda/D$ at 638 nm for a four quadrant phase mask in the laboratory.

Online material: color figures

1. INTRODUCTION

The 40 milliarcsecond diffraction limited resolution at $\lambda \simeq 1.6$ μm (λ = wavelength) provided by 8-meter class ground-based telescopes is theoretically sufficient for the direct detection and characterization of extrasolar planets in the habitable zones of nearby stars (<30 pc). Their direct imaging, however, is affected by the rapidly changing atmosphere as well as optical imperfections and residual quasistatic aberrations which limit the optical system's high contrast imaging capability. Accurate measurement and calibration of the wavefront is therefore required.

With Adaptive Optics (AO), the ability of current telescopes to reach the diffraction-limit has been improved greatly and post processing techniques such as differential imaging have made it possible to identify faint companions at angular separation $\gtrsim 10\lambda/\mathrm{D}$ from their parent star (D = Pupil diameter) (Marois et al. 2008; Lagrange et al. 2009).

The newly developed high performance small inner working angle (IWA) coronagraphs employed on Extreme Adaptive Optic Systems (ExAO) are trying to image exoplanets within a few λ/D. At such small angular separations, the telescope pointing errors make it difficult to center the stellar light on the occulting mask which creates a halo of speckles around the occulter preventing detection of companions. In other words, these high performance coronagraphs are extremely sensitive to tip-tilt errors (Lloyd & Sivaramakrishnan 2005; Shaklan & Green 2005; Sivaramakrishnan et al. 2005; Belikov et al. 2006; Guyon et al. 2006).

The absence of accurate pointing control degrades the coronagraph starlight rejection capability by allowing the planet's photons to mix with the starlight leaking around the coronagraph focal plane mask. Thus exoplanet direct imaging is often limited by how well low order wavefront aberrations upstream of a coronagraph are controlled and calibrated.

To address this issue, the LYOT project (Digby et al. 2006) proposed to reimage the starlight at the coronagraphic focal plane in order to track pointing errors. Current ExAO systems such as the Gemini Planet Imager (GPI) and the Subaru Coronagraphic Extreme Adaptive Optics (SCExAO) system use an adaption of the LYOT project's concept as outlined below.

[1] Subaru Telescope, National Astronomical Observatory of Japan, Hilo, HI 96720.
[2] Lesia, Observatoire de Paris-Meudon, 5 Place Jules Janssen, F-92195 Meudon Cedex, France.
[3] Laboratoire Lagrange, UMR7293, Université de Nice Sophia-Antipolis, CNRS, Observatoire de la Côte d'Azur, Bd. de l'Observatoire, 06304 Nice, France.
[4] Kyoto University, Kitashirakawa-Oiwakecho, Sakyo-ku, Kyoto 606-8502, Japan.

The Spectro-Polarimetric High-contrast Exoplanet Research (SPHERE) instrument for the Very Large Telescope (VLT) uses a Differential Tip-Tilt Sensor (DTTS) unit which is located as close to the coronagraphic focal plane mask as possible to minimize differential movement between elements. It measures the center of gravity to estimate the exact position of the beam on the coronagraph. Laboratory results of the DTTS have shown a centroid measurement precision of 0.14 mas/hr/axis if room temperature variations are kept below 0.5° C (Baudoz et al. 2010).

In contrast, GPI uses the starlight that passes through the focal plane mask and reimages the pupil on a Shack-Hartmann wavefront sensor in its calibration unit. GPI's laboratory results have shown a pointing accuracy of 2 mas in 20 s for an 8th magnitude star for an apodized-pupil coronagraph (Wallace et al. 2010).

The SCExAO system at Subaru Telescope is using the CLOWFS concept as described in Guyon et al. (2009) and Vogt et al. (2011). The CLOWFS uses a dual-zone focal plane mask which blocks the center of the point spread function (PSF), partially reflects the wings of the PSF with a reflective annulus, and allows off-axis sources to be transmitted towards the science camera. The recent laboratory demonstration of similarly designed CLOWFS on NASA's High Contrast Imaging Testbed at the Jet Propulsion Laboratory has shown the stabilization of tip-tilt with 0.001 λ/D residuals in closed loop at $\lambda = 808$ nm (Kern et al. 2013) with a phase-induced amplitude apodization coronagraph (PIAA Guyon et al., 2003, Guyon et al.,2005).

Despite the high level of tip/tilt control demonstrated on occulting coronagraphs, there is no solution yet in regards to tip/tilt sensing for phase mask coronagraphs (PMC). With the aim of imaging high contrast structures at 1 λ/D with phase mask-based coronagraphs, we introduce a new generation of CLOWFS which is compatible with PMC. It is based on a reflective Lyot stop (RLS) which re-images the diffractive focal plane mask. The new system is called the Lyot-based low order wavefront sensor (LLOWFS).

A common property of all PMCs is that they redistribute the energy spatially in the pupil plane downstream of the coronagraph, canceling on-axis light and diffracting it outside the geometric pupil which is then blocked by a conventional Lyot stop. To control pointing errors with a PMC, we have modified the Lyot design, so that the Lyot stop reflects the unused starlight towards a low-order sensor that reliably measures tip-tilt errors.

The RLS concept is presented in detail in section 2. The pointing error estimation is explained in section 2.2. We describe a typical generic LLOWFS optical configuration, numerical simulation, and the results in section 3. We then use realistic AO residuals as a simulation input to test the ability of our technique to measure the low order modes in section 3.3.3. Section 4 discusses the results of the preliminary implementation of the RLS with a four quadrant phase mask (FQPM) (Rouan et al. 2000) in a coronagraphic testbed at LESIA, France.

2. PRINCIPLE

2.1. A Reflective Lyot Stop Wavefront Sensor

In its simplest form, a coronagraph is an occulting disk in the focal plane of the telescope blocking the central airy disc of the star, combined with a Lyot stop which reduces the stellar glare by eliminating the rest of the diffracting light allowing detection of companions or disk structures.

The technique of using a reflective focal plane mask as a means of measuring and correcting the low order aberrations such as the CLOWFS concept has enabled high contrast imaging in 1–2λ/D region. However, for high performance PMCs, a reflective focal plane mask as used in CLOWFS is not applicable, hence a new solution is required. The LLOWFS instead accommodates the diffractive nature of the PMC focal plane mask in a manner illustrated in Figure 1. At the focal plane of the telescope, a phase mask diffracts starlight in a reimaged pupil plane. The starlight is then directed by the RLS towards a detector which is used for low-order sensing.

At this point it is possible to use the pupil plane image to drive the low order sensor as phase aberrations present in the intermittent focal plane are converted to intensity modulations via the phase mask used (e.g., the FQPM [Rouan et al. 2000], the Vortex [Mawet et al. 2010]). However, to maximize the signal-to-noise ratio and hence be able to operate on faint host stars, we conduct the wavefront sensing in a reimaged focal plane which offers the highest photon density per pixel.

For the accurate detection of the focus aberration, a deliberate defocus is introduced in the position of the detector in order to eliminate the sign ambiguity with respect to which side of the sensor the focus aberration is. The defocus in the detector position ensures that the image plane is on a single side of the focus at all times. A detailed study of the retrieval process with a defocused image is presented in Guyon et al. (2009).

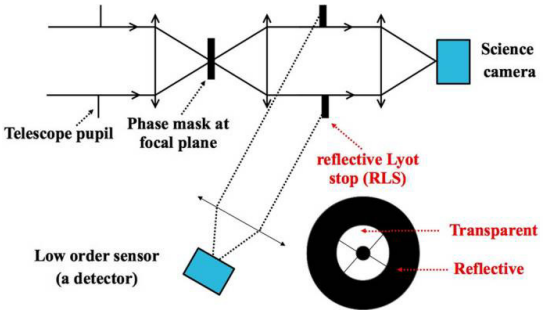

FIG. 1.—Schematic of the Lyot-based low order wavefront sensor (LLOWFS) consisting of a high performance coronagraph combined with a reflective Lyot stop (RLS) with a geometry that can be adapted according to the telescope pupil shape (central obstruction and spider arms) and diffraction pattern created by phase mask at focal plane. See the electronic edition of the *PASP* for a color version of this figure.

As we operate with a slight defocus the flux density per pixel is reduced, which only becomes an issue in the readout noise limited case. In addition, we do not expect cross talk to be introduced between the modes due to defocus but we have not quantified/investigated this thus far.

Guyon et al. (2009) also demonstrate a detailed closed loop operation on focus and the astigmatisms and, in principle, LLOWFS should be able to measure other modes such as focus and the astigmatisms apart from just pointing errors. However, our key motivation is to address the pointing errors only for this body of work, and the measurement of other low-order modes will be addressed in future work.

The configuration of LLOWFS that we will discuss in this paper is based on the revised SCExAO testbed (Jovanovic et al. 2013) which has been recently equipped with phase masks coronagraphs such as the Vortex, the eight octant phase mask (Murakami et al. 2008a), the phase-induced amplitude apodization with a variable focal plane mask (Newman et al. 2013, in preparation), and the four quadrant phase mask.

To make our simulations and experiments relevant to the SCExAO testbed, we used the pupil geometry (central obstruction and spider arms) of the Subaru Telescope. In addition, SCExAO is fed by a facility AO system known as AO188, which delivers post correction RMS wavefront errors of $\approx$200 nm in good seeing (Strehl ratio of $\approx 40\%$ in the H-band). These metrics were included in our simulations and will be used throughout this body of work.

2.2. Pointing Error Estimation Based on Linearity Approximation

In a post-AO correction scenario, residual phase errors can be assumed to be small ($\ll 1$ radian of rms wavefront error).

Simulations, as well as experimental results for the CLOWFS system, have demonstrated that for small pointing errors the intensity fluctuations in the reflective focal plane image are a linear function of low-order phase errors before the coronagraph. Applying the same principle to the LLOWFS, our estimates of the pointing errors are based on the linear relationship between sensor intensity and phase errors.

If we let I_0 represent a reflected reference image, acquired by the low-order sensor with no aberrations, and I_R the image with some aberrations, we assume that we can relate the difference between these two images by decomposing it into a linear combination of modes. If one considers tip-tilt alone, then we can write:

$$I_{R(\alpha_x,\alpha_y)} - I_0 = \alpha_x S_x + \alpha_y S_y \quad (1)$$

where S_x and S_y represent the sensor's response to tip and tilt, respectively. For any instant image I_R, one can therefore identify an unknown tip-tilt (α_x, α_y), by direct projection on the basis of modes, or using a least squares algorithm.

3. LYOT-BASED LOW ORDER WAVEFRONT SENSOR: OPTICAL ELEMENTS AND REALISTIC SIMULATIONS

In this section, we describe a simulation tool we have developed to test the functionality of our concept on a low IWA FQPM coronagraph. We discuss the factors that define the performance criteria of LLOWFS; for example, cross-talk between modes, linearity range of sensor response, and sensitivity towards aberrations upstream of the coronagraph.

3.1. Simulation Elements

A simplified optical layout of LLOWFS is shown in Figure 1 and the corresponding intensity distribution at each plane of a simulation element is shown is Figure 2. Below we briefly describe the simulation parameters considered.

The AO188 corrected beam is focused on a FQPM optimized for 1.6 μm. As shown in Figure 2*d*, the FQPM divides the focal plane in four quadrants and provides a π-phase shift between adjacent quadrants, resulting in self-destructive interference in the reimaged pupil. To account for typical manufacturing irregularities, we simulated the FQPM such that it included gaps of 1.8 μm (0.04 λ/D) between neighboring quadrants and gaps of 2.5 μm (0.06 λ/D) across the diagonal in the center of the mask seen in Figure 2*d*. These values correspond to the size of the defects in FQPM used in laboratory experiments. The mask creates a square diffraction pattern around the edge of the central obstruction in the pupil plane as can be seen in Figure 2*f*.

The unused diffracted starlight is then reflected via a RLS as shown in Figure 2*g*. The inner shape of the RLS is a square in order to block the square diffraction pattern around the obstruction. The outer diameter of the reflective area is chosen to be three times the diameter of the pupil in order to collect the majority of the light around the pupil. The image (Fig. 2*h*) shows what is seen by the sensor at the RLS plane.

The image (Fig. 2*i*) represents the RLS image (I_R) which has tip-tilt and other high order modes to be analyzed by the sensor. Note that the transition lines visible in the sensor image are related to the geometry of the FQPM. 5 radians rms of defocus were introduced in the sensor position to ensure that it is larger than the focus term to be measured to avoid sign ambiguities. Other higher order modes can also be measured; however, we estimated tip-tilt errors only in this paper.

3.2. Calibration Procedure

The LLOWFS is not an absolute pointing system. It is a differential sensor and requires calibration prior to estimating the best centering of the PSF on the coronagraph. To study the behavior of LLOWFS to the unknown tip-tilt errors upstream of the coronagraph, we calibrate the response of the sensor to the aberrations present in the wavefront at the entrance pupil.

The calibration procedure includes applying a phase map with a controlled amount of tip-tilt and other modes to our

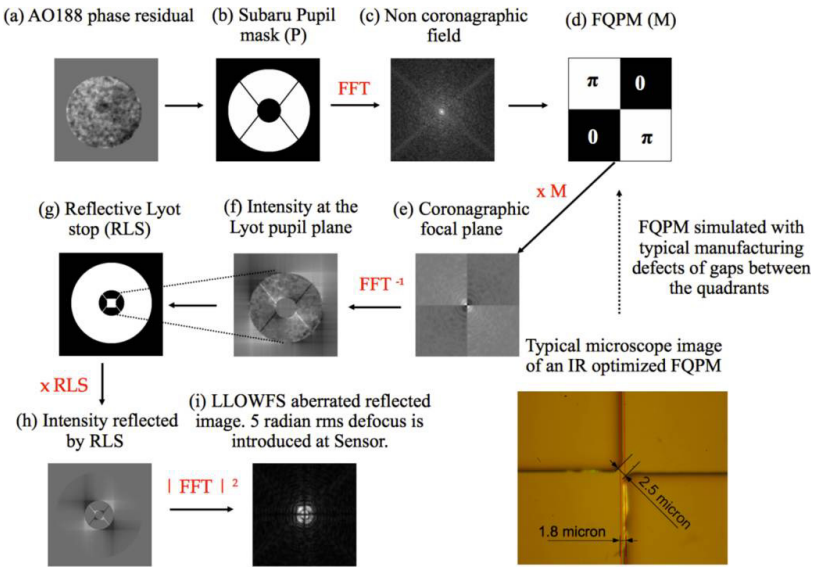

FIG. 2.—Intensity pattern at each plane of the simplified optical layout (Fig. 1) of the revised SCExAO system at Subaru Telescope showing the Lyot-based low order wavefront sensor (LLOWFS) with the four quadrant phase mask (FQPM) as an example. The input wavefront is the Subaru Telescope's Adaptive Optics System AO188 corrected residual phase map of 150 nm rms at 1.6 μm. The white surface in the reflected Lyot stop (RLS (*g*)) is reflective while the black surface is transmissive. See section 3.1 for more details (FFT stands for Fast Fourier Transforms). See the electronic edition of the *PASP* for a color version of this figure.

system in ideal conditions of no aberration and recording the calibration frames prior of studying the LLOWFS under aberrated conditions.

The sensor response S_x and S_y towards tip and tilt errors in equation (1) are estimated by obtaining the respective calibration frames after applying $\approx$0.01 radian rms of tip and tilt to our system. An example of the response is shown in Figure 3, for tip-tilt as well as other modes (defocus, astigmatism, etc.), showing that the LLOWFS is a versatile wavefront sensor which is capable of distinguishing tip-tilt errors from the other aberrations. In all of our simulations, we will use these calibration frames to estimate the tip-tilt errors in the wavefront.

LLOWFS relies on the shape of the reflected image, not its position on the sensor. However, during the calibration frames acquisition process, if environmental factors (temperature variations, flexure of the instrument) induce tip-tilt, then it will require the recalibration of the system with a new reference image.

3.3. LLOWFS Numerical Simulations

In our simulations, we have studied the LLOWFS without considering photon noise in this paper.

3.3.1. Ideal Case: Aberration-Free System

In the basic LLOWFS configuration shown in Figure 1, we considered no phase defects at the entrance pupil. First we acquired the on-axis image of the reflected light and recorded it as our reference image I_0 as shown in Figure 3*a*.

Next we applied a varying amount of tip between $\pm$0.5 radians rms ($\pm 0.3\lambda/D$) in the x direction with a step size of 0.01 radian rms and recorded a cube of 100 images as $I_{R\alpha_x}$. We then estimated tip-tilt aberrations α_x and α_y present in $I_{R\alpha_x}$ using equation (1) by solving them as a least squares problem.

The applied tip with respect to the estimated tip is shown in Figure 4. The residual tilt in the y direction which is almost negligible is also shown. The sensor showed a linear response to tip/tilt aberrations within $\pm$0.3 radians rms ($\pm 0.18\lambda/D$) of phase error with 1 % nonlinearity in measurement at 0.3 radian rms.

One of the properties of the LLOWFS technique is that it measures the modes independently from each other. There is no cross talk between measured modes in the low order aberration regime and the reconstruction of the image should work if the estimation of errors is done in the linear regime, more details of which can be found in the CLOWFS paper Guyon et al. (2009).

3.3.2. Sensor Linearity Under Low-Order Phase Errors

In this section, we study the response of the sensor to tip-tilt errors under the influence of multiple low-order phase aberrations such as tip, tilt, focus and astigmatism simultaneously. We consider an input wavefront as a cube of 100 phasemaps (image

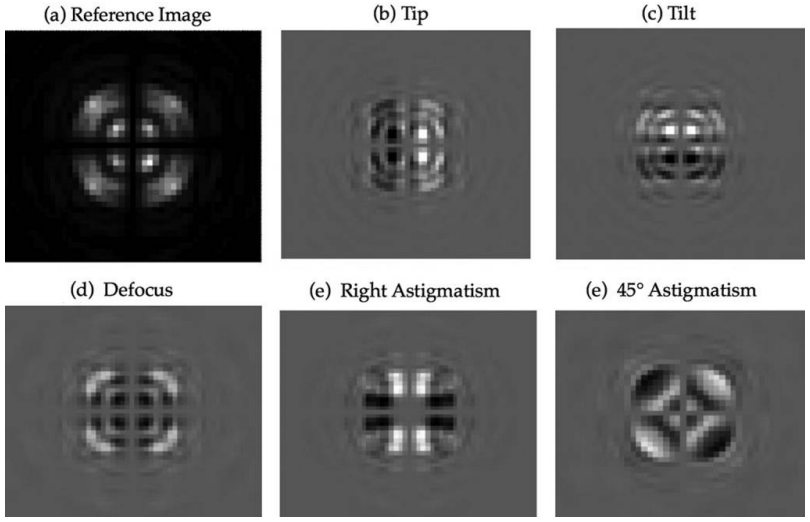

FIG. 3.—Simulated response of the LLOWFS sensor to the low-order modes which are obtained after applying 0.01 radian rms phase error per mode in an aberration-free system. These images are our calibration frames that we have used to measure the pointing errors present in the aberrated wavefront at the entrance pupil, as discussed in detail in section 3.3. 5 radian rms of defocus is introduced at the low-order sensor position. The images shown here have the same brightness scale.

cube I_R) of low order modes. Each phasemap has 5 low order errors with rms amplitude values increasing sequentially between ± 0.5 radians. For example, the first phasemap has all the modes with -0.5 radians (290 nm total phase error over the Subaru pupil), the 50th phasemap is free of aberrations and the 100th phasemap has $+0.5$ radians amplitude per mode.

Using equation (1), we estimated the tip-tilt coefficients through least squares methods and we present only the measured

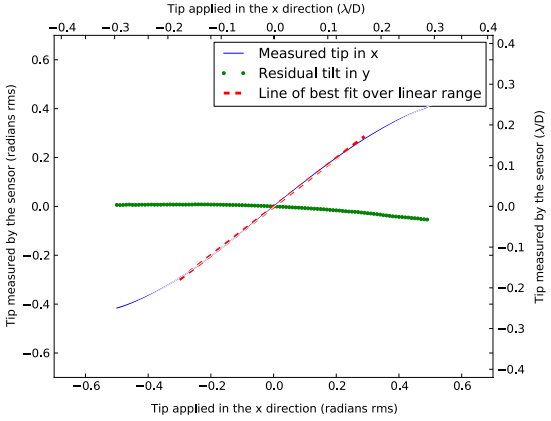

FIG. 4.—Response of the sensor to the tip aberration applied in the x direction at the entrance pupil. The sensor estimates the tip error linearly within ± 0.3 radian rms ($\pm 0.18\lambda/D$) of phase error with 1% nonlinearity at 0.3 radian rms. The residual tilt in the y direction shows no cross talk between the tip-tilt error measurements. The red dash line is the linear regression done within linearity range, i.e., ± 0.3 radians rms. See the electronic edition of the *PASP* for a color version of this figure.

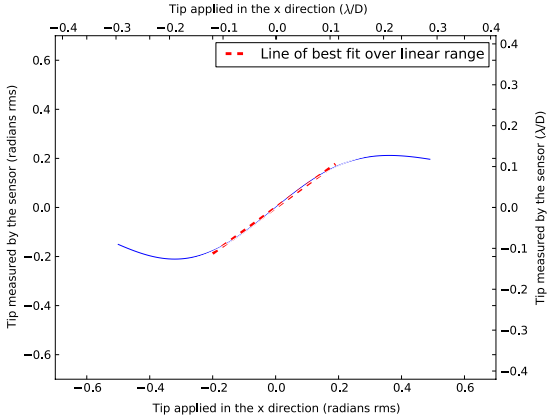

FIG. 5.—Linearity check of the sensor response to tip errors present in low-order phasemaps applied at the entrance pupil. The x-axis displays the tip aberrations applied in each phase map of the image cube. The corresponding y-axis shows the tip errors estimated by the LLOWFS. Under the influence of multiple low order aberrations, the sensor response becomes nonlinear beyond ± 0.2 radians rms ($\pm 0.12\lambda/D$). See the electronic edition of the *PASP* for a color version of this figure.

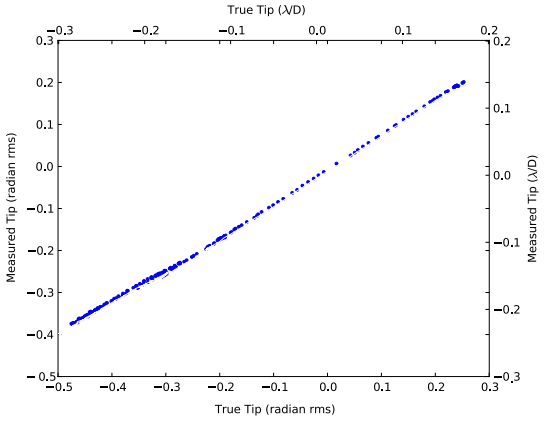

FIG. 6.—Linearity of sensor response to tip aberrations present in AO188 phase residuals. The x-axis represents phase error contributed by tip aberrations in each phasemap. The corresponding y-axis shows the response of the sensor to these tip errors. See the electronic edition of the *PASP* for a color version of this figure.

tip in the x direction in Figure 5. The plot showed compares the amount of tip present in the image cube with respect to the tip measured by the sensor. In the presence of low-order aberrations, the sensor response is linear for tip aberrations between ± 0.2 radians rms ($\pm 0.12\lambda/D$) with 14% nonlinearity in measurement at 0.2 radian rms and 32% nonlinearity at 0.3 radian rms. Unlike the single aberration case, the system response beyond ± 0.2 radians rms range becomes nonlinear in the presence of multiple low order aberrations and therefore makes the loop diverge.

We have repeated the tip-tilt error measurement analysis for different defocus positions in the sensor and noticed that the sensor linearity remains unaffected.

3.3.3. Post AO188 Phase Residuals as an Input Wavefront to the LLOWFS

The next step is to check the sensor linearity range and sensitivity towards high-order aberrations present in the residuals of the Subaru Telescope facility AO system. This is done by simulating a series of 200 post AO188 phasemaps with unknown low and high order aberrations with ≈ 180 nm rms amplitude. Figure 2*a* represents the first phase map of the series.

With the AO188 residual phasemap series as an input wavefront to our system, we measured the tip and tilt errors. Figure 6 plots the true tip aberrations present in the residual phasemaps versus tip aberrations measured by LLOWFS low-order sensor.

We also compare the sensor response to tip-tilt errors with their actual residual value for 200 phasemaps as shown in Figure 7. We notice that for small tip-tilt excursions, the sensor response to low-order aberrations provides a reliable measurement of the tip-tilt. The fidelity of the reconstruction degrades for larger tip-tilt excursion (beyond ± 0.2 radian rms), due to nonlinearity effects, but the sensor remains well behaved, and in closed loop, would converge toward the reference position, despite the nonlinearity. Under realistic simulations, the sensor delivered a measurement accuracy of $\approx 10^{-2}\lambda/D$ (2-12 nm at 1.6 μm) per mode as shown in Figure 7.

The higher order aberrations and large tip-tilt errors can affect the LLOWFS performance by introducing cross talk

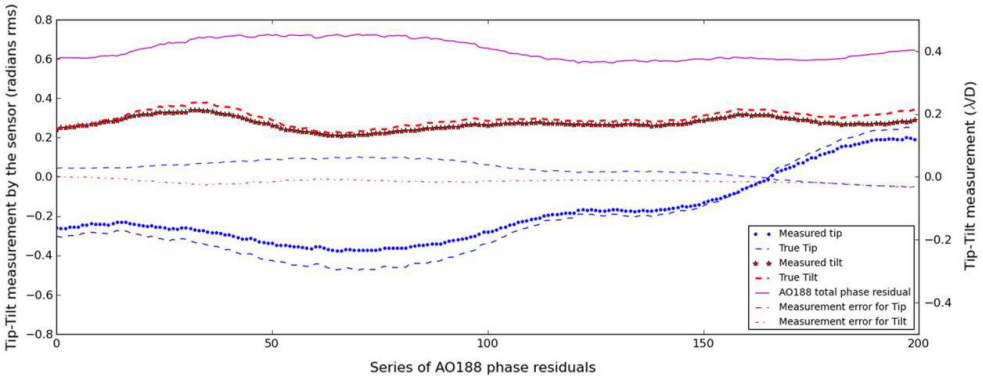

FIG. 7.—(*i*) Simulated sensor response to tip-tilt errors present in the realistic phase residuals of the Subaru Telescope AO188. The simulated series is comprised of 200 post AO phasemaps with unknown high and low order modes with ≈ 180 nm phase rms over the Subaru pupil. In the presence of high order modes and large tip-tilt errors, the predicted linearity of sensor decreases in the open loop regime. The measurement errors for tip and tilt shown are the difference between the measured and true tip/tilt errors. The standard deviation of this difference shows sensor's measurement accuracy of $\approx 10^{-2}\lambda/D$ per mode. See the electronic edition of the *PASP* for a color version of this figure.

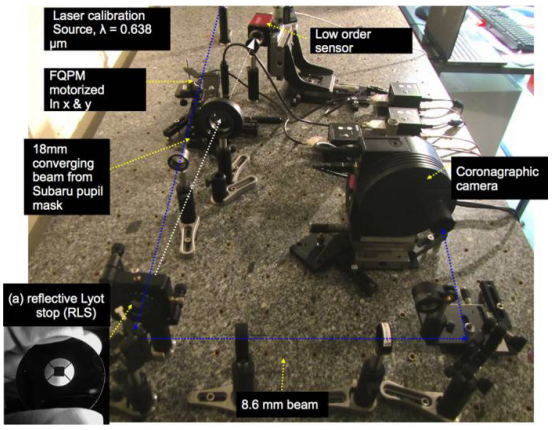

FIG. 8.—Laboratory setup of LLOWFS at Laboratoire d'études Spatiales et Instrumentation en Astrophysique (LESIA), Observatoire de Paris-Meudon (2013 June). See the electronic edition of the *PASP* for a color version of this figure.

between modes. Astigmatisms can be misinterpreted with higher order mode such as trefoil. We aim to study the behavior of sensor response to low-order aberrations under the influence of higher order aberrations in future work.

4. LLOWFS LABORATORY IMPLEMENTATION

An early version of the LLOWFS has been implemented on the coronagraphic testbed at LESIA, Observatoire de Paris. The optical design of our experiment is shown in Figure 1 and the laboratory setup is represented in Figure 8, which included:

1. Laser source of $\lambda = 0.638$ μm
2. Subaru pupil mask
3. FQPM (optimized at $\lambda = 0.635$ μm), mounted on two motors allowing it to move in the x and y directions
4. RLS (8.6 mm Lyot outer pupil diameter with 25.4 mm of reflective annulus around it) placed at an angle of 8° to reflect the light towards the low order sensor
5. The RLS is a fused silica disk of 1.5 mm thickness as shown in Figure 8*a*. The substrate flatness is better than 5 μm. The black region is reflective chrome with 60% reflectivity in near IR (1200 nm) while the white region is transparent.
6. Low-order sensor (pixel size = 7 μm). We introduced defocus in the sensor position and we estimated the value to be 5 ± 0.3 radians rms.

4.1. Procedure of Acquiring the Measurements

First the FQPM is aligned and the rejection of ≈30 has been obtained. The reasons for such suboptimal performance are: wavefront distortions, manufacturing accuracy of the mask, the FQPM rejection wavelength was not optimized for the laser source; in addition, the spiders and the secondary of the pupil affected the extinction capability of the coronagraph.

The intensity reflected by RLS is recorded as a reference image I_0 as shown in Figure 9*a*. Figure 9*b* shows the RLS having manufacturing defects: the angle between adjacent spider arms was 10° less than required. This meant that we could not mask

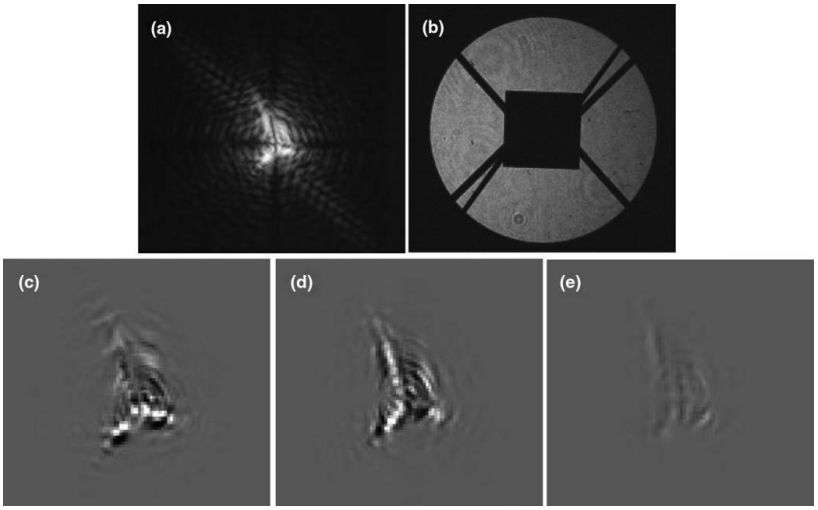

FIG. 9.—(*a*) Reference image acquired by LLOWFS. (*b*) RLS overlapped with the Subaru pupil mask. (*c*) Calibration frame for tip (0.12 λ/D). (*d*) Calibration frame for tilt (0.12 λ/D). (*e*) Difference between two reference images acquired before and after recording the mode measurements. (Exposure time for recording the images: 500 ms. The images shown here have the same brightness scale.)

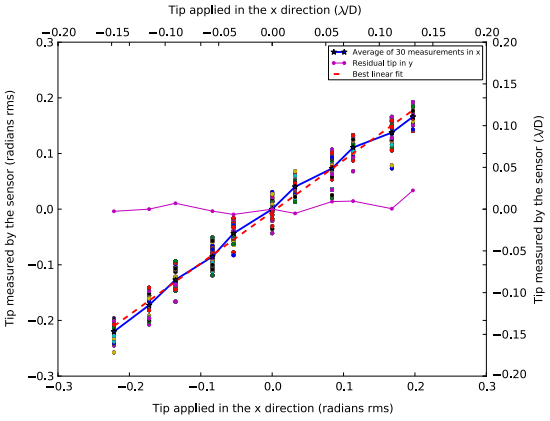

FIG. 10.—Laboratory results for tip errors: Graph shows the linearity of sensor response to the tip aberration applied to the FQPM in the x direction. The residual tilt in the y direction stays around zero for all the measurements for tip errors showing no cross talk between the modes. For each step, 30 images are taken showing dispersion of the measurement due to local turbulence. The red dash line is the linear regression done in the linearity range, i.e., within $\pm 0.12\lambda/D$ (± 0.19 radians rms). The sensor measurement accuracy for tip errors is 0.009 λ/D. See the electronic edition of the *PASP* for a color version of this figure.

all of the spider arms of the pupil, the traces of which are clearly visible in the reference image.

The FQPM is then moved in x with a step of 0.12 λ/D and the response of the sensor is acquired for tip as shown in Figure 9*c*. The sensor response obtained for the FQPM for the same step in the y direction is shown in Figure 9*d*.

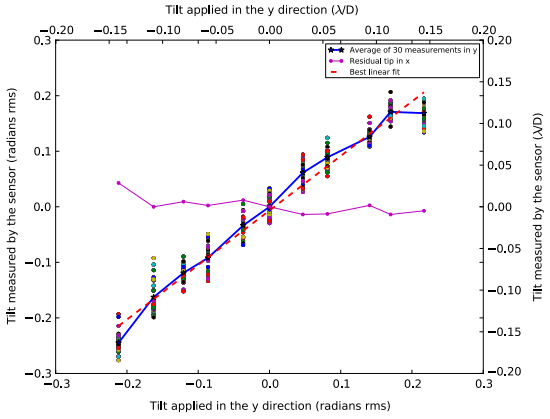

FIG. 11.—Laboratory results for tilt errors: Graph shows the linearity of sensor response to the tilt aberration applied in the y direction. The residual tip in x measured by the sensor stays around zero. The red dashed line is the linear regression done in the linearity range, i.e., within $\pm 0.12\lambda/D$ (± 0.19 radians rms). The sensor measurement accuracy for tilt errors in the y-direction is 0.011 λ/D. See the electronic edition of the *PASP* for a color version of this figure.

Note that our approach of obtaining sensor measurements in the x and y direction were identical. We registered the calibration frame for tip and tilt separately prior to testing the linearity of the sensor under large excursions in tip-tilt errors.

We then moved the FQPM in x within $\pm 0.2\lambda/D$ (± 0.32 radians rms) with a step size of $\approx 0.05\lambda/D$ and stored the image cube as I_{Rx}. We recorded two reference frames before and after taking our measurement. In Figure 9*e*, the difference clearly shows structure that can be explained by the local turbulence in the laboratory and thermal drifts of the mechanical elements driving the FQPM.

Figures 10 and 11 show the response of the sensor to tip and tilt in x and y studied independently. For every step applied in the x or y, a series of 30 images were recorded by the sensor. The dispersion in the data is a result of the local turbulence. For tip aberrations applied in the x direction, the tilt aberrations in the y direction stayed around zero. So we confirm the cross talk independency between tip-tilt error measurements as predicted in the simulation.

As can be seen, the sensor has a linear response over the majority of the aberration amplitude range tested with some possible nonlinearity creeping in at the beginning and end of the range under test. However, without more data this can not be concluded with any certainty. Nonetheless, this means the sensor can be used over a range of $\pm 0.12\lambda/D$ (≈ 0.19 radians phase rms over Subaru pupil) reliably.

4.2. Problems faced during LLOWFS Laboratory Implementation

The implementation of the LLOWFS in the laboratory was limited by various factors such as:

1. Local Turbulence
2. Non-optimized alignment of the testbed
3. Drift in the reference image of the LLOWFS over time
4. The substrate quality of RLS and its manufacturing defects
5. AR coatings on the FQPM were not optimized for the phase mask working wavelength.
6. Precision of the encoders on the stages driving the FQPM ($10^{-2}\lambda/D$)
7. Low-order sensor read out noise (15e-)

Even with all the limiting factors listed above, the LLOWFS implementation in the laboratory has efficiently demonstrated in open loop measurements an accuracy of $\approx 10^{-2}\lambda/D$ per mode for the FQPM at 638 nm.

5. GENERAL DISCUSSION

The Lyot-based low order wavefront sensor (LLOWFS) is highly photon efficient; as for pointing control it uses the starlight diffracted outside the phase mask which is otherwise

wasted in a conventional phase mask coronagraph (PMC). Our technique essentially requires a reflective Lyot stop and a low-order sensor which is simply a detector. The LLOWFS schematic layout presented in Figure 1 is adaptable to any PMC.

We showed that the LLOWFS measurement is not only limited to tip-tilt, as we could also potentially sense defocus and astigmatism which are distinguishable from tip-tilt signals as shown in Figure 3. However, the shortcomings of the LLOWFS that we noticed are: the maximum amplitude of tip/tilt excursions that can be measured is limited; there is a high risk of misinterpretation of astigmatism with higher order modes such as trefoil; and the sensor performance is influenced under high order aberrations which can introduce cross talk between modes. One more aspect that we have not studied yet is the photon sensitivity versus the sensor defocus position. The amount of defocus that we introduce will likely affect the sensitivity of the LLOWFS. We therefore aim to study the operation of the LLOWFS under the circumstances listed above in future work.

Our system can also be adapted as a post-processing technique (Vogt et al. 2011) to enhance the sensitivity of the coronagraph. The image reconstructed through the LLOWFS can be subtracted from the science image to calibrate out the low-order residuals.

The LLOWFS concept is reliable for high performance small inner working angle coronagraphs which provide $10^{-2}\lambda/\mathrm{D}$ of pointing measurement accuracy; hence, efficiently preventing the coronagraphic leaks which are the main cause of the degradation in the nulling performance. The combination of small IWA PMC plus sub milli-arcsecond level pointing stability of the LLOWFS applied to extremely large telescopes could enable the direct imaging of reflected light habitable zone planets.

The LLOWFS is indeed a necessity to control the pointing errors with PMC and an appealing solution for not only ground-based telescopes but also for space-based telescopes.

6. CONCLUSION

High throughput, low inner working angle (IWA) coronagraphs are essential to directly image and characterize (spectroscopy) exoplanets. However, their performance is affected due to lack of accurate pointing control. We addressed this issue by introducing a robust, easily adaptable technique to prevent the coronagraphic leaks for low IWA phase mask coronagraphs.

In this paper, we showed in simulations that with the realistic AO phase residuals as an input that the Lyot-based low order wavefront sensor (LLOWFS), by using the unused starlight reflected by the Lyot stop, is capable of measuring tip-tilt with the accuracy of $\approx 10^{-2}\lambda/D$ (2–12 nm at 1.6 μm) per mode on the four quadrant phase mask (FQPM).

We demonstrated the LLOWFS preliminary laboratory implementation and performance under a lack of stable environment. We estimated tip-tilt errors with a measurement accuracy of $\approx 10^{-2}\lambda/D$ at 638 nm per mode in an open loop regime with the FQPM.

Our simulation and laboratory performance show that the LLOWFS has reliable accuracy with the FQPM. Future work includes the simulation, performance verification, and contrast sensitivity of our technique with other phase masks such as the Roddier phase masks (Roddier & Roddier 1997), the vortex, the eight octant phase mask, and phase-induced amplitude apodization with a variable focal plane mask.

Aiming to make the LLOWFS more efficient and versatile, the measurement and correction of other low order aberrations such as focus and the astigmatisms will also be studied.

To further demonstrate our concept we have equipped the revised SCExAO testbed with the phase mask coronagraphs listed above together with their corresponding reflective Lyot stops. The laboratory tests under closed loop regime are currently ongoing and we aim to test the system on-sky soon.

REFERENCES

Belikov, R., Kasdin, N. J., & Vanderbei, R. J. 2006, ApJ, 652, 833

Baudoz, P., Dorn, R. J., Lizon, J. L., Fuscon, T., Dohlen, K., et al. 2010, Proc. SPIE, 7735, 77355 B

Digby, A. P., Hinkley, S., Oppenheimer, B. R., et al. 2006, ApJ, 650, 484

Guyon, O. 2003, A&A, 404, 379

———. 2005, ApJ, 629, 592

Guyon, O., Pluzhnik, E. A., Kuchner, M. J., Collins, B., & Ridgway, S. T. 2006, ApJ, 167, 81

Guyon, O., Matsuo, T., & Angel, R. 2009, ApJ, 693, 75

Jovanovic, N., Guyon, O., Martinache, Clergeon, C., Singh, G., Vievard, S., Kudo, T., Garrel, V., et al. 2013, Proc. of AO4ELT, 3, 13396

Kern, B., Guyon, O., Kuhnert, A., Niessner, A., Martinache, F., & Balasubramanian, K. 2013, Proc. SPIE, 8864, 88640 R

Lloyd, J. P., & Sivaramakrishnan, A. 2005, ApJ, 621, 1153

Lagrange, A., Gratadour, D., Chauvin, G., et al. 2009, A&A, 493, L 21

Marois, C., Macintosh, B., Barman, T., et al. 2008, Science, 322, 1348

Murakami, N., Uemura, R., Baba, N., Nishikawa, J., Tamura, M., Hashimoto, N., & Abe, L. 2008a, PASP, 120, 1112

Mawet, D., Serabyn, E., Liewer, K., et al. 2010, ApJ, 709, 53

Roddier, F., & Roddier, C. 1997, PASP, 109, 815

Rouan, D., Riaud, P., Boccaletti, A., Clénet, Y., & Labeyrie, A. 2000, PASP, 112, 1479

Shaklan, S. B., & Green, J. J. 2005, ApJ, 628, 474

Sivaramakrishnan, A., Soummer, R., Sivaramakrishnan, A. V., Lloyd, J. P., Oppenheimer, B. R., & Makidson, R. B. 2005, ApJ, 634, 1416

Vogt, F. P. A., Martinache, F., Guyon, O., et al. 2011, PASP, 123, 1434

Wallace, J. K., Angione, J., Bartos, R., Best, P., Burruss, R., Fregoso, F., Levine, B. M., Nemati, B., et al. 2010, Proc. SPIE, 7015, 70156 N

2.3 A reflective Lyot stop-based wavefront sensor

The general concept of the LLOWFS is described in detail in *Pub.* §2. Here, I will remind the principle of the LLOWFS in the context of a FQPM. Figure 2.1 describes the optical layout of the LLOWFS[2]. At the entrance, a pupil (P, Fig. 2.1 (a)) with central obscuration and spider arms is considered. The beam at the entrance of P is focused on a FQPM (M) which is situated at the first focal plane of the optical system in Fig. 2.1 (b). This phase mask divides the focal plane in four quadrants and provides a π-phase shift between adjacent quadrants. This π phase shifted coronagraphic focal plane image is shown in Fig. 2.1 c).

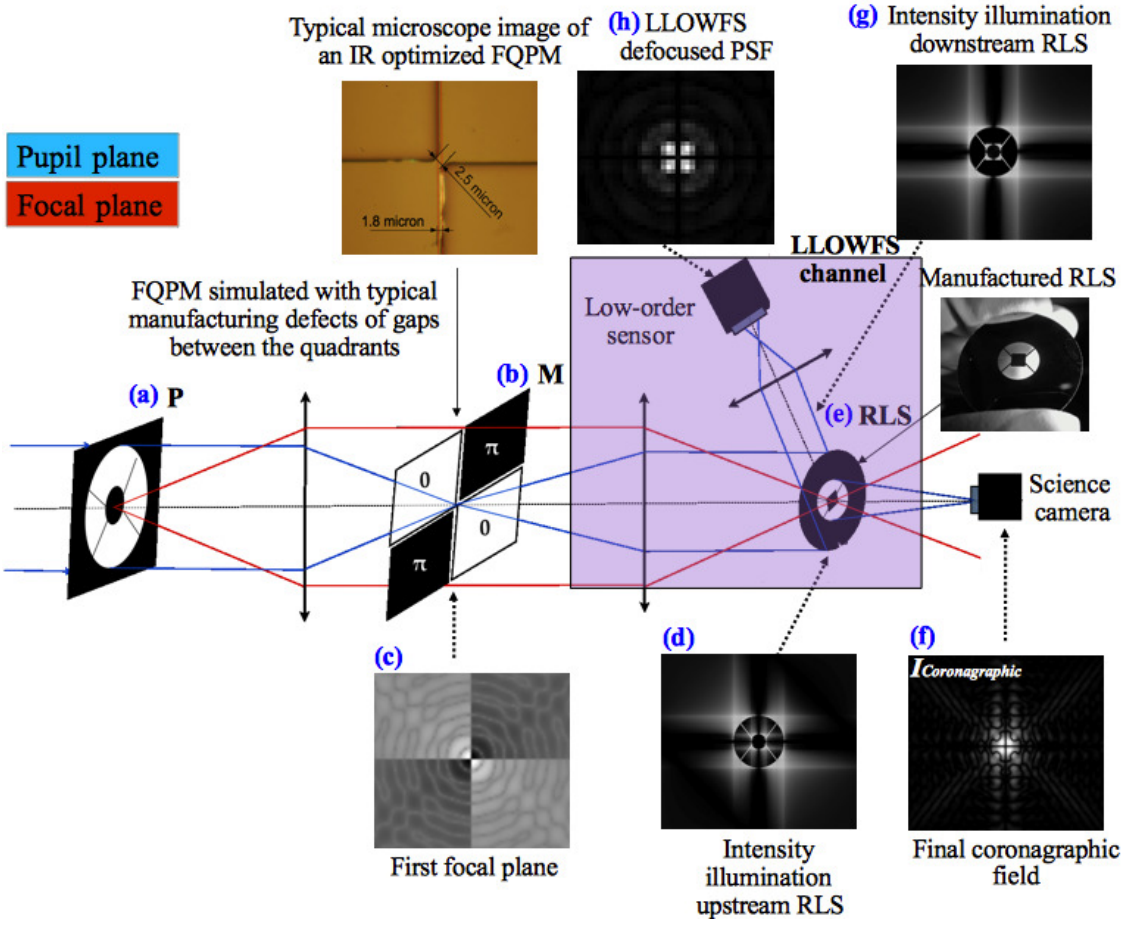

Figure 2.1: Optical layout of the LLOWFS with a FQPM. Shown are the intensities at respective focal and pupil planes. The FQPM in (b) is simulated with a typical manufacturing defects of 1.8 μm (0.04 λ/D) between adjacent quadrants and a gap of 2.5 μm (0.06 λ/D) across the diagonal of the mask. The RLS shown in (e) has the reflective surface appears to be black and the transmissive surface as white.

The FPM at the focal plane diffracts the starlight outside of the geometrical pupil. In a reimaged pupil plane downstream the FPM, the amplitude of the complex coronagraphic

[2]The description of each component of the optical system presented in Fig. 2.1 is described in more details in §2.4

field is shown in Fig. 2.1 (d)). A square pattern of diffracted intensity can be seen around the primary and secondary of the pupil due to the square geometry of the FQPM. At this plane, a reflective Lyot stop (Fig. 2.1 (e)) is situated, which instead of simply blocking the starlight, reflect it towards the low-order sensor (a detector), which I will refer as the LLOWFS camera in this thesis.

Now recalling the Eq. 1.18, which represents the electric field inside the Lyot plane in a coronagraphic imaging system

$$\frac{\psi_E(\xi,\lambda)}{\psi_0} = (P * \mathcal{F}^{-1}[M])L + i\,(\phi * \mathcal{F}^{-1}[M])L\,, \tag{2.1}$$

and the complex amplitude of the field at the Lyot plane is $A_E = \mathcal{F}[\psi_E]$. The intensity downstream the RLS in the science path is $I_{Coronagraphic} = |A_E|^2$ (Fig. 2.1 (f)).

However, outside of the Lyot stop, the electric field $\psi_R(\xi,\lambda)$ (Fig. 2.1 (g)) can be defined as

$$\frac{\psi_R(\xi,\lambda)}{\psi_0} = (P * \mathcal{F}^{-1}[M])(1-L) + i\,(\phi * \mathcal{F}^{-1}[M])(1-L)\,. \tag{2.2}$$

$\psi_R(\xi,\lambda)$ represents the complex field downstream of RLS in the LLOWFS channel highlighted in Fig. 2.1. Now expanding the Eq. 2.2

$$\frac{\psi_R(\xi,\lambda)}{\psi_0} = (P * \mathcal{F}^{-1}[M]) - P * \mathcal{F}^{-1}[M])L) + i\,(\phi * \mathcal{F}^{-1}[M])(1-L)\,, \tag{2.3}$$

where $P * \mathcal{F}^{-1}[M])L$ inside the Lyot pupil plane is zero. The term $(P * \mathcal{F}^{-1}[M])$, is independent of ϕ which dictates that even when the wavefront is perfect, there is already some light at the LLOWFS focal plane. The complex amplitude A_R at LLOWFS focal plane is then obtained by taking the Fourier transform of the complex electric field $\psi_R(\xi,\lambda)$ outside the Lyot pupil plane. A_R is then written as

$$\frac{A_R(x)}{\psi_0} = (\mathcal{F}[P]M) + i\,(\mathcal{F}[\phi]M) * \mathcal{F}[(1-L)]\,. \tag{2.4}$$

Replacing the term $(\mathcal{F}[P]M)$ by A_0 and $i\,(\mathcal{F}[\phi]M) * \mathcal{F}[(1-L)]$ by $G[\phi]$, Eq. 2.4 becomes

$$\frac{A_R(x)}{\psi_0} = A_0 + G[\phi]\,, \tag{2.5}$$

where A_0 the complex amplitude obtained by the LLOWFS camera for a perfect wavefront.

2.3.1 LLOWFS Hypothesis

By definition, any optical system is linear in complex amplitude. So the A_R obtained in LLOWFS camera plane is a linear function of the pupil plane complex amplitude A_E. The aberration-free complex amplitude distribution A_R in the LLOWFS camera and the change introduced on this complex amplitude by the low-order modes to be measured is nonorthogonal.

Since Eq. 2.5 is a linear function of ϕ in complex amplitude

$$\frac{A_R(x)}{\psi_0} = A_0 + mG[\phi] \,, \tag{2.6}$$

where m is a linear operator. The corresponding reflected light intensity $I_R = |A_R|^2$ (Fig. 2.1 (h)) in the LLOWFS camera is

$$I_R = I_0 + 2Re[A_0\overline{mG[\phi]}] + |mG[\phi]|^2 \,, \tag{2.7}$$

where I_0 corresponds to the reflected intensity with no wavefront aberration. I will call I_0 as a reflected reference image throughout the thesis. I_R is a linear function of $G[\phi]$ as long as

$$|mG[\phi]|^2 \ll Re[A_0\overline{mG[\phi]}] \,. \tag{2.8}$$

Equation 2.8 is satisfied if and only if $|mG[\phi]| \ll |A_0|$, which holds true only for small wavefront aberrations. The basis of LLOWFS theory is then

$$I_R = I_0 + 2Re[A_0\overline{mG[\phi]}] \,. \tag{2.9}$$

2.3.1.1 Linearity approximation

At the entrance of Fig. 2.1, lets consider small aberrations, $\phi \ll 1$ radian RMS (which is a typical value of a post-AO wavefront residuals). According to Eq. 2.9, the variations in the I_R downstream of a FPM is a linear function of the low-order aberrations that has caused these coronagraphic leaks.

Consider I_R as an aberrated image at any instant t. Then, the difference between I_R and I_0 in Eq. 2.9 can be decomposed into the linear combination of modes to be measured. If I consider only pointing errors, then I can write LLOWFS equation as

$$I_{R(\alpha_x,\alpha_y)} - I_0 = \alpha_x S_x + \alpha_y S_y + \nu \,, \tag{2.10}$$

where ν is the residual of higher order modes, $I_{R(\alpha_x,\alpha_y)}$ is the reflected image with unknown tip-tilt errors (α_x, α_y), which is recorded by the LLOWFS camera at an instant t. S_x and S_y are the calibrated responses (§2.3.2) of the sensor to the tip and tilt errors respectively. The unknown errors (α_x, α_y) in Eq. 2.10 are computed through a least-square fit of the measured pixel intensity values. In simulations, approximately a 30-pixel diameter disk is considered.

2.3.1.2 Defocus in the sensor position

If the requirement is to control only the pointing errors in a system, then the LLOWFS camera can be in the focal plane to estimate the tip-tilt modes. However, for centrosymmetric aberrations (focus and the spheric aberrations), LLOWFS camera can estimate their amplitudes but not their signs, because of their symmetry around the focal plane. As a result, these modes create an orthogonality between A_0 and $mG[\phi]$, which implies to $Re[A_0\overline{mG[\phi]}] = 0$, thus violating the Eq. 2.8. In that case, the LLOWFS image I_R in Eq. 2.7 becomes a quadratic function of the wavefront aberrations, $I_R = I_0 + |m\phi|^2$.

A way to break this orthogonality is to introduce a defocus in the position of the LLOWFS camera. The value for the defocus should be chosen carefully, which can be different for different coronagraphs as it depends on how a FPM is redistributing the starlight and where most of the light is concentrated[3] in the reimaged LLOWFS camera plane.

The defocus value is the tradeoff between the number of modes to be corrected and the speed of the sensor. A large defocus allows to correct more modes but spreads the signal over a larger number of pixels, which requires to integrate longer. A small defocus is more adapted for faint stars but does not allow to correct a lot of modes. Therefore, during on-sky closed-loop operations, the amount of sensor defocus should be selected depending on the detector and the brightness of the star. Figure 2.2 (a) shows simulated reference images (I_0) of the LLOWFS in case of a FQPM for different defocus position in the LLOWFS camera. I found out that 5 radian RMS of defocus produced clean modes and gave relatively better performance in sensor measurements with a FQPM, so I used this value for the rest of my simulations. §2.4.1 and §2.4.2 present the effect of different defocus values on the linear response of the LLOWFS in case of no aberration and Zernike aberrations respectively.

2.3.1.3 Measurement of the low-order modes other than pointing errors

At the entrance pupil of Fig. 2.1, lets consider that the wavefront is composed of low-order modes i of amplitude $\boldsymbol{\alpha} = (\alpha_1, \alpha_2 \cdots \alpha_n)$, where n is the total number of modes. Then, any reference subtracted LLOWFS image can be projected on to the basis of low-order modes i.e can be decomposed linearly on a base of orthonormal images S_i corresponding to the response of the sensor to the low-order modes. I can define a general mathematical equation following this formalism as follows

$$I_{R(\alpha)} - I_0 = \sum_{i=1}^{n} \alpha_i S_i + \nu_n \,, \tag{2.11}$$

where ν_n is the residual coming from the modes higher than the n-th mode. However, this equation is valid only if the reference image I_0 stays constant for the duration of the experiment. As the measurements are relative to a zero-point, the reference should be stable in order for the linear model in Eq. 2.11 to remain consistent. The LLOWFS image is an array of pixels values read from the LLOWFS camera (a detector). To avoid

[3]For a PIAA coronagraph, the reflected light is concentrated in an annulus whereas for a VVC, most of the light is at the center of the LLOWFS PSF.

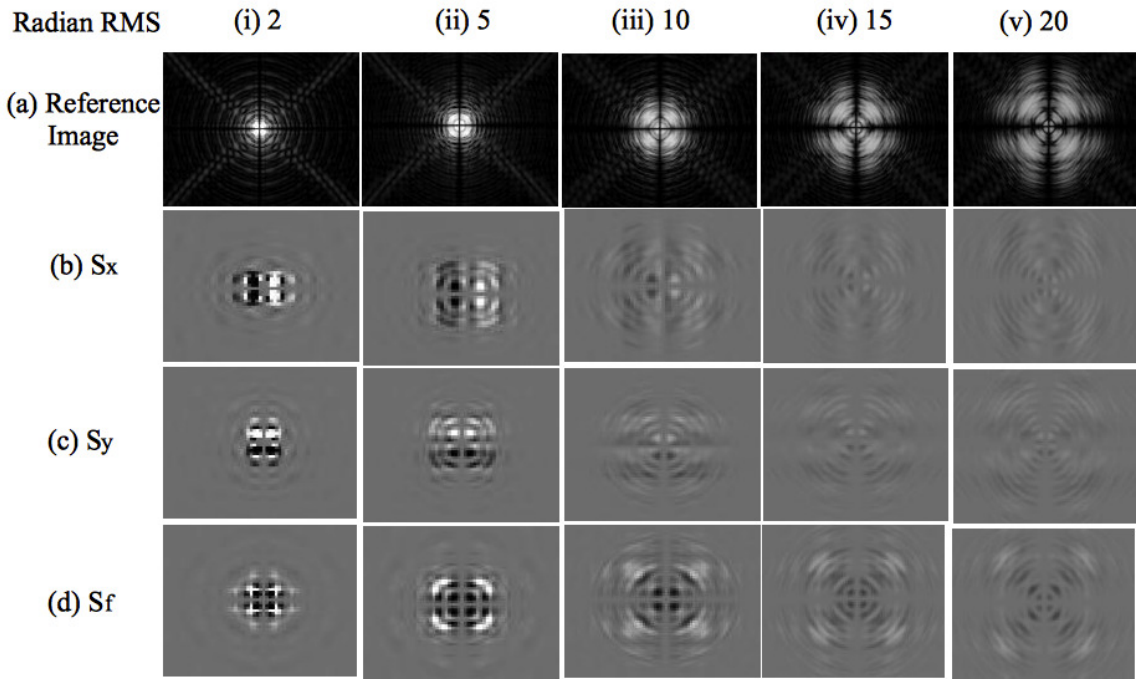

Figure 2.2: Simulated reference and response matrix for different defocus position of the low-order sensor for a FQPM. (a) Reference images under no phase aberration (§2.3.1.2). Images from (b) to (d) are the calibration frames for tip (S_x), tilt (S_y) and focus (S_f) respectively (§2.3.2) obtained after applying 0.01 radian RMS of respective Zernike phasemap. *Note: The images in each row is at same brightness scale.*

sensitivity to the variations of the source flux, low-level of processing such as the bias-subtraction, normalization to unity pixel values sum should be performed on the images.

For the correction of the estimated α_i for n number of modes, an active control is then provided by computing the control commands and actuating a correction device either a fast steering mirror or a deformable mirror to compensate for the aberrations (§2.3.4).

For my initial simulations during the first year of my thesis, I have used least-squares method to measure the first five Zernike low-order modes via Eq. 2.11 in an open-loop with the LLOWFS. Even for my laboratory experiments of LLOWFS in open-loop regime with different coronagraphs, I used least-squares method to measure low-order aberrations up to 35 modes (§4.5). However while working on the LLOWFS control loop (§2.3.4) during my last year, the measurements and correction using Eq. 2.11 were done by calculating a control matrix using a Singular Value Decomposition (SVD) method for optimal performance. The SVD allows to filter the lowest eigenvalues. Without filtering, the SVD is equivalent to the least squares method.

2.3.2 Calibration frames S_i (*Pub.* §3.2)

For the real time control of the low-order wavefront aberrations by the LLOWFS, calibrating the response of the system to the low-order modes prior of a closed-loop operation is

mandatory. This is achieved by first introducing known amount of aberrations upstream of a FPM and measuring the linear response of the sensor (S_i, for a low-order mode i) to the applied low-order modes. Using these responses, a LLOWFS image is then decomposed in to a linear sum of aberrations (Eqs. 2.10, 2.11)). This process will only require an actuating element to send controlled amount of aberration in the coronagraphic system in order to obtain sensor response to the applied aberration. In general, I will refer these sensor responses as calibration frames, whereas when I will explain the control loop theory, I will combine them to form the response matrix.

To compute sensor response S_i, I apply a pure Zernike phasemap upstream of the FPM for the mode i with an amplitude a_{ci}. I simulate the impact of that phasemap in the LLOWFS camera and normalize the response with the reference frame. I define a general equation as,

$$S_i = \frac{I_{Ri} - I_0}{a_{ci}} , \tag{2.12}$$

where I_{Ri} is the LLOWFS image recorded by the LLOWFS camera for the mode i and I_0 is the reference image. Equation 2.12 is used to compute the response S_i for any i^{th} mode.

For my simulations, I have obtained S_i for tip, tilt, focus, oblique and right astigmatisms for the coronagraphic system presented in Fig. 2.1 in ideal conditions with no aberrations. Figure. 2.2 (b-d) shows the sensor response to the first three Zernike modes: tip, tilt and focus respectively when applied to the system with an amplitude of 0.01 rad RMS. The image I_{Ri} for each S_i I simulated, is the average of 100 individual frames to reduce noise. I show these calibration frames for different defocus position of the sensor as well. It is clear that for large value of defocus, the calibration signals are distributed over a large area on the detector. LLOWFS measurements for the signals in Fig. 2.2 (b-d) (iii-v) will be limited by the camera dark current and readout noise.

Tip-tilt motions upstream of the FPM changes the shape of the LLOWFS PSF while downstream the FPM, Non Common Path (NCP) errors change the position of the PSF on the LLOWFS camera. These NCP errors in the LLOWFS channel can be introduced only by the motion of the lens or the camera. During measurements of the low-order aberrations, the response of the sensor does not depend on the position of the PSF on the LLOWFS camera but does relies on its shape. However, while acquiring the calibration frames (the response S_i and the reference I_0), if any external factor such as temperature variations and the instrument flexure changes the position of the low-order PSF by introducing tip-tilt errors (positional errors) then a new calibration should be reacquired, prior of estimating the unknown low-order aberrations. Since these errors are not compensated, the tip-tilt upstream and downstream the FPM is assumed to remain stable during the acquisition of the calibration.

Therefore, how often one needs to reacquire the calibration frames depends directly on the stability of the reference image on the detector. If these positional errors are out of the linear range (§2.3.3) and happen prior to closed-loop operation, then only the coronagraphic PSF need to be realigned behind the FPM and previously acquired calibration frames can be reused to close the loop. However such errors will not affect the closed-loop

operation as the low-order correction will compensate for them.

2.3.3 Sensor Linearity

An important metric for the characterization of the LLOWFS performance is the sensor linearity. It is important to understand –

- What is the linearity range of the sensor, i.e. the range over which the measurement is linear to $p\%$.
- Is it different for different modes,
- What are the factors that can affect this range and,
- How much crosstalk is introduced when trying to measure higher number of modes.

To check the linearity range of the sensor in my simulations (§2.4) and laboratory experiments (§4.3), I sequentially apply Zernike mode phasemaps with increasing amplitude (β_i) upstream of the FPM. For each phasemap applied, I record the corresponding LLOWFS image in another cube. With the help of the pre-computed S_i, I decompose this cube of aberrated LLOWFS images in Eq. 2.11. Using the measurements α_i, I estimate $\hat{\beta}_i$. I then compare the estimated amplitudes by the LLOWFS to the actual amplitudes of the Zernike coefficients introduced in the system. To check the linearity in the response of the sensor for each mode studied, I linearly fit the data points using a least square algorithm. To check the crosstalk between the different modes, I also analyze the residuals measured by the LLOWFS for the other modes. The open-loop measurement accuracy is calculated as σ_i of ($\hat{\beta}_i$ - β_i), where σ_i is the standard deviation calculated for each mode i.

2.3.4 Correction of the low-order modes

For the optimal performance of LLOWFS closed-loop operation, the measurements α_i of the low-order errors in Eq. 2.11 were done through the SVD method by pseudo-inverting the response matrix S (composed of the calibration frames S_i computed for each mode i) to provide the optimal solution to the least-squares problem in Eq. 2.11. Figure. 2.3 shows closed-loop control operation of the LLOWFS. The steps to acquire the calibration are the following:

- First, I record the reference image I_0, a 2-D image converted into a 1-D vector of N_{pix} total pixels.
- I record the response matrix S by successively sending n Zernike modes on the actuator. S then has a dimension of $N_{pix} \times n$.
- I compute the pseudo-inverse of the response matrix S to get the control matrix C of dimension $n \times N_{pix}$.

After acquiring the calibration frames, the loop is then closed using the following steps:

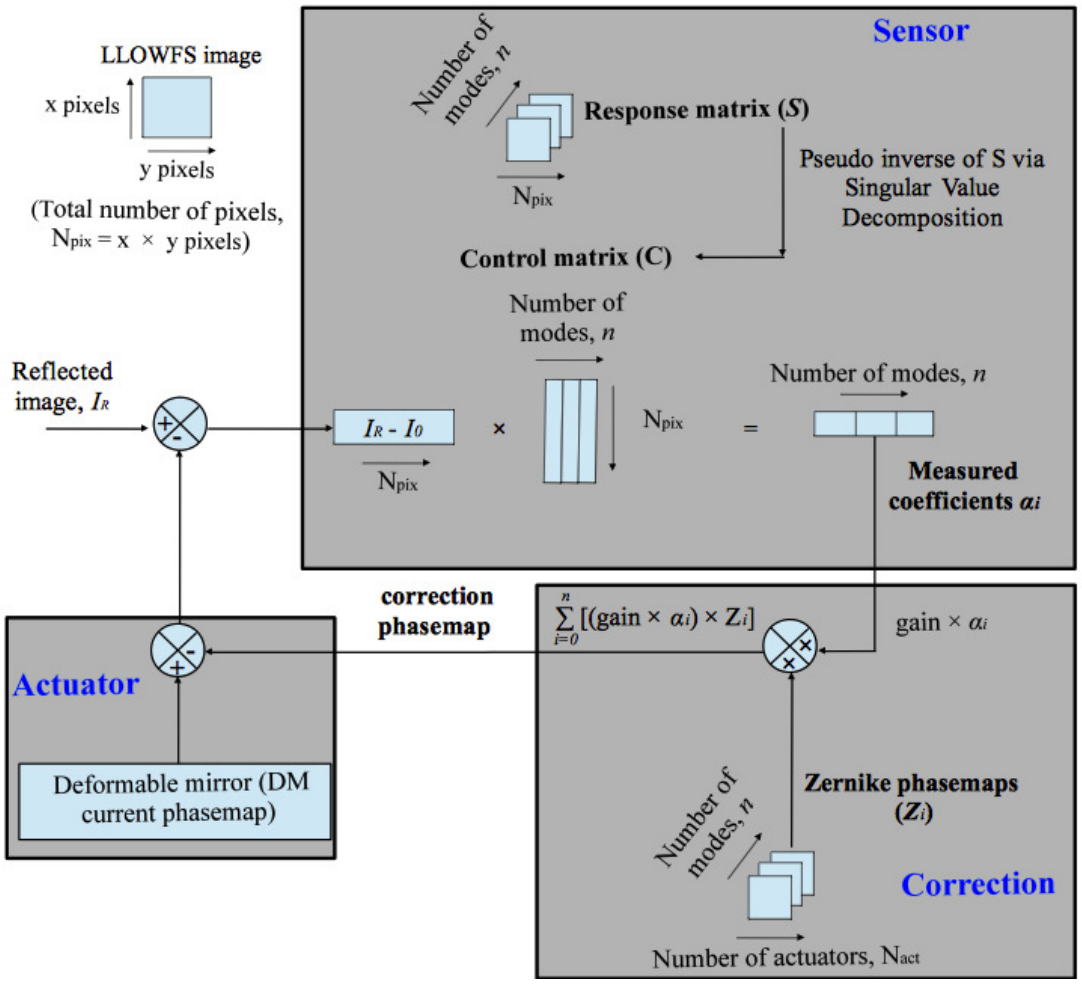

Figure 2.3: Control loop of the LLOWFS. In Eq. 2.11, the Pseudo inverse of the response matrix S through a singular value decomposition method returns the control matrix C, which in turn is used to get the measurements α_i of the unknown low-order errors. These measurements are used by an integrator controller to compute the correction, which are then sent to an actuating element such as a deformable mirror to compensate for the aberrations in the image I_R.

- If I_R is the aberrated image recorded on the LLOWFS detector, I convert this 2-D image into 1-D with total number of pixels as N_{pix}.

- The control matrix C is then multiplied with the reference subtracted 1-D LLOWFS image $I_R - I_0$. The result of this matrix multiplication is the vector of the measured low-order coefficients α_i with dimension $1 \times n$. This process is shown in the **Sensor** box of Fig. 2.3.

- This vector of measurements is then used by an integrator controller to compute the correction that should be applied to the actuator. In the **Correction** box of Fig. 2.3, the measurements α_i can either be multiplied with a flat gain or with modal gains (different gains for different modes). These corrections are then multiplied with a set of low-order Zernike phasemaps (Z_i) for which each α is measured. The Z

matrix has a dimension of $N_{act} \times n$, where N_{act} is the total number of actuators. The sum of all the Z_i phasemaps after their multiplication with the corresponding α is the final single 2-dimensional correction phasemap.

- The correction phasemap computed in the previous step is then subtracted from the current actuator phasemap of the actuator, for example a deformable mirror. The correction applied on the DM compensate for most of the low-order aberrations in image I_R.

I used the procedure presented here to measure and correct for the low-order aberrations using the LLOWFS images cropped to 40×40 pixels, and the 2000-actuators deformable mirror in §4.5 and §4.6. In the next section, I will present several of my simulations written in *Python language* to measure the low-order aberration in an open-loop scenario using the least-squares method.

2.4 Numerical simulations (*Pub.* §3.3)

To characterize the sensor linearity and the effect of different defocus positions of the sensor on the LLOWFS measurement, I have simulated the optical system presented in Fig. 2.1. In my simulations, I have considered the pupil geometry of the Subaru Telescope for the entrance of the system. In this thesis, the LLOWFS is developed for SCExAO, the extreme adaptive optics system of the Subaru Telescope, therefore my simulations are relevant to the SCExAO instrument.

The FQPM at the focal plane is optimized for a wavelength of 1.6 μm. The typical manufacturing defects of 1.8 μm (0.04 λ/D) between adjacent quadrants and a gap of 2.5 μm (0.06 λ/D) across the diagonal at the center of the phase mask is also taken into consideration. These values corresponds to the size of the defects in the FQPM I used in the laboratory. A microscopic image of a defected FQPM is shown in Fig. 2.1 (b).

At the re-imaged pupil plane, a RLS (Fig. 2.1 (e)) is simulated according to the intensity pattern diffracted around the central obscuration and spider arms. The outer edge of the pupil of the RLS is 5% undersized of the outer diameter of pupil P while the central obscuration and the spider arms are respectively 20% and 50% oversized. I defined the external diameter of the RLS as three times the outer diameter of the pupil P. I assumed that the reflective surface of the RLS is uniform and did not take into account the slight chromaticity of the reflective coating on the RLS.

Note: I did simulate a RLS with an infinite outer diameter, as well as twice and three times the outer diameter of P. I found out that the linearity results in all three cases were somewhat similar because the FQPM does not diffracts the starlight too far out of the geometrical pupil P. Therefore, in this case large amount of photons are available for RLS right outside the edge of the geometrical pupil to reflect them towards the LLOWFS camera.

The size of the RLS does depends on how far the FPM diffracts starlight outside of the pupil, which therefore defines the optimal outer diameter for the RLS. Depending on the constraint set by the coronagraphic system, either the FPM should be optimized to diffract

the starlight within the reflective zone of the RLS or the reflective diameter of the RLS should be designed to accommodate enough starlight photons. This problem is discussed in (§3.4.3.1 of Chapter 3) in case of a PIAA coronagraph where an unoptimized achromatic amplitude FPM (Newman *et al.*, 2013) diffracted most of the starlight outside of the reflective zone of the RLS, which affected the closed-loop performance of the LLOWFS.

With the elements of a coronagraphic optical system described above, I have performed four sets of LLOWFS simulations in *Python*, which are as follows:

- §2.4.1, Ideal condition: In this regime, no aberration is applied externally to the optical system, the wavefront at the entrance pupil is ideal.
- §2.4.2, Low-order Zernike phase defects: At the entrance of the pupil, phasemaps of tip, tilt, focus, oblique and right astigmatisms with varying amplitude are applied. The sensor linearity is then studied individually for each mode.
- §2.4.3, Post-AO188 phase residuals[4]: A series of 200 post-AO188 phasemaps with unknown low- and high-order aberrations with $\approx$ 180 nm rms amplitude is applied upstream of the FQPM. First five Zernike modes are then measured by the LLOWFS in each phasemap.
- Sensor defocus: All of the simulations mentioned above are retested under different values of the defocus position in the sensor.

None of my simulations presented in this chapter considered photon noise. Due to time constraints, I could not refine my simulator and perform photon noise tests. As after LLOWFS first publication, the foremost requirement was to implement it directly on the real system.

In Fig. 2.4, I present the visualization of the intensity illumination at each step of my simulation with some phase defects upstream of the FQPM. At the entrance, I show a post-AO188 phasemap of 0.59 radian RMS as ϕ. I used Fourier transform ($\mathcal{F}$) to go from pupil plane to focal plane and inverse transform ($\mathcal{F}^{-1}$) from focal plane to the pupil plane. To minimize the aliasing effect of the Fourier transform and to achieve large pixel sampling of both the pupil and the image plane, I used an image of 512×512 pixels with a pupil outer diameter of 128 pixels ($1\ \lambda/D = 4$ pixels).

In this figure, I show two optical paths –

- The science path (1), which shows the aberrated coronagraphic PSF of the FQPM at the final science detector plane,
- The LLOWFS path ((2) and (3)), which shows the final low-order PSFs for two different sizes of the RLS (Note that no sensor defocus is introduced in these paths. This is just to show the focused image with the LLOWFS).

  In the LLOWFS path (2), I considered that the RLS has an infinite reflective area outside of the geometrical Lyot pupil while in the LLOWFS path (3), I considered

[4]SCExAO is fed by AO system known as AO188, which delivers post correction RMS wavefront errors of $\approx$ 200 nm in good seeing (Strehl ratio of $\approx$ 40% in the H-band)

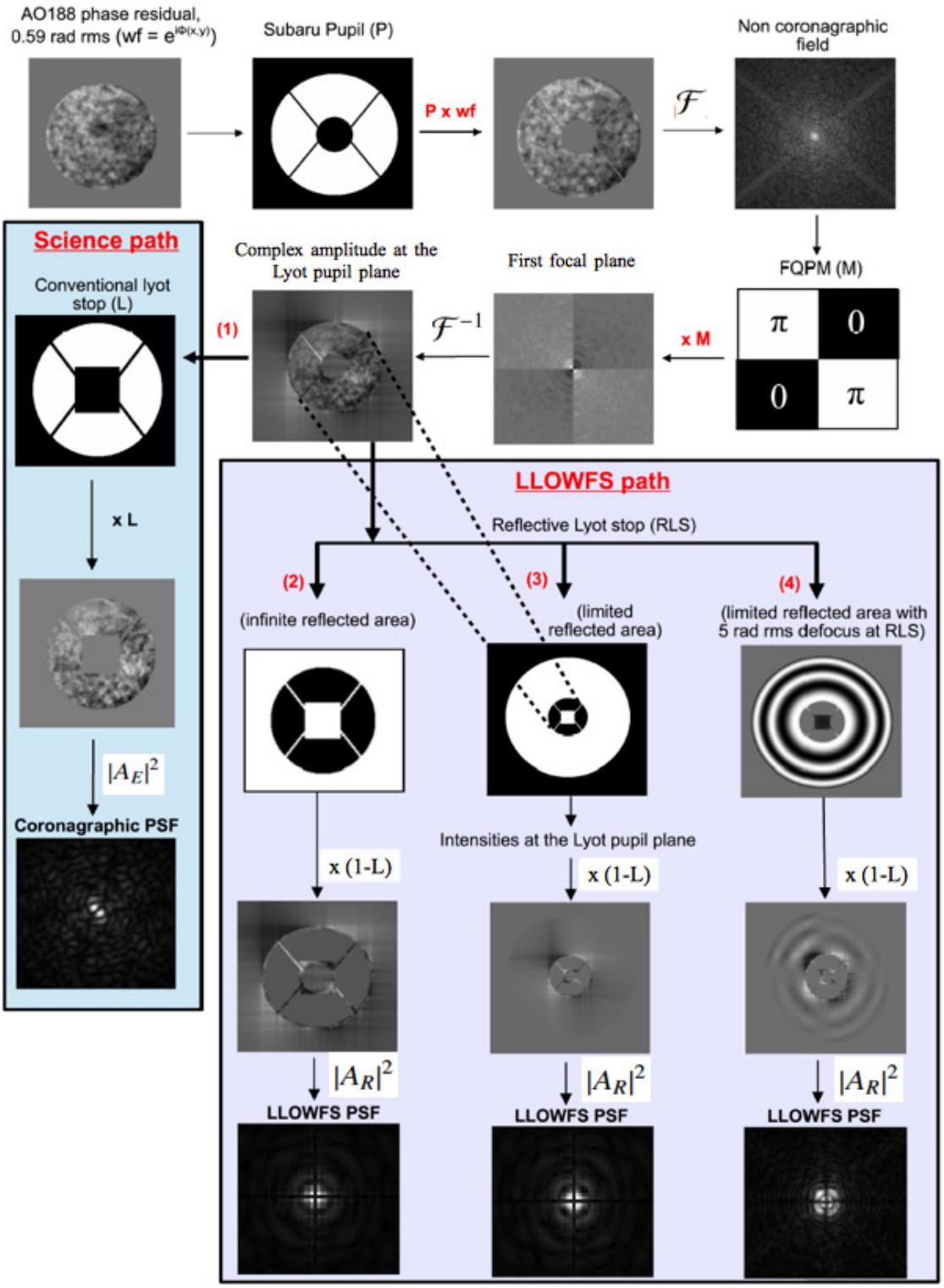

Figure 2.4: LLOWFS simulation showing intensity pattern at each step of the Fourier transform from pupil to image plane and vice versa. Two different sizes of the outermost reflective diameter of the RLS in LLOWFS path ((2) and (3)) shows the difference in sharpness in both low-order PSFs. *A_E and A_R are the complex amplitude at the final focal plane of the science and LLOWFS camera respectively.*

that the outermost reflective diameter of the RLS is three times the outer diameter of P. The shape of the low-order PSF is indeed sharper in path (2) than in (3) but in this case, it did not affect the linearity measurements of tip-tilt.

- The path in (4) is the same as in (3) but with a sensor defocus of 5 radian RMS.

For all of my simulations, I have performed the linearity tests with the low-order PSF shown in LLOWFS path (4) of Fig. 2.4.

2.4.1 Ideal case with no aberration (*Pub.* §3.3.1)

Following the LLOWFS path (4) of Fig. 2.4, I considered a perfect wavefront at the entrance ($\phi = 0$) and simulated a LLOWFS image. I recorded this image as I_0, which is shown in Fig. 2.2 (a)(ii). Then, using eq. 2.12, I computed the calibration frames S_i for tip, tilt, focus, oblique and right astigmatisms by applying successively 0.01 radian RMS of respective wavefront aberration upstream of the FQPM (Fig. 2.2 (b-d)(ii)).

Next, I sequentially applied tip aberration with amplitudes varying between ± 0.5 radian RMS (± 0.3 λ/D) at the entrance of P. This cube consisted of 100 images with step size of 0.01 radian RMS. Then, using eq. 2.11, I measured the α_i for tip and the residuals in tilt, focus, oblique and right astigmatism by least squares method.

The amplitude of estimated tip versus the applied tip is shown in *Pub.* Fig. 4. In this section, I show the linearity curves for the rest of the modes by repeating the same procedure as for tip mode. To study the sensor response to focus, I apply a cube of focus phasemaps with amplitudes varying between ± 0.5 radian RMS upstream of the FQPM. Then I measure the α_i for focus and residuals in tip, tilt, oblique and right astigmatisms by least squares. I repeat the same experiment for the other modes as well. Figures. 2.5 (a)(c), 2.6 (a)(c) shows the sensor linearity for the modes tilt, focus, oblique and right astigmatisms. In each figure, I also measure the residuals for the other modes.

For the FQPM coronagraph, just like tip mode, the sensor response to other modes except focus is also linear within ± 0.3 rad RMS (± 0.18 λ/D) of phase error with 1% of non-linearity in the measurement at 0.3 radian RMS. The accuracy of the linear fit is calculated as the ratio of the maximum output deviation divided by the full scale output, specified as a non linearity percentage. For focus, the linearity range is in between $\sim$ ± 0.15 rad RMS.

The right astigmatism mode is the dominating residual that is creating non-negligible crosstalk within the linear range of the measured modes in figures. 2.5 (a)(c), 2.6 (a). This is probably due to the symmetrical geometry of the FQPM mask. The signal at higher amplitude of aberration in tip, tilt, focus and oblique astig., is partially misinterpreted as right astigmatism due to non-linearities in the sensor signal. The crosstalk induced due to right astigmatism can be minimized by aligning the hairline of the FQPM with the spider arms of the pupil. I could not perform a test to confirm this assumption.

Nevertheless, I have repeated this test for eight different defocus position of the sensor from -5 to 20 radian RMS. Figures. 2.5 (b)(d), 2.6 (b)(d) shows the effects on the linearity of the modes studied due to different defocus position of the sensor. The linearity range

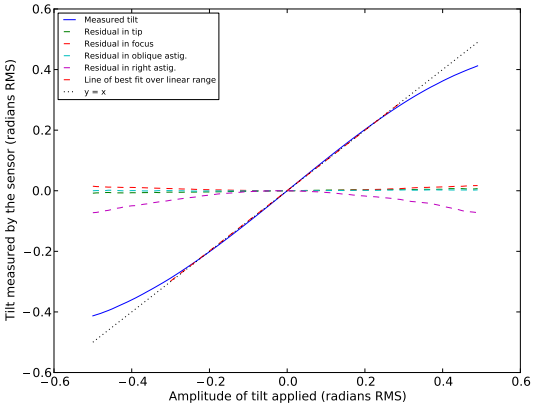

(a) Tilt measurement

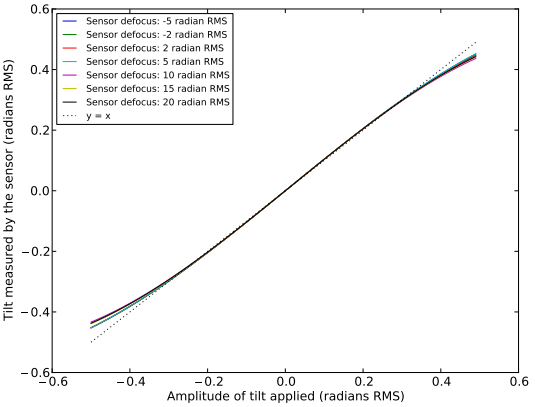

(b) Tilt measurement at different defocus position

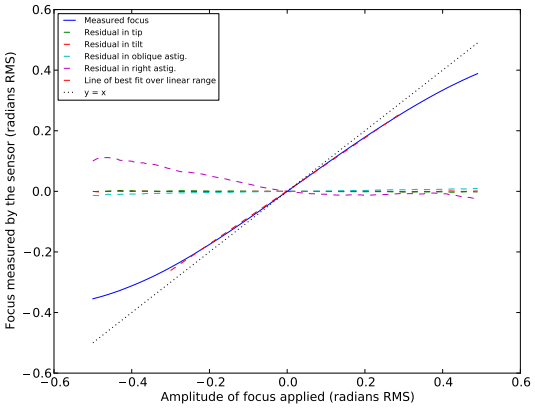

(c) Focus measurement

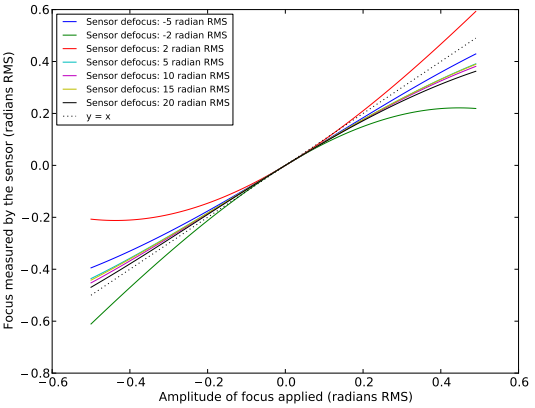

(d) Focus measurement at different defocus position

Figure 2.5: Response of the sensor to the aberrations applied individually in the system. (a) and (c) are the measurement of tilt and focus aberration at sensor defocus of 5 radian RMS respectively. The linearity of the sensor is ± 0.3 radian RMS for tilt and ± 0.2 radian RMS for focus. The residuals in other modes are also shown. (b) and (d) shows the effect of different defocus positions of sensor on the linearity range of the tilt and focus modes respectively. The linearity for focus mode in case of a FQPM does depend on the amount of defocus introduced in the system.

of tip, tilt and astigmatisms modes are not influenced at different defocus. However, it does have an effect on the focus because of its centrosymmetric property. In Fig. 2.6 (d), for the small defocus value in the sensor (± 2 radian RMS), the linearity range of focus measurement reduces because the defocus in the sensor is not enough to measure the focus aberration.

Note that these results are expected to be different for different coronagraphs.

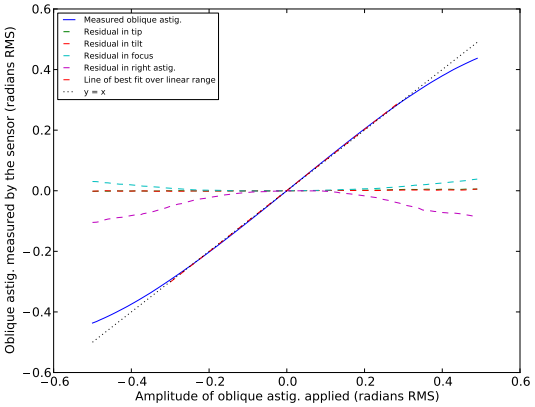

(a) Oblique astig. measurement

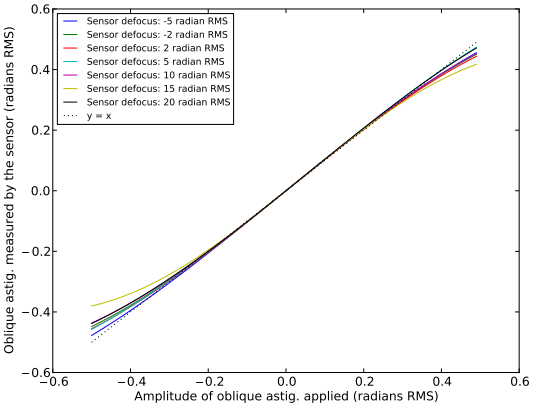

(b) Oblique astig. measurement at different defocus position

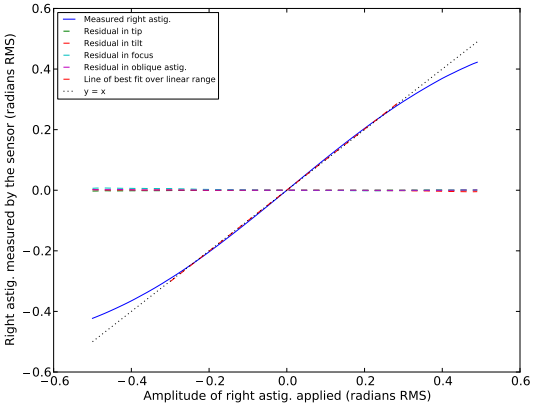

(c) Right astig. measurement

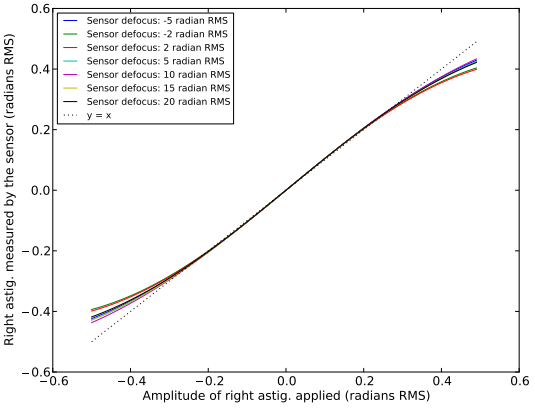

(d) Right astig. measurement at different defocus position

Figure 2.6: Response of the sensor to the aberrations applied individually in the system. (a) and (c) are the measurement of oblique and right astigmatism aberration at sensor defocus of 5 radian RMS respectively. The linearity of the sensor is ± 0.3 radian RMS for both astigs. The residuals in other modes are also shown. (b) and (d) shows little effect of different defocus positions of sensor on the linearity range of the oblique and right astigmatism modes respectively.

2.4.2 Sensor response to multiple Zernike aberrations (*Pub.* §3.3.2)

In this case, at the entrance pupil of the optical system in Fig. 2.1, ϕ is the sum of the phasemaps containing tip, tilt, focus, oblique and right astigmatisms errors in the input wavefront. A sequence of 100 phasemaps of these low-order errors, the amplitude of which is varied between ± 0.5 radian, is applied into the system. The first phasemap has all the modes with - 0.5 radian errors (290 nm total phase error over the Subaru pupil P), the 50th phasemap is free of aberrations and the 100^{th} phasemap has + 0.5 radian amplitude per mode. For each phasemap, I computed the corresponding I_R.

Using eq. 2.11, I measured α_i's for all the modes present in each I_R. The figure comparing the estimated tip mode to the amplitude of the applied tip mode is shown in *Pub.* Fig. 5. Here, I am showing the response of the rest of the modes. Figures 2.7 (a)(b)(c)(d) show the estimated tilt, focus, oblique and right astigmatisms versus the amplitude of the respective applied mode.

Under high amplitudes of the low-order errors, the linearity range is reduced from ± 0.3 radian RMS to ± 0.2 radian RMS (± 0.12 λ/D) for all the modes except focus. For tip-tilt, the non-linearity in measurement is 14% at 0.2 radian RMS and 32% at 0.3 radian RMS. The linearity range for the focus mode is reduced to ± 0.1 radian RMS with 45% of non-linearity at 0.2 radian RMS.

The aim of this simulation is to demonstrate two main points: – (1) The linearity range is affected under high amplitude of low-order aberrations, and – (2) Crosstalk is induced if the defocus value of the sensor is not chosen properly. In Fig. 2.7 (e), I show the linearity curve of the focus aberration for different defocus positions of the sensor. It is clear that under high amplitude of low-order errors, the non-linearities are introduced in the focus measurement. For smaller defocus value in the sensor position (between ± 2 radian RMS) and due to high amplitude of aberrations, large crosstalk can be noticed in the focus measurement. However, for high defocus value (≥ 5 radian RMS) in the sensor, a better estimation of the focus aberration is obtained with reduced crosstalk. Therefore, choosing the right value of defocus is important for the centrosymmetric aberrations such as focus and spherical.

2.4.3 Post-AO188 phase residuals (*Pub.* §3.3.3)

In this section, I present a test performed to analyze the LLOWFS sensitivity to low-order measurements under the realistic conditions where I apply a series of 200 phasemaps of simulated post-AO188 wavefront residual at the entrance of the system in Fig. 2.1. These phasmaps have unknown low- and high-order aberrations with ≈ 180 nm rms amplitude (average over all 200 phasemaps). Figure 2.4 shows one such phasemap of an AO188 phase residual of 0.59 radian RMS wavefront error. The PSF on the LLOWFS path (4) in this figure shows the corresponding aberrated reflected image I_R.

To measure the true amplitude of the aberration in each phasemap, I applied the least-squares method directly on the phasemaps projected over the Subaru pupil, to measure the true amount of aberration for five Zernike modes. Then, to estimate these errors via LLOWFS measurements, I recorded the I_R corresponding to each phasemap and decomposed it into low-order modes using Eq. 2.11.

In *Pub.* Fig. 6, I showed the tip mode estimated by the LLOWFS versus the true tip mode present in the wavefront. Also in *Pub.* Fig. 7, I compared the sensor measurements of the tip-tilt errors with the actual residual value present in the series of 200 phasemaps. Within the range of ± 0.2 radian RMS, the sensor reliably measured the tip-tilt errors. But for high amplitude errors (> 0.2 radian RMS), the response of the sensor to pointing errors degraded due to the non-linear effects.

In Fig. 2.8, I present the response of the sensor to (a) focus, (b) oblique astigmatism and (c) right astigmatism in the post-AO188 residual wavefront. The x-axis is the series

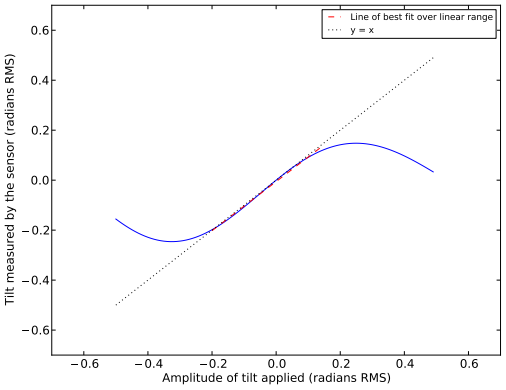

(a) Tilt measurement under phase defects

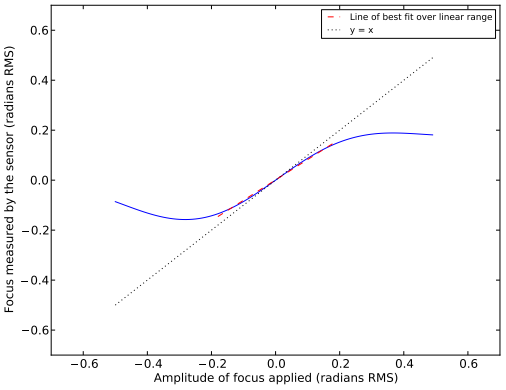

(b) Focus measurement under phase defects

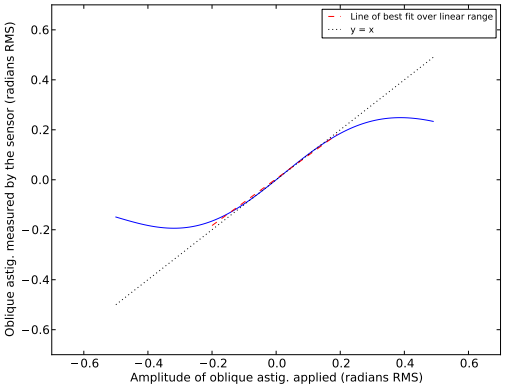

(c) Oblique astig. under phase defects

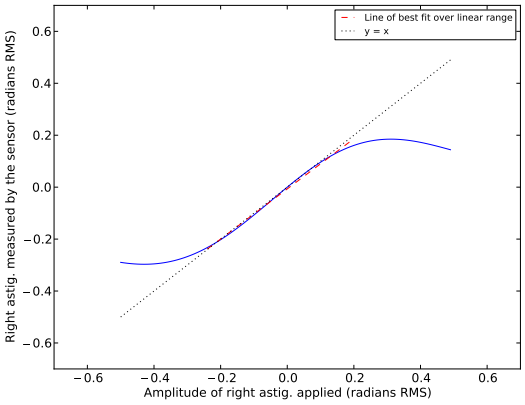

(d) Right astig. under phase defects

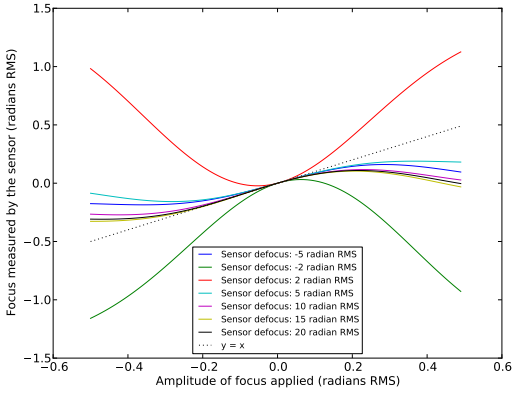

(e) Focus measurement under phase defects with different defocus position of sensor

Figure 2.7: Response of the sensor under the low-order phase errors upstream of the FQPM. (a)(b)(c)(d) are the measurement of tilt, focus, oblique and right astigmatism mode at sensor defocus of 5 radian RMS respectively. The linearity of the sensor reduced to ± 0.2 radian RMS for tilt and ± 0.1 radian RMS for focus. (e) shows the effect of different defocus position of the sensor on the linearity range of the focus mode. For sensor defocus between ± 2 radian RMS, strong crosstalk is introduced, indicating the importance of defocus in the sensor for the centrosymmetric aberrations like focus.

of phasemaps applied into the system and the y-axis shows the total error in radian RMS (red), the true value of the aberration present in the phasemaps (green) and the LLOWFS measurement (blue). The dashed line in each figure shows the measurement error per mode, which is the difference between the amplitude of the measured and true error in each phasemap.

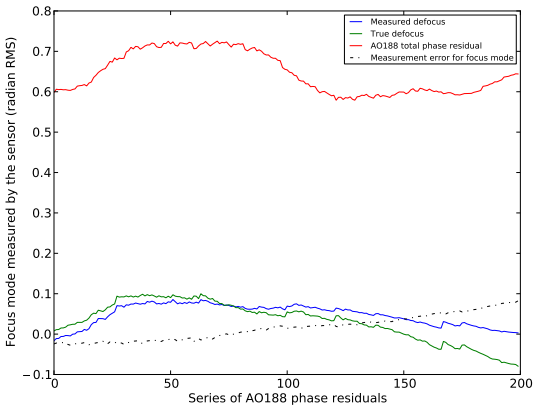

(a) Focus

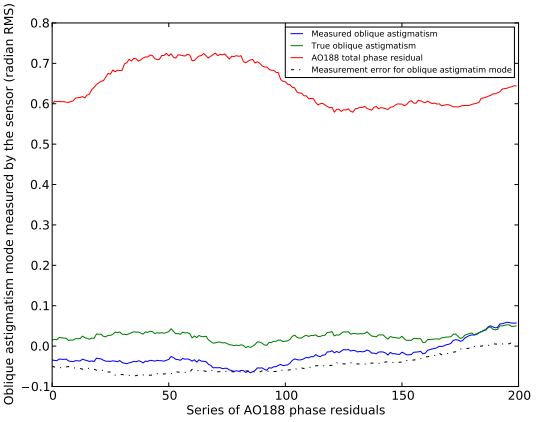

(b) Oblique astig.

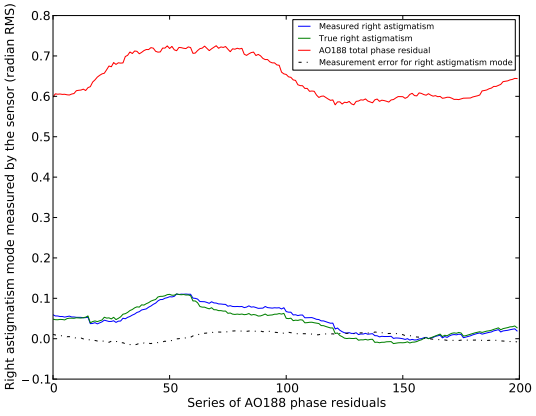

(c) Right astig.

Figure 2.8: Sensor response to (a) Focus, (b) Oblique and c) Right astigmatisms present in the realistic phase residuals of the Subaru Telescope AO188. The x-axis plots the simulated series of 200 post-AO phasemaps with unknown high- and low-order modes having $\approx$ 180 nm phase rms over the Subaru pupil. The y-axis in (a, b, c) shows the total error in radian RMS (red), the true amplitude of each aberration (green), the corresponding LLOWFS measurements (blue) and the measurement error (dashed line) per mode.

Each phasemap applied has random high-order aberrations. For errors > 0.7 radian RMS, and especially for oblique astigmatism, the measurement in Fig. 2.8 is affected due to crosstalk. High-order modes similar to astigmatisms like quadrafoil might have been misinterpreted as astigmatism.

Note that the LLOWFS is a coronagraphic low-order wavefront sensor which is designed to address the low-order aberrations in an ExAO corrected wavefront. Therefore, the quality of the measurement is degraded by the higher aberrations of the classical AO correction of AO188.

Moreover, for LLOWFS to provide exquisite control of the low-order errors, additional high-order correction is required which should bring down the total wavefront error in a post-AO wavefront residual from a typical level of 200 nm rms (at H band) to < 50 nm rms. This additional correction is generally provided by an ExAO system's highly sensitive high-order wavefront sensors. Even though these simulated post-AO188 phasemaps had uncorrected high-order errors, LLOWFS still measured the pointing errors with a measurement accuracy of $\approx 10^{-2}\ \lambda/D$ (2-12 nm at 1.6 μm).

2.5 First laboratory experiments (*Pub.* §4)

The very first laboratory test of the LLOWFS was performed at *LESIA, Observatoire de Paris* in June 2013. I setup this coronagraphic bench temporarily in the laboratory to measure the pointing errors with the LLOWFS. *Pub.* Figure 8 shows the coronagraphic bench, which was disassembled after my test. The FQPM used (developed by the laboratory *Galaxies, Etoiles, Physique et Instrumentation, Observatoire de Paris*) was optimized at 0.635 μm.

The pupil masks and the Lyot stop were designed to be compatible with the SCExAO bench. The design of the pupil mask is shown in Fig. 2.9 and the geometry in Fig. 2.10 (a). I have designed three sets of pupil masks (Fig. 2.9) –

- A mask with the original size of the pupil,
- A 2% undersize/oversize of the outer diameter of P and,
- A 1% undersize/oversize of the outer diameter of P.

The pupil masks 2 and 3 are designed to obscure the pupil alignment errors. For my tests at LESIA, I have used pupil mask 1 in *Pub.* Fig. 8.

For the first batch of the RLS, I had provided the geometry and coordinates of the Lyot stop for the FQPM to the manufacturer HTA Photomask, who first designed the mask with SolidWorks and later fabricated it. The RLS is a fused silica disk of 1.5 mm thickness (digitized version shown in Fig. 2.10 (a) and the manufactured stop in Fig. 2.10 c)). The substrate flatness is better than 5 μm. The black region is a substrate of reflective chrome with a 60% reflectivity in near IR (1200 nm) while the white region is transparent. Unfortunately, there was a manufacturing error in the angle of the spider arms which was off by 10° (*Pub.* Fig. 9(b)). *The transmission profile of the RLS for the FQPM can be found in §3.4.2 and the information on its size in Tab. 3.1.*

The complete description of the bench and the procedure to acquire the LLOWFS measurements is explained in detail in *Pub.* §4. The reference image and the calibration frames are shown in *Pub.* Fig. 9 (a, b, d, e). The linearity of the sensor to pointing errors is tested by applying tip-tilt errors within ± 0.2 λ/D (± 0.32 radian RMS). These errors

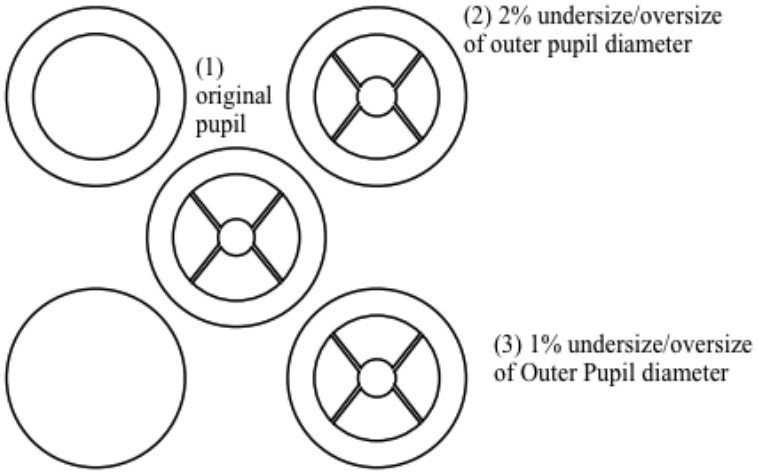

Figure 2.9: Design of the Subaru pupil opaque masks. The coordinates of these simulated masks were sent to a Laser cut machine that carved out these masks on a carbon fiber sheet. The Pupil mask 1 is the one I used for my first laboratory tests at LESIA.

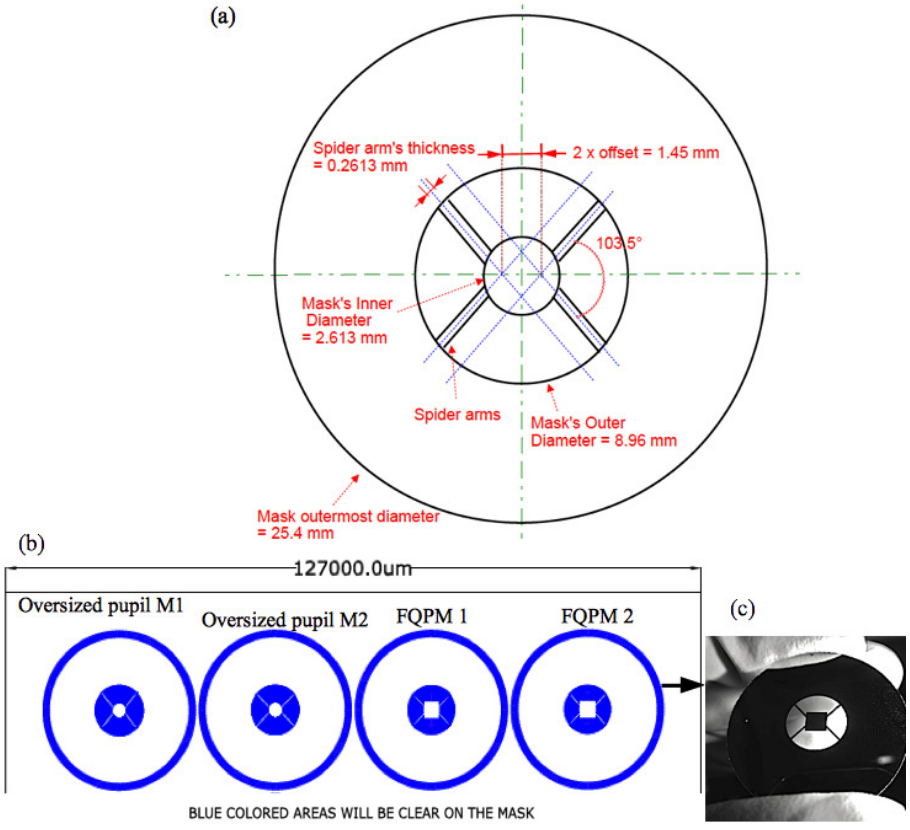

Figure 2.10: (a) Geometry of the Subaru pupil mask I have designed for my coronagraphic bench at LESIA and also for the SCExAO bench. (b) Digitized pattern of the RLS for the FQPM before their manufacturing. c) Manufactured RLS for the FQPM. The black surface is reflective chrome with 60% reflectivity in near IR (1200 nm).

were actually introduced by moving the FQPM itself, first in x-direction and then in y-direction. *Pub.* Fig. 10 and 11 show the sensor measurement in response to the tip-tilt errors applied on the bench.

This laboratory test was limited by the local turbulence in the laboratory and thermal drifts of the mechanical elements (*Pub.* §4.2). Even though, I proved experimentally that the linearity range of the LLOWFS for pointing errors is within ± 0.12 λ/D (≈ 0.19 radian RMS over the Subaru pupil) as predicted in my simulations in §2.4.2.

2.6 Discussion

In this chapter, I have introduced the concept and theory of the *Lyot-based low-order wavefront sensor* (§2.3) that I have developed to address the low-order wavefront aberrations for small IWA phase mask coronagraphs. I have presented the measurement of tip, tilt, focus, oblique and right astigmatism in an open-loop with a FQPM in simulations considering: – (1) no aberration (§2.4.1), – (2) low-order Zernike phase defects (§2.4.2) and – (3) post-AO wavefront residuals (§2.4.3) at the entrance pupil of a simulated coronagraphic system (Fig.2.1). I have also demonstrated the concept of the LLOWFS during a first laboratory experiment with a FQPM and found a similar linearity range than the one obtained with simulations, which is ± 0.12 λ/D for pointing errors (§2.5).

An important point to highlight is that it is possible to use the pupil plane image downstream of RLS in the LLOWFS channel, to drive the low-order sensor as phase aberrations present in the intermittent focal plane are converted to intensity modulations via the phase mask used. However, to maximize the signal-to-noise ratio and hence be able to operate on faint host stars, conducting the wavefront sensing in a reimaged focal plane offers the highest photon density per pixel.

In the next chapter, I will introduce the adaptive optics system (AO188), the extreme adaptive optics system (SCExAO) and the high contrast imager (HiCIAO) of the Subaru Telescope. I will describe how these three instruments are integrated with each other during on-sky observations of SCExAO. I will then explain in detail the implementation of the LLOWFS on the SCExAO instrument.

Chapter 3

Subaru Coronagraphic Extreme Adaptive Optics Instrument

"Any sufficiently advanced technology is indistinguishable from magic."
– Arthur C. Clarke, "Profiles of The Future", 1961
(Clarke's third law)

Contents

3.1 Introduction

The first high-contrast imager on the IR Nasmyth platform of the Subaru Telescope was HiCIAO infrared camera (Tamura *et al.*, 2007) used in conjunction with Subaru's adaptive optics system facility (called AO188 for its 188 actuators, Minowa *et al.* (2010)). HiCIAO is a PI-type science instrument, which combined a classical Lyot coronagraph with angular, polarization or spectral differential imaging modes. In operation with the AO188 under SEEDS survey, HiCIAO, although limited by its IWA have not only revealed the features of the inner parts of circumstellar disks in its PDI mode but also probed for companions at angular separations > 0.5" in ADI mode.

To study the innermost regions of the extrasolar system, which is unreachable by HiCIAO, an upgraded version: the Subaru Coronagraphic Extreme Adaptive Optics (SCExAO[1], Martinache & Guyon, 2009) instrument was introduced in 2009. Complementing AO188 and HiCIAO, SCExAO was primarily developed to combine a PIAA coronagraph and non-redundant aperture masking interferometry with its own 2000- actuator MEMS-based wavefront control system to probe the innermost (< 0.2") zones of the planetary systems, which the combination of AO188 and HiCIAO can not reach. SCExAO was basically designed to be used with the AO188 and HiCIAO and to provide an additional wavefront correction at/near the diffraction limit in order to enhance the parametric space of the SEEDS survey.

Currently, our instrument is not only equipped with the small IWA high performance coronagraphs optimized between 1-3 λ/D IWA but it also has the capability of providing exquisite wavefront control via a high-order visible Pyramid wavefront sensor operating at 3.6 kHz, speckle nulling control and a dedicated near infrared (NIR) coronagraphic low-order WFS operating at 170 Hz. SCExAO is a PI instrument and is currently under commissioning phase. SCExAO also complements GPI & SPHERE instruments in many aspects: – (1) scientifically due to its location in the Northern Hemisphere. – (2) in flexibility in the design which provides an opportunity to adapt it with new cutting edge detector/highly-sensitive wavefront sensing technologies. – (3) in its capability of exploring the region < 10 AU by giving access to the IWA as small as $\sim 1\ \lambda/D$. – (4) with its dedicated coronagraphic WFS for PMCs to provide closed-loop pointing accuracy of $\approx 10^{-3}\ \lambda/D$.

In this chapter, I will briefly explain the functioning of the AO188, HiCIAO and also the interfacing of SCExAO between these two instruments at the Nasmyth IR platform during the on-sky observations in §3.2. I will briefly describe the modules of SCExAO and will refer the relevant sections in our publication Jovanovic *et al.* (2015), which present SCExAO and its capabilities in great detail. I will emphasize on my contribution, which is the implementation of LLOWFS, its hardware and software interfacing and the characterization of its modes of operation on SCExAO in §3.4.

[1] http://www.naoj.org/Projects/SCEXAO/01project/

3.2 Subaru Telescope

Subaru Telescope[2] is one of the 8-meter world class ground-based observatories situated at the summit of Mauna Kea at an elevation of 4,205 meters on the Big-Island of Hawaii. Its a Ritchey-Chretien system mounted on a Alt-Az structure. One of the four foci of the telescope is the Nasmyth IR focus (F13.6, Fig. 3.1 (a)) where AO188 is located.

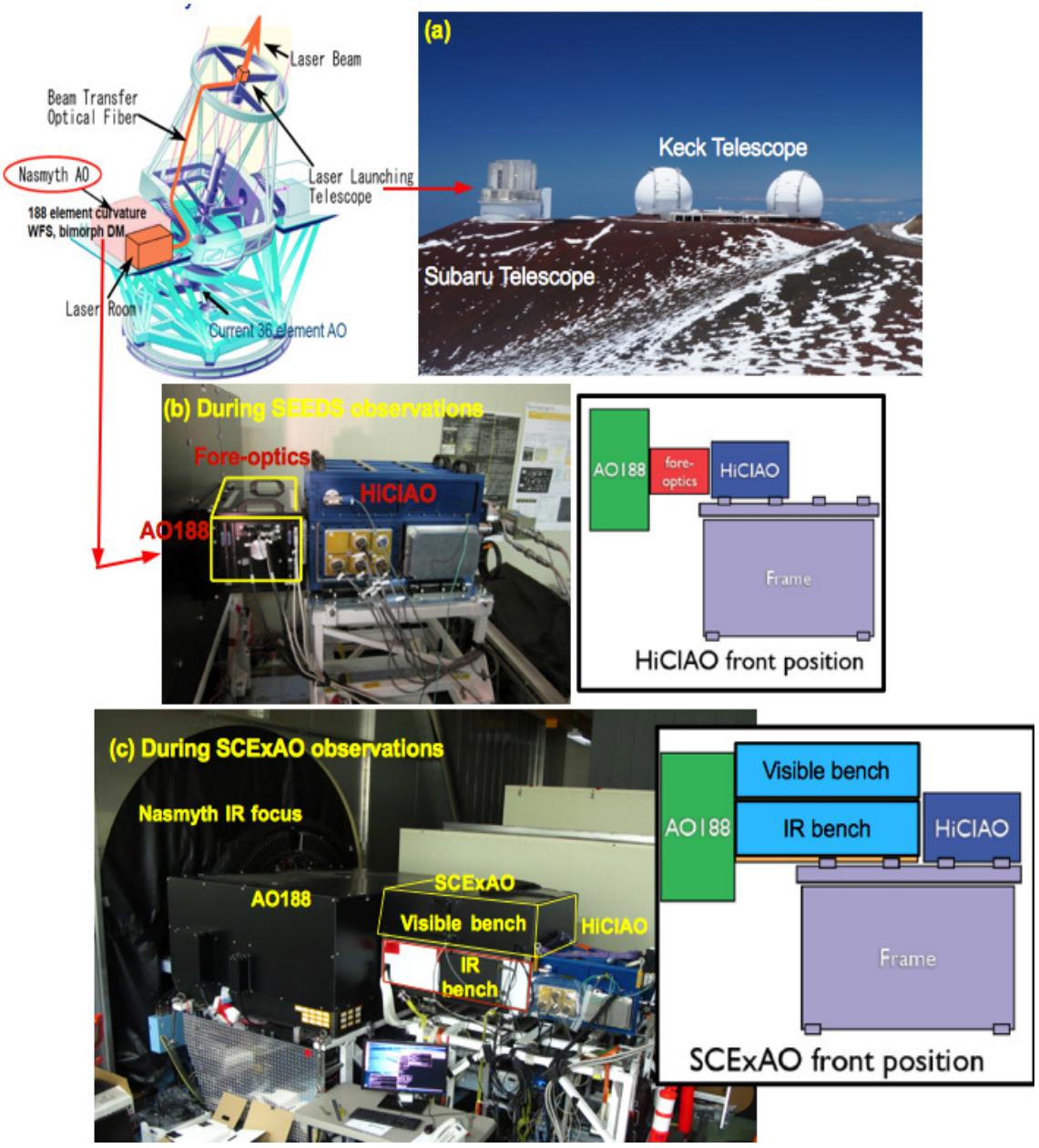

Figure 3.1: (a) Subaru observatory at the summit of Mauna Kea. (b) AO188 and HiCIAO configuration at the Nasmyth platform (right of the image) during SEEDS observations. c) SCExAO (both visible and IR benches) sandwiched between AO188 and HiCIAO during SCExAO engineering/science observations.

[2] http://www.naoj.org/Observing/Instruments/index.html

This is the principal adaptive optics instrument of the telescope which delivers corrected wavefront to several instruments such as IRCS (InfraRed Camera and Spectrograph, Kobayashi *et al.*, 2000), HiCIAO and SCExAO. AO188 sits at the Nasmyth platform and the rest of the instruments are craned downstream the AO188 path when required.

For now, I will refer these instruments as black boxes in order to explain their interface during the observations and later in the section, I will describe each instrument in detail. To fulfill the objectives of the SEEDS survey, HiCIAO is the principal instrument used with the AO188. The configuration of both instruments during SEEDS observation is shown in Fig. 3.1 (b). In this case, HiCIAO benefits only from the wavefront correction provided by AO188.

One of the goal to develop SCExAO is to enhance the detection sensitivity of HiCIAO by providing a second level of high-order correction at small angular separation. Some of the modules of the instrument are not commissioned yet, so during its on-sky testing and operations, SCExAO (both visible and IR benches) is transported from the Hilo base facility to the summit (Fig. 3.2 (a)(b)) and sandwiched between AO188 and HiCIAO (Fig. 3.1 (c)) typically a week before its observation. This basically requires to detach the delicate units first, such as the DM, cameras, external chassis containing RAID and graphics cards and all the electronics from the bench at Hilo, transporting all the modules to the summit, craning the whole unit between AO188 and HiCIAO at the Nasmyth platform (Fig. 3.2 (c)) and then assembling all the units back into a single piece.

Since January 2015, the instrument is staying at the telescope to limit transportation overheads. But during the first two years of my thesis, I received several opportunities to become a part of the process of transporting SCExAO as it has gone through several successful engineering and science nights since the starting of my thesis (September 2012). After craning SCExAO on the same platform as AO188 and HiCIAO, the next typical step is to align all three units to calibrate response matrixes for SCExAO's high- and low-order control loops to perform off-sky testings. The rough alignment of these units are done with an adjustable mechanical mounts with three degrees of freedom on the frame that holds the bench. The optical alignment between AO188 and the SCExAO bench is controlled remotely whereas HiCIAO is laterally and vertically aligned with the output collimated beam of SCExAO.

To avoid PSF movements due to mechanical and optical vibrations, the SCExAO bench is supported by four elastomer-based vibration isolators, which are used to damp high frequency mechanical vibrations from the surroundings. Also, to reduce the tip-tilt jitter from the cryocooler of HiCIAO, its pump is connected to the dewer by springs and metal bellows only (soft connections with low spring constants for maximum damping, Jovanovic *et al.*, 2014).

3.2.1 Facility Adaptive Optics system (AO188)

The adaptive optics system of Subaru, AO188 (Takami *et al.*, 2004), is based on an 188-elements curvature sensor with photon counting APD modules and a 188 element bimorph mirror, operating in natural (since October 2008) and laser guide star modes (FoV 2.7

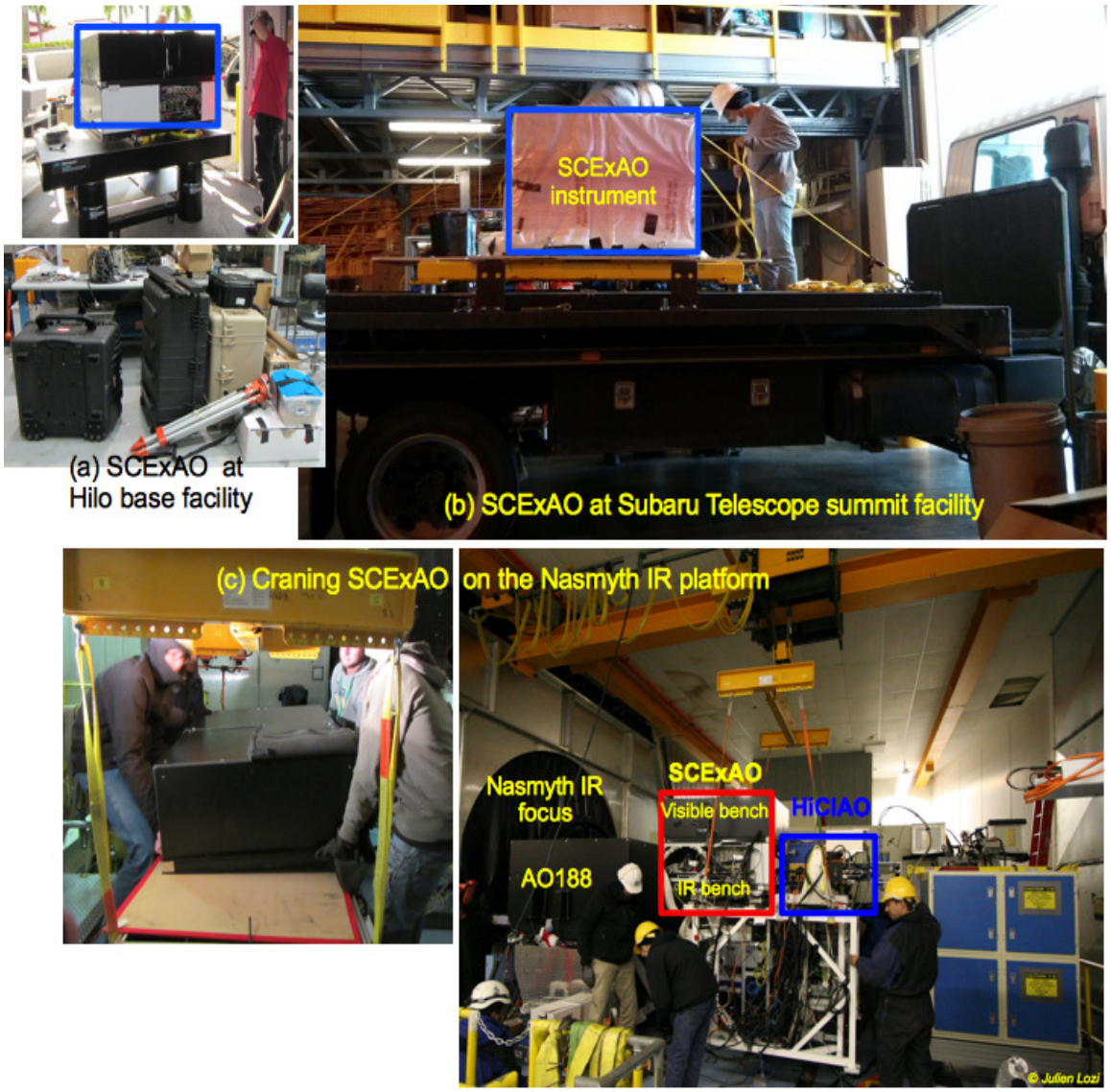

Figure 3.2: SCExAO instrument (a) at the Hilo base facility. (b) being transported to the Subaru Telescope facility at the summit of Mauna Kea. c) being craned at the Nasmyth IR platform of the telescope to be positioned between the AO188 and the HiCIAO.

arcminute in diameter). It is a classical single conjugated AO (SCAO) system, in which the DM is optically conjugated to the ground layer of turbulence. The system saw its first successful light in late 2006 with IRCS.

The field of view of SCExAO is < 10" and we always observe a bright enough target during SCExAO observations, therefore AO188 is used only in the NGS mode. Figure 3.3 present a simplified schematic diagram of the AO188 system in NGS mode.

A bright guide star (brighter than *R* magnitude of 16.5) during NGS mode provides wavefront measurement. A tip-tilt mirror corrects the low-order high-amplitude tip and tilt modes. The Bimorph mirror with 188 element is used as a deformable mirror to provide the wavefront correction. The bimorph mirror is made of two PZT (piezoelectric

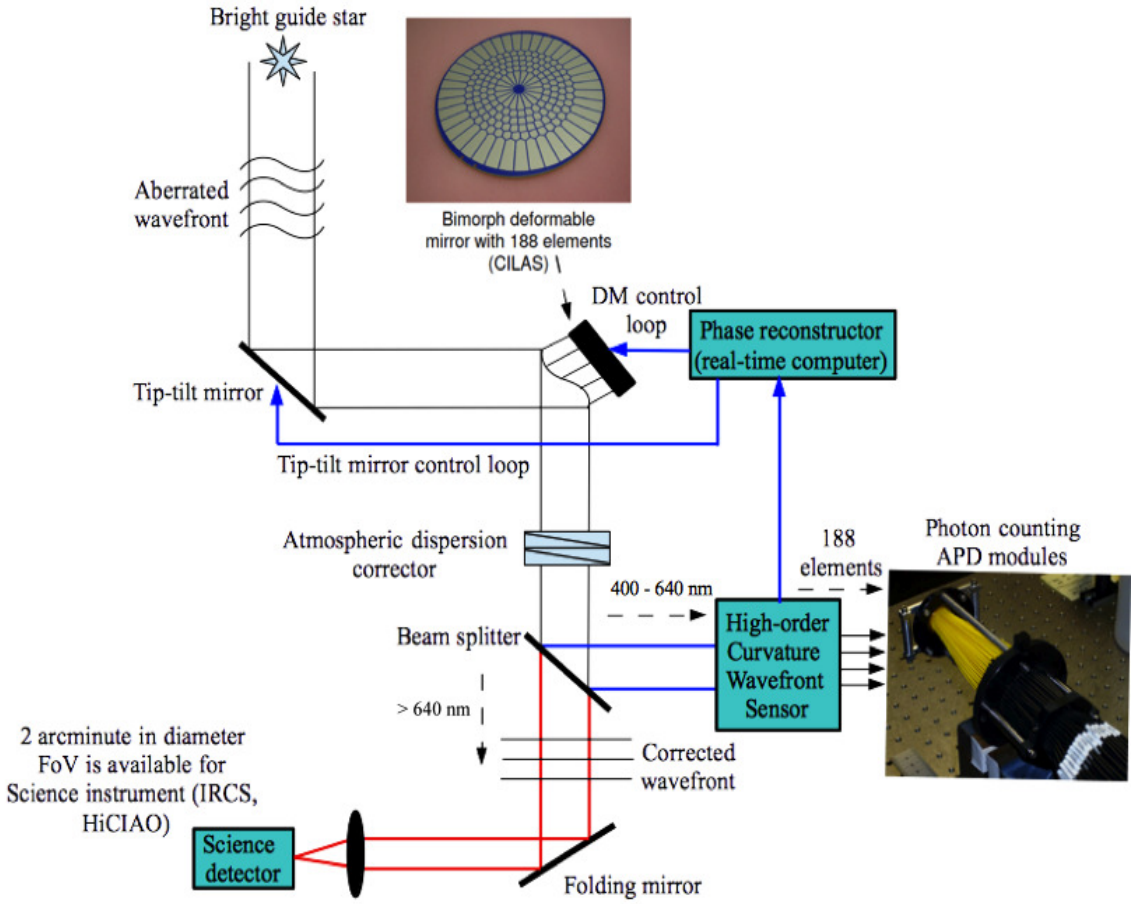

Figure 3.3: Simplified illustration of Subaru Telescope's AO188 system.

material) plates with a diameter of 130 mm (beam size 90 mm) and a total thickness of about 1.9 mm. The control electrodes are located between the two plates. The system has a conventional atmospheric dispersion corrector (ADC) downstream the DM to compensate for the atmospheric dispersion in both visible and infrared wavelength over 0.45 - 2.2 μm for both the science instrument and the WFS. A dichroic beam splitter in the beam reflects the optical light between 0.4 - 0.64 μm for wavefront sensing and transmits the optical and near-infrared light after 0.64 μm for science observations (Watanabe *et al.*, 2004).

A curvature WFS with 188 elements is used for the wavefront sensing. Optical fibers are placed at the focus of each subaperture to feed the output of the 188 elements to the photon-counting APDs. This wavefront sensor also has a guide star acquisition unit[3] to acquire a guide star from a 2 arcminute diameter field. A real-time computer (the control system) is used to analyze the wavefront measurements from the WFS to reconstruct the phase and then convert the measured phase into commands to send to each actuator at a speed of 1 kHz.

Figure 3.4 briefly summarizes the Strehl results of the AO188 taken under good seeing condition between 0.4 - 0.6". (a) and (b) shows the Strehl ratio as a function of m_V

[3]I have got the opportunity to work on these acquisitions units to track the laser spot of the Laser guide star during my Masters thesis in 2010.

and m_R of the NGS respectively for K-band (centered at 2.2 μm) between 2008-2009. AO188 typically provides 60% Strehl for $m_R < 10$ in K-band. Fig. 3.4 (c) shows the Strehl obtained for various observing wavelengths with NGS of $m_V = 5$ under a good seeing of 0.6". Around 1.6 μm, the Strehl is roughly 60%, however under moderate seeing, the Strehl in H-band is in between 30 - 40% and the total wavefront residual is ~ 200 nm RMS. That is a typical value we usually get as an output from the AO188 during SCExAO on-sky observations.

(a)

Conditions	Strehl ratio @K	Guide Star V_mag	Separation from GS	Sky Coverage
NGS (best)	~70%	8	<30"	<0.1%
NGS (moderate)	~40%	12	<30"	1 %
NGS (worst)	~10%	16	<30"	~ 30%
LGS (best)	~45%	14	<80"	~30%
LGS (moderate)	~30%	16	<80"	~50%
LGS (worst)	~10%	19	<80"	~100%

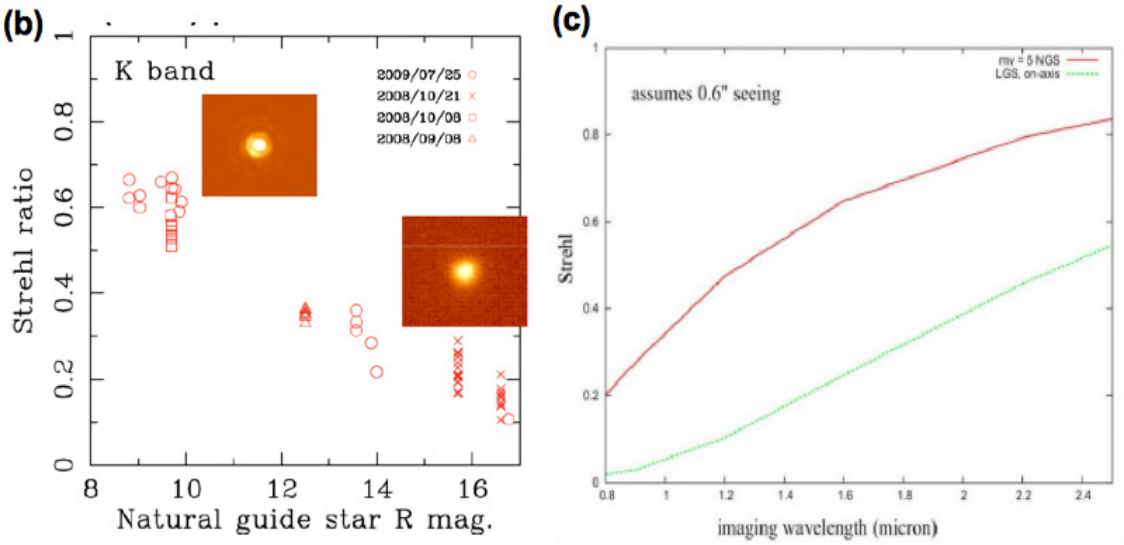

Figure 3.4: Strehl results in (a,b) K-band and c) H-band of Subaru Telescope's AO188 system[4] (Minowa *et al.*, 2010).

3.2.2 Facility Science instrument HiCIAO

HiCIAO is a high-contrast imaging instrument whose objective is to directly image young giant planets/brown dwarfs and circumstellar/debris disks around nearby stars. The instrument is composed of a – (1) warm coronagraph module (Fore optics in Fig. 3.5): consist of a field lens with the occulting spot deposited on its flat front surface (classical Lyot coronagraph, ~ 3-4 λ/D), a doublet collimator, and a doublet camera lens that delivers a collimated beam to the IR camera and – (2) a cryogenic IR camera module: consist of a

[4] http://www.naoj.org/Observing/Instruments/AO/performance.html

2048 × 2048-pixel HgCdTe array - HAWAII-2RG (HiCIAO dewar in Fig. 3.5)). The camera covers a wavelength range of 0.80 - 2.4 μm and has a readout noise of 15 e^- (Hodapp *et al.*, 2008).

The warm coronagraph module includes single and double Wollaston prisms which split the light into two or four directions for the differential imaging techniques. Two filter wheels in the cold module, located near the pupil and the detector allows spectral differential imaging mode as well as a normal imaging mode. Pupil viewer in the HiCIAO dewar is used to align the instrument Lyot stop with the telescope pupil that not only performs the coronagraphic suppression but also provide optimal reduction of thermal background.

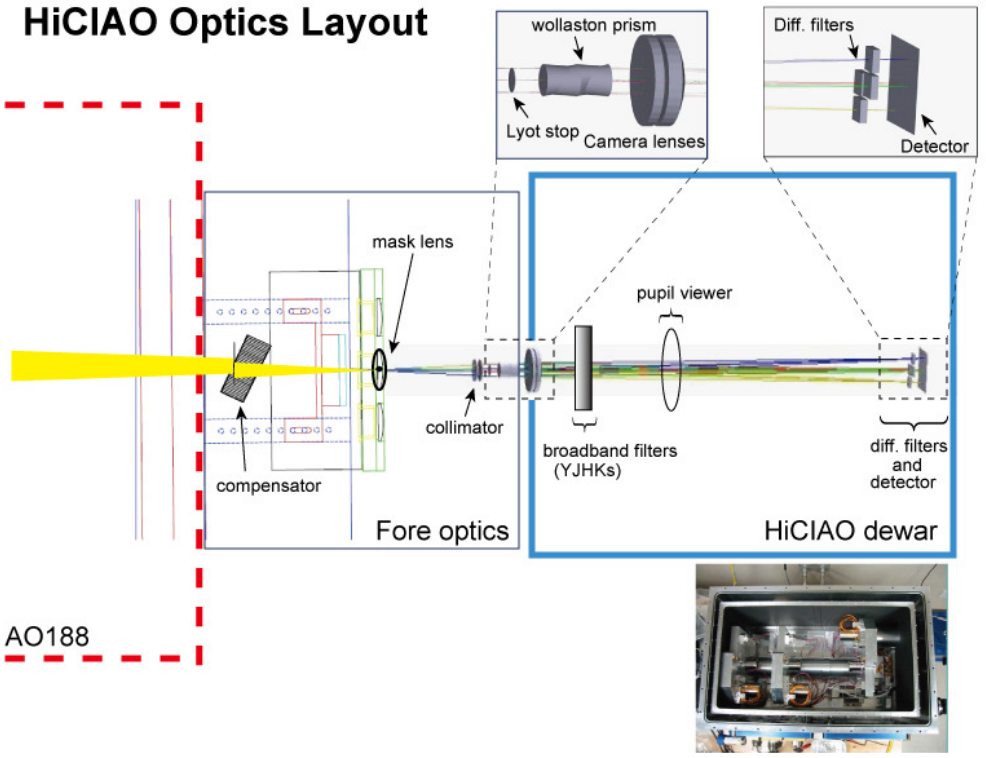

Figure 3.5: Optical layout of HiCIAO[5].

HiCIAO provides four modes of observations: – (1) Direct imaging mode (FoV of 20" × 20"), with or without a coronographic occulting spot and with a set of standard broadband filters in the near-infrared regime, – (2) PDI mode using a single Wollaston (FoV of 10" × 20"), – (3) SDI mode using double Wollaston (FoV of 5" × 5") and, – (4) ADI mode.

Combination of AO188 and HiCIAO have achieved an average Strehl of 40% and 67% in the H-band and K-band, respectively, with a guide star of R~5 under natural seeing of 0.5" in the H-band. The typical contrast achieved is of the order of 10^{-3} at 0.3" (6 λ/d) and 10^{-5} between 1" - 1.5" (20 - 30 λ/d) (Suzuki *et al.*, 2010). In five years, 120 nights of observations has allowed SEEDS to characterize giant planets around about 50

[5] http://www.naoj.org/staff/kudotm/SEEDSHiCIAOPVreport_final090923e.pdf

solar-type and massive stars in the outer regions of the extrasolar systems (a few 40 AU). Even with these impressive results, the instrument is limited by the IWA, low- and high-order wavefront residuals uncorrected by the AO188 and focal plane residual speckles. To address these limitations, SCExAO was proposed to provide: – (1) a second level of wavefront correction over post-AO188 residuals and – (2) a platform to develop and implement small IWA coronagraphs in order to exploit the differential imaging modes of HiCIAO to probe the region at/near the diffraction limit of the telescope.

3.2.3 SCExAO instrument

Apart from the founding members of the instrument, *Olivier Guyon* and *Frantz Martinache*, SCExAO has been developed by numbers of interns, PhD students and Postdocs. Though it was designed to improve the performance of HiCIAO, but its continuous development and implementation of newer technologies has given it a status of a prototype for ELT habitable planets spectroscopic characterizer. The SCExAO project started as a testbed to develop the PIAA technology and now it uniquely combines four techniques:

- **Extreme-AO**: to correct for the high-order wavefront aberrations via a visible Pyramid wavefront sensor (3.6 kHz),
- **Coronagraphy (IWA of 1-3 λ/D)**: to mask the on-axis starlight and suppress the diffraction effects of the telescope,
- **LLOWFS**: to keep the starlight centered on the FPM and record residual wavefront errors for post-processing and
- **Speckle control**: to modulate, suppress and calibrate residual speckles.

SCExAO consists of two optical benches: a lower IR bench and an upper visible bench, connected via a periscope. Different modules of the instrument are shown in Fig. 3.6. AO188 corrects 187 modes in the wavefront and feeds the residuals to SCExAO with a beam at $F/14$. SCExAO has its own 2000-actuator MEMS DM that provides actuation for all the wavefront sensing units i.e the PyWFS, LLOWFS and speckle nulling. The operation of SCExAO is completely independent from the AO188.

SCExAO's DM is also used to inject phase errors to simulate a dynamical turbulence for laboratory tests. The phase maps injected on the DM are built using a simulated phase screen, which follows the Kolmogorov profile. This phase screen can also be filtered to mimic the effects of the low and high spatial frequencies under pre/post-AO corrections. The simulated turbulence can run in the background independently of the corrections injected on the DM by the wavefront control loops. The final command sent to the DM is then the sum of the injected turbulence and the calculated corrections. For the turbulence injection, we control different parameters: strength (amplitude in nm RMS), wind speed (m/s) and an optional coefficient reducing the low-spatial frequencies to mimic the effect of the AO188 wavefront residuals. However, this simulation is limited by the maximum spatial frequency of the DM, which is 22.5 cycles/aperture.

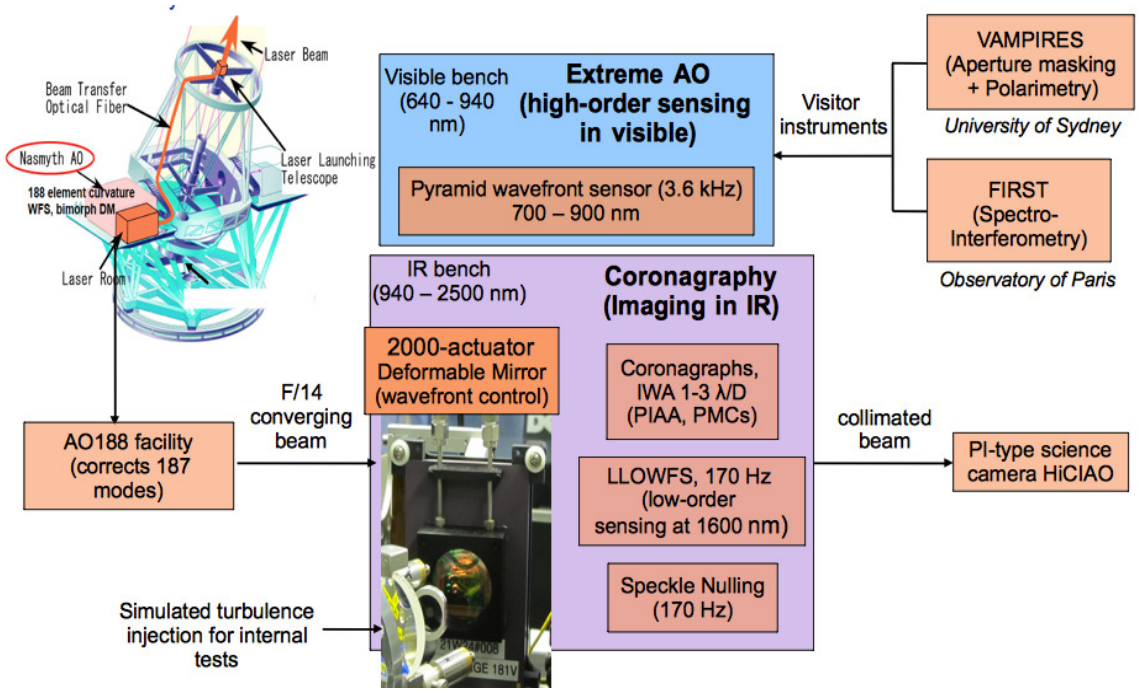

Figure 3.6: The different modules of the SCExAO instrument. It feeds on the wavefront corrected by the AO188 facility. The instrument uniquely combines extreme AO loop with coronagraphs optimized for IWA between 1-3 λ/D. The output of the instrument goes to the high contrast imager, HiCIAO.

The IR bench contains all NIR optics and coronagraphs, and is dedicated to high contrast imaging and NIR wavefront sensing via the LLOWFS and the speckle control at 170 Hz. The visible bench contains a high speed PyWFS (Clergeon *et al.*, 2013) as well as visible light interferometric science imaging modules: VAMPIRES (Visible Aperture Masking Polarimetric Interferometer for Resolving Exoplanetory Signatures, Norris *et al.*, 2015) and FIRST (Fibered Imager for a Single Telescope, Huby *et al.*, 2012)

All the three wavefront control loops use SCExAO's DM to correct for the wavefront. Therefore, they can not run simultaneously as only one control loop can command the DM for wavefront correction at a time. We neither have a tip-tilt mirror or a separate dedicated DM either for LLOWFS or for speckle nulling nor we can feed the low-order/speckle nulling correction to the upstream AO188 as there is no optical link between both instruments. Our goal is thus to combine the operation of all the WFSs so all of them can be addressed by a single global correction map that can be applied to the DM. We made initial efforts to integrate LLOWFS inside the PyWFS to address the differential tip-tilt errors in NIR via a differential pointing system (DPS). Chapter 5 is dedicated to this combination. Due to the relatively slow speed of the LLOWFS, this integration can correct differential pointing errors only at a speed of < 25 Hz. We are upgrading the design of the DPS in order to provide faster correction and the laboratory tests are currently undergoing.

To address chromaticity, SCExAO was converted from refractive to reflective relay optics in 2013. I have got the opportunity to work with the new optimized bench, especially on the IR bench. During the course of my thesis, I have designed, build and programmed the LLOWFS for the NIR bench. My job was to perform rigorous testing of LLOWFS

concept and characterize its performance with different coronagraphs in the laboratory and on-sky. For these three years, I was also the lead member of the team for operating the LLOWFS during on-sky engineering and science observations and later use the low-order residuals to post-process the raw data. For detailed description of LLOWFS on SCExAO, refer to §3.4.

SCExAO bench is described in great detail in our publication Jovanovic *et al.* (2015), which has recently been published in PASP. Below I will indicate the relevant figures and sections to follow the optical layout of all the modules of our instrument.

- The elements of SCExAO and its *detailed optical design* is described in *Pub.* §2.1, §2.2. Refer to §2.3 for *internal calibration*.
- *Pub.* Fig. 1 presents the system level flow diagram and commissioning status of several modules. *Pub.* Fig. 3 shows the schematic diagram of the calibration source, visible and IR benches of the SCExAO instrument.
- Refer to *Pub.* Table 1 for the characterization of all the detectors used in the system; Table 2 for plate scale and field of view; Table 4 and 5 for laboratory throughput of various arms of the IR and visible channels respectively; Table 8 for coronagraphs IWA and Table 9 for the complete commissioning status of SCExAO modes of operation and modules.
- The complete characterization of 2000-actuator DM and the technique adapted for humidity control is presented in *Pub.* §3.1.1 and §6.3
- *Pub.* §3.1.2 explains the design and status of the high-order correction provided by the PyWFS[6]. Figure 6 shows the Pyramid optics and the Strehl achieved under laboratory turbulence. Coherent speckle modulation and control is explained in *Pub.* §3.1.3 and in Martinache *et al.* (2014) as well.
- SCExAO's current and future coronagraphic capabilities are elaborated in *Pub.* §3.2.

[6]The thesis titled "Etude d'un analyseur de surface d'onde haute sensibilité pour l'optique adaptative extreme" dedicated to the development and implementation of PyWFS on SCExAO by Christophe Clergeon can be downloaded from `http://www.naoj.org/Projects/SCEXAO/`.

3.3 Jovanovic et al. (2015)

PUBLICATIONS OF THE ASTRONOMICAL SOCIETY OF THE PACIFIC, **127**:890–910, 2015 September

The Subaru Coronagraphic Extreme Adaptive Optics System: Enabling High-Contrast Imaging on Solar-System Scales

N. JOVANOVIC,[1,2] F. MARTINACHE,[3] O. GUYON,[1,4,5] C. CLERGEON,[1] G. SINGH,[1,6] T. KUDO,[1] V. GARREL,[7] K. NEWMAN,[5,8] D. DOUGHTY,[1,5] J. LOZI,[1] J. MALES,[4,9] Y. MINOWA,[1] Y. HAYANO,[1] N. TAKATO,[1] J. MORINO,[10] J. KUHN,[11] E. SERABYN,[11] B. NORRIS,[12] P. TUTHILL,[12] G. SCHWORER,[6,12] P. STEWART,[12] L. CLOSE,[4] E. HUBY,[6,13] G. PERRIN,[6] S. LACOUR,[6] L. GAUCHET,[6] S. VIEVARD,[6] N. MURAKAMI,[14] F. OSHIYAMA,[14] N. BABA,[14] T. MATSUO,[15] J. NISHIKAWA,[10] M. TAMURA,[10,16] O. LAI,[1,7] F. MARCHIS,[17] G. DUCHENE,[18,19] T. KOTANI,[10] AND J. WOILLEZ[20]

Received 2015 February 19; accepted 2015 June 23; published 2015 August 31

ABSTRACT. The Subaru Coronagraphic Extreme Adaptive Optics (SCExAO) instrument is a multipurpose high-contrast imaging platform designed for the discovery and detailed characterization of exoplanetary systems and serves as a testbed for high-contrast imaging technologies for ELTs. It is a multiband instrument which makes use of light from 600 to 2500 nm, allowing for coronagraphic direct exoplanet imaging of the inner $3\lambda/D$ from the stellar host. Wavefront sensing and control are key to the operation of SCExAO. A partial correction of low-order modes is provided by Subaru's facility adaptive optics system with the final correction, including high-order modes, implemented downstream by a combination of a visible pyramid wavefront sensor and a 2000-element deformable mirror. The well-corrected NIR (y-K bands) wavefronts can then be injected into any of the available coronagraphs, including but not limited to the phase-induced amplitude apodization and the vector vortex coronagraphs, both of which offer an inner working angle as low as $1\lambda/D$. Noncommon path, low-order aberrations are sensed with a coronagraphic low-order wavefront sensor in the infrared (IR). Low noise, high frame rate NIR detectors allow for active speckle nulling and coherent differential imaging, while the HAWAII 2RG detector in the HiCIAO imager and/or the CHARIS integral field spectrograph (from mid-2016) can take deeper exposures and/or perform angular, spectral, and polarimetric differential imaging. Science in the visible is provided by two interferometric modules: VAMPIRES and FIRST, which enable subdiffraction limited imaging in the visible region with polarimetric and spectroscopic capabilities respectively. We describe the instrument in detail and present preliminary results both on-sky and in the laboratory.

Online material: color figures

[1] National Astronomical Observatory of Japan, Subaru Telescope, 650 North A'Ohoku Place, Hilo, HI, 96720; jovanovic.nem@gmail.com.
[2] Department of Physics and Astronomy, Macquarie University, Sydney NSW 2109, Australia.
[3] Observatoire de la Cote d'Azur, Boulevard de l'Observatoire, Nice 06304, France.
[4] Steward Observatory, University of Arizona, Tucson, AZ 85721.
[5] College of Optical Sciences, University of Arizona, Tucson, AZ 85721.
[6] LESIA, Observatoire de Paris, 5 Place Jules Janssen, Meudon 92195, France.
[7] Gemini Observatory, c/o AURA, Casilla 603, La Serena, Chile.
[8] NASA Ames Research Center, Moffett Field, CA 94035.
[9] NASA Sagan Fellow.
[10] National Astronomical Observatory of Japan, 2-21-1 Osawa, Mitaka, Japan.
[11] Jet Propulsion Laboratory, California Institute of Technology, 4800 Oak Grove Dr., Pasadena, CA 91109.
[12] Sydney Institute for Astronomy (SIfA), Institute for Photonics and Optical Science (IPOS), School of Physics, University of Sydney, NSW 2006, Australia.
[13] Département d'Astrophysique, Géophysique et Océanographie, Université de Liège, 17 Allée du Six Août, 4000 Liège, Belgium.
[14] Division of Applied Physics, Faculty of Engineering, Hokkaido University, Kita-13, Nishi-8, Kita-ku, Sapporo, Hokkaido 060-8628, Japan.
[15] Kyoto University, Kitashirakawa-Oiwakecho, Sakyo-ku, Kyoto 606-8502, Japan.
[16] Department of Astronomy, University of Tokyo, 7-3-1 Hongo, Bunkyo, Tokyo 113-0033, Japan.
[17] Carl Sagan Center at the SETI Institute, Mountain View, CA 94043.
[18] Astronomy Department, University of California, Berkeley, CA 94720-3411.
[19] University Grenoble Alpes & CNRS, Institut de Planetologie et d'Astrophysique de Grenoble (IPAG), Grenoble F-3800, France.
[20] European Southern Observatory (ESO), Karl-Schwarzschild-Str. 2, Garching 85748, Germany.

1. INTRODUCTION

The field of high-contrast imaging is advancing at a great rate with several extreme adaptive optics systems having come online in 2014, including the Gemini Planet Imager (GPI) (Macintosh 2014), the Spectro-Polarimetric High-contrast Exoplanet REsearch instrument (SPHERE) (Beuzit et al. 2008), and the focus of this work, the Subaru Coronagraphic Extreme Adaptive Optics (SCExAO) system which join the already running P1640 (Dekany et al. 2013). These systems all share a similar underlying architecture: they employ a high-order wavefront sensor (WFS) and a deformable mirror (DM) to correct for atmospheric perturbations enabling high Strehl ratios in the near-infrared (NIR) ($>90\%$), while a coronagraph is used to suppress on-axis starlight downstream. The primary motivation for such instrumentation is the direct detection of planetary mass companions at contrasts of 10^{-5}–10^{-6} with respect to the host star, at small angular separations (down to 1–$5\lambda/D$) from the host star.

The era of exoplanetary detection has resulted in ∼1500 planets so far confirmed (Han et al. 2014). The majority of these were detected via the transit technique with instruments such as the *Kepler Space Telescope* (Borucki et al. 2010). The radial velocity method (Mayor & Queloz 1995) has also been prolific in detection yield. Both techniques are indirect in nature (the presence of the planet is inferred by its effect on light from the host star) and hence often deliver limited information about the planets themselves. It has been shown that it is possible to glean insights into atmospheric compositions via techniques such as transit spectroscopy (Charbonneau 2001), whereby star light from the host passes through the upper atmosphere of the planet as it propagates to Earth, albeit with limited signal-to-noise ratio. The ability to directly image planetary systems and conduct detailed spectroscopic analysis is the next step toward understanding the physical characteristics of their members and refining planetary formation models.

To this end, so far <50 substellar companions have been directly imaged (see Fig. 3 in Pepe et al. [2014]). The challenge lies in being able to see a companion, many orders of magnitude fainter, at very small angular separations ($<1''$), from the blinding glare of the host star. Indeed, the Earth would be $>10^9\times$ fainter than the sun if viewed from outside the solar system in reflected light. Although these levels of contrast cannot be overcome from ground-based observations at small angular separations ($<0.5''$), it is possible to circumvent this by imaging the thermal signatures instead and targeting bigger objects. Indeed, all planets imaged thus far were large Jupiter-like planets (which are brightest) detected at longer wavelengths (in the near-IR H and K-bands and the mid-IR L and M-bands) in thermal light (a subset of detections include Kraus & Ireland [2012]; Lagrange et al. [2009]; Marois et al. [2008]). To overcome the glare from the star which results in stellar photons swamping the signal from the companion, adaptive optics systems (AO) are key (Lagrange et al. 2009). Although angular differential imaging is the most commonly used technique for imaging planets thus far (Marois et al. 2008), coronagraphy (Lafreniere et al. 2009; Serabyn et al. 2010a) and aperture-masking interferometry (Kraus & Ireland 2012) have also been used to make detections. With the direct detection of the light from the faint companion itself, spectroscopy becomes a possibility and indeed preliminary spectra have been taken for some objects as well (Barman et al. 2011; Oppenheimer et al. 2013).

In addition to planetary spectroscopy, how disks evolve to form planetary systems is a key question that remains unanswered. Thus far coronagraphic imagers like HiCIAO at the Subaru Telescope have revealed intricate features of the inner parts of circumstellar disks using polarization differential imaging (under the SEEDS project [Tamura et al. 2009]). These solar-system scale features include knots and spiral density waves within disks like MWC758 and SAO 206462 (Grady et al. 2013; Muto et al. 2012). How such features are affected by or lead to the formation and evolution of planets can only be addressed by high-contrast imaging of the inner parts (up to 15 AU from the star) of such disks. To address the lack of information in this region, high-contrast imaging platforms equipped with advanced wavefront control and coronagraphs are pushing for smaller inner working angles (IWA). In the limit of low wavefront aberrations, currently achieved with AO systems operating in the near-IR, coronagraphs are the ideal tool for imaging the surrounding structure/detail as they are unrivaled in achievable contrast. Both the contrast and IWA are dependent on the level of wavefront correction available. With wavefront corrections typically offered by facility adaptive optics (AO) systems on 5–10-m class telescopes (∼30–40% in H-band), previous generations of coronagraphic imagers, such as the Near-Infrared Coronagraphic Imager (NICI) on the Gemini South telescope (Artigau 2008), were optimized for an IWA of 5–$10\lambda/D$. However, with extreme AO (ExAO) correction offering high Strehl ratio and stable pointing, GPI and SPHERE have been optimized for imaging companions down to angular separations of ∼$3\lambda/D$ (>120 mas in the H-band). SCExAO utilizes several more sophisticated coronagraphs including the Phase-Induced Amplitude Apodization (PIAA) (Guyon 2003) and vector vortex (Mawet et al. 2010), which drive the IWA down to just below $1\lambda/D$. At a distance of 100 pc, the PIAA/vortex coronagraphs on SCExAO would be able to image from 4 AU outward (approximately the region beyond the orbit of Jupiter). Further, in the case of the HR8799 system, the IWA would be 1.6 AU (the distance of Mars to our Sun) making it possible for SCExAO to image the recently hypothesized fifth planet at 9 AU (mass between 1 and 9 Jupiter masses) (Gozdziewski & Migaszewski 2014) if it is indeed present as predicted.

Despite the state-of-the-art IWA offered by these coronagraphs in the near-IR, the structure of disks and the distribution of planets at even closer separations than $1\lambda/D$ will remain inaccessible with coronagraph technology alone. This scale is scientifically very interesting as it corresponds to the inner parts of the solar system where the majority of exoplanets have been

found to date based on transit and radial velocity data (Han et al. 2014). To push into this regime, SCExAO uses two visible wavelength interferometric imaging modules known as VAMPIRES (Norris et al. 2012a) and FIRST (Huby et al. 2012). VAMPIRES is based on the powerful technique of aperture masking interferometry (Tuthill et al. 2000), while FIRST is based on an augmentation of that technique, known as pupil remapping (Perrin et al. 2006). Operating in the visible part of the spectrum, the angular resolution of these instruments on an 8-m class telescope approaches a territory previously reserved for long baseline interferometers (15 mas at $\lambda = 700$ nm) and expands the type of target that can be observed to include massive stars. Although the modules operate at shorter wavelengths where the wavefront correction is of a lower quality, interferometric techniques allow for subdiffraction limited imaging (10 mas resolution using $\lambda/2D$ criteria as conventionally used in interferometry) even in this regime, albeit at lower contrasts ($\sim 10^{-3}$), making optimal use of the otherwise discarded visible light. Despite the lower contrasts, aperture-masking interferometry has already delivered faint companion detections at unprecedented spatial scales (Kraus & Ireland 2012). Each module additionally offers a unique capability. For example, the polarimetric mode of VAMPIRES is designed to probe the polarized signal from dusty structures such as disks around young stars and shells around giant stars (Norris et al. 2012b, 2015) at a waveband where the signal is strongest. This is a visible analog of that offered by the SAMPol mode on the NACO instrument at the VLT (Lenzen et al. 2003; Norris et al. 2012b; Tuthill et al. 2010). FIRST, on the other hand, offers the potential for broadband spectroscopy and is tailored to imaging binary systems and the surface features of large stars. Such capabilities greatly extend SCExAO beyond that of a regular ex-AO facility.

Finally, with a diffraction-limited point-spread-function (PSF) in the near-IR, and a large collecting area, SCExAO is ideal for injecting light into fiber-fed spectrographs such as the Infrared Doppler instrument (IRD) (Tamura et al. 2012). In addition, this forms the ideal platform for exploring photonic-based technologies such as photonic lanterns (Leon-Saval et al. 2013) and integrated photonic spectrographs (Cvetojevic et al. 2012) for next-generation instrumentation.

The aim of this publication is to outline the SCExAO instrument and its capabilities in detail and offer some preliminary results produced by the system. In this vein, § 2 describes the key components of SCExAO while § 3 highlights the functionalities and limitations of the instrument. § 4 outlines plans for future upgrades and the paper concludes with a summary in § 5.

2. THE ELEMENTS OF SCEXAO

In order to understand the scientific possibilities and limitations of the SCExAO instrument, it is important to first understand the components and their functionalities. To aid the discussion, a system level diagram of SCExAO is shown in Figure 1, and an image of the instrument at the Nasmyth platform is shown in Figure 2. A detailed schematic of the major components is shown in Figure 3. The components and functionalities of SCExAO have been undergoing commissioning as will be outlined throughout this publication. A summary of

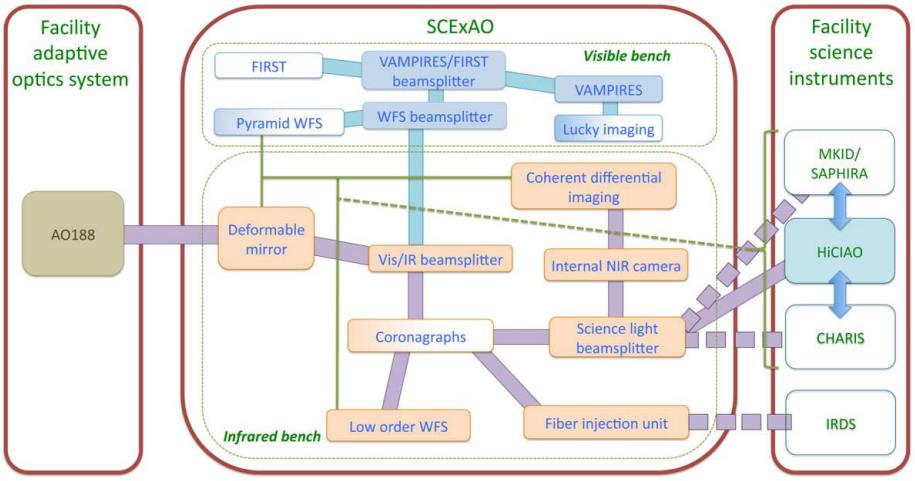

FIG. 1.—System level flow diagram of the SCExAO instrument. *Thick purple and blue lines* depict optical paths while thin green lines signify communication channels. *Dashed lines* indicate that a connection does not currently exist but it is planned for the future. *Filled boxes* indicate commissioning status. *Solid boxes*: commissioned; *graded boxes*: partially commissioned; *white background*: not commissioned. See the electronic edition of the *PASP* for a color version of this figure.

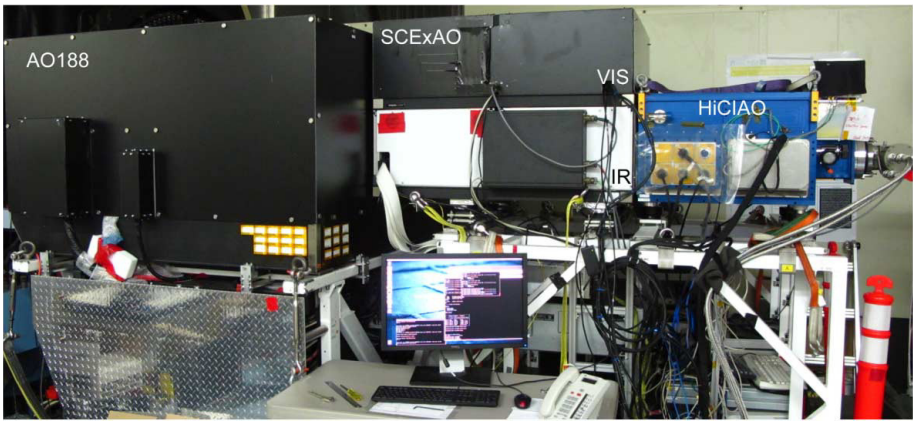

FIG. 2.—Image of SCExAO mounted at the Nasmyth IR platform at Subaru Telescope. To the left is AO188, which injects the light into SCExAO (center), and HiCIAO is shown on the right. The FIRST recombination bench is not shown for visual clarity. See the electronic edition of the *PASP* for a color version of this figure.

the commissioning status of each mode of operation or module of SCExAO can be found in the tables.

The main aim of SCExAO is to exploit the well-corrected wavefront enabled by the high-order WFS to do high-contrast imaging with light across a broad spectrum: from 600 to 2500 nm. As such, there are a number of instrument modules within SCExAO that operate in different wavebands simultaneously while the coronagraph is collecting data. This hitchhiking mode of operation enables maximum utilization of the stellar flux, which allows for a more comprehensive study of each target.

2.1. SCExAO at a Glance

The SCExAO instrument consists of two optical benches mounted on top of one another, separated by ∼350 mm. The bottom bench (IR bench) hosts the deformable mirror, coronagraphs, and a Lyot-based low-order wavefront sensor (LLOWFS) while the top bench (visible bench) hosts the pyramid WFS, VAMPIRES, FIRST, and lucky imaging (see Fig. 3). The benches are optically connected via a periscope.

The light from the facility adaptive optics system (AO188) is injected into the IR bench of SCExAO and is incident on the 2000 element deformable mirror (2k DM) before it is split by a dichroic into two distinct channels: light shorter than 940 nm is reflected up the periscope and onto the top bench while light longer than 940 nm is transmitted. The visible light is then split by spectral content by a range of long- and short-pass dichroics which send the light to the pyramid WFS (PyWFS) and visible light science instruments. The PyWFS is used for the high-order wavefront correction and drives the DM on the IR bench. The VAMPIRES and FIRST modules utilize the light not used by the PyWFS. Lucky imaging/PSF viewing makes use of light rejected by the aperture masks of VAMPIRES.

The IR light that is transmitted by the dichroic on the IR bench propagates through one of the available coronagraphs. After the coronagraphs, the light reflected by the Lyot stop is used to drive a LLOWFS in order to correct for the chromatic and noncommon errors (such as tip/tilt) between the visible and IR benches (Singh et al. 2014). The light transmitted by the coronagraphs is then incident on the science light beamsplitter which determines the spectral content and exact amount of flux to be sent to a high frame rate internal NIR camera as compared to a science grade detector such as the HAWAII 2RG in the HiCIAO instrument and soon to be commissioned CHARIS. The internal NIR camera can then be used to drive various coherent differential imaging algorithms.

2.2. Detailed Optical Design

The instrument is designed to receive partially corrected light from the facility adaptive optics system, AO188 (188 actuator deformable mirror). The beam delivered from AO188 converges with a speed of $f/14$. Typical H-band Strehl ratios are ∼30–40% in good seeing (Minowa et al. 2010). The beam is collimated by an off-axis parabolic mirror (OAP1, $f = 255$ mm) creating an 18 mm beam. Details of the OAPs can be found in the appendix. The reflected beam is incident upon the 2k DM, details of which are in § 3.1.1. The surface of the DM is placed one focal length from OAP1 which conjugates it with the primary mirror of the telescope (i.e., it is in a pupil plane). Once the beam has reflected off the DM, it is incident upon a fixed pupil mask which replicates the central obstruction and spiders of the telescope, albeit slightly oversized. This mask is permanently in the beam (both on-sky and in the laboratory)

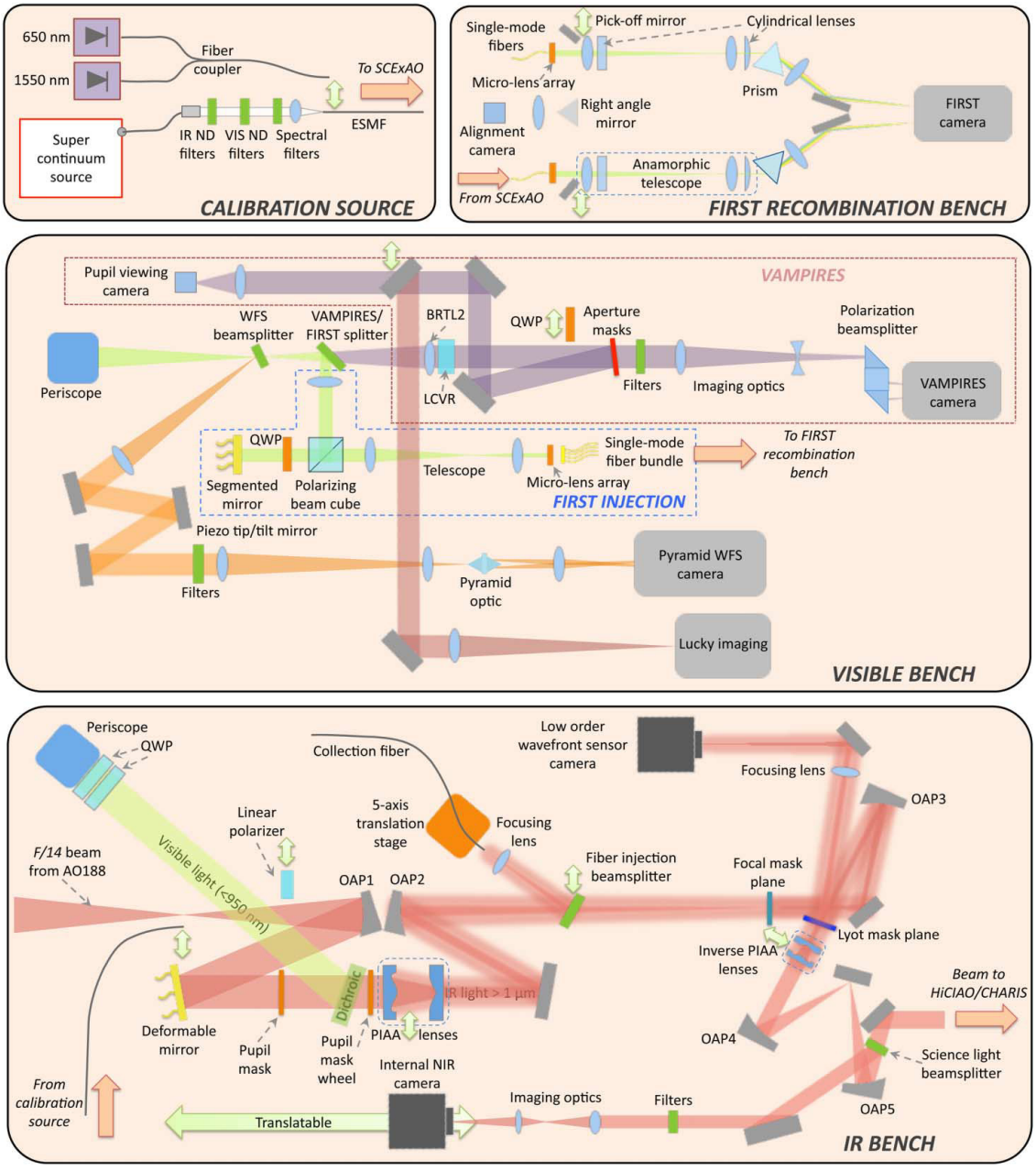

FIG. 3.—Schematic diagram of the SCExAO instrument. Top box (left): Portable calibration source layout. Top box (right): FIRST recombination bench. Middle box: layout of the visible optical bench which is mounted on top of the IR bench. Bottom box: IR bench layout. *Dual head green arrows* indicate that a given optic can be translated in/out of or along the beam. *Orange arrows* indicate light entering or leaving the designated bench at that location. See the electronic edition of the *PASP* for a color version of this figure.

so that response matrices collected for the various wavefront sensors with the internal light source in SCExAO can be used on-sky as well. It is positioned as close to the pupil plane as possible (~70 mm away from the DM) and forms the primary pupil for the instrument. The image/pupil rotator in AO188 is used to align the telescope pupil with the fixed internal mask when on-sky (i.e., SCExAO operates with a fixed pupil and rotating image when observing).

Immediately following the mask is a dichroic beamsplitter (50 mm diameter, 7 mm thick) which reflects the visible light (<940 nm) and transmits the IR (>940 nm). In the transmitted beam path, there is a mask wheel after the dichroic which hosts numerous masks including the shaped pupil coronagraphic mask. The automated mounts for the phase-induced amplitude apodization (PIAA) coronagraph lenses are adjacent to the mask wheel. They too were placed as close to the DM pupil as possible. The PIAA lenses themselves will be described in detail, for now it is important to note that they can be retracted from the beam entirely. A flat mirror is used to steer the light onto OAP2 which focuses the beam ($f = 519$ mm). A variety of coronagraphic focal plane masks, used to suppress the on-axis star light, are housed in a wheel which also has three axes of translation in the focal plane (the masks are outlined in § 3.2). OAP3 recollimates the beam to a 9 mm diameter beam ($f = 255$ mm). A wheel with Lyot plane masks is situated in the collimated beam such that the masks are conjugated with the pupil plane. The Lyot wheel can be adjusted in lateral alignment via motorized actuators. Light diffracted by the focal plane mask and reflected from the Lyot stop is imaged onto a nonscience grade (i.e., relatively high noise), high frame rate detector which is used for low-order wavefront sensing. The light transmitted by the Lyot stop is next incident upon the inverse PIAA lenses (detailed in § 3.2). They are mounted on stages which allow motorized control of the lateral positioning and are conjugated to the PIAA lenses upstream and can also be retracted from the beam entirely. OAP4 and OAP5 reimage the telescope pupil for the HiCIAO/CHARIS camera. On its way to the camera, the beam is intercepted by the science light beamsplitter which is used to control the flux and spectral content sent to a high frame rate internal NIR camera and the facility science instruments. Detectors in a high-contrast imaging instrument are among the most important components, and therefore, the performance of those used in SCExAO is summarized in Table 1.

The light directed to the internal NIR camera passes through a filter wheel for spectral selectivity. The content of the filter wheel and the science light beamsplitter wheels are reported in Table 2. An image is formed on the internal NIR camera via a pair of IR achromatic lenses (see appendix for details). The sampling and field-of-view on this and other cameras is summarized in Table 3. The internal NIR camera is mounted on a translation stage allowing it to be conjugated to any location between the focal and pupil planes.

The light reflected by the dichroic on the bottom bench (which splits the visible and IR channels) is directed toward a periscope which transports it to the upper bench. An achromatic lens (50 mm diameter, $f = 500$ mm) is mounted in the periscope to reimage the pupil onto the top bench. A wheel hosts a range of dichroic beamsplitters at the focus of the beam on the top bench to select the spectral content to be directed toward the PyWFS (named WFS beamsplitter; content listed in Table 2). The light reflected is collimated by an achromatic lens ($f = 200$ mm) and the pupil image is located on a piezo-tip/tilt mirror used to modulate the PyWFS. The reflected beam is routed to focusing optics which form a converging beam with $f/40$ (a combination of achromatic lenses with focal lengths of $f = 400$ and $f = 125$ mm are used for this). A double pyramid prism shaped optic (Esposito et al. 2010) is placed at the focus of the beam such that the vertex is on the optical axis. An image of the resulting four pupils is generated via one additional lens ($f = 300$ mm) on the detector. The PyWFS is discussed in more detail in § 3.1.2.

The light which is not directed to the WFS is split between two modules: VAMPIRES and FIRST. The basic optical layouts are outlined here and details in regards to specifics, including

TABLE 1
DETECTOR CHARACTERISTICS USED WITHIN SCEXAO

Detector name	Technology	Detector size (pixels)	Pixel size (μm)	Read-out noise (e^-)	Full frame (Frame rate [Hz])	Operating wavelengths (nm)	Manufacturer (Product name)
Internal NIR camera	InGaAs (CMOS)	320×256	30	114	170	900–1700	Axiom Optics (OWL SW1.7HS)
LOWFS camera	InGaAs (CMOS)	320×256	30	140	170	900–1700	Axiom Optics (OWL SW1.7HS)
HiCIAO/CHARIS	HgCdTe (CMOS)	2048×2048	18	15–30	<3	850–2500	Teledyne (HAWAII 2RG)
PyWFS (previous)	Si (sCMOS)	2560×2160 (128×128)	6.5	1.2	100 (1700)	350–1000	Andor (Zyla)
PyWFS (current)	Si (EMCCD)	240×240 (120×120)	24	<0.3	2000 (3700)	350–1000	Firstlight Imaging (OCAM2K)
Lucky imaging	Si (EMCCD)	512×512	16	<1	35	300–1000	Andor (iXon3 897)
VAMPIRES	Si (EMCCD)	512×512	16	<1	56	300–1000	Andor (iXon Ultra 897)
FIRST	Si (EMCCD)	512×512	16	<1	31.9	300–1000	Hamamatsu (ImagEM C9100-13)

NOTES. —The values in the table are taken from manufacturer specifications/measurements. Values in parentheses indicate the subframed (previous PyWFS) or binned (current PyWFS) image size and corresponding frame rate used. Read-out noise quoted for EMCCDs is with gain applied. Quantum efficiencies for these detectors are shown in Table 7.

TABLE 2
FILTER AND BEAMSPLITTER WHEEL CONTENTS

Slot	Internal camera filters	Science light beamsplitters	Wavefront sensor beamsplitter	VAMPIRES/FIRST splitter
1	Open	AR-coated window (900–2600 nm)	Open	Silver mirror
2	T = y-band	$T, R = 50\%$ (900–2600 nm)	Silver mirror	$T, R = 50\%$, 600–950 nm
3	T = J-band	$T = 10\%$, $R = 90\%$ (900–2600 nm)	$T, R = 50\%$, 600–950 nm	$T < 700$ nm, $R > 700$ nm
4	T = H-band	$T = 90\%$, $R = 10\%$ (900–2600 nm)	$T < 650$ nm, $R > 650$ nm	$T > 700$ nm, $R < 700$ nm
5	50 nm bandpass at 1600 nm	$T > 90\%$ (1400–2600 nm), $R > 95\%$ (900–1400 nm)	$T < 700$ nm, $R > 700$ nm	AR-coated window (600–950 nm)
6	–	$T > 90\%$ (1900–2600 nm), $R > 95\%$ (900–1900 nm)	$T < 750$ nm, $R > 750$ nm	Open
7	–	Gold mirror	$T < 800$ nm, $R > 800$ nm	–
8	–	–	$T < 850$ nm, $R > 850$ nm	–
9	–	–	$T > 750$ nm, $R < 750$ nm	–
10	–	–	$T > 800$ nm, $R < 800$ nm	–
11	–	–	$T > 850$ nm, $R < 850$ nm	–

NOTES. —The values in the table are based on the final measurements made by the manufacturer. T, transmission; R, reflection; AR, anti-reflection. Items 5 and 6 of the science light beamsplitter have not been delivered yet.

calibration and performance, are given in other publications (Huby et al. 2012; Norris et al. 2015). For engineering purposes, a gray beamsplitter is used to divide the light between VAMPIRES and FIRST ($50/50$), but can be swapped for several other optics if the science demands it (contents of the VAMPIRES/FIRST splitter wheel are shown in Table 2).

The light transmitted by the splitter is used by the VAMPIRES module. It is first collimated (by BRTL2) and then passes through a series of optics including a liquid crystal variable retarder (LCVR), pupil masks, and spectral filters before being focused by a combination of a converging and diverging lens onto a low noise detector. A polarization beamsplitter, consisting of a polarizing beam cube and three right-angled prisms, is placed in the beam after the final focusing lens and is used to spatially separate the two orthogonally polarized components on the detector. The VAMPIRES module combines aperture-masking interferometry with polarimetry. The sparse aperture masks are housed in the pupil wheel where an assortment of masks with various throughputs and Fourier coverage can be found (please see Norris et al. [2015] for details). The module operates on 50 nm bandwidths of light selected within the 600–800 nm range, via a set of spectral filters in order to maintain fringe visibility, while maximizing the signal-to-noise ratio. At 650 nm, VAMPIRES can achieve an angular resolution of 8.4 mas (Fizeau criteria) and has a field-of-view in masking mode which ranges from 80 mas to 460 mas depending on the mask selected (larger fields-of-view, ~1–2″ are possible in normal imaging mode, no mask). Rather than simply blocking the unwanted light from the pupil, the masks are reflective mirrors with transmissive subapertures so that the unwanted light is redirected to a pupil-viewing camera (PtGrey, Flea, FL3-U3-13S2M-CS) which allows for fine alignment of the masks with the pupil. The pupil-viewing mode of VAMPIRES is only used when aligning the masks. To utilize the light when pupil-viewing is not being used a mirror is translated into the beam to direct the light to the Lucky imaging module/point-spread-function (PSF) viewer (described in detail in § 3.3).

TABLE 3
PLATE SCALE AND FIELD-OF-VIEW

Detector	Sampling (mas/pixel)	Field-of-view (″)
Internal NIR camera	12.1 ± 0.1	4×3
HiCIAO	8.3 ± 0.1	$>10 \times 10$
VAMPIRES (M)	–	0.08–0.46
VAMPIRES (NM)	6.0	2×1
FIRST	–	0.1

NOTES. —All values in this table were measured off-sky by moving the calibration source laterally in the input focal plane (AO188 focal plane) and determining this motion in pixels on the detector. This motion is converted to a plate scale based on the knowledge of the AO188 plate scale which is well known to be $1.865''$/mm. This method yields consistent values to those obtained by looking at astrometric binaries. M, with aperture masks; NM, no masks. Range of field-of-view is dependent on choice of mask. Please see Norris et al. (2015) for more details.

The high angular resolution imaging capability of VAMPIRES is boosted by an advanced polarimetric capability. This gains its strength from the multitiered differential calibration scheme which is utilized. First, two quarter wave plates (HWP) mounted in front of the periscope on the bottom bench can be used to compensate for the birefringence induced by the mirrors in AO188 and SCExAO. The setting of these plates is done by careful calibration beforehand. Fast polarization modulation (~50 Hz) comes from the LCVR which is switched between every image. The analyzer splits the signal into two distinct interferograms on the detector with orthogonal polarizations. Finally, a HWP positioned in front of AO188, used for HiCIAO polarimetric imaging in the NIR, was determined to work well in the visible and is used as the main polarization switching component in VAMPIRES. The quarter wave plate (QWP) before the aperture mask wheel and the polarizer on the bottom bench are used for calibrating the polarization systematics with the internal calibration source and can be swung into the beam when off-sky (they are not used on-sky). For more details about

the nested differential calibration procedure please refer to Norris et al. (2015).

The light reflected by the beam splitter is sent to the FIRST module. It is collimated before entering a polarizing beamsplitter cube. The main beam is reflected at 90° onto a 37-element segmented mirror (Iris AO [Helmbrecht 2011]) which is conjugated to the pupil plane. A QWP placed between the polarizing beamsplitter and the segmented mirror is used to rotate the polarization so that the beam passes through the cube when reflected off the segmented mirror. A beam-reducing telescope compresses the beam so that a single segment of the mirror has a one-to-one correspondence with a microlens in the microlens array (MLA) used for injecting into the bundle of single-mode polarization maintaining fibers (see Fig. 3). This architecture allows the segmented mirror to fine-tune the coupling into each of the fibers with small tip/tilt control. Currently 18 of the 30 available fibers (2 sets of 9 fibers each) are used and they transport the light to a separate recombination bench (see Fig. 3) where the interferograms are formed and data collected. A description of the recombination bench is beyond the scope of this work. The instrument offers an angular resolution of 9 mas at 700 nm with a 100 mas field-of-view ($\sim 6\lambda/D$ in radius). In addition, broadband operation from 600 to 850 nm, with a spectral resolving power of 300, offers a new avenue to maximizing data output while using standard bispectrum analysis techniques (and hence precision/contrast) while simultaneously allowing spectra to be collected.

FIRST has had several successful observing campaigns on close binary stars at Lick Observatory. It has now made the move from the Cassegrain focus of the Shane telescope to the gravitationally invariant Nasmyth platform of Subaru Telescope, which minimizes mechanical flexure and hence instrumental instabilities. A more comprehensive description of the instrument including the recombination bench, how it works, and the initial science results is presented in Huby et al. (2012, 2013).

Despite all the advanced wavefront control, interferometers and coronagraphs in SCExAO, the performance of the system is highly dependent on the stability of the PSF. Vibrations can plague high-contrast imaging testbeds via flexure, windshake of mirrors, or moving parts (e.g., cryocoolers). For this reason several key efforts have been made to address PSF stability in SCExAO. First, four elastomer-based vibration isolators (Newport, M-ND20-A) are used to support the SCExAO bench at the Nasmyth platform. These elastomers have a natural frequency 9–12 Hz and are used to damp high-frequency mechanical vibrations from the surrounding environment. Second, the mounts for the OAP-based relay optics in the instrument were custom made from a single piece to minimize the drift of the PSF. Finally, the mounting scheme for the HiCIAO cryocooler was rebuilt such that the pump was connected to the dewer by springs and metal bellows only (soft connections with low spring constants for maximum damping). This reduced the tip/tilt jitter observed on the NIR internal camera by a factor of 10 at 10 Hz and up to 100 at a resonant frequency of 23 Hz (Jovanovic et al. 2014a). These steps have improved overall PSF stability against long-term drifts and vibrations above a few Hz. However, there are small residual resonances which will be addressed with a linear quadratic Gaussian (LQG) controller (Poyneer et al. 2014) implemented to the LLOWFS loop in future.

2.3. Internal Calibration

An important feature of any high-contrast testbed is the ability to internally calibrate it off-sky. The SCExAO instrument can be aligned/calibrated with its internal calibration source. The source can be seen in Figure 3 and consists of a standalone box which houses a super continuum source (Fianium–Whitelase micro) for broadband characterization, and two fiber-coupled laser diodes (675 and 1550 nm) for alignment. The light from the super continuum source is collimated and passes through a series of wheels which house neutral density filters for both visible and IR wavelengths as well as a selection of spectral filters. The light is coupled into an endlessly single-mode photonic crystal fiber (NKT photonics - areoGUIDE8) which transports the light to the SCExAO bench. The fiber is mounted on a translation stage and can be actuated into the focus of the AO188 beam (see Fig. 3) when internal calibration is performed or the instrument is not at the telescope. The endlessly single-mode fiber is ideal for this application as it offers a diffraction-limited point source at all operating wavelengths of the super continuum source and SCExAO (600–2500 nm).

The effects of atmospheric turbulence can also be simulated. This is achieved by using the DM to create a large phase-screen with the appropriate statistical fluctuations. A single-phase screen Kolmogorov profile is used where the low spatial frequencies can be attenuated, to mimic the effect of an upstream AO system like AO188. A 50×50 pixel subarray (corresponding to the actuators of the DM) is extracted from the larger phase screen. By scanning the subarray across the phase map, a continuous and infinite sequence of phase screens can be generated. The amplitude of the RMS wavefront map, the magnitude of the low spatial frequency modes, and the speed of the subarray passing over the map (i.e., windspeed) are all free parameters that can be adjusted. This simulator is convenient as it allows great flexibility when characterizing SCExAO modules. Note that, due to the limited stroke of the DM (which is discussed in § 3.1.1), the turbulence simulator cannot be used to simulate full seeing conditions but provides a level of wavefront perturbation that is representative of post AO188 observing conditions. Finally, although the simulator can provide turbulence with the correct spatial structure pre- or post-AO, it does not take into account the temporal aspects of the correction provided by an upstream AO system (i.e., AO corrects low temporal frequencies leaving only higher frequencies).

2.4. Instrument Throughput

To plan observing schedules and determine the limitations of the instrument, the throughput was accurately characterized. As SCExAO has many branches, Tables 4 and 5 summarize the measured internal system throughput for each. Although not explicitly listed, the throughputs include all flat mirrors required to get the light to a given module. In addition, Table 6 highlights the measured throughputs of the optics upstream from SCExAO which includes the effects of the atmosphere, telescope, AO188 HWP, atmospheric dispersion compensator (ADC), AO188 optics, as well as HiCIAO. To determine the total throughput to a given detector plane of the instrument, one should first use Table 2 to select the appropriate beamsplitter, and then find the corresponding throughput for that branch from Table 4 or 5. This value should then be multiplied by the relevant throughputs in Table 6. To convert to photoelectrons, the quantum efficiencies for the detectors used in SCExAO are listed in Table 7. Finally, the throughputs of the focal plane masks used for the coronagraphs are not shown in Table 4 as they are specifically designed to attenuate the light. Indeed, the throughput of these masks depends on the distance from the optic axis, and for this, we refer the reader to literature such as Guyon (2005).

From the tables, we can determine the throughput to several focal planes within SCExAO as an example of the system performance and a demonstration of how to use the tables. One commonly used observing mode involves directing the majority

TABLE 4
THROUGHPUT OF THE VARIOUS ARMS OF THE IR CHANNEL OF SCEXAO MEASURED IN THE LABORATORY FROM THE INTERNAL CALIBRATION SOURCE

Path (elements)	Band	Throughput (%)
From calibration source input to…		
Internal NIR camera		
(OAPs, DM, SLB2)	y	35.3
(OAPs, DM, SLB3)	y	60.6
(OAPs, DM, SLB4)	y	4.5
(OAPs, DM, SLB7)	y	71.1
(OAPs, DM, SLB2)	J	27.2
(OAPs, DM, SLB3)	J	53.7
(OAPs, DM, SLB4)	J	5.9
(OAPs, DM, SLB7)	J	50.4
(OAPs, DM, SLB2)	H	32.8
(OAPs, DM, SLB3)	H	56.2
(OAPs, DM, SLB4)	H	9.4
(OAPs, DM, SLB7)	H	63.4
Facility science instruments		
(OAPs, DM, SLB1)	y	72.1
(OAPs, DM, SLB2)	y	34.9
(OAPs, DM, SLB3)	y	7.6
(OAPs, DM, SLB4)	y	67.2
(OAPs, DM, SLB1)	J	66.9
(OAPs, DM, SLB2)	J	33.4
(OAPs, DM, SLB3)	J	6.2
(OAPs, DM, SLB4)	J	60.5
(OAPs, DM, SLB1)	H	65.2
(OAPs, DM, SLB2)	H	31.8
(OAPs, DM, SLB3)	H	5.0
(OAPs, DM, SLB4)	H	58.2
Single-mode injection		
(OAPs, DM, FIB)	J	77.0
(OAPs, DM, FIB)	H	78.3
Components in isolation		
(PIAA + Binary Mask + IPIAA)	y	53.2
(PIAA + Binary Mask + IPIAA)	J	52.2
(PIAA + Binary Mask + IPIAA)	H	52.5

NOTES. —OAPs, off-axis parabolic mirrors used to relay the light; DM, the window and mirror of the DM; SLB, science light beamsplitter; the number designates the slot (see Table 2); FIB, fiber injection beamsplitter.

TABLE 5
THROUGHPUT OF THE VARIOUS ARMS OF THE VISIBLE CHANNEL OF SCEXAO MEASURED IN THE LABORATORY FROM THE INTERNAL CALIBRATION SOURCE

Path (elements)	Band	Throughput (%)
From calibration source input to…		
Pre-WFSBS		
(PTTB)	R	57.8
	I	65.4
	z	65.6
PyWFS camera		
(PTTB + PyWFS optics WFSBS 2)	R	43.0
	I	47.1
	z	47.6
(PTTB + PyWFS optics, WFSBS 3)	R	20.5
	I	23.0
	z	25.2
(PTTB + PyWFS optics, WFSBS 4, 9, 10 or 11)	R	42.4
(PTTB + PyWFS optics, WFSBS 4, 5, 6 or 7)	I	49.1
(PTTB + PyWFS optics, WFSBS 4, 5, 6, 7 or 8)	z	48.7
VAMPIRES camera		
(PTV + WFSBS 3)	R	12.6
	I	15.3
	z	15.2
(PTV + WFSBS 5, 6, 7, or 8)	R	25.3
(PTV + WFSBS 8)	I	27.5
(PTV + WFSBS 9, 10, or 11)	z	30.6)
FIRST input		
(PTF + WFSBS 3)	R	12.6
	I	15.3
	z	13.4
(PTF + WFSBS 5, 6, 7 or 8)	R	27.1
(PTF + WFSBS 8)	I	29.0
(PTF + WFSBS 9, 10 or 11)	z	28.6

NOTES. —OAP1, the first off-axis parabolic mirror used to relay the light; DM, the window and mirror of the DM; WFSBS, wavefront sensor beamsplitter; the number designates the slot (see Table 2); BRTL1: beam-reducing telescope lens 1, which is located in the periscope. Path to top bench (PTTB): OAP1, DM, dichroic, QWP ×2, periscope mirrors, BRTL1. Path to VAMPIRES (PTV): OAP1, DM, dichroic, QWP ×2, periscope mirrors, BRTL1 & 2, 50/50 BS, and focusing lenses. Path to FIRST (PTF): OAP1, DM, dichroic, QWP ×2, periscope mirrors, BRTL1, 50/50 BS, and collimating lens. Note that the throughput is only quoted to the input of FIRST. Also, the throughputs of the aperture masks for VAMPIRES were not included; please see Norris et al. (2015) for these values.

TABLE 6
THROUGHPUT OF THE ATMOSPHERE, TELESCOPE, AO188 HWP, ATMOSPHERIC DISPERSION COMPENSATOR (ADC), AO188 OPTICS, AND HiCIAO AS A PERCENTAGE

Band	Atmos.	Tele.	HWP	ADC	AO188	HiCIAO
R	91	82	93	95	68	–
I	96	75	95	95	69	–
z	97	79	95	95	69	–
y	98	80	94	95	72	–
J	95	91	96	94	77	87
H	97	92	94	92	79	78
K	92	93	92	70	82	82

NOTES. —The atmospheric transmission in R, I, Z bands is estimated from Buton et al. (2012). The throughput of the atmosphere in the y-, J-, H-, and K-bands assumes an airmass of 1.5 and precipitable water vapor content of 1.6 mm (data taken from Gemini Observatory website) (Lord 1992). The throughput of the telescope is calculated from the reflectivity of the material used for the coating and does not include effects like diattenuation from M3, for example. The throughputs for the HWP and ADC were measured on-sky. The throughputs for R, I, Z, and y band for AO188 have been calculated from materials. J-, H-, and K-band throughputs for AO188 were measured.

of the postcoronagraphic light toward HiCIAO for H-band imaging. In this case, one would select the 90% transmitting beamsplitter in the science light beamsplitter wheel (Slot 4 from Table 2). In this case, the throughput of SCExAO would be 9.4% to the internal NIR camera and 58.2% to HiCIAO (from Table 4). To determine the total throughput from the top of the atmosphere, one would need to multiply the SCExAO throughputs by those listed for the atmosphere (97%), telescope (92%), HWP (94%), ADC (92%), AO188 (79%), and HiCIAO optics/filters (78%) by those listed in Table 6, which yields values of 4.5% and 27.7%, respectively. From here, one would need to take into account the losses of the focal plane and Lyot masks which are coronagraph-specific. Finally, it is possible to use the quantum efficiencies listed in Table 7 to convert the throughput of the instrument into the number of photoelectrons on the HiCIAO detector for a given magnitude target.

In addition to flux at the detector plane, the throughput to the primary wavefront sensor is a useful piece of information for appropriate target selection. Since the PyWFS does most of its sensing at 850–900 nm, one could operate with an 800 nm short-pass filter in the wavefront sensor beamsplitter wheel (slot 7 from Table 2). The throughput of SCExAO to the WFS detection plane with this splitter would be 48.7% in the z-band (from Table 5). The associated throughput as measured from the top of the atmosphere would be 23.2% (including the z-band throughputs from Table 6). This relatively low throughput is attributed to the fact the PyWFS is a long way downstream of the telescope and even within SCExAO. In the future, if SCExAO were to be rebuilt, one could imagine moving the WFS to be the first element after the telescope and ADC which would no doubt improve the throughput by a factor of 2 at least. This would allow the PyWFS to operate with high performance on a 1 magnitude fainter star.

TABLE 7
QUANTUM EFFICIENCY AS A FUNCTION OF WAVEBAND FOR THE DETECTORS IN SCEXAO AS A PERCENTAGE

Detector	R	I	z	y	J	H	K
Internal NIR camera	–	–	–	58	73	73	–
LOWFS camera	–	–	–	58	73	73	–
HiCIAO/CHARIS	–	–	–	–	46	68	68
PyWFS (current)	98	96	77	–	–	–	–
Lucky imaging	93	74	47	–	–	–	–
VAMPIRES	93	74	42	–	–	–	–
FIRST	91	70	42	–	–	–	–

NOTES. —Values were taken from manufacturer specifications.

3. THE FUNCTIONALITIES OF SCEXAO

Key to the successful implementation of a high-performance coronagraph or interferometer for high-contrast imaging is a wavefront control system to correct for both atmospheric as well as instrumental aberrations. Wavefront control comprises two primary components: sensing and correction. The former is taken care of by a wavefront sensor, a device designed to map the spatial profile of the phase corrugations, while the latter by an adaptive element such as a DM. In this section, we describe how the elements of SCExAO function.

3.1. Wavefront Control

3.1.1. Wavefront Correction

The deformable mirror is the proverbial heart of any adaptive optics system. The 2k DM used in SCExAO (Fig. 4) is manufactured by Boston Micromachines Corporation based on MEMS technology. The DM is enclosed in a sealed chamber in order to control its environment. The critical parameter to control is the humidity level and is kept below 20% as advanced aging of MEMS actuators has been observed when high voltages (180 V is the maximum that can be applied), required to actuate individual elements, are applied in a moist environment (Shea et al. 2004). A desiccant is used to filter the compressed air of moisture. A circuit monitors both humidity and pressure and is set up to interlock the power to the DM based on these two metrics (see Appendix).

The chamber window is optimized for transmission across the entire operating range of SCExAO, 550–2500 nm (antireflection-coated, IR-fused silica). The DM's silicon membrane is gold coated and hosts 2000 actuators within the 18 mm diameter beam (there are others outside the pupil but they are not connected). The membrane is bonded to the $\sim$250 μm square-shaped actuators, which are on a pitch of 400 μm. This means that there are 45 and 45.5 actuators across the 18 mm beam in the vertical and horizontal directions, respectively. The number of actuators across the DM defines the highest spatial frequency

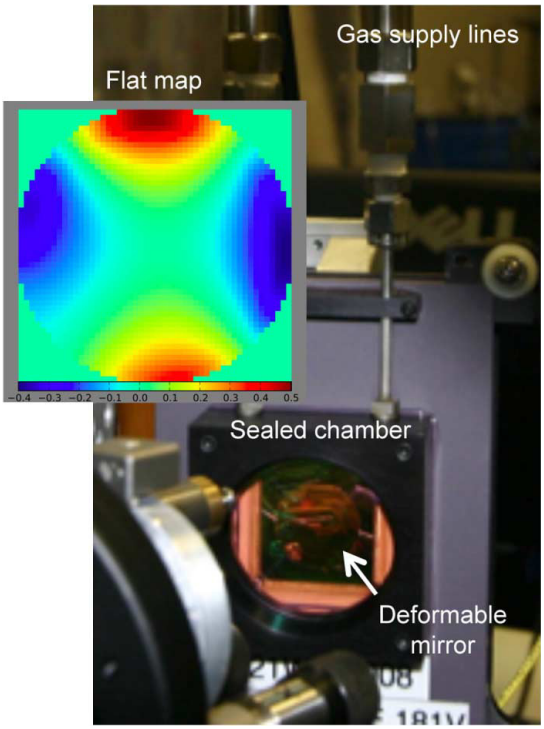

FIG. 4.—2k DM mounted in the SCExAO instrument. The gas supply lines to the sealed chamber can be seen along with the gold surface of the DM itself. Inset: The map applied to the DM in order to compensate for the DM surface figure. The map shows the magnitude of the modulation of the actuators in microns. The window is 50 actuators in diameter corresponding to the functioning region of the DM. The map required to flatten the DM surface is dominated by the Zernike which represents astigmatism. See the electronic edition of the *PASP* for a color version of this figure.

components which can be probed/controlled by the DM and hence the region of control in the focal plane. For our case, the 45 actuator pupil diameter means that the fastest modulation that can be Nyquist sampled by the DM consists of 22.5 cycles across the diameter. This means that spatial frequencies out to $22.5\lambda/D$ from the PSF can be addressed, which defines the radius of the control region in the focal plane (0.9″ in H-band, highlighted in Fig. 5). Figure 5 shows the surface of the DM, where the five dead actuators (actuators that cannot be modulated) are clearly visible. Fortunately, it was possible to position three of the actuators behind the secondary or outside the pupil and one is partially blocked by the spiders of the telescope, leaving only one dead segment in the illuminated pupil. Dead segments compromise the maximum contrast achievable post-coronagraph as they diffract light and hence the 1–2 illuminated for SCExAO is close to ideal. Note that most coronagraph Lyot stops currently installed in SCExAO do not mask out the actuators, but there are plans to include such masks in the future. In addition, the resolution of the DM can be qualitatively examined in Figure 5 where a bitmap image of the PI, Guyon's face, and the bat symbol have been imprinted in phase. The camera used to capture the image is not conjugated to the plane of the DM so that phase information gets recorded as amplitude information on the camera. The resolution of the images generated by the DM demonstrates the high level of sophistication MEMS technology has reached.

The surface of the unpowered DM is not flat. The inset to Figure 4 shows the voltage map that needs to be applied to obtain a flat DM in units of microns of stroke, known as a flatmap. The distortion of the surface of the DM is clearly dominated by astigmatism. Images of the PSF of SCExAO taken without and with the flat map applied are shown in the top left panels of Figure 5. The image without the flatmap is consistent with the presence of strong astigmatism. The PSF post flatmap is diffraction-limited. It is clear that the maximum stroke required for correction near the edges approaches 0.5 μm. This means that 25% of the 2 μm stroke of the actuators is used up to flatten the DM.

3.1.2. Wavefront Sensing

Wavefront correction within the SCExAO instrument comes in two stages: low spatial and temporal frequencies are partially corrected by AO188 prior to being injected into SCExAO where a final correction including higher order modes is implemented. In good seeing conditions, AO188 can offer 30–40% Strehl ratios in the H-band. The high-order wavefront correction, which is the focus of this section, is facilitated by a pyramid wavefront sensor (PyWFS). The PyWFS is chosen because of its large dynamic range and its sensitivity properties (Guyon 2005). In its standard implementation, a tip/tilt mirror modulates the location of the PSF in a circular trajectory which is centered on the apex of the pyramid. This implementation has been used to correct seeing-limited light to Strehl ratios as high as 90% in very good seeing on LBTAO (Esposito et al. 2011) and MagAO (Close et al. 2013). By removing modulation, however, the range over which the sensor responds linearly to aberrations is greatly reduced. Hence, to utilize a PyWFS without modulation, the wavefronts must be partially corrected by another sensor initially. With AO188 providing such a correction upstream, this implementation is possible with the PyWFS on SCExAO. SCExAO incorporates a piezo-driven mirror mount (shown in Fig. 3) to provide the modulation functionality, with the driver carefully synchronized to the frame rate of the camera. The implementation allows for continuous changes of the modulation radius (see Fig. 6). Such an architecture enables the possibility to start with a modulated PyWFS that has a larger range of linearity and slowly transition to a nonmodulated sensor for maximum sensitivity and the highest Strehl ratio, as wavefront errors are gradually reduced.

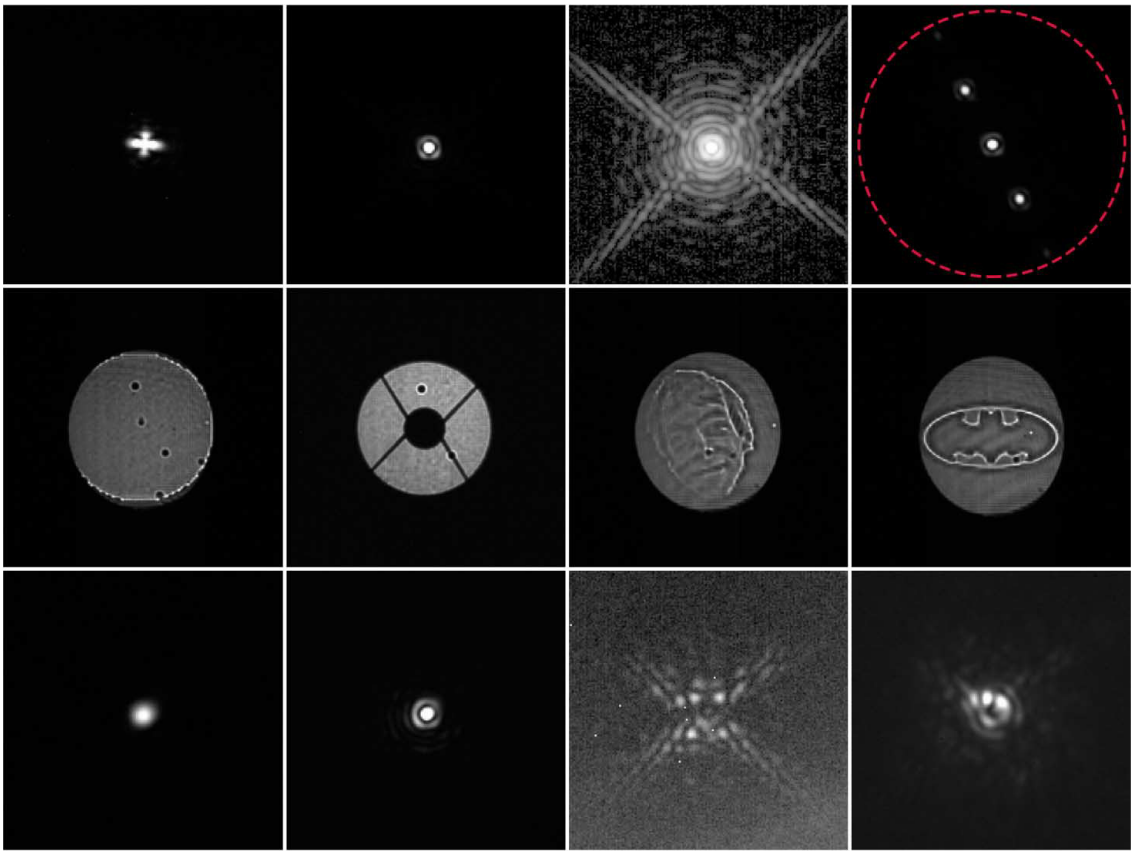

FIG. 5.—Top row: PSF of SCExAO at 1550 nm with the unpowered DM surface (left). Strong astigmatism is clearly visible. An image of the instrument PSF taken with the optimum flat map applied with linear (middle-left) and logarithmic (middle-right) scaling. The image is diffraction-limited and numerous Airy rings can be seen. Image with several artificial speckles applied (right). The *dashed ring* designates the edge of the control region of the DM corresponding to a radius of $22.5\lambda/D$ or 900 mas at 1550 nm. Second row: Pupil images showing the unmasked surface of the DM with five dead actuators (left), the internal spider mask in place masking several actuators (middle-left), an image of the PI Guyon (middle-right), and the bat symbol (right). These two images demonstrate the resolution of the DM. Bottom row: Image of the PSF taken in the laboratory with a laser at 1550 nm, after the conventional PIAA lenses (left), with the IPIAA lenses (middle-left) as well as with the achromatic focal plane mask (AFPM) ($1.9\lambda/D$ IWA) (*middle-right*). Right: An image with the PIAA, IPIAA, and AFPM is shown taken on-sky on the night of July 25, 2013, with the full H-band. See the electronic edition of the *PASP* for a color version of this figure.

The PyWFS has undergone laboratory and initial testing on-sky. In its initial format, it exploited a microlens array instead of a pyramid optic as it was easier to obtain (pyramid optics need to be custom made). However, it was determined that although small microlenses have good interlens quality, which keeps diffraction effects at a minimum, they have a limited field-of-view which limits their use with modulation. On the other hand, larger microlenses remove this limitation but the interlens quality is poor and results in strong diffraction. Hence, it was not possible from the two microlens arrays tested to simultaneously obtain a large field-of-view and low diffraction (there may indeed be microlenses on the market that can achieve both) (Clergeon 2014). For this reason, a dedicated pyramid optic was obtained. The pyramid optic presented here is a double pyramid, as shown in Figure 6, and is a replica of the one used on MagAO (Close et al. 2013; Esposito et al. 2010). The pyramid optic segments the PSF and generates four images of the pupil on the camera (see Fig. 6). The OCAM^{2}k from FirstLight imaging (see full specs in Table 1) is used as the detector and is capable of photon counting, with low read noise, high frame rate, and low latency (<1 frame) which enables the correction of high temporal frequencies and allows operation on faint

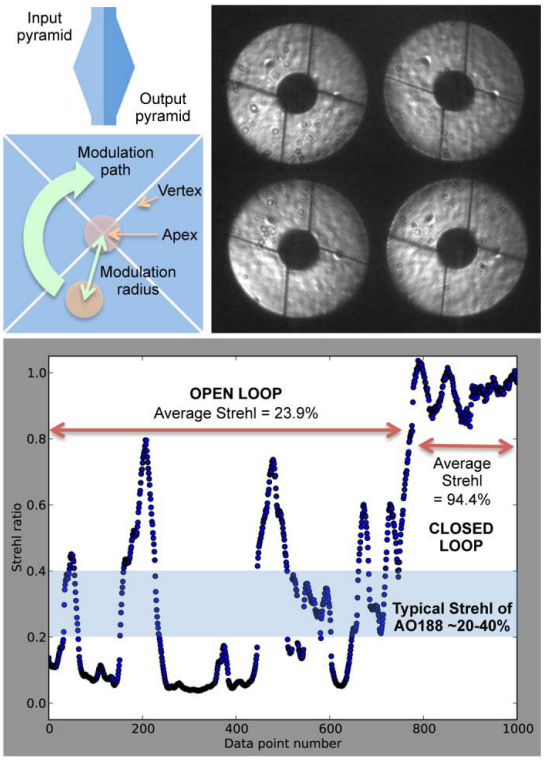

FIG. 6.—(Top left) A side view of the double pyramid. A very shallow angle (~1°) is required which is hard to produce so two steeper pyramids are used such that the cumulative effect of refraction between them is equivalent to a single shallower sloped pyramid optic (Esposito et al. 2010). Below this a front view of the pyramid is shown. The circles represent the PSF position without modulation (red spot) and with modulation (orange spot). The green arrow shows the path of the PSF across the front face of the pyramid optic when modulation is applied. (Top right) An image of the four pupils generated by the pyramid optic taken with modulation applied. (Bottom image) Strehl measured for the internal source with 300 nm RMS wavefront error applied to the turbulence simulator and the PyWFS loop open and then closed. NB, the Strehl ratio calculation procedure has a limited accuracy of about 5–7% when the Strehl ratio is >90%. Hence, values >1 are possible in this regime as shown in the above chart and should simply be interpreted as regions of high Strehl, with no emphasis put on the exact value. See the electronic edition of the *PASP* for a color version of this figure.

guide stars. To facilitate full-speed PyWFS loop operation (limited by camera frame rate), fast computations are required and for this a bank of GPUs is utilized. Details of the control loop architecture for the PyWFS are beyond the scope of this work. Here we focus on the recent performance of the loop.

In laboratory testing, the PyWFS successfully closed the loop with modulation (amplitude of $1.7\lambda/D$) on up to 830 modes. Our modal basis consisted of linearly independent modes obtained by singular value decomposition of an input basis consisting of five Zernike coefficients (tip, tilt, focus, astigmatisms) and the remainder Fourier modes (sine waves) up to a given spatial frequency of the DM. Nonorthogonality between input modes was addressed by rejecting (not controlling) low-eigenvalue modes. This basis set was chosen purely for convenience. This was achieved with the turbulence simulator generating 300 nm RMS wavefront error maps with a wind speed of 5 m/s and the low-order spatial frequencies scaled to 30% of the Kolmogorov power spectrum value to simulate upstream low-order wavefront correction. Light with wavelengths between 800 and 940 nm was used for the tests and the loop was run at 1 kHz. The Strehl of the images captured by the internal NIR camera was measured in the open- and closed-loop regime and the results depicted in Figure 6. The average Strehl in the open-loop regime was 23% which is consistent with the value predicted from Marechal's approximation (Hardy 1998) (22.7%) given 300 nm of wavefront error at 1550 nm. When the loop is closed on 830 modes, the Strehl improved to >90% on average confirming that given realistic post-AO correction, the PyWFS can indeed achieve extreme AO performance as required.

The nonmodulated mode was also tested with the turbulence simulator in the laboratory. However, due to the smaller linear range of the sensor without modulation the amplitude of wavefront errors was reduced. For the purposes of the test, it was set to 60 nm (windspeed 5 m/s and low-order Kolmogorov frequencies set to 30%). The loop was successfully closed at 1.5 kHz on the turbulence simulator on 1030 modes (which include five Zernikes). In this regime, it was clear that the speckles in the halo surrounding the PSF were held very static. The loop speed is constantly being improved by optimizing the code and removing delays. An operational speed as high as 3.5 kHz with minimal delay should be possible in the near future. Since the WFS detector operates in photon-counting mode, the loop will be able to run at full speed (3.5 kHz) even on faint targets (I-mag ~10), albeit at lower loop gain. Fainter targets still will require lower loop speeds. An optimal modal gain integrator will also be implemented soon.

Thus far the PyWFS has undergone some initial on-sky testing and has performed well on up to 130 modes (with modulation, 1.7 λ/D radius). However, as the speed of the loop was the same as AO188 (i.e., 1 kHz) and there were fewer modes than are corrected by AO188, a negligible improvement in Strehl was observed. Most of the gain came in the form of reduced tip/tilt jitter which was clearly visible in long integration time images. With further improvements in the AO loop code, the PyWFS should perform as demonstrated in the laboratory more recently, on-sky.

Noncommon path and chromatic low-order errors between the visible PyWFS and the IR coronagraphs are measured with the LLOWFS on the IR channel. The LLOWFS utilizes the light diffracted by the focal plane masks of the coronagraphs (discussed in detail in § 3.2), which is otherwise thrown away.

A reflective Lyot stop is used to direct the diffracted light to the LOWFS camera (Singh et al. 2014). In this way, a reimaged PSF formed on the camera can be used to drive low-order, including tip/tilt, corrections by looking at the presence of asymmetries in the image. It has been tested thoroughly both in the laboratory and on-sky. Indeed, it was used on-sky in conjunction with the vector vortex coronagraph on Vega, on the nights of April 14 and 15, 2014, and produced residual RMS tip/tilt wavefront errors of $0.01\lambda/D$ (Singh et al. 2015).

In addition to the PyWFS and LLOWFS, we are testing other wavefront sensing techniques. One such technique is known as focal plane wavefront sensing which exploits eigenphase imaging techniques (Martinache 2013). The focal plane wavefront sensor relies on establishing a relationship between the phase of the wavefront in the pupil plane and the phase in the Fourier plane of the image. Although it has a limited range of linearity ($\sim\pi$ radians), which means that the wavefront must first be corrected to the 40% Strehl ratio level before this sensor can be utilized, it can boost the Strehl ratio to $>95\%$ in the H-band by correcting low-order modes. In addition, it operates just as effectively in the photon noise regime and is extremely powerful as noncommon path errors are eliminated. This wavefront sensor is currently under development and has been successfully tested on both the internal calibration source, in which case the aberrations due to the internal SCExAO optics were corrected as well as on-sky, where the static aberrations due to the telescope, AO188 optics, and SCExAO were all corrected. Some additional detail of this work can be found in Martinache et al. (2014a).

3.1.3. Coherent Speckle Modulation and Control

As a booster stage to the primary wavefront control loops, SCExAO makes use of coherent speckle modulation and control to both measure and attenuate residual starlight in the instrument's postcoronagraph focal plane. The 2k DM actuators are used to remove starlight from a predefined region, referred to as the dark hole (Malbet et al. 1995). Active modulation, induced by the 2k DM, creates coherent interferences between residual speckles of unknown complex amplitude and light added by modifying the DM's shape (this component's complex amplitude is known from a model of the DM response and the coronagraph optics). By iterating cycles of measurement and correction, starlight speckles that are sufficiently slow to last multiple cycles are removed from the dark hole area. This approach, developed and perfected in the last 20 yrs (Borde & Traub 2006; Codana & Kenworthy 2013; Give'on et al. 2007; Guyon et al. 2010; Malbet et al. 1995), is well suited to high-contrast imaging as it effectively targets slow speckles, which are the dominant source of confusion with exoplanets. It also allows coherent differential imaging (CDI), a powerful postprocessing diagnostic allowing true sources (incoherent with the central starlight) to be separated from residual starlight (Guyon et al. 2010). Compared to passive calibration techniques, such as angular differential imaging, CDI offers more flexibility, and achieves faster averaging of speckle noise. This is especially relevant at small angular separations, where ADI would require very long observation time to achieve the required speckle diversity. An example of a pair of speckles being generated by a periodic corrugation applied to the DM and used for starlight suppression is shown in the top right inset of Figure 5.

In SCExAO, coherent speckle control is implemented as discrete speckle nulling: The brightest speckles are identified in the dark hole region, and simultaneously modulated by the 2k DM, revealing their complex amplitudes. The 2k DM nominal shape is then updated to remove these speckles, and successive iterations of this loop gradually remove slow and static speckles. While discrete speckle nulling is not as efficient as more optimal global electric field inversion algorithms, it is far easier to implement and tune, and thus more robust for ground-based systems which have much larger wavefront errors than laboratory testbeds or space systems. This approach has been validated on SCExAO both in the laboratory (Martinache et al. 2012) and on-sky (Martinache et al. 2014b) and is a means of carving out a dark hole on one side of the PSF to boost contrast in that region. A recently taken image demonstrating the successful implementation of speckle nulling without a coronagraph on RX Boo is shown in the lower panel of Figure 7. The region where the nulling process was performed is outlined by the dashed white line and spans from 5–$22.5\lambda/D$. An image without the nulling applied is shown in the top panel of Figure 7 for comparison. This result was obtained on June 2, 2014, in favorable seeing conditions (seeing $<0.7''$). The nulling process reduced the average flux over the entire controlled area by 30% and by 58% in the region between 5–$12\lambda/D$, where the nulling was most effective. With better wavefront correction and the use of a coronagraph, the improvement in the contrast will grow.

The current limitations to achieving high-quality speckle nulling on-sky are wavefront correction, readout noise, and loop speed. As high-sensitivity cameras in the NIR are currently limited in regards to maximum frame rate (the Axiom cameras used are among the fastest commercially available at the time of writing), it is not possible for the active speckle nulling algorithm to pursue atmospherically induced speckles as they change from frame-to-frame. Hence, the current implementation of speckle nulling on SCExAO aims at removing the static and quasi-static speckles induced by diffraction from the secondary and spiders as well as optical aberrations. For this reason, it is important to have a high level of atmospheric wavefront correction on-sky so that the persistent speckles due to static and quasi-static aberrations can be easily identified. As the speckles are $\sim 1000\times$ fainter than the PSF core, a magnitude limit for speckle nulling of 3–4 in the H-band is imposed by the current cameras used due to the high readout noise ($114\ e^-$). This places a severe limitation on potential targets of scientific interest. To alleviate these issues, SCExAO is acquiring a Microwave Kinetic Inductance Detector (MKID) which is a photon counting, energy

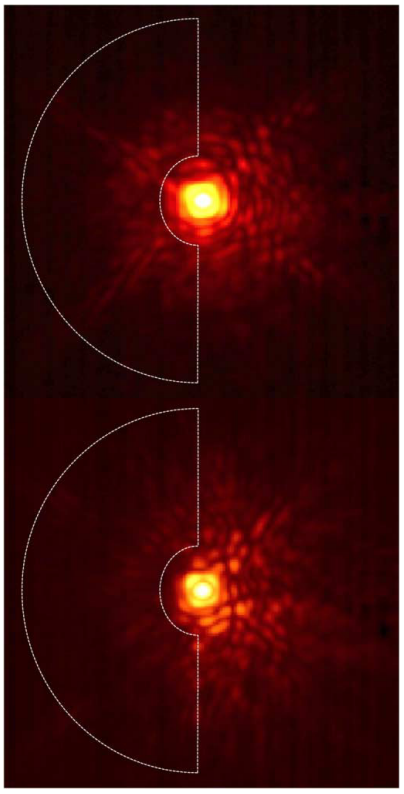

FIG. 7.—Top: RX Boo with no speckle nulling applied. Bottom: RX Boo with speckle nulling performed on the region enclosed by the *white dashed line*. Each image is a composite of 5000, 50 μs frames which have been shifted and added together. Each panel has a square root stretch applied to it and the maximum and minimum values are clipped for optimum viewing contrast. See the electronic edition of the *PASP* for a color version of this figure.

discriminating NIR array (Mazin et al. 2012). The MKID array will offer almost no readout noise or dark current and is capable of high frame rates ($>$1 kHz). This enables speckle nulling to be performed on fainter, more scientifically relevant targets, and for noncommon speckles due to chromatic dispersion in the atmosphere to be corrected for the first time, allowing for a significant improvement in detectability of faint companions. As the developmental time for the MKID array is several years, speckle control is being tested with a SAPHIRA (SELEX) array of avalanche photodiodes in the interim (Atkinson et al. 2014).

In contrast to speckle suppression, the addition of artificial speckles to the focal plane image can be utilized for precision astrometry when the on-axis starlight has been suppressed post-coronagraph. Further, by modulating the phase of the speckles during an exposure, they can be made incoherent with the speckles in the halo offering superior astrometric performance. In addition, by carefully calibrating the flux ratio between the PSF core and speckles, it is also possible to use these speckles for photometry and hence retrieving the contrast of companions as well (Martinache et al. 2014b). As opposed to diffractive grids utilized by other high-contrast imagers (Wang et al. 2014), the adaptive nature of the DM allows the speckle position, and brightness to be carefully tailored to each science case.

3.2. Coronagraphs

The advanced wavefront control techniques utilized on SCExAO build the foundation for high-contrast (10^{-5}–10^{-6}) imaging of faint companions with the onboard coronagraphs. The coronagraphs available in SCExAO are listed in Table 8. The performance of the coronagraphs used in SCExAO is limited by the level of wavefront control achieved. The PIAA/PIAACMC and the Vortex offer the lowest IWA and highest throughput but are more sensitive to wavefront error. On the other hand, the shaped pupil has a larger IWA and lower throughput but is less sensitive to residual wavefront error. Hence, the coronagraphs available are designed to span a large range of residual wavefront error and should be chosen accordingly.

The two key coronagraphs are the phase-induced amplitude apodization (PIAA) and the vector vortex types. PIAA refers to the act of remapping a flat-top pupil to a soft-edged pupil in order to remove the diffraction features associated with a hard-edged aperture (i.e., Airy rings) (Guyon 2003). These diffraction features make it difficult to suppress all of the light via a coronagraphic mask in the focal plane without blocking a close, faint companion. A combination of aspheric lenses are used to achieve the remapping in SCExAO and are referred to as PIAA lenses. SCExAO offers several types of remapping lenses. The first type is referred to as the conventional PIAA design and was presented in Lozi et al. (2009). Conventional PIAA lenses offer the most aggressive remapping, eliminating the secondary and converting the post-PIAA pupil into a prolate spheroid (a near-Gaussian which is finite in extent). An image depicting the remapping process between the two PIAA lenses in the laboratory is shown in Figure 8, while a radial profile of the apodization function is shown in Figure 9.

TABLE 8
DETAILS OF SCEXAO CORONAGRAPHS

Coronagraph type	Inner working angle (λ/D)	Waveband (s)
PIAA	1.5	y-K
PIAACMC	0.8	y-K
Vortex	2	H
MPIAA + vortex	1	H
MPIAA + 8-octant	2	H
4-Quadrant	2	H
Shaped pupil	3	y-K

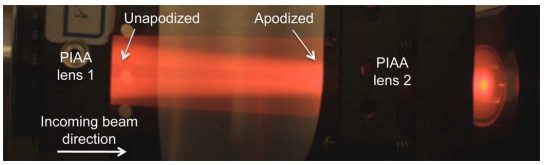

FIG. 8.—Picture of a visible beam being apodized by the conventional PIAA lenses in the laboratory (side view). The image is taken between the two lenses. The beam enters from the left of the image where the intensity across the beam is uniform except for the faint part in the middle of the beam (behind the secondary) and at the right hand side of the image, the beam is concentrated in the middle (i.e., apodized). See the electronic edition of the *PASP* for a color version of this figure.

To complete the softening of the edges of the beam, a binary mask is used which has a radially variant attenuation profile. Note that the binary mask is used to reduce the demand on the curvature changes across the aspheric surfaces of the PIAA lenses, and it is possible to eliminate it at the expense of increased manufacturing complexity of the PIAA lenses. As outlined in Guyon (2003), once the on-axis star has been suppressed with a focal plane mask, it is important to reformat the pupil to its original state in order to preserve the field-of-view. This can be done by using another set of PIAA lenses in reverse and the ensemble of lenses are referred to as the inverse PIAA lenses (IPIAA). The position of the PIAA and inverse PIAA lenses can be seen in Figure 3. Due to the low material dispersion of CaF_2, the conventional PIAA lens design used in SCExAO is achromatic across the NIR (y-K bands). However, an appropriate focal

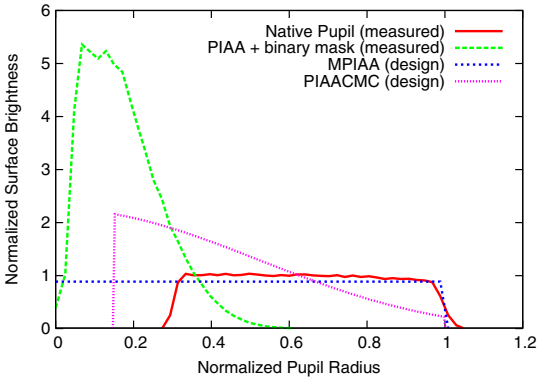

FIG. 9.—The figure shows a comparison of the radial apodization profiles of the various PIAA lenses as compared to the Subaru telescope pupil. The PIAA (*green line*) pulls the light inwards most aggressively, almost entirely removing the secondary and softening the edges of the beam. The PIAACMC (*pink line*) pulls some of the light inwards but does not entirely remove the presence of the secondary or soften the edges completely. The MPIAA (*blue line*) removes the presence of the secondary but does not soften the edges at all. See the electronic edition of the *PASP* for a color version of this figure.

plane mask must be chosen to achieve this. If an ordinary opaque mask is used, then the size of the mask is wavelength dependent, and so is the IWA. To circumvent this issue, SCExAO uses focal plane masks that consist of a central cone surrounded by a ring of pits periodically positioned around the cone, made from a transmissive material on a substrate which refracts rather than reflects the on-axis star light (Newman et al. 2015). In this way, a variable focal plane mask which is achromatic across H-band can be achieved. In addition, since the light is strongly diffracted outwards by the focal plane masks, it can be redirected toward the LLOWFS via a reflective Lyot mask (Singh et al. 2014).

Despite the fact that the conventional PIAA offered in SCExAO has an IWA of $1.5\lambda/D$, due to the aggressive remapping which causes an abrupt phase step in the central part of the beam post-PIAA, the contrast at $1.5\lambda/D$ is limited to 1×10^{-5} and is very sensitive to tip/tilt. To alleviate these issues, a modified version of the PIAA coronagraph can be used. It is referred to as the PIAA complex mask coronagraph (PIAACMC) and is outlined in greater detail in Guyon et al. (2010). The major difference is that the PIAA lenses used for the PIAACMC are less aggressive, which means the remapped pupil has soft edges but the secondary is still present as shown in Figure 9. The lenses themselves are in the same mounts as those for the PIAA so they can be replaced on the fly. The focal plane mask is now replaced with a partially transmissive, phase shifting mask which is manufactured via electron beam etching. The IWA of the coronagraph can be tuned by varying the opacity of the focal plane mask and in the limit when the mask is fully transmissive, the IWA is minimized at the expense of sensitivity to tip/tilt. Nonetheless, the PIAACMC offers a contrast of 1×10^{-6} at $1\lambda/D$, is less sensitive to tip/tilt than the PIAA, and is fully achromatic from y-K band. It is scheduled to be installed and commissioned in the near future.

A third and final type of PIAA is used to remap the pupil into a flat top without a central obstruction for an 8-octant coronagraph which is discussed in the following section (Oshiyama et al. 2014). The lenses are referred to as MPIAA lenses and reside in the same mounts as the other two. Despite the remapping, these optics are not apodizers as the pupil retains its hard edge post remapping. A comparison of the various apodization schemes is shown in Figure 9.

Other coronagraphs include the vortex (Mawet et al. 2009, 2010), 4-quadrant (Rouan et al. 2000), 8-octant (Murakami et al. 2010), and shaped pupil (Carlotti et al. 2012) versions. The vortex, 4-quadrant, and 8-octant coronagraphs are phase-mask coronagraphs as opposed to occulting coronagraphs and consist of two primary elements: a focal plane and Lyot stop mask. All focal plane masks are situated in a wheel in the focal plane while the Lyot stop masks are located in the Lyot mask wheel and the positions of both are shown in Figure 3.

The vortex coronagraph in SCExAO uses a H-band optimized, topographic charge two focal plane mask. This mask is constructed from a birefringent liquid crystal polymer material,

i.e., a waveplate where the optical axis (fast axis) orientation is spatially dependent and in this case a function of the azimuthal coordinate (Mawet et al. 2009). Although an IWA of $0.9\lambda/D$ is achievable with an unobstructed pupil with nonmanufacturing defects, it is limited to $2.0\lambda/D$ with the pupil geometry at the Subaru Telescope. However, the vector vortex on SCExAO could be used in conjunction with the MPIAA lenses to circumvent this issue and regain the inherent IWA. The vector vortex mask is more achromatic than a scalar mask and hence can operate across the full H-band (Mawet et al. 2009). As the nulling process is based on interference of light from different parts of the mask, best performance is achieved with higher Strehl ratios and stable centering of the PSF on the mask (5 mas tip/tilt error or below in this case).

The 8-octant coronagraph focal plane mask employed on SCExAO is based on photonic crystal technology (Murakami et al. 2010). It consists of eight triangular segments that comprise half-wave plates where the optical axes of a given segment are always orthogonal to its two nearest neighbors. This creates a π phase shift between adjacent segments for the transmitted beam which destructively interferes in the reimaged focal plane to null out the on-axis star. The 8-octant itself is not achromatic but broadband operation can be realized by placing a polarizer and analyzer before and after the mask respectively (Murakami et al. 2008) (note this is also true for the vortex coronagraph). This coronagraph exploits the pupil-reformatting MPIAA lenses described above to achieve an IWA of $\sim 2\lambda/D$ and offers very high-contrasts at these angular scales. Similar to the vector vortex it is also sensitive to tip/tilt and hence active control is the preferred mode of operation.

The 4-quadrant focal plane mask is a scalar mask which consists of segments that phase shift the light by π with respect to the neighboring segments. Although a perfectly manufactured 4-quadrant mask could offer an IWA of as low as $1\lambda/D$ if used in conjunction with the MPIAA lenses mentioned above, the mask in SCExAO has manufacturing defects and so cannot achieve such performance. The 4-quadrant in SCExAO is a prototype which serves its purpose for internal testing only.

The Lyot stop masks for the vector vortex, 4-quadrant, and 8-octant coronagraphs are designed to reflect rejected light toward the LOWFS camera for fine tip/tilt guiding which is discussed in the subsequent section. The vector vortex and 4-quadrant Lyot stop masks consist of a replica mask to the Subaru Telescope pupil geometry with slight modifications. Both masks have a slightly oversized secondary and spiders for better rejection; however, the 4-quadrant has a square secondary instead of a circular one. On the other hand, as the secondary is eliminated thanks to the MPIAA lenses, then the Lyot stop for the 8-octant is simply a slightly undersized circular aperture.

Finally, shaped pupil coronagraphs can also be tested on SCExAO. These coronagraphs are located in the pupil plane mask wheel and any focal or Lyot plane masks required are placed in the appropriate wheel. For further details, please see Carlotti et al. (2012).

3.3. Lucky Fourier Imaging

An important element of all adaptive optics systems is a real-time PSF monitoring camera. This is depicted as the Lucky imaging camera in Figure 3, the specifications of which are listed in Table 1. Currently, a narrowband of light ($\sim$30–50 nm) is steered toward this camera from the pupil plane masks of VAMPIRES and the PSF imaged. The camera runs at a high frame rate, subframed, and collects images rapidly which are primarily used for monitoring the PSF. The frames can subsequently also be used for traditional lucky imaging. However, a more advanced version of this technique named Lucky Fourier Imaging is commonly utilized (Garrel et al. 2012). The technique relies on looking for the strongest Fourier components of each image, and then synthesizing a single image with the extracted Fourier information. In this way, diffraction-limited images at 680 nm of targets like Vega (bottom image in Fig. 10) and Betelgeuse have been synthesized in 2″ seeing (Garrel 2012). This is clearly an extremely powerful tool and we propose to advance this imaging capability by adding multiple spectral channels.

3.4. Fiber Injection Unit

In addition to direct imaging, long baseline interferometry and high-precision radial velocity both stand to gain significantly from a stable and 90% Strehl PSF on an 8-m class telescope. For example, long baseline interferometers like the Optical Hawaiian Array for Nanoradian Astronomy (OHANA) combine beams from multiple telescopes once it has been transported to the combination room via single-mode optical fibers (Woillez et al. 2004). However, coupling efficiently into single-mode fibers is no mean feat, but with access to a stable PSF with 90% Strehl, it can be achieved. Indeed, this is already being exploited for the purposes of nulling interferometry on P1640 (Serabyn et al. 2010). Once the light has been coupled into a single-mode fiber, it could be used as an alternative feed for a conventional multimode fiber-fed spectrograph. The nontemporally and spatially varying PSF provided by a single-mode fiber can be used in precision radial velocity measurements to eliminate modal-noise, a limiting factor in achieving high precisions. For these reasons, we are developing a single-mode injection unit on the SCExAO platform.

To inject light into the fiber, it is tapped off with a retractable dichroic on its way to focus after OAP2 (see Fig. 3). A dichroic which reflects y, J, and H-short bands is currently used for this. An achromatic lens ($f = 10$ mm) is used to adjust the $f/\#$ of the beam before it is injected into the fiber which sits atop a stage. The 5-axis stage allows for XYZ translation via precise stepper motor actuators and course alignment of tip/tilt. The stage can be scanned through focus to maximize coupling into the fiber.

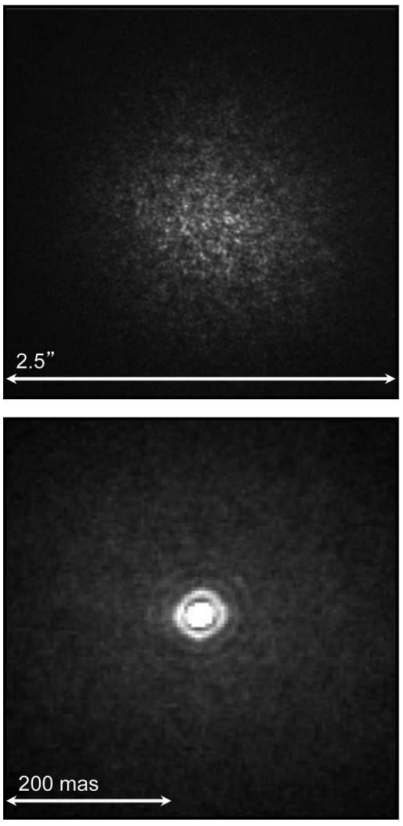

FIG. 10.—Top image: Vega in 2″ seeing at 680 nm. Bottom image: Synthesized image of Vega at 680 nm in the presence 2″ seeing. Image was reconstructed from a 1% selection of Fourier components across the 10^4 frames collected. A diffraction-limited PSF with a FWHM of 17 mas is obtained post-reconstruction (note: the scale of the bottom image differs from the top one). The data was acquired on 2012 February 5 and 6.

A further advantage of implementing such a module on SCExAO is that we can use the conventional PIAA lenses to more closely match the intensity distribution of the collection fiber and hence boost the coupling to a theoretical value of 100%. To make this useful on-sky, this injection system relies on the PyWFS delivering a high Strehl beam. The fine tip/tilt control is provided by the LLOWFS by using the transmitted H-band light. This unit is currently operational and may be utilized by instruments such as the high-precision spectrograph IRD for the survey it will undertake (Tamura et al. 2012). In addition, by developing such a unit, it becomes possible to exploit numerous other photonics technologies on-sky (Cvetojevic et al. 2012; Marien et al. 2012). The injection unit is described in more detail in Jovanovic et al. (2014b).

TABLE 9
COMMISSIONING STATUS OF SCEXAO MODES OF OPERATION AND MODULES

Module/mode	Commissioning status (completion date)
Wavefront control	
LLOWFS	Complete
SN	Complete
PyWFS	Partially complete (2015 fall)
PyWFS + LLOWFS	Partially complete (2015 fall)
SN + PyWFS + LLOWFS	Incomplete (late 2015)
Coronagraphs	
PIAA	Complete
Vortex	Complete
4-Quadrant	Complete
Shaped pupil	Complete
PIAACMC	Incomplete (2015 fall)
MPIAA + Vortex	Incomplete (late 2015)
MPIAA + 8-octant	Incomplete (2015 fall)
Visible imagers	
VAMPIRES	Complete
Lucky imaging	Partially complete (late 2015)
FIRST	Incomplete (late 2015)
NIR fiber injection	Complete
NIR science imagers	
CHARIS	Expected delivery early 2016 (mid-2016)
MKID	Expected delivery late 2016 (2017)

NOTES. —+ signifies that these modes/modules are operating in conjunction. SN-speckle nulling, PIAA will be replaced by the PIAACMC.

4. COMMISSIONING STATUS AND FUTURE EXTENSIONS

SCExAO is clearly a complex instrument with modules at various stages of commissioning. Table 9 summarizes the commissioning status/plan of the various modes of operation and modules of SCExAO.

Table 9 shows that the integral field spectrograph known as CHARIS will replace the HiCIAO imager from mid 2016. This instrument segments the focal plane with an array of microlenses, before dispersing each PSF and then reimaging onto a detector (see Table 1) (Peters et al. 2012). This allows for spatially resolved spectral information, albeit at low resolving powers. Such an instrument has three key advantages. First, background stars in a given image can quickly be identified. Second, owing to the fact that the instrument operates over a very broadband (J-K bands), the presence of a planet can be inferred by detecting the fixed speckle within a spectral data cube. Finally, low-resolution spectra of gas giants can be taken, enabling the atmospheres of these planets to be constrained and better understood (Brandt et al. 2014; McElwain et al. 2012). Indeed, presently operating integral field spectrographs such as OSIRIS at the Keck Telescope, the units in P1640 and GPI have been used to characterize the atmospheres of known planetary systems like HR8799 (Barman et al. 2011; Ingraham et al. 2014; Oppenheimer et al. 2013).

Although not included in the table, it has been proposed to outfit the IR arm of SCExAO with a polarimetric mode of

operation to study scattered dust in circumstellar disks. This mode, known as polarization differential imaging (PDI), has been hugely successful for the HiCIAO imager (Grady et al. 2013), and we aim to preserve this capability while offering a superior IWA. This IR polarimetric mode will complement one of the VAMPIRES offered in the visible, albeit on different spatial scales.

5. SUMMARY

The SCExAO instrument is a versatile high-contrast imaging platform which hosts advanced wavefront control systems, IR coronagraphs, and visible interferometers that are ideal for imaging at $<3\lambda/D$ (solar-system scales). The extreme adaptive optics system delivers the necessary wavefront correction to be able to push detection limits for ground-based observations at small angular separations and interferometer precisions. Such instruments will be critical to understanding the inner structure of circumstellar disks and planetary systems and how they form. In addition, they will provide the appropriate avenue to collecting spectra from planetary candidates and determining their physical properties for the first time. Further, the SCExAO platform is an ideal testbed for demonstrating and prototyping technologies for future ELTs and space-missions. SCExAO is the only high-contrast imager of its kind and will be uniquely positioned to contribute to exoplanetary science.

We are grateful to B. Elms for his contributions to the fabrication of parts for the SCExAO rebuild. The SCExAO team thanks the Subaru directorate for funding various grants to realize and develop the instrument.

APPENDIX

A.1. Off-Axis Parabolic Mirrors

All OAPs in the SCExAO instrument were manufactured via diamond turning of aluminum and overcoating with gold, are 50 mm in diameter, and were designed to work at a nominal off-axis angle of 17°. OAPs 1, 3, 4, and 5 have a $f = 255$ mm while OAP2 has a $f = 519$ mm. Although there is no data on the wavefront error of these optics, each optic was initially used to form an image in the visible and it was determined from this that the RMS wavefront error was $<\lambda/20$ at 630 nm over a 20 mm beam size corresponding to that which is used in SCExAO.

A.2. Internal NIR Camera Lenses

The focusing lenses for the science camera include a $f = 150$ and 50 mm converging, achromatic doublet which are AR-coated for the NIR region (1–1.65 μm). The distance between the lenses is set to be just larger than the sum of their focal lengths so that a slow beam is formed ($f/65$).

A.3. Deformable Mirror Environmental Controls

An interlock system which monitors the environmental conditions in the DM chamber (pressure, humidity) was put in place to prolong the life of the DM as they are known to age rapidly in high-humidity environments (Shea et al. 2004). A low-pressure regulator (Fairchild-M4100) was used to offer fine control of the injected dry air pressure to the DM chamber at the <1 psi level (with respect to ambient). The pressure is set to 0.4 psi above ambient when operating and monitored by a precise pressure sensor (FESTO–SDE1). Such low-pressure differentials are used so that the chamber does not deform significantly and hence induce any extra errors to the wavefront. A 1 psi pressure differential relief valve is used as a hard limit in case of over pressure in the circuit. The humidity in the circuit is measured with a moisture probe (Edgetech–HT120). The alarms for both the pressure and humidity sensors are used to control the power supplied to the DM electronics. When the humidity is below 15% and the pressure between 0.2 and 0.8 psi, the DM electronics will be powered and the actuators can be driven. However, if the humidity rises above 15% and/or the pressure goes above 0.8 psi or below 0.2 psi, then the alarms on the sensors will trigger a relay switch, to which the DM electronics are connected, to trip and cut the power to the DM. As a final level of reassurance, a low flow rate (250 mL/ min) flow controller is connected to the end of the line to insure that there is a very slow flow over the DM membrane and no turbulence in the chamber. A rapid flow could tear the thin silicon membrane (3 μm) and/or cause turbulence in the chamber which would be equivalent to seeing. The window to the chamber is 50 mm in diameter, made from a 12 mm thick piece of IR-fused silica which is AR-coated across the operating range.

REFERENCES

Artigau, E., Biller, B. A., Wahhaj, Z., Hartung, M., Hayward, T. L., Close, L. M., Chun, M. R., Li, M. C., et al. 2008, Proc. SPIE, 70141 Z
Atkinson, D., Hall, D., Baranec, C., Baker, I., Jacobson, S., & Riddle, R. 2014, Proc. SPIE, 915419 A
Barman, T. S., Macintosh, B., Konopacky, Q. M., & Marois, C. 2011, ApJ, 733, 65 B
Beuzit, J.-L., Feldt, M., Dohlen, K., Mouillet, D., Pugeta, P., Wildi, F., Abee, L., Antichif, J., et al. 2008, Proc. SPIE, 701418
Borde, P. J., & Traub, W. A. 2006, ApJ, 638, 488 B

Borucki, B., Koch, D., Basri, G., Batalha, N., Brown, T., Caldwell, D., Caldwell, J., Christensen-Dalsgaard, J., et al. 2010, Science, 327, 977
Brandt, T., McElwain, M., Janson, M., Knapp, G., Mede, K., Limbach, M., Groff, T., Burrows, A., et al. 2014, Proc. SPIE, 9148-49
Buton, C., et al. 2012, A&A, 549A, 5 B
Carlotti, A., Kasdin, N. J., Martinache, F., Vanderbei, R. J., Young, E. J., Che, G., Groff, T. D., & Guyon, O. 2012, Proc. SPIE, 84463 C
Charbonneau, D., Brown, T. M., Noyes, R. W., & Gillilna, R. L. 2001, ApJ, 568, 377
Clergeon, C. 2014, Ph.D. dissertation
Close, L. M., Males, J. R., Morzinski, K., Kopon, D., Follette, K., Rodigas, T. J., Hinz, P., Wu, Y.-L., et al. 2013, ApJ, 774, 94 C
Codana, J. L., & Kenworthy, M. 2013, ApJ, 767, 100 C
Cvetojevic, N., Jovanovic, N., Betters, C., Lawrence, J. S., Ellis, S., Robertson, G., & Bland-Hawthorn, J. 2012, A&A, 544, L 1
Dekany, R., Roberts, J., Burruss, R., Antonin, T., Baranec, C., Guiwits, S., Hale, D., Angione, J., et al. 2013, ApJ, 776, 130 D
Esposito, S., Riccardi, A., Fini, L., Puglisi, A. T., Pinna, E., Xompero, M., Briguglio, R., Quirs-Pacheco, F., et al. 2010, Proc. SPIE, 7736-09 F
Esposito, S., Riccardi, A., Pinna, E., Puglisi, A., Quirs-Pacheco, F., Arcidiacono, C., Xompero, M., Briguglio, R., et al. 2011, Proc. SPIE, 8149-02 E
Garrel, V., Guyon, O., & Baudoz, P. 2012, PASP, 124, 861
Garrel, V. 2012, PhD dissertation
Give'on, A., Kern, B., Shaklan, S., Moody, D. C., & Pueyo, L. 2007, Proc. SPIE, 66910 A
Gozdziewski, K., & Migaszewski, C. 2014, MNRAS, 440, 3140
Grady, C. A., Muto, T., Hashimoto, J., Fukagawa, M., Currie, T., Biller, B., Thalmann, C., Sitko, M. L., et al. 2013, ApJ, 762, 48
Guyon, O. 2003, A&A, 404, 379
———. 2005, ApJ, 629, 592
Guyon, O., Martinache, F., Belikov, R., & Soummer, R. 2010, ApJS, 190, 220
Guyon, O., Pluzhnik, E., Martinache, F., Totems, J., Tanaka, S., Matsuo, T., Blain, C., & Belikov, R. 2010, PASP, 122, 71 G
Han, E., Wang, S., Wright, J. T., Feng, Y. K., Zhao, M., Fakhouri, O., Brown, J. I., & Hancock, C. 2014, PASP, 126, 827
Hardy, J. W. 1998, Adaptive Optics for Astronomical Telescopes (New York: Oxford University Press)
Helmbrecht, M. A., Min, H., Carl, K., & Marc, B. 2011, Proc. SPIE, 793108
Huby, E., Duchene, G., Marchis, F., Lacour, S., Perrin, G., Kotani, T., Choquet, E., Gates, E. L., et al. 2013, A&A, 560, A 113
Huby, E., Perrin, G., Marchis, F., Lacour, S., Kotani, T., Duchene, G., Choquet, E., Gates, E. L., et al. 2012, A&A, 541A, A 55
Ingraham, P., et al. 2014, ApJ, 794L, 15 I
Jovanovic, N., Guyon, O., Martinache, F., Clergeon, C., Singh, G., Kudo, T., Newman, K., Kuhn, J., et al. 2014a, Proc. SPIE, 9147-1 Q
Jovanovic, N., Guyon, O., Martinache, F., Schwab, C., & Cvetojevic, N. 2014b, Proc. SPIE, 9147, 9147-287
Kraus, A., & Ireland, M. J. 2012, ApJ, 745, 1
Lafreniere, D., Marois, C., Doyon, R., & Barman, T. 2009, ApJ, 694L, 148 L
Lagrange, A.-M., Gratadour, D., Chauvin, G., Fusco, T., Ehrenreich, D., Mouillet, D., Rousset, G., Rouan, D., et al. 2009, A&A, 493, 21 L
Lenzen, R., Hartung, M., Brandner, W., Finger, G., Hubin, N., Lacomber, F., Lagrange, A.-M., Lehnert, M., et al. 2003, Proc. SPIE, 4841-944 L
Leon-Saval, S. G., Argyros, A., & Bland-Hawthorn, J. 2013, Nanophotonics, 2, 429
Lord, S. D. 1992, NASA Technical Memorandum 103957
Lozi, J., Marinache, F., & Guyon, O. 2009, PASP, 121, 1232
Macintosh, B., et al. 2014, Proc. Natl. Acad. Sci., 111, 12661
Malbet, F., Yu, J. W., & Shao, M. 1995, PASP, 107, 386 M
Mariën, G., Jovanović, N., Cvetojević, N., Williams, R., Haynes, R., Lawrence, J., Parker, Q., & Withford, M. J. 2012, MNRAS, 421, 3641
Marois, C., Macintosh, B., Barman, T., Zuckerman, B., Song, I., Patience, J., Lafrenière, D., & Doyon, R. 2008, Science, 322, 1348 M
Martinache, F. 2013, PASP, 125, 422 M
Martinache, F., Guyon, O., Clergeon, C., & Blain, C. 2012, PASP, 124, 1288
Martinache, F., Guyon, O., Jovanovic, N., Clergeon, C., Singh, G., Kudo, T., Currie, T., Thalmann, C., et al. 2014a, Proc. SPIE, 9148, 914870
Martinache, F., Guyon, O., Jovanovic, N., Clergeon, C., Singh, G., Kudo, T., Currie, T., Thalmann, C., et al. 2014b, PASP, 126, 565
Mawet, D., Serabyn, E., Liewer, K., Burruss, R., Hickey, J., & Shemo, D. 2010, ApJ, 709, 53
Mawet, D., Serabyn, E., Liewer, K., Hanot, Ch., McEldowney, S., Shemo, D., & O'Brien, N. 2009, Opt. Exp., 17, 1902
Mayor, M., & Queloz, D. 1995, Nature, 378, 355
Mazin, B. A., Bumble, B., Meeker, S. R., O'Brien, K., McHugh, S., & Langman, E. 2012, Opt. Exp., 20, 1503
McElwain, M. W., Brandt, T. D., Janson, M., Knapp, G. R., Peters, M. A., Burrows, A. S., Carlotti, A., Carr, M. A., et al. 2012, Proc. SPIE, 84469 C
Minowa, Y., Hayano, Y., Oya, S., Watanabe, M., Hattori, M., Guyon, O., Egner, S., Saito, Y., et al. 2010, Proc. SPIE, 77363 N
Murakami, N., Nishikawa, J., Yokochi, K., Tamura, M., Baba, N., & Abe, L. 2010, ApJ, 714, 772
Murakami, N., Uemura, R., Baba, N., Nishikawa, J., Tamura, M., Hashimoto, N., & Abe, L. 2008, PASP, 120, 1112
Muto, T., Grady, C. A., Hashimoto, J., Fukagawa, M., Hornbeck, J. B., Sitko, M., Russell, R., Werren, C., et al. 2012, ApJ Lett., 748, L 22
Newman, K., Guyon, O., Balasubramanian, K., Belikov, R., Jovanovic, N., Martinache, F., & Wilson, D. 2015, PASP, 127, 437
Norris, B., Schworer, G., Tuthill, P., Jovanovic, N., Guyon, O., Stewart, P., & Martinache, F. 2015, MNRAS, 447, 2894 N
Norris, B., Tuthill, P. G., Ireland, M. J., Lacour, S., Zijlstra, A. A., Lykou, F., Evans, T. M., Stewart, P., et al. 2012a, Proc. SPIE, 844503 N
Norris, B., Tuthill, P. G., Ireland, M. J., Lacour, S., Zijlstra, A. A., Lykou, F., Evans, T. M., Stewart, P., et al. 2012b, Nature, 484, 220
Oppenheimer, B. R., Baranec, C., Beichman, C., Brenner, D., Burruss, R., Cady, E., Crepp, J. R., Dekany, R., et al. 2013, ApJ, 768, 24 O
Oshiyama, F., Murakami, N., Guyon, O., Martinache, F., Baba, N., Matsuo, T., Nishikawa, J., & Tamura, M. 2014, PASP, 126, 270
Pepe, F., Ehrenreich, D., & Meyer, M. R. 2014, Nature, 513, 358
Perrin, G., Lacour, S., Woillez, J., & Thiebaut, E. 2006, MNRAS, 373, 747 P

Peters, M. A., Groff, T., Kasdin, N. J., McElwain, M. W., Galvin, M., Carr, M. A., Lupton, R., Gunn, J. E., et al.2012, Proc. SPIE, 8446E, 7UP
Poyneer, L. A., De Rosa, R. J., Macintosh, B., Palmer, D. W., Perrin, M. D., Sadakuni, N., Savransky, D., Bauman, B., et al. 2014, Proc. SPIE, 9148E, 0KP
Rouan, D., Riaud, P., Boccaletti, A., Clenet, Y., & Labeyrie, A. 2000, PASP, 112, 1479
Serabyn, E., Mawet, D., & Burruss, R. 2010a, Nature, 464, 1018
Serabyn, E., Mennesson, B., Martin, S., Liewer, K., Mawet, D., Hanot, C., Loya, F., Colavita, M. M., et al. 2010b, Proc. SPIE, 77341 E
Shea, H. R., Gasparyan, A., Chan, H. B., Arney, S., Frahm, R. E., Lopez, D., Jin, S., & McConnell, P. 2004, Trans. on Dev. & Mat. Rel., 4, 198
Singh, G., Martinache, F., Baudoz, P., Guyon, O., Matsuo, T., Jovanovic, N., & Clergeon, C. 2014, PASP, 126, 586
Singh, G., Lozi, J., Guyon, O., Jovanovic, N., Baudoz, P., Martinache, F., Kudo, T., Serabyn, E., et al. 2015, PASP, 127, 857
Tamura, M. 2009, Proc. AIPC, 1158, 11 T
Tamura, M., Suto, H., Nishikawa, J., Kotani, T., Sato, B., Aoki, W., Usuda, T., Kurokawa, T., et al. 2012, Proc. SPIE, 84461 T
Tuthill, P., Monnier, J. D., Danchi, W. C., Wishnow, E. H., & Haniff, C. A. 2000, PASP, 112, 555
Tuthill, P., Lacour, S., Amico, P., Ireland, M., Norris, B., Stewart, P., Evans, T., Kraus, A., et al. 2010, Proc. SPIE, 7735, 1O–T
Wang, J. J., Rajan, A., Graham, J. R., Savransky, D., Ingraham, P. J., Ward-Duong, K., Patience, J., De Rosa, R. J., et al. 2014, Proc. SPIE, 9147, 15
Woillez, J. M., Perrin, G., Guerin, J., Lai, O., Reynaud, F., Wizinowich, P. L., Neyman, C. R., Le Mignant, D., et al. 2004, Proc. SPIE, 5491, 1425

SCExAO's current status

In *April 2015*, SCExAO has completed *Phase 1* of the project which was the on-sky correction of the low-order wavefront aberrations by the LLOWFS and low-speed speckle control on the post-AO188 wavefront residuals. With no additional ExAO loop, LLOWFS corrected low-order aberrations on the post-AO188 residuals and stabilized the starlight on the FPM. *Phase 1* provided a moderate contrast improvement over HiCIAO for NIR planet detection.

During upcoming on-sky observation in *July, September and October 2015*, we are going to address the *Phase 2* of the project which is to provide durable correction and a significant contrast improvement to HiCIAO, enhancing the SR to more than 90% via a faster, low latency and better tuned ExAO loop. We will achieve this result by combining our three control loops: LLOWFS + PyWFS+ Speckle nulling. This capability should lead us towards the NIR planet imaging at high contrast and visible light interferometry, polarimetry to detect circumstellar disks. We are also going to test SAPHIRA (Finger *et al.*, 2014), a NIR photon counting camera developed in collaboration with the Institute for Astronomy in Hilo, to enable high speed speckle control.

Phase 3 of the project is expected to begin in *2017* when HiCIAO will be replaced by – (1) MKIDs (Microwave Kinetic Inductance Detectors, Mazin *et al.*, 2013), which is a NIR/visible photon counting detector with wavelength resolution from 0.7 to 1.4 μm which will be delivered by the University of California, Santa Barbara in 2016 and – (2) CHARIS (Coronagraphic High Angular Resolution Imaging Spectrograph, Peters-Limbach *et al.*, 2013), a NIR integral field spectrograph from Princeton University. This will provide an opportunity to our instrument to obtain spectra within the wavelength range of 0.8 - 2.7 μm. We should be able to perform NIR spectroscopic characterization of the reflected light with high contrast ($\sim 10^{-8}$) at small angular separations.

3.4 LLOWFS elements on SCExAO

In this section and onwards, I will focus on my contribution to the SCExAO instrument which is the implementation of the LLOWFS on its IR bench. First of all, I will briefly revise the optical layout of the LLOWFS on SCExAO. The optomechanical design of the IR bench is shown in Fig. 3.7. From the right, the input light source can either be a calibrated fiber coupled laser diode (1550 nm) or the f/14 converging beam from AO188. The beam is collimated by an off-axis parabola ($f = 255\ mm$). This collimated 18 mm diameter beam meets the DM at a pupil plane conjugated with the primary mirror of the telescope. The beam reflected off the DM meets a mask mimicking the shape of the Subaru pupil, which I designed and presented in Fig. 2.9 (2) of §2.5. The mask sits permanently in the beam so that the response matrices for the PyWFS and the LLOWFS obtained in the laboratory can be reused during the on-sky loop closure. The dichroic which is located after the pupil mask separates IR beam (940 -2500 nm) from the visible (640 -940 nm). The procedure to align the IR bench is described in §3.5.1.

The transmitted IR beam then meets the PIAA optics mounted in a wheel that can be moved in or out to apodize the beam. At the focal plane is located a wheel that can select several PMCs (§3.4.3) such as the VVC, the FQPM and the EOPM coronagraphs.

This wheel can be adjusted in x, y and z directions to finely align the FPMs remotely via motorized actuators. For all the vertical (y) actuators on SCExAO, a movement of 20,000 steps of the motor corresponds to 1 mm whereas for horizontal (x) and focus (z) actuators, 1 mm distance is covered by moving the motor 10,000 steps.

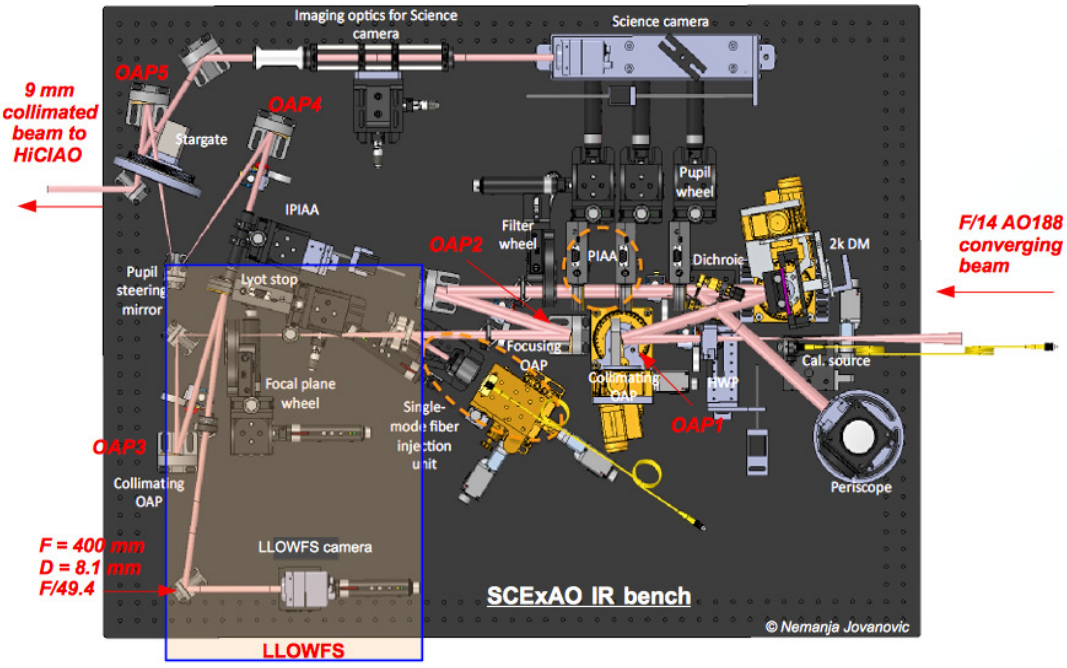

Figure 3.7: The optomechanical layout of the LLOWFS on the IR bench of SCExAO. The LLOWFS optical path is highlighted with a blue box.

The phase masks at the focal plane diffracts the starlight outside of the geometrical pupil. An OAP sitting in the beam downstream the FPMs wheel, recollimates this residual starlight to a 9 mm diameter beam ($f = 255\ mm$). Further in a downstream reimaged pupil plane, the collimated beam encounters a pupil wheel, which sits at an angle of 6°. This wheel consists of the RLSs (§3.4.2) corresponding to each FPMs at the focal plane. The RLS at the pupil plane does not just block the diffracted starlight, it actually reflects it towards a lens ($f = 400\ mm$) that focuses the starlight onto the LLOWFS camera (highlighted at the bottom of the bench in Fig. 3.7), which sits at a defocused position.

However, the light transmitted by the RLS meet the inverse PIAA lenses, which are also mounted on a stage allowing a motorized control of the lateral positioning and are conjugated to the PIAA lenses upstream. The pupil plane of PIAA is ≈ 60 mm behind the RLSs pupil wheel. These pair of inverse PIAA lenses can also be retracted from the beam entirely when not in use. The nulled coronagraphic PSF is directed towards two different NIR imaging optics via a selection of beamsplitters that can select the spectral content and the amount of flux between the two optical paths. One relayed optical path is towards the high frame rate internal NIR imaging camera and another one is towards HiCIAO.

The LLOWFS camera and the internal NIR imaging camera are InGaAs CMOS detectors with a resolution of 320×256 pixels, a frame rate of up to 170 Hz and a read out noise of 140 e^-. The internal NIR camera is actually mounted on a translation stage, which allows it to be conjugated to any location between the focal and pupil planes. This feature

is actually very helpful in going back and forth from pupil to focal plane and vice versa while aligning the FPMs remotely.

3.4.1 Deformable Mirror

SCExAO uses a 2k-actuator DM from *Boston MicroMachine (BMC)*. It has a square array of 50×50 actuators, however 500 actuators in the corners are not connected. It has a stroke of 1.2 μm and can run at several kHz. There are 5 dead actuators. Fortunately, two are outside of the pupil, one is behind the central obscuration and we aligned the spiders so that one of the remaining two is partially masked. SO we have only one and a half dead actuator in the FOV. SCExAO is the only instrument using this model of MEMS from BMC. The complete characterization of the DM and the technique adapted for humidity control is presented in *Pub.* §3.1.1 and §6.3.

3.4.2 Reflective Lyot Stops

The first batch of RLSs designed for the FQPM are presented in *Pub.* Fig. 9(b), they had a manufacturing error where the angle of the spider arms were off by 10°. The second batch of RLSs for the VVC, the FQPM and the PIAA coronagraphs (are presented in Figs. 3.8, 3.9, 3.10 respectively), I designed them in SolidWorks and created the *DXF (Drawing eXchange Format)* file, which is an extension for graphic image format typically used with AutoCAD (Computer Assisted Drafting) software. With these files, the manufacturer deposited the masks directly on the glass. The masks are actually made by lithographing a layer of chrome on a fused silica disk of 1.5-mm thickness. The chrome, corresponding to the reflective surface in the manufactured RLSs (Figs. 3.8, 3.9, 3.10) has a reflectivity of only 60% in NIR while the rest of the light is being absorbed.

I have designed two sets of reflective Lyot masks for each coronagraph. One set is a simple oversized mask and another set has two extra discs (also reflective) inside the geometrical pupil to mask the diffraction due to two dead actuators. For the majority of my tests, I use the RLSs that does not masks the dead actuators as the transmitted signal is not much affected by their scattering of the starlight.

I present the size of the RLSs for the VVC, the FQPM and the PIAA coronagraphs adapted on SCExAO in table 3.1. The undersize/oversize factor is with respect to the outer diameter, the central obscuration and the spider arms of the Subaru pupil mask. All these RLSs have an outer most reflective annulus of diameter 25.4 mm. I have also taken in to account an extra 2% undersize/oversize factor (included in the values presented in table 3.1) to be less sensitive to pupil alignment errors.

Figure 3.11 presents the reflective profile of the chrome layer coating on the RLSs, measured with a spectrophotometer between 0.5 - 2.5 μm. The chrome is only $\sim$ 60% reflective around 1.6 μm and is chosen over aluminum, silver or gold coating due to cost constraints. We are planning to have AR coated aluminum/gold material RLSs to reduce flux losses in the LLOWFS and the science channels for future upgrade.

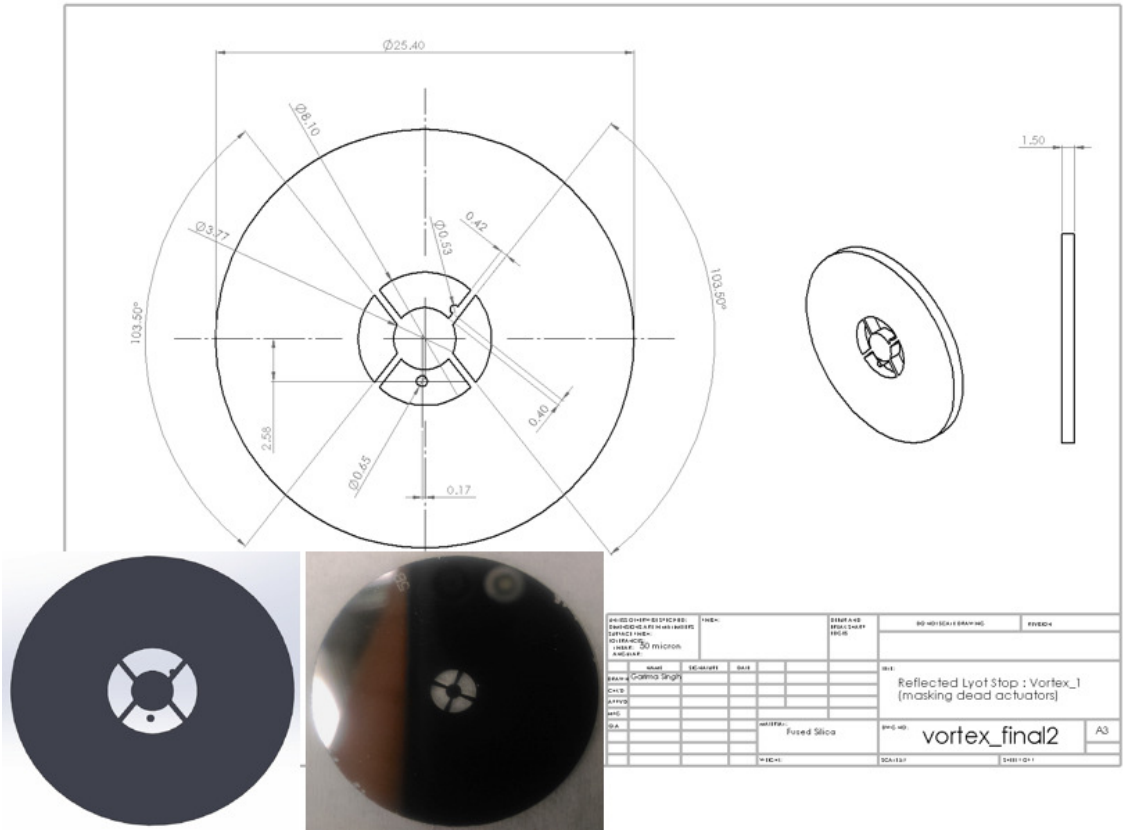

Figure 3.8: Reflective Lyot stop designed and manufactured for a VVC installed on SCExAO.

Table 3.1: Sizes of the RLSs for different coronagraphs on SCExAO

Pupil	VVC	FQPM	PIAA
	(%)	(%)	(%)
Outer diameter, D_L (undersize)	9	9	12
Central Obscuration (oversize)	42	32	37
Spider Arms (oversize)	60	65	50

The throughputs[7] of clear glass (first row) and chrome layer (second row) of the RLSs in y, J and H band are compared in Fig. 3.12. The flux in the focal plane images are compared through both regions, using a 10-pix diameter circular mask around the PSF to remove noisy pixels. The internal NIR science camera is used to acquire these images by adjusting the exposure time to optimize the SNR for the PSF through glass and through chrome. The transmission of the starlight through the chrome layer is negligible as compared to the transparent region. Table 3.2 present the throughput and the optical density (OD) of the chrome layer. OD is another definition of the transmission of optical material, usually optical densities (transmission = 10^{-OD}).

[7]This analysis has been done with the help from a SCExAO member, Julien Lozi.

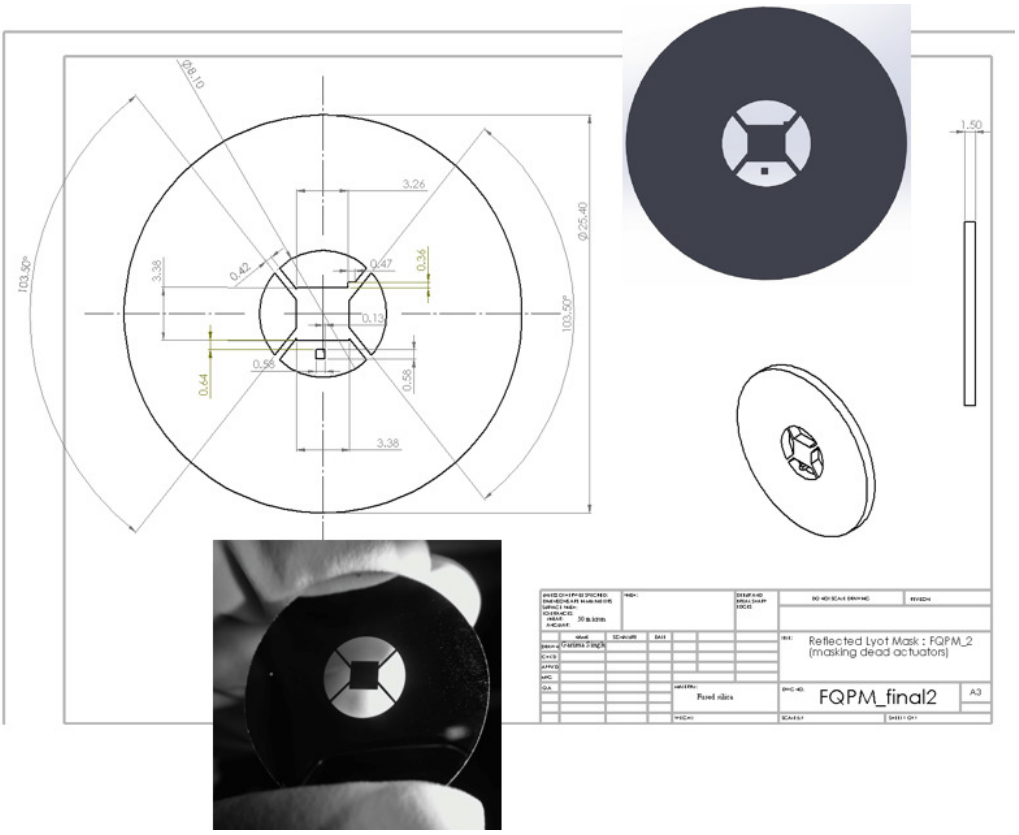

Figure 3.9: Reflective Lyot stop designed and manufactured for a FQPM coronagraph installed on SCExAO.

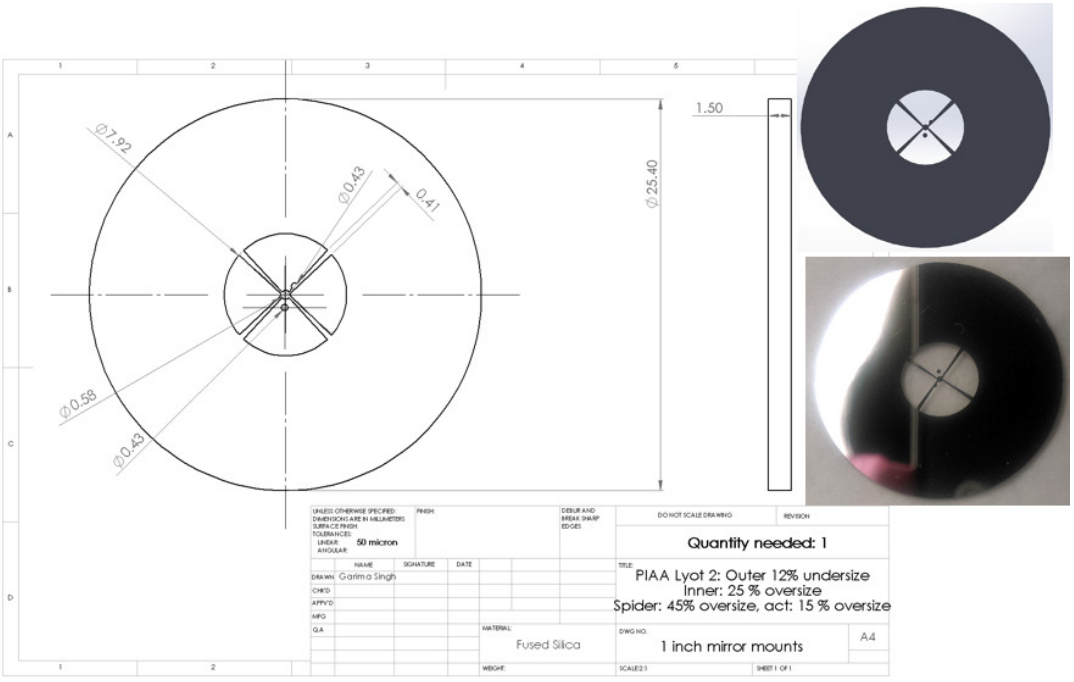

Figure 3.10: Reflective Lyot stop designed and manufactured for a PIAA coronagraph installed on SCExAO.

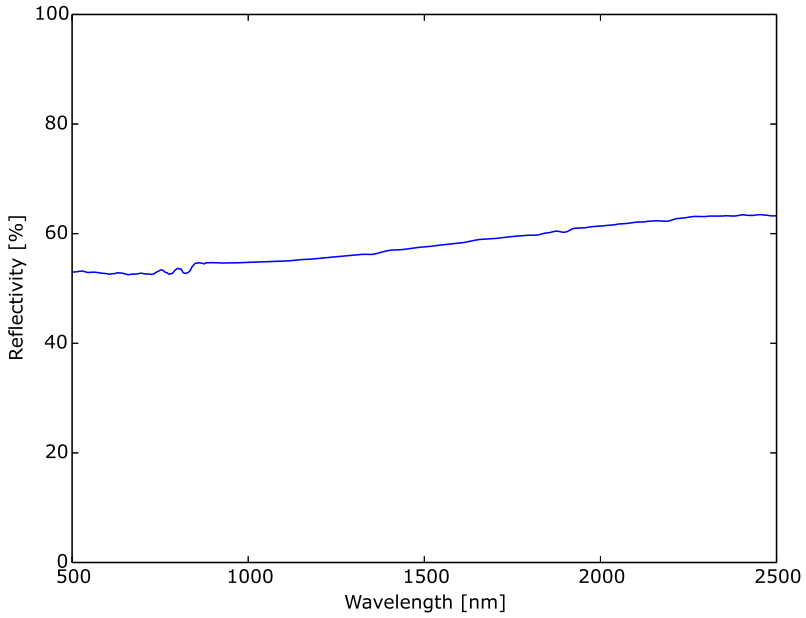

Figure 3.11: Reflectivity of the chrome layer of the RLSs, measured with the spectrometer.

Table 3.2: Throughput and optical density of the chrome layer on the RLS through three different filters.

Filter	Chrome coating on RLS	
	Throughput (%)	Optical density
Y	0.0089	4.09
J	0.022	3.66
H	0.038	3.42

The throughput of the glass substrate on which these masks are digitized is also measured through the spectrophotometer between 0.5 and 2.5 μm, and shown in Fig. 3.13. The throughput is coherent with a 4% loss per surface, with a transmission of about 93% in average. The throughput of an off-axis source reduced by the geometry of the RLSs for different coronagraphs is obtained by dividing the total flux through the RLS by the transmission of the glass. Top row of Fig. 3.14 shows pupil images with the Subaru pupil mask only (reference), middle and bottom rows present the pupils through the RLSs of the VVC and the FQPM coronagraphs. Note that the RLS studied here for the FQPM have a disk masking the dead actuator, but my design had a defect, the manufactured RLS was the mirror copy of what it should have been. I considered the front face of the design as reflective and facing the incoming beam, however the manufactured RLS was done considering the opposite. Table 3.3 summarizes the throughput measurements. The transmission of the glass (only the clear region of the RLS) is ~ 91% (Fig. 3.13) while the total throughput in presence of the RLS is about 63% in H band (geometric throughput of

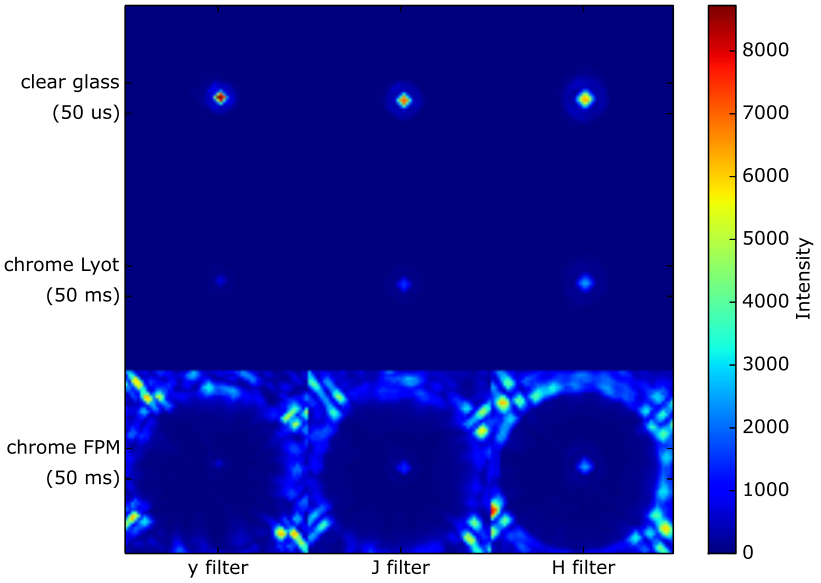

Figure 3.12: The first row of images present PSFs through clear glass of the RLS (exposure time 50 μs) in three different bands. The second row shows PSFs through the chrome coated region of the RLS (exposure time 50 ms) and the bottom row is the chrome coated amplitude FPM (§3.4.3). The middle row shows negligible transmission through the chrome layer comparatively to the clear region of the RLS.

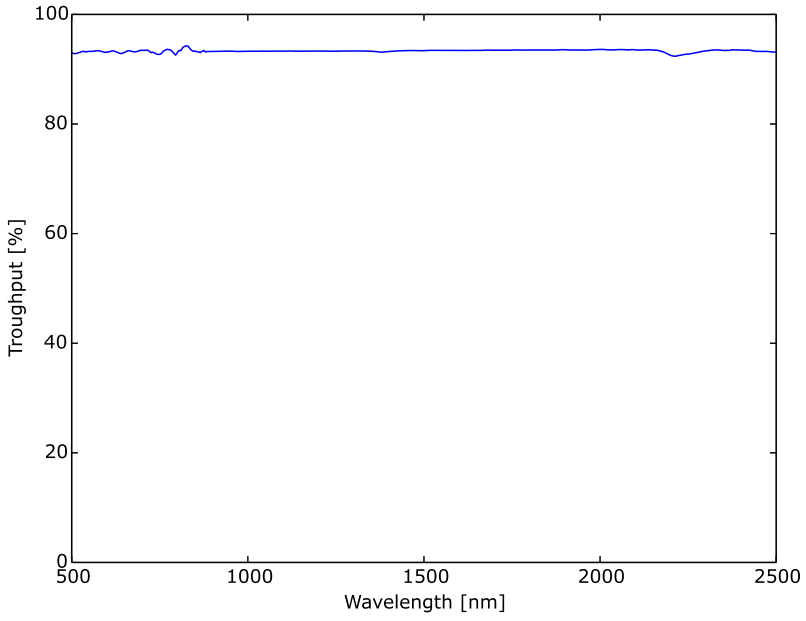

Figure 3.13: Throughput of the glass substrates used for manufacturing the RLSs.

~ 70%).

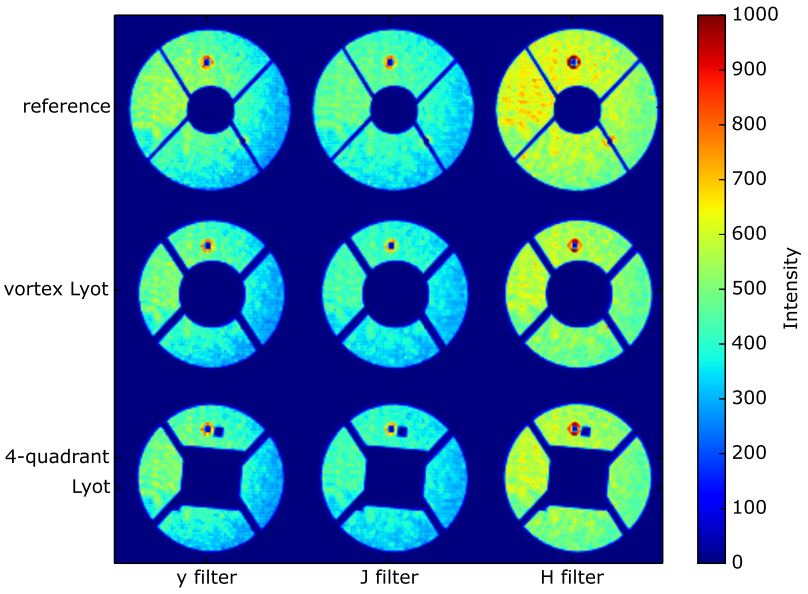

Figure 3.14: Pupil images for the VVC and the FQPM coronagraphs, comparing throughput reduced by the geometry of their corresponding RLSs through three different filters. My design of RLS for the FQPM had a design flaw where the position of the disk to mask one of the dead actuator is a bit off.

Table 3.3: Throughput of the RLSs for the VVC and the FQPM coronagraphs through three different filters.

Filter	VVC			FQPM		
	Glass Substrate (%)	RLS geometry(%)	total (%)	Glass Substrate (%)	RLS geometry(%)	total (%)
y	92.0	70.1	64.5	91.8	69.9	64.2
J	91.0	69.8	63.5	90.3	69.6	62.8
H	90.8	69.9	63.2	91.1	69.4	63.2

The transmission of the RLS for the PIAA coronagraph is shown separately in Fig. 3.15 as it first requires to align the PIAA optics and its apodizer with a binary FPM (§3.4.3). The PIAA optics with an apodizer upstream of the FPM condenses the starlight mostly at the center in a Gaussian-like shape as can be seen in the remapped pupil plane shown in middle row of Fig. 3.15. So the shape of the central obscuration of a RLS plays an important role in the throughput measurement as most of the light is concentrated at the center of the pupil. The loss in throughput due to the geometry of the RLS (bottom row of Fig. 3.15) downstream the binary mask is measured by dividing the total throughput through the RLS by the transmission of the glass in the remapped PIAA pupil plane. Table 3.4 summarizes the throughput.

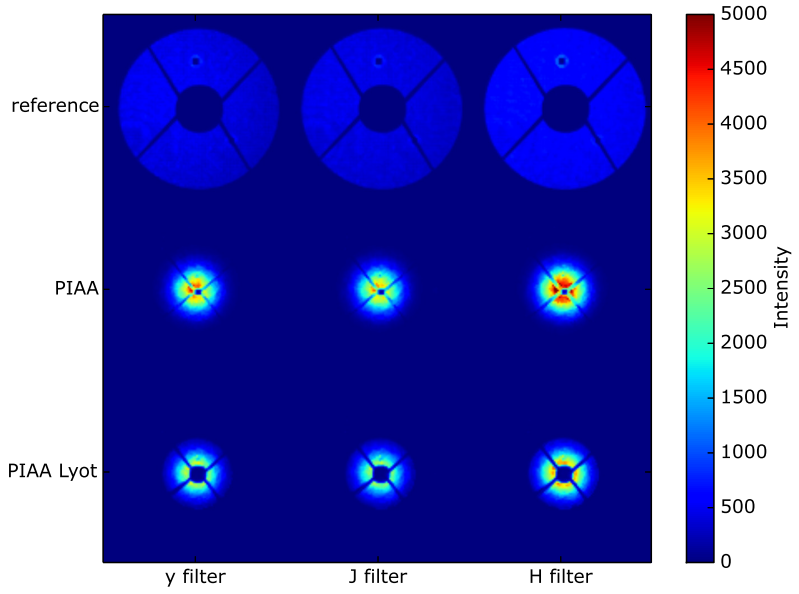

Figure 3.15: Pupil images through the PIAA lenses (middle row) and the PIAA RLS (bottom row). Throughput is studied for three different filters.

Table 3.4: Throughput of the PIAA optics and its RLS through three different filters.

Filter	PIAA optics	PIAA RLS		
	(%)	Glass Substrate (%)	RLS geometry (%)	total (%)
y	59.2	91.0	78.9	71.8
J	58.1	91.0	79.2	72.1
H	58.1	90.0	80.1	72.1

The flux is reduced significantly by the PIAA optics and its apodizer in the beam (throughput < 60%). The central obscuration of the PIAA's RLS is not aggressive in this design, hence the transmission of an off-axis source due to its geometry is 79%, which is a bit higher than the RLS of VVC and FQPM as presented in table 3.3.

The geometry of these RLSs are actually not carefully optimized to prevent loss in throughput of the coronagraphs on SCExAO. My main focus was to optimize it for LLOWFS purpose. However, these three years of my experience with the LLOWFS on SCExAO has allowed us to gain understanding in coronagraph optimization without loss in the LLOWFS performance for future upgrades.

3.4.3 Focal plane masks

For SCExAO, the PIAA coronagraph is the heart of the instrument since 2006. However, in 2013, several small IWA phase mask coronagraphs were also installed on the instrument: the FQPM in collaboration with *Pierre Baudoz* at *LESIA, Observatoire de Paris*, the EOPM in collaboration with *Naoshi Murakami* at *Hokkaido University, Japan* and the VVC with *Eugene Serabyn* at *Jet Propulsion Laboratory*. The VVC on SCExAO is a rotating half-waveplate structure that has a vectorial phase spiral described in Mawet *et al.* (2009b). There is a 25 μm diameter opaque metallic spot deposited at the center to mask the central defect. The presence of these coronagraphs on SCExAO has given me the opportunity to test LLOWFS concept for different small IWA coronagraphs on the same platform under the same environmental conditions.

3.4.3.1 LLOWFS compatibility with amplitude FPMs

Previously, SCExAO was using the CLOWFS technique to deal with the low-order wavefront aberrations for the PIAA technology before the installation of these PMCs. As CLOWFS can not address low-order aberrations for the PMCs, we changed the hardware and implemented the LLOWFS, which is more diverse than the CLOWFS in terms of providing correction not only to the PMCs but to amplitude apodized coronagraphs as well.

To make the LLOWFS compatible with the PIAA coronagraph, the size of the amplitude mask used at the focal plane plays an important role. An amplitude mask bigger than the PSF core blocks most of the starlight and diffracts only a small fraction of it in the reimaged pupil plane. The LLOWFS, in that case, will not get enough starlight photons, hence will not provide an optimal solution.

A way to make the LLOWFS efficient with the amplitude masks is to use a conic-shaped FPM that diffracts the starlight in a ring around the pupil in the Lyot plane. Such a mask should theoretically provide an optimal number of photons for the LLOWFS independently of the size of the mask. Newman *et al.* (2015a) has manufactured an achromatic FPM which is a substitute for a conventional hard-edge opaque mask. The effective size of the mask scales with wavelength to match the size of the stellar PSF. An isometric view of profilometry of such a mask is shown in Fig. 3.16 (a). The pattern of a set of achromatic FPMs for different IWA (diameter in λ/D) developed for the PIAA on SCExAO is shown in Fig. 3.16 (b). These images were obtained off-sky on SCExAO, under the illumination of the sodium lamp of AO188. The masks are etched into a silicon wafer and consists of a central cone-shaped structure surrounded by an azimuthally periodic binary pattern. FPM 4 has a manufacturing defect.

The cone of such kind of a FPM is designed to reject all the starlight and diffract it outside the pupil. The angle of the cone determines the radial position of the diffracted light in the RLS plane. A shallow angle moves the starlight closer to the edge of the geometrical pupil whereas a steeper angle moves the starlight farther out. Therefore, how closer or farther a FPM diffracts the starlight outside of the geometrical pupil defines the sensing capability of the LLOWFS. If the starlight is diffracted far out of the collecting optics (reflective zone) of a RLS, then there will not be much starlight available for sensing.

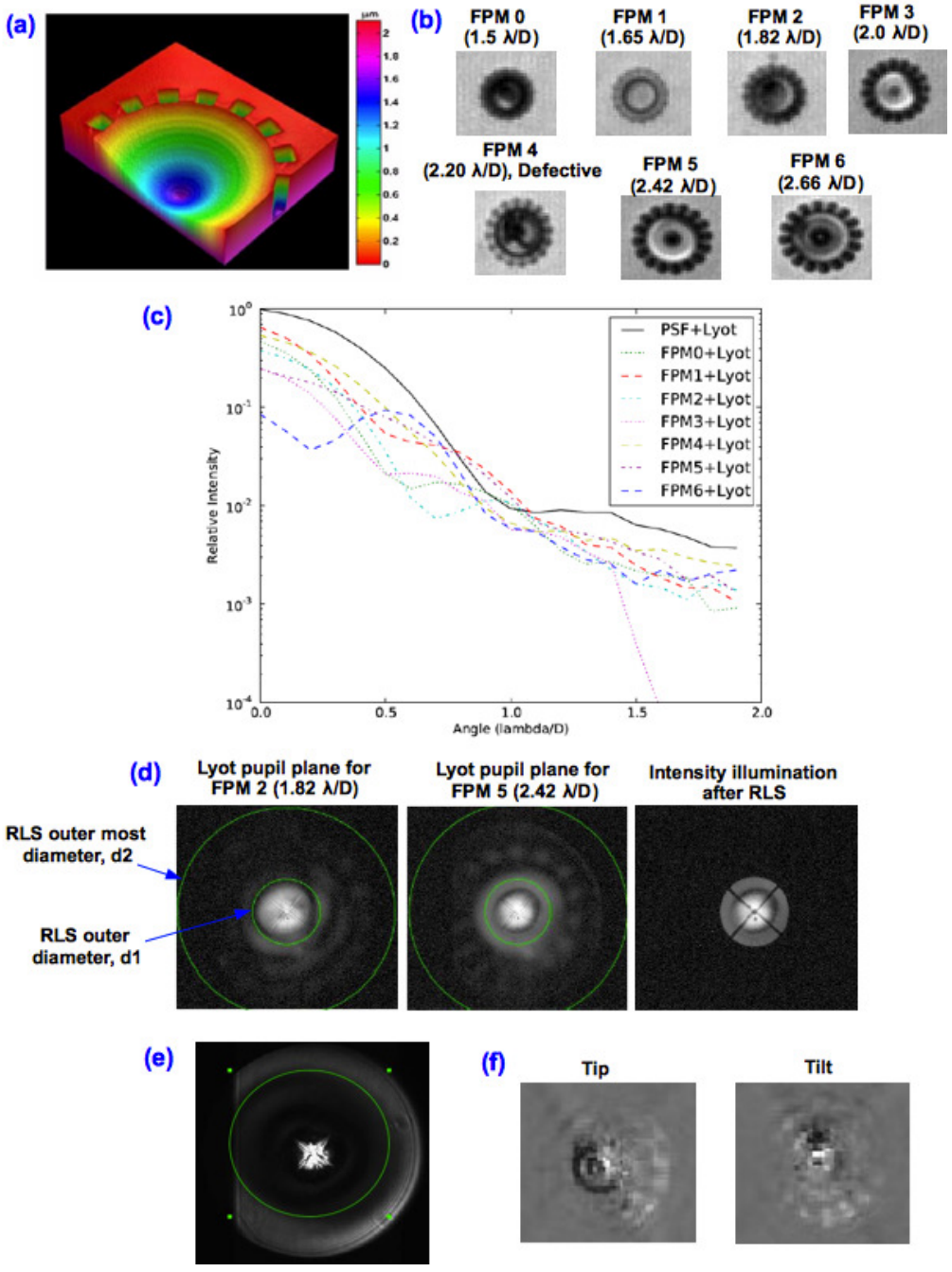

Figure 3.16: Performance of the achromatic focal plane masks designed for the PIAA coronagraph. a) Isometric view of mask profilometry (Newman *et al.*, 2015a). b) Achromatic FPMs geometry illumination under the sodium lamp of AO188. c) Radial average azimuthal profile of the PSF obtained with PIAA + different FPMs (in (b)) and corresponding RLS in the beam. d) An example of a FPM that diffracts most of the starlight inside the geometrical pupil, which severely affects the throughput of an off-axis source. e) An example of a FPM which diffracts the starlight far out of the reflective annulus of a RLS does not provide enough photons for low-order sensing. f) Unoptimized FPM like in (d) affects the response matrix of the modes as well. The signal tends to be noisier.

I tested two sets of achromatic FPMs for PIAA on SCExAO *(in July 2013 and September 2014)*. Unfortunately, both sets had large manufacturing defects. The reasons are not completely understood yet as this kind of technology is new and not entirely explored. The masks shown in Fig. 3.16 (b) were not optimized and leaked most of the starlight inside the geometrical pupil. For the PIAA coronagraph, the radial azimuthal profile of the PSFs through each of these FPM downstream PIAA RLS is shown in Fig. 3.16 (c). The contrast is very poor for each of these masks because a large part of the starlight still falls on the internal science NIR detector. Fig. 3.16 (d) present the intensity illumination at the Lyot plane downstream FPM 2 (first image) and FPM 5 (middle image) without a RLS. The inner circle in green is the outer diameter of the RLS whereas the outer green circle outlines the outermost reflective diameter of the RLS. It is visible that the cone of the angle is too shallow and most of the starlight is diffracted inside the pupil. There is still some starlight diffracted due to the teeth pattern of the FPM5 but its not sufficient for optimal LLOWFS performance.

A second set of FPM in Fig. 3.16 (e) diffracts the starlight outside of the reflective zone of the RLS. In this case, there was no light to reflect towards the low-order sensor. The green circle is highlighting the outermost reflective diameter of the RLS. Unoptimized FPMs not only affects the rejection capability of a coronagraph but also prevent optimal low-order sensing. The quality of the response matrix shown in Fig. 3.16 (f) obtained with a signal through the FPM 5 in Fig. 3.16 (d) is also affected, which means that the tip-tilt and other low-order aberration signals during calibration will be noisier and a bad signal like this can induce cross coupling in the calibration frames.

To test the LLOWFS with the PIAA coronagraph, we installed *in April 2015* a set of chrome coated amplitude FPM with diameters from 1.5 to 6 λ/D diameter (170 to 690 μm at 1.6 μm. The transmission profile of the chrome layer on these mask is same as described in Tab. 3.2.

3.4.3.2 Throughput of coronagraphs on SCExAO

The signal from an off-axis source through different FPMs on SCExAO is mimicked by misaligning the PSF upstream of the FPMs. The throughput in that case is measured by the ratio of flux in the pupil plane with and without the FPM. Figure 3.17 shows the pupil illumination without a FPM in first row of images through different filters y, J and H. Then four different FPMs are analyzed: the VVC, the FQPM, the EOPM and the amplitude mask (array of opaque disks for the PIAA) in a sequential order from top to bottom in Fig. 3.17. For an EOPM, there is some diffraction pattern visible in the pupil plane. Due to the geometry of the EOPM, it was difficult to have an off-axis PSF passing though only one octant of the mask, especially in H-band where the PSF is larger than at y or J band. So an off-axis signal for an EOPM is falling between the octant geometry of the mask, which diffracts the light around the edge of the spider arms.

Except for the vortex FPM, all the other FPMs have a similar high throughput in all bands. The vortex FPM, optimized for the H-band, has a poor transmission ($< 20\%$) at shorter wavelengths. Table 3.5 resumes the measured FPM transmissions through the different filters. The FQPM does not have an AR coating, hence it has a throughput of about 89% in three bands whereas for the AR coated EOPM, the transmission in J- and H-band

is 96 and 99% respectively. For the amplitude FPM, which does not have an AR coating either, its throughout is about 92.5% in all the bands, which is coherent with a 4% loss per surface.

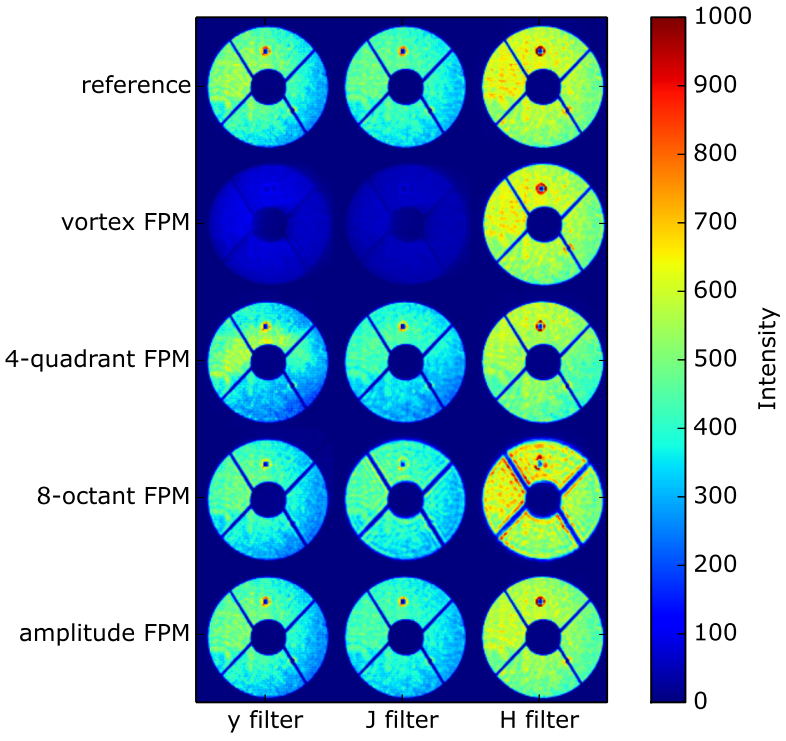

Figure 3.17: Pupil images downstream of different FPMs on SCExAO. The PSF is misaligned upstream of a FPM to mimic the signal from an off-axis source in order to analyze its throughput through 3 different filters for three different coronagraphs.

Table 3.5: Focal plane mask throughputs on SCExAO, through 3 different filters.

Filter	VVC	FQPM	EOPM	Amplitude FPM
	(%)	(%)	(%)	(%)
y	17.2	89.3	88.7	92.5
J	13.0	89.0	95.9	92.3
H	98.9	89.7	99.3	92.5

3.4.4 LLOWFS camera

For low-order wavefront sensing purposes, *Axiom Optics's (OWL SW1.7HS)* InGaAs CMOS detector[8] is chosen. As sensing is performed in a defocus plane, the PSF is sampled with more pixels than at the focus. A lens with a 400-mm focal length is selected (Fig. 3.7) to be more than Nyquist sampled in the focal plane, the pixel size being 30 μm.

$$Sampling = \frac{\lambda\,(f/D)}{camera\ pixel\ pitch} = \frac{1.6\,\mu m\ \times\ 400\,mm}{30\,\mu m \times 8\,m} = 2.6\ pixels \qquad (3.1)$$

This sensor has a detector size of 320×256 pixels and runs at a speed of 170 Hz. Figure 3.18 shows (a) the specifications of the LLOWFS camera and (b) the camera itself on the IR bench. I have reused the code written in *C language* for a previous CLOWFS camera (Xenics, 100 Hz) and upgraded the interface with low-level programming to obtain the images from the camera for the sensing purpose.

(a)

Sensor Type	InGaAs PIN-Photodiode
Camera Setup/control	CameraLink
Active pixel	320 x 256
Pixel Pitch	30 x 30 μm
Spectral response	0.4 – 1.7 μm
Read out noise (RMS)	140 electrons
Quantum efficiency	> 70% @ 1.5 μm
Exposure time	500 *ns* to more than 500 *ms*
Dynamic range	14 bit
Power supply	12V DC ± 10%
Frame rate	170 Hz
Operating temperature	-20°C to + 55°C
Dimensions	50 x 50 x 78.5 *mm*
Weight (no lens)	275g
Cost	USD 27650.00

(b)

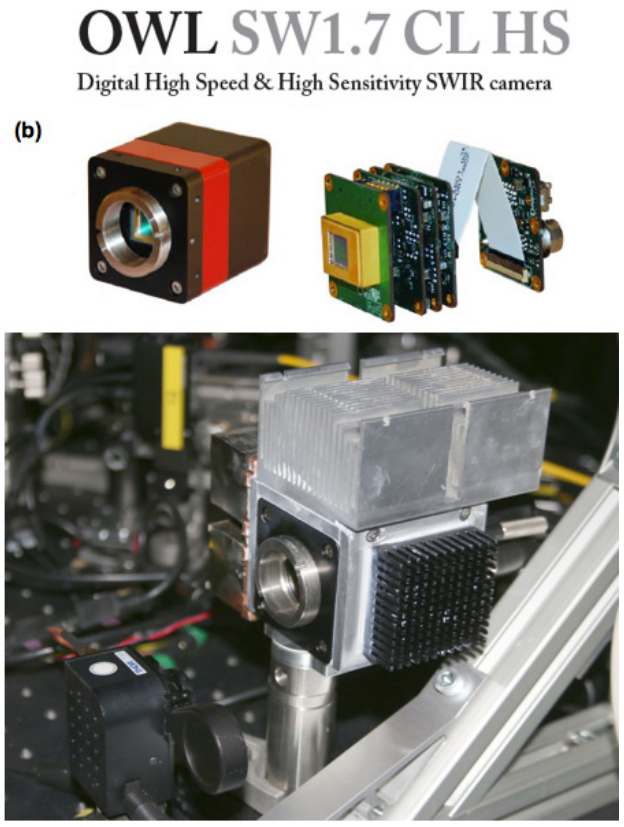

Figure 3.18: Specifications of the LLOWFS camera on SCExAO instrument.

Figure 3.19 presents a noise analysis I performed on the LLOWFS camera. To perform this analysis, I put some flux on the camera and recorded sets of images at different exposure times. Then for each pixel, I analyzed the average flux and the variance in the counts and the result are plotted in this figure.

[8]The exact same detector is used as our internal science NIR camera as well.

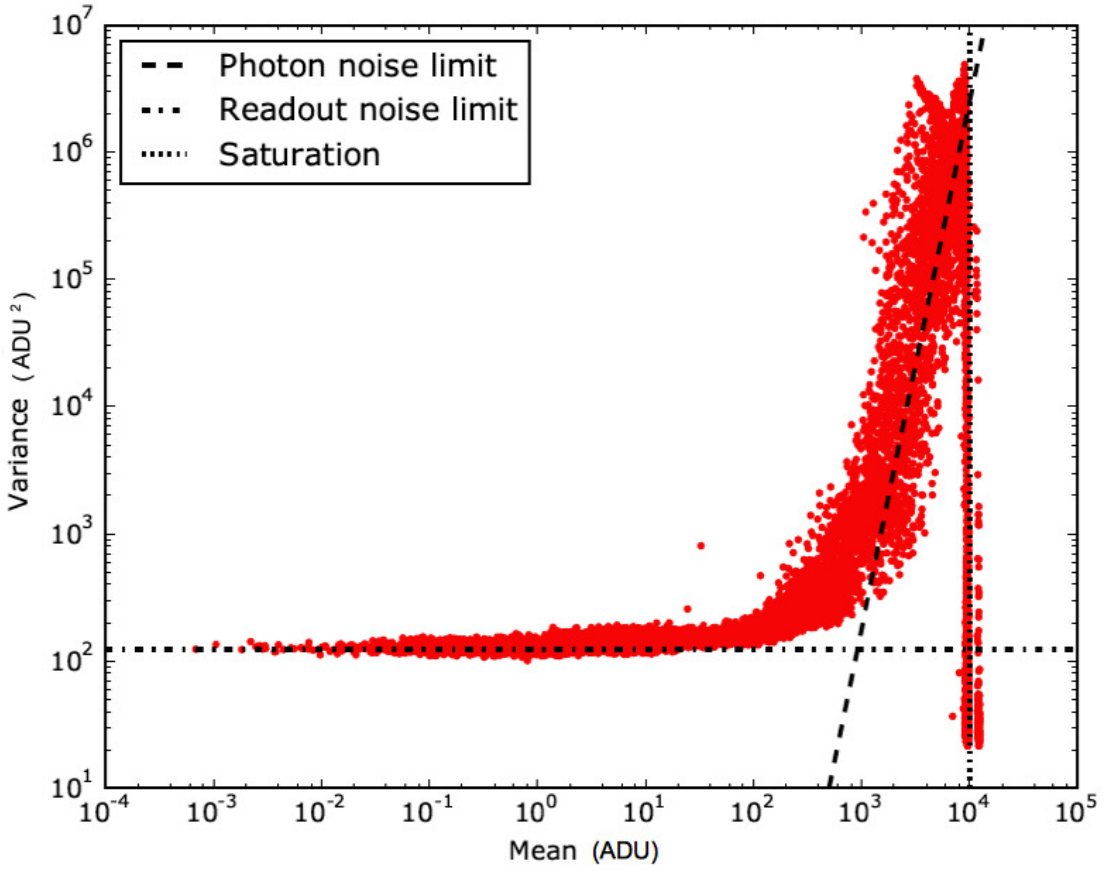

Figure 3.19: Noise characterization of the LLOWFS camera.

Three states are visible. For low counts, the variance is constant and corresponds to the readout noise limit. For higher counts, the variance is linear with the averaged counts, indicating the photon noise limit. Finally, the saturation is observed at around 10^4 counts.

3.5 Alignment procedures

3.5.1 Aligning the IR bench

When SCExAO is placed between the AO188 and the HiCIAO, then for off-sky testings, SCExAO is aligned with the internal calibration source (at 1.5 μm) of the AO188. When the converging beam from AO188 enter the SCExAO IR bench, then the stages of OAP1, the off-axis parabola direct collimates the beam and conjugate the pupil on the DM, as well as the DM itself are moved in pitch and yaw directions remotely until the PSF and the pupil falls on their respective hotspot on the internal NIR science camera. However, note that the internal source of AO188 shifts the focus of its output beam, which is actually compensated by applying a defocus phasemap on the DM of the AO188. As long as the beam is collimated inside the AO188, the collimation inside SCExAO does not have to be tweaked. During on-sky observations, the focus offset is pre-calibrated for different instruments downstream AO188.

During SCExAO observations, only the cryogenic dewar of HiCIAO is used without the Fore optics. To align SCExAO with HiCIAO, first the HiCIAO instrument is moved laterally and vertically to align the pupil with the collimated beam coming out of the SCExAO. Once the pupil is aligned, then the PSF on the hotspot of the HiCIAO camera is aligned by manually tip-tilting a mirror before the science camera (Fig. 3.7) until the PSF is aligned with the optical axis of HiCIAO.

3.5.2 Aligning the FPMs and RLSs

The PIAA/Inverse PIAA optics, the FPMs and the RLSs are aligned remotely by moving their respective motorized wheels driven by stepper motors[9]. Figure 3.20 shows the pupil and focal plane wheels on SCExAO. The fine alignment of the coronagraphs is done by moving these wheels in x, y and z direction remotely and checking the focal and pupil plane images by moving the stage of the internal science camera back and forth. This feature is very helpful to align precisely the on-axis source at the center of the FPMs.

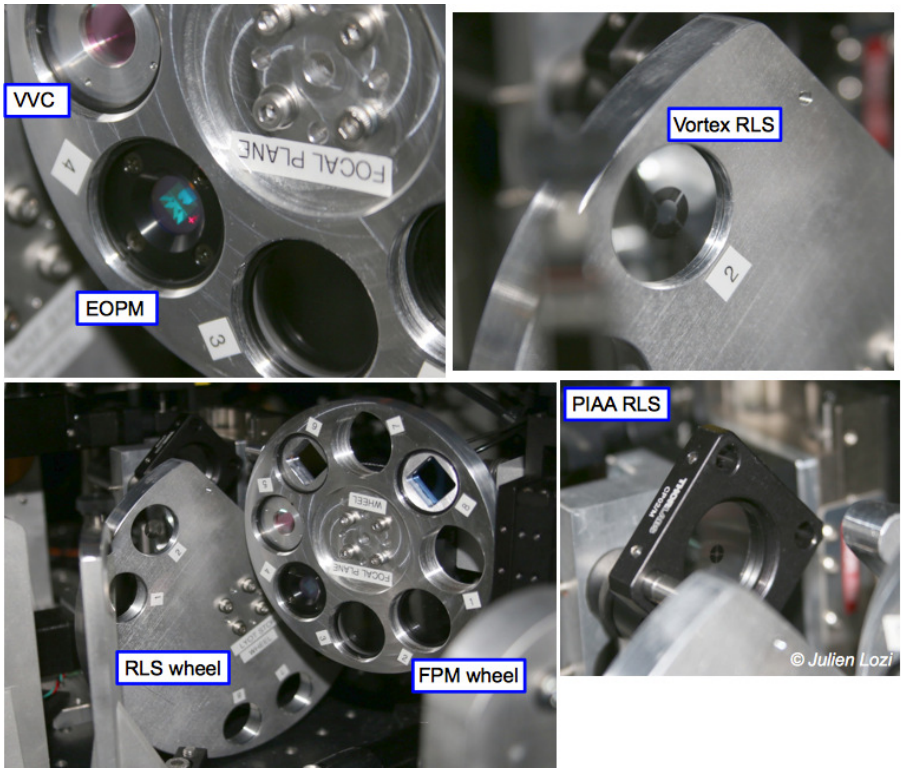

Figure 3.20: FPM and RLS wheel on SCExAO.

Before aligning any FPM on SCExAO, it is crucial to align the PSF on the hotspot of the camera. This is done by moving the DM stage in a closed-loop fashion to align the beam with the optical axis. This step takes few seconds as it also takes into account the backlash of the actuators that moves the DM stage. Once the PSF (Fig. 3.21 (b)(i)) is aligned, the next step is to move the corresponding FPM slot in the wheel.

[9]The interface of communicating with the wheels remotely is written in Python by Frantz Martinache.

To align the VVC:

- I move our internal science camera to the pupil plane to grossly find the vortex by moving the actuators of the FPM wheel in x and y to search for shadowing stripes. Then, I move back to the focal plane to roughly align the mask to get an image-plane "doughnut". I refine x and y positions at the focal plane to optimize the symmetry of the doughnut (Fig. 3.21 (a)(i)).

- I move back to the pupil plane to adjust the focus stepwise until the pupil is evenly dark and most of the light is ejected out of it. I optimize the alignment by moving the focus by + z and - z to check if they are similarly worse. I check for the gradient of light inside the pupil and finely tune the position in x, y and z till I notice a symmetric leak around the secondary and the outer edge of the pupil (Fig. 3.21 (a)(iv)).

  A deliberate misalignment in y direction of the vortex at the focal plane and the pupil plane is shown in Fig. 1.28 (b) and (c) respectively. The pupil image is not completely dark inside and there is an intensity ramp visible on the right edge of the pupil. In this case the misalignment is visible. However, for small misalignment errors, the second Airy ring in Fig. 1.28 (b) might look symmetric, giving a misleading impression that the vortex is aligned. It is tricky to obtain the reference (Fig. 1.28 (a)) during on-sky operations. The aligned vortex is of "doughnut" shape without the Lyot stop whereas with a RLS, the pattern at the center is square, which is obtained with very fine movements of the actuators.

- To align the Lyot stop, I move the RLS pupil wheel and aligns the corresponding slot which contains the RLS of the VVC with the pupil illumination shown in Fig. 3.21 (a)(iv) by moving the pupil wheel in x and y direction.

  The angle of the RLSs in each slot of the wheel were carefully aligned with the Subaru pupil mask when they were placed inside the wheel. Small alignment errors are generally masked by the oversized Lyot stops. In case, if a RLS is off in rotation then the wheel is moved by a few degrees to align the illuminated central obscuration and spider arms of the geometrical pupil behind the RLS geometry. The alignment of the RLS takes less than a minute.

  Figure 3.21 (a)(ii) shows the PSF with the RLS (no FPM) and Fig. 3.21 (a)(iii) shows the final coronagraphic PSF of the VVC with the vortex and Lyot stop in the beam. All the focal plane images shown in Fig. 3.21 (a) are of same brightness scale.

Note: The FPMs and RLSs wheels are very stable. Once the fine alignment is done, the actuator positions for both wheels are automatically stored in a file with date and UT timestamp. These values when reused, generally puts back the FPM slot and its corresponding RLS roughly in a previously aligned position. The refined adjustments of the coronagraph then consume less time.

To align the FQPM/EOPM coronagraph:

- I move the internal science camera to the focal plane and scan all the positions of either the x or the y actuator to look for the fine crosshair in that particular direction.

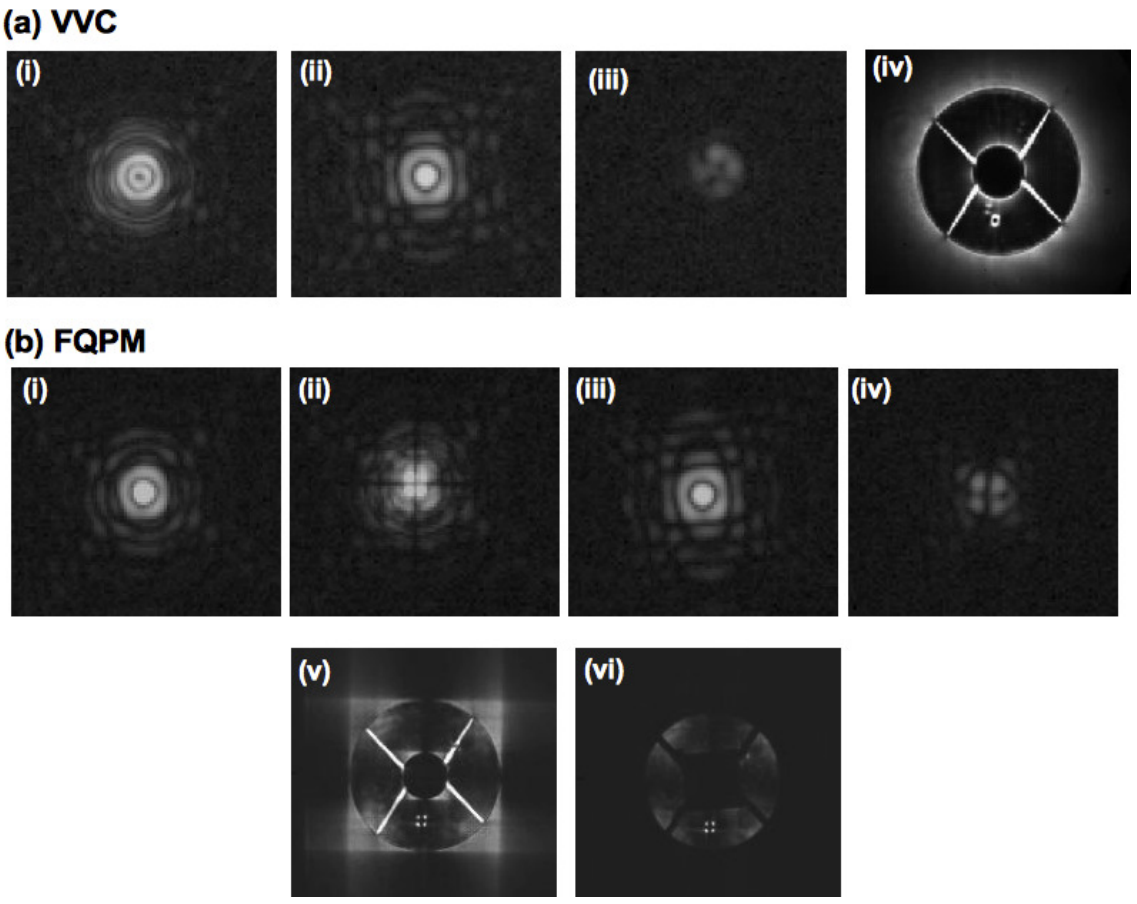

Figure 3.21: Focal and pupil plane images of the aligned (a) VVC and (b) FQPM coronagraphs in the laboratory on SCExAO. (a)(i) Vector vortex aligned on the PSF. (a)(ii) PSF only with RLS of the VVC (without a FPM). (a)(iii) Final coronagraphic PSF with FPM and corresponding RLS in the beam for the VVC. (a)(iv) Illumination at the pupil plane after fine alignment of the vector vortex. (b)(i) Non-coronagraphic PSF on SCExAO. (b)(ii) FQPM aligned on the PSF. (b)(iii) PSF taken only with the RLS of the FQPM (no FPM). (b)(iv) Final coronagraphic PSF of the FQPM. (b)(v) Illumination of the pupil plane downstream the FQPM. The square intensity pattern around the edges of the pupil is due to the geometry of the FQPM. (b)(vi) Pupil image after putting the RLS of the FQPM in the beam. *Note: – The intensity leakage inside the geometrical pupil in (a)(iv) and (b)(v) are the diffraction patterns of the FPM around the edge of a dead actuator. – All the focal plane images in (a) and in (b) are of same brightness scale.*

Then, I repeat the procedure to find the crosshair of the FQPM in the other direction as well (Fig. 3.21 (b)(ii)).

- I move to the pupil plane and scan the positions in z direction to look for the location where there is a sharp square pattern around the edges (outer and inner) of the geometrical pupil and less intensity is scattered inside the pupil (Fig. 3.21 (b)(v)).
- I move back to the focal plane and perform the fine alignment of the crosshair at the center of the PSF by tweaking the x and y actuators of the FPM wheel.

A deliberate misalignment in the y direction of the simulated FQPM at the pupil and the focal plane is shown in Fig. 1.22 (b) and (c) respectively. Most of the starlight is scattered inside the geometrical pupil.

- The RLS of the FQPM is then aligned by moving the x and y actuators of the pupil wheel (Fig. 3.21 (b)(vi)). A square diffraction pattern is visible inside the geometrical pupil. This is the scattering of the starlight downstream the FQPM around the dead actuator.

  Figure 3.21 (b)(iii) shows the PSF with the RLS (no FPM) and Fig. 3.21 (b)(iv) shows the final coronagraphic PSF of the FQPM with its corresponding RLS in the beam. All the focal plane images shown in Fig. 3.21 (b) are of same brightness scale.

To align the PIAA coronagraph:

The alignment of PIAA coronagraph is different from the procedure explained above for the PMCs. The first step is to align the two lenses of the PIAA optics, which is performed by moving the respective wheels in x and y direction and also the distance between them. This step takes a few minutes as the first lens of PIAA optics is aligned using the pupil plane whereas the second lens of PIAA is aligned using the focal plane, which once again is tweaked delicately with very small steps in x and y direction. When the distance between the two lenses are accurate, a gaussian spot with no diffraction rings appears at the focal plane.

Before aligning FPM and RLS, inverse PIAA optics are first aligned very carefully by tip-tilting the tube containing both lenses. If the distance between the two lenses are correct, a regular Airy pattern should reappear.

The PSF after the first set of PIAA lenses is then blocked by placing an amplitude FPM (with sizes varying between 1.5 - 6 λ/D). The FPM in this case is easy to align as it is an opaque mask. I look for the symmetric "doughnut" around the edge of the opaque mask. Then, I move back to the pupil plane and align the corresponding RLS.

Aligning the VVC and the FQPM on-sky, takes usually less than five minutes (depending on the seeing) as the previously stored positions of the x, y and z actuators of the FPM wheel are quite stable and the alignment on-sky is usually less cumbersome. However, aligning the PIAA, the FPM and the Inverse PIAA usually takes more time (roughly 10 minutes) as it is a delicate procedure. Apodized PSF downstream the PIAA optics is very sensitive to seeing, vibrations and environmental factors. The alignment time I mentioned here also includes the time to move the corresponding wheels to put the required FPM and RLS in the beam.

3.6 LLOWFS operation on SCExAO

There are two modes of operating LLOWFS on SCExAO. These modes are specifically applicable to the SCExAO instrument because of its optical design. Figure 3.22 describes the systematic flowchart of operating LLOWFS in Non-ExAO and ExAO regime.

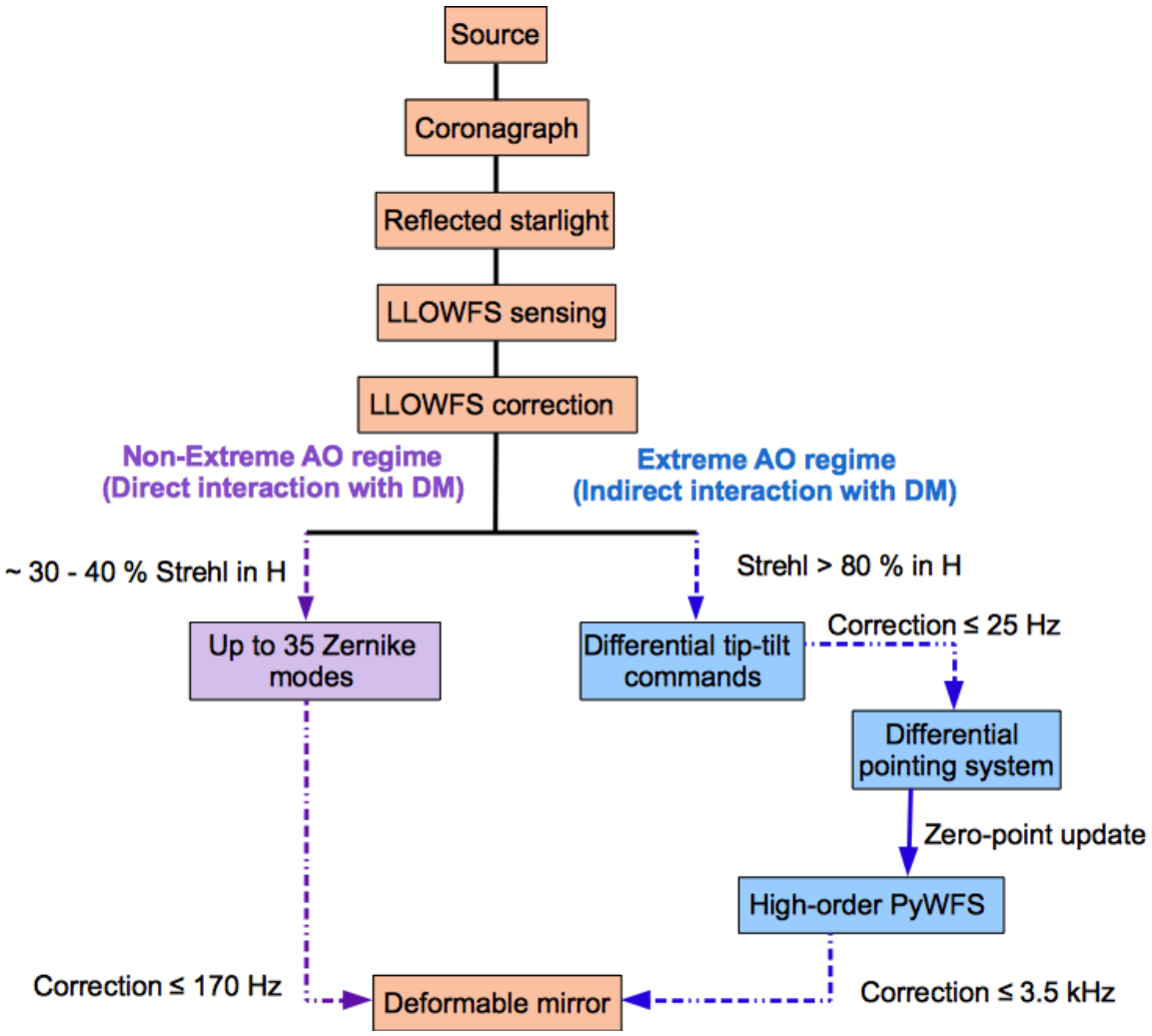

Figure 3.22: The LLOWFS operation on the SCExAO instrument under Extreme AO (blue) and Non-extreme AO (purple) regimes.

As I explained in §3.2.3, because there is only one correcting unit (DM) on SCExAO, all the WFSs (PyWFS, LLOWFS and Speckle nulling) can not use it simultaneously to apply their respective corrections. Our ultimate goal is thus to unite the operation of all the WFSs so that a combined correcting phasemap can be produced to apply a global correction to the system. Addressing this goal, we made an initial effort to integrate the LLOWFS inside the high-order PyWFS, which led to the second mode of LLOWFS operation on SCExAO.

3.6.1 Non-Extreme AO regime

In this configuration, the LLOWFS is the only sensor which is sensing the low-order wavefront aberrations in a post-AO188 residuals. There is no additional high-order correction by the PyWFS. The LLOWFS is the primary sensor which interacts with the DM directly to compensate for aberrations < 200 nm RMS. The maximum sensing and correction speed is 170 Hz in this case. As AO188 provides a typical Strehl of ~ 30 - 40%

at H band, LLOWFS only stabilizes a partially corrected PSF behind the FPM and cannot provide significant improvement over contrast.

In the laboratory, the LLOWFS sensed up to 35 Zernike modes for the VVC, FQPM, EOPM and up to 15 modes for the PIAA coronagraph, and corrected them by directly commanding the DM. On-sky, the sensing and correction of 10 Zernike modes has been done for the VVC in H-band and 5 Zernike modes for the PIAA in J-band on the same target.

Chapter 4 present the open-, closed-loop results and spectral analysis of the LLOWFS performance in the laboratory and on-sky for different coronagraphs. I demonstrated the stabilization of the on-axis star at the center of the FPM with a pointing accuracy of sub-milliarcseond at 1.6 μm.

3.6.2 Extreme AO regime

In this case, the LLOWFS does not interact with the DM directly. The main WFS that controls the DM is the visible high-order PyWFS. The LLOWFS after sensing the differential tip-tilt errors, sends the command to a Differential Pointing System (DPS), which is connected with the PyWFS optically. DPS, after receiving the tip-tilt command from the LLOWFS, physically changes the position of the beam falling at the apex of the Pyramid optics thereby changing its zero-point (reference). Upon sensing the change in its zero-point, the PyWFS compensate it by commanding the DM to move by the corresponding amount to bring the reference back to its nominal position.

The differential tip-tilt command is sensed at $\leq$ 170 Hz, however, the correction by the DPS is communicated to the PyWFS at $\leq$ 25 Hz because of the slow response of the DPS Piezo controller. In this regime, PyWFS corrects the high-order aberration in the visible at a frequency $\leq$ 3.5 kHz and the LLOWFS addresses the pointing errors only at a frequency $\leq$ 25 Hz. LLOWFS operates on the PSF with a typical SR $>$ 80% in H-band.

Chapter 5 present the successful implementation of the LLOWFS inside the PyWFS and demonstrate the correction of the differential pointing errors on the IR bench in the laboratory and on-sky. This combination also allowed me to characterize high frequency telescope vibrations during the transit of a target that eventually affected LLOWFS corrections.

The two methods of LLOWFS operation that are discussed in this thesis are implemented in accordance with the design of the SCExAO instrument. The low-order wavefront sensing approach presented in the non-ExAO regime can easily be implemented on any coronagraphic ExAO instrument that either can feed the tip-tilt signals to their existing AO/ExAO tip-tilt mirror or has a dedicated DM for the low-order modes correction. However, the second approach for the ExAO regime is valid when the pointing and NCP errors are not sensed inside the ExAO loop and therefore requires a separate sensor to measure the aberrations and a technique to feedback the correction to the ExAO loop without interrupting its operation.

Nevertheless, both techniques of the LLOWFS are well implemented on SCExAO and

has successfully demonstrated the correction of the low-order aberrations on-sky. These techniques can be adapted to any direct imaging instrument, which is aiming to control and calibrate the low-order wavefront aberrations at/near the diffraction limit.

3.6.3 LLOWFS Control and Graphical User Interface

For my laboratory experiments for the first two years, I have coded the control loop in *Python language*, which was not optimized for closing the loop during on-sky operations. So to provide high speed computation with low latency for on-sky testings during my third year, I have used the skeleton of control loop for the PyWFS written in *C* by *Olivier Guyon*. The PyWFS and the LLOWFS share the same code architecture for their core control loop, envisioning an optimal usage of the on-sky time during future operations. The input parameters to the control loop are different but both WFSs follows common memory data structure in C to compute the control commands by pseudo-inverting the response matrix via a SVD method (as explained in §2.3.4 in chapter 2).

The process of reading the images from their respective detectors, performing reference and dark image subtractions and then normalization, removing hot pixels, commanding the DM to obtain the calibration frames (either off-sky or on-sky), computing the control matrix, selecting the gain, sending correction phasemaps to the DM and saving the residuals are common features for both sensors.

The PyWFS control is complex as it corrects a mixture of Zernike and Fourier modes ($\sim$ 1600) with modal gain approach. It is still under progress and going through an optimization process. The LLOWFS loop is simplified, and unlike the PyWFS loop that is using GPUs for fast matrix multiplications, it is only using CPUs for its calculations.

The Fig. 3.23 and 3.24 display three windows of the Graphical User Interface (GUI) for the LLOWFS that I have written in bash script. Figure 3.23 shows: Select Parameter GUI, Fig. 3.24 (a) Configuration GUI and, Fig. 3.24 (b) Control GUI. The Select Parameter GUI allows the user to select several parameters and perform a calibration. The selectable parameters are: – type of coronagraph, – correction unit (DM or DPS), – number of modes to be corrected (default is 2 if the correction unit is the DPS), – the amplitude (in nm) to obtain the response matrix and, – number of images to average in the response matrix. Using these variables, the response matrix is acquired and the control matrix is computed. Each of these parameters and corresponding matrices are automatically stored in a configuration file.

From the Configuration GUI (Fig. 3.24 (a)), a pre-configured file can be selected and loaded directly to the control loop without requiring to reselect the variables in Fig. 3.23.

After loading the required configuration from Fig. 3.24 (a), the Control GUI is used to drive the LLOWFS control loop. A parameter, *"loop max lim"* (in Fig. 3.24 (b)) allows to select a threshold (in μm) to the amplitude of the aberration that can be corrected in order to prevent a saturation of the DM. This GUI also allows to inject either a Zernike aberration in the system or a realistic turbulence for laboratory testings. The control loop operations such as select *"gain"* and *"open", "close", "kill"* the loop are performed by clicking the corresponding button. This bash script functions in conjunction with LLOWFS control loop in *C language*.

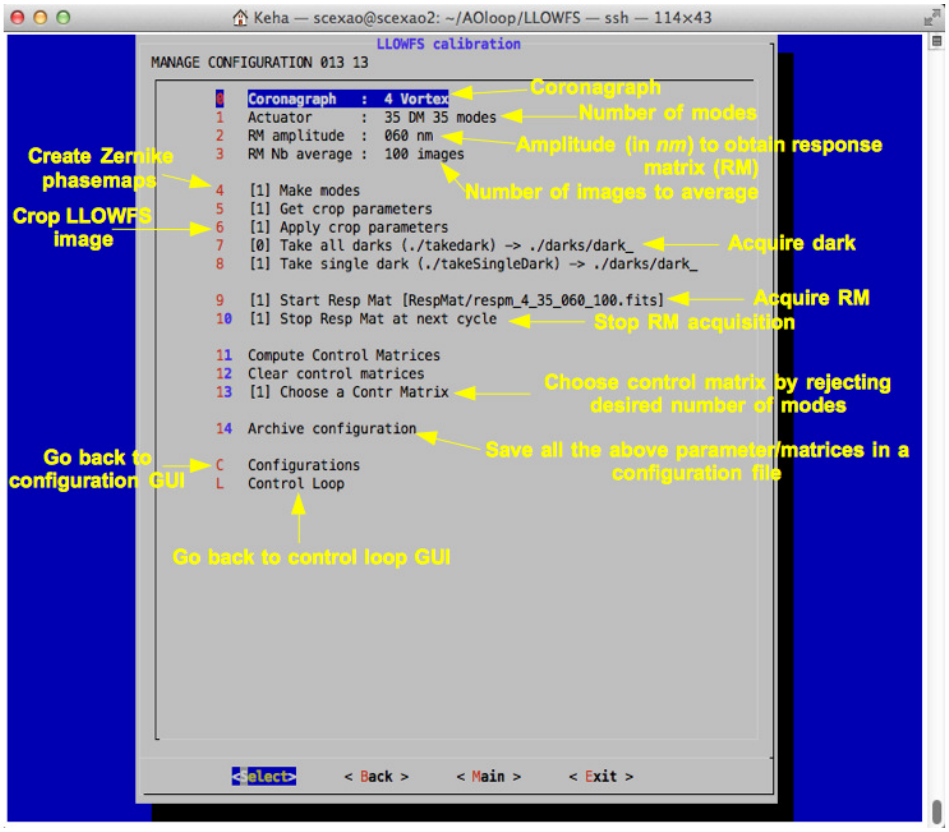

Figure 3.23: "Select Parameter" GUI window for the LLOWFS written in bash script.

To display the real time telemetry of the low-order aberrations, I used the residuals saved by the control loop in *C code*. These residuals are also used to characterize the LLOWFS performance by comparing open- and closed-loop results. I perform all of this high-level processing in *Python language*.

In the next chapter, I present the detailed analysis of the low-order wavefront control with different coronagraphs followed by the results obtained in the laboratory and on-sky using the LLOWFS under the Non-ExAO regime on SCExAO.

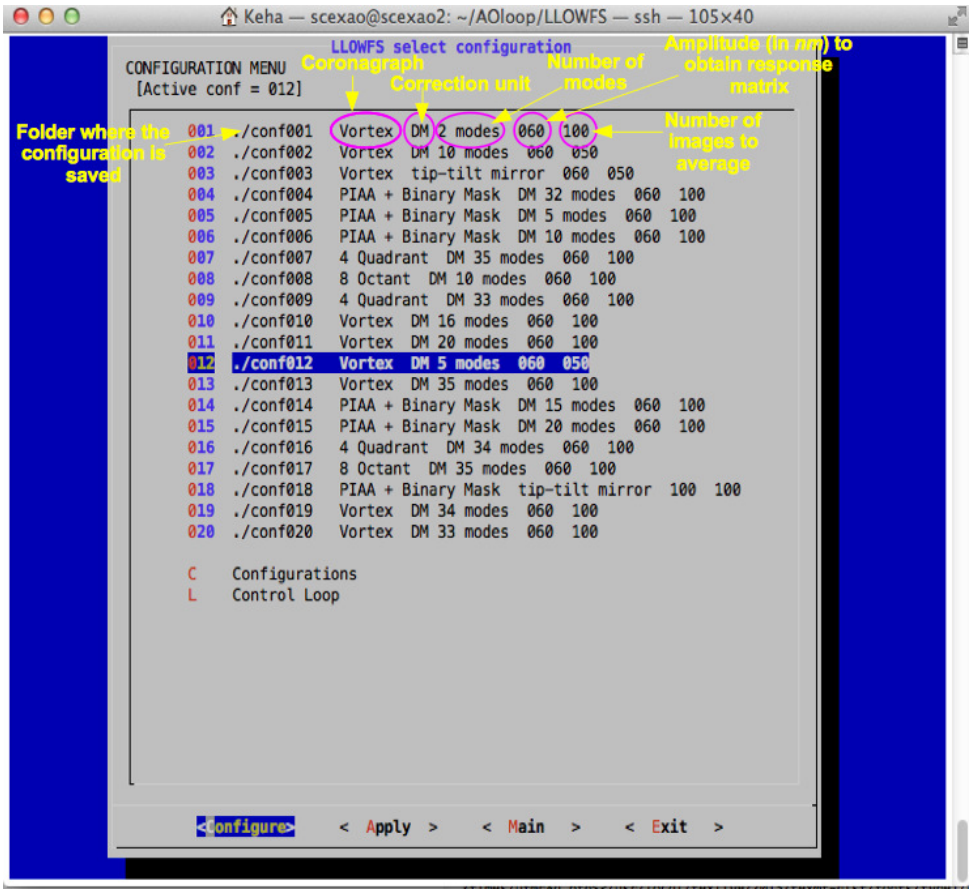

(a) Configuration GUI

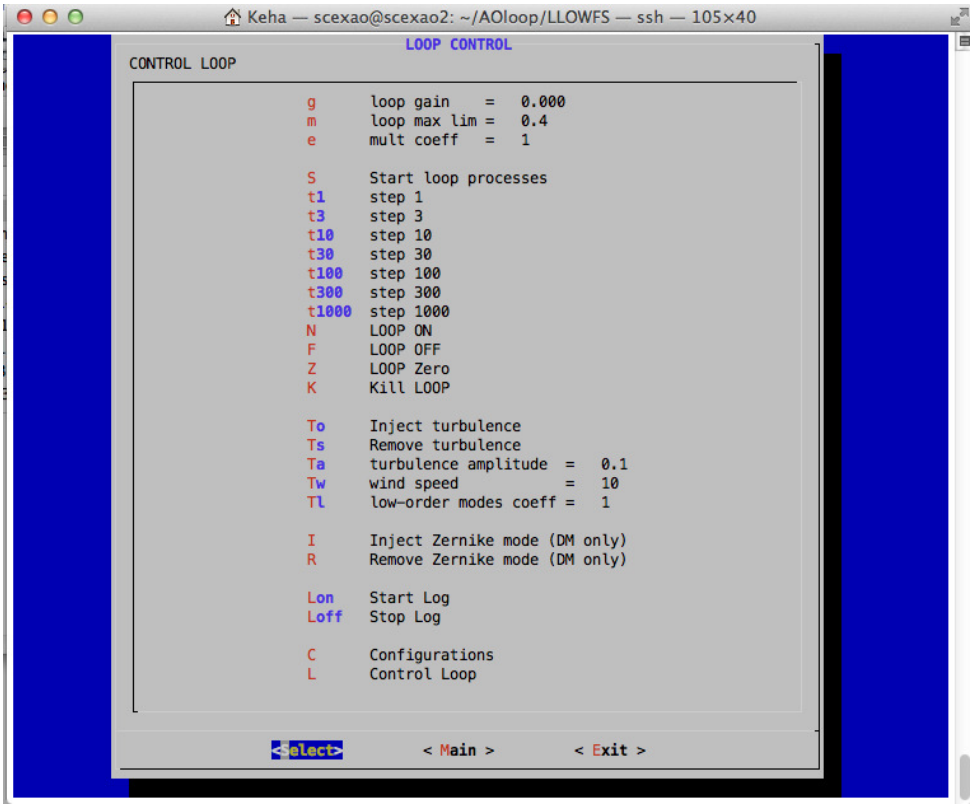

(b) Control GUI

Figure 3.24: Control GUI window for LLOWFS written in bash script.

Chapter 4

Laboratory and on-sky results of the LLOWFS used in a non-ExAO regime

"It was like a new world opened to me, the world of science, which I was at last permitted to know in all liberty."

– Marie Curie

As quoted in Marie and Pierre Curie and the Discovery of Polonium and Radium, Nobel Lecture

Contents

4.1 Introduction

So far, I presented the LLOWFS concept, its simulations with a FQPM and the first laboratory experiments at LESIA in Chapter 2, where I demonstrated the measurement of tip-tilt errors only. Then, I described the SCExAO instrument, the throughput of its coronagraphs and reflective Lyot stops and a detail description of the LLOWFS implementation on the instrument in Chapter 3. Now, in the current chapter I will present the experiments I have performed on SCExAO in order to characterize the LLOWFS performance with different coronagraphs in a non-ExAO regime. I got several opportunities to test the LLOWFS on-sky and since September 2014 its successful closed-loop operations has allowed SCExAO to provide stable coronagraphic PSF during engineering and science nights.

This chapter is an extension of the publication Singh *et al.* (2015), which presents the LLOWFS results obtained in the laboratory and on-sky on SCExAO. I presented the temporal measurements and the spectral analysis of the open- and closed-loop residuals obtained by the LLOWFS in the non-ExAO and ExAO regimes. This paper demonstrated only the experimental results of LLOWFS mostly on engineering targets because of the high level of uncorrected high order aberrations. No significant improvement in the contrast is achieved during on-sky operations. First I will grossly outline the presentation of the publication and then in the rest of the chapter, I will describe the detailed performance analysis of the LLOWFS for different coronagraphs in the laboratory and on-sky.

- *Pub.* §2.2 introduces the LLOWFS implementation on SCExAO. This is a brief summary of the details presented in §3.4 of Chapter 3. *Pub.* Fig. 1 summarizes the LLOWFS setup on SCExAO.

- *Pub.* Fig. 2 shows a flowchart of the LLOWFS operation in non-ExAO configuration. *Pub.* §3 present the results obtained with the LLOWFS under this regime where it interacts with the DM directly to compensate for the low-order errors. A Linearity test (*Pub.* Fig. 4) is presented in *Pub.* §3.3.1 while temporal measurements and a spectral analysis in the laboratory (*Pub.* Fig. 6, 7 and 8) and on-sky (*Pub.* Fig. 9, 10 and 11) with a VVC is presented in *Pub.* §3.3.3 and §3.3.4 respectively.

- *Pub.* Fig. 12 in §3.4 presents the processed frames with the internal science NIR camera. These on-sky images were obtained with AO188 and the LLOWFS both in closed-loop, which has stabilized the starlight behind the FPM. The star in *Pub.* Fig. 12 (b) was misaligned prior of LLOWFS closed-loop operation.

This chapter will present a similar analysis than in the paper for the FQPM/EOPM and the PIAA coronagraphs under non-ExAO regime (§4.5 and §4.6)). I will also characterize the sources of vibrations (§4.5.2) that affected LLOWFS measurements in the laboratory and on-sky.

- *Pub.* §4 presents the integration of the LLOWFS inside the visible high-order PyWFS to address the differential tip-tilt errors. *Pub.* Fig. 13 shows a flowchart describing how the LLOWFS is integrated inside PyWFS. Chapter 5 is dedicated to the LLOWFS operations in the ExAO regime where I present the stable and durable on-sky results obtained with the LLOWFS so far.

4.2 Singh et al. 2015

PUBLICATIONS OF THE ASTRONOMICAL SOCIETY OF THE PACIFIC, **127**:857–869, 2015 September

On-Sky Demonstration of Low-Order Wavefront Sensing and Control with Focal Plane Phase Mask Coronagraphs

GARIMA SINGH,[1,2] JULIEN LOZI,[1] OLIVIER GUYON,[1] PIERRE BAUDOZ,[2] NEMANJA JOVANOVIC,[1] FRANTZ MARTINACHE,[3] TOMOYUKI KUDO,[1] EUGENE SERABYN,[4] AND JONAS KUHN[5]

Received 2015 April 18; accepted 2015 June 11; published 2015 August 12

ABSTRACT. The ability to characterize exoplanets by spectroscopy of their atmospheres requires direct imaging techniques to isolate planet signal from the bright stellar glare. One of the limitations with the direct detection of exoplanets, either with ground- or space-based coronagraphs, is pointing errors and other low-order wavefront aberrations. The coronagraphic detection sensitivity at the diffraction limit therefore depends on how well low-order aberrations upstream of the focal plane mask are corrected. To prevent starlight leakage at the inner working angle of a phase mask coronagraph, we have introduced a Lyot-based low-order wavefront sensor (LLOWFS), which senses aberrations using the rejected starlight diffracted at the Lyot plane. In this article, we present the implementation, testing, and results of LLOWFS on the Subaru Coronagraphic Extreme Adaptive Optics system (SCExAO) at the Subaru Telescope. We have controlled 35 Zernike modes of a H-band vector vortex coronagraph in the laboratory and 10 Zernike modes on-sky with an integrator control law. We demonstrated a closed-loop pointing residual of 0.02 mas in the laboratory and 0.15 mas on-sky for data sampled using the minimal 2-s exposure time of the science camera. We have also integrated the LLOWFS in the visible high-order control loop of SCExAO, which in closed-loop operation has validated the correction of the noncommon path pointing errors between the infrared science channel and the visible wavefront sensing channel with pointing residual of 0.23 mas on-sky.

Online material: color figures

1. INTRODUCTION

One of the goals of the next generation of ground- and space-based missions is the direct detection and spectrophotometric characterization of rocky-type exoplanets in the habitable zone (HZ) of a parent star. The scientific motivation is to study the chemical compositions of their atmospheres to search for bio-signatures. Disentangling rocky-type extrasolar planets from M-type and solar-type star at 10 parsec requires the angular resolution and sensitivity of a 30-m telescope from the ground and 2–4 meters telescope in space, respectively. However, resolution alone is not sufficient enough for their detection in the HZ. The direct imaging of such exoplanets is limited by the ability to identify planet signal above the bright stellar background at small angular separation, which therefore requires high-contrast imaging (HCI) near the diffraction limit.

Coronagraphs are used to block the starlight and suppress the diffraction effects of the telescope, making the planet signal more accessible. Small inner working angle (IWA) coronagraphs can reach to within the first couple of Airy rings of the star. However, the exploitation of this region relies on the ability of efficiently controlling and calibrating the residual low-order wavefront errors (Guyon et al. 2006). These aberrations occurring upstream of a focal plane mask (FPM) are a common issue for both ground- and space-based coronagraphs, which result in starlight leaking around the coronagraphic mask. The aim of this article is to present the results of a unique low-order wavefront sensor applicable to phase mask coronagraphs (PMCs), including the vortex coronagraph, with which it is tested here.

First efforts have been made to reduce the quasi-static pointing aberrations at Palomar well-corrected subaperture (WCS), on the Hale telescope, and achieved a residual of $0.02\ \lambda/D$ (6 mas) with a vortex coronagraph (Serabyn et al. 2010). The current ground-based extreme adaptive optics (ExAO) instruments such as Gemini Planet Imager (GPI, Macintosh et al. [2014]) at the Gemini Observatory and Spectro-Polarimetric High-contrast Exoplanet Research (SPHERE, Beuzit et al. [2010]) at the Very Large Telescope are now predictively correcting the dynamic low-order wavefront aberrations.

[1] National Astronomical Observatory of Japan, Subaru Telescope, 650 N A'Ohoku Place, Hilo, HI 96720.
[2] Lesia, Observatoire de Paris-Meudon, 5 Place Jules Janssen, F-92195 Meudon Cedex, France.
[3] Observatoire de la Côte d'Azur, Boulevard de l'Observatoire, 06300 Nice, France.
[4] Jet Propulsion Laboratory, California Institute of Technology, 4800 Oak Grove Drive, Pasadena, CA 91109-8099.
[5] Institute for Astronomy, Swiss Federal Institute of Technology, Wolfgang-Pauli-Strasse 27, CH-8093 Zurich, Switzerland.

GPI is equipped with a 7×7 low-order Shack-Hartmann (SH) wavefront sensor that has demonstrated the corrections of the noncommon path aberrations down to <5 nm root mean square (rms) for spatial frequencies <3 cycles/pupil under simulated turbulence. By implementing a Linear Quadratic Gaussian algorithm (LQG, Petit et al. [2009]) in the AO system, they have demonstrated on-sky corrections of common-path vibrations at 60, 120, and 180 Hz to under 1 mas per axis for tip-tilt residuals and a reduction of focus aberration down to 3 nm rms wavefront error at the 60 Hz peak (Poyneer et al. 2014).

SPHERE's SAXO (SPHERE AO for eXoplanet Observation) uses a 40×40 visible SH wavefront sensor and demonstrated an on-sky residual jitter of 11 mas with an integrator controller and 9 mas with an LQG algorithm (Petit et al. 2014).

The Subaru Coronagraphic ExAO (SCExAO, Jovanovic et al. [2015]) instrument at the Subaru Telescope, the Exoplanetary Circumstellar Environments, and Disk Explorer (EXCEDE, Belikov et al. [2014]; Lozi et al. [2014]) testbed at NASA Ames and the High-Contrast Imaging Testbed (HCIT, Kern et al. [2013]) at JPL have implemented a coronagraphic low-order wavefront sensor (CLOWFS, Guyon et al. [2009]), which senses the rejected starlight reflected by the FPM. With the use of a Phase-Induced Amplitude Apodization (PIAA, Guyon [2003]) coronagraph, residuals $\leq 10^{-3}\ \lambda/D$ for the tip and tilt modes have been demonstrated in closed-loop in the laboratory operation.

However, these existing solutions are not compatible with the nonreflective PMCs, which are the type of coronagraphs that diffracts the rejected starlight in the postcoronagraphic pupil plane. To address this issue, Singh et al. (2014a) have introduced the concept of a Lyot-based low-order wavefront sensor (LLOWFS), which senses aberrations using the residual starlight reflected by the Lyot stop. Its first implementation has demonstrated an open-loop measurement pointing accuracy of $10^{-2}\ \lambda/D$ at 638 nm with a Four Quadrant Phase Mask (FQPM, Rouan et al. [2000]) coronagraph. The preliminary implementation of the LLOWFS on the SCExAO instrument has also demonstrated an on-sky closed-loop pointing accuracy of $\sim 7 \times 10^{-3}\ \lambda/D$ (Singh et al. 2014b) with a vector vortex coronagraph (VVC, Mawet et al. [2010]).

The aim of this article is to present the laboratory and on-sky results of an improved version of the LLOWFS on the SCExAO instrument. In § 2, we remind the reader about the principle of the LLOWFS concept and its integration in the SCExAO instrument. Then, § 3 presents the results in laboratory and on-sky for the configuration where the aberrations sensed by the LLOWFS are directly corrected by the Deformable Mirror (DM). Finally, § 4 presents the on-sky results for a second configuration where the LLOWFS is integrated in the ExAO loop to correct for the noncommon path and chromatic errors between the visible wavefront sensor of the ExAO and the imaging wavelengths.

2. LYOT-BASED LOW-ORDER WAVEFRONT SENSOR

2.1. Principle

LLOWFS is a coronagraphic wavefront sensor which is designed to sense the pointing errors and other low-order wavefront aberrations at the IWA of the PMCs. The coronagraphic mask at the focal plane diffracts starlight outside the geometrical pupil in the downstream pupil plane. Unlike conventional coronagraphs, the diffracted starlight in the reimaged pupil plane, instead of being simply blocked by an opaque Lyot stop, is reflected via a reflective Lyot stop (RLS) toward a reimaged focal plane. This reflected light is collected by a detector and used to measure the low-order aberrations.

LLOWFS is a linear wavefront reconstructor that relies on the assumption that if the post-AO wavefront residuals are $\ll 1$ radian rms then the intensity variations in the reflected light are a linear combination of the low-order aberrations occurring upstream of the focal plane phase mask.

An image I_R affected by the low-order modes i of amplitude $\boldsymbol{\alpha} = (\alpha_1, \alpha_2 \ldots \alpha_n)$ is subtracted from a reference image I_0 and decomposed into a linear combination on a base of orthonormal images S_i corresponding to the response of the sensor to the low-order modes. So the difference between an image at any instant and the reference follows the equation

$$I_R(\boldsymbol{\alpha}) - I_0 = \sum_{i=1}^{n} \alpha_i S_i. \tag{1}$$

The measurements are then used to compute the control commands via an integrator control law.

This paper focuses on the empirical approach of the LLOWFS only. For a detailed theoretical description, the reader may refer to the publication Singh et al. (2014a).

2.2. SCExAO Instrument with Integrated LLOWFS

SCExAO is a versatile high-contrast imaging instrument which features an ExAO control loop using a Pyramid wavefront sensor (PyWFS, Clergeon et al. [2013]) that provides a high and stable Strehl ratio, a speckle nulling routine to improve the contrast on one half of the field of view, and a LLOWFS to stabilize the starlight behind the coronagraphic mask. These different wavefront sensors are implemented on SCExAO to address the issues that degrade the point spread function (PSF) quality: the PyWFS measures the dynamical high-order wavefront aberrations, speckle nulling suppresses the quasi-static speckles, and the LLOWFS measures the coronagraphic leaks. This publication focuses only on the LLOWFS and its integration with the PyWFS. More details about the PyWFS and the speckle nulling loop can be found in Jovanovic et al. (2015).

The SCExAO instrument is located at the Nasmyth platform of the Subaru Telescope. The instrument is sandwiched between

Subaru's 188-actuator adaptive optics facility (AO188, Guyon et al. [2014]) and HiCIAO (Hodapp et al. 2008), a high-contrast coronographic imager for AO offering angular/spectral/polarization differential imaging modes. Figure 1 shows the simplified version of the optical ray path on SCExAO which is described as follows. AO188, using the light below 640 nm and correcting 187 modes, stabilizes the PSF with a typical Strehl ratio of 30% in H-band. The AO corrected diffraction-limited F/14 beam is then fed to SCExAO as an input. The beam, collimated by an off-axis parabola (OAP), strikes SCExAO's 2000-actuator DM at the pupil plane. The beam reflected from the DM meets the dichroic that separates the visible light (640–940 nm) from the Infrared (IR) light (940–2500 nm). The visible light is reflected toward the upper bench via a periscope while the IR light is transmitted to the lower bench. The visible upper bench includes a nonmodulated PyWFS which is capable of measuring ∼1600 aberrated modes with a frame rate of up to 3.6 kHz at ∼850 nm. The lower IR bench supports the LLOWFS and the speckle nulling control loop working at 1.6 μm. The bench includes a variety of coronagraphs optimized for very small IWA (1–3 λ/D, i.e., 40–120 mas at 1.6 μm): PIAA, Shaped pupil (Kasdin et al. 2004), VVC, FQPM, and eight octant phase mask (8OPM, Murakami et al. 2010). The VVC on SCExAO is a rotating half-waveplate structure that has a vectorial phase spiral. There is a 25-μm diameter opaque metallic spot deposited at the center to mask the central defect (Mawet et al. 2009). We used this coronagraph for the results presented in this article.

After the dichroic, the PIAA optics mounted in a wheel can be moved in or out to apodize the IR beam. At the focal plane, all the PMCs mentioned earlier sit in a wheel that can be adjusted in the x, y, and z directions via motorized actuators. The on-axis starlight diffracted by the FPMs in a downstream reimaged pupil plane encounters a pupil wheel, which sits at an angle of 6° as shown in Figure 1. This pupil wheel consists of the RLSs corresponding to each FPMs at the focal plane. These pupil masks are made by lithographing a layer of chrome on a fused silica disk of 1.5-mm thickness. Figure 1 shows an example of a RLS for the VVC coronagraph. The chrome, corresponding to the reflective surface in this image, has a reflectivity of only 60% in near infrared, while the rest is being absorbed.

The RLS at the pupil plane blocks the diffracted starlight rejected outside of the geometrical pupil. This unused masked starlight is reflected toward a Near Infrared (NIR) detector in a reimaged focal plane for low-order wavefront sensing. This detector will be referred to as the LLOWFS camera throughout the paper. The nulled coronagraphic PSF is directed toward two different NIR imaging optics via a selection of beamsplitters that can select the spectral content and the amount of flux between the two optical paths. One relayed optical path is toward the high frame rate internal NIR imaging camera and another one is toward HiCIAO.

The LLOWFS camera and the internal NIR imaging camera are InGaAs CMOS detectors with a resolution of 320× 256 pixels, a frame rate of up to 170 Hz and a read out noise of 140 e^-. They are used for the alignment of the coronagraphs as well as the testing and calibration of the low-order control loop either with the internal calibration source or directly on the sky. On the other hand, HiCIAO uses a HAWAII 2RG

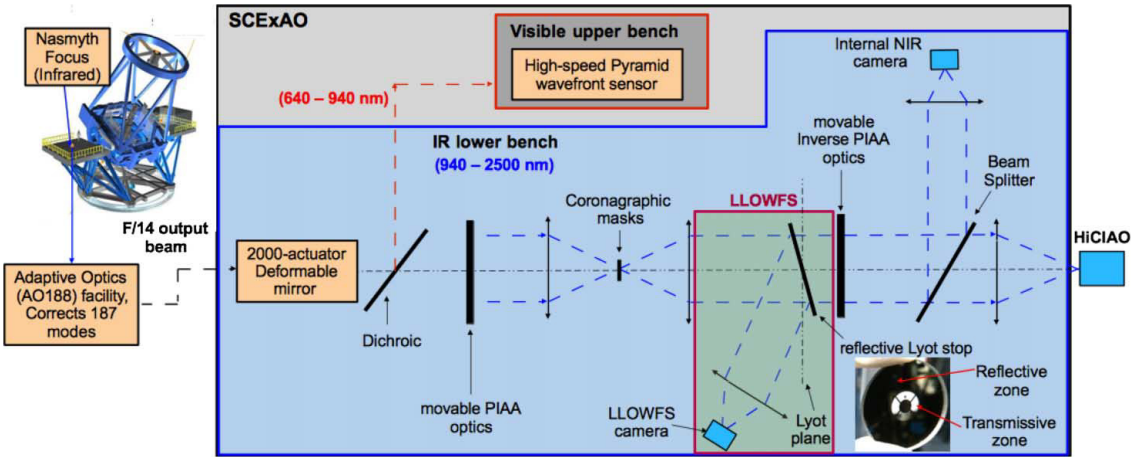

FIG. 1.—Simplified optical ray path of SCExAO. The instrument is situated at the Nasmyth platform of the Subaru Telescope and feeds on the beam from AO188. The output of the instrument goes to the high-contrast imager, HiCIAO. SCExAO has two benches: visible and IR. The coronagraphic masks at the focal plane are interchangeable PMCs such as VVC, FQPM, and 8OPM. LLOWFS is shown on the IR channel simply requiring a reflective Lyot stop (RLS), relay optics, and a detector. The RLS presented in the figure is the Lyot stop designed for the VVC. See the electronic edition of the *PASP* for a color version of this figure.

detector with a resolution of 2048×2048 pixels, a frame rate $\ll 3$ Hz, and a read out noise of 15–30 e^-. HiCIAO is a facility science instrument we used to perform the differential imaging and to collect the postcoronagraphic data during the on-sky operations. The advantage of having both the internal NIR camera and the HiCIAO is that the former can be used to track the high temporal frequencies in the atmospheric turbulence while the latter is ideal for tracking the slow varying spatial frequency components with much better sensitivity.

The SCExAO instrument is developed with an ultimate goal of being rapidly adaptable to the future extremely large telescopes (Guyon & Martinache 2013). Further details of the SCExAO instrument and its future capabilities are beyond the scope of this article and are described in detail in Jovanovic et al. (2015).

2.3. Deformable Mirror as a Wavefront Corrector and a Turbulence Generator

The DM of SCExAO can be used not only to control the aberrations up to the highest spatial frequency of 22.5 λ/D but also to inject phase errors to simulate a dynamical turbulence for laboratory tests. The phase maps injected on the DM are built using a simulated phase screen, which follows the Kolmogorov profile. This phase screen can also be filtered to mimic the effects of the low and high spatial frequencies under pre-/post-AO corrections. The simulated turbulence can run in the background independently of the corrections injected on the DM by the wavefront control loops. The final command sent to the DM is then the sum of the injected turbulence and the calculated corrections. For the turbulence injection, we control different parameters: strength (amplitude in nm rms), wind speed (m/s), and an optional coefficient reducing the low-spatial frequencies to mimic the effect of the AO188 wavefront residuals. However, this simulation is limited by the spatial frequency of the DM, which is 22.5 cycles/aperture.

2.4. LLOWFS Operation on SCExAO

SCExAO has a dedicated low-order wavefront correction loop, which uses the measurement of the LLOWFS to calculate the control commands. The measured aberrations are compensated by actuating the DM by the following two methods:

1. Direct interaction with the DM: The low-order wavefront corrections are sent directly to the DM. In this case, 35 Zernike modes in the laboratory and 10 Zernike modes on-sky can be controlled thus far. The method and the results obtained are described in detail in § 3.

2. Indirect interaction with the DM: The second avenue of communication is when the LLOWFS controls the piezo-driven tip-tilt mount of the dichroic, which separates visible and IR channels, to offset the zero-point of the PyWFS. With this configuration, the axis of the PyWFS is changed by moving the dichroic in tip-tilt with the corresponding amount of measured pointing residuals. This pointing shift in the visible channel is then compensated by the DM in closed-loop, hence indirectly controlling the differential pointing errors in the IR channel. We demonstrate the concept and the first on-sky results with this preliminary setup, known as the differential pointing system, in § 4.

The second approach of low-order wavefront control is the one that will be used in the final configuration of SCExAO during the scientific observations. Indeed, the different wavefront sensors on SCExAO use the same DM for the wavefront correction, and therefore cannot run simultaneously as separate units. Nevertheless, the first approach is still valid for coronagraphic ExAO designs that have a dedicated DM for the low-order correction.

3. LOW-ORDER CORRECTION USING DIRECT INTERACTION WITH THE DM

3.1. Configuration

Figure 2 summarizes the configuration in a simplified flowchart. The starlight rejected by the coronagraph is reflected toward the LLOWFS camera. The reflected intensity at any instant is then sensed at the rate of 170 Hz. The low-order estimations are done by first obtaining the response matrix, also called calibration frames. These frames are acquired by applying a known amplitude of each Zernike mode independently to the DM. The reference subtracted response of the sensor is saved as a response matrix. The measurements are obtained using the Singular Value Decomposition (SVD) method, and used by an integrator controller to compute the corrections. These corrections are then sent to the DM, which compensates for the low-order aberrations.

3.2. Calibration Frames Acquisition

Figure 3 presents the response of the LLOWFS to probe the low-order Zernike modes. These frames are acquired prior to

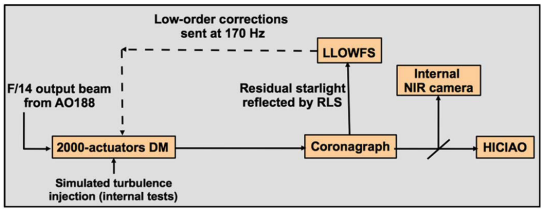

FIG. 2.—Flowchart of the configuration when the LLOWFS is directly coupled to the DM as the actuator on the IR channel of SCExAO. The LLOWFS camera senses the starlight reflected by the Lyot stop and measures the low-order aberrations. Calculated corrections are then sent to the DM. In this configuration, we use a simple integrator control law. See the electronic edition of the *PASP* for a color version of this figure.

closing the control loop. In the laboratory, without any simulated turbulence, we apply a phasemap with an amplitude of 60 nm rms for the 35 Zernike modes separately to the DM. The effect of these modes on the low-order images is subtracted from the reference frame to calibrate the LLOWFS response to the low-order modes. Figure 3*a* shows the response matrix obtained in the laboratory for 10 Zernike modes only. This figure shows a clear distinction between the calibration frames, indicating no confusion in the response of the LLOWFS to different low-order modes.

In a similar manner, Figure 3*b* shows the on-sky calibration frames obtained by applying phasemaps with an amplitude of 60 nm rms for the 10 Zernike mode on the DM while observing the science target Epsilon Leonis (1.5 mas rms of tip-tilt angle on-sky). These calibration frames were obtained with the AO188 loop closed.

The on-sky response matrix looks noisier than the one obtained in the laboratory. It is actually dominated by uncorrected phase errors, since the AO188 is the only loop providing wavefront correction. Even if the on-sky signal is not as strong as in the laboratory, the modes are quasi-orthogonal and still can be used to close the loop.

3.3. Measurements

In order to characterize the performance of a low-order wavefront sensor for coronagraphic purpose, it is important to understand how efficiently the pointing errors are measured and mitigated. We analyzed the properties like the linear response of the sensor, the cross coupling between the low-order modes, and the requirement of how often the calibration frames should be reacquired.

3.3.1.Linearity

Figure 4 presents the linearity of the sensor to the tip aberration studied in case of the VVC. We applied phasemaps of tip aberrations with amplitudes between ± 150 nm rms to the DM. The impact of each phasemap on the low-order images was recorded. Using the response matrix acquired in Figure 3*a*, the amount of the tip error as well as the residual in the other modes was estimated through SVD. The experiment was repeated 20 times and the plotted data are the average of the 20 measurements acquired.

The linearity range of the sensor is around 150 nm rms (from -50 nm to 100 nm rms) for the tip mode in *x*. The residuals of the modes tilt in *y*, focus, oblique, and right astigmatism extracted through SVD are $\sim$1 nm rms within the linearity range which is a tolerable amount of cross-coupling between the modes. The shift in the center of the linear range toward one direction could be caused by misalignments of the beam with respect to the FPM, or by the 25-μm metallic dot not being perfectly centered with the vortex half-waveplate. We repeated the linearity test with the rest of the modes and observed a similar behavior in the range of linearity and the shift of the zero point.

Therefore, the stability of the reference image on the low-order camera dictates how often the LLOWFS should reacquire calibration frames. During the acquisition of the calibration, if the environmental factors, such as temperature variation and the flexure of the instruments, introduce tip-tilt errors in the reference PSF, then the system needs to be recalibrated. If these drifts happen prior to closed-loop operation and are out of the linearity range, then only the PSFs need to be realigned behind the FPM and previously acquired calibration frames can be reused to close the loop. However, such drifts will not affect the closed-loop operation as the low-order correction will compensate for them.

3.3.2. Turbulence Injection in the Laboratory

All of our experiments in the laboratory are conducted with simulated dynamic phase errors that were applied on the DM. For the turbulence simulation, we chose 150 nm rms as the amplitude, 10 m/s as the wind speed, and we allowed all the low-spatial frequency components of the turbulence to be left uncorrected mimicking the case with no AO correction

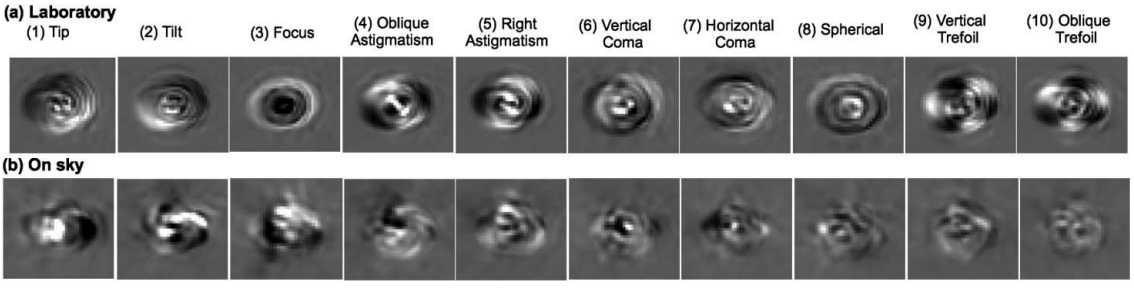

FIG. 3.—Response matrix for the VVC obtained (*a*) in the laboratory and (*b*) on-sky for 10 Zernike modes. Note: These frames have the same brightness scale.

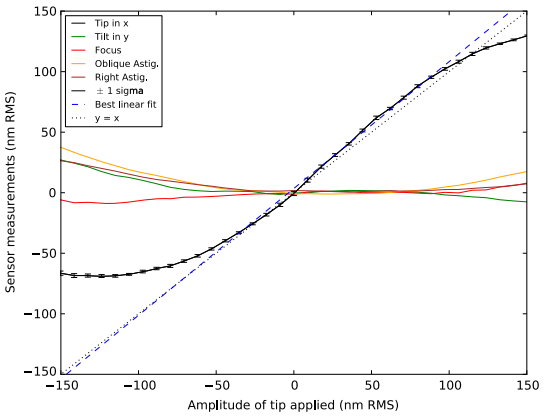

FIG. 4.—Linear response of the sensor to the tip aberrations in the case of the VVC. The Y-axis shows the measurements estimated for five modes. The residuals of tilt, focus, oblique, and right astigmatisms are ∼1 nm rms within the linear range. The *blue dash line* shows the best linear fit within the linear range (from −50 nm to 100 nm rms) of the sensor. Note: The plotted data are the average of the aberrations estimated in a set of 20 measurements. See the electronic edition of the *PASP* for a color version of this figure.

upstream. Figure 5*a* is the visualization of a phasemap of the simulated turbulence applied on the DM.

3.3.3. Spectral Analysis in the Laboratory

For the laboratory test presented here, the low-order control loop is correcting 35 Zernike modes at 170 Hz, the frequency of the camera. The gain of the integrator controller is set to 0.7. We can push the gain to high values because the latency of the control loop is very low, ∼1.1 frames.

Figure 5*b* shows the correction phasemap computed by the LLOWFS control loop corresponding to the turbulence applied in Figure 5*a*. As expected, the color map in both images is opposite to each other, i.e., the control command cancels the injected turbulence. In closed-loop operation, the final command applied to the DM is the sum of these two phasemaps.

The frequency of the LLOWFS (170 Hz) is much higher than the maximum frequency resolved by the minimal exposure time of the science detector HiCIAO (<0.5 Hz for an exposure time of 2 s). So to have a meaningful evaluation of the residuals in open- and closed-loop, we will analyze them in two temporal bands:

1. 0–0.5 Hz : corresponds to slow varying frequency components temporally resolved by the science camera, i.e., the dynamical contribution of the turbulence in the science images of HiCIAO.

2. 0.5–85 Hz : corresponds to the faster motions resolved by the LLOWFS, but averaged by the exposure time of the science

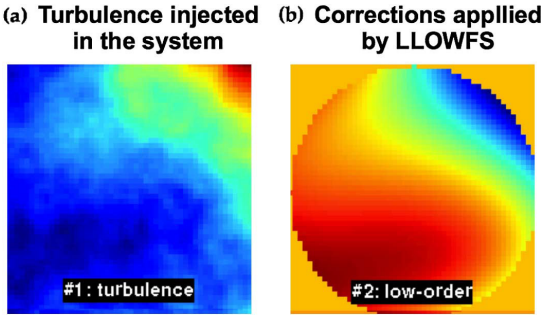

FIG. 5.—(*a*) The figure shows one phase map of the dynamic turbulence injected into the system (on the DM) and (*b*) the corrections computed using the LLOWFS in the laboratory. During closed-loop operation of the LLOWFS, the final command that is being sent to the DM is the sum of these phasemaps. See the electronic edition of the *PASP* for a color version of this figure.

camera, i.e., the static contribution of the turbulence and the vibrations in the science images.

Figure 6 presents a temporal measurement of the open- and closed-loop residuals for 35 Zernike modes. These measurements (*red lines*) are filtered by a moving average of 2 s to match the minimal exposure time of HiCIAO (*black lines*). In closed-loop operations, the stability of the residuals improved noticeably for all the modes.

Figure 7 summarizes the open- and closed-loop residuals for all 35 Zernike modes. We obtained a reduction by a factor of 30–500 (median of 200) on all the modes for the low frequencies (<0.5 Hz), leaving only subnanometer residuals. For the higher frequencies (>0.5 Hz), the factor of improvement is only between 3 and 12 (median of 5), because it is dominated by the vibrations that are not corrected by the controller. These vibrations, mostly coming from the resonance at 60 Hz of a Stirling cooler, are introduced by mechanical motions of the optical elements on the bench. In fact, the vibrations above 10 Hz are actually amplified by the overshoot of the controller. The pointing residuals for open- and closed-loop sampled at 0.5 Hz are about $10^{-2}\ \lambda/D$ rms (0.8 mas) and a few $10^{-4}\ \lambda/D$ rms (0.02 mas), respectively.

The high speed of the LLOWFS helps us to analyze the vibrations induced either by mechanical (cryo-coolers, motors, etc.) or environmental (telescope structure due to wind-shaking) factors. In order to analyze the spectral distribution, we study the Power Spectral Density (PSD) of the residuals. The PSD is calculated as the square modulus of the Fourier transform of the residuals. A Welch smoothing is performed on the PSD to reduce the noise. Figure 8 presents the PSDs of the open- and closed-loop data of only the tilt mode in the laboratory. The improvement is about two orders of magnitude at 0.5 Hz while high frequencies >10 Hz are slightly amplified.

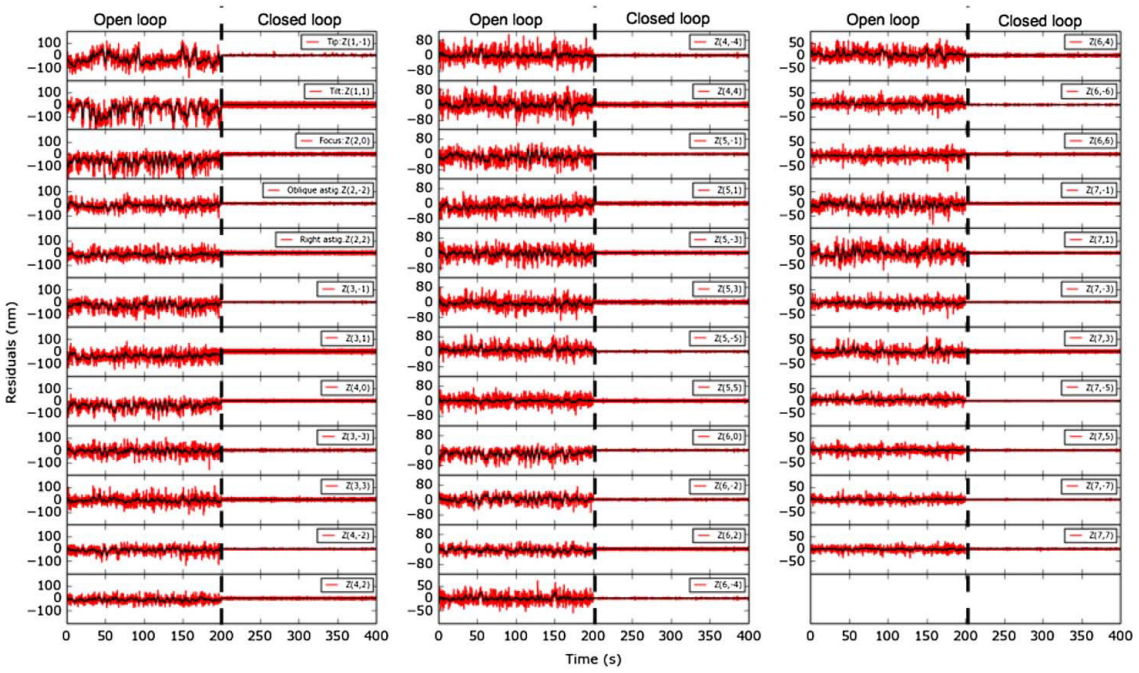

FIG. 6.—Residuals in open- and closed-loop for 35 Zernike modes obtained in the laboratory with dynamic turbulence. The *red lines* are the raw residuals while the *black lines* are the moving average of the residuals using a 2-s window. Figure 7 quantifies the open- and closed-loop residuals for the measurements presented here. See the electronic edition of the *PASP* for a color version of this figure.

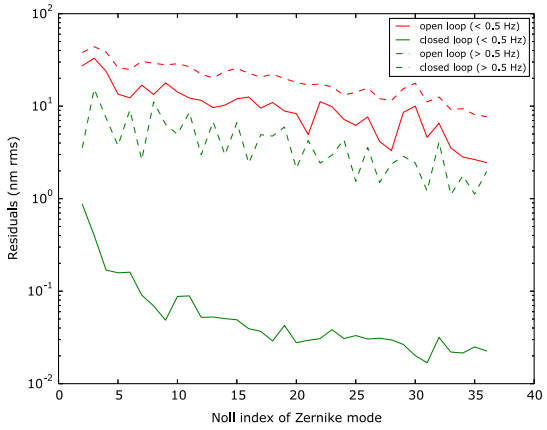

FIG. 7.—Open- and closed-loop residuals for 35 Zernike modes corrected under the laboratory turbulence. The correction at low frequencies is about two orders of magnitude, leaving subnanometer residuals for all the modes. See the electronic edition of the *PASP* for a color version of this figure.

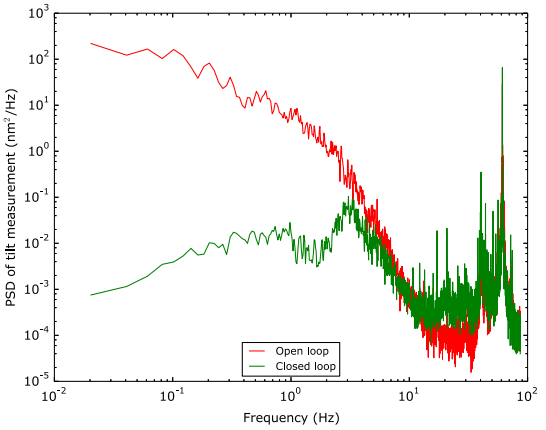

FIG. 8.—PSD of the open- and closed-loop for the tilt aberration under the laboratory turbulence. Significant improvement is visible in closed-loop operation at frequencies <3 Hz. The vibrations beyond 10 Hz are amplified due to the overshoot of the controller. See the electronic edition of the *PASP* for a color version of this figure.

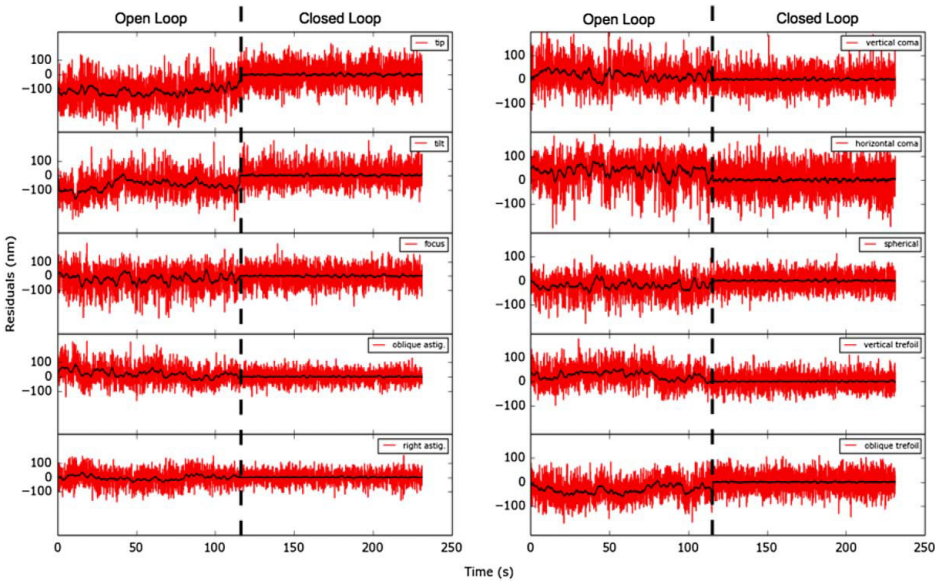

FIG. 9.—On-sky open and closed-loop residuals for 10 Zernike modes for the science target Epsilon Leonis. The *red lines* are the raw residuals whereas the *black lines* are the moving average with a 2-s window. Fig. 10 quantifies the residuals presented here. Note: The open-loop is the post-AO188 raw residuals and the amplitude variations of the residuals are sometimes outside of the linear range of LLOWFS, which cause the underestimation of their measurement. See the electronic edition of the *PASP* for a color version of this figure.

We have yet to identify the source of vibrations occurring beyond 10 Hz, which are probably due to optical elements vibrating inside the instrument. These oscillations are for now beyond the bandwidth of the low-order wavefront controller and therefore amplified by its overshoot. We are currently optimizing this control loop with a LQG controller to correct for the vibrations of the telescope and the instrument. The LQG, based on a Kalman filter, uses the real-time low-order telemetry to calculate a model of the disturbance (pointing errors, turbulence, and vibrations) and predicts the best correction to apply. Further discussions of LQG implementation on SCExAO will be the focus of a future publication.

3.3.4. Spectral Analysis On-Sky

After having tested the LLOWFS in the laboratory conditions, we analyzed its performance during an on-sky engineering run in 2015 April. The results presented here were taken on the science target Epsilon Leonis ($m_H = 1.23$). In this case, AO188 closed the loop on 187 modes providing a Strehl ratio of $\sim 40\%$ (500 nm rms wavefront error) in H-band. The LLOWFS then closed the loop on this wavefront residuals at 170 Hz with 10 Zernike modes. Since the gain of the loop is tuned manually at present, a conservative gain of 0.05 is used for this demonstration to ensure the stability of the closed-loop operation.

Figure 9 presents the on-sky open- and closed-loop residuals. Similar to Figure 6, the results are smoothed by a moving average using a window of 2 s to match the minimal exposure time of HiCIAO. The improvement in the closed-loop residuals is visible in the on-sky data. However, the residuals are more disturbed by vibrations, and hence are noisier than those collected in the laboratory.

The same analysis as the one explained in § 3.3.3, i.e., separating low frequencies below 0.5 Hz resolved by HiCIAO and the high frequencies above 0.5 Hz averaged by HiCIAO, was performed on the on-sky data and is presented in Figure 10. For low frequencies, we obtained a reduction by a factor of 2.5 to 4.4 (median of 3.1) for all the modes, while for the higher frequencies, closing the loop corrected the residuals by a factor of 1.2 only. This is expected due to the small gain value of the integrator controller. However, we demonstrate that the slow varying pointing errors are reduced down to a few $10^{-3}\ \lambda/D$ rms (0.15 mas).

In Figure 11, we present the on-sky PSD for the open- and closed-loop for the tilt aberration only. The profile of the disturbance is different from the laboratory experiment presented in Figure 8. A new vibration around 6 Hz, due to the telescope structure, appeared in the on-sky PSD. The vibration at 60 Hz was reduced because the Stirling cooler causing it was removed from the instrument. Moreover, the shape of the

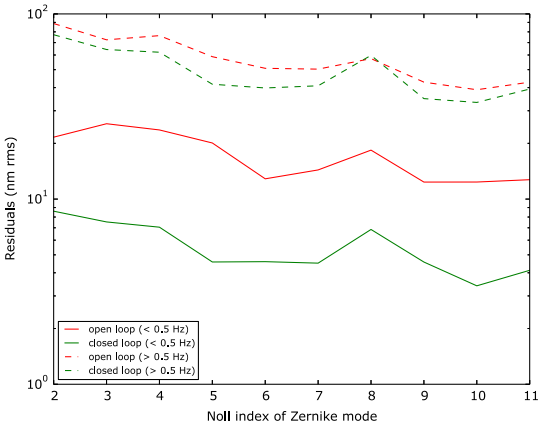

FIG. 10.—Open- and closed-loop residuals obtained on-sky for 10 Zernike modes. The correction provides a significant improvement at low frequencies but slightly amplifies the higher frequencies. See the electronic edition of the *PASP* for a color version of this figure.

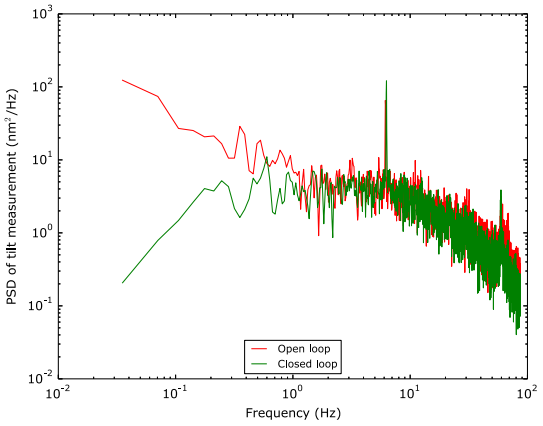

FIG. 11.—On-sky PSD of the open- and closed-loop presented for the tilt aberration only. A telescope vibration around 6 Hz appeared during the on-sky operation. In closed-loop, an improvement can be noticed at frequencies <0.5 Hz. Due to the effects of the nonlinearities in LLOWFS response, the real amplitude of the residuals are underestimated, causing the slope of the PSD to appear smaller than the one obtained in the laboratory. See the electronic edition of the *PASP* for a color version of this figure.

pointing errors is different from the turbulence generated in the laboratory. Indeed, the general slope of the PSD is smaller than a typical Kolmogorov distribution. The amplitude of the variations are sometimes larger than the linear range of the LLOWFS ($\pm$170 nm rms on the wavefront), which causes an underestimation of the real amplitude and a modification of the shape of the PSD. Due to a smaller gain value, the LLOWFS could not correct for the vibrations occurring beyond 0.5 Hz, but the PSD shows a significant improvement below that frequency. Figure 11 summarizes the residuals in open- and closed-loop. However, because of the amplitude of the variations outside of the linear range, the values in the figure are probably underestimated.

3.4. Processed Science Frames

In this section, we present the impact of the tip-tilt and other low-order residuals on the frames acquired by the SCExAO's internal NIR camera. Figure 12 presents the standard deviation per pixel in a cube of 1000 science frames (2 ms of integration time) for open- and closed-loop, in the laboratory (Fig. 12*a*) and on-sky for Epsilon Leonis (Fig. 12*b*), Aldebaran (Fig. 12*c*), and Altair (Fig. 12*d*). These images show lower standard deviation for closed-loop images (hence darker than the open loop images) and a better centered beam behind the VVC in closed-loop. However, for the target Epsilon Leonis, the coronagraph was not centered perfectly when the reference frame was acquired.

These images were obtained without the correction of high-order modes by the PyWFS. The LLOWFS in closed-loop only stabilizes the beam upstream of the VVC, without showing any significant contrast improvement in the absence of an ExAO loop. Therefore, the on-sky contrast enhancement of the VVC cannot be evaluated with these results.

4. LLOWFS INTEGRATION WITH THE HIGH-ORDER PYRAMID WAVEFRONT SENSOR

The final goal of the LLOWFS is to work in close interaction with a high-order wavefront sensor like PyWFS to correct for the noncommon path and chromatic errors occurring between the imaging and wavefront sensing channels. The control of noncommon path aberrations is essential because the PyWFS is using the visible light while the coronagraph uses the NIR light. Also, the PyWFS is not sensitive enough to low-order modes, and leaves a part of them uncorrected. So these uncorrected aberrations (static and dynamic) create unwanted stellar leakage around the coronagraphic mask in NIR. We integrated the LLOWFS with PyWFS to address these noncommon path and chromatic errors.

4.1. Configuration

SCExAO's high-order PyWFS, currently under development, is capable of controlling $\sim$1600 modes at 3.6 kHz. For the results presented in this article, we used an earlier version of the PyWFS running at 1.7 kHz and correcting only tip-tilt.

In this preliminary setup, PyWFS is the only system communicating with the DM. So instead of sending commands to the DM, the LLOWFS uses the differential pointing system to offset the zero-point of the PyWFS. Figure 13 presents the flowchart

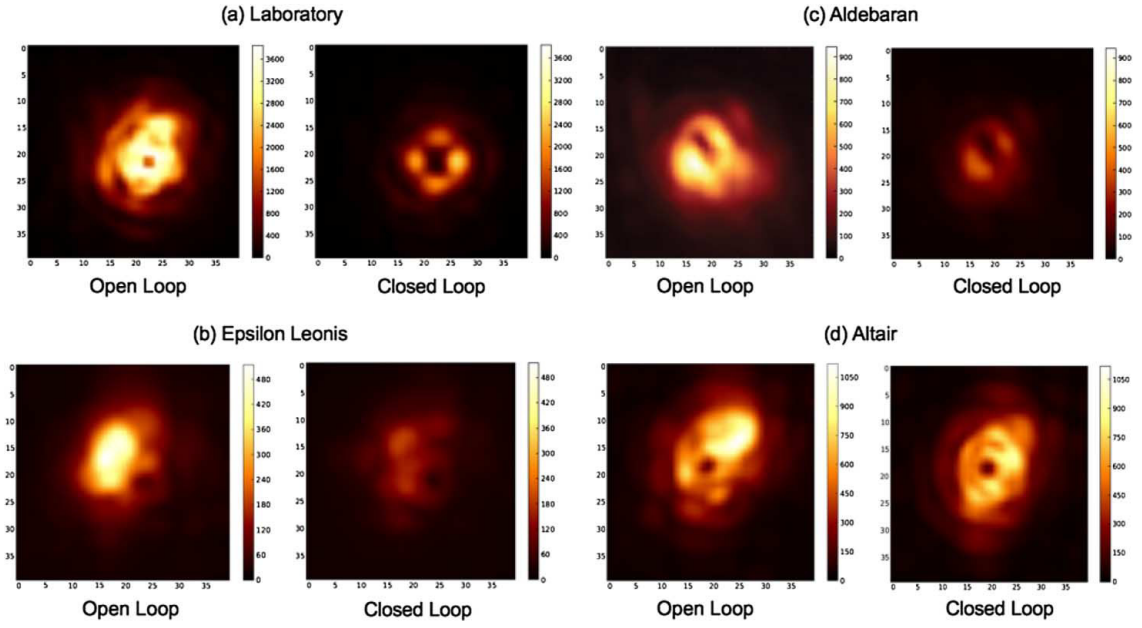

FIG. 12.—Comparison of the standard deviation of the intensity for 1000 frames of the NIR camera (*a*) laboratory, (*b*) science target Epsilon Leonis ($m_H = 1.23$), (*c*) science target Aldebaran ($m_H = -2.78$), and (*d*) science target Altair ($m_H = 0.10$). Note: Each set of open- and closed-loop images are of same brightness scale. Closed-loop images are expected to be darker than the open-loop images. Black spot at the middle of all the frames is the metallic dot at the center of the VVC to mask its central defects. See the electronic edition of the *PASP* for a color version of this figure.

of the LLOWFS integration inside the high-order control loop. The blue arrow shows the first regime described earlier in § 3.1 (cf., Fig. 2), where LLOWFS sends commands directly to the DM. The red arrows describe the configuration of the second regime where the high-order loop corrects for tip-tilt aberrations in visible and the low-order loop send commands to the differential pointing system to compensate for chromatic errors in IR.

4.2. On-Sky Demonstration

We pointed the telescope to the variable star χ Cyg ($m_H = -1.1$ during this observation). AO188 closed the loop on 187 modes with a seeing of $0.8''$ at 1.6 μm. The PyWFS closed its loop only on tip-tilt in the visible with a 1.7 kHz loop speed. The PyWFS was not optimized at this point, and hence provided only a partial correction of tip-tilt modes.

Similar to the first configuration explained in § 3.1, the LLOWFS first acquired a response matrix in order to measure the noncommon path errors. The on-sky reference is moved in x and y with an angle of 1.5 mas to obtain the calibration frames for differential tip and tilt. Using this response matrix, we closed the LLOWFS loop with a gain value of 0.03. A small gain was used because of the slow response of the piezo driver, controlled only up to 5 Hz. Figure 14 shows the successful loop closure of the PyWFS and the LLOWFS. Once again, the data presented here are smoothed to simulate an exposure time of 2 s. When PyWFS loop is closed, we see a slight improvement in the stability, but a significant amount of noncommon path residuals are still visible. These differential errors are improved when low-order loop is closed.

Table 1 summarizes the open and closed-loop residuals for high- and low-order control loops. Once again, we analyzed the data at two different spectral bands. This table shows that we have achieved a factor 3–4 improvement in correcting differential tip-tilt residuals with the gain of 0.03 for the slow varying frequencies. As expected, the improvement for the higher frequencies is not significant due to the small gain used.

Due to the fact that the variations are larger than the linear range of the LLOWFS, the residuals in Table 1 are probably underestimated again. Even in such circumstances, closed-loop pointing residuals are only about 6×10^{-3} λ/D (0.23 mas) when the dataset is sampled at the frame rate of the science camera (0.5 Hz).

We present the on-sky PSD of the high- and low-order integrated control loops for the differential tip aberration in Figure 15. Compared to Figure 11, the fast high-order control loop has diminished the telescope vibrations previously noticed at 6 Hz. When we close the loop using the LLOWFS, we observe a significant reduction of the residual turbulence for low

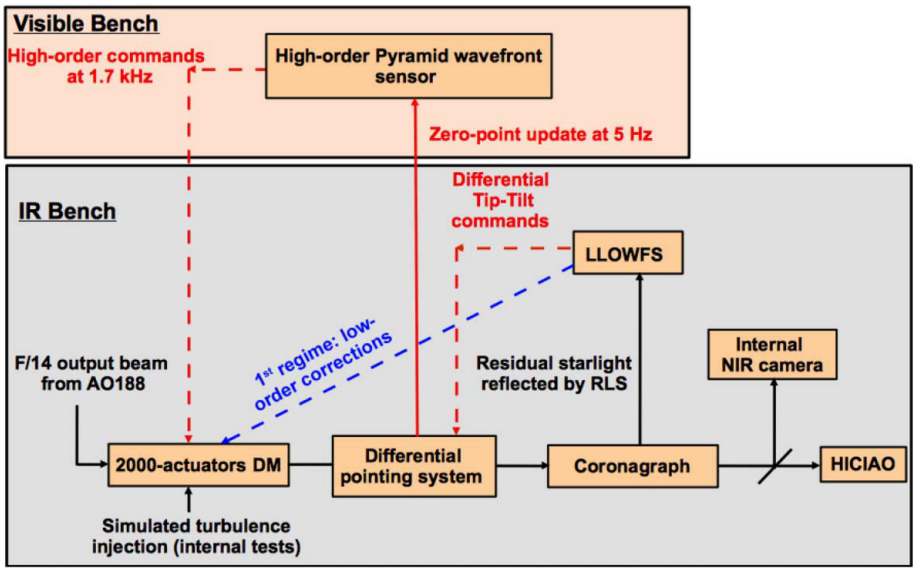

FIG. 13.—Flowchart of the LLOWFS functioning in two configurations on SCExAO. The *black arrows* depict the common flow of the low-order control loop in both regimes. Configuration 1 (*blue arrow*) is when the LLOWFS is used directly with the DM to correct for the low-order aberrations as presented in § 3.1. Configuration 2 (*red arrows*) is when LLOWFS, after sensing differential tip-tilt errors in IR channel, updates the zero-point of the PyWFS using a differential pointing system. To compensate for the beam shift in the visible channel, the high-order loop commands the DM to correct for the chromatic errors. See the electronic edition of the *PASP* for a color version of this figure.

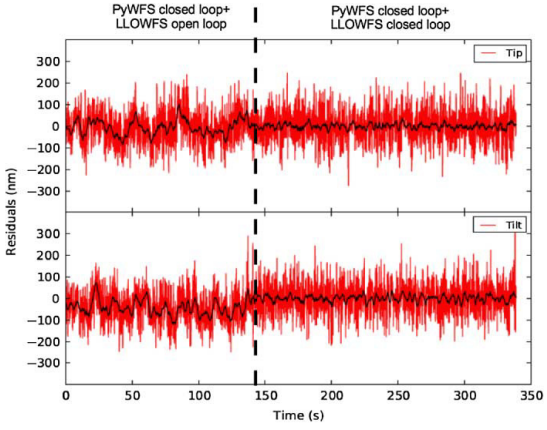

FIG. 14.—On-sky open- and closed-loop residuals of low-order control integrated in the high-order corrections of post-AO188 wavefront residuals. The black data are the moving average of residuals with 2-s window while the red data are the raw residuals. When the low-order loop is open then the high-order loop is correcting the pointing errors only in the visible leaving chromatic errors uncorrected. These chromatic errors are significantly reduced when the loop is also closed using the LLOWFS. Table 1 summarizes low-order residuals for the differential tip-tilt modes. (science target: χ Cyg.) See the electronic edition of the *PASP* for a color version of this figure.

frequencies (<0.5 Hz). In closed-loop, an overshoot between 1 and 2 Hz is also visible. This is due to the mismatch between the frequency of the sensor (170 Hz) and the frequency of the actuator (5 Hz). A gain of 0.03 actually corresponds to a gain of 1 at the speed of the actuator, which explains the overshoot.

4.3. Limitations with the Initial Setup

The performance of the LLOWFS with its preliminary integration with the PyWFS was constrained due to several factors.

1. Due to the slow response of the piezo driver (every 0.2 s), the LLOWFS could not control tip-tilt aberrations faster than 1 Hz. In the current configuration, we updated the differential pointing system by replacing the control of the tip-tilt from the piezo-driven dichroic to a tip-tilt mirror which is used for the modulation of the PyWFS. This will increase the loop rate up to 100 Hz.

2. Using either the dichroic or the tip-tilt mirror, the low-order control is limited to only tip and tilt modes. To correct other low-order aberrations as well and to improve the speed, we are currently upgrading the way the LLOWFS interacts with the PyWFS. The LLOWFS will send its corrections directly to the PyWFS that will then overwrite its reference point to compensate for these corrections with the DM.

TABLE 1
ON-SKY OPEN- AND CLOSED-LOOP RESIDUALS OF DIFFERENTIAL TIP-TILT WITH THE LOW-ORDER LOOP INTEGRATED WITH THE HIGH-ORDER LOOP

		Low freq. (<0.5 Hz) (Resolved in HiCIAO)		High freq. (>0.5 Hz) (Averaged in HiCIAO)	
Mode	Unit	Open-loop	Closed-loop	Open-loop	Closed-loop
Tip	nm	26.1	9.4	144	142
	λ/D	1.6×10^{-2}	5.9×10^{-3}	9.0×10^{-2}	8.8×10^{-2}
	mas	0.66	0.24	3.6	3.6
Tilt	nm	36.3	9.3	170	166
	λ/D	2.3×10^{-2}	5.8×10^{-3}	10.6×10^{-2}	10.4×10^{-2}
	mas	0.91	0.23	4.3	4.2

NOTE.—The correction is only significant for low frequencies.

3. The PyWFS, in its initial stage, corrected only tip-tilt in the visible, which could not provide significant improvement for LLOWFS in the IR channel. Hence, the LLOWFS performance in both configurations was dominated by the uncorrected higher order modes.

5. LLOWFS COMPATIBILITY WITH CORONAGRAPHS

The LLOWFS is compatible with a family of small IWA PMCs. Similar closed-loop laboratory performance has been obtained for the FQPM and the 8OPM coronagraphs as demonstrated for the VVC in § 3.3.3. Detailed closed-loop performance analysis of the LLOWFS with different PMCs is intended for the future publication.

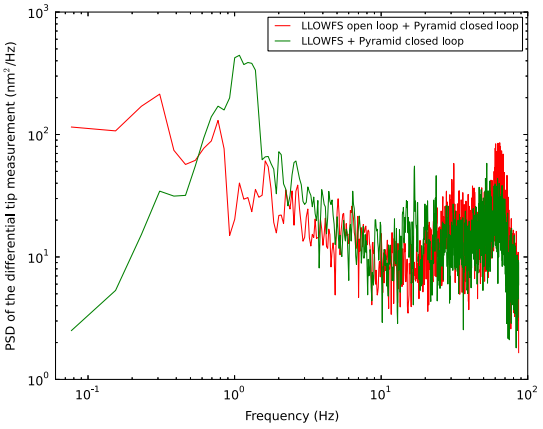

FIG. 15.—On-sky open- and closed-loop PSD of the differential tip aberration in case of the PyWFS integration with the LLOWFS. Closing the loop with the PyWFS reduces the telescope vibrations at 6 Hz shown in Fig. 11. The low-order correction provides significant improvement at frequencies <0.5 Hz and an overshoot around 1 Hz because of the difference in the sensing (170 Hz) and the correction (5 Hz) frequency. See the electronic edition of the *PASP* for a color version of this figure.

However, for coronagraphs such as the PIAA using an amplitude mask, the LLOWFS sensing capability depends on the size of the FPM. An amplitude mask bigger than the PSF core blocks most of the starlight and diffracts only a small fraction of it in the reimaged pupil plane. LLOWFS, in that case, does not get enough starlight photons, and hence cannot provide an optimal solution. However, we have closed the loop with PIAA and shaped pupil with an opaque binary FPM about half of the size of the PSF in the laboratory. For this type of coronagraph, the CLOWFS would be a more efficient wavefront sensor. However, it requires some hardware changes on SCExAO that will not be compatible with the PMCs.

A way to also make LLOWFS efficient with the amplitude masks is to use a conic-shaped FPM that diffracts the starlight in a ring around the pupil in the Lyot plane. Such a mask provides an optimal number of photons for LLOWFS independent of the size of the mask. We have tested this solution with an achromatic phase-shifting focal plane mask (AFPM, Newman et al. [2014]), which is based on a diffractive optical filtering technique scaling the size of the FPM linearly with the wavelength. This mask has a cone structure at its center with an angle optimized for the residual starlight to fall within the reflective zone of the RLS. The testing of AFPMs with PIAA and shaped pupil are currently ongoing on our instrument and the performance of the low-order correction in the laboratory and on the sky will be discussed in future publications.

6. CONCLUSION

Small IWA phase mask coronagraphs, which enable high-contrast imaging at small angular separations, are extremely sensitive to tip-tilt errors. It is crucial to decrease these effects using all the rejected starlight available, which is typically discarded in a coronagraph. Hence, to overcome the consequences of wavefront aberrations at/near the diffraction limit, implementing LLOWFS-like technology is crucial to control starlight leakage around the coronagraphic mask. We have demonstrated the first successful on-sky closed-loop test of low-order corrections using LLOWFS with the vector vortex coronagraph on the SCExAO instrument.

Both in the laboratory and on-sky, we showed an improvement of the low-order slow varying residuals (<0.5 Hz),

dynamically resolved by the exposure time of the science camera HiCIAO. In the laboratory, we obtained a correction of about 2 orders of magnitude for 35 Zernike modes, while on-sky, due to the use of a small conservative gain for the controller, the improvement is only a factor of 3 for 10 Zernike modes.

We also demonstrated the capacity of the low-order control loop to be combined with the high-order loop for the correction of the noncommon path and chromatic aberrations between this high-order loop and the coronagraph. We obtained a factor of 3–4 improvement in a preliminary setup, using a slow differential pointing system. These results are expected to improve with the better integration of the low-order differential control in the high-order loop.

Corrections of high-order modes other than just tip-tilt by PyWFS should provide a Strehl ratio $>90\%$. Moreover, the implementation of a LQG control law in the low-order correction should significantly reduce the coronagraphic leakage in the IR channel. Further performance testing of the integrated control loop on-sky is scheduled for the upcoming observational nights at the Subaru Telescope. A significant enhancement in the detection sensitivity of the SCExAO instrument is expected during the future science observations.

7. FUTURE DEVELOPMENT

Future work related to the LLOWFS is focused on three areas which are envisioned to provide high contrast at small angular separation. The goals are optimal control of the low-order aberrations, point spread function calibration close to/near the IWA using low-order telemetry (Vogt et al. 2011), and interaction between speckle calibration and low-order control.

We are currently in the process of implementing a LQG controller for the LLOWFS on SCExAO. In order to improve the postprocessing of the science images, we will use the low-order telemetry of the residuals left uncorrected by the control loop to calibrate the amount of starlight leakage at small angular separations. We are also currently studying the interaction of speckle calibration with the LLOWFS especially for the correction of speckles at small IWA.

The development and the implementation of the above-mentioned technologies on SCExAO should significantly improve the contrast around the first couple of Airy disks of the star. Such advancements will allow SCExAO to detect young Jupiters (a few M_j) by a factor of ∼3 closer to their host stars than is currently possible with other ground-based ExAO systems.

Our goal is to demonstrate innovative wavefront control approaches that are central to future high-contrast systems. To maximize the performance of the coronagraphs by efficiently controlling and calibrating the wavefront at the small angular separations, we aim to search the best instrumental parameter space to combine the optimized LLOWFS control with the PSF calibration and speckle nulling. A precursor of these approaches implemented on the next-generation extremely large telescopes and future larger space missions should enable direct imaging and low-resolution spectroscopy of Earthlike planets in the HZ of M-type and F, G, K-type nearby stars, respectively.

The SCExAO team would like to thank the AO188 scientists and engineers for operating the AO system and diagnosing the issues faced during the observations. We gratefully acknowledge the support and help from the Subaru Observatory staff. This research is partly supported by a Grant-in-Aid for Science Research in a Priority Area from MEXT, Japan.

REFERENCES

Belikov, R., Lozi, J., Pluzhnik, E., et al. 2014, Proc. SPIE, 9143, 23
Beuzit, J.-L., Boccaletti, A., Feldt, M., et al. 2010, in ASP Conf. Ser. 430, Pathways Towards Habitable Planets, ed. V. Coudé du Foresto, D. M. Gelino, & I. Ribas (San Francisco: ASP), 231
Clergeon, C., Guyon, O., Martinache, F., et al. 2013, in Proceedings of the Third AO4ELT Conference, eds. S. Esposito, & L. Fini, 95
Guyon, O. 2003, A&A, 404, 379
Guyon, O., Hayano, Y., Tamura, M., et al. 2014, Proc. SPIE, 9148, 1
Guyon, O., & Martinache, F. 2013, Am. Astron. Soc. Meeting Abstracts, 221
Guyon, O., Matsuo, T., & Angel, R. 2009, ApJ, 693, 75
Guyon, O., Pluzhnik, E. A., Kuchner, M. J., Collins, B., & Ridgway, S. T. 2006, ApJS, 167, 81
Hodapp, K. W., Suzuki, R., Tamura, M., et al. 2008, Proc. SPIE, 7014, 701419-1
Jovanovic, N., Guyon, O., Martinache, F., et al. 2015, PASP, 127, 890
Kasdin, N. J., Vanderbei, R. J., Littman, M. G., Carr, M., & Spergel, D. N. 2004, Proc. SPIE, 5487, 1312–1321
Kern, B., Guyon, O., Kuhnert, A., Niessner, A., Martinache, F., & Balasubramanian, K. 2013, Proc. SPIE, 8864
Lozi, J., Belikov, R., Thomas, S. J., et al. 2014, Proc. SPIE, 9143, 22
Macintosh, B., Graham, J. R., Ingraham, P., et al. 2014, Proc. Natl. Acad. Sci., 111, 12661
Mawet, D., Serabyn, E., Liewer, K., Burruss, R., Hickey, J., & Shemo, D. 2010, ApJ, 709, 53
Mawet, D., Serabyn, E., Liewer, K., et al. 2009, Opt. Express, 17, 1902
Murakami, N., Guyon, O., Martinache, F., et al. 2010, Proc. SPIE, 7735, 33
Newman, K., Belikov, R., Pluzhnik, E., Balasubramanian, K., & Wilson, D. 2014, Proc. SPIE, 9151, 5
Poyneer, L. A., De Rosa, R. J., Macintosh, B., et al. 2014, Proc. SPIE, 9148
Petit, C., Conan, J.-M., Kulcár, C., & Raynaud, H.-F. 2009, J. Opt. Soc. Am. A, 26, 1307
Petit, C., Sauvage, J.-F., Fusco, T., et al. 2014, Proc. SPIE, 9148
Rouan, D., Riaud, P., Boccaletti, A., Clénet, Y., & Labeyrie, A. 2000, PASP, 112, 1479
Serabyn, E., Mawet, D., & Burruss, R. 2010, Nature, 464, 1018
Singh, G., Guyon, O., Baudoz, P., et al. 2014b, Proc. SPIE, 9148, 48
Singh, G., Martinache, F., Baudoz, P., et al. 2014a, PASP, 126, 586
Vogt, F. P. A., Martinache, F., Guyon, O., et al. 2011, PASP, 123, 1434

4.3 Sensor Linearity

This section further elaborates *Pub.* §3.3.1, which talks about the linearity of the sensor. I tested the linearity of four different coronagraphs with the LLOWFS on SCExAO. The VVC's linear response to the tip aberration applied in x direction is presented in *Pub.* §3.3.1. The linearity range for the VVC is measured to be about 150 nm RMS (from - 50 nm to 100 nm RMS) with crosstalks between the modes to be ~ 1 nm RMS within the linear range. This linear range, 150 nm RMS (0.1 λ/D) is actually consistent with the linearity range demonstrated for tip-tilt measurements with a FQPM in Singh *et al.* (2014). In this section, first I will explain the procedure to acquire the low-order frames for the linearity test and then I will present the linearity results obtained with the other coronagraphs of SCExAO.

In this thesis, I studied the low-order response to 35 Zernike modes for the PMCs and 15 Zernike modes for the PIAA coronagraph. The measurement of 35 Zernike modes is not the limit of LLOWFS for low-order sensing for a PMC. Due to time limitations, I could not perform more experiments to explore the highest number of Zernike mode that can be measured by the LLOWFS without getting affected by the cross coupling and aliasing of Zernike coefficients (Herrmann, 1981). However, for PIAA, the limit to correct Zernike modes is around 15.

The linearity range of the different modes on the different coronagraphs is somewhat same and the cross coupling of low-order Zernike modes with higher modes does not affect the measurements within the linearity range. However, the LLOWFS measurements obtained using the wavefront corrected by AO188 can be underestimated, because the wavefront provided by the AO is still too aberrated to stay comfortably in the linear range of the LLOWFS.

4.3.1 Procedure to measure the linearity

The procedure to perform the linearity test is explained below:

- First of all, I align the studied coronagraph by following the steps explained in §3.5.2 of Chapter 3. I record a low-order reference image using the LLOWFS camera. Then, using Eq. 2.12, I obtain the response of the sensor for each Zernike mode[1].

  In Fig. 4.1, I present the calibration frames obtained in the laboratory for (a) a VVC, (b) a PIAA and (c) a FQPM coronagraphs. For each of these coronagraphs, I acquired the response of the sensor by applying 60 nm RMS of amplitude for each Zernike mode using the DM of SCExAO. I have used these calibration frames in the rest of the chapter to demonstrate the loop closure with the LLOWFS in the laboratory.

- Prior of starting the linearity test, I created a cube of phasemap per Zernike mode with amplitudes varying between ± 150 nm rms such that the first, the middle and

[1] A procedure to calibrate the response of the sensor is explained in detail in §2.3.2 in Chapter 2.

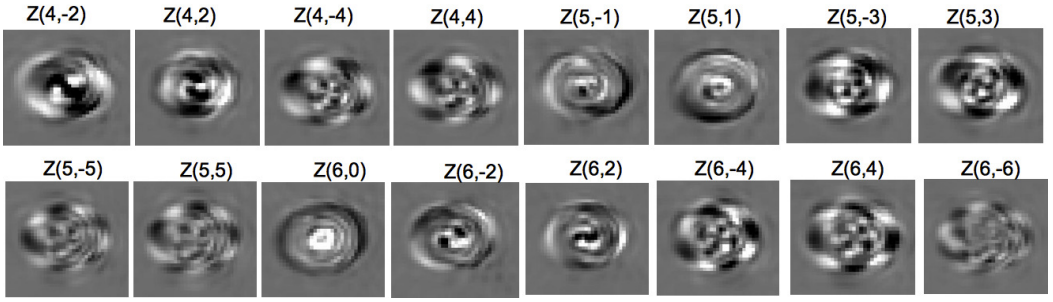

(a) VVC: 26 Zernike modes (first 10 Zernike modes are shown in Pub. Fig. 3)

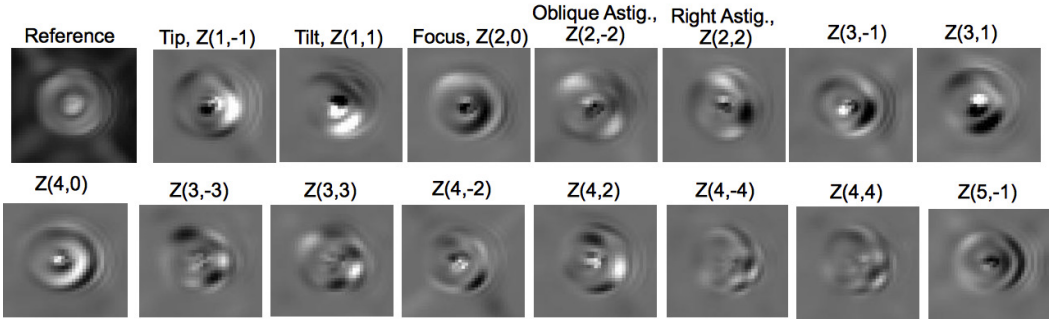

(b) PIAA: 15 Zernike modes (Reference image is in log scale.)

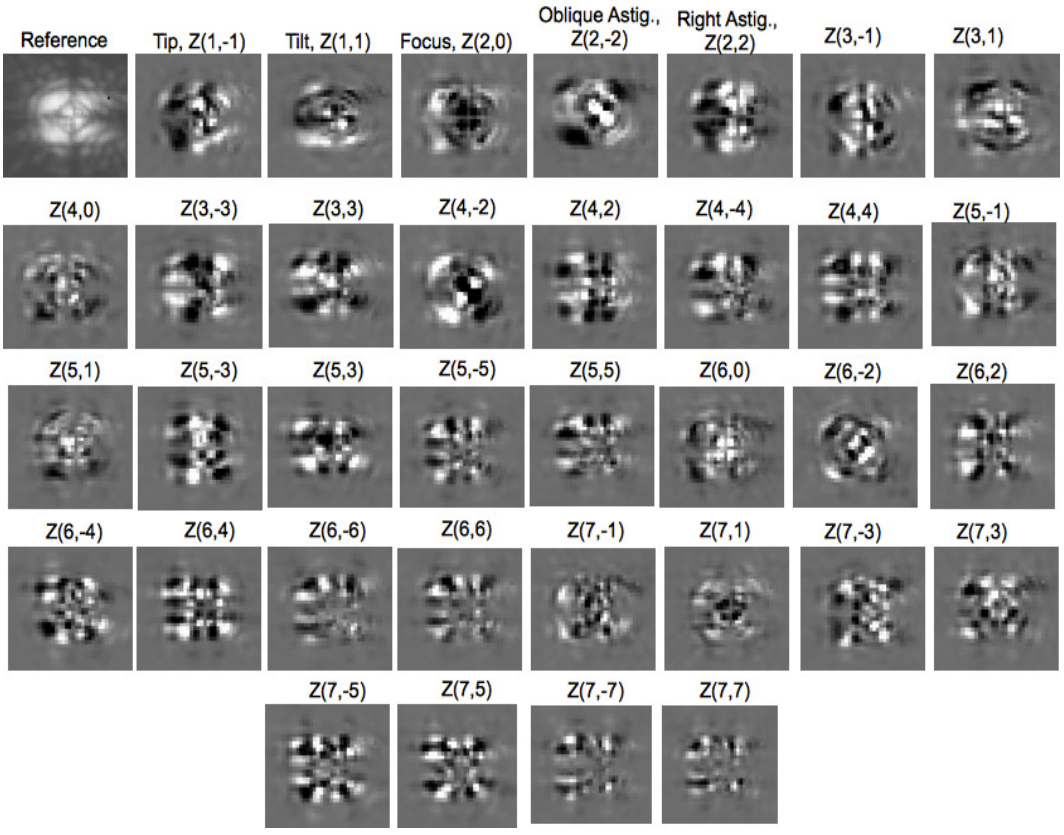

(c) FQPM: 35 Zernike modes (Reference image is in log scale.)

Figure 4.1: Response matrices up to 35 modes obtained in the laboratory for the (a) VVC, (b) PIAA and (c) the FQPM coronagraphs by applying 60 nm RMS of amplitude for each Zernike mode on the DM. *Note that all the calibration frames shown for each coronagraph are of same brightness scale.*

the last phasemaps have respectively - 150, 0 and + 150 nm RMS of error for each Zernike mode over the Subaru pupil.

This simulated phasemap in a cube is 50 × 50 pixels array such that each pixel in the image correspond to each actuator of the DM. Fig. 4.2 shows an example of simulated Zernike phasemaps.

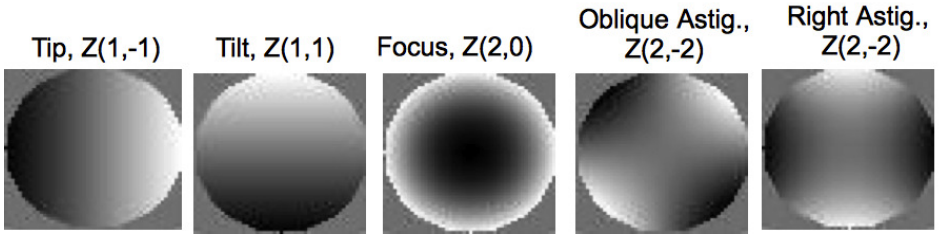

Figure 4.2: Simulated Zernike phasemap applied on the DM to perform the linearity test.

- After creating the wavefront errors with Zernike modes, I apply each phasemap of the cube of each Zernike mode on the DM and record its effect on the corresponding low-order image in another cube. Each image recorded is the average of 100 images.
- I repeat the above step 20 times, so that in the end I have 20 measurements for each amplitude of Zernike phasemaps applied on the DM on SCExAO. These 20 values helps to define the dispersion of the measurements.
- I process low-order images in *Python*. For each image of a cube, I subtract the reference image and decompose the result into a linear combination of Zernike modes using Eq. 2.11. Using the least squares method, I estimate the low-order errors in each image per cube. So in each cube, I get the measurement of the mode actuated, and also the other modes to study cross couplings. For each Zernike studied individually, I average the 20 separate measurements to get a more precise result.
- I compare the amplitude measured with the LLOWFS to the real amplitude applied on the DM. The standard deviation of difference between the two gives me the measurement accuracy of the mode studied. I also perform a linear fit within the linear range using the least squares method.

4.3.2 Results

I present the response of the LLOWFS only to the tip aberration for the PIAA, the FQPM and the EOPM coronagraphs in Fig. 4.3 and 4.4. The linearity is found to be similar than for the VVC presented in *Pub.* Fig. 4, which is 150 nm RMS (from - 50 nm to 100 nm RMS). However, all the coronagraphs have different crosstalks between modes. For the VVC, I showed in the publication that the residuals of tilt, focus and astigmatisms are ∼ 1 nm RMS within the linearity range.

However, for other coronagraphs in Fig. 4.3 and 4.4, the measurement accuracy of the sensor response to tip aberration within the linearity range is – (1) 4.1 nm RMS for the

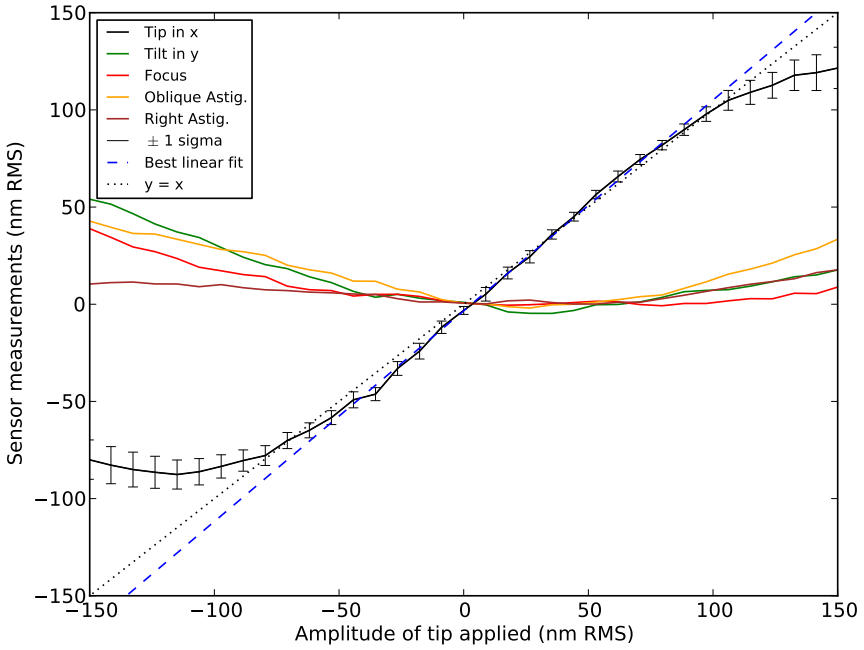

(a) PIAA coronagraph

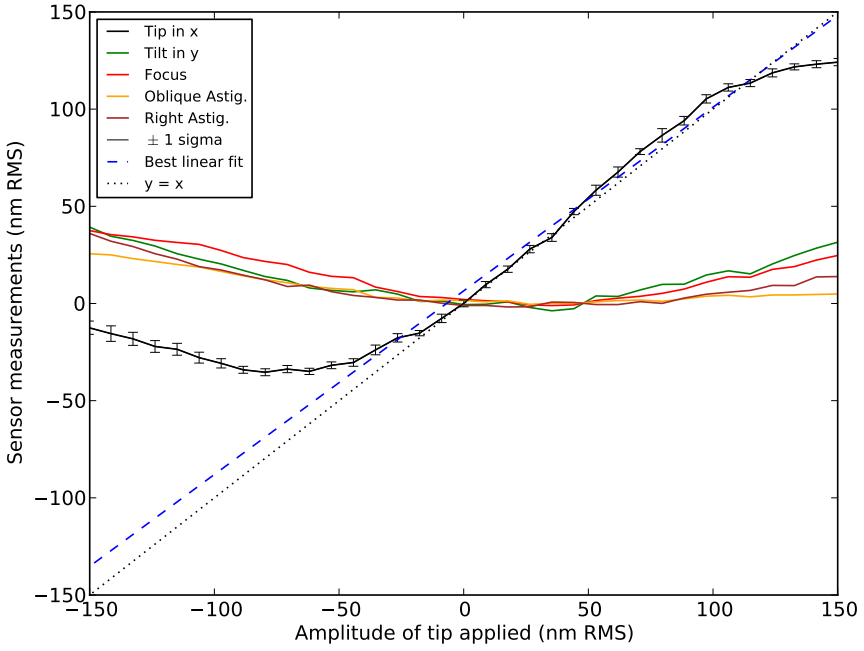

(b) FQPM coronagraph

Figure 4.3: Sensor linearity in response to tip aberration for the (a) PIAA and (b) FQPM coronagraphs. Cross coupling with other four Zernike modes are also presented. The linearity of the sensor is roughly 150 nm RMS (from - 50 nm to 100 nm RMS).

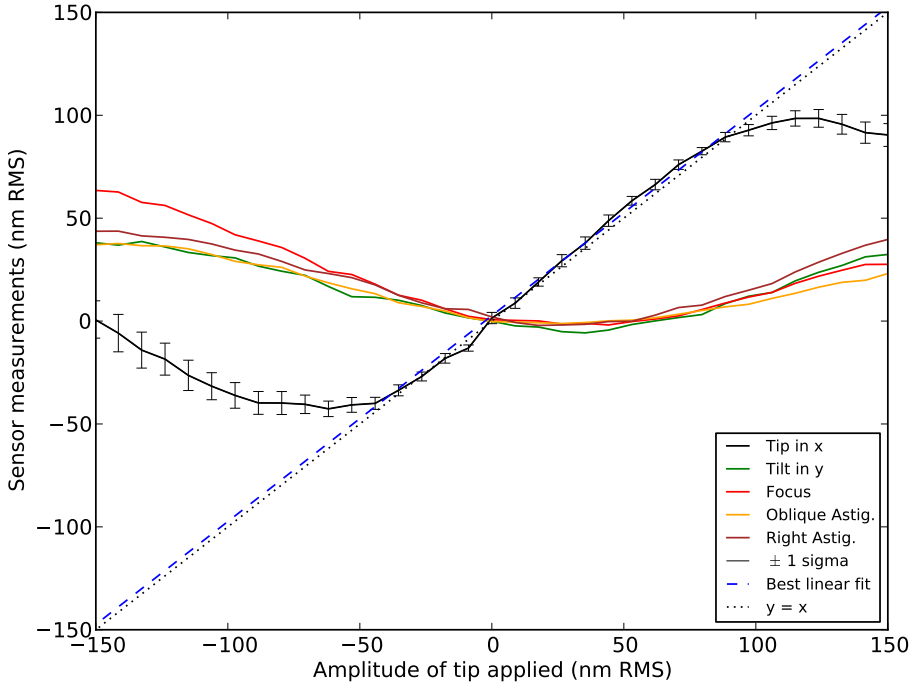

Figure 4.4: Sensor linearity in response to tip aberration for the EOPM coronagraph. Cross coupling with other four Zernike modes are also presented. The linearity of the sensor is roughly 150 nm RMS (from - 50 nm to 100 nm RMS).

PIAA, – (2) 5.7 nm RMS for the FQPM and – (3) 3.4 nm RMS for the EOPM coronagraphs.

Whereas the measurement accuracy of the sensor response to the residuals in other modes within the linearity range is – (1) ~ 46 nm RMS for the PIAA, – (2) ~ 45 nm RMS for the FQPM and – (3) ~ 47 nm RMS for the EOPM coronagraphs.

For this experiment, the tip aberration showed a strong crosstalk with other Zernike modes for all the coronagraphs. A shift in the linearity range is also noticed. I have found a similar shift in all the linearity curves of other Zernike modes for all the coronagraphs presented here. For the FQPM/EOPM coronagraphs, there is even a slight shift in the zero point of the residuals, which means that the sensor measured some residue even when there was no aberration applied.

For all the coronagraphs, this could be caused by factors such as: – (1) misalignments of the beam upstream of the FPM, – (2) surface quality of the RLSs, – (3) the amplitude of the defocus that might create this shift and– (4) may be the manufacturing defects at the center of the FPMs (which is unlikely to be a reason for the shift). After several tests with different defocus and alignments, I could not conclude on the origin of this shift. The level of crosstalk, which is in the linear range of the sensor, is tolerable and therefore in closed-loop operation with LLOWFS, the errors within 150 nm RMS should be compensated and the aberrated beam should converge back to its reference.

4.4 Closing the loop with the LLOWFS

4.4.1 Correction of Zernike modes and Turbulence

To compute the correction for the low-order aberrations to apply in close-loop operations, I follow the control loop procedure explained in Fig. 2.3 in §2.3.4. For my tests in the laboratory, I apply simulated dynamic phase errors on the DM (*Pub.* §3.3.2). For this simulated turbulence, which follows a Kolmogorov profile, I have chosen the amplitude of the turbulence as 150 nm RMS and the wind speed as 10 m/s. In Fig. 4.5 (a), I present the visualization of the phasemaps of the simulated turbulence applied on the DM.

To have the meaningful assessment of the LLOWFS performance under laboratory turbulence, I analyze the same number of data in the open- and closed-loop. To obtain the data, I run the control loop (§3.6.3) and set the gain to 0, then I record LLOWFS measurements in open-loop for some amount of time. In the next step, I chose a nominal gain value and closes the loop with it. Then, I save the closed-loop residuals measured by LLOWFS for the same amount of time than for open-loop measurements.

Figure 4.5 shows the example of the wavefront errors applied on the DM and the correction phasemap computed by the LLOWFS. (a) shows various dynamic phasemaps of the simulated turbulence. (b) shows the additional Zernike errors injected into the system (applied on top of the turbulent phase-screen) and (c) shows the combined correction phase map computed by the LLOWFS corresponding to the total error (in (a) and (b)) applied into the system. The information should be read row wise as each row corresponds to the input ((a) and (b)) and output ((c)) of a single test.

For a good correction, the color of the phasemap in (c) should be opposite of the combined phasemap in (a) and (b), which simply means that the control commands computed by the LLOWFS cancels the wavefront errors injected into the system. In this figure, I simply present the snapshots of two different ways of introducing known aberrations into the system and test the correction computed by the LLOWFS. For the first three rows in Fig. 4.5 (b), I only inject a Zernike mode with an amplitude of 100 nm RMS into the system and show the corresponding correction phasemap in (c), perfectly canceling the applied error. However, in 4^{th} and 5^{th} row, on top of the 100 nm RMS Zernike mode, I also induce the simulated turbulence with 150 nm RMS amplitude. So that the error injected into the system is the total of the phasemap in (a) and (b). In this case, the colormap of the corresponding correction phasemap in (c), is not perfectly opposite of the sum in (b) and (c) because LLOWFS corrected the low-order errors in the turbulence but could not control high amplitude errors that are outside of its linear range.

Note that the operation of applying wavefront errors on the DM and computing corrections via the LLOWFS are two different process and run independent of each other. During the closed-loop operations in the laboratory, the final command that is applied on the DM is the sum of the phasemaps in (a), (b) and (c).

4.4.2 Criteria of low-order telemetry analysis

In this and the next Chapter 5, I have performed three basic analysis with the LLOWFS open- and closed-loop residuals to characterize the performance of the low-order control

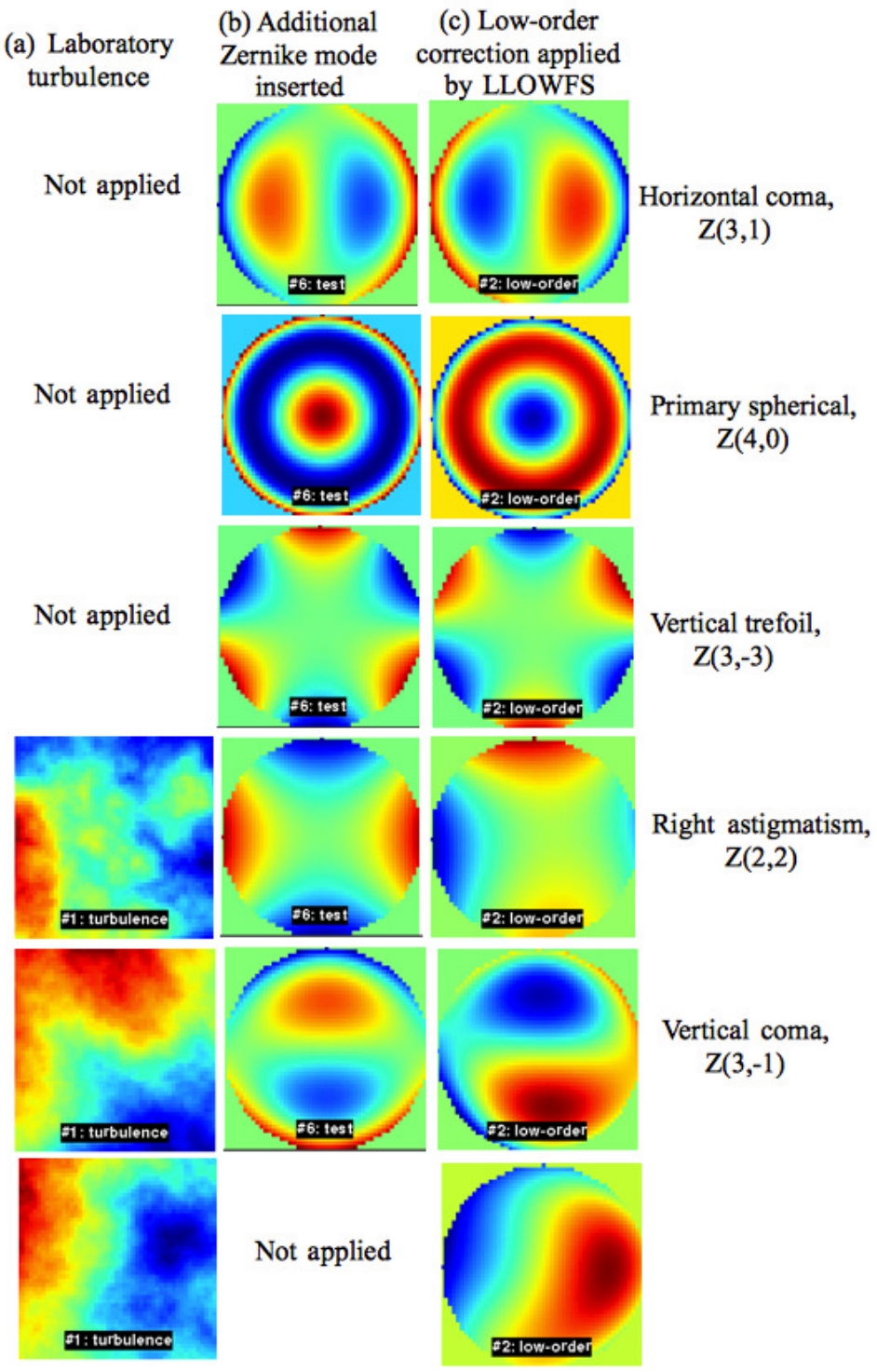

Figure 4.5: (a) Examples of the phasemaps of the simulated dynamic phase-screens applied on the DM. (b) Additional Zernike phase error inserted on top of the turbulence applied in (a). (c) The combined correction phasemap computed using the LLOWFS in the laboratory. During LLOWFS closed-loop operations, the final command sent to the DM is the sum of the phasemaps in rows of (a), (b) and (c). Note that the figure is to be read row wise as each row belongs to the input/output of a single test.

loop, which are as follows:

Temporal Measurements

I analyze the raw open- and closed-loop residuals measured by the LLOWFS. The raw data show already a reduction in the level of the amplitude of the aberrations after closing the loop. I also compute the moving average of the raw residuals using a window of 2-seconds to match the minimal exposure time of HiCIAO. The moving average shows how well the loop performs at low frequencies.

Power spectral density (PSD) analysis of the residuals

I study the PSD of the time series of the residuals in order to analyze their spectral distribution. This function, in units of residuals (here in nm) squared per hertz, is calculated as the square modulus of the Fourier transform of the residuals. A Welch smoothing is performed on the PSD to reduce the noise. This smoothing is improving the signal to noise ratio in the PSD by averaging a number of PSDs calculated over a smaller moving window. Here I choose a window of 400 points moving every 200 points. To improve even more the quality of the PSD, I apply a *Hann* windowing on every set of 400 points. I then compare the smoothed PSD of the closed-loop residuals to the PSD of the open-loop residuals to determine the cutoff frequency, the highest frequency where the low-order loop provides a significant correction.

To understand the impact of the vibrations on the residuals, I also calculate the cumulative integral of the PSD, which not only identifies the strongest vibration distinctively but also provide the direct value of the strength of the vibration. The peaks in the PSD corresponding to each vibration actually appears as steps in the cumulative integral function, with amplitudes corresponding to their powers in the residual.

The maximum value of the cumulative integral corresponds to the variance of the residual. Also, the square root of the cumulative integral, called the cumulative standard deviation provides a direct information of the standard deviation of the residuals for any sampling frequency. The last data point on the cumulative standard deviation plot corresponds to the standard deviation of the time series of the residuals.

I have used the PSDs and the cumulative integral plots to analyze the performances of the control loop, and to identify the vibrations affecting the LLOWFS performance on SCExAO.

Processing the science frames

I study the impact of the open- and closed-loop residuals on the images acquired by the internal NIR science and the LLOWFS camera. I analyze the images by computing the average and the standard deviation per pixel in a cube with 1000 science/LLOWFS frames. In the non-ExAO regime, it can be difficult to see the impact of the low-order correction on the average of a cube, because the PSF is dominated by high-order aberrations. This is why I will study the standard deviation. Indeed, images having low standard deviation will be visually darker than the images with comparatively high standard deviation. A good low-order correction will appear when the closed-loop standard deviation images are significantly darker than the open-loop standard deviation images. Also, in closed-

loop, the beam will be well centered behind the FPM.

I have analyzed the performance of the low-order loop by comparing the data using the tools described earlier. The LLOWFS maximum frequency is 170 Hz, which is much higher than the maximum frequency resolved by the minimal exposure time typically used by HiCIAO (< 0.5 Hz for an exposure time of 2 seconds). So to evaluate the results also with the point of view of the science camera, I have studied the open- and closed-loop residuals in two temporal bands.

– (1) 0 - 0.5 Hz: to analyze the slow varying frequency components temporally resolved by HiCIAO, i.e. the dynamical contribution of the turbulence in the science images of HiCIAO and,

– (2) 0.5 - 85 Hz: to analyze the faster motions of the turbulence resolved by the LLOWFS, which are in contrary averaged by the long exposures of HiCIAO. The static contribution of the turbulence and the vibrations in the science images will be addressed (85 Hz is the LLOWFS Nyquist frequency).

I will emphasize on the results obtained in the temporal band 0 - 0.5 Hz for closed-loop pointing accuracy, since it is where the loop performs the better and where it is the most critical for the science camera. However, I will also study the vibrations and their impact on LLOWFS correction in temporal band 0.5 - 85 Hz.

4.5 Spectral analysis in the laboratory

4.5.1 Closing the loop on PIAA, FQPM and EOPM coronagraphs

Figure 4.6 (a), 4.7 (a) and 4.8 (a) shows the temporal measurements of 15 Zernike modes for the PIAA and 35 Zernike modes for the FQPM and the EOPM coronagraphs respectively. After closing the low-order loop[2], the residuals average around zero for all the modes for the three coronagraphs. These figures can also be compared with the temporal measurement obtained with the VVC, which is presented in *Pub.* Fig. 6.

Figure 4.6 (b), 4.7 (b) and 4.8 (b) summarizes the open- and closed-loop residuals in two temporal bands:

– (1) For the PIAA (with a 1.8 λ/D binary mask): the reduction obtained is a factor of 14 to 110 (median 66) on all the modes for frequencies < 0.5 Hz. However, for higher frequencies, the factor of improvement is only between 2.1 and 10 (median 2.9). The pointing residuals for open- and closed-loop sampled at 0.5 Hz are about $10^{-2}\lambda/D$ RMS (1 mas) and $10^{-3}\lambda/D$ RMS (0.07 mas) respectively.

– (2) For the FQPM: at low frequencies (< 0.5 Hz) a factor of improvement of 21 to 600 (median 140) is obtained while for higher frequencies, the improvement is only in between 5 and 20 (median 10). The pointing residuals for open- and closed-loop sampled at 0.5 Hz are a few $10^{-2}\lambda/D$ RMS (2.3 mas) and a few $10^{-4}\lambda/D$ RMS (0.02 mas) respectively.

– (3) For the EOPM: improvement is in between 133 - 500 (median 220) for frequencies < 0.5 Hz and in between 1.6 and 10 (median 6.6) for frequency > 0.5 Hz. The

[2]LLOWFS camera defocus value > 15 rad RMS.

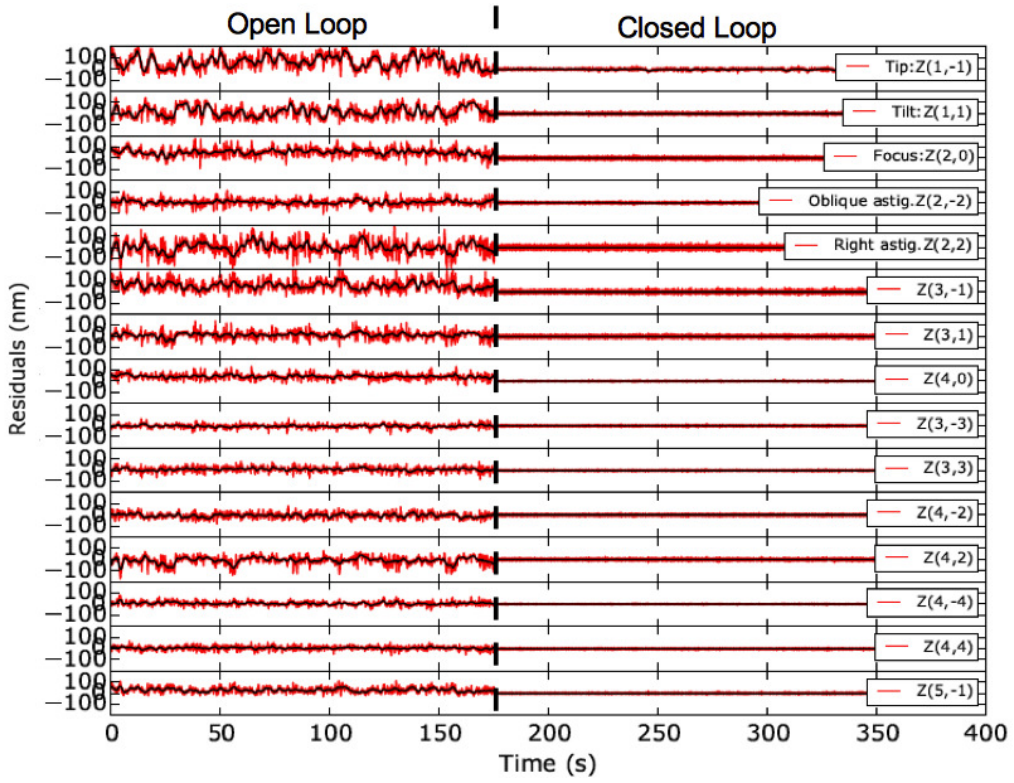

(a) Open- and closed-loop raw residuals (in red) and their moving average using a 2 seconds window (in black).

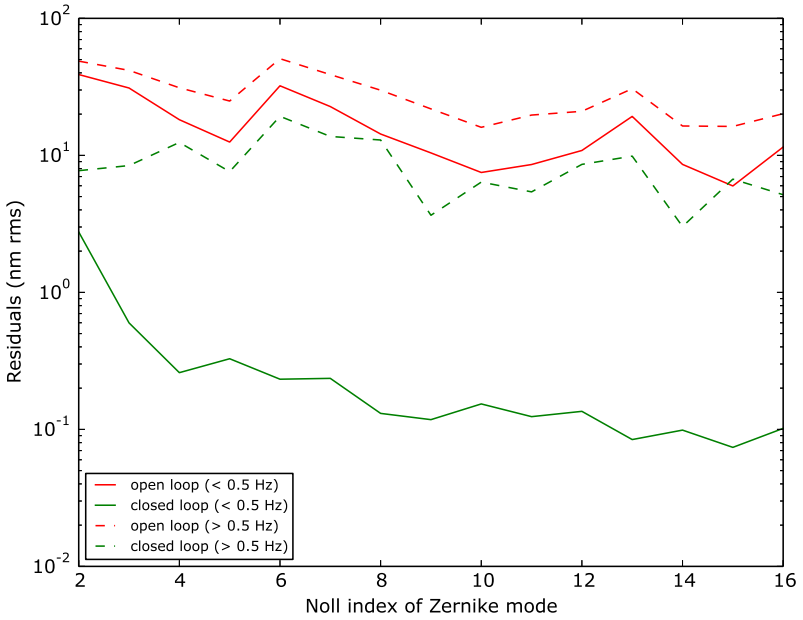

(b) Standard deviation of the residuals for each Zernike mode. The correction at low frequencies (< 0.5 Hz) is roughly one order of magnitude.

Figure 4.6: Open- and closed-loop residuals for 15 Zernike modes obtained under the dynamic turbulence applied on to the DM in the laboratory for a PIAA coronagraph. A gain of 0.7 was used for the closed-loop operation.

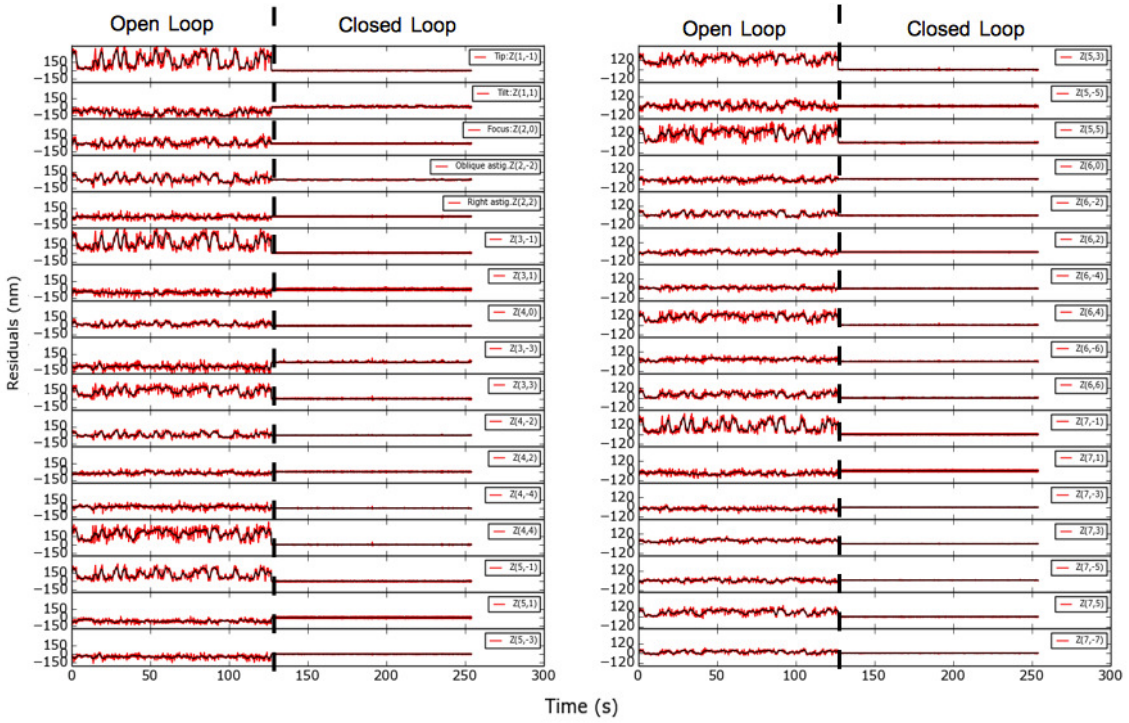

(a) Open- and closed-loop raw residuals (in red) and their moving average using a 2 seconds window (in black).

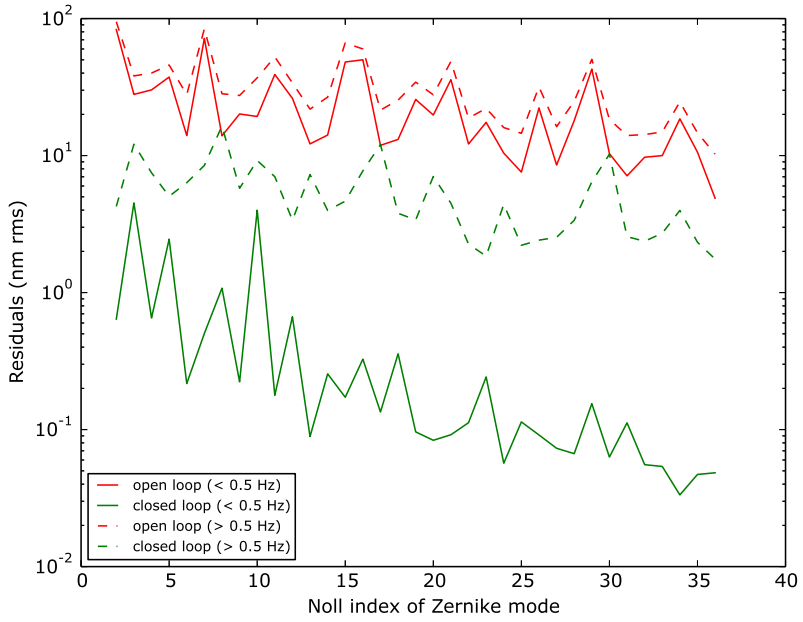

(b) Standard deviation of the residuals for each Zernike mode. The correction at low frequencies (< 0.5 Hz) is ~ 2 order of magnitude

Figure 4.7: Open- and closed-loop residuals for 35 Zernike modes obtained under the dynamic turbulence applied on to the DM in the laboratory for a FQPM coronagraph. A gain of 0.7 was used for the closed-loop operation.

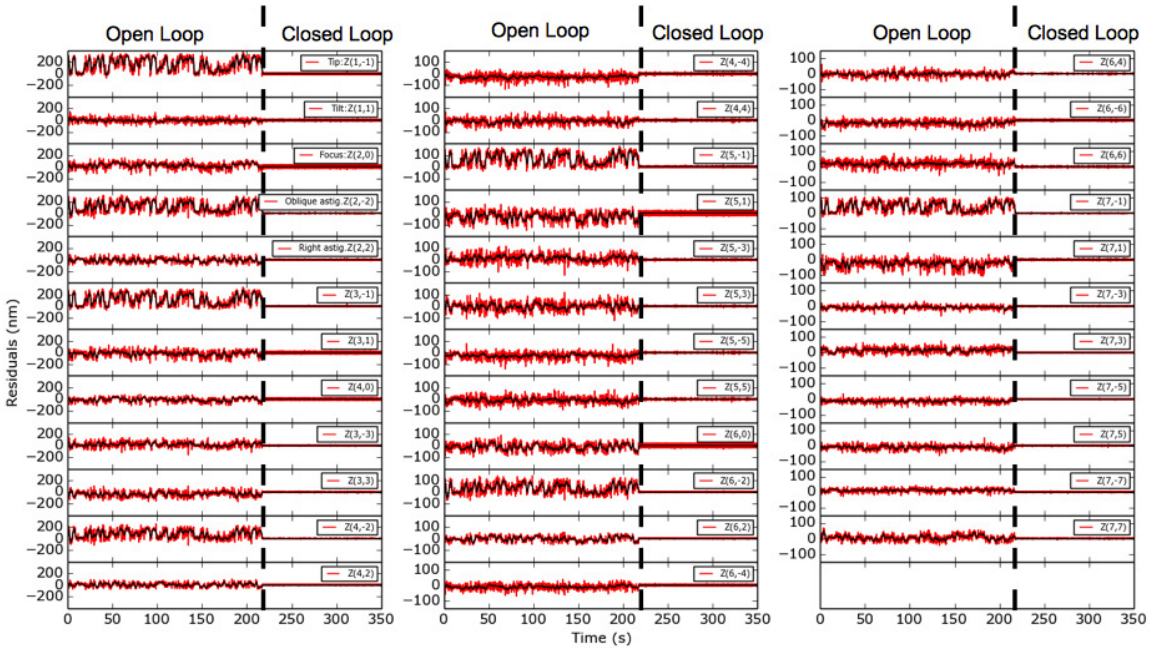

(a) Open- and closed-loop raw residuals (in red) and their moving average using a 2 seconds window (in black).

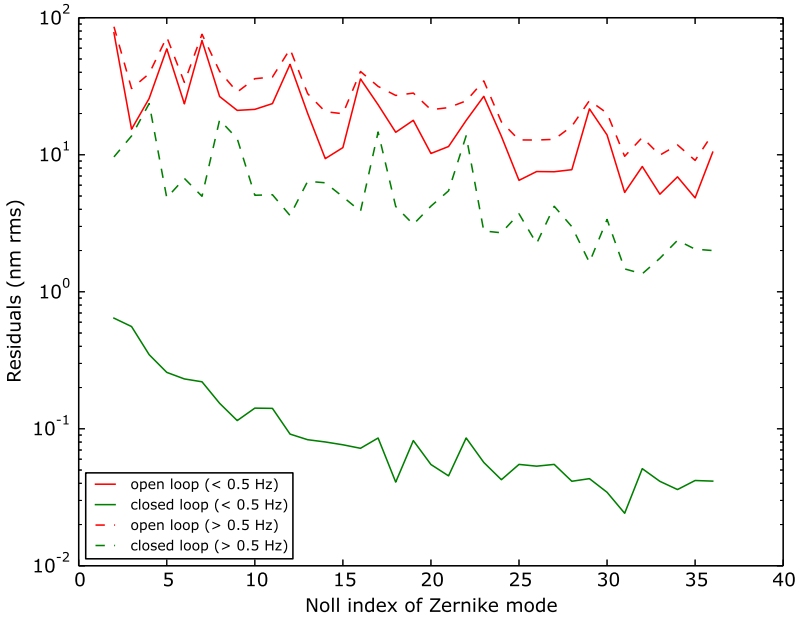

(b) Standard deviation of the residuals for each Zernike mode. The correction at low frequencies (< 0.5 Hz) is ~ 2 orders of magnitude

Figure 4.8: Open- and closed-loop residuals for 35 Zernike modes obtained under the dynamic turbulence applied on to the DM in the laboratory for a EOPM coronagraph. A gain of 0.7 was used for the closed-loop operation.

pointing residuals for open- and closed-loop sampled at 0.5 Hz are a few $10^{-2}\lambda/D$ RMS (2 mas) and $10^{-4}\lambda/D$ RMS (0.02 mas) respectively.

In Fig. 4.9 (a) and (b) and Fig. 4.10 (a) and (b), I show the PSDs for a tip aberration for the VVC, the PIAA, the FQPM and the EOPM coronagraphs. In all four PSDs, significant improvement in closed-loop is visible for frequencies < 1 Hz.

Note: The PSD presented in Fig. 4.9 (a) is the same as shown in Pub. Fig. 8. The additional information I presented in this figure is the closed-loop result using different gains. I explained in the control loop procedure in §2.3.4 that the loop has an option to put either a flat gain for all the modes or choose a modal gain. Currently for the low-order loop, we can only apply a flat gain. I tested the low-order loop with different gain values on several occasions and I obtained the optimal correction with gain values between 0.5 - 0.8. The reason I can push the gain to high values is because the latency of the control loop is very low, ~ 1.1 frames. Therefore, for all the PSD figures presented for the tests in the laboratory, I have used the gain value of 0.7. The gain higher than 0.8 created an overshoot and amplified the higher frequencies.

In PSD plots, the improvement is about two orders of magnitude at 0.5 Hz for the PIAA and three orders of magnitude for the FQPM and the EOPM coronagraphs. The high frequencies after 10 Hz are slightly amplified. The vibration at 60 Hz, which is already high in open loop, gets particularly amplified by the overshoot of the controller. The reason for the smaller corrections at high frequencies as shown in Fig. 4.6 (b), 4.7 (b) and 4.8 (b) is because of the dominating vibrations that are not corrected by the controller and are beyond its bandwidth. In closed-loop, the vibrations ≥ 10 Hz are actually amplified by the overshoot of the controller. The possible source of the vibration between 40 - 80 Hz is discussed in §4.5.2[3].

In Fig. 4.9 (b) and Fig. 4.10 (c) and (d), I present the cumulative standard deviation of closed-loop for 15 Zernike modes for PIAA and 35 Zernike modes for the FQPM and the EOPM coronagraphs. In these figures, each vibration can be seen distinctively as a step. Up to 30 Hz, all the modes have approximately the same contributions to the total wavefront errors except for the first few Zernike modes such as tip, tilt focus and astigmatisms. The amplitude of these aberrations are higher than that of the higher order of Zernike modes in the simulated turbulence. Therefore, the residuals of those modes are also higher, especially for the PIAA and the FQPM in Fig. 4.9 (b) and Fig. 4.10 (c) and contribute more to the total error. After 30 Hz, all the modes are affected by the same vibration harmonics (50 and 60 Hz for the strongest ones), with different strengths.

I also present the standard deviation of the internal NIR science and the LLOWFS camera frames for the VVC and the PIAA coronagraphs in Fig. 4.11 and for the FQPM and the EOPM in Fig. 4.12. I have taken 10 cubes (each cube has 1000 frames recorded at 170 Hz) from the internal science and the LLOWFS camera and averaged them using a window of 2 seconds to simulate the impact of the correction at low frequency resolved by HiCIAO. With 30 frames as a result in a simulated HiCIAO averaged cube, I calculate the standard deviation per pixel in this cube. As expected, the closed-loop images are darker

[3]Note that LLOWFS data for PSDs I presented here were obtained during off-sky operations with SCExAO at the Nasmyth platform. Some vibrations were introduced temporarily due to environmental factors as some of the team members were present around the instrument to work on other modules.

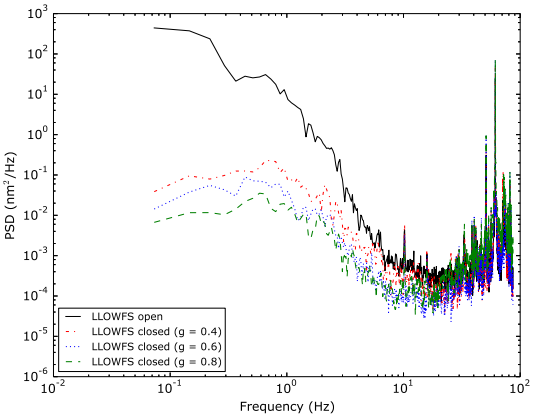

(a) Smoothed PSD of tip aberration for the VVC for different gains

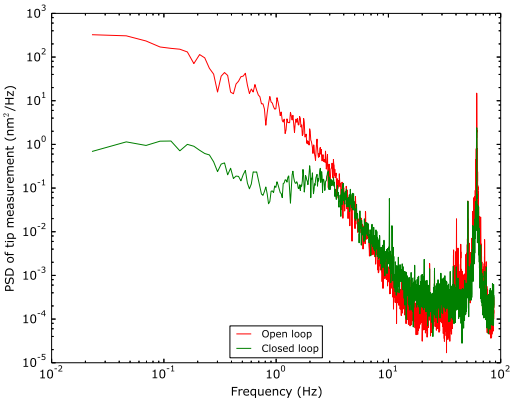

(b) Smoothed PSD of tip aberration for the PIAA for a gain of 0.7

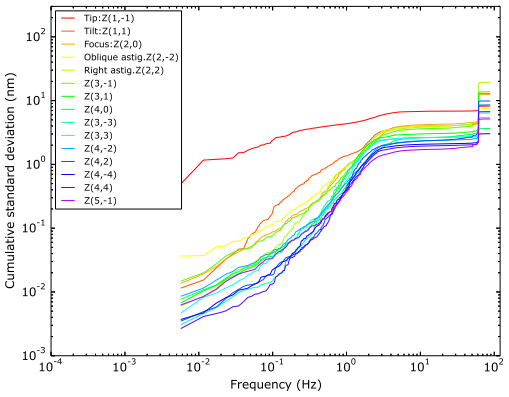

(c) Cumulative standard deviation in closed-loop

Figure 4.9: (a) The power spectral density of tip aberration for a VVC, same as in *Pub.* Fig. 8 but here I presented the closed-loop for different gain values. (b) The PSD for tip aberration and (c) the cumulative standard deviation for 15 Zernike modes are presented for a PIAA coronagraph. The results are obtained under laboratory turbulence.

than the open-loop images which means that the standard deviation for closed-loop images are lower than the one in the open-loop. These images are at the same brightness scale, saturating the open-loop images. The information presented here is not the comparison of the shape of the PSF in open- and closed-loop but the correction quality provided by the LLOWFS.

Figure 4.13 compares the mean of the open- and closed-loop images of the internal NIR science camera for the four coronagraphs. These frames are the average of 10,000 frames. The correction by LLOWFS is visible in the closed-loop images of all the coronagraphs. After closing the loop, the PSFs are well aligned upstream of the FPM and converge back to their reference. For PIAA, the PSF was slightly misaligned prior of starting the closed-loop operation with LLOWFS. Hence, the starlight leakage due to misaligned PSF

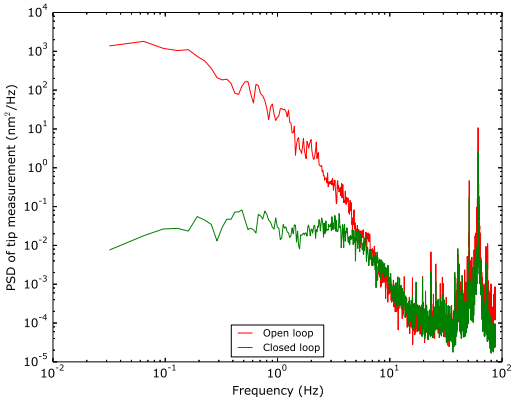

(a) Smoothed PSD of tip aberration for the FQPM for a gain of 0.7.

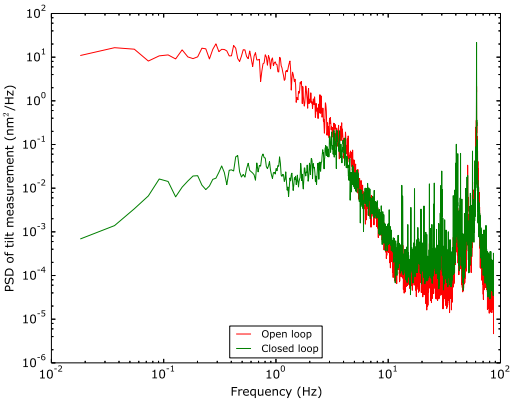

(b) Smoothed PSD of tip aberration for the EOPM for a gain of 0.7.

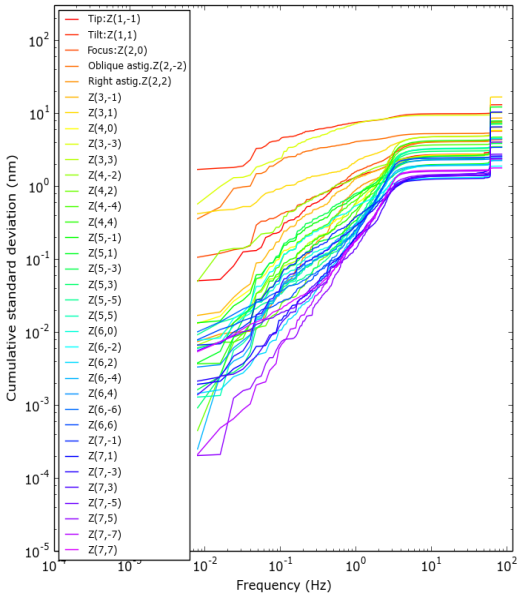

(c) Cumulative standard deviation of 35 modes for FQPM in closed-loop

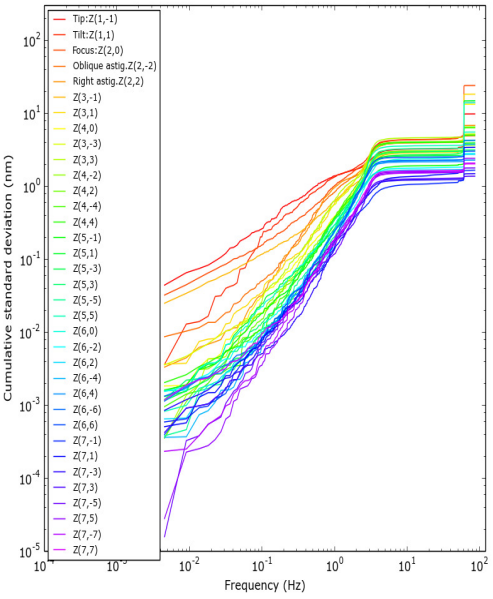

(d) Cumulative standard deviation of 35 modes for EOPM in closed-loop

Figure 4.10: (a) (b) The power spectral density for tip aberration for FQPM and EOPM coronagraph respectively. (c) (d) the cumulative standard deviation for 35 Zernike modes in open- and closed-loop are presented for FQPM and EOPM coronagraph. The results are obtained under laboratory turbulence.

is visible both in the open- and closed-loop images.

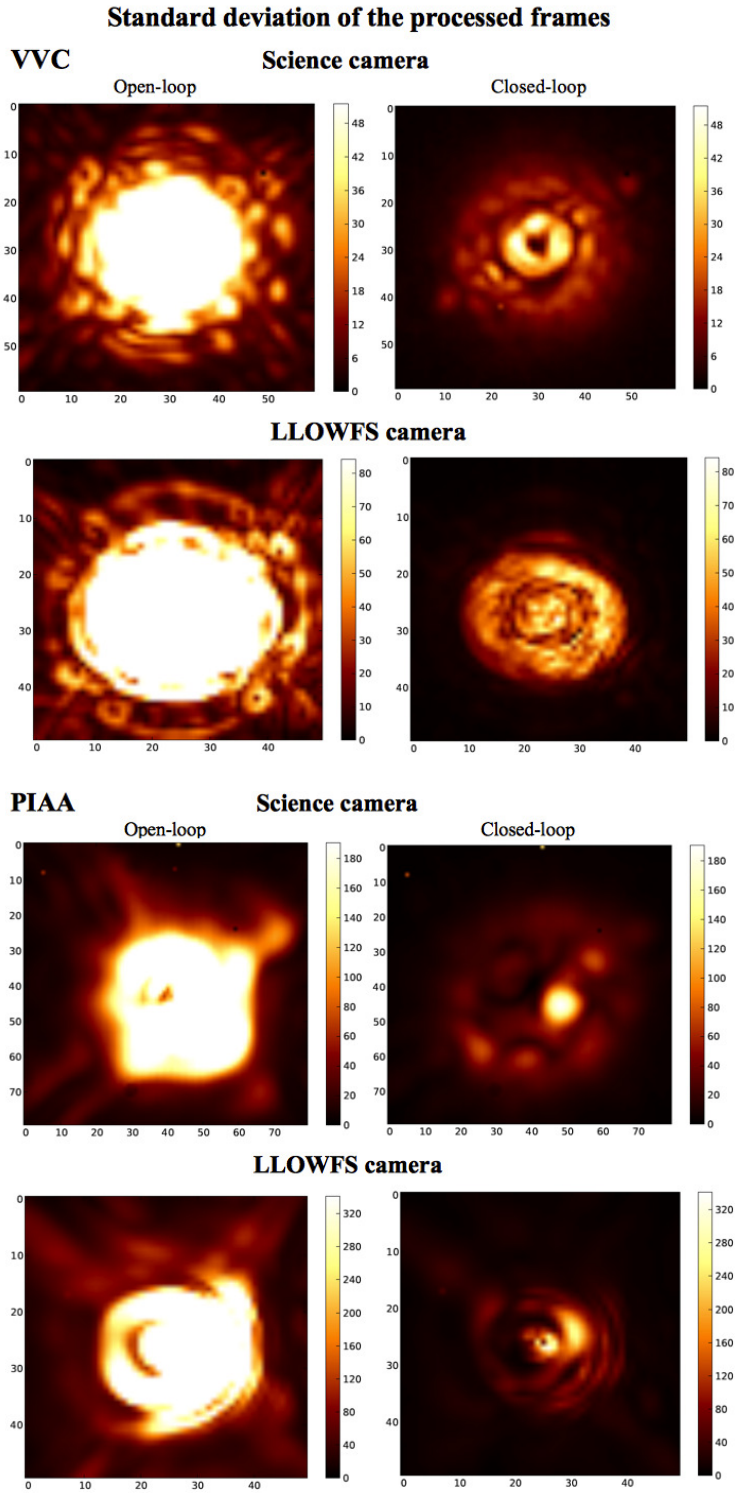

Figure 4.11: Standard deviation of the processed frames (internal science and LLOWFS camera) in open- and closed-loop regime for the VVC and the PIAA coronagraphs obtained under laboratory turbulence. Each image presented here is the standard deviation per pixel in a cube of HiCIAO simulated averaged frames. The darker images for closed-loop depicts a lower standard deviation than for the images in open-loop. *Note: Each set of open- and closed-loop images are of same brightness scale.*

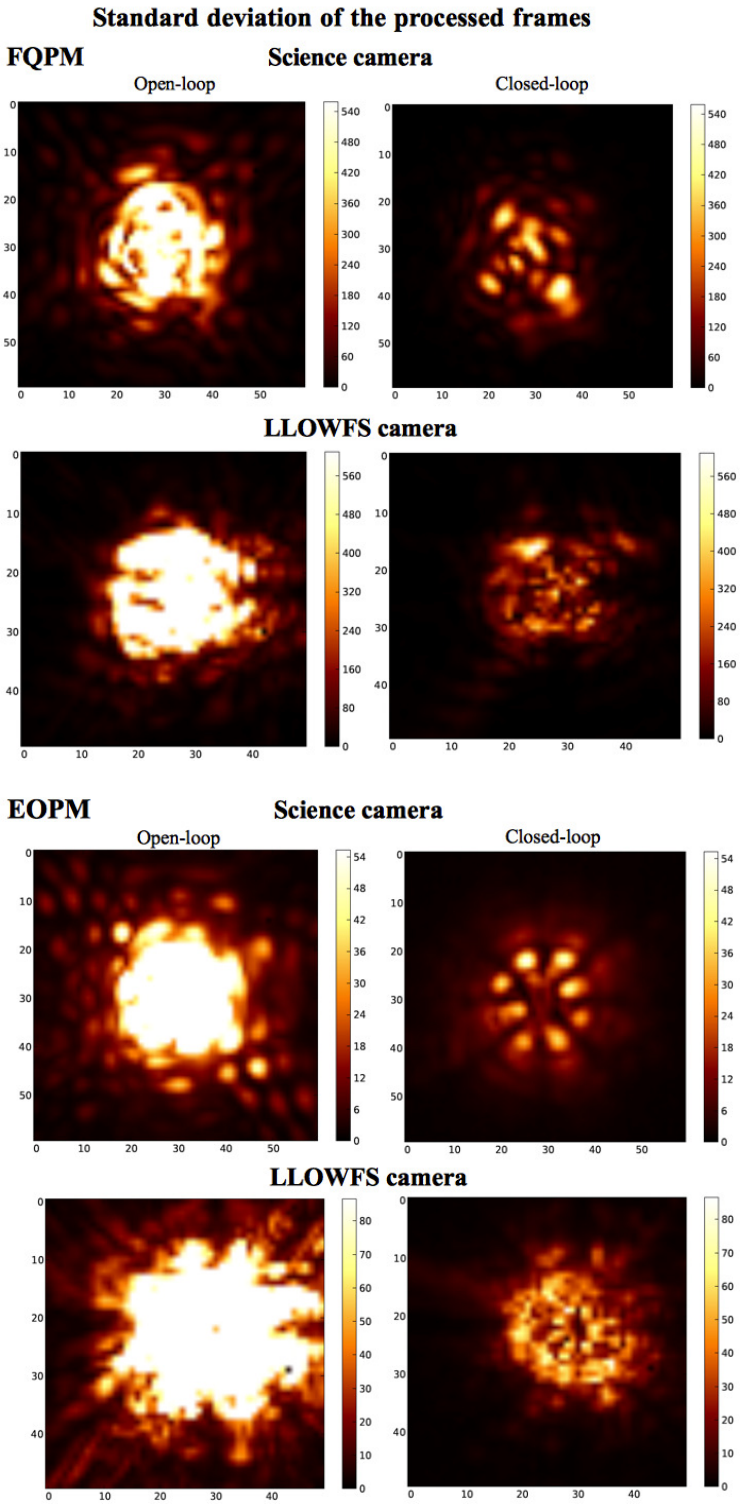

Figure 4.12: Standard deviation of the processed frames (internal science and LLOWFS camera) in open- and closed-loop regime for the FQPM and the EOPM coronagraphs obtained under laboratory turbulence. Each image presented here is the standard deviation per pixel in a cube of HiCIAO simulated averaged frames. The darker images for closed-loop depicts a lower standard deviation than for the images in open-loop. *Note: Each set of open- and closed-loop images are of same brightness scale.*

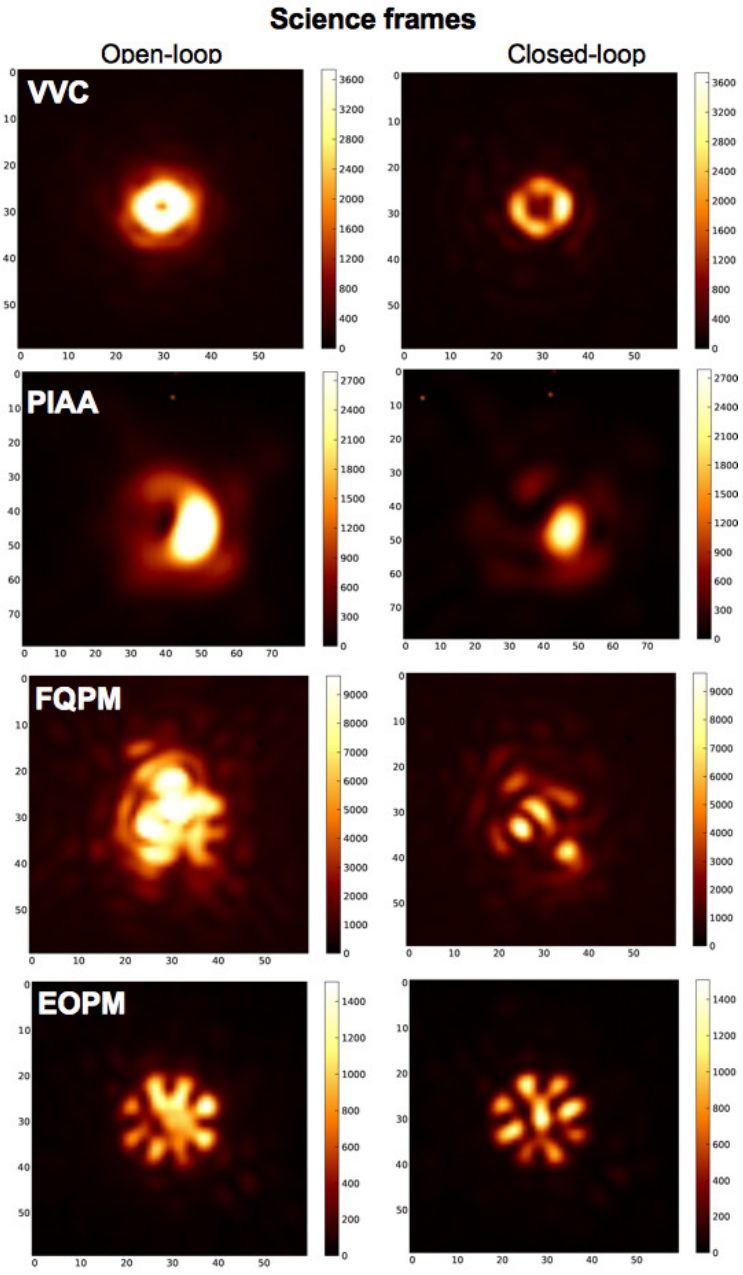

Figure 4.13: Comparing the mean of the open- and closed-loop processed frames of the internal NIR science camera for the four coronagraphs. Each image is the average of 10,000 frames acquired over 60 s. Each set of open- and closed-loop images are of same brightness scale. The FPM for PIAA was slightly misaligned prior of starting LLOWFS test in the laboratory. Also these sets of images correspond to the temporal measurements presented in *Pub.* Fig. 6 and Fig. 4.6 (a), and 4.7 (a) and 4.8 (a) respectively. *Note: Plate scale is 12 mas/pixel.*

4.5.2 Sources of vibration in the laboratory

The results for different coronagraphs I presented so far in §4.5 (including the VVC presented in the publication), are deduced from experiments that were executed under the

laboratory turbulence with an internal source, when the instrument was already in place at Subaru's Nasmyth platform. These tests were performed within hours during the same day to have similar environmental conditions for the comparison of results.

The vibrations observed at frequencies ≥ 40 Hz are probably induced by the optical and mechanical elements such as cryo-coolers and motors on the bench. A dominating vibration that is observed at 60 Hz in all the PSDs (open- and closed-loop) presented so far was mostly excited by the Stirling cooler of the camera SAPHIRA. During my testings, this camera replaced HiCIAO for its off-sky testings on the bench. I got an opportunity to turn off its cooler almost for half an hour and obtain open- and closed-loop residuals with LLOWFS to verify the source of vibration at 60 Hz.

I aligned the VVC, ran the LLOWFS control loop and saved open- and closed-loop residuals for several minutes. I present the open- and closed-loop PSD of tip aberration in Fig. 4.14. Indeed the strong vibration that was observed in Fig. 4.9 (b), Fig. 4.10 (a) and (b) and *Pub.* Fig. 8 at 60 Hz is reduced after the cooler was turned off. But since 60 Hz is the frequency of the electrical power, other sources can induce the same vibration with different strength at this frequency. This test was done off-sky, so SAPHIRA cooler was the main source of the vibration at 60 Hz. However, during on-sky operations, other possible sources such as tip-tilt mirror of AO188, optical mounts of coronagraphs optics especially PIAA optics and motors can also cause the vibration at 60 Hz. In Fig. 4.14, there is still some leftover vibration at 60 Hz that also might be due to the electronics.

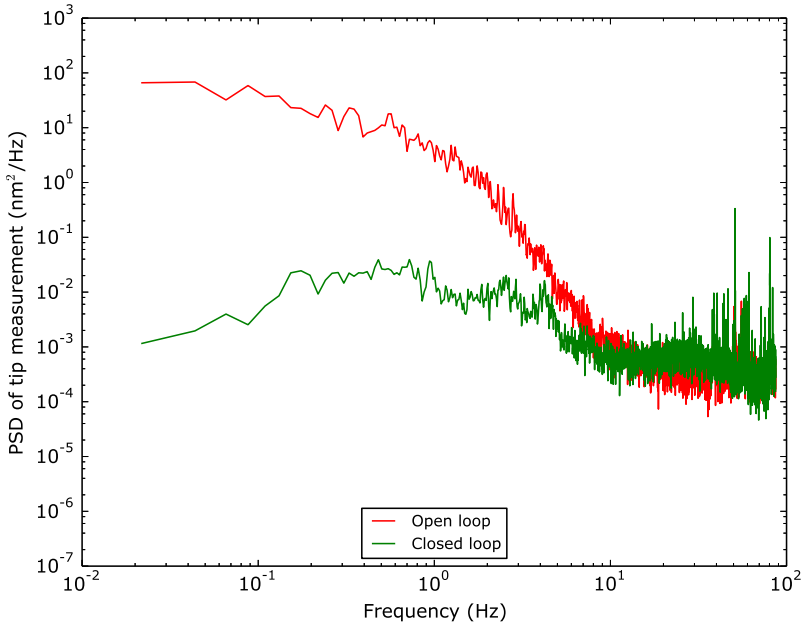

Figure 4.14: Open- and closed-loop PSD of tip aberration for a VVC with SAPHIRA Stirling cooler turned off. Dominating vibration observed in Fig. 4.9 (a), (b) and Fig. 4.10 (a), (b) at 60 Hz has disappeared in this test.

The definite source of the vibrations at 40, 50 and 80 Hz are not known yet. It is difficult to predict if they were excited temporarily due to environmental factors at the

Nasmyth platform during day time testings or if they were induced by optical elements that are vibrating occasionally. The PSD for the PIAA and the EOPM in Fig. 4.9 (b) and Fig. 4.10 (b) does not have a vibration at 80 Hz as there is in Fig. 4.10 (a) and Fig. 4.14.

To also understand how LLOWFS correction respond to different flux levels, I performed another experiment[4] where I analyzed the PSD of tip aberration in closed-loop at different exposures of the LLOWFS camera with a source at a fix flux, which is equivalent to simulating different star brightnesses. The result of this test is presented in Fig. 4.15, which is performed under no simulated turbulence for a VVC. For long exposures (when there is enough photons), the correction is mainly dominated by the vibrations whereas for shorter exposures (where the star is very faint), the correction is limited by detector noise. In the red plot for exposure of 5 ms, the effect of vibration at 40 and 80 Hz are prominent. Unfortunately, due to the Nyquist frequency of the LLOWFS camera at 85 Hz, reducing the exposure time is not strictly equivalent to fainter stars. Indeed very short exposure times can discriminate other vibrations at higher frequency than the Nyquist frequency. This is what we see at 10 Hz, the amplitude of the vibration is dependent on the exposure time, indicating that it is the folded frequency of of a vibration at 160 or 180 Hz.

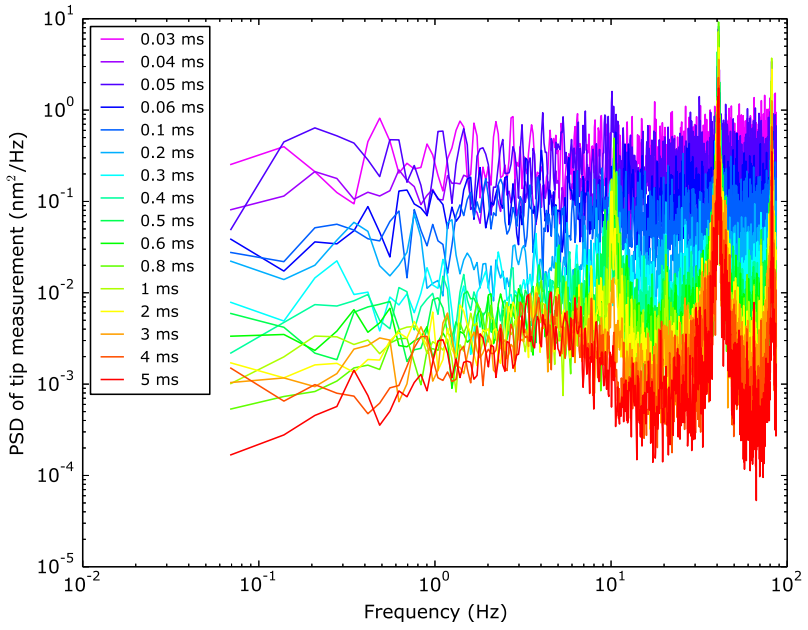

Figure 4.15: PSD of the tip aberration in closed-loop obtained for different exposures under no laboratory turbulence for a VVC. For long exposures, the correction is limited by the vibrations while for short exposures, its limited by the photon noise.

[4]Not on the same day as the one performed in §4.5

4.5.3 Discussion

So far in this chapter, I analyzed – (1) the linearity of the sensor, – (2) the open- and closed-loop temporal measurements, – (3) the spectral domain with PSDs and cumulative integrals and – (4) the stability of the processed open- and closed-loop images of the internal NIR science and LLOWFS camera in the laboratory for four different coronagraphs on SCExAO.

I also demonstrated the measurement and the correction of 35 Zernike modes for the PMCs. However, based on the knowledge of the general statistics of the aberration, decomposing the atmospheric wavefront into higher order of Zernike polynomials is not the best solution for wavefront reconstruction. The signal for higher Zernike modes lies mostly at the pupil periphery and is mostly flat at the center of the pupil, which is hardly the case with the on-sky wavefront.

A more optimal solution would be to decompose the wavefront into Fourier modes, which is an infinite expansion representing a complex wave aberration by breaking it into its frequency components. I performed a preliminary test to correct the wavefront with the LLOWFS by decomposing it into a set of Fourier modes. I used a set of Fourier modes (in DM space), which is used by the PyWFS for high-order correction. The first five modes were the Zernike modes (tip, tilt, focus and astigmatisms) and the rest were the Fourier modes. For large defocus values of the sensor (> 15 rad RMS), the LLOWFS measured and corrected 5 Zernike modes in addition with – (1) 12 Fourier modes with the PIAA, – (2) 28 modes (with 8 modes rejected in the SVD decomposition) and 52 modes (17 modes rejected) with the VVC and – (3) 52 Fourier modes (17 modes rejected) for the FQPM coronagraph. There are two reasons for low number of Fourier modes correction. – (1) For large cycles per aperture, the speckles are created farther from the FPM, hence there was no signal for LLOWFS to sense. In that case speckle nulling is required to run in conjunction with the LLOWFS. This integration is currently ongoing. – (2) the modal gain values should have been used to give more weightage to the low-order modes such as tip-tilt. I used a flat gain for the Zernike and Fourier modes correction which conceptually can not produce a stable correction. This feature of using a modal gain does not exist in the LLOWFS control loop yet. I could not perform more tests to better understand the LLOWFS correction with Fourier modes.

Nevertheless, the LLOWFS proved to be a versatile linear wavefront reconstructor, which can not only sense the aberrations for PMCs but also for the amplitude apodized coronagraphs (PIAA-type). In the laboratory, for frequencies ≤ 0.5 Hz, closed-loop pointing residuals between $10^{-3}\lambda/D$ and $10^{-4}\lambda/D$ is achieved for the PIAA, the VVC, the FQPM and the EOPM coronagraphs.

4.6 On-sky spectral analysis with VVC and PIAA

In this section, I will present the spectral analysis of the results I obtained for the VVC and the PIAA coronagraph during several on-sky engineering nights with SCExAO in combination with AO188 and HiCIAO/SAPHIRA at the Subaru Telescope. For all of the results presented below, the AO188 provided a typical Strehl ratio of ~ 30 - 40% in H-band with a ~ 200 nm RMS wavefront error. The LLOWFS then closed the loop on these post-AO188 residuals with a maximum speed of 170 Hz.

Note: The closed-loop pointing residuals that I will present in each of the results will be for slow varying errors i.e for the dataset that will be sampled at the maximum frame rate of HiCIAO (0.5 Hz).

4.6.1 Observation of a δ Scuti variable star, m_H = 1.92

During one of the science night in April 2015, we observed a white main-sequence star in the constellation Leo. After AO188 closed its loop (0.35" seeing in IR), first I aligned the VVC and then I obtained the response matrix for 10 Zernike modes by applying an amplitude of 60 nm RMS (corresponding to 1.6 mas RMS on sky for the tip-tilt modes) for each Zernike mode on the DM. These frames are similar to the response matrix shown in *Pub.* Fig. 3 (b). I closed the loop on 10 modes with a gain of 0.5 at 170 Hz (exposure time of 5 ms on LLOWFS camera and a maximum threshold on the correction set at 300 nm. This is the maximum amplitude of the aberration that can be corrected in order to prevent saturation of the DM.

Figure 4.16 (a) shows the temporal measurement of all the modes in closed-loop for 10 minutes. I did not plot the open-loop residuals for comparison because I could not save enough data points in open-loop due to observing time constraints. Figure 4.16 (b) summarizes the closed-loop results for all the modes in two temporal bands. The LLOWFS was running fast and with a high gain, so for low frequencies (< 0.5 Hz), the correction is roughly 2 orders of magnitude better than the correction at higher frequencies. Below 0.5 Hz, the level of residuals for all the modes are approximately the same (< 0.2 nm RMS). For this observation, a closed-loop pointing residual of $10^{-4}\lambda/D$ is obtained. This is the best on-sky pointing residuals obtained by the LLOWFS so far.

A smooth closed-loop PSD for the tip aberration is also presented in Fig. 4.17 (a). Indeed for frequencies (< 0.5 Hz), the slope of the PSD is very low as compared with the on-sky PSD presented in the publication (*Pub.* Fig. 11) where I also demonstrated closed-loop with 10 Zernike modes with a VVC for a different science target. The result in the publication is obtained with a very small gain of 0.05 to ensure the stability of closed-loop operation due to unstable seeing. However, the closed-loop result with a VVC in this section is obtained with a gain value of 0.5 explaining the higher quality of correction than the result in the publication.

There is only one significant telescope vibration excited at a frequency of 6 Hz, the source of which is discussed in §4.6.4. As SAPHIRA camera was off the instrument, the strength of the vibration at 60 Hz is reduced. There is possibly another source that is creating the 60 Hz vibration as some residual can still be noticed. Moreover, the vibrations

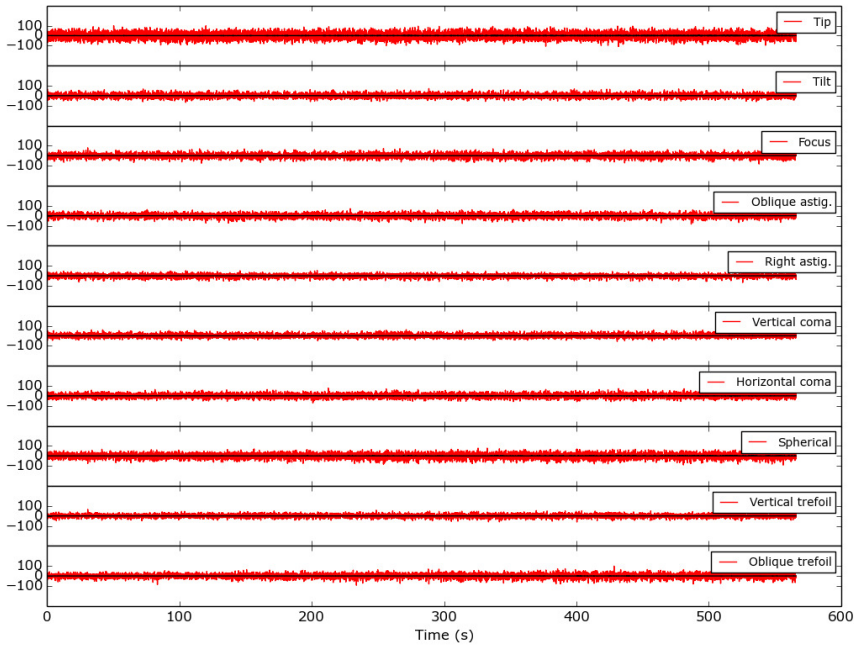

(a) Closed-loop temporal measurement of the raw residuals (in red) and their moving average using a window of 2 seconds (black). The correction of 10 Zernike modes is demonstrated.

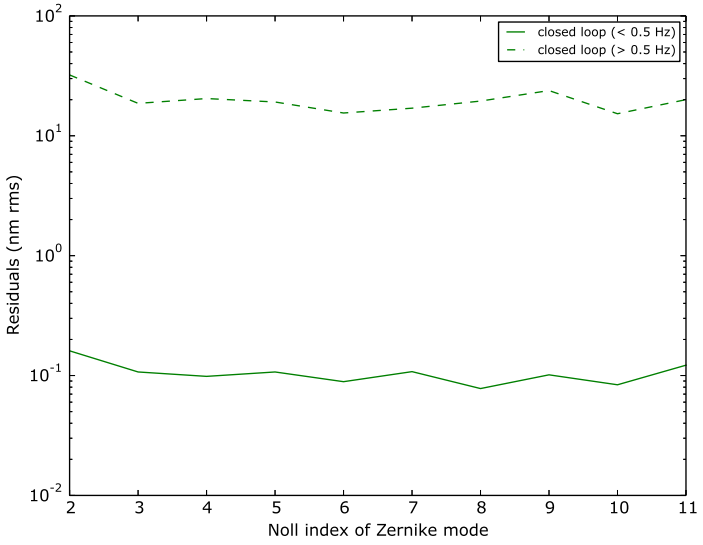

(b) Closed-loop residuals for each Zernike mode. For frequencies < 0.5 Hz, the correction is roughly two orders of magnitude better than at higher frequencies.

Figure 4.16: (a) On-sky closed-loop residuals of 10 Zernike modes obtained with LLOWFS (at 170 Hz with a gain of 0.5) for a VVC. (b) In closed-loop, the correction for all the modes at frequencies < 0.5 Hz is approximately the same (< 0.2 nm RMS). A closed-loop pointing residuals of $10^{-4}\lambda/D$ is obtained for slow varying errors.

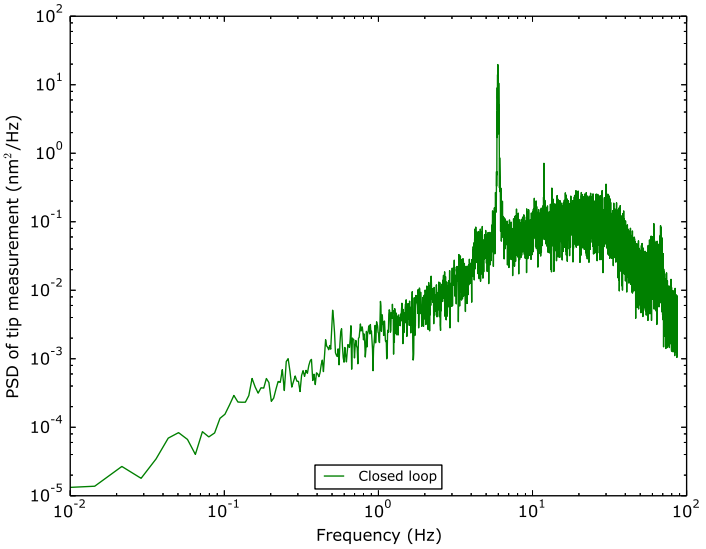

(a) Closed-loop PSD of tip aberration showing a telescope vibration at 6 Hz. A gain of 0.5 is used for the closed-loop operation.

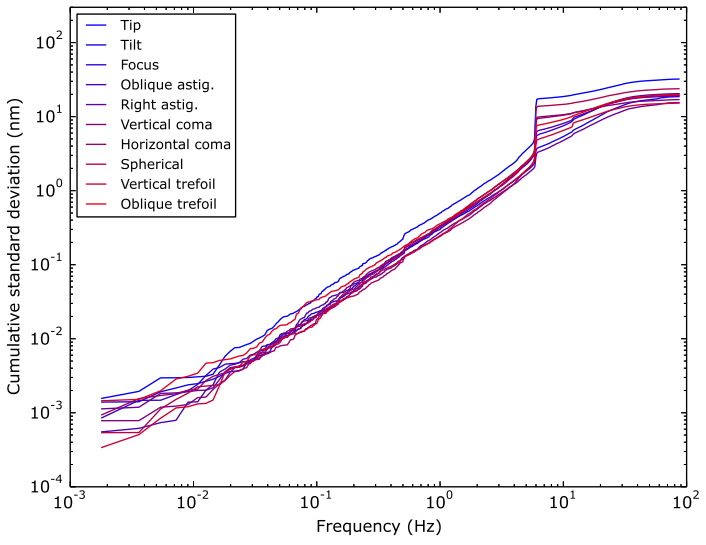

(b) Cumulative standard deviation of all the Zernike modes in closed-loop

Figure 4.17: (a) On-sky closed-loop PSD for a tip aberration corresponding to the residuals obtained in Fig. 4.16 (a) for a VVC. Only one strong telescope vibration is observed at 6 Hz. No other high frequency vibration affected the LLOWFS correction. (b) Cumulative standard deviation of 10 Zernike modes in closed-loop. The vibration at 6 Hz is visible as a step in this plot. The correction of all the modes are affected above 6 Hz with different strengths.

at 40, 50 and 80 Hz seen before are not noticeable here. As I summarized earlier in §4.5.2, they might have been excited temporarily due to local disturbances (team members working at the Nasmyth platform) during the time I performed my tests in the laboratory. This is one more reason for the good quality of on-sky correction, which is the absence of high frequency vibrations. *I will show in §5.6 of Chapter 5, how LLOWFS performance is affected in the presence of high frequency vibrations excited by telescope motors and encoders during the transit of the target.*

I also present the cumulative standard deviation of all the modes in closed-loop in Fig. 4.17 (b). The only strong vibration at 6 Hz can be seen as a vertical step in this figure. Below 6 Hz, all the modes have approximately similar contribution to the total wavefront error. However, above 6 Hz, the correction of all the modes are affected with different strengths. This figure also confirms the closed-loop pointing residual of $10^{-4}\lambda/D$ (1.6 nm) for frequencies ≤ 0.5 Hz.

In Fig. 4.18, I present the processed science frames from – (a)(b) the internal NIR camera and from – (c)(d) the HiCIAO camera. As I mentioned, I could not save open-loop residuals for the same amount of time (10 minutes) as for the closed-loop, so for comparison I processed only 2 cubes (1000 frames each, at exposure of $0.1s$) of open- and closed-loop images with the internal science camera. In (a), I present the standard deviation per pixel of 2000 frames. In open-loop, starlight leakage is fairly visible around the first few Airy rings, which are significantly suppressed in closed-loop. In (b), I present the average of 2000 frames. The closed-loop image looks less bright than the open-loop image. The leakage in the starlight possibly occurred due to the telescope vibration at 6 Hz noticed in the PSD (Fig. 4.16 (c)).

The saturated HiCIAO frames in Fig. 4.18 (c)(d) are de-striped, flat fielded with bad pixels removed. Again to compare the open-loop images with the closed-loop, I could process only 4 frames (a few seconds of exposure time). The time difference between the acquisition of the HiCIAO frames and the internal science frames was less than a minute. Even though I did not have enough HiCIAO frames, I still show the standard deviation per pixel in 4 frames in Fig. 4.18 (c) where closed-loop image is indeed darker than the open-loop image, indicating comparatively stable standard deviation. I show the improvement in variance by an order of magnitude, therefore, the detection sensitivity should improve by the same factor.

Also, a significant improvement can be noticed in the average of HiCIAO frames in Fig. 4.18 (d). In closed-loop, the scattered starlight is reduced and the spider arms together with the region surrounding the central star looks more sharper than in the open-loop image.

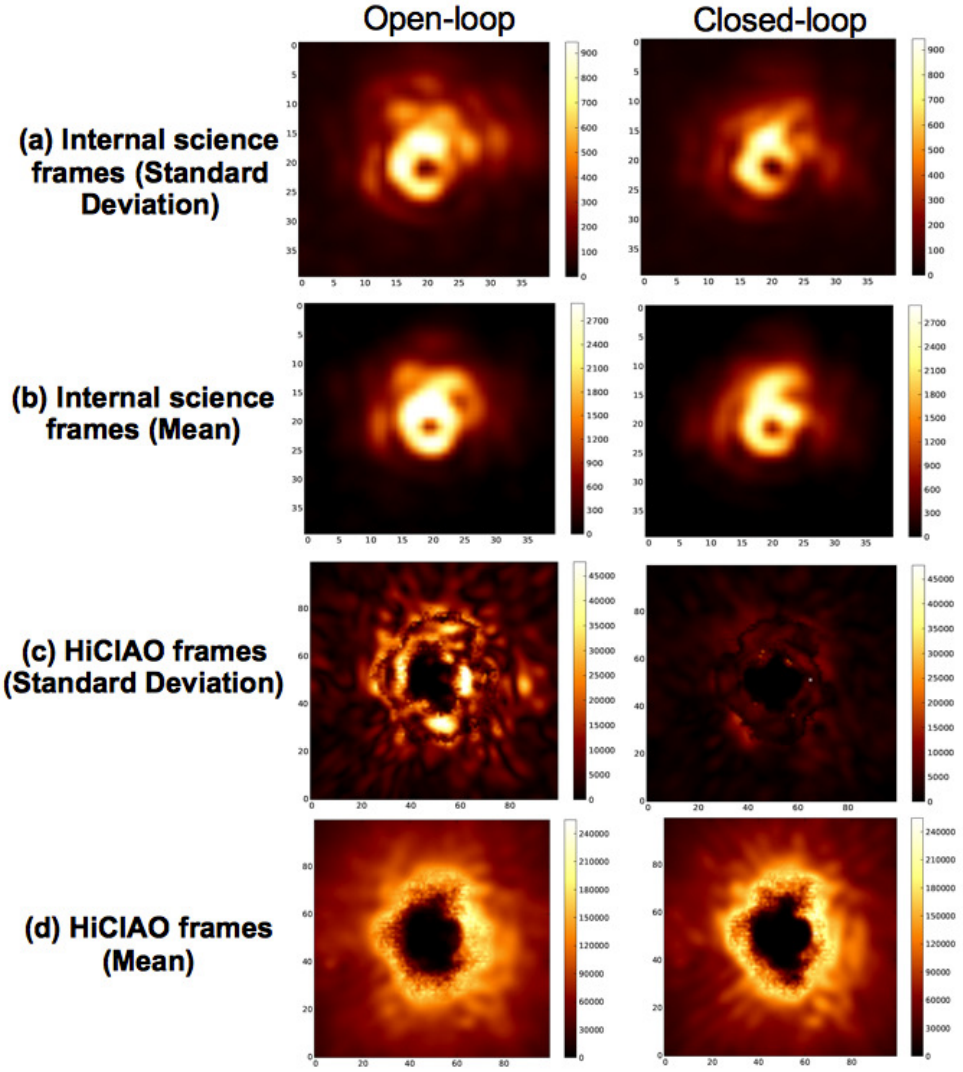

Figure 4.18: On-sky open- and closed-loop processed images from the internal NIR science camera and HiCIAO for a VVC. (a)(b) standard deviation and average per pixel of 2 cubes (2000 frames) of the internal science camera respectively. (c)(d) standard deviation and mean per pixel of HiCIAO frames respectively (4 frames only). In (a)(b), starlight leakage due to residual turbulence around the first few Airy rings in open-loop is corrected in closed-loop. In (c), the closed-loop image is darker than the open-loop image depicting a lower standard deviation. In (d), the scattering is reduced and the spider arms look sharper in closed-loop image. *These images are obtained with AO188 and the LLOWFS in closed-loop only. No additional ExAO loop provided high-order wavefront correction.* (*Plate scale is 12 mas/pixel for internal science camera and 8.3 mas/pixel for HiCIAO.)*

4.6.2 ε Boo, a G9II-III multiple star system, $m_V = 2.35$

We observed a yellow bright giant star in the constellation Boötes during one of the engineering night in April 2015 (moderate seeing). On this target, I got the opportunity to close the loop on 10 modes with both VVC and PIAA coronagraphs in H-band with a speed of 170 Hz. During this observation, HiCIAO was replaced by SAPHIRA camera for its first few on-sky testing downstream SCExAO. We stayed on this target for 1 hour to perform LLOWFS engineering with both coronagraphs on the same target.

Firstly I used the PIAA coronagraph. The PIAA optics, binary mask (1.8 λ/D diameter), PIAA[5] and RLS were aligned on the target. Then I acquired the response matrix (Fig. 4.19) for 10 Zernike modes by applying an amplitude of 60 nm RMS (1.5 mas RMS tip-tilt angle on-sky) for each Zernike mode on the DM. I closed the loop at 170 Hz with a gain of 0.05 (the threshold in the correction was set to 400 nm). I used a small gain to ensure the stability of the loop as the seeing was unstable. The open- and closed-loop residuals (raw in red and moving average in black) are presented in Fig. 4.20 (a). The values of residuals per mode are also summarized in Fig. 4.20 (b). For frequencies < 0.5 Hz, all the closed-loop residuals are < 4 nm RMS and the improvement is by a factor of 6 to 7. However, the correction at low frequencies is more than 1 order of magnitude better than at higher frequency (> 0.5 Hz). A closed-loop pointing residual of $10^{-3}\lambda/D$ is obtained for slow varying pointing errors (the level of correction obtained in §4.6.1 is better due to good seeing).

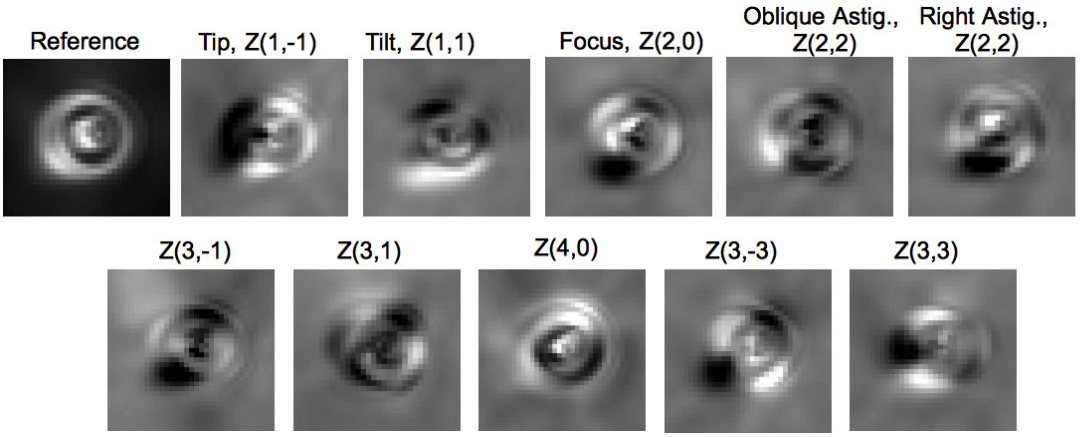

Figure 4.19: On-sky reference and response matrix for 10 Zernike modes with the PIAA coronagraph. These matrices are obtained by applying amplitude of 60 nm RMS (1.5 mas RMS tip-tilt angle on-sky) of respective Zernike modes on the DM.

To test the LLOWFS performance with the VVC, first I removed all the optics related to PIAA out of the beam and then aligned the vector vortex mask with its corresponding RLS. Second, I acquired the response matrix for 16 Zernike modes and attempted to close the loop with it. The loop kept breaking due to high amplitude of uncorrected high-order modes. So, during the inversion of the response matrix before computing the control matrix, I actually rejected 6 modes with low eigenvalues and then closed the loop again

[5]Inverse PIAA was not aligned as the optics was not ready.

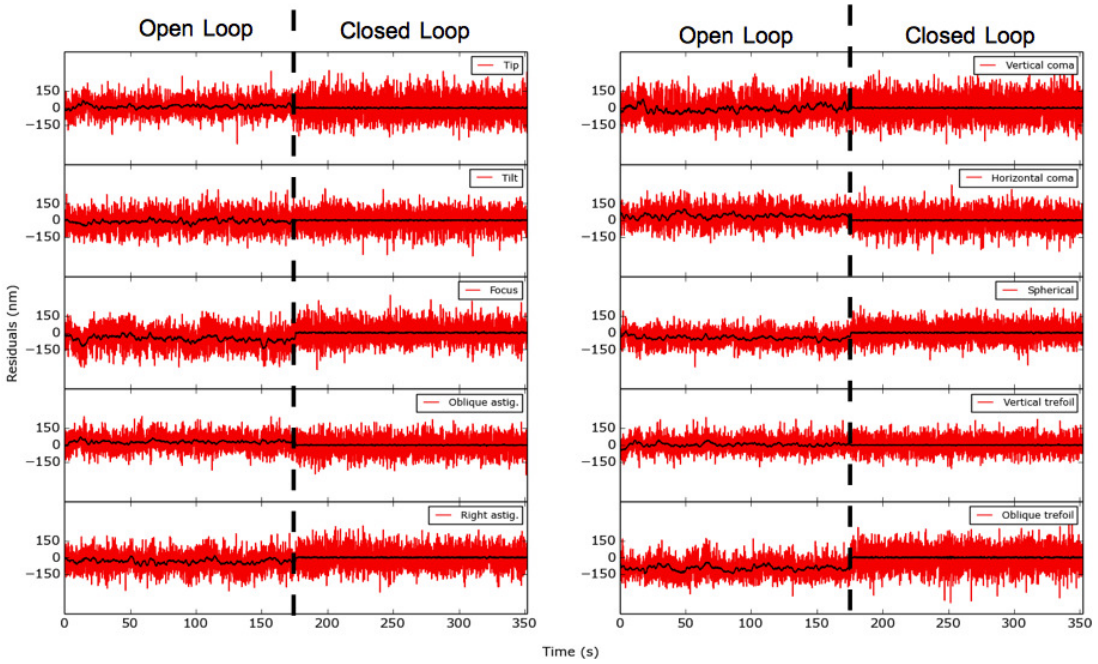

(a) Open- and closed-loop raw residuals of 10 Zernike modes (in red) and their moving average using a 2 seconds window (in black) for the PIAA coronagraph.

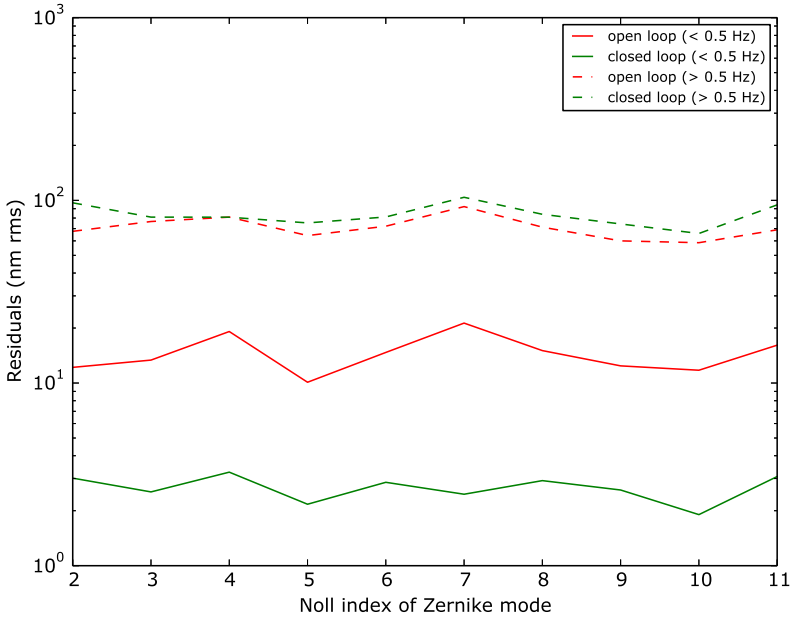

(b) Standard deviation of the residuals for each Zernike mode. The correction for frequency < 0.5 Hz is more than 1 order of magnitude better than at high frequency (> 0.5 Hz)

Figure 4.20: On-sky open- and closed-loop temporal measurement of 10 Zernike modes obtained with the LLOWFS for the PIAA coronagraph. A closed-loop pointing residuals of $10^{-3}\lambda/D$ is obtained for frequency < 0.5 Hz.

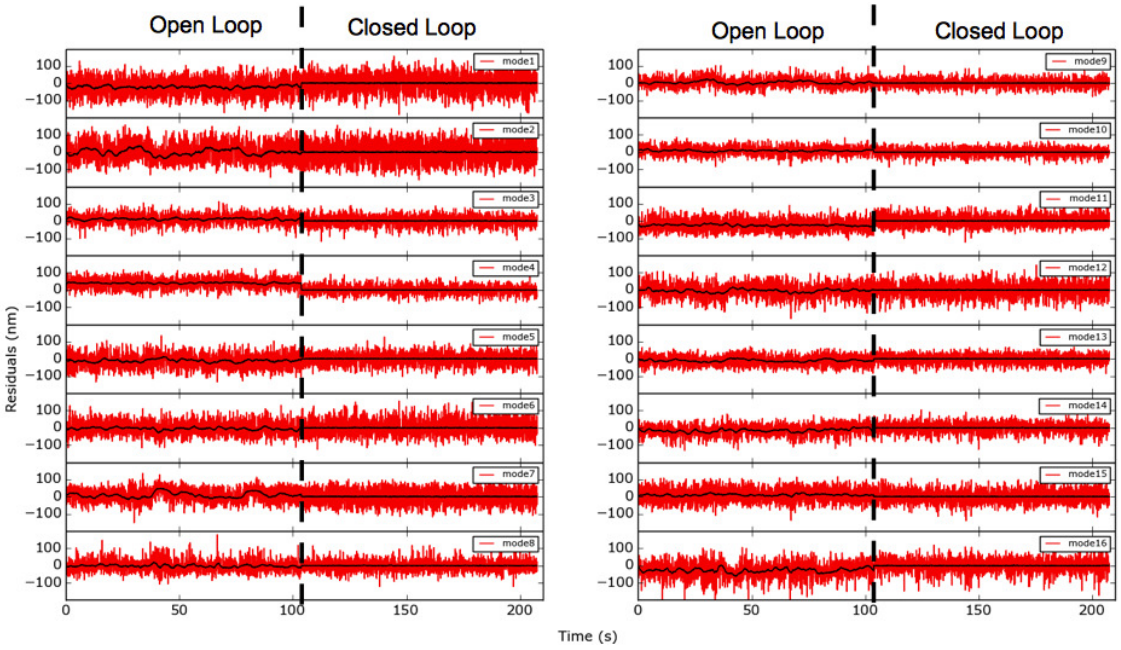

(a) Open- and closed-loop raw residuals of 16 modes (in red) and their moving average using a 2 seconds window (in black) for the VVC. 6 modes are rejected during the inversion of the response matrix, so the modes corrected here are not purely Zernike.

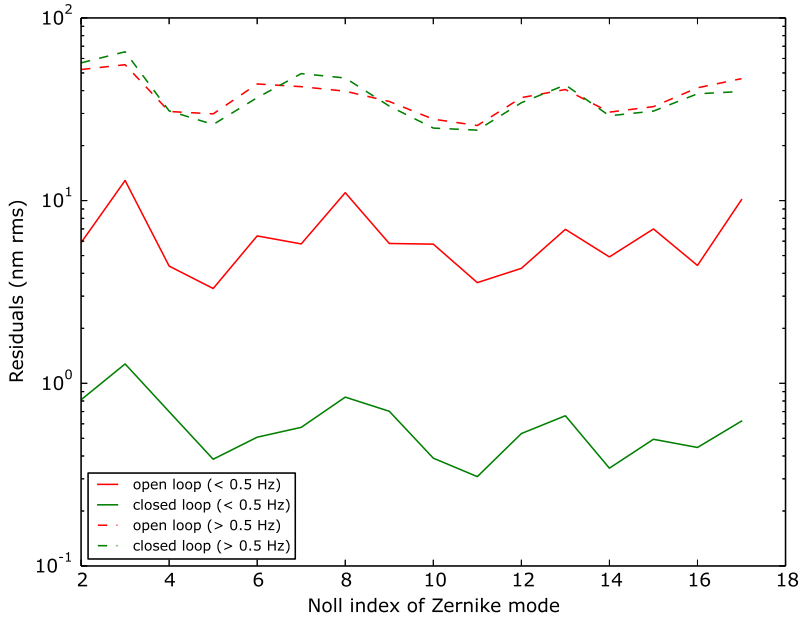

(b) Standard deviation of the residuals for each Zernike mode. The correction for frequency < 0.5 Hz is more than 1 order of magnitude better than at high frequency (> 0.5 Hz)

Figure 4.21: On-sky open- and closed-loop temporal measurement of 16 modes obtained with the LLOWFS for the VVC coronagraph. The residual values for all the modes for frequency < 0.5 Hz in (b) are approximately around 1.5 nm RMS, so the closed-loop pointing residual should be around $10^{-3}\lambda/D$.

with effectively 10 modes with a gain of 0.1. The modes corrected were no longer purely Zernike modes as I rejected 6 modes from the control matrix. Figure. 4.21 (a) present the open- and closed-loop temporal measurements of 16 modes. Also, the residual value obtained for each mode in closed-loop is presented in Fig. 4.21 (b) for two temporal bands. The closed-loop residual for all the modes is approximately less than 1.5 nm RMS for frequencies < 0.5 Hz, so the pointing residual should be around $10^{-3}\lambda/D$.

Figure. 4.22 (a)(b) shows the open- and closed-loop PSD of the tip aberration and mode 1 in case of the PIAA and the VVC respectively. In both figures, two common vibrations are visible. One at 6 Hz, which is a telescope vibration and another one at 60 Hz that can either be excited by the SAPHIRA cooler or by optical mounts in AO188 or by the PIAA optics especially in Fig. 4.22 (a) for PIAA. Indeed, a new vibration is visible only when the PIAA optics are in the beam, indicating that they originate from their mounts.

One more vibration is induced around 12 Hz in both PSDs and another one at around 1.8 Hz only during the observation with VVC that might be due to the pointing motors of the telescope. Due to these vibrations, the temporal measurements shown in Fig. 4.20 (a) and Fig. 4.21 (a) are more disturbed and hence noisier than the one obtained in the laboratory. The shape of the PSDs are also modified as compared with the one obtained in the laboratory (Fig. 4.9 (a)(b) and Fig. 4.10 (a)(b)), which is due to the underestimation of the real amplitude.

The amplitude of the variations are sometimes larger than the linear range of the sensor ($\sim \pm$ 170 nm RMS on the wavefront) and the measurements might be underestimated by the LLOWFS. Due to a small gain value, LLOWFS could not correct the vibrations and therefore the closed-loop PSDs are slightly amplified. This also explains the amplification in closed-loop residuals at higher frequencies (> 0.5 Hz) that can be noticed in Fig. 4.20 (b) and Fig. 4.21 (b).

I also present the cumulative standard deviation of all the modes corrected in Fig. 4.20 (b) and Fig. 4.21 (b) for PIAA and VVC respectively. For both measurements, the dominating vibration is at 6 Hz, as the step at that frequency is quite prominent. The correction of all the modes are affected by this vibration with different strengths. For the VVC, modes 1, 2 and 3 are much more affected by the vibrations at 1.8 and 6 Hz. The vibration at 60 Hz in this case is not strong and therefore does not affect the closed-loop residuals.

Due to limited bandwidth of the controller, these vibrations were not corrected. Nonetheless a closed-loop pointing residual of $10^{-3}\lambda/D$ is demonstrated for slow varying errors for both coronagraphs.

Figure 4.23 shows the standard deviation of the open- and closed-loop images of the internal NIR science camera for PIAA and VVC. I took 6 cubes (1000 frames each) of the camera, and simulated HiCIAO frames by performing the moving average on the 6000 frames using a window of 2 seconds. In the final cube containing 17 simulated frames, I took the standard deviation per pixel in the cube. The correction of low-order aberrations is significantly visible for both coronagraphs. *Note: The science target was not perfectly aligned with the VVC before LLOWFS closed-loop operation.*

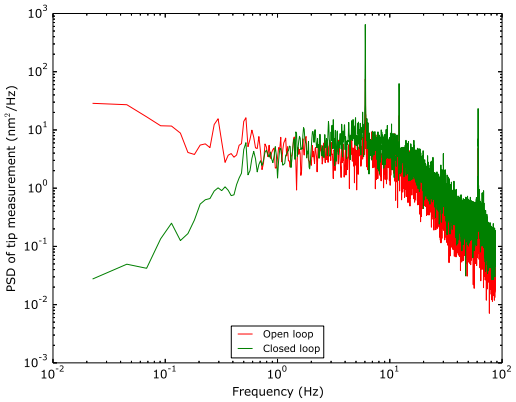

(a) Smoothed PSD of tip aberration for the PIAA coronagraph. A gain value of 0.05 is used for the closed-loop operation.

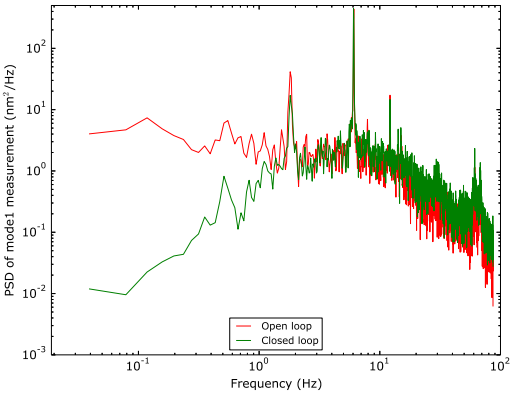

(b) Smoothed PSD of mode 1 for the VVC. A gain of 0.1 is used for the closed-loop operation.

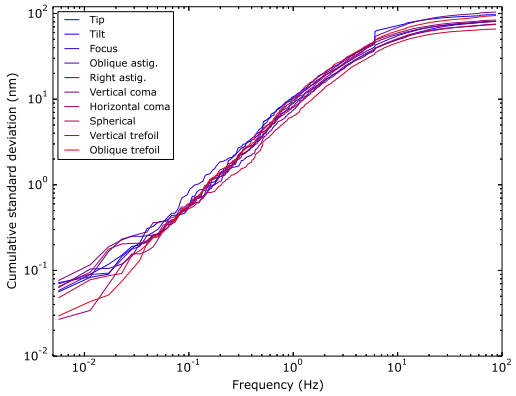

(c) Cumulative standard deviation of 10 Zernike modes in closed-loop.

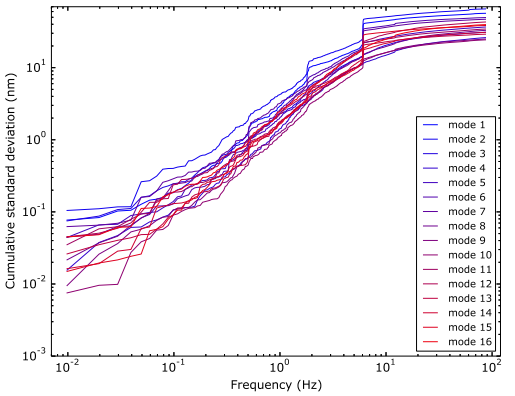

(d) Cumulative standard deviation of 16 modes in closed-loop. 6 modes are rejected during the inversion of the response matrix, so the 10 modes corrected here are not purely Zernike.

Figure 4.22: Comparison of PSDs and cumulative standard deviation of the residuals of 10 modes corrected on-sky for the PIAA and the VVC on the same target. (a)(b) PSD of tip aberration and mode 1 for the PIAA and the VVC respectively. A common telescope vibration at 6 Hz is observed during the observation in both figures. A vibration at 1.8, 12 and 60 Hz are also visible. (c)(d) shows the closed-loop cumulative standard deviation of 10 Zernike modes for the PIAA and 16 modes for the VVC. The vibration at 6 Hz is the strongest vibration which affects all the modes with different strength.

4.6.3 RX Boo, a semi-regular pulsating Star, $m_H = -1.55$

We also observed a M7 type star in the constellation Boötes during one of the engineering nights in April 2015 (moderate seeing) and I closed the loop on 5 Zernike modes with the PIAA coronagraph. This result is interesting because it is the first time I closed the loop

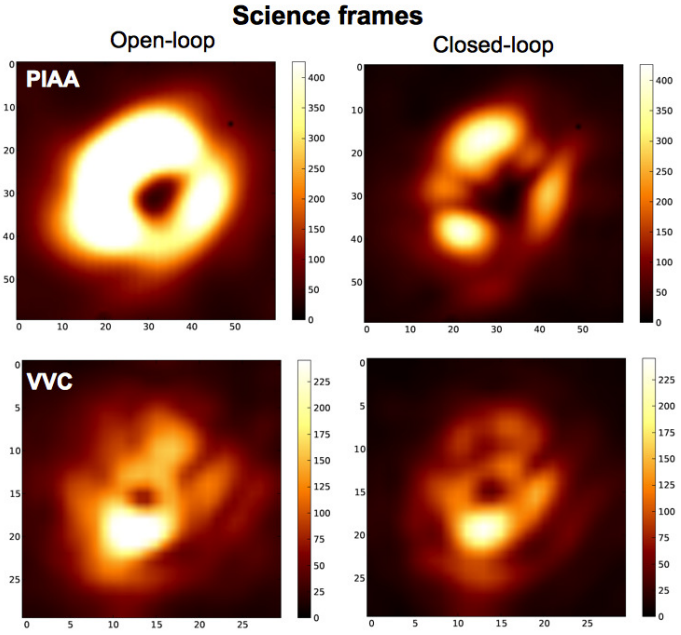

Figure 4.23: On-sky open- and closed-loop standard deviation of the images from the internal NIR science camera, comparing the results of the PIAA and the VVC on the same target. These frames are simulated HiCIAO images, which are obtained by the moving average of internal science images in 6 cubes (1000 frames each), using a window of 2 seconds. LLOWFS sensed 10 modes at 170 Hz in H-band for both coronagraphs. The VVC was slightly misaligned prior of closing the loop with LLOWFS. *Each set of open- and closed-loop images are at the same brightness scale.*

in J-band[6], with a speed of 100 Hz and for a gain of 0.05. The open- and closed-loop temporal measurements are shown in Fig. 4.24. Closed-loop pointing residual of a few $10^{-3}\lambda/D$ is obtained for frequencies < 0.5 Hz. Fig. 4.25 shows the open- and closed-loop images of the internal science camera. I took the moving average with a 2-second window on the science frames and simulated 61 HiCIAO frames. Then I calculated the standard deviation per pixel of the 61 simulated frames to show the corrections at low frequency that are resolved by HiCIAO.

4.6.4 Sources of vibration on-sky

The vibration at 6 Hz on the Subaru Telescope is very well characterized in Kanzawa *et al.* (2006). Two accelerometers were installed temporarily on the top ring of the telescope to measure the vibration in the azimuth (AZ) and elevation (EL) direction, shown in Fig. 4.26 (a). The broken circles in this figure shows the location of AZ and EL encoders, which are used to measure the absolute angle and the speed of each axis.

The vibration noticed at 6 and 12 Hz in all the on-sky PSDs occurs in the EL direction and is actually excited by periodic errors in incremental encoders which is used to

[6]The J-Band was then used by the single mode fiber injection unit of SCExAO discussed in §3.4 of §3.3.

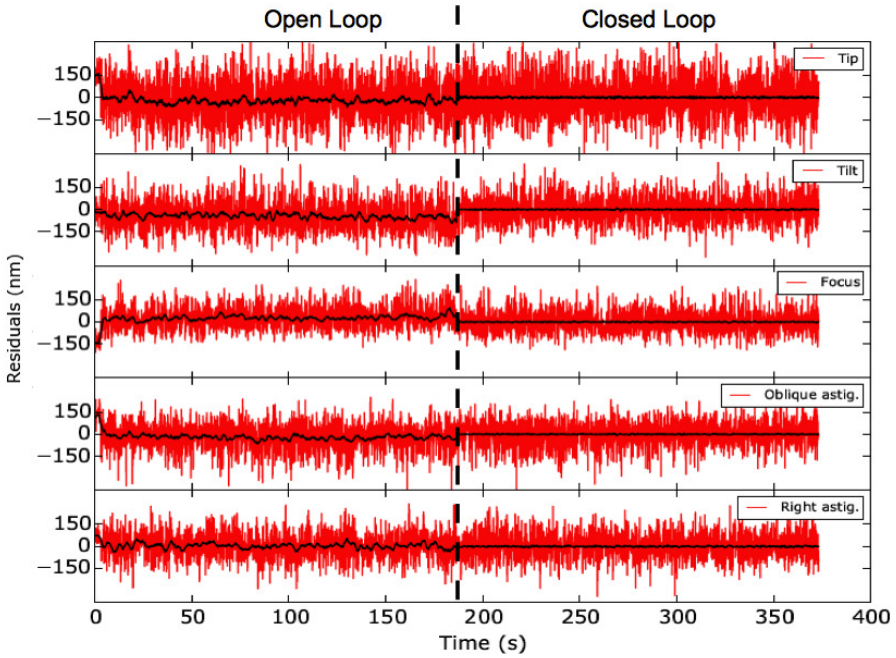

(a) Open- and closed-loop residuals of 5 Zernike modes with the PIAA coronagraph. The red data present the raw residuals whereas the black ones are the moving average of raw residuals using a window of 2 seconds.

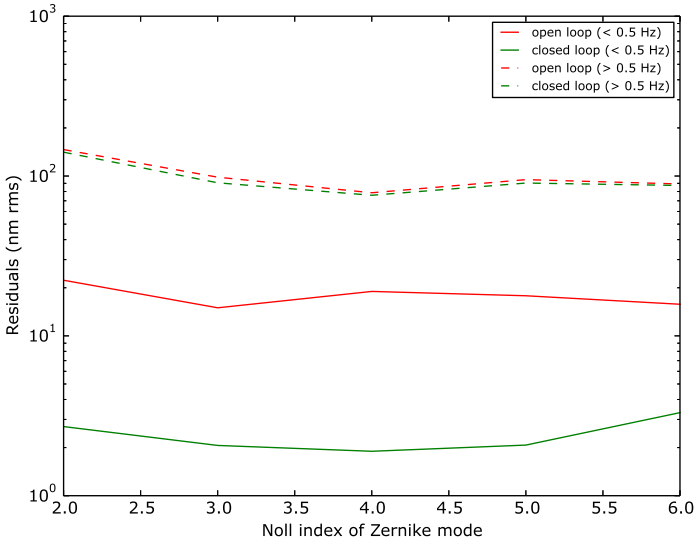

(b) Open- and closed-loop residuals for each Zernike mode.

Figure 4.24: On-sky open- and closed-loop temporal measurements of 5 Zernike modes in J-Band with the LLOWFS for the PIAA coronagraph. A closed-loop pointing residual of a few $10^{-3}\lambda/D$ is obtained for frequencies < 0.5 Hz in (b).

measure the velocity of telescope rotation. The spectra of these vibrations in EL direction detected by the accelerometer is shown in Fig. 4.26 (b). It is also concluded that – (1) these vibrations are excited when the wind speed at the top ring is 2 - 4 m/sec and – (2) the frequencies of these vibrations are proportional to the rotation speed of the EL

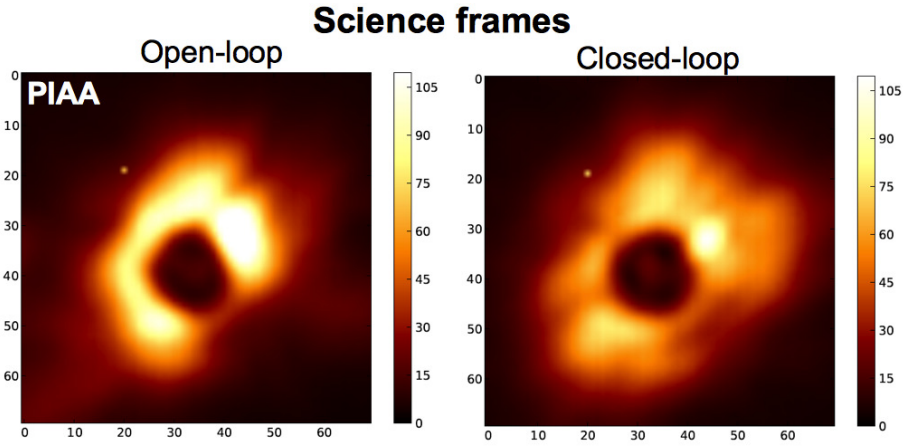

Figure 4.25: On-sky open- and closed-loop processed images of the internal science camera. LLOWFS corrected 5 Zernike modes with PIAA coronagraph in J-band. These images are the standard deviation per pixel of 61 simulated frames of HiCIAO.

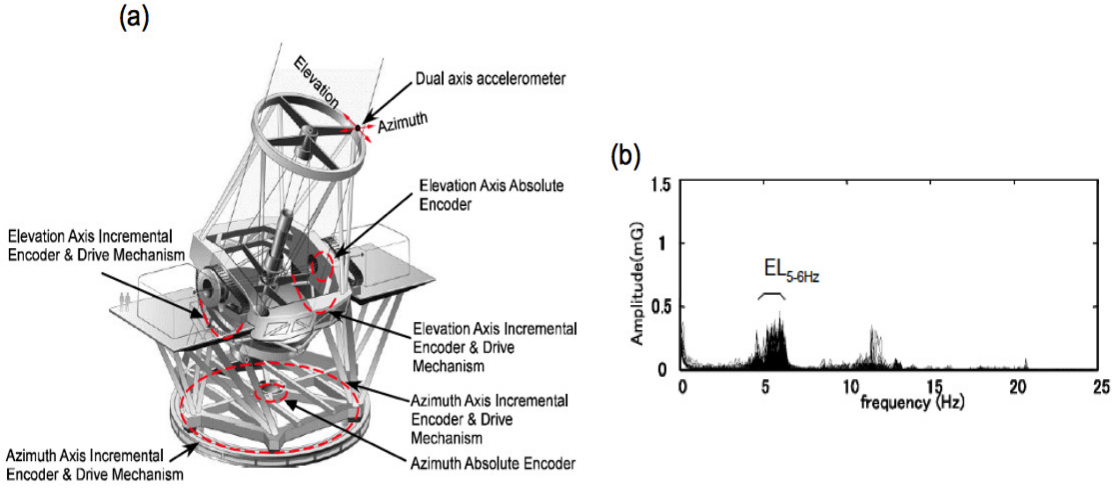

Figure 4.26: (a) Position of the two accelerometers on the top ring in the AZ and EL direction to measure the vibration at the Subaru Telescope. The broken rings show the position of the encoders used to measure the angle and the speed of both axes. (b) Acceleration in EL direction with peaks at 6 and 12 Hz. (Kanzawa *et al.*, 2006)

axis. These frequencies are equal to $V_{EL}/2.23$ arcsecond, where V_{EL} is the rotation speed of the EL axis (12 - 15 arcsec/second).

Apart from these known vibrations, other sources of vibration at higher frequency might be the optical/mechanical elements inside AO188 or SCExAO itself that are vibrating occasionally with different straights. I could not perform further studies to identify the definite sources of the vibrations.

These vibrations are one of the major causes of the degradation in the performance of the LLOWFS. The high amplitude variations (about 1 λ/D) caused by them are outside

of the linear range of the LLOWFS, which makes it difficult to obtain a stable correction with the LLOWFS in a non-ExAO regime. We will see in Chapter 5, even when using the ExAO regime, these vibrations cause image motion of more than 4 mas (0.1 λ/D in H-band) and affects the pointing stability of low-order loop. These vibrations can not be corrected by the low-order loop due to limited bandwidth of its controller and the underestimation of the amplitude because of the limited linear range of the LLOWFS.

4.7 Conclusion

In this chapter, I compared the LLOWFS performance in open- and closed-loop scenario in the laboratory for the VVC, the PIAA, the FQPM and the EOPM coronagraphs. In the laboratory, LLOWFS closed the loop on a simulated turbulence, which had a strength of 150 nm RMS, wind speed of 10 m/s and was mostly dominated by the low-order modes. Under such conditions, I demonstrated – (1) a closed-loop pointing residuals between $10^{-3}\lambda/D$ and $10^{-4}\lambda/D$ for all the coronagraphs for slow varying errors and – (2) that the correction for frequencies < 0.5 Hz is 2 orders of magnitude better than the correction at higher frequencies.

However, on-sky I have closed the loop on the post-AO188 wavefront residuals for the VCC and the PIAA coronagraphs only. The AO188 typically provides a SR of ~ 30 - 40% in H-band with a ~ 200 nm RMS wavefront error. As there was no additional high-order correction, therefore the low-order control loop partially stabilized the beam upstream of the coronagraph. During on-sky operations, some of the results were obtained with a slightly misaligned FPM. Even in such cases, the low-order loop provided stable correction.

On-sky, the correction is around 1 orders of magnitude better at frequencies < 0.5 Hz than at frequencies higher than 0.5 Hz. LLOWFS correction is mostly limited by the high frequency jitter and telescope vibrations. Eventhough, under good seeing and for bright targets ($m_H \leq 2$), the closed-loop residuals of $10^{-4}\lambda/D$ is obtained with the LLOWFS as presented in §4.6.1. For moderate seeing conditions, LLOWFS can routinely provide the closed-loop pointing residuals of $10^{-3}\lambda/D$ as demonstrated in *Pub.* §3.3.4 and Figure 9 and 10, §4.6.2 and §4.6.3.

In the next chapter, I will present the integration of the LLOWFS with the high-order PyWFS control loop and will demonstrate the control of pointing errors in the ExAO regime in the laboratory and ultimately on-sky. I will also discuss the factors and circumstances under which LLOWFS can not provide an optimal correction.

Chapter 5

LLOWFS integration inside the visible high-order Pyramid Wavefront Sensor: On-sky results in ExAO regime

"The most incomprehensible thing about the world is that it is comprehensible."
– Albert Einstein
In Banesh Hoffmann and Helen Dukas, Albert Einstein: Creator and Rebel (1972, 1973)

Contents

5.1 Introduction

The SCExAO instrument has three main wavefront sensors as stated in §3.2.3 of Chapter 3. A PyWFS to measure the high-order wavefront aberrations in the visible, a SN loop to suppress the speckle halo and a LLOWFS to address the low-order wavefront aberrations in the NIR. However, all these sensors cannot run simultaneously, independently from each other, as there is only one DM to correct for the measured aberrations.

The LLOWFS during its operation, as discussed in Chapter 4, was the only wavefront sensing unit that was interacting with the DM to compensate for the low-order aberrations. In this non-ExAO regime, only the low frequencies were corrected from the post-AO residual wavefront. During the closed-loop correction of the low-order modes, the PSF was well stabilized upstream of the coronagraphic mask but no significant quantitative analysis such as Strehl improvement and contrast enhancement could have been performed due to the lack of the simultaneous correction of the higher-order aberrations.

However, in the present configuration of SCExAO during the scientific observations, the high-order PyWFS is now the only sensor that interacts with the DM to compensate for ~ 1600 modes. In this ExAO regime, when the wavefront aberrations are sensed in the visible while the coronagraphic science is performed in the NIR, the Non-Common Path (NCP) errors that are also chromatic errors are introduced in the NIR science channel.

The high-order modulating PyWFS, in its current mode of operation on SCExAO, does provide a wide linear and dynamical range but at the expense of the sensitivity Guyon (2005). Being less sensitive to the low spatial frequencies, the modulating PyWFS in closed-loop operation require more photons to make the same measurement as in the non-modulated (fixed) PyWFS. The strategy on SCExAO will be to reduce the modulation at the minimum while closing the loop to increase the sensitivity. In any case, the PyWFS corrects most of the low-order aberrations in the visible. Even with a perfect correction, NCP errors (that are also chromatic errors because of the different paths used by the visible and the NIR) are bound to be introduced in the NIR imaging channel due to the chromaticity of the atmosphere. For small IWA coronagraphs, these uncorrected NCP errors (static and dynamic) leak the rejected starlight around the FPM, limiting the contrast that a coronagraph is designed to achieve. Therefore, during closed-loop operations with the PyWFS, it is essential to address these NCP errors and chromatic errors to enhance the detection sensitivity of the instrument.

To control the low-order NCP errors in the ExAO regime, we have integrated the LLOWFS inside the visible ExAO loop of SCExAO. In this chapter, I will discuss the two different approaches of integrating low-order loop inside the high-order loop (§5.2 and §5.3) that has been implemented and tested in the laboratory (§5.5) and finally on-sky to correct only the tip-tilt (§5.6).

5.2 Differential Pointing system to integrate the LLOWFS inside the PyWFS

To control the pointing errors in the NIR channel during the ExAO closed-loop scenario, a Differential Pointing System (DPS) has been implemented to establish the connection

between the LLOWFS and the PyWFS. LLOWFS, instead of sending the commands to the DM, controls the DPS to interact with the PyWFS for the correction of the pointing errors. For this thesis, two versions of the DPS have been tested that will be presented in this chapter.

Figure 5.1 presents a general flowchart of the use of the DPS by the LLOWFS to connect indirectly with the DM (via the PyWFS). The steps to control the pointing errors in this case are explained below.

- The LLOWFS first measures the commands to control the differential tip-tilt errors. These measurements are sent to the DPS, which physically changes the nominal position of the visible PSF falling on the Pyramid optics.
- In closed-loop, this change in the zero-point of the visible PSF is sensed by the PyWFS, which sends the control commands to the DM to compensate for it, thereby correcting the differential pointing errors in the IR.

In this configuration, though the PyWFS and the LLOWFS closed-loop operation sets the visible and IR on their respective zero-points with appropriate offsets. However, this correction optimizes the aberrations in the IR channel but degrades slightly the performances in the visible channel. The visible instruments (VAMPIRES and FIRST) are less sensitive to aberrations than the coronagraph.

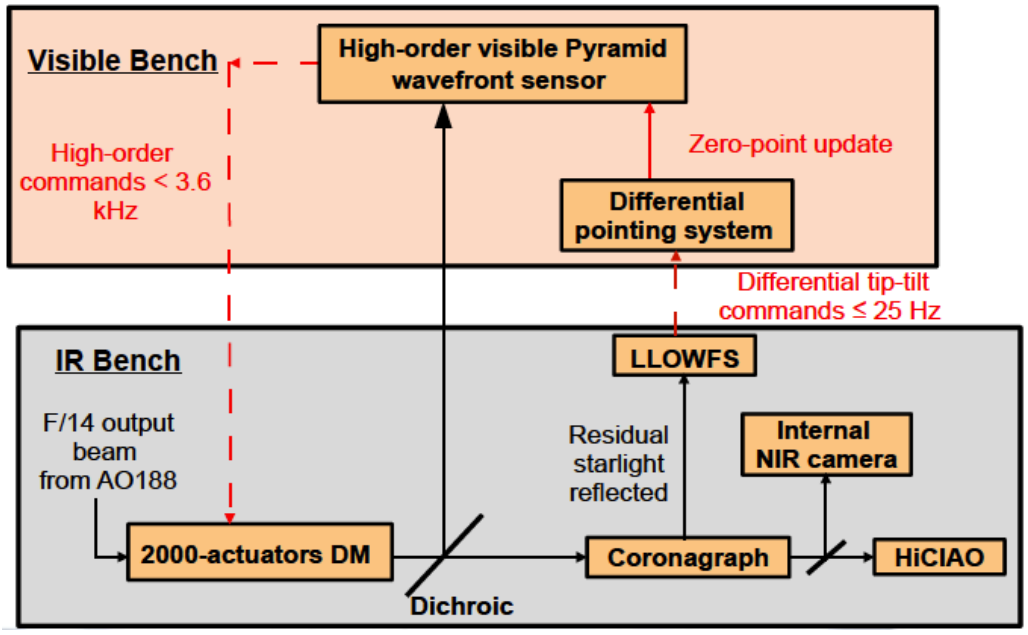

Figure 5.1: Flowchart of the Differential pointing system that connects the LLOWFS with the PyWFS to address the differential pointing errors in the ExAO closed-loop regime.

The first version of the DPS included the control of the piezo-driven dichroic that separates the visible light from the IR, which is situated on the IR bench as shown in Fig. 3.7. When the LLOWFS send the commands to the DPS, it controlled the pitch/yaw of the piezo, which moved the dichroic accordingly. This dichroic movement physically

changed the position of the beam falling on the pyramid optics of the PyWFS, hence changing the reference by changing the relative flux in each of the four pupils on the camera.

The use of the piezo-driven dichroic as a DPS was the initial effort to run the LLOWFS and the PyWFS simultaneously as an independent unit. The testing of this first version of the DPS with the non-modulating PyWFS was attempted directly on-sky in September 2014. The results are discussed in detail in §5.6.1.

In the current ExAO mode, we use a modulating PyWFS to be able to exploit the wider linear range of the sensor. In order to do so, a separate piezo-driven tip-tilt mirror on the visible bench has been installed to modulate the visible PSF at the apex of the Pyramid optics. By applying a series of continuous sine and cosine waves using the tip-tilt servo-controller, the PSF is moved on a circle around the apex of the pyramid optics with a radius of 1.6 λ/D. I will address the piezo-driven tip-tilt mirror unit as a tip-tilt modulator (TTM) in the rest of the thesis.

Due to the slow response of the piezo controller ($< 5\ Hz$) of the first version of the DPS, we adapted the TTM as the DPS for the LLOWFS. Figure 5.2 presents the optical ray path of the light on the visible bench, also highlighting the TTM unit integrated with the PyWFS. For the rest of the section, I will focus on the hardware architecture, featuring the subunits of the SCExAO's visible bench.

The visible light reflected by the dichroic as shown in *Pub.* Figure 3 is reflected towards the top bench via a periscope. To re-image the pupil plane on the visible bench, an achromatic lens (50 mm diameter, $f = 500$ mm) is mounted inside the periscope. At the focus of the beam, a WFS pickoff wheel consisting of a range of dichroic beamsplitters allows the separation of the spectral content between the PyWFS from the FIRST/VAMPIRES units. The 850 nm (40 nm bandwidth) beam reflected off the WFS wheel is collimated by an achromatic lens ($f = 200$ mm), which create a pupil image at the TTM plane. The TTM is mounted on four piezoelectric actuators, located at the corners of a square. To apply a tip-tilt in a particular direction requires a synchronized movement of the two diagonally opposite actuators. This symmetrical design is chosen because the pivot point of the mirror is fixed and the drifts introduced on the piezos due to the temperature change will be compensated and will not affect the modulation of the PSF on the Pyramid optics.

The relayed focusing optics (a combination of achromatic lenses with focal lengths of $f = 400$ and $f = 125$ mm) downstream the TTM forms a converging beam ($F/\# = 40$) and focuses it on the vertex of the double pyramid prism shaped optics (Esposito *et al.*, 2010). The Pyramid optics is custom made and is a replica of the one used on MagAO (Close *et al.*, 2013). There is a pupil lens ($f = 300$ mm) mounted on a x/y stage, which finally images the four pupils separated by the pyramid optics on the Pyramid camera, OCAM2K. The movable stage of this lens is used to align the pupils on the OCAM2K during its remote operation. The specification of the camera is described in Table 1 of §3.3.

During the ExAO closed-loop operation, when the LLOWFS controls the current version of the DPS i.e the TTM, then it changes the zero-point of the modulating PSF. The detailed theory of the control is explained in the next section. The DPS using the TTM does provide a better control (25 Hz) than the previous version but is not fast enough to

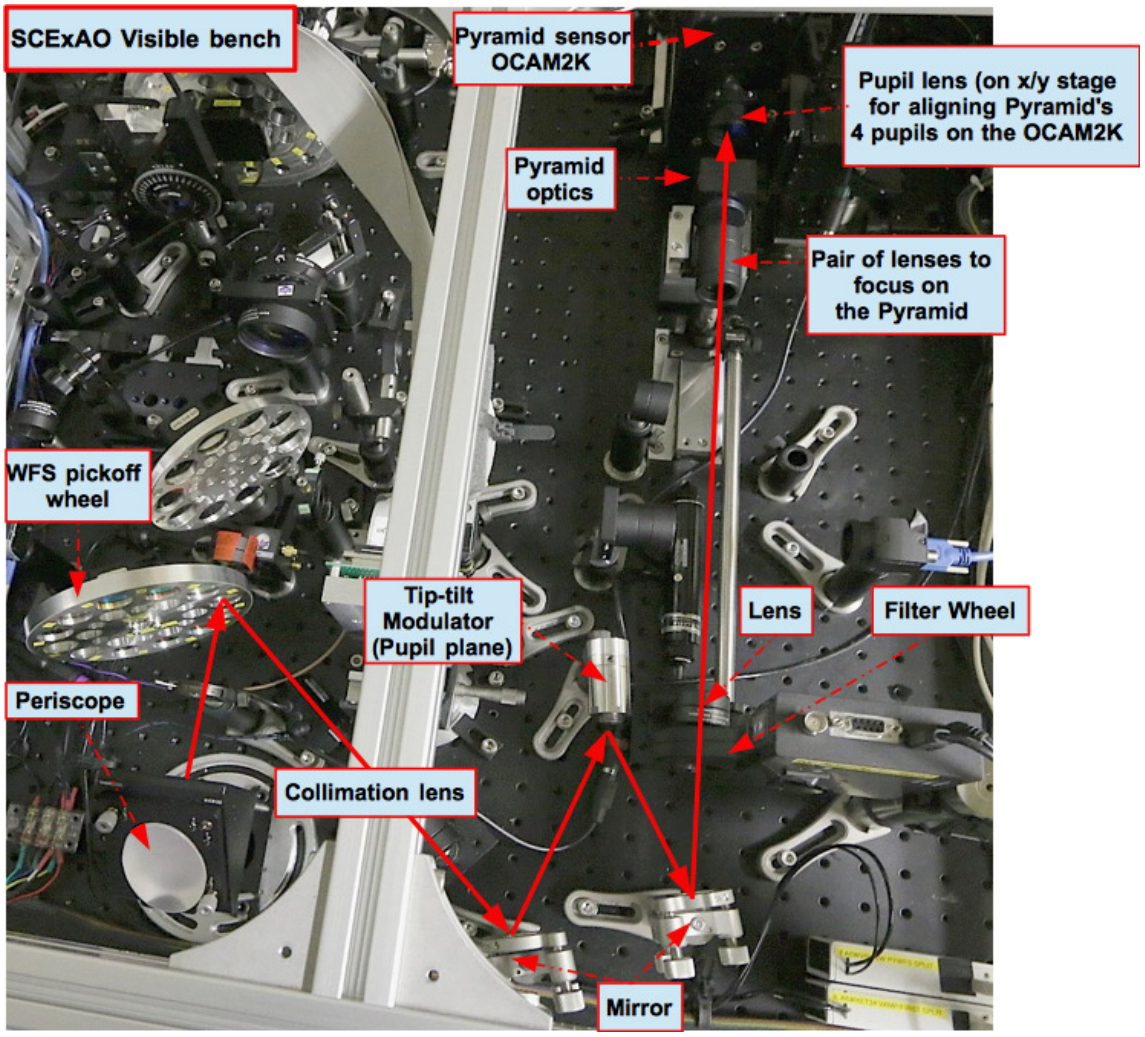

Figure 5.2: Optical ray path of the SCExAO's visible bench. The Tip-Tilt Modulator (TTM), which modulates the PSF at the apex of the Pyramid optics is also used as a Differential Pointing System (DPS) to address the differential tip-tilt errors in the IR.

control the high temporal frequencies of the turbulence.

5.3 Control theory of the low-order loop integrated inside the high-order loop in the ExAO regime

In the previous section, I have introduced how the DPS establishes the physical communication between the LLOWFS and the PyWFS. In this section, I will explain in detail how the control loop of the LLOWFS and the PyWFS are associated with each other. The important point to note here is that the LLOWFS uses the same code to sense the aberrations and to compute the commands as explained in the §3.6.3. Minor software changes were made in order for the LLOWFS to interact with the DPS instead of the DM. To be able to use the LLOWFS code globally, I have added an option in the LLOWFS GUI to choose

the controller on the fly (*"Actuator"* field in Fig. 3.23). In the case where we are using the DPS as a controller, the default value of the axis to be corrected is only two (tip and tilt) at present.

Figure 5.3 explains the control approach that the LLOWFS adapted to address the differential tip-tilt errors while the PyWFS loop is closed. The procedure is explained in the following steps.

- Input: I have taken an aberrated coronagraphic PSF. The PyWFS has corrected the high-order wavefront aberrations in the visible and provided a Strehl of about 60% under a median seeing. In the IR, the vector vortex mask can be seen at the top right of the coronagraphic PSF, clearly depicting that there is still a large tip-tilt error uncorrected which has misaligned the beam upstream of the VVC. The effect of the wavefront aberrations can also be seen in the LLOWFS PSF, which has introduced the asymmetries in its shape.

- Calibration: To correct the differential tip-tilt in the IR, first the reference image and the response matrix are acquired. In order to do that, the DPS has been selected as a controller and voltages equivalent to a 60 nm amplitude are sent to the tip-tilt piezos to calibrate the response of the sensor to the tip-tilt errors.

- Sensor: Using the reference image and the response matrix obtained in the calibration step, the LLOWFS PSF is then decomposed through the SVD into the linear combination of the tip-tilt modes. The tip-tilt errors present in the image are then measured at a maximum frame rate of 170 Hz.

- Control: The measurements are used to compute the control commands via an integrator control law, tuned by a gain common to both axes. The commands computed are then sent to the DPS (TTM), which updates the position of the modulating PSF on the Pyramid optics at a speed of 25 Hz, thereby changing the flux in the four pupils on the OCAM2K.

- PyWFS, after sensing the change in its reference image, immediately sends the corresponding commands to the DM at a frame rate < 3.6 kHz, to compensate for its zero-point update, which also corrects the offsets in the IR. A good low-order control stabilizes the PSF behind the coronagraphic mask and also brings the low-order PSF back to its reference position, as can be seen in the corrected PSFs in Fig. 5.3.

The measured residuals by LLOWFS is updated every 5.7 ms while the piezo actuators responds every 40 ms due to the slow communication with the piezo electronics. In closed-loop, the measurements are accumulated and by the time the actuator responds, the gathered residuals are averaged and sent every 7^{th} residual value (170 Hz $\times$ 40 ms). To avoid the divergence of the loop, the gain should be < 0.1 in order to send the right measurement that the controller can correctly respond to. In this case, the latency is very small, around 1 frame, because the loop is running very slow. The bandwidth and the vibrations are the reason the small gain is used in order to avoid the overshoot of the controller.

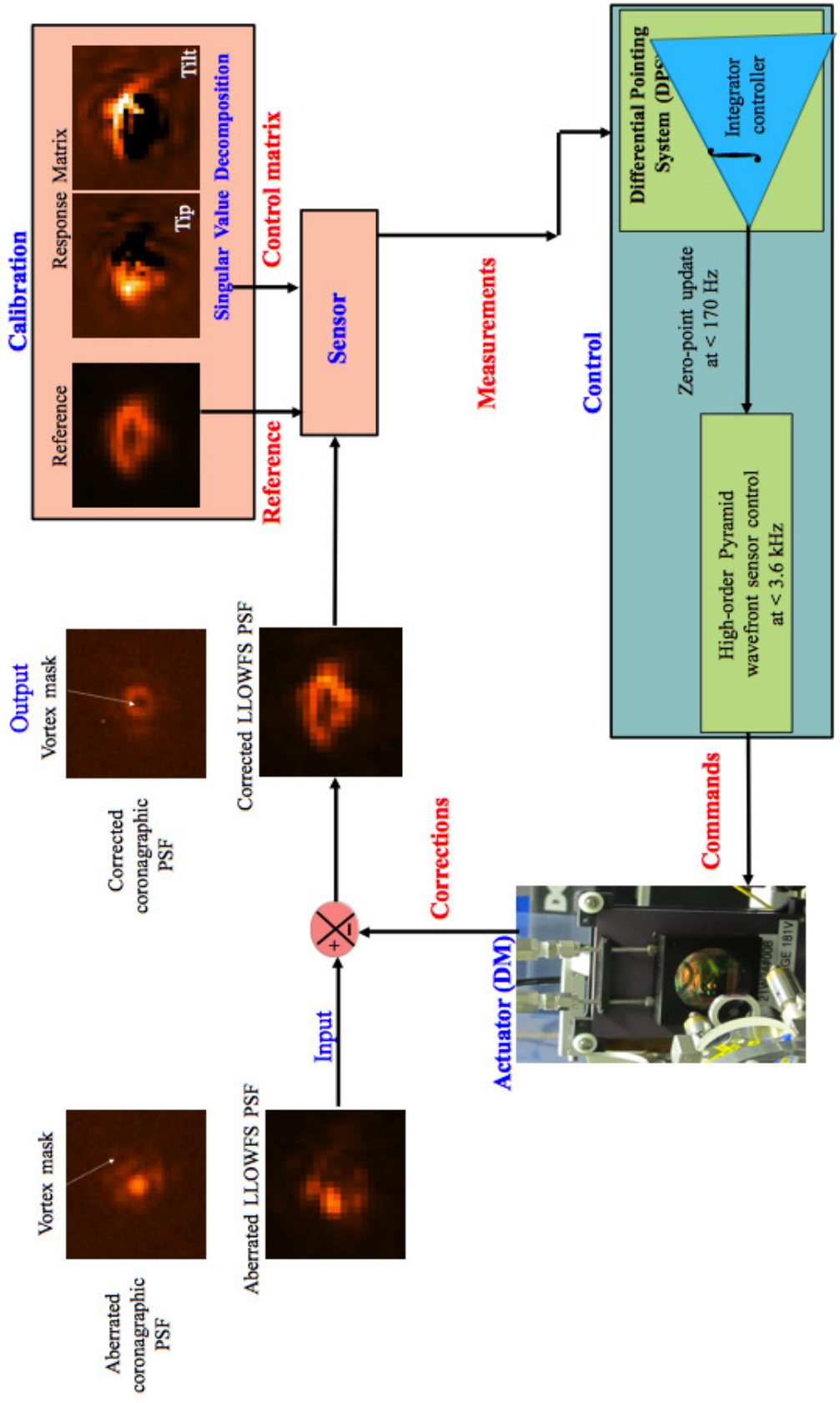

Figure 5.3: Flowchart presenting the control loop of the integrated low-order and high-order loop in the ExAO closed-loop regime on the SCExAO.

At the moment, the gain values for LLOWFS control are selected manually from the LLOWFS GUI. In the current version of the LLOWFS code, we do not have a feature of selecting different gains for different modes, hence the same gain is used for the correction of tip and tilt.

During the observations, the quality of the low-order correction is interpreted visually by – (1) looking at the stability and the positioning of the PSF behind the coronagraphic mask and – (2) by monitoring the real-time telemetry of the tip-tilt residuals. I will discuss the factors that affects LLOWFS closed-loop performance under the ExAO mode in §5.7. Nevertheless, in the ExAO regime, LLOWFS suppresses the NCP residuals and stabilizes the beam upstream of the coronagraph.

NOTE: The LLOWFS and the internal NIR camera PSF that I have taken as an example in Fig. 5.3 are the actual on-sky PSF of a K5/M0III spectral type star ($\mathbf{m_H = 3.87}$*). The coronagraphic PSF at the entrance of the Fig. 5.3 is after the correction from the AO188 and the PyWFS. I demonstrate additional correction by the LLOWFS.*

5.4 Laboratory experiment with the Tip-tilt modulator as a Differential Pointing System

With the configuration of the DPS as a controller for the LLOWFS, as explained in the sections 5.2 and 5.3, I will now present the tests performed and the results obtained in the ExAO mode in the laboratory. The procedure followed during the experiment of simultaneously closing the loop of the PyWFS and the LLOWFS is explained below in a sequential manner.

- Source: We switch on the Super continuum source (*Pub.* Fig. 3) and adjust its setting in order to simulate a star with an apparent magnitude of $m_H \simeq 2$. The exposure time of the internal NIR camera is set to 5 ms (170 Hz). The star fainter than $m_H \simeq 2$ is not simulated here because we wish to sense the commands at the fastest frame rate of the camera (at 170 Hz) in order to study the vibrations in the instrument at higher frequencies.

- Coronagraph: I align the vector vortex mask and its corresponding RLS on the PSF using the internal NIR camera. The procedure of aligning a VVC is explained in §3.5.2.

- PyWFS: We align the four pupils of the PyWFS on the OCAM2K by moving the x/y stage of the pupil lens located in front of the camera. We acquire a new reference image, load a previously acquired response matrix and close the loop with the PyWFS, thereby correcting $\sim$ 800 modes in the visible (the PyWFS was not fully operational for the experiments presented in this chapter, it was correcting 800 modes at 700 Hz instead of 1600 modes at 3.5 Hz). Under these settings, I then acquire a reference image and a response matrix with the LLOWFS by commanding the DPS.

- Laboratory turbulence: The simulated dynamic phase errors are applied on the DM in the next step. I choose 150 nm RMS as the amplitude of the turbulence, 10 m/s as

the wind speed and allow all the low-spatial frequency components of the turbulence to be left uncorrected.

- LLOWFS: I choose the limit of 0.6 volts (170 nm) as the maximum amplitude that should be applied on the DPS for the correction. After saving the PyWFS closed-loop + LLOWFS open-loop residuals for a few minutes, I close the loop with the LLOWFS. I tested the loop performance with different gain settings and the results are discussed later in this section.

The procedure to set up both the WFSs and close their respective loops takes less than 10 minutes. This time limit is very important for the efficient use of the observing time during the science nights at the telescope. If the loop breaks either due to the high amplitude variations of the turbulence or due to the high gain value, the time it takes to reset all the loops is within 2 minutes as there is no requirement to load extra parameters. It only requires to put the gain value to 0.0, stop the loop, zero the last applied correction on the DM and then turn on the loop again with a small initial gain.

5.5 Spectral analysis of the low-order control loop in the laboratory

I would like to remind the reader that the data analysis, both temporal and spectral, is following the same procedure as explained in §4.4.2. I will analyze the residuals for open- and closed-loop in two temporal bands. The first band, between 0 and 0.5 Hz corresponds to the slow varying frequency components resolved by the science camera, HiCIAO. This band addresses the dynamical contribution of the turbulence in the science images of HiCIAO. The second band, between 0.5 and 85 Hz, corresponds to the faster motions resolved by the internal NIR camera but averaged by HiCIAO. The static contribution of the turbulence and the vibration in the science images will be addressed here.

Figure. 5.4 shows the differential tip-tilt residuals measured by the LLOWFS in open- and closed loop. These raw residuals (red lines) are filtered by a moving average of 2 seconds to match the minimal exposure time of HiCIAO (black lines). The asymmetries in the measurement of tilt mode might be due to the shift in the linearity of the sensor as noticed in §4.3.2

The LLOWFS, in open-loop, measured the uncorrected NCP errors during the PyWFS closed-loop mode. These NCPs are stabilized when the LLOWFS also closed its loop. The performance of the loop has been tested with several gain values. Figure 5.5 shows the gain versus the standard deviation of the open- and closed-loop residuals for the tilt mode in the two temporal bands. There are two important points to note here: – (1) Compared to the other gains, the closed-loop residual is lower for the gain value of 0.05, that is why I show the temporal measurement of open- and closed-loop for that gain only in Fig. 5.4 and – (2) The residuals are shown for the two different temporal bands. As stated before, the closed-loop residuals for the band 0 - 0.5 Hz (resolved by HiCIAO) are much lower than the one calculated for the high frequency band (blue line) for all the gain values. The same behavior has been noticed with the mode tip as well.

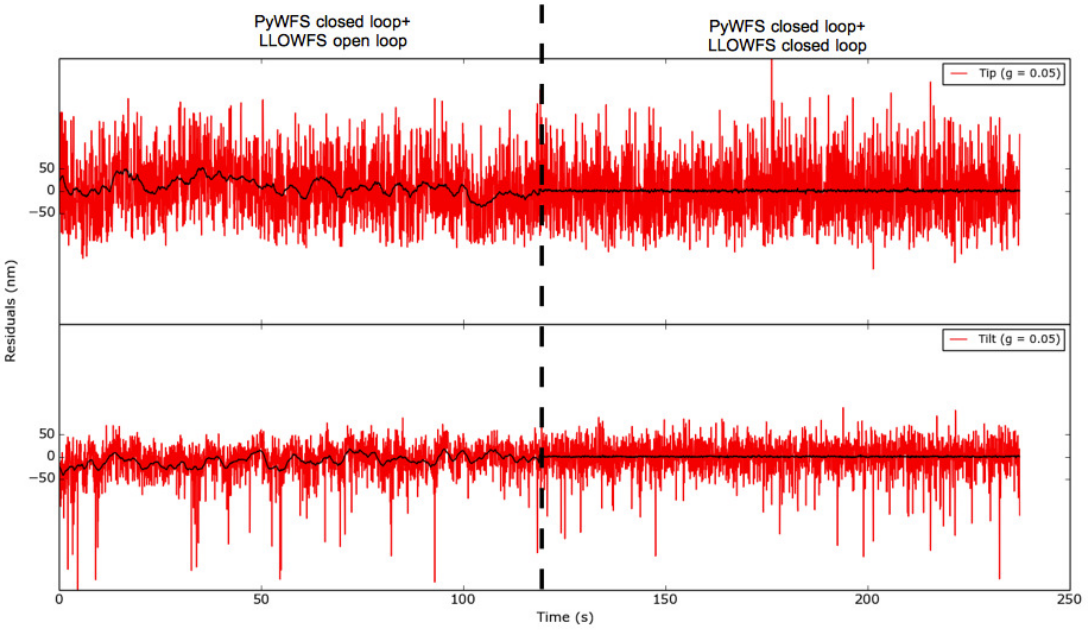

Figure 5.4: Differential tip-tilt residuals measured by the LLOWFS in the ExAO closed-loop regime under the laboratory turbulence. The red lines are the raw residuals measured while the black lines are the moving average of the raw residuals with a 2 second window to simulate the residuals seen by the science detector HiCIAO. A gain of 0.05 was used for the closed-loop operation.

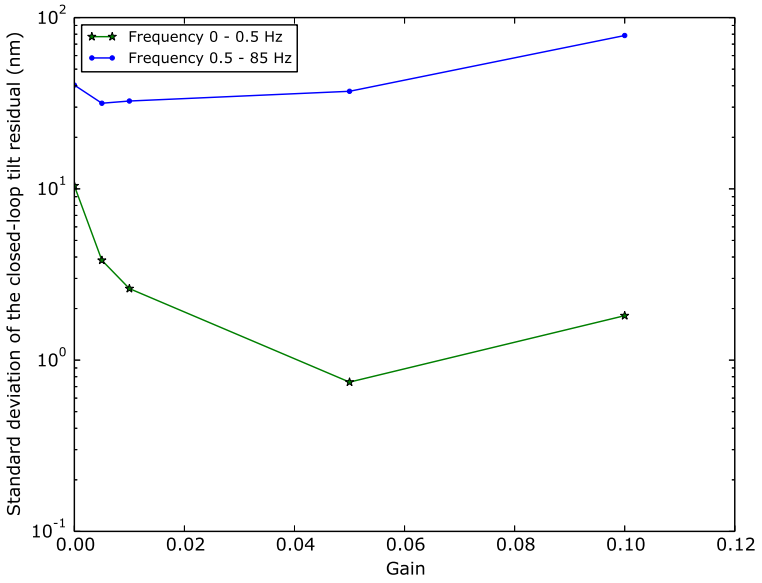

Figure 5.5: Gain versus the standard deviation of the LLOWFS open- and closed-loop for the differential tilt residual in the ExAO regime under the laboratory turbulence. The closed-loop residual is lower for the gain of 0.05, correcting low frequencies (0 - 0.5 Hz) comparatively better than at the other gain values. Not much improvement has been noticed at the higher frequencies due to the limited bandwidth of the controller.

Table 5.1 summarizes the open- and closed-loop residuals measured by the LLOWFS for the differential tip-tilt under the ExAO-regime. The residuals are again presented for the two temporal bands. For the slow varying frequencies, a factor of 11 to 14 improvement has been achieved in suppressing the NCP errors, which was left uncorrected by the PyWFS closed-loop. However, no improvement was achieved in correcting the high varying frequency components. This is because of the vibrations over 5 Hz, which are not corrected by the controller due to its limited bandwidth. For the frequencies at < 0.5 Hz, the pointing residuals for open- and closed-loop are about 7.7×10^{-3} λ/D (0.31 mas) and 6.6×10^{-4} λ/D (0.03 mas) for tip and tilt respectively.

Table 5.1: Laboratory open- and closed-loop differential tip-tilt residuals of the low-order loop when integrated inside the high-order loop. The correction is only significant for the low frequencies.

		Low Freq. (< 0.5 Hz) (Resolved in HiCIAO)		**High Freq. (> 0.5 Hz) (Averaged in HiCIAO)**	
Mode	Unit	**Open loop**	**Closed loop**	**Open loop**	**Closed loop**
Tip	nm	14.1	1.3	65.6	66.4
	λ/D	8.8×10^{-3}	8.1×10^{-4}	4.1×10^{-2}	4.2×10^{-2}
	mas	0.36	**0.03**	1.7	**1.7**
Tilt	nm	10.4	0.75	39.0	37.1
	λ/D	6.5×10^{-3}	4.7×10^{-4}	2.4×10^{-2}	2.3×10^{-2}
	mas	0.26	**0.02**	1.0	**0.95**

Next, I analyzed the PSDs of the tip-tilt residuals under the open- and closed-loop operation of the LLOWFS. Figure 5.6 shows the closed-loop residuals at four different gains. For the gain value of 0.05, the correction is significantly visible for the frequency below 1 Hz as compared at the other gains. However, an overshoot occurred at the frequencies above 1 Hz. This is due to the mismatch between the frequency of the sensor (170 Hz) and the frequency of the actuator (25 Hz). A gain of 0.05 actually corresponds to a gain of 0.3 at the speed of the actuator, which explains the overshoot.

In open-loop, vibrations between frequencies 55 - 60 Hz are also visible only in one axis (tilt) here, which are amplified in the closed-loop (for gain = 0.1) due to the overshoot in the correction of the controller. The sources of these vibrations are discussed in §4.5.2.

I have also analyzed the cumulative integral of the PSDs presented in the Fig. 5.6, to understand the impact of the vibrations on the residuals. Figure 5.7 presents the cumulative integral in the open- and closed-loop regime for the tip-tilt residuals at different gains. For the tip aberration (Fig. 5.7(a)), no steps are visible as there is no vibration. However,

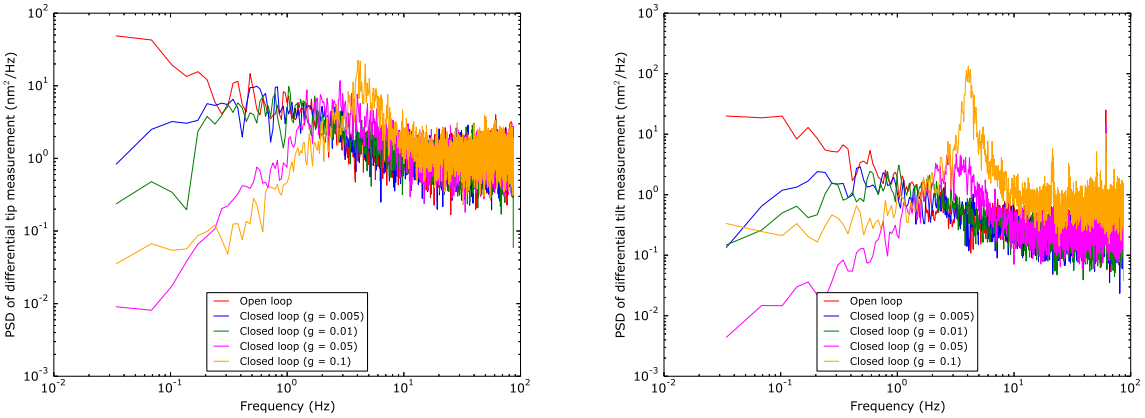

(a) Tip ***(b)*** Tilt

Figure 5.6: PSDs of the open- and closed-loop tip-tilt residuals for the different gain values under the laboratory turbulence. Significant suppression of the residuals is visible below 1 Hz for the gain of 0.05. The vibrations beyond 10 Hz for the tilt residuals (at gain = 0.1) are amplified due to the overshoot of the controller.

the tilt aberration (Fig. 5.7(b)) is affected by the vibration harmonics between 55 - 60 Hz for all the gain values but with different strengths. In both axes, the correction is better for frequencies < 1 Hz at the gain of 0.05.

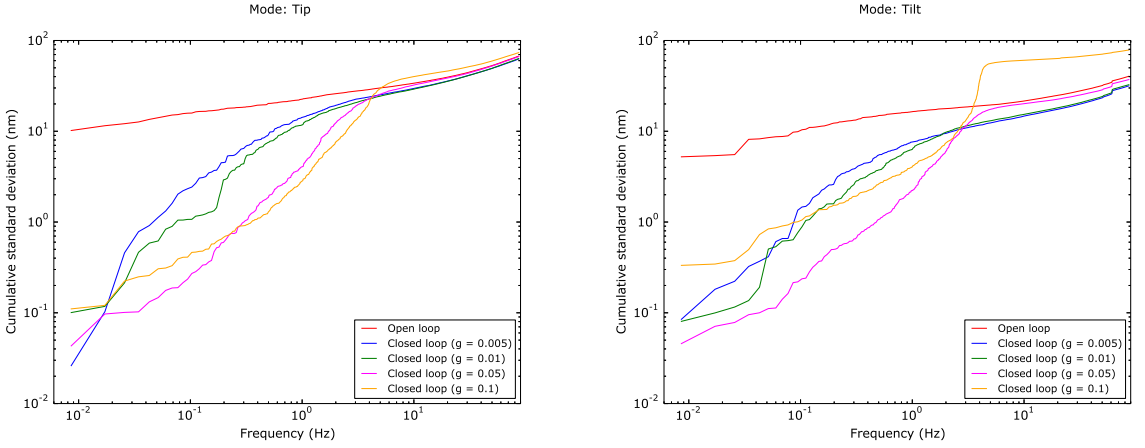

(a) TIP ***(b)*** Tilt

Figure 5.7: Cumulative integral of the PSDs in open- and closed-loop for the tip-tilt residuals under the laboratory turbulence. The cumulative standard deviation presents how strongly the vibrations are affecting the tip-tilt residuals for the different gain values.

Figure 5.8 shows the performance of the LLOWFS control via a transfer function for the different gain values. At both gains, 0.05 and 0.1, the correction is exactly one orders of magnitude corresponding to the one order magnitude of the frequency at < 0.5 Hz, as per the theory of the integrator controller. The overshoot for the gain 0.05 (amplitude of

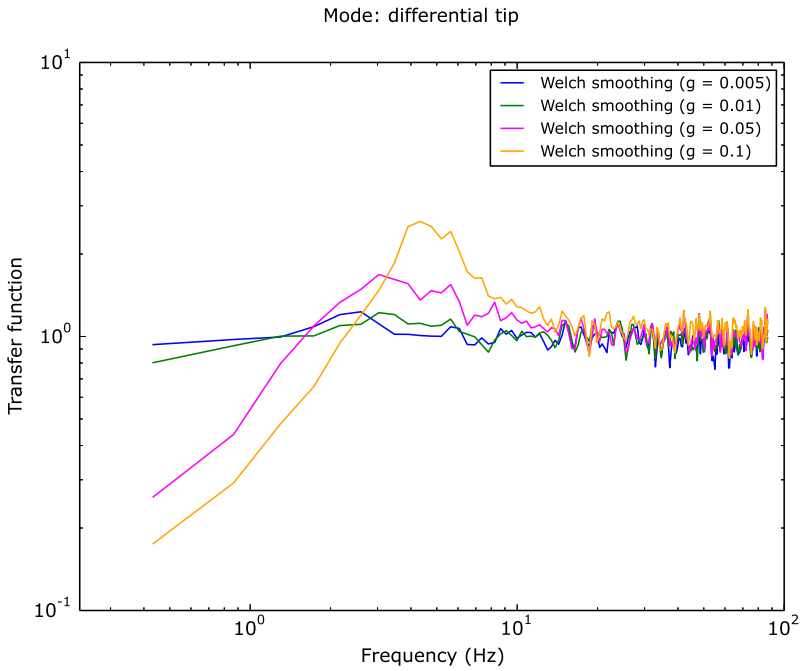

Figure 5.8: Transfer function of the LLOWFS control for the tip residual obtained at different gain values under the laboratory turbulence.

1.6 at 3.2 Hz) is smaller as compared for the gain 0.1 (amplitude 2.5 at 4.5 Hz), therefore, it is compensated by the correction between 0.5 and 1.6 Hz, without affecting much the residuals for higher frequencies. However, for the gain 0.1, the overshoot is important and the residuals for the high frequencies (> 4.5 Hz) are amplified.

The bandwidth frequency i.e. the frequency at which the closed-loop magnitude response is equal to -3 dB, is 1.2 Hz for the gain of 0.05.

After characterizing the performance of the LLOWFS by studying its spectral analysis, I now present the impact of the NCP tip-tilt residuals on the internal NIR science camera in the Fig. 5.9. The PyWFS loop was closed for all these frames. I compared the LLOWFS open-loop (left column) and closed-loop (right column) under the two temporal bands as usual. The exposure time of the internal NIR camera was 0.2s.

To simulate the minimal exposure time of HiCIAO, the internal NIR frames are averaged using a window of 2 seconds. The first row (Fig. 5.9(a)) present the average per pixel in a cube of HiCIAO simulated averaged frames. No significant improvement is visible due to the uncorrected high-frequency components. However, the difference in the open- and closed-loop frame is visible in the standard deviation (Fig. 5.9(b)) per pixel of the HiCIAO simulated averaged cube. The closed-loop image show lower standard deviation (hence darker than the open-loop image).

I also analyzed the standard deviation (Fig. 5.9 (c)) of each pixel in a raw cube of the frames from the internal NIR camera, to visualize the effects of the higher frequencies resolved by it. The standard deviation of the closed-loop is indeed higher than the open-loop image. These results are expected because the residuals at high frequency are amplified by the overshoot.

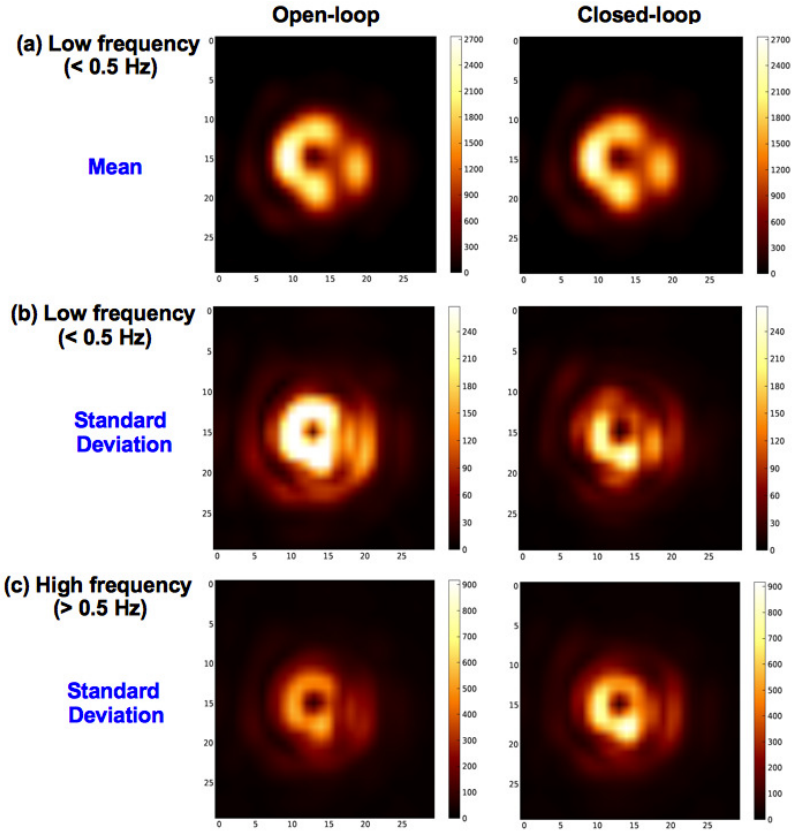

Figure 5.9: Processed frames of the internal NIR science camera presenting the LLOWS performance in the open- and closed-loop under the ExAO regime. The frames in the first two rows are averaged using a window of 2 seconds to simulate the effects of the low frequencies as seen by the HiCIAO. The improvement after closing the loop is not visible in the (a) average, however (b) the standard deviation is lower (hence the image is darker) as compared with the open loop image. Also as expected, c) the standard deviation of the closed-loop for the higher frequencies are amplified due to the overshoot.

5.6 On-sky spectral analysis of the low-order loop integrated inside the high-order control loop

In this section, I will present the on-sky analysis of the LLOWFS performance under the ExAO regime (§3.6.2) i.e. with the AO188 and PyWFS in closed-loop. To remind the reader again, the AO188 runs upstream of the SCExAO instrument and its operation are independent from SCExAO's WFSs. I will present the on-sky processed residuals and the corresponding HiCIAO science frames accquired during several engineering and science nights from September 2014 to April 2015.

The PyWFS is currently under development. However, it has now started to provide a diffraction-limited PSF on the sky in the visible since April 2015. During the engineering nights in September 2014, under which the LLOWFS and the PyWFS control loop integration was performed and analyzed, the PyWFS was in its initial phase of testing and provided a corrections of the tip-tilt modes only. Nevertheless, with the correction of higher number of modes other than just tip-tilt by the PyWFS in April 2015, the LLOWFS has corrected the NCP errors in the IR and provided a stable and durable correction during the science nights.

5.6.1 Variable star χ Cyg, $m_H = -1.93$ (September 2014 observation)

During this engineering night, when we observed the target χ Cyg, the AO188 closed the loop on 187 modes with a seeing of 0.8" at 1.6 µm. We used the VVC to occult the PSF. The PyWFS closed its loop only on tip-tilt in the visible with a loop speed of 1.7 kHz. As I have already mentioned, the PyWFS was not optimized at this point and hence provided only a partial correction of the tip-tilt modes. Also, for this observation, the LLOWFS used the first version of the DPS (piezo-driven dichroic) as its controller as explained in §5.2.

Figure 5.10 presents the temporal measurement of the open- and closed-loop of the LLOWFS. The data presented here are smoothed to simulate an exposure time of 2 seconds. The PyWFS closed the loop on the post-AO188 wavefront residuals and improved the stability of the residuals as measured by the LLOWFS in its open-loop. The NCP errors that were left uncorrected by the PyWFS were significantly reduced when the low-order loop was also closed. A small gain of 0.03 was used for LLOWFS control because of the slow response of the piezo driver (first version of the DPS), controlled only up to 5 Hz.

Table 5.2 summarizes the open and closed-loop residuals for the low-order control loop performance only. The data is analyzed at two different spectral bands. An improvement by a factor of 3 to 4 has been achieved in correcting the differential tip-tilt residuals for the slow varying frequencies. As expected, the improvement for the higher frequencies is not significant due to the small gain used.

We noticed the variations in the Fig. 5.10 that are sometimes larger than the linear range of the LLOWFS (± 170 nm rms), so the residuals in table 5.2 are probably underestimated. Even in such circumstances, the closed-loop pointing residuals are only about 6×10^{-3} λ/D (0.23 mas) when the dataset is sampled at the frame rate of the science camera (0.5 Hz).

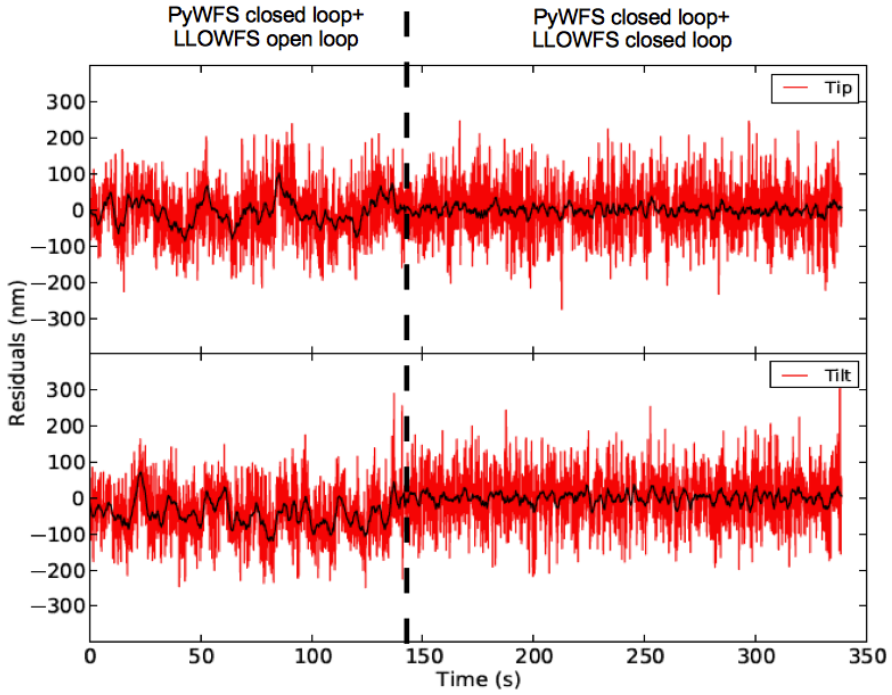

Figure 5.10: On-sky tip-tilt residuals obtained by the LLOWFS open- and closed-loop control, when it is integrated inside the high-order PyWFS control. When the low-order loop is open, the visible high-order is correcting only the tip-tilt errors in the post-AO188 wavefront residuals, leaving behind the uncorrected NCP errors in the IR. The LLOWFS in closed-loop, minimizes these errors significantly. A gain of 0.03 was used for the closed-loop operation.

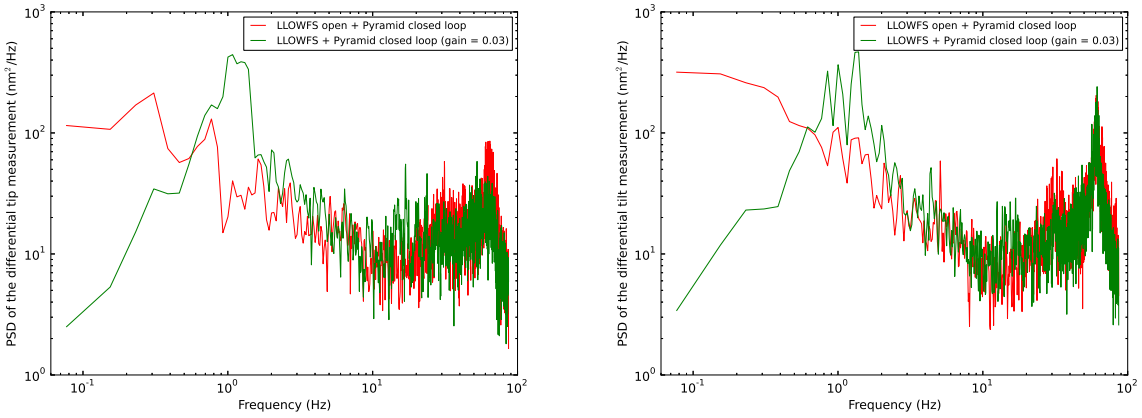

(a) TIP ***(b)*** Tilt

Figure 5.11: On-sky PSDs of the differential tip-tilt residuals obtained for the LLOWFS open- and closed-loop control under the ExAO regime. The low-order correction provides a significant improvement at frequencies < 0.5 Hz.

Table 5.2: On-sky open- and closed-loop residuals of differential tip-tilt with the low-order loop integrated with the high-order loop. The closed-loop pointing residual is 6×10^{-3} λ/D (0.23 mas) for the low frequencies.

		Low Freq. (< 0.5 Hz) (Resolved in HiCIAO)		**High Freq. (> 0.5 Hz) (Averaged in HiCIAO)**	
Mode	Unit	**Open loop**	**Closed loop**	**Open loop**	**Closed loop**
Tip	nm	26.1	9.4	144	142
	λ/D	1.6×10^{-2}	5.9×10^{-3}	9.0×10^{-2}	8.8×10^{-2}
	mas	0.66	**0.24**	3.6	**3.6**
Tilt	nm	36.3	9.3	170	166
	λ/D	2.3×10^{-2}	5.8×10^{-3}	10.6×10^{-2}	10.4×10^{-2}
	mas	0.91	**0.23**	4.3	**4.2**

Figure 5.11 presents the closed-loop analysis using the PSDs of the differential tip-tilt. The low-order correction provides a significant improvement at frequencies < 0.5 Hz and an overshoot around 1 Hz because of the mismatch in the sensing (170 Hz) and the correction (5 Hz) frequency. A vibration at 60 Hz is visible, which was excited by a Stirling cooler could not be corrected by the LLOWFS. The general slope of the PSD is probably affected by the non-linearities of the sensor. This is because of the amplitude of the variations that are sometimes larger than the linear range of the LLOWFS, which caused an underestimation of the real amplitude and a modification of the shape of the PSD.

5.6.2 A K5/M0III spectral type star, m_H = 3.87 (April 2015 observation)

This target was observed during one of the science nights in April 2015. With a seeing of ~ 0.5", the PyWFS closed the loop on ~ 800 modes and provided a Strehl of 60% in H band. The LLOWFS used the new version of the DPS (TTM) and comparatively provided a faster control (25 Hz) than the previous version of the DPS. However, the LLOWFS sensed the aberrations at 20 Hz only (50 ms exposure on the low-order camera). Also, to increase the sensitivity to the tip-tilt sensing, I reduced the defocus in the low-order image to have a higher density of photons per pixels. Figure 5.12 shows the reference image and the response matrix obtained directly on-sky.

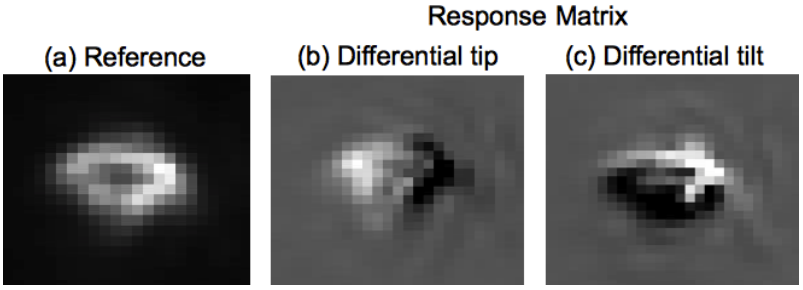

Figure 5.12: On-sky reference and response matrix (1.5 mas angle on-sky) with a VVC

We stayed on this target for almost 2 hours and the observer allowed us to perform the engineering tasks as the PyWFS and the LLOWFS required the tuning of their respective loops to stabilize the PSF behind the vector vortex mask. With the LLOWFS, I have collected ~ 35 minutes of open- and closed-loop data with two different gain values to analyze the LLOWFS performance. Figure 5.13 presents the temporal measurement of the on-sky residuals obtained under the LLOWFS open- and closed-loop.

I have tested the loop with a gain of 0.05 and 0.01. The correction is relatively more stable during the closed-loop operation at the gain of 0.05 than at the gain of 0.01. Figure 5.13 shows the suppression of the NCP errors better with the gain of 0.05 than with the gain 0.01.

Table 5.3 summarizes the residuals obtained under the open- and closed-loop operation by the LLOWFS. An improvement of factor 1.5 to 2 is obtained while correcting the low frequencies. Closed-loop pointing residuals of only about 1.2×10^{-2} λ/D (0.43 mas) has been obtained. Figure 5.14 comparing the PSDs of the closed-loop tip-tilt residuals at two different gains. The closed-loop at gain 0.05 (green plot) corrected the low frequencies convincingly better than the gain of 0.01 (blue plot). There is no overshoot detected as the sensing and the control was done at the same frequency (~ 20 Hz). A known telescope vibration emerged in one of the axis (tilt) at 5-6 Hz in the Fig. 5.14(b), which could not be corrected by the controller. The closed-loop PSD in Fig. 5.14(b) is also amplified at the frequencies < 0.1 Hz for both gains due to the large variations in the amplitude of the turbulence which was out of the linear range of the sensor.

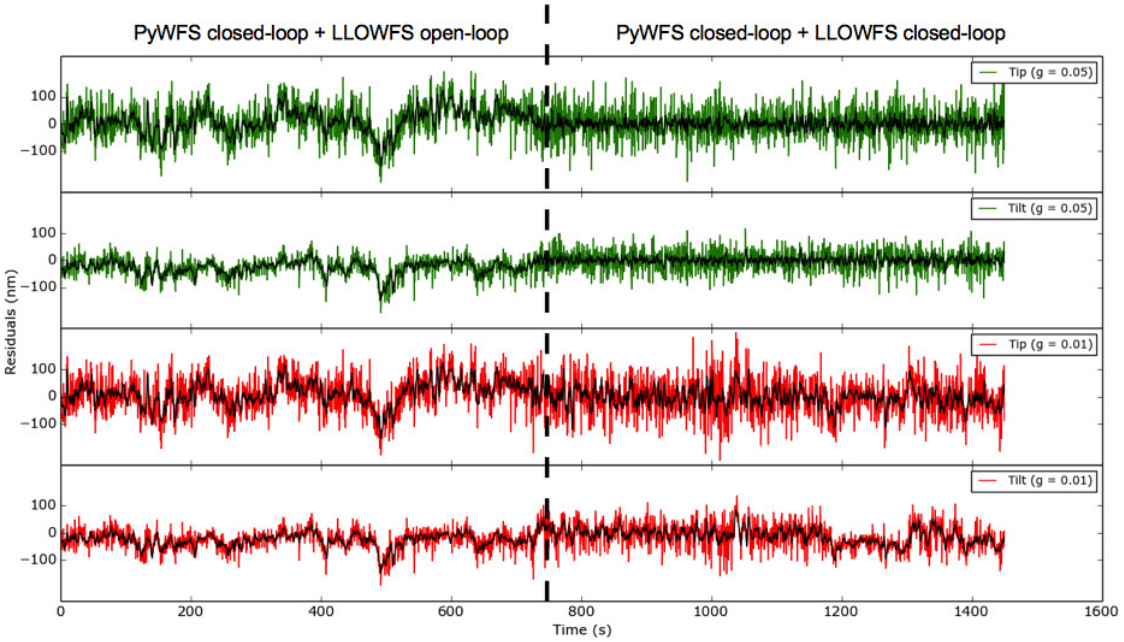

Figure 5.13: On-sky Residuals of the LLOWFS open- and closed-loop under the ExAO regime. The LLOWFS closed-loop is tested with two different gain. The gain of 0.05 provides a more stable correction than the gain of 0.01.

Table 5.3: On-sky open- and closed-loop residuals of differential tip-tilt with the low-order loop integrated with the high-order loop. The closed-loop pointing residual is 1.2×10^{-2} λ/D (0.48 mas) for the low frequencies.

		Low Freq. (< 0.5 Hz) (Resolved in HiCIAO)		**High Freq. (> 0.5 Hz) (Averaged in HiCIAO)**	
Mode	Unit	**Open loop**	**Closed loop**	**Open loop**	**Closed loop**
Tip	nm	33.6	20.2	55.1	53.9
	λ/D	2.1×10^{-2}	1.3×10^{-2}	3.5×10^{-2}	3.4×10^{-2}
	mas	0.86	**0.51**	1.4	**1.3**
Tilt	nm	18.5	13.2	29.5	36.1
	λ/D	1.2×10^{-2}	8.2×10^{-3}	1.8×10^{-2}	2.3×10^{-2}
	mas	0.47	**0.34**	0.75	**0.92**

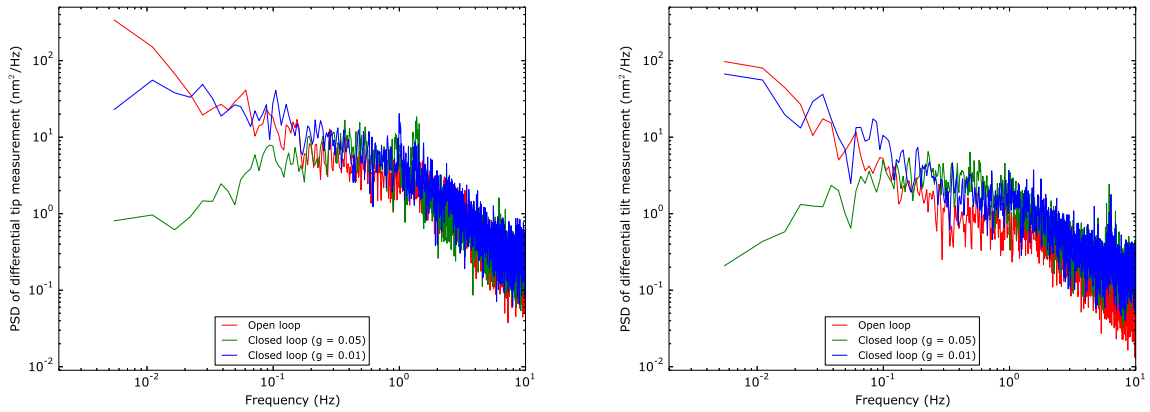

(a) TIP ***(b)*** Tilt

Figure 5.14: On-sky open- and closed-loop PSDs of the differential tip-tilt residuals measured by the LLOWFS under the ExAO regime. Closed-loop with gain of 0.05 provides better correction than the gain of 0.01 at frequencies < 0.1 Hz.

5.6.3 Comparing the two versions of the Differential Pointing System

The on-sky results obtained in §5.6.1 when the piezo-driven dichroic is used as a DPS can not be compared with the on-sky results obtained in §5.6.2 when the TTM is used as a DPS by the LLOWFS. For both the observations, the PyWFS delivered very different performances. The seeing conditions were also quite different. The sensing were done at different frequencies. The vibration at 60 Hz that appeared in the PSDs of the Fig. 5.11 of the first version of the DPS could not be detected in the PSD of the Fig. 5.14 of the second version due the slower sensing frequency (20 Hz).

Moreover, the residuals obtained in the table 5.2, in case of the first version of the DPS might be underestimated due to the variations that were sometimes outside of the linear range of the sensor. However, the non-linearities also affected the temporal results in the second version as well (Fig. 5.14 (b)) but their effects were less prominent than in the first version.

Detailed qualitative comparison either in the laboratory or on-sky could not be performed because of the – (1) PyWFS that was in the developing phase and was going through rigorous testing and – (2) limited available time to perform more tests as both techniques were either tested directly on-sky or a day prior of the observation.

5.6.4 A G8V C spectral type variable star, $m_H = 5.098$ (April 2015 observation)

In April 2015, during one of the science nights, the observation of this particular target has provided a very interesting dataset. The PyWFS, like for the previous target, corrected $\sim$ 1600 modes and provided a Strehl of $\sim$ 60 % in H under a median seeing of 0.6". With this target, I have not only obtained the best results with the LLOWFS in terms of the stability and durability but have also gained an understanding in characterizing the sources of the vibrations. This is one of the faintest target on which the LLOWFS closed its loop even though the sensing was done at 20 Hz only. The LLOWFS loop remain closed for 1 hour 45 minutes till the observer decided to move on to the next target.

As the target was faint, I focused the low-order image to the maximum allowable focus (not exactly at focus, due to space constraints on the bench) to gather more photons. Figure 5.15 shows the reference image and the response matrix obtained on-sky with the so called focused low-order image.

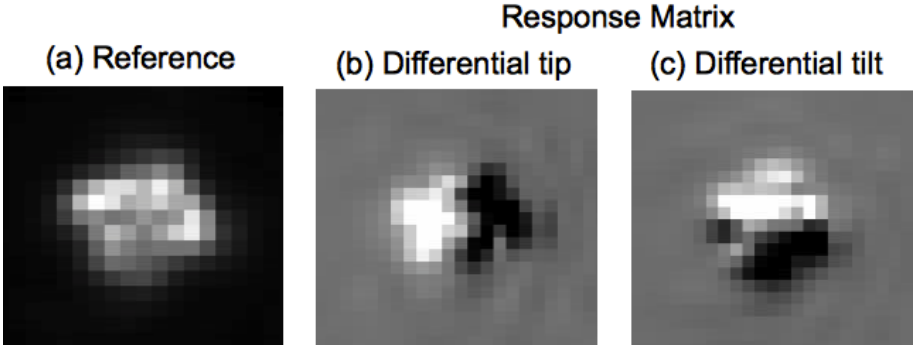

Figure 5.15: On-sky reference and response matrix (1.5 mas angle on-sky) with a VVC. (Target: G8V C spectral type variable star, $\mathbf{m_H = 5.098}$)

Both tip and tilt modes, which are defined by the axes of the TTM, are actually not aligned with the azimuth and elevation of the telescope. To characterize LLOWFS measurement of the differential tip-tilt residuals into elevation (EL) and azimuth (AZ) directions, the coordinates of the measured values were rotated by 37°. So that,

$$EL = tip \times \cos(37^\circ) - tilt \times \sin(37^\circ) \; and, \; AZ = tip \times \cos(37^\circ) + tilt \times \sin(37^\circ) \quad (5.1)$$

Figure 5.16 shows the temporal measurement of the LLOWFS closed-loop residuals obtained in elevation and azimuth direction during the observation of this particular science target for 1 hour 45 minutes. The curve in red/green is the raw residual while the one in black is the moving average of the residuals with a window of 2-seconds. There was no latency in the loop as the sensing and the correction frequency was the same ($\sim$ 20 Hz), which has also allowed to push the gain to 0.2.

The observation started approximately 16 minutes before the transit of the target, i.e. the point of maximum elevation. An interesting pattern has been observed in the temporal measurements of the residuals during the maximum of the transit in the EL direction (bottom image of Fig. 5.16, which is the zoomed version of the image on the top). High

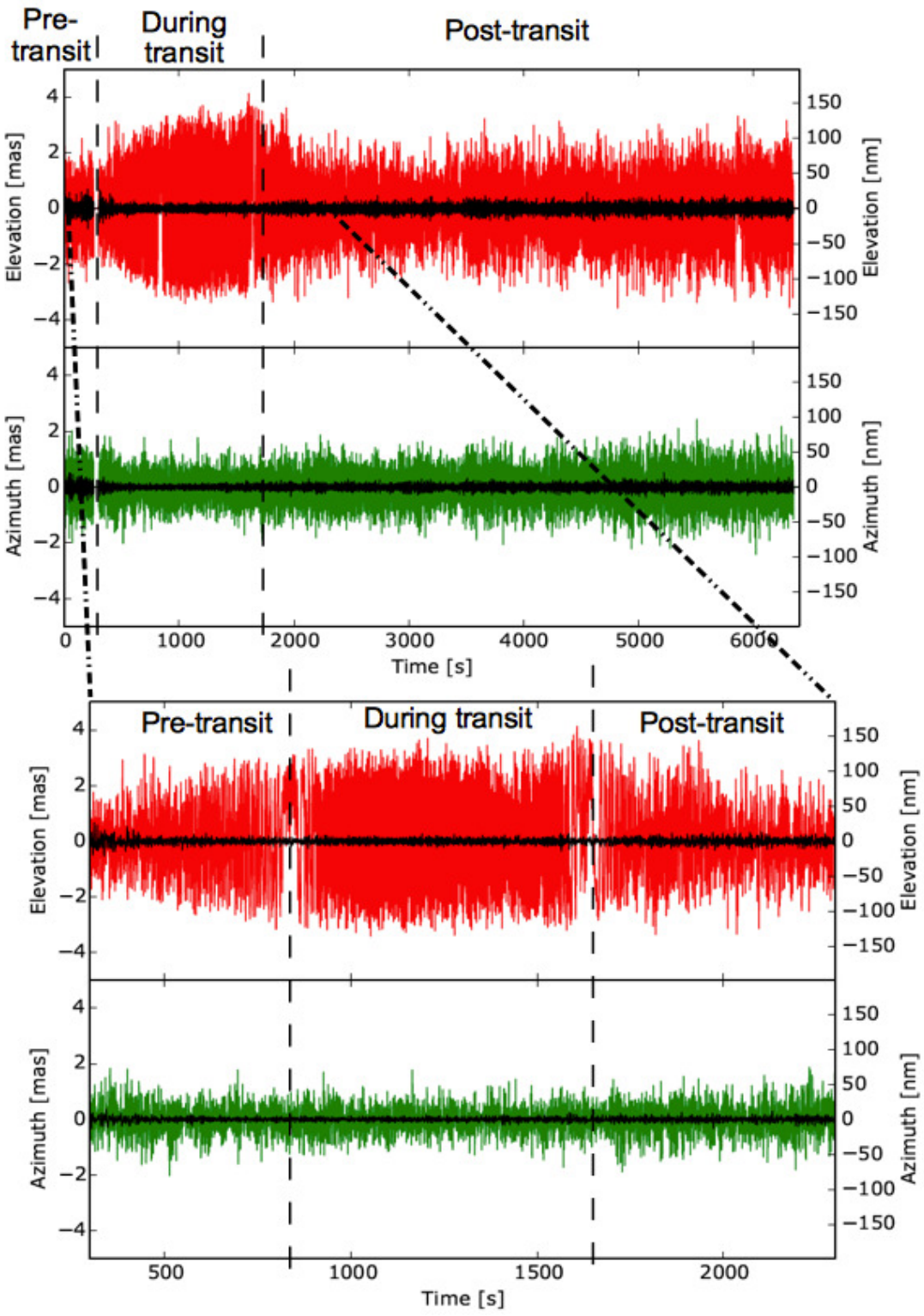

Figure 5.16: On-sky closed-loop differential residuals in elevation and azimuth directions as measured by the LLOWFS at the time of the Pre-, Post- and during the transit of the science target. The curve in red/green is the raw residual while the one in black is the moving average of the residuals with a window of 2-seconds. The LLOWFS loop remain closed for 1 hour 45 minutes, which was the full duration of the observation of this target.

frequency variation of the closed-loop residuals has been observed, which indicated that some additional stronger vibrations were introduced during the transit.

Figure. 5.17 shows the PSD of the LLOWFS closed-loop residual obtained for the immediate pre-, post- and during the transit of the target. For the – (1) pre- and post-transit, the vibrations occurred at the frequencies 3.8 Hz, 7.6 Hz and 8 Hz and – (2) during the transit, the vibrations were excited at 4.4, 5.2, 8 and 9.6 Hz.

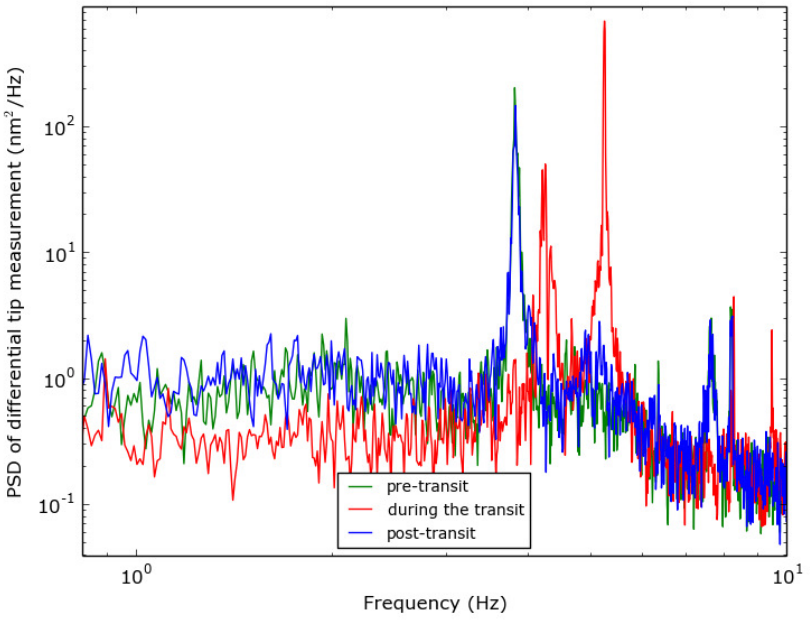

Figure 5.17: Closed-loop PSD of the residual measured by the LLOWFS at the time of the Pre- (16 minutes), Post- (16 minutes) and during (9 minutes) the transit of a science target. The frequency of the vibrations shifts and gets amplified during the transit.

The cumulative standard deviation of the PSD (in Fig. 5.17), which is the square root of the cumulative sum of the PSD is shown in Fig. 5.18 (a). The vibration at 3.8 Hz, which is of the same strength at pre- and post-transit (green and blue plot respectively) has not only shifted to 5.2 Hz but its power also gets amplified by a factor of ~ 2 during the transit (red plot). This factor is calculated directly from the cumulative variance plot in the Fig. 5.18 (b), by visualizing the size of both the steps linearly for the frequency before and after the shift. The step size is about ~ 1000 nm^2 at pre- and post-transit while during the transit, its amplified to ~ 3000 nm^2.

An additional vibration at 4.4 Hz that occurs only during the transit can also be seen as a step in the cumulative variance of the PSD in Fig. 5.18 (b), which is 5 times weaker than the vibration at the shifted frequency 5.2 Hz. The power of the other vibrations either during the transit (8, 9.6 Hz) or at the pre-/post-transit (7.6, 8 Hz) are weaker and their contribution to the overall variations are not prominent.

An important study that I could not perform with this data is analyzing the vibrations beyond 20 Hz and especially between 50-60 Hz that we have noticed during the previous

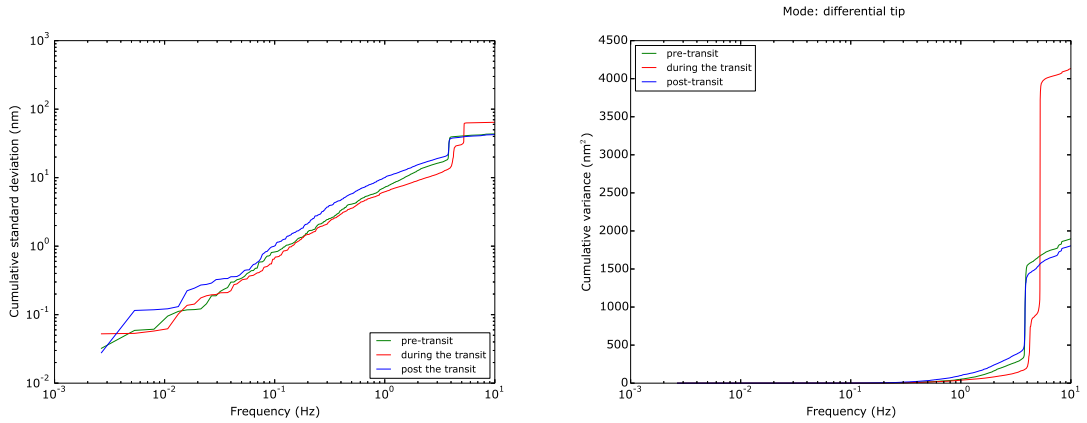

(a) Cumulative standard deviation

(b) Cumulative variance

Figure 5.18: On-sky closed-loop cumulative integral of the PSD of the measured residual at the time of Pre-, Post- and during the transit of a science target. The vibration at 3.8 Hz for the pre- and post-transit shifts to 5.2 Hz during the transit and gets amplified by 2 times in power. This amplification is clearly visible as the size of the step, which can be linearly compared in plot (b), which is the cumulative variance of the PSD in Fig. 5.17.

on-sky results in §4.6.2. The target was faint for the LLOWFS camera and the exposure time was 0.05s that is why LLOWFS could sense the aberrations at 20 Hz only.

Finding sources of the vibrations during the transit

The analysis presented so far, however, doesn't provide information about the evolution in frequency and amplitude of the vibrations. To analyze these time series of data, the evolution of the vibrations is studied by calculating the PSD and the cumulative standard deviation on a moving window of 1000 points. The result is a 3-dimensional plot, with the frequency in X, the time evolution in Y, and the amplitude of the function (either the PSD or the cumulative standard deviation) in Z[1].

The evolution of the PSD with time in Elevation and Azimuth directions is shown in the Fig. 5.19 and Fig. 5.20 respectively. There are several conclusions that can be drawn out of these plot for this particular observation.

- In *EL* direction (Fig. 5.19), the vibration at 3.8 Hz started about 16 minutes before the transit. While the target was transiting, this vibration at 3.8 Hz, first shifted to 4.4 Hz, then becomes amplified and jumped to 5.2 Hz for $\sim$ 9 minutes around the maximum of the transit. At the immediate post-transit, the vibration at 5.2 Hz went back to 4.4 Hz and down to 3.8 Hz, before disappearing completely 16 minutes after the transit.

- The harmonics of vibrations at 3.8, 4.4, 5.2 Hz can be seen (Fig. 5.19) at almost

[1]This analysis was performed with the help from Julien Lozi, one of the SCExAO member.

double of these values, starting at 7.6 Hz, going up to more than 8 Hz, then jumping to 9.6 Hz (probably 10.4 Hz folded by the temporal resolution of the sensor), then going back down to 7.6 Hz. This vibration is probably due to the encoder on the elevation axis. Because around the transit, the motion of the telescope is very small and the encoder might be hitting its resolution limit.

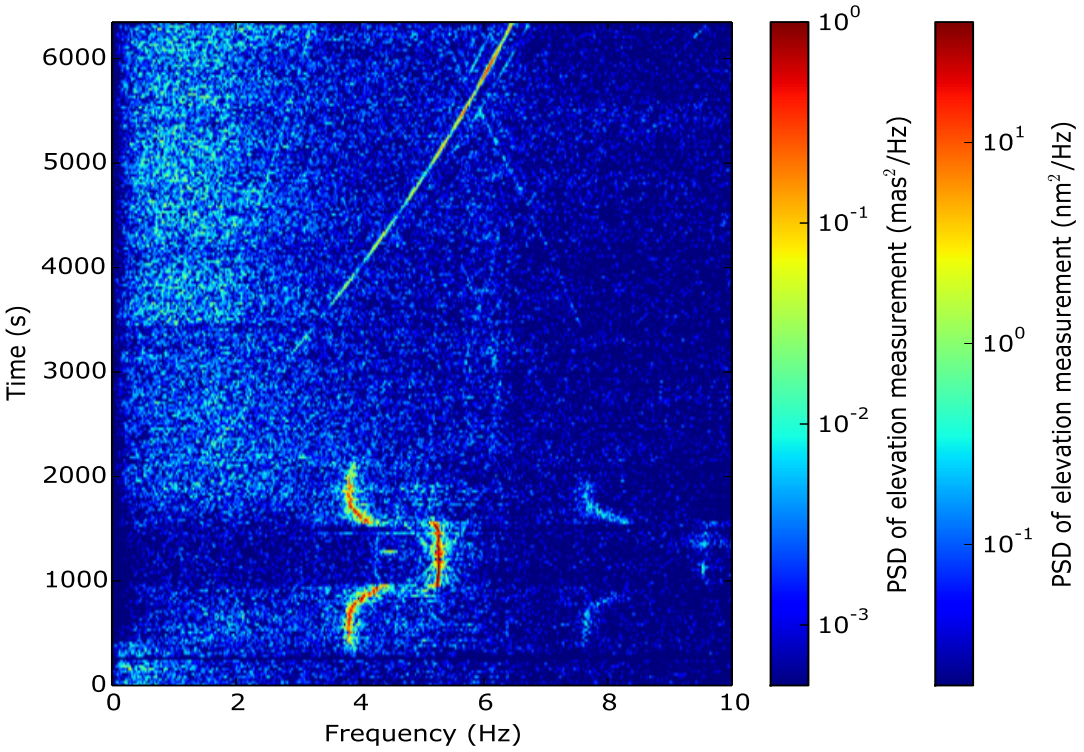

Figure 5.19: On-sky evolution of the closed-loop PSD depicting strong vibrations in Elevation direction. The vibration at 3.8 Hz occurred at pre-/post- transit of the target and its frequency shifted to 5.2 Hz and with 2 times more power during the transit.

- Another vibration appeared after the transit in *EL* direction, which kept evolving from 0 to a maximum frequency of 6.4 Hz throughout the observation. Another faint vibration can be seen at half that frequency, indicating a common source. These vibrations are due to the telescope motors themselves, rotating faster as telescope move far from the transit.

- In *AZ* direction shown in Fig. 5.20, the vibrations are less visible. The amplitude of a vibration at 8.3 Hz is strongest at the transit that goes to about 5.2 Hz at the end of this observation. Another fainter vibration can be seen between 3.4 Hz and 9.6 Hz, which is probably the folded harmonics of the strongest vibration, going from 16.6 Hz down to 10.4 Hz. These two components are probably introduced by the motors driving the azimuth of the telescope, because they have to rotate faster around the transit of the target.

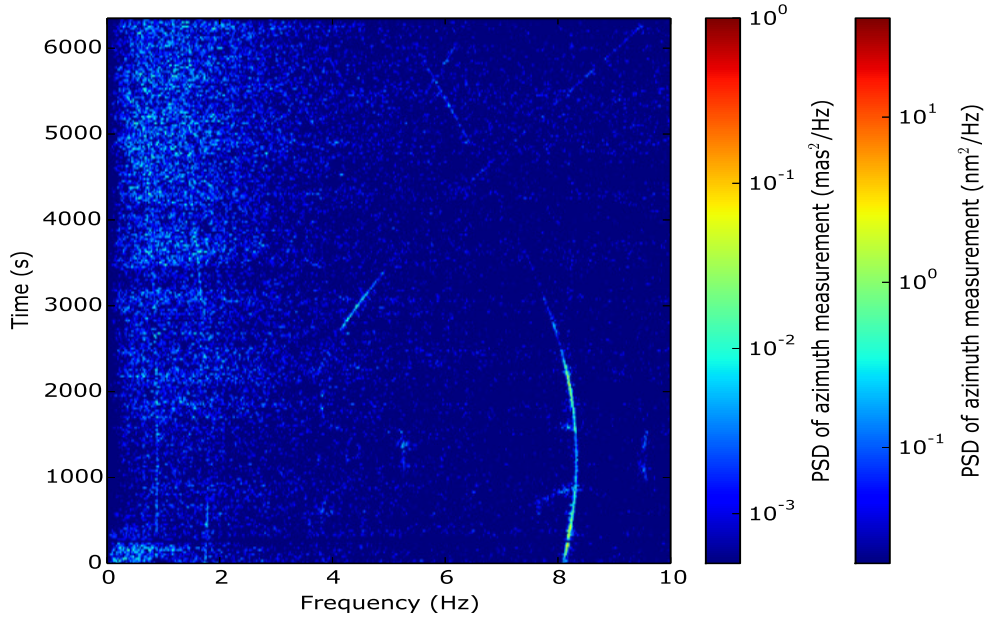

Figure 5.20: On-sky evolution of closed-loop PSD depicting no strong vibrations in Azimuth direction.

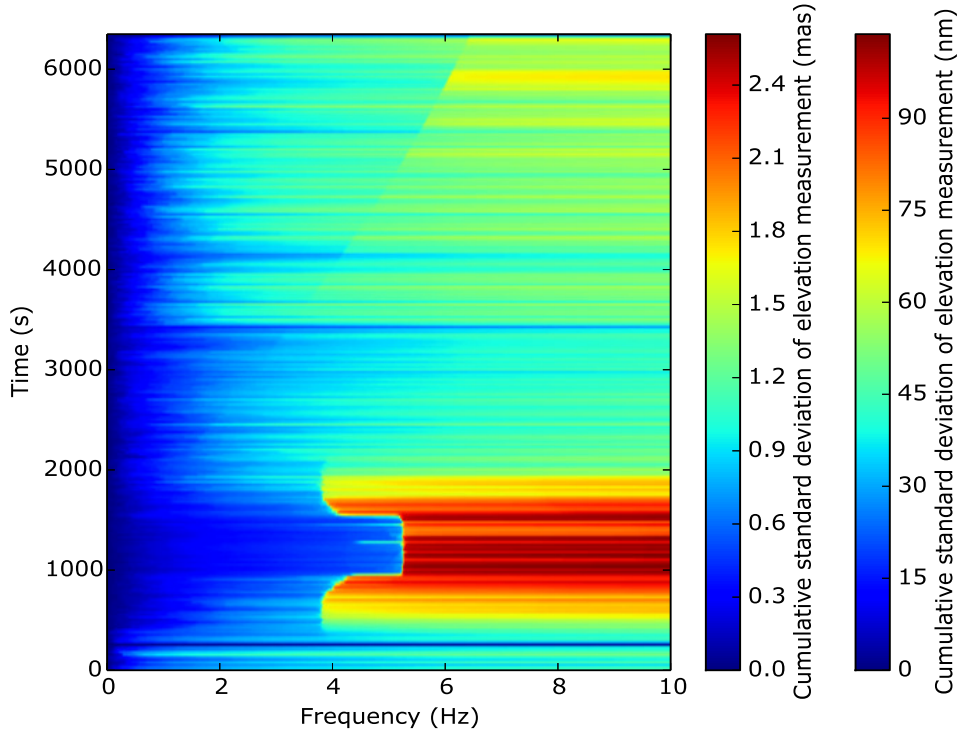

Figure 5.21: On-sky evolution of the closed-loop cumulative standard deviation of the tip aberration obtained throughout the observation of the target. The strongest vibration visible is at 5.2 Hz that occurred during the transit.

- From Fig. 5.21, which shows the evolution of the cumulative standard deviation of the measurements with time, it can easily be interpreted that the vibration at 5.2 Hz in *EL* direction during the transit is the strongest. As already discovered by Kanzawa *et al.* (2006), this vibration is due to the encoders of the elevation axis. Indeed, at transit, the elevation is almost constant, and the fix pitch of the encoders create an oscillation when their measurement is between pitches. This vibration increases the residual by more than a factor of 2 (probably underestimated because the high frequency vibrations are outside the linear domain of the LLOWFS). The main vibration of the motors is also visible after the transit, which only increased the residual by a factor of 1.5 at the maximum frequency.

Table 5.4 summarizes the closed-loop measurements of the residual in the elevation and the azimuth direction for pre-/post- and during the transit of the target for two temporal bands. For low frequencies (0 - 0.5 Hz) in *EL*, in spite of the excitation of strong vibrations, the closed loop residuals appears to be corrected comparatively better during the transit than at pre-/post-transit, whereas for the high-frequencies, the correction is better at pre-/post-transit. The correction should actually be about the same, but it is underestimated for higher frequencies because of their high amplitude, which is out of the linear range of the LLOWFS.

The PSD during the transit (red plot in Fig. 5.17) also seems to provide a little better correction at the frequencies < 3 Hz than for pre- and post-transit even though the vibrations introduce strong variations at the higher frequencies. This might be either due to – (1) the change in the seeing or – (2) the lower turbulence strength because of the low air mass during the transit or – (3) the non-linearities that seems to increase the variations of the residuals for the post-transit data (black curve in the Fig. 5.16).

Nevertheless, closed-loop pointing residuals of ~ 1.5 × 10^{-3} λ/D (0.06 mas) has been achieved at frequencies < 0.5 Hz under strong vibrations excited in EL direction.

In *EL*, almost 2 mas (0.05 λ/D) of image motion has been measured by the LLOWFS during the transit for higher frequencies (> 0.5 Hz). These vibrations has influenced the science observation for at least 30 minutes. Not only the contrast degraded but also the data for the ADI got affected because the planet has the largest motion in the science images during the transit. As LLOWFS can not run faster (≤ 25 Hz) in the ExAO regime, the impact of these vibrations is even stronger for faint targets. Because of non-linearities, the amplitude of these measured residuals might be underestimated due to the limited bandwidth of the LLOWFS control loop. The plate scale of the internal NIR camera is 12 mas/pixel and during the transit, motion of the PSFs (low-order and internal science camera images) over a few pixels had been observed visually. This motion is probably larger than 10 mas, but LLOWFS could not measure it due to the above stated reasons.

In AZ, a closed-loop pointing accuracy of ~ 0.9 × 10^{-3} λ/D (0.04 mas) has been achieved for lower frequencies (< 0.5 Hz), which is better than the pointing accuracy accquired in the EL direction as the effects due to vibrations in AZ were less strong.

Table 5.4: On-sky closed-loop residual in the elevation and the azimuth direction for pre-/post- and during the transit of the science target. The closed-loop pointing residual of 1.5×10^{-3} λ/D has been achieved at frequencies < 0.5 Hz.

		Low Freq. (< 0.5 Hz) (Resolved in HiCIAO)			**High Freq. (> 0.5 Hz)[a] (Averaged in HiCIAO)**		
Direction	Unit	**Pre-transit**	**During transit**	**Post-transit**	**Pre-transit**	**During transit**	**Post-transit**
EL	nm	5.0	3.4	4.6	51.9	79.1	47.3
	λ/D	3.1×10^{-3}	2.1×10^{-3}	2.9×10^{-3}	3.3×10^{-2}	5.0×10^{-2}	3.0×10^{-2}
	mas	**0.13**	**0.09**	**0.12**	**1.3**	**2.0**	**1.2**
AZ	nm	3.0	2.3	3.0	21.8	18.8	24.2
	λ/D	1.9×10^{-3}	1.5×10^{-3}	1.9×10^{-3}	1.4×10^{-2}	1.2×10^{-2}	1.5×10^{-2}
	mas	**0.08**	**0.06**	**0.08**	**0.6**	**0.5**	**0.6**

[a]These values might be underestimated because of the high amplitude of the high frequencies which LLOWFS could not correct due to its limited bandwidth.

Figure 5.22 shows de-striped, flat fielded and bad pixels removed HiCIAO frames. Fig. 5.22 (a) are the frames acquired only with the VVC's Lyot stop in the beam. (a)(i) is the single science frame acquired with an exposure time of 1.5 s during PyWFS closed loop and LLOWFS open-loop. Approximately 60% Strehl was achieved at H band. (b)(ii) presents the single frame during PyWFS and LLOWFS closed-loop. A slight improvement in the PSF stability is visible when LLOWFS loop is closed in (b)(ii).

Fig. 5.22 (b) present saturated coronagraphic HiCIAO frames for Pre-, during and post-transit with both PyWFS and LLOWFS loop closed. These frames are the average of 60 frames at exposure of 1.5s. The effect of additional vibrations introduced during the transit is not quite prominent in frame (b(ii)), however, a slight increase in the intensity is still noticeable in b(ii) as compared with the frames acquired during Pre- and Post-transit (b(ii)(iii)).

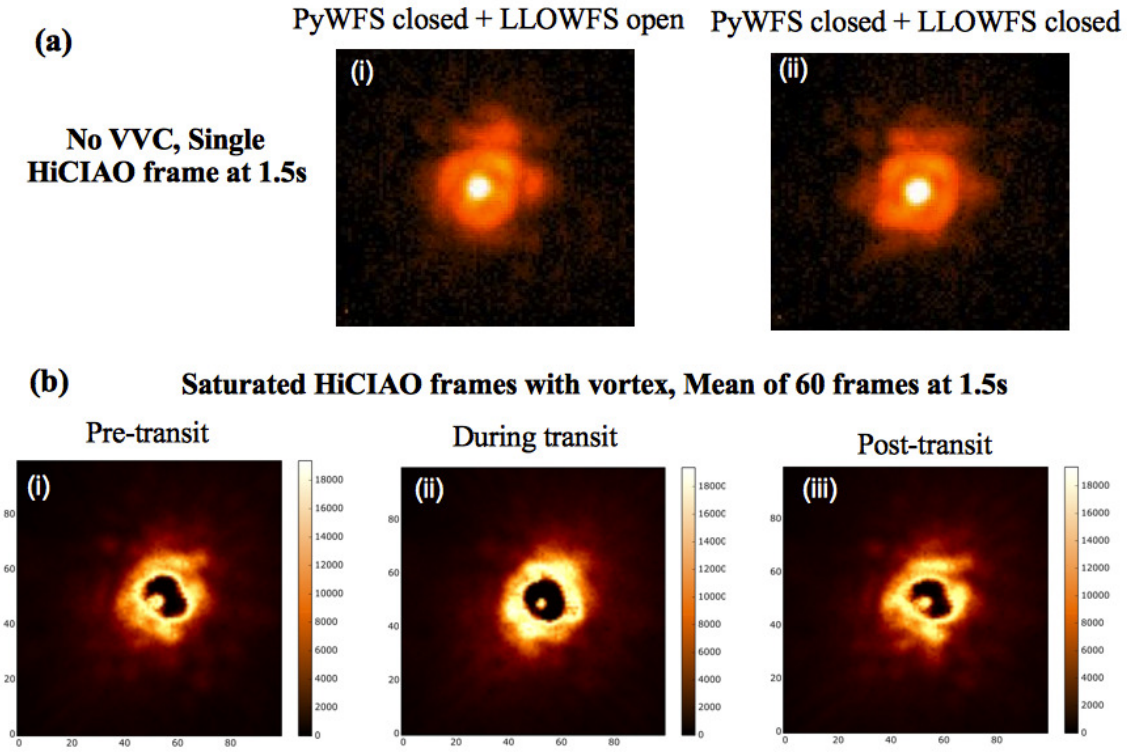

Figure 5.22: HiCIAO processed science frames during the PyWFS and the LLOWFS closed-loop operation. (a) are the PSFs only with the VVC's Lyot stop in the beam. Image in (a)(i) is acquired during the PyWFS closed- and LLOWFS-open-loop operation and (a(ii)) is the image when both loops are closed. A slight improvement in the stability of the PSF can be noticed in a(ii) as compared with the one in (a)(i). (b) Shows the saturated HiCIAO frames with a VVC and a Lyot stop in the beam. These frames are the average of 60 frames acquired with an exposure of 1.5 s for the Pre-, During and Post-transit of the target. Both PyWFS and LLOWFS loops are closed providing Strehl of $\sim$ 60% at 1.6 μm. Starlight spillover and a slight increase in the intensity of the image during the transit (b(ii)) can be seen which is due to the strong vibrations excited during the transit. Images in b(i)(iii) are comparatively darker. (*Plate scale is 8.3 mas/pixel for HiCIAO.)*

5.6.5 A variable star of α^2 CVn type, m_H = 6.281 (April 2015 observation)

This is the faintest science target for which the LLOWFS has corrected the differential tip-tilt residuals (at 20 Hz) under the ExAO-regime. We stayed on this target for 55 minutes, and the PyWFS + LLOWFS remain closed for the full duration. This particular target also transited during its observation and we noticed that some of the vibrations that occurred while observing the target as described in § 5.6.4 did not occur with the current target. The reason is because this target was 10° lower in the sky as compared to the previous target and the transit occurred in the south direction instead of the north.

Figure 5.23 (a) presents the PSD of the residual obtained at pre-/post-transit (green and blue plot respectively) and during the transit (red plot) of the target. These expected vibrations in *EL* direction at 3.8, 4.4 Hz also occurred at pre-/post-transit, which again shifted to the frequency 5.2 Hz during the transit (for 8 minutes). The strength of the vibration can be visualized from the cumulative variance of the PSD shown in the Fig. 5.23 (b). The vibration at 3.8 Hz has shifted to 5.2 Hz and got amplified by a factor of 2.3. Moreover, the power of the vibration at 3.8 Hz at the pre-transit was reduced by a factor of 1.3 at the post-transit. This observation confirmed that the encoders are creating these vibrations, because the frequency is related to the regular spacing of the features on the incremental encoders.

In *AZ* direction, the main frequency of the motors driving this axis occurred between 8.7 Hz and 8 Hz. This is probably due to the lower elevation of the target, requiring a faster speed for the azimuthal motors.

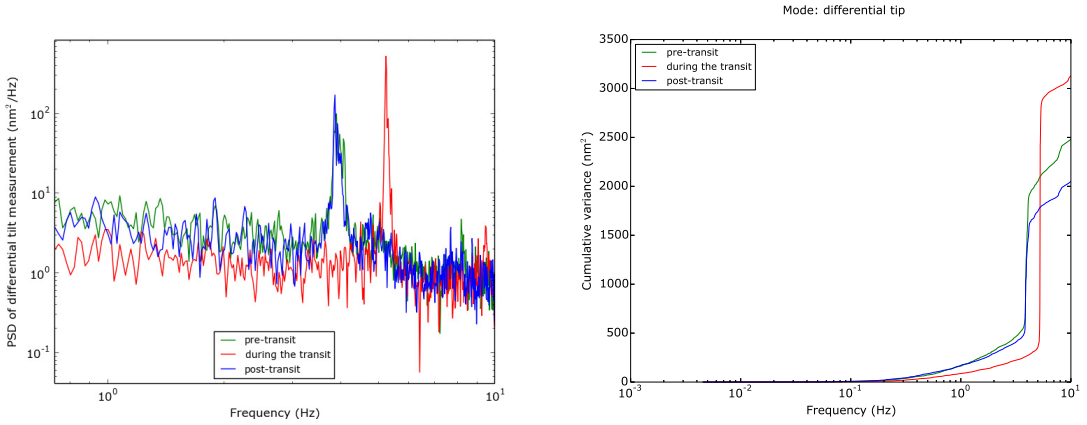

(a) PSD of the Tip residual

(b) Cumulative variance of the PSD in (a)

Figure 5.23: (a) Closed-loop PSD of the residual measured by the LLOWFS at the time of the Pre-, Post- (16 minutes) and during (8 minutes) the transit of a science target. The frequency of the vibrations shifts and gets amplified during the transit of the target. (b) Cumulative variance of the PSD in (a), which shows that the vibration is shifted from 3.8 to 5.2 Hz and gets amplified by a factor of 2.3 during the transit.

The frequencies of the vibrations, especially during the transit that are observed in §5.6.4 and §5.6.5 actually matches with the frequencies of the vibrations detected in the

study by Kanzawa *et al.* (2006) at the Subaru Telescope. They measured and characterized these vibrations via accelerometers and concluded that the vibrations are excited – (1) due to the periodic errors in the incremental encoders of the elevation and azimuth direction that are used to measure the velocity of the telescope rotation and – (2) due to the motors that steer the telescope in azimuth and elevation direction.

The accelerometers were installed temporarily at the telescope to measure the vibrations. To address this issue, the observatory is planning to adapt one of the following solutions: – (1) Either tune the current encoders or replace them with a precise one with smaller tripe pitches. – (2) Tweak the gain of the pointing control of the telescope during the transit. – (3) Install accelerometers permanently on the telescope to control the vibrations. After measuring the vibrations, the tip-tilt signal can be send either to the IR secondary of the telescope or to the AO188 system for the correction.

5.7 Factors affecting LLOWFS performance under ExAO regime

I have successfully feedbacked the low-order correction inside the high-order control loop under the ExAO operation of the SCExAO instrument. In the laboratory and on-sky, I have demonstrated a closed-loop pointing residuals of a few 10^{-4} λ/D and 10^{-3} λ/D respectively. Though the LLOWFS provided a stable and a durable correction of the differential tip-tilt errors in the IR but only with a maximum speed of 25 Hz. There are several factors that can affect the performance of LLOWFS, which are summarized below.

- LLOWFS stability depends on the correction provided by the AO188 and the PyWFS. Any interruption in their control loop will halt the LLOWFS loop due to uncorrected high frequency variations.
- The limited speed of the LLOWFS controller ($\sim$ 25 Hz).
- Mismatch in the frequency of the sensing (170 Hz) and the correction (25 Hz) for the bright targets, which may cause an overshoot of the controller.
- Excitation of the vibrations due to telescope motion especially during transit (at maximum elevation) of a target.
- Noisy on-sky reference and response matrix due to bad seeing. Asymmetries in the response matrix can introduce non-linearities in the calibrated response of the sensor.
- Tuning of the loop by setting the gain manually. Not knowing whether the gain applied is optimal or if it will make the loop unstable.

LLOWFS correction is a trade off between the defocus of the sensor, speed of the loop and number of modes to be corrected. For bright targets, large defocus ($>$ 10 radian) can be introduced in the position of the LLOWFS camera to correct more number of modes (demonstrated correction of 10 modes on-sky under non ExAO regime) at fast speed. However, for faint targets, the LLOWFS camera should be placed closer to focus in order to concentrate high density of photons over small number of pixels. In this case, only few modes can be corrected due to insufficient defocus in the sensor position. The correction of only 2-3 modes has been demonstrated at slow speed.

5.8 Upgrades to improve LLOWFS performance

Below are the upgrades that have already been performed during the writing process of my thesis.

- In the ExAO regime, either using the dichroic or the tip-tilt mirror as a DPS by the LLOWFS, the low-order control was limited to only tip and tilt modes. To correct other low-order aberrations as well and to improve the speed, software upgrades of the way the LLOWFS interacts with the PyWFS has already been performed. To

enable its full potential in the ExAO regime, the LLOWFS without being in physical contact with the PyWFS, now simultaneously send the correction to the DM and update the zero point of the PyWFS. LLOWFS is now measuring 16 modes in the ExAO regime in the laboratory.

- To increase the SNR, LLOWFS camera is cooled and the reflectivity of the RLS is improved by replacing chrome coated RLS with the gold coated substrate.
- Initial integration of both LLOWFS and speckle nulling loop inside the PyWFS control loop has been performed to provide the stability of the contrast.

Near-future upgrades includes:

- Implementation of a LQG controller for the low-order loop in order to provide an optimal control of the vibrations.
- The use of the low-order telemetry to calibrate the uncorrected low-order aberrations in real-time.
- Replacement of the current LLOWFS camera with a 10 kHz high frame rate camera.

Conclusion

In a decade, the current ground-based extreme adaptive optics instruments will be able to directly image young EGPs in the habitable zones of their host star. However, to achieve this goal, they will have to be equipped with high performance small IWA coronagraphs in order to gain access to the immediate surroundings (< 10 AU) of the star. Coronagraphs alone will not be sufficient as they are extremely sensitive to the tip-tilt errors and require an exquisite control of the low-order wavefront aberrations at/near their IWA.

Even after the high-order wavefront correction from the AO/ExAO, a dedicated coronagraphic wavefront sensor is often required to provide a stable and durable control of low-order aberrations, especially pointing errors upstream of a FPM. In §1.4.3, I presented the state of the art in dealing with pointing errors. None of the techniques adapted by the current instruments discussed in this section can measure low-order aberrations beyond tip-tilt for small IWA phase mask coronagraphs. Addressing this problem, I worked on a concept aimed at measuring low-order aberrations using the starlight reflected by the Lyot stop.

In this thesis, I introduced a Lyot-based Low-Order WaveFront Sensor (LLOWFS). I presented its principle (§2.3), simulations (§2.4), its implementation on the *SCExAO instrument* at the *Subaru Telescope* (§3.4), its very first laboratory results (§2.5, §4.5, §5.5) and very first on-sky results (§4.6, §5.6). The LLOWFS is a versatile wavefront sensor and a linear reconstructor of the wavefront. It can measure the aberrations for different families of coronagraphs (apodized/amplitude/phase) as it only requires a reflective Lyot stop to collect the rejected starlight and relay optics to direct the starlight towards an imaging camera to accumulate photons.

During the first year of my thesis, I studied thoroughly the LLOWFS concept, diagnosed the problem of low-order aberrations with the FQPM through simulations and performed the first preliminary testings in the laboratory at *LESIA, Observatoire de Paris*. For the next two years of my research, I have studied two ways of integrating the LLOWFS on the SCExAO instrument. I implemented the sensor on the instrument, programmed the control loop using sensor measurements and performed rigorous testings in the laboratory and on-sky with several coronagraphs.

In the first approach of integration, the LLOWFS relied on the post AO188 wavefront residuals (SR of 30% - 40% in H-band with a $\sim$ 200 nm RMS wavefront error) and used SCExAO's 2k-actuator DM for the correction of the low-order modes.

Under this non-ExAO regime, I have validated the closed-loop performance of the LLOWFS for 15 Zernike modes with the PIAA and for 35 Zernike modes with the VVC,

the FQPM and the EOPM coronagraphs. I obtained this result in the laboratory under the simulated turbulence (amplitude of 150 nm RMS and wind speed of 10 m/s) mimicking the post-AO correction scenario but also allowing low-spatial frequency components of the turbulence to be left uncorrected. Under such circumstances, I obtained a closed-loop pointing residual between $10^{-3}\lambda/D$ and $10^{-4}\lambda/D$ in H-band at 170 Hz for slow-varying errors (frequencies < 0.5 Hz) for all the coronagraphs.

On the on-sky post-AO188 residuals, I demonstrated the correction of 10 Zernike modes with the VVC and the PIAA coronagraph in H-band on the same target (§4.6.2) and obtained a closed-loop tip-tilt residuals of a few $10^{-3}\lambda/D$ for slow varying errors. LLOWFS performance was limited by the vibrations from the telescope (6 Hz, 12 Hz) and the optical/mechanical elements (40 - 60 Hz) inside the instrument. Even in these circumstances, I demonstrated that under good seeing and for bright target ($m_H < 2$), the low-order control provides a closed-loop pointing residuals of $10^{-4}\lambda/D$ (1.6 nm). Under moderate seeing and for targets brighter than $m_H < 2.5$, the low-order control routinely provide a closed-loop residual of $10^{-3}\lambda/D$.

All the results obtained in the non-ExAO regime are presented in Chapter 4. No significant improvement in the contrast is observed as there was no high-order wavefront correction. With the AO188 and the LLOWFS in closed-loop, the starlight was well aligned upstream of the FPM during on-sky operations.

In the second approach, I integrated the LLOWFS with SCExAO's high-order Pyramid WaveFront Sensor (PyWFS) control loop. Instead of directly commanding the DM for the low-order correction, LLOWFS communicated its correction to the PyWFS via a Differential Pointing System (DPS). This method is applicable for any extreme adaptive optics instruments that has several wavefront sensing units with only one dedicated DM for the wavefront correction. With this preliminary setup, the non-common path errors in tip-tilt between the visible wavefront sensing channel and the infrared science channel are corrected. In the laboratory, an improvement of roughly one order of magnitude has been achieved in compensating the chromatic errors when LLOWFS closed the loop on residuals of the PyWFS (§5.5).

On-sky with the VVC, I have demonstrated the improvement of tip-tilt errors by a factor of 5 to 6 in the ExAO regime. During a science night, for the observation of two faint targets (m_H = 5.09 (§5.6.4) and m_H = 6.3 (§5.6.5)), the PyWFS and the LLOWFS loop remain closed for 1 hour 45 minutes and 55 minutes respectively. These are the most durable and stable results I have obtained with the LLOWFS during the course of my research. Downstream the AO188, the PyWFS corrected ~ 800 modes in the visible and provided a SR between 60 - 70% in H-band under a median seeing of 0.6". On these residuals, I demonstrated a closed-loop pointing residuals of $10^{-3}\lambda/D$ in the infrared channel. However, these observations were dominated by high amplitude vibrations (frequencies between 3.8 and 9.6 Hz) introduced occasionally by the elevation incremental encoders of the telescope mainly during the transit of the target. Under such circumstances, the LLOWFS obtained a closed-loop pointing residuals of a few $10^{-3}\lambda/D$ (< 5 nm) for slow varying errors. The results that I presented in these sections might be underestimated as non-linearities induced by the vibrations could not be controlled by the low-order loop due to its limited bandwidth (~ 25 Hz). Due to these vibrations, the LLOWFS measured an image motion of ~ 2 mas (0.05 λ/D), however, at least 10 mas of image motion was

observed on the science camera.

Throughout my research, SCExAO was under a development phase. That is why, I developed two modes of operating the LLOWFS on the instrument. The results presented in the ExAO regime were obtained during the engineering and science nights in April 2015 when the PyWFS started to provide a SR of more than 60%. However, during the July 2015 run (1.5 weeks ago), a SR of > 90% has been achieved in the H-band. With such a stable PSF, the LLOWFS is envisioned to provide pointing residuals of 10^{-4} λ/D on a regular basis.

However, with the current integration of the PyWFS and the LLOWFS, only pointing errors are addressed in the imaging channel. In the near future, the LLOWFS, instead of interacting with the DPS, will interact directly with the control loop of the PyWFS. The LLOWFS will measure more low-order errors than just pointing errors, and will send its correction directly inside the control loop software of the PyWFS, changing its zero-point. This upgrade will not require any additional hardware but only few software changes. We are planning to test this new mode in the September and October 2015 runs (I have one night in September, I intend to try the LLOWFS on-sky, and probably test in open- and closed-loop on a long period).

One aspect that I could not study in this thesis is the interaction of the LLOWFS with the speckle nulling loop. It is interesting to close the loop with LLOWFS and freeze the speckle pattern. During July 2015 run, efforts have been made to integrate the speckle nulling loop with the PyWFS. Precomputed speckle nulling maps were sent to the PyWFS to change its zero-point offset. This integration with active speckle control is in progress and intended to be tested during the next couple of runs.

The next crucial requirement for SCExAO is – (1) to implement a LQG controller for the low-order loop to provide an optimal control of the aberrations and – (2) to integrate both LLOWFS and speckle nulling loop inside the PyWFS control loop so that all the three wavefront sensing units can run simultaneously. In this configuration, both speckle nulling and LLOWFS will overwrite their respective correction inside the control loop of the PyWFS and only the PyWFS will then control the DM for the compensation of the wavefront aberrations. This upgrade in the near future should allow SCExAO to detect young Jupiters (a few Mj) by a factor of ~ 3 closer to their host stars than is currently possible.

Despite the constant evolution on SCExAO, I have accomplished the goal I set in §1.4.2.3. On the basis of the assumptions that if the planet detection is limited by the stellar angular size (stellar angular radius of ~ 0.15 mas for a M spectral type star at 10 pc), then the allowable jitter should be 0.0036 λ/D for a 8-m telescope. Even under the presence of uncorrected turbulence and high amplitude vibrations, I achieved an on-sky pointing residual of 10^{-3} λ/D in H-band.

Perspective

To control the starlight leakage near the coronagraphic IWA, both LLOWFS approaches presented in this thesis can easily be implemented on any existing extreme adaptive optics instrument that has either a dedicated low-order DM or has the possibility to feed the low-order correction to their existing DM or to a tip/tilt mirror. The Keck Planet Imager, which is an upcoming upgrade of the Keck AO system has already acknowledged the benefits of the LLOWFS (Mawet *et al.*, 2014b).

For the upcoming ELTs, in order to image the rocky-type habitable planets around the M-type main sequence stars using the coronagraphs optimized for $\sim 1\ \lambda/D$ IWA (Guyon *et al.*, 2012), the implementation of the LLOWFS-like technology can enhance the image quality at/near the IWA by providing an unprecedented control of the low-order wavefront aberrations. This feature can help the direct imagers of the ELTs to probe the region at the angular separation of ~ 1 AU.

The PICTURE-C (Mendillo *et al.*, 2015) mission, which is an high-altitude ballon carrying a high performance vortex coronagraph has already considered the LLOWFS to deal with the pointing errors left uncorrected by the Wallops Arc Second Pointer (WASP) system. To control the low-order aberrations for the VVC, they have selected the LLOWFS over a SHWFS and a Curvature WFS for their second flight planned in 2019.

This technique is equally relevant for the next generation HCI instruments aboard space telescopes such as WFIRST-AFTA, Exo-C and ACESat. One of the challenges foreseen for these coronagraphs is the low-order aberrations induced by the thermal drifts and the telescope pointing. All the three missions are considering to use a PIAACMC optimized between ~ 1.6 - $2\ \lambda/D$ IWA. They will benefit directly from the LLOWFS as it is an ideal technology to control the low-order aberrations for the PMCs. The study of the linear range I performed with the LLOWFS on SCExAO can give the requirement on the pointing of the spacecraft, while the level of correction demonstrated on SCExAO can be scaled to space conditions to give specifications on the acceptable level of vibrations.

The coronagraphic wavefront sensor presented in this thesis has opened a new instrumental parameter space to define the best approaches for wavefront control and calibration in conjunction with the existing technologies.

In order to improve the post processing of the science images, the low-order telemetry of the residuals left uncorrected by the control loop can be used to calibrate the amount of starlight leakage at small angular separations. Synchronized LLOWFS measurements and science camera frames can be used to build a library of response of the residuals on the starlight leakage. During the observation of the science target, LLOWFS residuals can

then be fitted with the best match in the library. The corresponding science equivalents can be subtracted from the science image to reconstruct the PSF.

The interaction of speckle calibration with LLOWFS especially for the corrections of speckles at small IWA can reduce the duration of control loop iteration which is essential when the coronagraph requires long exposures to collect enough photons. Thus, the number of accessible targets can be increased by using fewer images per iteration.

The cross fertilization of the techniques such as the LLOWFS optimization, the PSF calibration and the speckle suppression at small IWA on the current/future ExAO instruments implemented on the 8-m class observatories should enable the detection of the EGPs in the habitable zone of their host stars within a decade and of Earth-like planets around M-dwarfs in the HZ on the next generation of ELTs.

"New ideas pass through three periods: 1) It can't be done. 2) It probably can be done, but it's not worth doing. 3) I knew it was a good idea all along!"

- Arthur C. Clarke

List of Publications

Peer-reviewed Papers

- "Lyot-based low order wavefront sensor for phase mask coronagraphs: Principle, Simulations and Laboratory Experiments"
  Singh, G., Martinache, F., Baudoz, P., Guyon, O., Matsuo, T., Jovanovic N., Clergeon, C. *Publications of the Astronomical Society of the Pacific*, vol. 126, pp. 586-594, June 2014.

- "On-Sky speckle nulling demonstration at small angular separation with SCExAO"
  Martinache, F., Guyon, O., Jovanovic, N., Clergeon, C., **Singh, G.**, Kudo, T., Currie, T., Thalmann, C., McElwain, M., Tamura, M. *Publications of the Astronomical Society of the Pacific*, vol. 126, pp. 565-572, June 2014.

- "On-Sky Demonstration of Low-Order Wavefront Sensing and Control with Focal Plane Phase Mask Coronagraphs"
  Singh, G., Lozi, J., Guyon, O., Baudoz, P., Jovanovic N., Martinache, F., Kudo, T., Serabyn, E., & Kuhn, J. *Publications of the Astronomical Society of the Pacific*, Volume 127, issue 955, pp.857-869, 2015.

- "The Subaru Coronagraphic Extreme Adaptive Optics System: Enabling High-Contrast Imaging on Solar-System Scales"
  Jovanovic, N., Martinache, F., Guyon, O., Clergeon, C., **Singh, G.**, Kudo, T., et al. *Publications of the Astronomical Society of the Pacific*, Volume 127, issue 955, pp.890-910, 2015.

Conference Proceedings

- "Lyot-based Low Order Wavefront Sensor: Implementation on the Subaru Coronagraphic Extreme Adaptive Optics System and its Laboratory Performance"
  Singh, G., Guyon, O., Baudoz, P., Jovanovic, N., Martinache, F., Kudo T., Serabyn, E., Kuhn,J. G.
  Proc. SPIE 9148, Adaptive Optics Systems IV, 914848, doi:10.1117/12.2057211 (August 2014).

- “Development and recent results from the Subaru coronagraphic extreme adaptive optics system"
  N. Jovanovic, O. Guyon, F. Martinache, C. Clergeon, **G. Singh**, T. Kudo, K. Newman, J. Kuhn, E. Serabyn, B. Norris, P. Tuthill, P. Stewart, E. Huby, G. Perrin, S. Lacour, S. Vievard, N. Murakami, O. Fumika, Y. Minowa, Y. Hayano, J. White, O. Lai, F. Marchis, G. Duchene, T. Kotani, J. Woillez
  Proc. SPIE 9147, Ground-based & Airborne Instrumentation for Astronomy V, 91471Q, doi:10.1117/12.2057249, July 2014.

- “Recent progress on phase-mask coronagraphy based on photonic-crystal technology"
  N. Murakami; J. Nishikawa; M. Tamura; E. Serabyn; W. A. Traub; K. M. Liewer; D. C. Moody; J. T. Trauger; O. Guyon; F. Martinache; N. Jovanovic; **G. Singh**; F. Oshiyama; H. Shoji; M. Sakamoto, S. Hamaguchi; K. Oka; N. Baba
  Proc. SPIE 9143, Optical, Infrared, and Millimeter Wave, 914334, doi: 10.1117/12.2054790, August 2014.

- “On-sky speckle nulling with the Subaru Coronagraphic Extreme AO (SCExAO) instrument"
  Martinache, F., Guyon, O., Jovanovic, N., Clergeon, C., **Singh, G.**, Kudo, T.
  Proc. SPIE 9148, Adaptive Optics Systems IV, id. 914821, August 2014.

- “SCExAO: First Results and On-Sky Performance
  Thayne, C., Guyon, O., Martinache,F., Clergeon, C., Mi Jovanovic, N., **Singh, G.**, Kudo, T.

- “Lyot-based Ultra-Fine Pointing Control System for Phase Mask Coronagraphs"
  Singh, G., Martinache, F., Baudoz, P., Guyon, O., Matsuo, T., Clergeon, C.
  Proc. of AO4ELT3, DOI: 10.12839/AO4ELT3.12667, 2013

- “SCExAO as a precursor to an ELT exoplanet direct imaging instrument"
  Jovanovic, N., Guyon, O., Martinache, F., Clergeon, C., **Singh, G.**
  Proc. of AO4ELT3, DOI: 10.12839/AO4ELT3.13396, 2013

- ‘The Subaru Coronagraphic Extreme Adaptive Optics Imager: First Results and On-Sky Performance"
  Thayne, C., Guyon, O., Martinache, F., Clergeon, C., McElwain, M., Thalmann, C., Jovanovic, N., **Singh, G.**, Kudo,T.
  Proceedings of the International Astronomical Union, 8(S299):34-35, 2013.

Bibliography

Aime, C., & Soummer, R. 2004 (Oct.). Multiple-stage apodized pupil Lyot coronagraph for high-contrast imaging. *Pages 456–461 of:* Bonaccini Calia, D., Ellerbroek, B. L., & Ragazzoni, R. (eds), *Advancements in Adaptive Optics*. Society of Photo-Optical Instrumentation Engineers (SPIE) Conference Series, vol. 5490.

Aime, C., Soummer, R., & Ferrari, A. 2002. Total coronagraphic extinction of rectangular apertures using linear prolate apodizations. *aap*, **389**(July), 334–344.

Angel, J. R. P. 1994. Ground-based imaging of extrasolar planets using adaptive optics. *nat*, **368**(Mar.), 203–207.

Angel, R. 2003. Imaging Extrasolar Planets from the Ground. *Pages 543–556 of:* Deming, D., & Seager, S. (eds), *Scientific Frontiers in Research on Extrasolar Planets*. Astronomical Society of the Pacific Conference Series, vol. 294.

Appourchaux, T., Michel, E., Auvergne, M., Baglin, A., Toutain, T., Baudin, F., Benomar, O., Chaplin, W. J., Deheuvels, S., Samadi, R., Verner, G. A., Boumier, P., García, R. A., Mosser, B., Hulot, J.-C., Ballot, J., Barban, C., Elsworth, Y., Jiménez-Reyes, S. J., Kjeldsen, H., Régulo, C., & Roxburgh, I. W. 2008. CoRoT sounds the stars: p-mode parameters of Sun-like oscillations on HD 49933. *aap*, **488**(Sept.), 705–714.

Baba, N., & Murakami, N. 2003. A Method to Image Extrasolar Planets with Polarized Light. *pasp*, **115**(Dec.), 1363–1366.

Babcock, H. W. 1953. The Possibility of Compensating Astronomical Seeing. *pasp*, **65**(Oct.), 229.

Bailey, V., Meshkat, T., Reiter, M., Morzinski, K., Males, J., Su, K. Y. L., Hinz, P. M., Kenworthy, M., Stark, D., Mamajek, E., Briguglio, R., Close, L. M., Follette, K. B., Puglisi, A., Rodigas, T., Weinberger, A. J., & Xompero, M. 2014. HD 106906 b: A Planetary-mass Companion Outside a Massive Debris Disk. *apjl*, **780**(Jan.), L4.

Baranne, A., Queloz, D., Mayor, M., Adrianzyk, G., Knispel, G., Kohler, D., Lacroix, D., Meunier, J.-P., Rimbaud, G., & Vin, A. 1996. ELODIE: A spectrograph for accurate radial velocity measurements. *aaps*, **119**(Oct.), 373–390.

Baudoz, P., Rabbia, Y., & Gay, J. 2000a. Achromatic interfero coronagraphy I. Theoretical capabilities for ground-based observations. *aaps*, **141**(Jan.), 319–329.

Baudoz, P., Rabbia, Y., Gay, J., Burg, R., Petro, L., Bely, P., Fleury, B., Madec, P.-Y., & Charbonnier, F. 2000b. Achromatic interfero coronagraphy. II. Effective performance on the sky. *aaps*, **145**(Aug.), 341–350.

Baudoz, P., Galicher, R., Baudrand, J., & Boccaletti, A. 2008 (July). Theory and laboratory tests of the multi-stage phase mask coronagraph. *Page 6 of: Society of Photo-Optical Instrumentation Engineers (SPIE) Conference Series*. Society of Photo-Optical Instrumentation Engineers (SPIE) Conference Series, vol. 7015.

Baudoz, P., Dorn, R. J., Lizon, J.-L., Fusco, T., Dohlen, K., Charton, J., Beuzit, J.-L., Puget, P., Mouillet, D., Felt, M., Wildi, F., Barrufolo, A., Kasper, M., & Hubin, N. 2010 (July). The differential tip-tilt sensor of SPHERE. *Page 5 of: Society of Photo-Optical Instrumentation Engineers (SPIE) Conference Series*. Society of Photo-Optical Instrumentation Engineers (SPIE) Conference Series, vol. 7735.

Belikov, R., Kasdin, N. J., & Vanderbei, R. J. 2006. Diffraction-based Sensitivity Analysis of Apodized Pupil-mapping Systems. *apj*, **652**(Nov.), 833–844.

Belikov, R., Lozi, J., Pluzhnik, E., Hix, T. T., Bendek, E., Thomas, S. J., Lynch, D. H., Mihara, R., Irwin, J. W., Duncan, A. L., Greene, T. P., Guyon, O., Kendrick, R. L., Smith, E. H., Witteborn, F. C., & Schneider, G. 2014 (Aug.). EXCEDE technology development III: first vacuum tests. *Page 23 of: Society of Photo-Optical Instrumentation Engineers (SPIE) Conference Series*. Society of Photo-Optical Instrumentation Engineers (SPIE) Conference Series, vol. 9143.

Bendek, e. a. 2014. Search for Life Beyond the Solar System. Exoplanets, Biosignatures & Instruments conference, http://www.ebi2014.org, id.4.15.,. *In: Optical, Infrared, and Millimeter Space Telescopes*.

Beuzit, J.-L., Lacombe, F., Mariotti, J.-M., Perrier, C., & Rouan, D. 1991. A search for substellar objects with a coronographic near infrared camera. *Pages 316–318 of:* Elston, R. (ed), *Astronomical Society of the Pacific Conference Series*. Astronomical Society of the Pacific Conference Series, vol. 14.

Beuzit, J.-L., Mouillet, D., Lagrange, A.-M., & Paufique, J. 1997. A stellar coronograph for the COME-ON-PLUS adaptive optics system. *aaps*, **125**(Oct.), 175–182.

Beuzit, J.-L., Feldt, M., Dohlen, K., Mouillet, D., Puget, P., Antici, J., Baruffolo, A., Baudoz, P., Berton, A., Boccaletti, A., Carbillet, M., Charton, J., Claudi, R., Downing, M., Feautrier, P., Fedrigo, E., Fusco, T., Gratton, R., Hubin, N., Kasper, M., Langlois, M., Moutou, C., Mugnier, L., Pragt, J., Rabou, P., Saisse, M., Schmid, H. M., Stadler, E., Turrato, M., Udry, S., Waters, R., & Wildi, F. 2006. SPHERE: A 'Planet Finder' Instrument for the VLT. *The Messenger*, **125**(Sept.), 29–+.

Beuzit, J.-L., Mouillet, D., Oppenheimer, B. R., & Monnier, J. D. 2007. Direct Detection of Exoplanets. *Protostars and Planets V*, 717–732.

Biasi, R., Gallieni, D., Salinari, P., Riccardi, A., & Mantegazza, P. 2010 (July). Contactless thin adaptive mirror technology: past, present, and future. *Page 2 of: Society of*

Photo-Optical Instrumentation Engineers (SPIE) Conference Series. Society of Photo-Optical Instrumentation Engineers (SPIE) Conference Series, vol. 7736.

Blain, C. 2013. *Modelling MEMS deformable mirrors for astronomical adaptive optics*. Ph.D. thesis, University of Victoria (Canada.

Blandford, R. D. 2009 (Jan.). Astronomy and Astrophysics 2010 Launch. *Page #213.01 of: American Astronomical Society Meeting Abstracts # 213*. Bulletin of the American Astronomical Society, vol. 41.

Boccaletti, A., Riaud, P., Baudoz, P., Baudrand, J., Rouan, D., Gratadour, D., Lacombe, F., & Lagrange, A.-M. 2004. The Four-Quadrant Phase Mask Coronagraph. IV. First Light at the Very Large Telescope. *pasp*, **116**(Nov.), 1061–1071.

Bonneau, D., Josse, M., & Labyrie, A. 1975 (Dec.). Lock-In Image Subtraction Detectability of Circumstellar Planets with the Large Space Telescope. *Page 403 of:* de Jager, C., & Nieuwenhuijzen, H. (eds), *Image Processing Techniques in Astronomy*. Astrophysics and Space Science Library, vol. 54.

Borucki, W. J., Koch, D., Basri, G., Batalha, N., Brown, T., Caldwell, D., Caldwell, J., Christensen-Dalsgaard, J., Cochran, W. D., DeVore, E., Dunham, E. W., Dupree, A. K., Gautier, T. N., Geary, J. C., Gilliland, R., Gould, A., Howell, S. B., Jenkins, J. M., Kondo, Y., Latham, D. W., Marcy, G. W., Meibom, S., Kjeldsen, H., Lissauer, J. J., Monet, D. G., Morrison, D., Sasselov, D., Tarter, J., Boss, A., Brownlee, D., Owen, T., Buzasi, D., Charbonneau, D., Doyle, L., Fortney, J., Ford, E. B., Holman, M. J., Seager, S., Steffen, J. H., Welsh, W. F., Rowe, J., Anderson, H., Buchhave, L., Ciardi, D., Walkowicz, L., Sherry, W., Horch, E., Isaacson, H., Everett, M. E., Fischer, D., Torres, G., Johnson, J. A., Endl, M., MacQueen, P., Bryson, S. T., Dotson, J., Haas, M., Kolodziejczak, J., Van Cleve, J., Chandrasekaran, H., Twicken, J. D., Quintana, E. V., Clarke, B. D., Allen, C., Li, J., Wu, H., Tenenbaum, P., Verner, E., Bruhweiler, F., Barnes, J., & Prsa, A. 2010. Kepler Planet-Detection Mission: Introduction and First Results. *Science*, **327**(Feb.), 977–.

Bowler, B. P., Liu, M. C., Dupuy, T. J., & Cushing, M. C. 2010. Near-infrared Spectroscopy of the Extrasolar Planet HR 8799 b. *apj*, **723**(Nov.), 850–868.

Burrows, A., Marley, M., Hubbard, W. B., Lunine, J. I., Guillot, T., Saumon, D., Freedman, R., Sudarsky, D., & Sharp, C. 1997. A Nongray Theory of Extrasolar Giant Planets and Brown Dwarfs. *apj*, **491**(Dec.), 856–875.

Burrows, A., Ibgui, L., & Hubeny, I. 2008a. Optical Albedo Theory of Strongly Irradiated Giant Planets: The Case of HD 209458b. *apj*, **682**(Aug.), 1277–1282.

Burrows, A., Budaj, J., & Hubeny, I. 2008b. Theoretical Spectra and Light Curves of Close-in Extrasolar Giant Planets and Comparison with Data. *apj*, **678**(May), 1436–1457.

Charbonneau, D., Brown, T. M., Latham, D. W., & Mayor, M. 2000. Detection of Planetary Transits Across a Sun-like Star. *apjl*, **529**(Jan.), L45–L48.

Chew, T. Y., Clare, R. M., & Lane, R. G. 2006. A comparison of the Shack Hartmann and pyramid wavefront sensors. *Optics Communications*, **268**(Dec.), 189–195.

Chilcote, J., Barman, T., Fitzgerald, M. P., Graham, J. R., Larkin, J. E., Macintosh, B., Bauman, B., Burrows, A. S., Cardwell, A., De Rosa, R. J., Dillon, D., Doyon, R., Dunn, J., Erikson, D., Gavel, D., Goodsell, S. J., Hartung, M., Hibon, P., Ingraham, P., Kalas, P., Konopacky, Q., Maire, J., Marchis, F., Marley, M. S., Marois, C., Millar-Blanchaer, M., Morzinski, K., Norton, A., Oppenheimer, R., Palmer, D., Patience, J., Perrin, M., Poyneer, L., Pueyo, L., Rantakyrö, F. T., Sadakuni, N., Saddlemyer, L., Savransky, D., Serio, A., Sivaramakrishnan, A., Song, I., Soummer, R., Thomas, S., Wallace, J. K., Wiktorowicz, S., & Wolff, S. 2015. The First H-band Spectrum of the Giant Planet β Pictoris b. *apjl*, **798**(Jan.), L3.

Clergeon, C., Guyon, O., Martinache, F., Veran, J.-P., Gendron, E., Rousset, G., Correia, C., & Garrel, V. 2013 (Dec.). The Subaru Coronagraphic Extreme AO High Speed and High Sensitivity Wavefront Sensors. *Page 95 of:* Esposito, S., & Fini, L. (eds), *Proceedings of the Third AO4ELT Conference*.

Close, L. M., Males, J. R., Morzinski, K., Kopon, D., Follette, K., Rodigas, T. J., Hinz, P., Wu, Y.-L., Puglisi, A., Esposito, S., Riccardi, A., Pinna, E., Xompero, M., Briguglio, R., Uomoto, A., & Hare, T. 2013. Diffraction-limited Visible Light Images of Orion Trapezium Cluster with the Magellan Adaptive Secondary Adaptive Optics System (MagAO). *apj*, **774**(Sept.), 94.

Close, L. M., Follette, K. B., Males, J. R., Puglisi, A., Xompero, M., Apai, D., Najita, J., Weinberger, A. J., Morzinski, K., Rodigas, T. J., Hinz, P., Bailey, V., & Briguglio, R. 2014. Discovery of Hα Emission from the Close Companion inside the Gap of Transitional Disk HD 142527. *apjl*, **781**(Feb.), L30.

Cooper, C. S., & Showman, A. P. 2006. Dynamics and Disequilibrium Carbon Chemistry in Hot Jupiter Atmospheres, with Application to HD 209458b. *apj*, **649**(Oct.), 1048–1063.

Crepp, J. R., Pueyo, L., Brenner, D., Oppenheimer, B. R., Zimmerman, N., Hinkley, S., Parry, I., King, D., Vasisht, G., Beichman, C., Hillenbrand, L., Dekany, R., Shao, M., Burruss, R., Roberts, L. C., Bouchez, A., Roberts, J., & Soummer, R. 2011. Speckle Suppression with the Project 1640 Integral Field Spectrograph. *apj*, **729**(Mar.), 132.

Crossfield, I. J. M. 2013. On high-contrast characterization of nearby, short-period exoplanets with giant segmented-mirror telescopes. *aap*, **551**(Mar.), A99.

Currie, T., Lisse, C. M., Kuchner, M., Madhusudhan, N., Kenyon, S. J., Thalmann, C., Carson, J., & Debes, J. 2015. Direct Imaging and Spectroscopy of a Young Extrasolar Kuiper Belt in the Nearest OB Association. *apjl*, **807**(July), L7.

de Zeeuw, T., Tamai, R., & Liske, J. 2014. Constructing the E-ELT. *The Messenger*, **158**(Dec.), 3–6.

Defrère, D., Absil, O., Hinz, P., Kuhn, J., Mawet, D., Mennesson, B., Skemer, A., Wallace, K., Bailey, V., Downey, E., Delacroix, C., Durney, O., Forsberg, P., Gomez, C., Habraken, S., Hoffmann, W. F., Karlsson, M., Kenworthy, M., Leisenring, J., Montoya, M., Pueyo, L., Skrutskie, M., & Surdej, J. 2014 (July). L'-band AGPM vector vortex coronagraph's first light on LBTI/LMIRCam. *Page 3 of: Society of Photo-Optical Instrumentation Engineers (SPIE) Conference Series*. Society of Photo-Optical Instrumentation Engineers (SPIE) Conference Series, vol. 9148.

Dekany, R., Roberts, J., Burruss, R., Truong, T., & Palmer, Guiwits, H. H. D. A. J. B. C. C. E. D. J. T. C. Z. J. H. J. M. D. B. A. H. D. 2011 (Sept.). Palm-3000 on-sky results. *Page 4 of: Second International Conference on Adaptive Optics for Extremely Large Telescopes. Online at <A href="http://ao4elt2.lesia.obspm.fr">http://ao4elt2.lesia.obspm.fr</A>, id.4*.

Dekany, R., Burruss, R., Shelton, J. C., Oppenheimer, B., Vasisht, G., Metchev, S., Roberts, J., Tesch, J., Truong, T., Milburn, J., Hale, D., Baranec, C., Hildebrandt, S., Wahl, M., Beichman, C., Hillenbrand, L., Patel, R., Hinkley, S., Cady, E., & Parry, I. 2013 (Dec.). First exoplanet and disk results with the PALM-3000 adaptive optics system. *Page 52 of:* Esposito, S., & Fini, L. (eds), *Proceedings of the Third AO4ELT Conference*.

Dicke, R. H. 1975. Phase-contrast detection of telescope seeing errors and their correction. *apj*, **198**(June), 605–615.

Digby, A. P., Hinkley, S., Oppenheimer, B. R., Sivaramakrishnan, A., Lloyd, J. P., Perrin, M. D., Roberts, Jr., L. C., Soummer, R., Brenner, D., Makidon, R. B., Shara, M., Kuhn, J., Graham, J., Kalas, P., & Newburgh, L. 2006. The Challenges of Coronagraphic Astrometry. *apj*, **650**(Oct.), 484–496.

Esposito, S., & Riccardi, A. 2001. Pyramid Wavefront Sensor behavior in partial correction Adaptive Optic systems. *aap*, **369**(Apr.), L9–L12.

Esposito, S., Riccardi, A., Fini, L., Puglisi, A. T., Pinna, E., Xompero, M., Briguglio, R., Quirós-Pacheco, F., Stefanini, P., Guerra, J. C., Busoni, L., Tozzi, A., Pieralli, F., Agapito, G., Brusa-Zappellini, G., Demers, R., Brynnel, J., Arcidiacono, C., & Salinari, P. 2010 (July). First light AO (FLAO) system for LBT: final integration, acceptance test in Europe, and preliminary on-sky commissioning results. *Page 9 of: Society of Photo-Optical Instrumentation Engineers (SPIE) Conference Series*. Society of Photo-Optical Instrumentation Engineers (SPIE) Conference Series, vol. 7736.

Esposito, S., Mesa, D., Skemer, A., Arcidiacono, C., Claudi, R. U., Desidera, S., Gratton, R., Mannucci, F., Marzari, F., Masciadri, E., Close, L., Hinz, P., Kulesa, C., McCarthy, D., Males, J., Agapito, G., Argomedo, J., Boutsia, K., Briguglio, R., Brusa, G., Busoni, L., Cresci, G., Fini, L., Fontana, A., Guerra, J. C., Hill, J. M., Miller, D., Paris, D., Pinna, E., Puglisi, A., Quiros-Pacheco, F., Riccardi, A., Stefanini, P., Testa, V., Xompero, M., & Woodward, C. 2013. LBT observations of the HR 8799 planetary system. First detection of HR 8799e in H band. *aap*, **549**(Jan.), A52.

Ferrari, A., Soummer, R., & Aime, C. 2007. An introduction to stellar coronagraphy. *Comptes Rendus Physique*, **8**(Apr.), 277–287.

Finger, G., Baker, I., Alvarez, D., Ives, D., Mehrgan, L., Meyer, M., Stegmeier, J., & Weller, H. J. 2014 (Aug.). SAPHIRA detector for infrared wavefront sensing. *Page 17 of: Society of Photo-Optical Instrumentation Engineers (SPIE) Conference Series*. Society of Photo-Optical Instrumentation Engineers (SPIE) Conference Series, vol. 9148.

Foo, G., Palacios, D. M., & Swartzlander, Jr., G. A. 2005. Optical vortex coronagraph. *Optics Letters*, **30**(Dec.), 3308–3310.

Fried, D. L. 1978. Probability of getting a lucky short-exposure image through turbulence. *J. Opt. Soc. Am.*, **68**(12), 1651–1657.

Galicher, R., Rameau, J., Bonnefoy, M., Baudino, J.-L., Currie, T., Boccaletti, A., Chauvin, G., Lagrange, A.-M., & Marois, C. 2014. Near-infrared detection and characterization of the exoplanet HD 95086 b with the Gemini Planet Imager. *aap*, **565**(May), L4.

Gay, J., & Rabbia, Y. 1996. An interferometric method for coronography. *Academie des Sciences Paris Comptes Rendus Serie B Sciences Physiques*, **322**(Feb.), 265–271.

Give'on, A., Kern, B., Shaklan, S., Moody, D. C., & Pueyo, L. 2007 (Sept.). Broadband wavefront correction algorithm for high-contrast imaging systems. *Page 0 of: Society of Photo-Optical Instrumentation Engineers (SPIE) Conference Series*. Society of Photo-Optical Instrumentation Engineers (SPIE) Conference Series, vol. 6691.

Golimowski, D. A., Clampin, M., Durrance, S. T., & Barkhouser, R. H. 1992. High-resolution ground-based coronagraphy using image-motion compensation. *ao*, **31**(Aug.), 4405–4416.

Green, J. J., & Shaklan, S. B. 2003 (Nov.). Optimizing coronagraph designs to minimize their contrast sensitivity to low-order optical aberrations. *Pages 25–37 of:* Coulter, D. R. (ed), *Techniques and Instrumentation for Detection of Exoplanets*. Society of Photo-Optical Instrumentation Engineers (SPIE) Conference Series, vol. 5170.

Guyon, O. 2003. Phase-induced amplitude apodization of telescope pupils for extrasolar terrestrial planet imaging. *aap*, **404**(June), 379–387.

Guyon, O. 2005. Limits of Adaptive Optics for High-Contrast Imaging. *apj*, **629**(Aug.), 592–614.

Guyon, O. 2011. Instrument Tip-Tilt Control Demonstration at the sub-Milli-arcsecond level. https://exep.jpl.nasa.gov/links/. *Whitepaper*.

Guyon, O., & Roddier, F. J. 2000 (July). Direct exoplanet imaging possibilities of the nulling stellar coronagraph. *Pages 377–387 of:* Léna, P., & Quirrenbach, A. (eds), *Interferometry in Optical Astronomy*. Society of Photo-Optical Instrumentation Engineers (SPIE) Conference Series, vol. 4006.

Guyon, O., Pluzhnik, E. A., Kuchner, M. J., Collins, B., & Ridgway, S. T. 2006. Theoretical Limits on Extrasolar Terrestrial Planet Detection with Coronagraphs. *apjs*, **167**(Nov.), 81–99.

Guyon, O., Angel, J. R. P., Backman, D., Belikov, R., Gavel, D., Giveon, A., Greene, T., Kasdin, J., Kasting, J., Levine, M., Marley, M., Meyer, M., Schneider, G., Serabyn, G., Shaklan, S., Shao, M., Tamura, M., Tenerelli, D., Traub, W., Trauger, J., Vanderbei, R., Woodruff, R. A., Woolf, N. J., & Wynn, J. 2008 (July). Pupil mapping Exoplanet Coronagraphic Observer (PECO). *Page 1 of: Society of Photo-Optical Instrumentation Engineers (SPIE) Conference Series*. Society of Photo-Optical Instrumentation Engineers (SPIE) Conference Series, vol. 7010.

Guyon, O., Matsuo, T., & Angel, R. 2009. Coronagraphic Low-Order Wave-Front Sensor: Principle and Application to a Phase-Induced Amplitude Coronagraph. *apj*, **693**(Mar.), 75–84.

Guyon, O., Pluzhnik, E., Martinache, F., Totems, J., Tanaka, S., Matsuo, T., Blain, C., & Belikov, R. 2010a. High-Contrast Imaging and Wavefront Control with a PIAA Coronagraph: Laboratory System Validation. *pasp*, **122**(Jan.), 71–84.

Guyon, O., Martinache, F., Belikov, R., & Soummer, R. 2010b. High Performance PIAA Coronagraphy with Complex Amplitude Focal Plane Masks. *apjs*, **190**(Oct.), 220–232.

Guyon, O., Martinache, F., Cady, E. J., Belikov, R., Balasubramanian, K., Wilson, D., Clergeon, C. S., & Mateen, M. 2012 (July). How ELTs will acquire the first spectra of rocky habitable planets. *Page 1 of: Society of Photo-Optical Instrumentation Engineers (SPIE) Conference Series*. Society of Photo-Optical Instrumentation Engineers (SPIE) Conference Series, vol. 8447.

Guyon, O., Hayano, Y., Tamura, M., Kudo, T., Oya, S., Minowa, Y., Lai, O., Jovanovic, N., Takato, N., Kasdin, J., Groff, T., Hayashi, M., Arimoto, N., Takami, H., Bradley, C., Sugai, H., Perrin, G., Tuthill, P., & Mazin, B. 2014 (Aug.). Adaptive optics at the Subaru telescope: current capabilities and development. *Page 1 of: Society of Photo-Optical Instrumentation Engineers (SPIE) Conference Series*. Society of Photo-Optical Instrumentation Engineers (SPIE) Conference Series, vol. 9148.

Hagan, J., Thormann, A., Soummer, R., Pueyo, L., & Marois, C. 2010 (Oct.). Direct Detections of the HR8799 planets using the LOCI algorithm on NICMOS data. *Page 24 of: In the Spirit of Lyot 2010*.

Hardy, A., Schreiber, M. R., Parsons, S. G., Caceres, C., Retamales, G., Wahhaj, Z., Mawet, D., Canovas, H., Cieza, L., Marsh, T. R., Bours, M. C. P., Dhillon, V. S., & Bayo, A. 2015. The First Science Results from Sphere: Disproving the Predicted Brown Dwarf Around V471 Tau. *apjl*, **800**(Feb.), L24.

Hardy, J. W. 1998. *Adaptive Optics for Astronomical Telescopes*.

Hart, M. H. 1978. The evolution of the atmosphere of the earth. *icarus*, **33**(Jan.), 23–39.

Hartung, M., Macintosh, B., Langlois, P., Sadakuni, N., Gavel, D., Wallace, J. K., Palmer, D., Poyneer, L., Savransky, D., Thomas, S., Dillon, D., Dunn, J., Hibon, P., Rantakyrö, F., & Goodsell, S. 2014 (Aug.). On-sky low order non-common path correction of the GPI calibration unit. *Page 5 of: Society of Photo-Optical Instrumentation Engineers (SPIE) Conference Series*. Society of Photo-Optical Instrumentation Engineers (SPIE) Conference Series, vol. 9148.

Hayward, T. L., Brandl, B., Pirger, B., Blacken, C., Gull, G. E., Schoenwald, J., & Houck, J. R. 2001. PHARO: A Near-Infrared Camera for the Palomar Adaptive Optics System. *pasp*, **113**(Jan.), 105–118.

Herrmann, J. 1981. Cross coupling and aliasing in modal wave-front estimation. *Journal of the Optical Society of America (1917-1983)*, **71**(Aug.), 989.

Hinkley, S., Oppenheimer, B. R., Zimmerman, N., Brenner, D., Parry, I. R., Crepp, J. R., Vasisht, G., Ligon, E., King, D., Soummer, R., Sivaramakrishnan, A., Beichman, C., Shao, M., Roberts, L. C., Bouchez, A., Dekany, R., Pueyo, L., Roberts, J. E., Lockhart, T., Zhai, C., Shelton, C., & Burruss, R. 2011. A New High Contrast Imaging Program at Palomar Observatory. *pasp*, **123**(Jan.), 74–86.

Hinkley, S., Bowler, B. P., Vigan, A., Aller, K. M., Liu, M. C., Mawet, D., Matthews, E., Wahhaj, Z., Kraus, S., Baraffe, I., & Chabrier, G. 2015. Early Results from VLT SPHERE: Long-slit Spectroscopy of 2MASS 0122-2439 B, a Young Companion Near the Deuterium Burning Limit. *apjl*, **805**(May), L10.

Hodapp, K. W., Suzuki, R., Tamura, M., Abe, L., Suto, H., Kandori, R., Morino, J., Nishimura, T., Takami, H., Guyon, O., Jacobson, S., Stahlberger, V., Yamada, H., Shelton, R., Hashimoto, J., Tavrov, A., Nishikawa, J., Ukita, N., Izumiura, H., Hayashi, M., Nakajima, T., Yamada, T., & Usuda, T. 2008 (July). HiCIAO: the Subaru Telescope's new high-contrast coronographic imager for adaptive optics. *Page 19 of: Society of Photo-Optical Instrumentation Engineers (SPIE) Conference Series*. Society of Photo-Optical Instrumentation Engineers (SPIE) Conference Series, vol. 7014.

Howard, A. W., Marcy, G. W., Bryson, S. T., Jenkins, J. M., Rowe, J. F., Batalha, N. M., Borucki, W. J., Koch, D. G., Dunham, E. W., Gautier, III, T. N., Van Cleve, J., Cochran, W. D., Latham, D. W., Lissauer, J. J., Torres, G., Brown, T. M., Gilliland, R. L., Buchhave, L. A., Caldwell, D. A., Christensen-Dalsgaard, J., Ciardi, D., Fressin, F., Haas, M. R., Howell, S. B., Kjeldsen, H., Seager, S., Rogers, L., Sasselov, D. D., Steffen, J. H., Basri, G. S., Charbonneau, D., Christiansen, J., Clarke, B., Dupree, A., Fabrycky, D. C., Fischer, D. A., Ford, E. B., Fortney, J. J., Tarter, J., Girouard, F. R., Holman, M. J., Johnson, J. A., Klaus, T. C., Machalek, P., Moorhead, A. V., Morehead, R. C., Ragozzine, D., Tenenbaum, P., Twicken, J. D., Quinn, S. N., Isaacson, H., Shporer, A., Lucas, P. W., Walkowicz, L. M., Welsh, W. F., Boss, A., Devore, E., Gould, A., Smith, J. C., Morris, R. L., Prsa, A., Morton, T. D., Still, M., Thompson, S. E., Mullally, F., Endl, M., & MacQueen, P. J. 2012. Planet Occurrence within 0.25 AU of Solar-type Stars from Kepler. *apjs*, **201**(Aug.), 15.

Huby, E., Perrin, G., Marchis, F., Lacour, S., Kotani, T., Duchêne, G., Choquet, E., Gates, E. L., Woillez, J. M., Lai, O., Fédou, P., Collin, C., Chapron, F., Arslanyan,

V., & Burns, K. J. 2012. FIRST, a fibered aperture masking instrument. I. First on-sky test results. *aap*, **541**(May), A55.

Jenkins, C. 2008. Optical vortex coronagraphs on ground-based telescopes. *mnras*, **384**(Feb.), 515–524.

Jovanovic, N., Guyon, O., Martinache, F., Clergeon, C., Singh, G., Kudo, T., Newman, K., Kuhn, J., Serabyn, E., Norris, B., Tuthill, P., Stewart, P., Huby, E., Perrin, G., Lacour, S., Vievard, S., Murakami, N., Fumika, O., Minowa, Y., Hayano, Y., White, J., Lai, O., Marchis, F., Duchene, G., Kotani, T., & Woillez, J. 2014 (July). Development and recent results from the Subaru coronagraphic extreme adaptive optics system. *Page 1 of: Society of Photo-Optical Instrumentation Engineers (SPIE) Conference Series*. Society of Photo-Optical Instrumentation Engineers (SPIE) Conference Series, vol. 9147.

Jovanovic, N., Martinache, F., Guyon, O., Clergeon, C., Singh, G., Kudo, T., Garrel, V., Newman, K., Doughty, D., Lozi, J., Males, J., Minowa, Y., Hayano, Y., Takato, N., Morino, J., Kuhn, J., Serabyn, E., Norris, B., Tuthill, P., Schworer, G., Stewart, P., Close, L., Huby, E., Perrin, G., Lacour, S., Gauchet, L., Vievard, S., Murakami, N., Oshiyama, F., Baba, N., Matsuo, T., Nishikawa, J., Tamura, M., Lai, O., Marchis, F., Duchene, G., Kotani, T., & Woillez, J. 2015. The Subaru Coronagraphic Extreme Adaptive Optics System: Enabling High-Contrast Imaging on Solar-System Scales. *pasp*, **127**(Oct.), 890–910.

Kalas, P., Graham, J. R., Chiang, E., Fitzgerald, M. P., Clampin, M., Kite, E. S., Stapelfeldt, K., Marois, C., & Krist, J. 2008. Optical Images of an Exosolar Planet 25 Light-Years from Earth. *Science*, **322**(Nov.), 1345–.

Kane, S. R., & Gelino, D. M. 2012. The Habitable Zone Gallery. *pasp*, **124**(Apr.), 323–328.

Kanzawa, T., Tomono, D., Usuda, T., Takato, N., Negishi, S., Sugahara, S., & Itoh, N. 2006 (June). Improvement of the pointing accuracy of the Subaru Telescope by suppressing vibrations. *Page 3 of: Society of Photo-Optical Instrumentation Engineers (SPIE) Conference Series*. Society of Photo-Optical Instrumentation Engineers (SPIE) Conference Series, vol. 6267.

Kasting, J. F., Whitmire, D. P., & Reynolds, R. T. 1993. Habitable Zones around Main Sequence Stars. *icarus*, **101**(Jan.), 108–128.

Kenknight, C. E. 1977. Methods of detecting extrasolar planets. I - Imaging. *icarus*, **30**(Feb.), 422–433.

Kern, B., Guyon, O., Kuhnert, A., Niessner, A., Martinache, F., & Balasubramanian, K. 2013 (Sept.). Laboratory demonstration of Phase Induced Amplitude Apodization (PIAA) coronagraph with better than 10^{-9} contrast. *Page 0 of: Society of Photo-Optical Instrumentation Engineers (SPIE) Conference Series*. Society of Photo-Optical Instrumentation Engineers (SPIE) Conference Series, vol. 8864.

Kobayashi, N., Tokunaga, A. T., Terada, H., Goto, M., Weber, M., Potter, R., Onaka, P. M., Ching, G. K., Young, T. T., Fletcher, K., Neil, D., Robertson, L., Cook, D., Imanishi, M., & Warren, D. W. 2000 (Aug.). IRCS: infrared camera and spectrograph for the Subaru Telescope. *Pages 1056–1066 of:* Iye, M., & Moorwood, A. F. (eds), *Optical and IR Telescope Instrumentation and Detectors*. Society of Photo-Optical Instrumentation Engineers (SPIE) Conference Series, vol. 4008.

Kolmogorov, A. N. 1991. The local structure of turbulence in incompressible viscous fluid for very large Reynolds numbers. *Royal Society of London Proceedings Series A*, **434**(July), 9–13.

Kopparapu, R. K., Ramirez, R., Kasting, J. F., Eymet, V., Robinson, T. D., Mahadevan, S., Terrien, R. C., Domagal-Goldman, S., Meadows, V., & Deshpande, R. 2013. Habitable Zones around Main-sequence Stars: New Estimates. *apj*, **765**(Mar.), 131.

Kopparapu, R. K., Ramirez, R. M., SchottelKotte, J., Kasting, J. F., Domagal-Goldman, S., & Eymet, V. 2014. Habitable Zones around Main-sequence Stars: Dependence on Planetary Mass. *apjl*, **787**(June), L29.

Krist, J. E., Trauger, J. T., Unwin, S. C., & Traub, W. A. 2012 (Sept.). End-to-end coronagraphic modeling including a low-order wavefront sensor. *Page 53 of: Society of Photo-Optical Instrumentation Engineers (SPIE) Conference Series*. Society of Photo-Optical Instrumentation Engineers (SPIE) Conference Series, vol. 8442.

Kuchner, M. J., & Traub, W. A. 2002. A Coronagraph with a Band-limited Mask for Finding Terrestrial Planets. *apj*, **570**(May), 900–908.

Kuchner, M. J., Crepp, J., & Ge, J. 2005. Eighth-Order Image Masks for Terrestrial Planet Finding. *apj*, **628**(July), 466–473.

Lafrenière, D., Marois, C., Doyon, R., Nadeau, D., & Artigau, É. 2007. A New Algorithm for Point-Spread Function Subtraction in High-Contrast Imaging: A Demonstration with Angular Differential Imaging. *apj*, **660**(May), 770–780.

Lagrange, A.-M., Gratadour, D., Chauvin, G., Fusco, T., Ehrenreich, D., Mouillet, D., Rousset, G., Rouan, D., Allard, F., Gendron, É., Charton, J., Mugnier, L., Rabou, P., Montri, J., & Lacombe, F. 2009. A probable giant planet imaged in the β Pictoris disk. VLT/NaCo deep L'-band imaging. *aap*, **493**(Jan.), L21–L25.

Leconte, J., Soummer, R., Hinkley, S., Oppenheimer, B. R., Sivaramakrishnan, A., Brenner, D., Kuhn, J., Lloyd, J. P., Perrin, M. D., Makidon, R., Roberts, Jr., L. C., Graham, J. R., Simon, M., Brown, R. A., Zimmerman, N., Chabrier, G., & Baraffe, I. 2010. The Lyot Project Direct Imaging Survey of Substellar Companions: Statistical Analysis and Information from Nondetections. *apj*, **716**(June), 1551–1565.

Lemarquis, F., Lequime, M., Albrand, G., Escoubas, L., Simon, J.-J., Baudrand, J., Riaud, P., Rouan, D., Boccaletti, A., Baudoz, P., & Mawet, D. 2004 (Feb.). Manufacturing of four-quadrant phase mask for nulling interferometry in the thermal infrared. *Pages 435–443 of:* Amra, C., Kaiser, N., & Macleod, H. A. (eds), *Advances in Optical Thin*

Films. Society of Photo-Optical Instrumentation Engineers (SPIE) Conference Series, vol. 5250.

Lena, P. 1988. *Observational astrophysics*.

Lloyd, J. P., & Sivaramakrishnan, A. 2005. Tip-Tilt Error in Lyot Coronagraphs. *apj*, **621**(Mar.), 1153–1158.

Lloyd, J. P., Gavel, D. T., Graham, J. R., Hodge, P. E., Sivaramakrishnan, A., & Voit, G. M. 2003 (Feb.). Four-quadrant phase mask coronagraph: analytical calculation and pupil geometry. *Pages 171–181 of:* Schultz, A. B. (ed), *High-Contrast Imaging for Exo-Planet Detection.* Society of Photo-Optical Instrumentation Engineers (SPIE) Conference Series, vol. 4860.

Lozi, J., Martinache, F., & Guyon, O. 2009. Phase-Induced Amplitude Apodization on Centrally Obscured Pupils: Design and First Laboratory Demonstration for the Subaru Telescope Pupil. *pasp*, **121**(Nov.), 1232–1244.

Lozi, J., Belikov, R., Thomas, S. J., Pluzhnik, E., Bendek, E., Guyon, O., & Schneider, G. 2014 (Aug.). Experimental study of a low-order wavefront sensor for high-contrast coronagraphic imagers: results in air and in vacuum. *Page 22 of: Society of Photo-Optical Instrumentation Engineers (SPIE) Conference Series*. Society of Photo-Optical Instrumentation Engineers (SPIE) Conference Series, vol. 9143.

Lyot, B. 1932. Étude de la couronne solaire en dehors des éclipses. Avec 16 figures dans le texte. *zap*, **5**, 73.

Lyot, B. 1939. The study of the solar corona and prominences without eclipses (George Darwin Lecture, 1939). *mnras*, **99**(June), 580.

Macintosh, B., Zuckerman, B., Becklin, E. E., & McLean, I. S. 1992 (May). Searches for Brown Dwarfs in the Hyades. *Page 773 of: American Astronomical Society Meeting Abstracts #180*. Bulletin of the American Astronomical Society, vol. 24.

Macintosh, B., Graham, J. R., Ingraham, P., Konopacky, Q., Marois, C., Perrin, M., Poyneer, L., Bauman, B., Barman, T., Burrows, A. S., Cardwell, A., Chilcote, J., De Rosa, R. J., Dillon, D., Doyon, R., Dunn, J., Erikson, D., Fitzgerald, M. P., Gavel, D., Goodsell, S., Hartung, M., Hibon, P., Kalas, P., Larkin, J., Maire, J., Marchis, F., Marley, M. S., McBride, J., Millar-Blanchaer, M., Morzinski, K., Norton, A., Oppenheimer, B. R., Palmer, D., Patience, J., Pueyo, L., Rantakyro, F., Sadakuni, N., Saddlemyer, L., Savransky, D., Serio, A., Soummer, R., Sivaramakrishnan, A., Song, I., Thomas, S., Wallace, J. K., Wiktorowicz, S., & Wolff, S. 2014. First light of the Gemini Planet Imager. *Proceedings of the National Academy of Science*, **111**(Sept.), 12661–12666.

Macintosh, B., Graham, J., Palmer, D., Doyon, R., Gavel, D., Larkin, J., Oppenheimer, B., Saddlemyer, L., Wallace, J. K., Bauman, B., Evans, J., Erikson, D., Morzinski, K., Phillion, D., Poyneer, L., Sivaramakrishnan, A., Soummer, R., Thibault, S., & Veran, J.-P. 2006. The Gemini Planet Imager. vol. 6272. Proc. Soc. Photo-Opt. Instrum. Eng.

Madhusudhan, N., Knutson, H., Fortney, J. J., & Barman, T. 2014. Exoplanetary Atmospheres. *Protostars and Planets VI*, 739–762.

Maire, A.-L., Skemer, A. J., Hinz, P. M., Desidera, S., Esposito, S., Gratton, R., Marzari, F., Skrutskie, M. F., Biller, B. A., Defrère, D., Bailey, V. P., Leisenring, J. M., Apai, D., Bonnefoy, M., Brandner, W., Buenzli, E., Claudi, R. U., Close, L. M., Crepp, J. R., De Rosa, R. J., Eisner, J. A., Fortney, J. J., Henning, T., Hofmann, K.-H., Kopytova, T. G., Males, J. R., Mesa, D., Morzinski, K. M., Oza, A., Patience, J., Pinna, E., Rajan, A., Schertl, D., Schlieder, J. E., Su, K. Y. L., Vaz, A., Ward-Duong, K., Weigelt, G., & Woodward, C. E. 2015. The LEECH Exoplanet Imaging Survey. Further constraints on the planet architecture of the HR 8799 system. *aap*, **576**(Apr.), A133.

Malbet, F. 1996. High angular resolution coronography for adaptive optics. *aaps*, **115**(Jan.), 161.

Males, J. R., Close, L. M., Morzinski, K. M., Wahhaj, Z., Liu, M. C., Skemer, A. J., Kopon, D., Follette, K. B., Puglisi, A., Esposito, S., Riccardi, A., Pinna, E., Xompero, M., Briguglio, R., Biller, B. A., Nielsen, E. L., Hinz, P. M., Rodigas, T. J., Hayward, T. L., Chun, M., Ftaclas, C., Toomey, D. W., & Wu, Y.-L. 2014. Magellan Adaptive Optics First-light Observations of the Exoplanet β Pic B. I. Direct Imaging in the Far-red Optical with MagAO+VisAO and in the Near-ir with NICI. *apj*, **786**(May), 32.

Marley, M. S., Saumon, D., Guillot, T., Freedman, R. S., Hubbard, W. B., Burrows, A., & Lunine, J. I. 1996. Atmospheric, Evolutionary, and Spectral Models of the Brown Dwarf Gliese 229 B. *Science*, **272**(June), 1919–1921.

Marois, C., Lafrenière, D., Doyon, R., Macintosh, B., & Nadeau, D. 2006. Angular Differential Imaging: A Powerful High-Contrast Imaging Technique. *apj*, **641**(Apr.), 556–564.

Martinache, F., & Guyon, O. 2009 (Aug.). The Subaru Coronagraphic Extreme-AO Project. *Page 0 of: Society of Photo-Optical Instrumentation Engineers (SPIE) Conference Series*. Society of Photo-Optical Instrumentation Engineers (SPIE) Conference Series, vol. 7440.

Martinache, F., Guyon, O., Jovanovic, N., Clergeon, C., Singh, G., Kudo, T., Currie, T., Thalmann, C., McElwain, M., & Tamura, M. 2014. On-Sky Speckle Nulling Demonstration at Small Angular Separation with SCExAO. *pasp*, **126**(June), 565–572.

Mas, M., Baudoz, P., Mazoyer, J., Galicher, R., & Rousset, G. 2012a (Sept.). Experimental results on wavefront correction using the self-coherent camera. *Page 89 of: Society of Photo-Optical Instrumentation Engineers (SPIE) Conference Series*. Society of Photo-Optical Instrumentation Engineers (SPIE) Conference Series, vol. 8446.

Mas, M., Baudoz, P., Rousset, G., & Galicher, R. 2012b. Tip-tilt estimation and correction using FQPM coronagraphic images. *aap*, **539**(Mar.), A126.

Mawet, D., Lenaerts, C., Moreau, V., Renotte, Y., Rouan, D., & Surdej, J. 2003. Achromatic Four Quadrant Phase Mask Coronagraph using the Dispersion of Form Birefringence. *Pages 117–128 of:* Aime, C., & Soummer, R. (eds), *EAS Publications Series*. EAS Publications Series, vol. 8.

Mawet, D., Riaud, P., Absil, O., & Surdej, J. 2005a. Annular Groove Phase Mask Coronagraph. *apj*, **633**(Nov.), 1191–1200.

Mawet, D., Riaud, P., Absil, O., Baudrand, J., & Surdej, J. 2005b (Aug.). The four-quadrant ZOG and annular groove phase mask coronagraphs. *Pages 502–511 of:* Coulter, D. R. (ed), *Techniques and Instrumentation for Detection of Exoplanets II*. Society of Photo-Optical Instrumentation Engineers (SPIE) Conference Series, vol. 5905.

Mawet, D., Riaud, P., Baudrand, J., Baudoz, P., Boccaletti, A., Dupuis, O., & Rouan, D. 2006. The four-quadrant phase-mask coronagraph: white light laboratory results with an achromatic device. *aap*, **448**(Mar.), 801–808.

Mawet, D., Serabyn, E., Liewer, K., Hanot, C., McEldowney, S., Shemo, D., & O'Brien, N. 2009a. Optical Vectorial Vortex Coronagraphs using Liquid Crystal Polymers: theory, manufacturing and laboratory demonstration. *Optics Express*, **17**(Feb.), 1902–1918.

Mawet, D., Serabyn, E., Liewer, K., Hanot, C., McEldowney, S., Shemo, D., & O'Brien, N. 2009b. Optical Vectorial Vortex Coronagraphs using Liquid Crystal Polymers: theory, manufacturing and laboratory demonstration. *Optics Express*, **17**(Feb.), 1902–1918.

Mawet, D., Serabyn, E., Liewer, K., Burruss, R., Hickey, J., & Shemo, D. 2010a. The Vector Vortex Coronagraph: Laboratory Results and First Light at Palomar Observatory. *apj*, **709**(Jan.), 53–57.

Mawet, D., Pueyo, L., Moody, D., Krist, J., & Serabyn, E. 2010b (July). The Vector Vortex Coronagraph: sensitivity to central obscuration, low-order aberrations, chromaticism, and polarization. *Page 14 of: Society of Photo-Optical Instrumentation Engineers (SPIE) Conference Series*. Society of Photo-Optical Instrumentation Engineers (SPIE) Conference Series, vol. 7739.

Mawet, D., Pueyo, L., Lawson, P., Mugnier, L., Traub, W., Boccaletti, A., Trauger, J. T., Gladysz, S., Serabyn, E., Milli, J., Belikov, R., Kasper, M., Baudoz, P., Macintosh, B., Marois, C., Oppenheimer, B., Barrett, H., Beuzit, J.-L., Devaney, N., Girard, J., Guyon, O., Krist, J., Mennesson, B., Mouillet, D., Murakami, N., Poyneer, L., Savransky, D., Vérinaud, C., & Wallace, J. K. 2012 (Sept.). Review of small-angle coronagraphic techniques in the wake of ground-based second-generation adaptive optics systems. *Page 4 of: Society of Photo-Optical Instrumentation Engineers (SPIE) Conference Series*. Society of Photo-Optical Instrumentation Engineers (SPIE) Conference Series, vol. 8442.

Mawet, D., Shelton, C., Wallace, J., Bottom, M., Kuhn, J., Mennesson, B., Burruss, R., Bartos, R., Pueyo, L., Carlotti, A., & Serabyn, E. 2014a (Aug.). Demonstration

of vortex coronagraph concepts for on-axis telescopes on the Palomar Stellar Double Coronagraph. *Page 2 of: Society of Photo-Optical Instrumentation Engineers (SPIE) Conference Series*. Society of Photo-Optical Instrumentation Engineers (SPIE) Conference Series, vol. 9143.

Mawet, D., Bowler, B., Dekany, R., Wallace, J., Vasisht, G., Serabyn, E., & Wizinowich, P., e. a. 2014b. Keck Planet Imager. *Whitepaper*.

Mayor, M., & Queloz, D. 1995. A Jupiter-mass companion to a solar-type star. *nat*, **378**(Nov.), 355–359.

Mayor, M., Pepe, F., Queloz, D., Bouchy, F., Rupprecht, G., Lo Curto, G., Avila, G., Benz, W., Bertaux, J.-L., Bonfils, X., Dall, T., Dekker, H., Delabre, B., Eckert, W., Fleury, M., Gilliotte, A., Gojak, D., Guzman, J. C., Kohler, D., Lizon, J.-L., Longinotti, A., Lovis, C., Megevand, D., Pasquini, L., Reyes, J., Sivan, J.-P., Sosnowska, D., Soto, R., Udry, S., van Kesteren, A., Weber, L., & Weilenmann, U. 2003. Setting New Standards with HARPS. *The Messenger*, **114**(Dec.), 20–24.

Mazin, B. A., Meeker, S. R., Strader, M. J., Szypryt, P., Marsden, D., van Eyken, J. C., Duggan, G. E., Walter, A. B., Ulbricht, G., Johnson, M., Bumble, B., O'Brien, K., & Stoughton, C. 2013. ARCONS: A 2024 Pixel Optical through Near-IR Cryogenic Imaging Spectrophotometer. *pasp*, **125**(Nov.), 1348–1361.

Mazoyer, J., Baudoz, P., Galicher, R., Mas, M., & Rousset, G. 2013. Estimation and correction of wavefront aberrations using the self-coherent camera: laboratory results. *aap*, **557**(Sept.), A9.

Mazoyer, J., Baudoz, P., Galicher, R., & Rousset, G. 2014. High-contrast imaging in polychromatic light with the self-coherent camera. *aap*, **564**(Apr.), L1.

Meadows, V., & Seager, S. 2010. *Terrestrial Planet Atmospheres and Biosignatures*. Pages 441–470.

Mendillo, C. B., Brown, J., Martel, J., Howe, G. A., Kuravi, H., Finn, S. C., A., C., Chakrabarti.S., Douglas, E. S., Mawet, D., Guyon, G., Singh, G., Lozi, J., Cahoy, K. L., & Marinan, A. D. 2015. The low-order wavefront sensor for the PICTURE-C mission. *In: Society of Photo-Optical Instrumentation Engineers (SPIE) Conference Series*. Society of Photo-Optical Instrumentation Engineers (SPIE) Conference Series, vol. 9605.

Minowa, Y., Hayano, Y., Oya, S., Watanabe, M., Hattori, M., Guyon, O., Egner, S., Saito, Y., Ito, M., Takami, H., Garrel, V., Colley, S., Golota, T., & Iye, M. 2010 (July). Performance of Subaru adaptive optics system AO188. *Page 3 of: Society of Photo-Optical Instrumentation Engineers (SPIE) Conference Series*. Society of Photo-Optical Instrumentation Engineers (SPIE) Conference Series, vol. 7736.

Morzinski, K. M., Close, L. M., Males, J. R., Kopon, D., Hinz, P. M., Esposito, S., Riccardi, A., Puglisi, A., Pinna, E., Briguglio, R., Xompero, M., Quirós-Pacheco, F., Bailey, V., Follette, K. B., Rodigas, T. J., Wu, Y.-L., Arcidiacono, C., Argomedo, J.,

Busoni, L., Hare, T., Uomoto, A., & Weinberger, A. 2014 (July). MagAO: Status and on-sky performance of the Magellan adaptive optics system. *Page 4 of: Society of Photo-Optical Instrumentation Engineers (SPIE) Conference Series*. Society of Photo-Optical Instrumentation Engineers (SPIE) Conference Series, vol. 9148.

Mouillet, D., Lagrange, A. M., Augereau, J. C., & Ménard, F. 2001. Asymmetries in the HD 141569 circumstellar disk. *aap*, **372**(June), L61–L64.

Mulders, G. D., Pascucci, I., & Apai, D. 2015. A Stellar-mass-dependent Drop in Planet Occurrence Rates. *apj*, **798**(Jan.), 112.

Murakami, N., Uemura, R., Baba, N., Nishikawa, J., Tamura, M., Hashimoto, N., & Abe, L. 2008. An Eight-Octant Phase-Mask Coronagraph. *pasp*, **120**(Oct.), 1112–1118.

Murakami, N., Nishikawa, J., Yokochi, K., Tamura, M., Baba, N., & Abe, L. 2010. Achromatic Eight-octant Phase-mask Coronagraph using Photonic Crystal. *apj*, **714**(May), 772–777.

Nakajima, T., Durrance, S. T., Golimowski, D. A., & Kulkarni, S. R. 1994. A coronagraphic search for brown dwarfs around nearby stars. *apj*, **428**(June), 797–804.

Narita, N., Sato, B., Hirano, T., & Tamura, M. 2009. First Evidence of a Retrograde Orbit of a Transiting Exoplanet HAT-P-7b. *pasj*, **61**(Oct.), L35–L40.

Newman, K., Belikov, R., Guyon, O., Balasubramanian, K., & Wilson, D. 2013 (Sept.). Achromatic focal plane mask for exoplanet imaging coronagraphy. *Page 1 of: Society of Photo-Optical Instrumentation Engineers (SPIE) Conference Series*. Society of Photo-Optical Instrumentation Engineers (SPIE) Conference Series, vol. 8864.

Newman, K., Guyon, O., Balasubramanian, K., Belikov, R., Jovanovic, N., Martinache, F., & Wilson, D. 2015a. An Achromatic Focal Plane Mask for High-Performance Broadband Coronagraphy. *pasp*, **127**(May), 437–444.

Newman, K., Belikov, R., Guyon, O., & Pluzhnik, E. 2015b (Jan.). Performance characterization of a PIAA complex focal plane mask. *Page 258.11 of: American Astronomical Society Meeting Abstracts*. American Astronomical Society Meeting Abstracts, vol. 225.

Noll, R. J. 1976. Zernike polynomials and atmospheric turbulence. *Journal of the Optical Society of America (1917-1983)*, **66**(Mar.), 207–211.

Norris, B., Schworer, G., Tuthill, P., Jovanovic, N., Guyon, O., Stewart, P., & Martinache, F. 2015. The VAMPIRES instrument: imaging the innermost regions of protoplanetary discs with polarimetric interferometry. *mnras*, **447**(Mar.), 2894–2906.

Oppenheimer, B. R., Digby, A. P., Newburgh, L., Brenner, D., Shara, M., Mey, J., Mandeville, C., Makidon, R. B., Sivaramakrishnan, A., Soummer, R., Graham, J. R., Kalas, P., Perrin, M. D., Roberts, Jr., L. C., Kuhn, J. R., Whitman, K., & Lloyd, J. P. 2004 (Oct.). The Lyot project: toward exoplanet imaging and spectroscopy. *Pages*

433–442 of: Bonaccini Calia, D., Ellerbroek, B. L., & Ragazzoni, R. (eds), *Advancements in Adaptive Optics*. Society of Photo-Optical Instrumentation Engineers (SPIE) Conference Series, vol. 5490.

Palacios, D. M. 2005 (Aug.). An optical vortex coronagraph. *Pages 196–205 of:* Coulter, D. R. (ed), *Techniques and Instrumentation for Detection of Exoplanets II*. Society of Photo-Optical Instrumentation Engineers (SPIE) Conference Series, vol. 5905.

Paresce, F., & Burrows, C. 1986 (Sept.). Multi-color, High Spatial Resolution Imaging of the Beta Pictoris Circumstellar Disk. *Page 1027 of: Bulletin of the American Astronomical Society*. Bulletin of the American Astronomical Society, vol. 18.

Paresce, F., & Burrows, C. 1987. Coronography at La Silla - High resolution imaging of faint features near bright objects. *The Messenger*, **47**(Mar.), 43–46.

Perrin, M. D., Duchene, G., Millar-Blanchaer, M., Fitzgerald, M. P., Graham, J. R., Wiktorowicz, S. J., Kalas, P. G., Macintosh, B., Bauman, B., Cardwell, A., Chilcote, J., De Rosa, R. J., Dillon, D., Doyon, R., Dunn, J., Erikson, D., Gavel, D., Goodsell, S., Hartung, M., Hibon, P., Ingraham, P., Kerley, D., Konapacky, Q., Larkin, J. E., Maire, J., Marchis, F., Marois, C., Mittal, T., Morzinski, K. M., Oppenheimer, B. R., Palmer, D. W., Patience, J., Poyneer, L., Pueyo, L., Rantakyrö, F. T., Sadakuni, N., Saddlemyer, L., Savransky, D., Soummer, R., Sivaramakrishnan, A., Song, I., Thomas, S., Wallace, J. K., Wang, J. J., & Wolff, S. G. 2015. Polarimetry with the Gemini Planet Imager: Methods, Performance at First Light, and the Circumstellar Ring around HR 4796A. *apj*, **799**(Feb.), 182.

Peters-Limbach, M. A., Groff, T. D., Kasdin, N. J., Driscoll, D., Galvin, M., Foster, A., Carr, M. A., LeClerc, D., Fagan, R., McElwain, M. W., Knapp, G., Brandt, T., Janson, M., Guyon, O., Jovanovic, N., Martinache, F., Hayashi, M., & Takato, N. 2013 (Sept.). The optical design of CHARIS: an exoplanet IFS for the Subaru telescope. *Page 1 of: Society of Photo-Optical Instrumentation Engineers (SPIE) Conference Series*. Society of Photo-Optical Instrumentation Engineers (SPIE) Conference Series, vol. 8864.

Petit, C., Conan, J.-M., Kulcsár, C., & Raynaud, H.-F. 2009. Linear quadratic Gaussian control for adaptive optics and multiconjugate adaptive optics: experimental and numerical analysis. *Journal of the Optical Society of America A*, **26**(May), 1307.

Petit, C., Sauvage, J.-F., Fusco, T., Sevin, A., Suarez, M., Costille, A., Vigan, A., Soenke, C., Perret, D., Rochat, S., Barrufolo, A., Salasnich, B., Beuzit, J.-L., Dohlen, K., Mouillet, D., Puget, P., Wildi, F., Kasper, M., Conan, J.-M., Kulcsár, C., & Raynaud, H.-F. 2014 (Aug.). SPHERE eXtreme AO control scheme: final performance assessment and on sky validation of the first auto-tuned LQG based operational system. *Page 0 of: Society of Photo-Optical Instrumentation Engineers (SPIE) Conference Series*. Society of Photo-Optical Instrumentation Engineers (SPIE) Conference Series, vol. 9148.

Poyneer, L. A., De Rosa, R. J., Macintosh, B., Palmer, D. W., Perrin, M. D., Sadakuni, N., Savransky, D., Bauman, B., Cardwell, A., Chilcote, J. K., Dillon, D., Gavel, D., Goodsell, S. J., Hartung, M., Hibon, P., Rantakyrö, F. T., Thomas, S., & Veran, J.-P.

2014 (July). On-sky performance during verification and commissioning of the Gemini Planet Imager's adaptive optics system. *Page 0 of: Society of Photo-Optical Instrumentation Engineers (SPIE) Conference Series*. Society of Photo-Optical Instrumentation Engineers (SPIE) Conference Series, vol. 9148.

Prieto, J. L., Stanek, K. Z., Kochanek, C. S., Weisz, D. R., Baruffolo, A., Bechtold, J., Burwitz, V., De Santis, C., Gallozzi, S., Garnavich, P. M., Giallongo, E., Hill, J. M., Pogge, R. W., Ragazzoni, R., Speziali, R., Thompson, D. J., & Wagner, R. M. 2008. LBT Discovery of a Yellow Supergiant Eclipsing Binary in the Dwarf Galaxy Holmberg IX. *apjl*, **673**(Jan.), L59–L62.

Pueyo, L., Kasdin, N. J., & Shaklan, S. 2011. Propagation of aberrations through phase-induced amplitude apodization coronagraph. *Journal of the Optical Society of America A*, **28**(Feb.), 189.

Quintana, E. V., Barclay, T., Raymond, S. N., Rowe, J. F., Bolmont, E., Caldwell, D. A., Howell, S. B., Kane, S. R., Huber, D., Crepp, J. R., Lissauer, J. J., Ciardi, D. R., Coughlin, J. L., Everett, M. E., Henze, C. E., Horch, E., Isaacson, H., Ford, E. B., Adams, F. C., Still, M., Hunter, R. C., Quarles, B., & Selsis, F. 2014. An Earth-Sized Planet in the Habitable Zone of a Cool Star. *Science*, **344**(Apr.), 277–280.

Racine, R., Walker, G. A. H., Nadeau, D., Doyon, R., & Marois, C. 1999. Speckle Noise and the Detection of Faint Companions. *pasp*, **111**(May), 587–594.

Ragazzoni, R. 1996. Pupil plane wavefront sensing with an oscillating prism. *Journal of Modern Optics*, **43**(Feb.), 289–293.

Riaud, P., Boccaletti, A., Rouan, D., Lemarquis, F., & Labeyrie, A. 2001. The Four-Quadrant Phase-Mask Coronagraph. II. Simulations. *pasp*, **113**(Sept.), 1145–1154.

Riaud, P., Boccaletti, A., Baudrand, J., & Rouan, D. 2003. The Four-Quadrant Phase Mask Coronagraph. III. Laboratory Performance. *pasp*, **115**(June), 712–719.

Roberts, Jr., L. C., & Neyman, C. R. 2002. Characterization of the AEOS Adaptive Optics System. *pasp*, **114**(Nov.), 1260–1266.

Roddier, F. 1988. Curvature sensing and compensation: a new concept in adaptive optics. *ao*, **27**(Apr.), 1223–1225.

Roddier, F. 2004. *Adaptive Optics in Astronomy*.

Roddier, F., & Roddier, C. 1997. Stellar Coronograph with Phase Mask. *pasp*, **109**(July), 815–820.

Rogers, L. A. 2015. Most 1.6 Earth-radius Planets are Not Rocky. *apj*, **801**(Mar.), 41.

Rouan, D., Riaud, P., Boccaletti, A., Clénet, Y., & Labeyrie, A. 2000. The Four-Quadrant Phase-Mask Coronagraph. I. Principle. *pasp*, **112**(Nov.), 1479–1486.

Rousset, G., Fontanella, J. C., Kern, P., Gigan, P., & Rigaut, F. 1990. First diffraction-limited astronomical images with adaptive optics. *aap*, **230**(Apr.), L29–L32.

Sabelhaus, P. A., & Decker, J. E. 2004 (Oct.). An overview of the James Webb Space Telescope (JWST) project. *Pages 550–563 of:* Mather, J. C. (ed), *Optical, Infrared, and Millimeter Space Telescopes*. Society of Photo-Optical Instrumentation Engineers (SPIE) Conference Series, vol. 5487.

Schöck, M., Els, S., Riddle, R., Skidmore, W., Travouillon, T., Blum, R., Bustos, E., Chanan, G., Djorgovski, S. G., Gillett, P., Gregory, B., Nelson, J., Otárola, A., Seguel, J., Vasquez, J., Walker, A., Walker, D., & Wang, L. 2009. Thirty Meter Telescope Site Testing I: Overview. *pasp*, **121**(Apr.), 384–395.

Seager, S. 2013. Exoplanet Habitability. *Science*, **340**(May), 577–581.

Serabyn, E., Wallace, K., Troy, M., Mennesson, B., Haguenauer, P., Gappinger, R., & Burruss, R. 2007. Extreme Adaptive Optics Imaging with a Clear and Well-Corrected Off-Axis Telescope Subaperture. *apj*, **658**(Apr.), 1386–1391.

Serabyn, E., Mawet, D., & Burruss, R. 2010. An image of an exoplanet separated by two diffraction beamwidths from a star. *nat*, **464**(Apr.), 1018–1020.

Shack, R. V. 1971. Production and use of a lenticular Hartmann screen. *OSA*, **61**, 656.

Shaklan, S. B., & Green, J. J. 2005. Low-Order Aberration Sensitivity of Eighth-Order Coronagraph Masks. *apj*, **628**(July), 474–477.

Showman, A. P. 2008. Extrasolar planets: A whiff of methane. *nat*, **452**(Mar.), 296–297.

Singh, G., Martinache, F., Baudoz, P., Guyon, O., Matsuo, T., Jovanovic, N., & Clergeon, C. 2014. Lyot-based Low Order Wavefront Sensor for Phase-mask Coronagraphs: Principle, Simulations and Laboratory Experiments. *pasp*, **126**(June), 586–594.

Singh, G., Lozi, J., Guyon, O., Baudoz, P., Jovanovic, N., Martinache, F., Kudo, T., Serabyn, E., & Kuhn, J. 2015. On-Sky Demonstration of Low-Order Wavefront Sensing and Control with Focal Plane Phase Mask Coronagraphs. *pasp*, **127**(Oct.), 857–869.

Sivaramakrishnan, A., Koresko, C. D., Makidon, R. B., Berkefeld, T., & Kuchner, M. J. 2001. Ground-based Coronagraphy with High-order Adaptive Optics. *apj*, **552**(May), 397–408.

Sivaramakrishnan, A., Soummer, R., Sivaramakrishnan, A. V., Lloyd, J. P., Oppenheimer, B. R., & Makidon, R. B. 2005. Low-Order Aberrations in Band-limited Lyot Coronagraphs. *apj*, **634**(Dec.), 1416–1422.

Skemer, A. J., Hinz, P. M., Esposito, S., Burrows, A., Leisenring, J., Skrutskie, M., Desidera, S., Mesa, D., Arcidiacono, C., Mannucci, F., Rodigas, T. J., Close, L., McCarthy, D., Kulesa, C., Agapito, G., Apai, D., Argomedo, J., Bailey, V., Boutsia, K., Briguglio, R., Brusa, G., Busoni, L., Claudi, R., Eisner, J., Fini, L., Follette, K. B., Garnavich, P., Gratton, R., Guerra, J. C., Hill, J. M., Hoffmann, W. F., Jones, T., Krejny, M., Males, J., Masciadri, E., Meyer, M. R., Miller, D. L., Morzinski, K., Nelson, M., Pinna, E., Puglisi, A., Quanz, S. P., Quiros-Pacheco, F., Riccardi, A., Stefanini, P., Vaitheeswaran, V., Wilson, J. C., & Xompero, M. 2012. First Light LBT AO Images

of HR 8799 bcde at 1.6 and 3.3 μm: New Discrepancies between Young Planets and Old Brown Dwarfs. *apj*, **753**(July), 14.

Skemer, A. J., Hinz, P., Esposito, S., Skrutskie, M. F., Defrère, D., Bailey, V., Leisenring, J., Apai, D., Biller, B., Bonnefoy, M., Brandner, W., Buenzli, E., Close, L., Crepp, J., De Rosa, R. J., Desidera, S., Eisner, J., Fortney, J., Henning, T., Hofmann, K.-H., Kopytova, T., Maire, A.-L., Males, J. R., Millan-Gabet, R., Morzinski, K., Oza, A., Patience, J., Rajan, A., Rieke, G., Schertl, D., Schlieder, J., Su, K., Vaz, A., Ward-Duong, K., Weigelt, G., Woodward, C. E., & Zimmerman, N. 2014 (July). High contrast imaging at the LBT: the LEECH exoplanet imaging survey. *Page 0 of: Society of Photo-Optical Instrumentation Engineers (SPIE) Conference Series*. Society of Photo-Optical Instrumentation Engineers (SPIE) Conference Series, vol. 9148.

Skrutskie, M. F., Jones, T., Hinz, P., Garnavich, P., Wilson, J., Nelson, M., Solheid, E., Durney, O., Hoffmann, W., Vaitheeswaran, V., McMahon, T., Leisenring, J., & Wong, A. 2010 (July). The Large Binocular Telescope mid-infrared camera (LMIRcam): final design and status. *Page 3 of: Society of Photo-Optical Instrumentation Engineers (SPIE) Conference Series*. Society of Photo-Optical Instrumentation Engineers (SPIE) Conference Series, vol. 7735.

Soummer, R. 2005. Apodized Pupil Lyot Coronagraphs for Arbitrary Telescope Apertures. *apjl*, **618**(Jan.), L161–L164.

Soummer, R., Dohlen, K., & Aime, C. 2003a. Achromatic dual-zone phase mask stellar coronagraph. *aap*, **403**(May), 369–381.

Soummer, R., Aime, C., & Falloon, P. E. 2003b. Stellar coronagraphy with prolate apodized circular apertures. *aap*, **397**(Jan.), 1161–1172.

Spergel, D., Gehrels, N., Breckinridge, J., Donahue, M., Dressler, A., Gaudi, B. S., Greene, T., Guyon, O., Hirata, C., Kalirai, J., Kasdin, N. J., Moos, W., Perlmutter, S., Postman, M., Rauscher, B., Rhodes, J., Wang, Y., Weinberg, D., Centrella, J., Traub, W., Baltay, C., Colbert, J., Bennett, D., Kiessling, A., Macintosh, B., Merten, J., Mortonson, M., Penny, M., Rozo, E., Savransky, D., Stapelfeldt, K., Zu, Y., Baker, C., Cheng, E., Content, D., Dooley, J., Foote, M., Goullioud, R., Grady, K., Jackson, C., Kruk, J., Levine, M., Melton, M., Peddie, C., Ruffa, J., & Shaklan, S. 2013. Wide-Field InfraRed Survey Telescope-Astrophysics Focused Telescope Assets WFIRST-AFTA Final Report. *ArXiv e-prints*, May.

Stapelfeldt, K. R., Brenner, M. P., Warfield, K. R., Dekens, F. G., Belikov, R., Brugarolas, P. B., Bryden, G., Cahoy, K. L., Chakrabarti, S., Dubovitsky, S., Effinger, R. T., Hirsch, B., Kissil, A., Krist, J. E., Lang, J. J., Marley, M. S., McElwain, M. W., Meadows, V. S., Nissen, J., Oseas, J. M., Serabyn, E., Sunada, E., Trauger, J. T., & Unwin, S. C. 2014 (Aug.). Exo-C: a probe-scale space mission to directly image and spectroscopically characterize exoplanetary systems using an internal coronagraph. *Page 2 of: Society of Photo-Optical Instrumentation Engineers (SPIE) Conference Series*. Society of Photo-Optical Instrumentation Engineers (SPIE) Conference Series, vol. 9143.

Stevenson, D. J. 1999. Life-sustaining planets in interstellar space? *nat*, **400**(July), 32.

Suzuki, R., Kudo, T., Hashimoto, J., Carson, J., Egner, S., Goto, M., Hattori, M., Hayano, Y., Hodapp, K., Ito, M., Iye, M., Jacobson, S., Kandori, R., Kusakabe, N., Kuzuhara, M., Matsuo, T., Mcelwain, M., Morino, J.-I., Oya, S., Saito, Y., Shelton, R., Stahlberger, V., Suto, H., Takami, H., Thalmann, C., Watanabe, M., Yamada, H., & Tamura, M. 2010 (July). Performance characterization of the HiCIAO instrument for the Subaru Telescope. *Page 30 of: Society of Photo-Optical Instrumentation Engineers (SPIE) Conference Series*. Society of Photo-Optical Instrumentation Engineers (SPIE) Conference Series, vol. 7735.

Swartzlander, Jr., G. A. 2006. Achromatic optical vortex lens. *Optics Letters*, **31**(July), 2042–2044.

Takami, H., Watanabe, M., Takato, N., Colley, S., Eldred, M., Kane, T., Guyon, O., Hattori, M., Goto, M., Iye, M., Hayano, Y., Kamata, Y., Arimoto, N., Kobayashi, N., & Minowa, Y. 2004 (Oct.). Laser guide star AO project at the Subaru Telescope. *Pages 837–845 of:* Bonaccini Calia, D., Ellerbroek, B. L., & Ragazzoni, R. (eds), *Advancements in Adaptive Optics*. Society of Photo-Optical Instrumentation Engineers (SPIE) Conference Series, vol. 5490.

Tamura, M. 2009 (Aug.). Subaru Strategic Exploration of Exoplanets and Disks with HiCIAO/AO188 (SEEDS). *Pages 11–16 of:* Usuda, T., Tamura, M., & Ishii, M. (eds), *American Institute of Physics Conference Series*. American Institute of Physics Conference Series, vol. 1158.

Tamura, M., Hodapp, K., Suzuki, R., Abe, L., Takami, H., Suto, H., Guyon, O., Kandori, R., Morino, J., Hashimoto, J., Stahlberger, V., Jacobson, S., Yamada, H., Shelton, R., Tavrov, A., Murakami, N., Nishikawa, J., Hayashi, M., Usuda, T., Yamada, T., & Nishimura, T. 2007 (June). HiCIAO and Exoplanet/Disk Searches on Subaru. *Page 34 of: In the Spirit of Bernard Lyot: The Direct Detection of Planets and Circumstellar Disks in the 21st Century*.

Thalmann, C., Carson, J., Janson, M., Goto, M., McElwain, M., Egner, S., Feldt, M., Hashimoto, J., Hayano, Y., Henning, T., Hodapp, K. W., Kandori, R., Klahr, H., Kudo, T., Kusakabe, N., Mordasini, C., Morino, J.-I., Suto, H., Suzuki, R., & Tamura, M. 2009. Discovery of the Coldest Imaged Companion of a Sun-like Star. *apjl*, **707**(Dec.), L123–L127.

Thalmann, C., Janson, M., Buenzli, E., Brandt, T. D., Wisniewski, J. P., Moro-Martín, A., Usuda, T., Schneider, G., Carson, J., McElwain, M. W., Grady, C. A., Goto, M., Abe, L., Brandner, W., Dominik, C., Egner, S., Feldt, M., Fukue, T., Golota, T., Guyon, O., Hashimoto, J., Hayano, Y., Hayashi, M., Hayashi, S., Henning, T., Hodapp, K. W., Ishii, M., Iye, M., Kandori, R., Knapp, G. R., Kudo, T., Kusakabe, N., Kuzuhara, M., Matsuo, T., Miyama, S., Morino, J.-I., Nishimura, T., Pyo, T.-S., Serabyn, E., Suto, H., Suzuki, R., Takahashi, Y. H., Takami, M., Takato, N., Terada, H., Tomono, D., Turner, E. L., Watanabe, M., Yamada, T., Takami, H., & Tamura, M. 2011. Images of the Extended Outer Regions of the Debris Ring around HR 4796 A. *apjl*, **743**(Dec.), L6.

Thalmann, C., Mulders, G. D., Janson, M., Olofsson, J., Benisty, M., Avenhaus, H., Quanz, S. P., Schmid, H. M., Henning, T., Buenzli, E., Ménard, F., Carson, J. C., Garufi, A., Messina, S., Dominik, C., Leisenring, J., Chauvin, G., & Meyer, M. R. 2015. Optical imaging polarimetry of the LkCa 15 protoplanetary disk with SPHERE ZIMPOL. *ArXiv e-prints*, July.

Traub, W. A., & Oppenheimer, B. R. 2010. *Direct Imaging of Exoplanets*. Pages 111–156.

Vanderbei, R. J., Kasdin, N. J., & Spergel, D. N. 2004. Checkerboard-Mask Coronagraphs for High-Contrast Imaging. *apj*, **615**(Nov.), 555–561.

Vérinaud, C., Le Louarn, M., Korkiakoski, V., & Carbillet, M. 2005. Adaptive optics for high-contrast imaging: pyramid sensor versus spatially filtered Shack-Hartmann sensor. *mnras*, **357**(Feb.), L26–L30.

Vogt, F. P. A., Martinache, F., Guyon, O., Yoshikawa, T., Yokochi, K., Garrel, V., & Matsuo, T. 2011. Coronagraphic Low-Order Wavefront Sensor: Postprocessing Sensitivity Enhancer for High-Performance Coronagraphs. *pasp*, **123**(Dec.), 1434–1441.

Vogt, S. S., Allen, S. L., Bigelow, B. C., Bresee, L., Brown, B., Cantrall, T., Conrad, A., Couture, M., Delaney, C., Epps, H. W., Hilyard, D., Hilyard, D. F., Horn, E., Jern, N., Kanto, D., Keane, M. J., Kibrick, R. I., Lewis, J. W., Osborne, J., Pardeilhan, G. H., Pfister, T., Ricketts, T., Robinson, L. B., Stover, R. J., Tucker, D., Ward, J., & Wei, M. Z. 1994 (June). HIRES: the high-resolution echelle spectrometer on the Keck 10-m Telescope. *Page 362 of:* Crawford, D. L., & Craine, E. R. (eds), *Instrumentation in Astronomy VIII*. Society of Photo-Optical Instrumentation Engineers (SPIE) Conference Series, vol. 2198.

Wallace, J. K., Rao, S., Jensen-Clem, R. M., & Serabyn, G. 2011 (Sept.). Phase-shifting Zernike interferometer wavefront sensor. *Page 0 of: Society of Photo-Optical Instrumentation Engineers (SPIE) Conference Series*. Society of Photo-Optical Instrumentation Engineers (SPIE) Conference Series, vol. 8126.

Watanabe, M., Takami, H., Takato, N., Colley, S., Eldred, M., Kane, T., Guyon, O., Hattori, M., Goto, M., Iye, M., Hayano, Y., Kamata, Y., Arimoto, N., Kobayashi, N., & Minowa, Y. 2004 (Oct.). Design of the Subaru laser guide star adaptive optics module. *Pages 1096–1104 of:* Bonaccini Calia, D., Ellerbroek, B. L., & Ragazzoni, R. (eds), *Advancements in Adaptive Optics*. Society of Photo-Optical Instrumentation Engineers (SPIE) Conference Series, vol. 5490.

Watson, S. M., Mills, J. P., Gaiser, S. L., & Diner, D. J. 1991. Direct imaging of nonsolar planets with infrared telescopes using apodized coronagraphs. *ao*, **30**(Aug.), 3253–3262.

Zsom, A., Seager, S., de Wit, J., & Stamenković, V. 2013. Toward the Minimum Inner Edge Distance of the Habitable Zone. *apj*, **778**(Dec.), 109.

Appendices

Appendix A

Third AO4ELT Conference - Adaptive Optics for Extremely Large Telescopes (2013)

Third AO4ELT Conference - Adaptive Optics for Extremely Large Telescopes
Florence, Italy. May 2013
ISBN: 978-88-908876-0-4
DOI: 10.12839/AO4ELT3.12667

LYOT-BASED ULTRA-FINE POINTING CONTROL SYSTEM FOR PHASE MASK CORONAGRAPHS

Garima Singh[1,2a], Frantz Martinache[1], Pierre Baudoz[2], Olivier Guyon[1], Taro Matsuo[3], and Christophe Clergeon[1,2]

[1] National Astronomical Observatory of Japan, Subaru Telescope, 650 N A'Ohoku Pl, Hilo, HI 96720, USA
[2] LESIA, Observatoire de Paris-Meudon, 5 Place Jules Janssen, F-92195 Meudon Cedex, France
[3] Kyoto University, Kitashirakawa-Oiwakecho, Sakyo-ku, Kyoto 606-8502, Japan

Abstract. High performance coronagraphic imaging at small inner working angle requires efficient control of low order aberrations. The absence of accurate pointing control at small separation not only degrades coronagraph starlight rejection but also increases the risk of confusing planet's photons with starlight leaking next to the coronagraph focal plane mask center. Addressing this issue is essential for preventing coronagraphic leaks, and we have thus developed a new concept, the Lyot-based pointing control system (LPCS), to control pointing errors and other low order aberrations within a coronagraph. The LPCS uses residual starlight reflected by the Lyot stop at the pupil plane. Our simulation has demonstrated pointing errors measurement accuracy between 2-12 nm for tip-tilt at 1.6 μm with a four quadrant phase mask coronagraph.

1 Introduction

The direct detection and characterization of extrasolar planets is affected by the rapidly changing atmosphere. The optical systems can not perform the high contrast imaging without the accurate measurement and calibration of the wavefront. But with the help of Adaptive Optics, the optical system are able to reach the diffraction-limit and the post processing techniques such as Differential Imaging has made it possible to identify faint companions at angular separation $\gtrsim$10 λ/D from their parent star (Marois et al. 2008 and Lagrange et al. 2009). Moreover, the newly developed small inner working angle (IWA) coronagraphs employed on Extreme Adaptive Optic Systems (ExAO) have improved their ability to image exoplanets within a few λ/D. But Guyon et al. (2006) addresses the following challenges that limits coronagraphic performance: stabilizing starlight at the center of the coronagraph; isolating companion's photons by calibrating speckles from star; obtaining high star-planet contrast (10^{-6} in IR) over large spectral bandwidth.

The closer the search area is to the star, the more difficult it is to image the companions because high performance coronagraphs are extremely sensitive to tip/tilt errors (Lloyd & Sivaramakrishnan 2005; Shaklan & Green 2005; Sivaramakrishnan et al. 2005; Belikov et al. 2006; Guyon et al. 2006). Thus, their performance is limited by how well the low order wavefront aberrations are controlled and calibrated.

The Subaru Telescope Coronagraphic Extreme AO (SCExAO) is a flexible, high performance coronagraphic system that can detect high contrast structures as close as 1λ/D and which uses a coronagraphic low-order wavefront sensor (CLOWFS) as described in Guyon

[a] singh@naoj.org

et al. (2009) and Vogt et al. (2011) to suppress low order aberrations in the coronagraph. The CLOWFS uses a dual-zone focal plane mask and analyzes the defocused image of the unused partially reflected starlight. The recent laboratory demonstration of CLOWFS on NASA's High Contrast Imaging Testbed (HCIT) at JPL has shown the stabilization of tip-tilt with 0.001λ/D residual in closed loop for λ = 808 nm on Phase Induced Amplitude Apodization (PIAA)-type coronagraph (Kern et al. 2013).

To further enhance the IWA of SCExAO, we have modified the instrument to support phase mask coronagraphy with a goal IWA $< 1\lambda$/D. To be able to take advantage of the small IWA offered by phase mask coronagraphs (PMCs), we introduce a new generation of CLOWFS to do the pointing control which is compatible with PMCs. It is based on the idea of re-imaging the starlight reflected by the Lyot Stop towards an imaging camera at a defocused position. We call our new system as Lyot-based pointing control system (LPCS). The common property of the PMCs is that they diffract starlight outside of the geometrical pupil which is then blocked by the conventional Lyot stop. For super fine controlling of the pointing errors, we have modified the Lyot design for them. We used a reflective Lyot stop (RLS) which fully reflects the unused starlight towards the low order wave front sensor measuring the low order modes accurately.

The concept of RLS and pointing error estimation theory is presented in section 2. We describe the LPCS optical configuration, numerical simulation and their results in section 3. All of our simulations are done without considering photon noise.

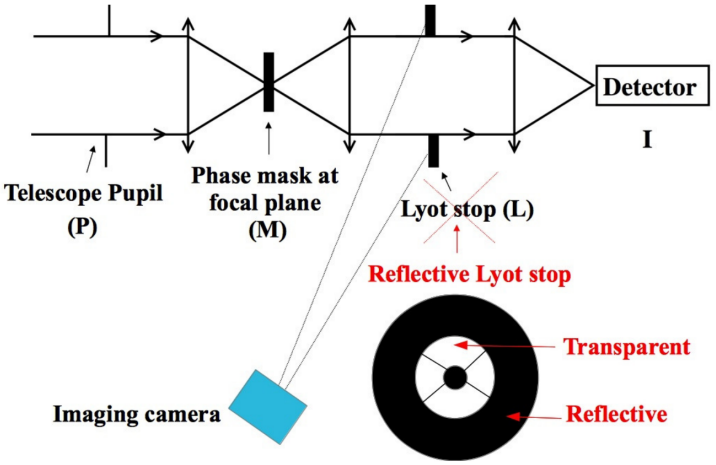

Fig. 1. Basic design of the LPCS consisting of a high performance coronagraph combined with reflective Lyot stop whose geometry can be adopted considering telescope pupil with central obstruction and spider arms.

2 Principle

2.1 A reflecting Lyot stop wavefront sensor

Atmospheric turbulence and telescope pointing errors make it difficult to center the stellar light on occulting mask which creates halo of speckles around the occulter preventing detection of companion. SCExAO's CLOWFS has successfully used a focal plane mask as a means of

measuring and correcting the low order aberrations and has made planet detection possible within the 1 - 2λ/D region. Its possible to reach the region $\lesssim 1\lambda$/D with high performance PMCs, but the sensitivity to tip-tilt errors make it mandatory to correct for low order aberrations to obtain the best starlight rejection. However a reflective focal plane mask as used in SCExAO is not feasible to measure pointing errors for PMCs, hence a new solution is needed.
The PMCs have the tendency to redistribute the energy spatially in the telescope pupil, canceling on-axis light and diffracting it outside the aperture which is then absorbed by the Lyot stop. We introduce a new concept where we fully utilize the unused diffracted light by reflecting it via Lyot stop (called as reflective Lyot stop) towards an imaging camera to accurately measure pointing errors. Fig. 1 describes the basic concept of LPCS. At the focal plane of the telescope, a phase mask diffracts starlight in a re-imaged pupil plane. This residual starlight is then collected by the RLS (L) and then reflected towards the camera which acquires a defocused starlight image.

2.2 Pointing errors estimation based on linearity approximation

In a post-AO correction scenario, residual phase errors can be assumed to be small (<<1 radian phase rms at pupil). Simulation work, as well as preliminary experimental results show that our Lyot-based pointing control system (LPCS) is a linear wavefront sensor. For small pointing errors, intensity fluctuations in the RLS image appear to be a linear function of low-order phase errors before the coronagraph. Calling I_0 our reference image, acquired by the LPCS camera with no tip-tilt, and I_R the instant LPCS image, we can relate the difference between these two images to a linear combination of modes. If one considers tip-tilt alone, then we can for instance write:

$$I_{R(\alpha_x,\alpha_y)} - I_0 = \alpha_x S_x + \alpha_y S_y \quad (1)$$

where S_x and S_y represent the sensor's respective response to tip and tilt. For any instant image I_R, one can therefore identify unknown tip-tilt (α_x, α_y), by direct projection on the basis of modes, or using a least square algorithm. S_x and S_y are obtained during a calibration step, after applying a controlled amount of tip and tilt modes. Example of response modes are shown in Fig. 3, for tip-tilt as well other modes: defocus and astigmatism, showing that the LPCS is a versatile sensor.

3 Lyot-based pointing control system

3.1 Optical Configuration

We have developed a simulation tool by reproducing the revised SCExAO system (Jovanovic et al. 2013) at Subaru Telescope to test LPCS concept. A simplified optical configuration of the LPCS is shown in Fig. 2. The optical components are described as follows:

- Entrance Pupil (*a*): $f14$ beam of 18 mm diameter as an input to SCExAO which is the output of 8-meter Subaru Telescope's Adaptive Optics AO188 system)
- Phase Mask Coronagraph (*b*): FQPM (Optimized wavelength λ=1.6 μm). The FQPM divides the focal plane in four quadrant and provides a π phase shift in the two opposite quadrants, resulting in self-destructive interference in the relay pupil (Rouan et al. 2000). To be more realistic, we simulated a FQPM with manufacturing defects: gap of 2.5 μm in the transition

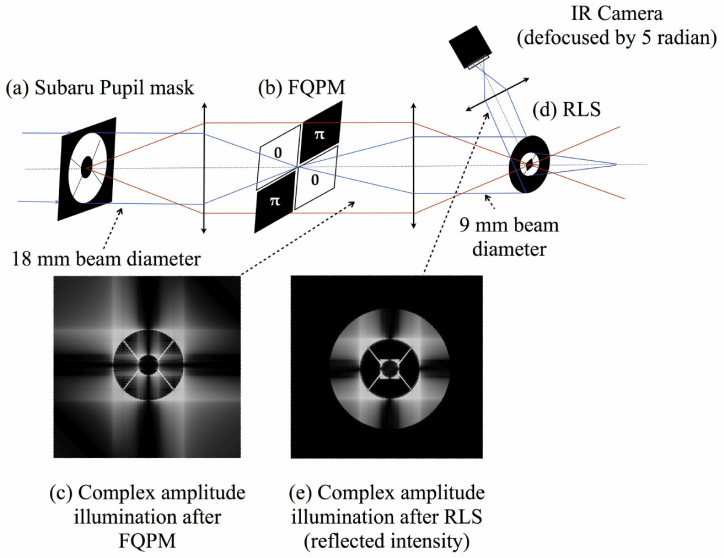

Fig. 2. Simplified optical layout of revised SCExAO system showing LPCS with FQPM as an example. (a) Subaru pupil mask. (b) Four quadrant phase mask (FQPM). (c) Intensity pattern after FQPM. (d) Reflected Lyot Stop (RLS). (e) Complex amplitude as seen at RLS plane. See section 3.1 for more details.

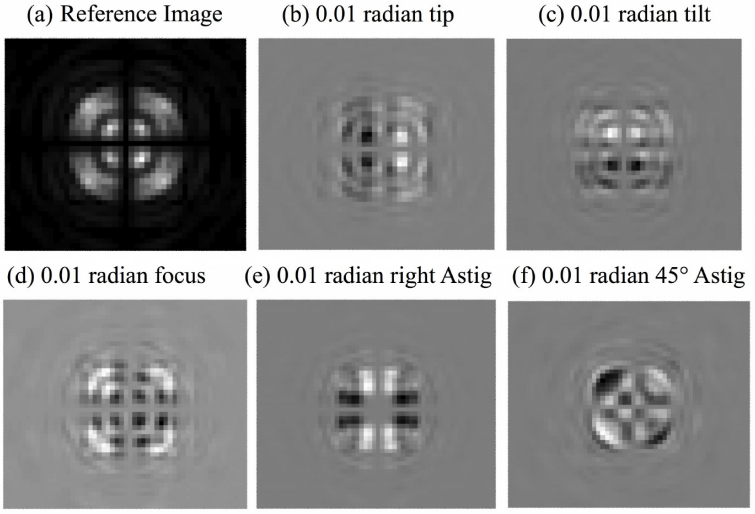

Fig. 3. Response of the LPCS to the low-order modes which are our calibration frames to measure the unknown aberrations present in the entrance pupil.

zone of the opposite quadrants and the shift of ≈1.8 μm between the layers deposited on the two adjacent quadrants.

– Reflective Lyot stop (*d*): *f*28 beam of 9 mm diameter. The black surface is reflective chrome while white surface is transparent. The geometry of RLS adopted for FQPM: Lyot outer pupil diameter (5% undersized), Lyot central obstruction diameter (12% oversized), Spider arms (50% oversized).The outer most diameter of RLS is considered to be 3 x Lyot outer pupil diameter.

Image (*c*) is the complex amplitude after FQPM clearly showing the square intensity pattern diffracted by central obstruction. Image (*e*) is what is seen by the clowfs at RLS plane.

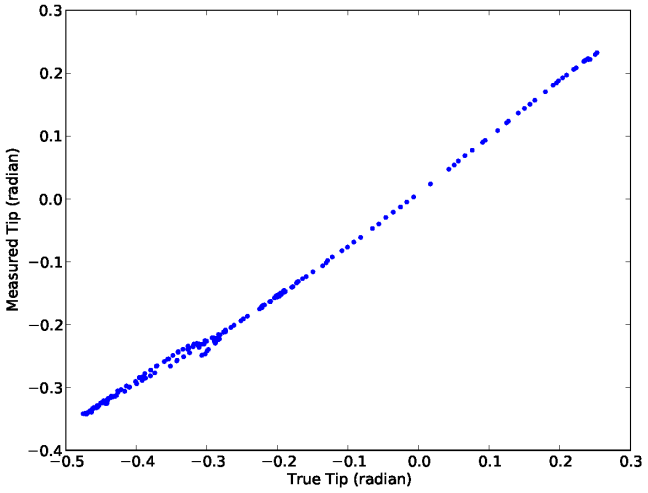

Fig. 4. Linearity of LPCS response to tip in post-AO188 phase residual.

3.2 LPCS Numerical Simulations: Subaru Telescope's AO188-post processed residual phase as wavefront error to LPCS

To check the performance of the LPCS, we use the Subaru Telescope's realistic AO188 residual phase series as input to our system. The series consist of 200 residual phase maps with unknown low and high order aberrations (≈ 180 *nm* phase rms at λ= 1.6 μm). The residual wavefront after encountering the FQPM at the focal plane interfere self-destructively inside the pupil. A wavefront aberration of 0.72 radians is added after FQPM to mimic the quasi-static speckles. The unused diffracted light is then reflected via RLS towards the imaging camera which then measures the tip-tilt that is originally present in the residual phase map. Fig. 4 shows the true tip aberration present in the residual phase map versus tip aberration measured by LPCS showing the linearity range of ±0.1 radians. We also compare the LPCS response to tip-tilt with their actual residual value for 200 phasemaps as shown in Fig. 5. The LPCS measurement accuracy for tip-tilt is: *0.05 rad rms* for tip, *0.01 rad rms* for tilt. Fig. 5 shows that for small tip-tilt

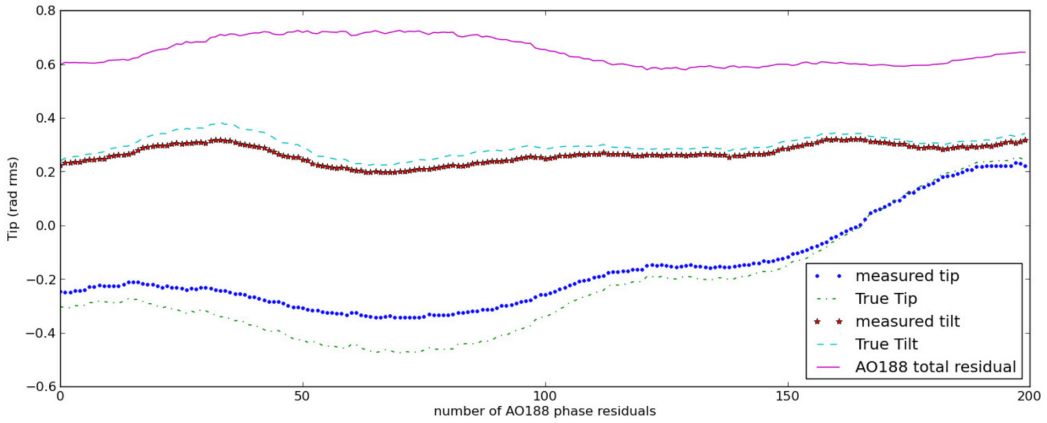

Fig. 5. Response of LPCS to tip-tilt in the realistic AO188 phase residual of 200 image series.

excursions, the LPCS response to low-order aberrations provides a reliable measurement of the tip-tilt. The fidelity of the reconstruction degrades for larger tip-tilt excursion (beyond ± 0.1 radians), due to non-linearity effects, but the sensor remains well behaved, and in close-loop, would converge toward the reference position, despite the non-linearity. Overall, our system showed the measurement accuracy of 2-12 nm per mode at 1.6 μm for FQPM.

4 Conclusion

The lack of accurate pointing control degrades the ability of low inner working angle (IWA) coronagraphs to directly image and characterize exoplanets. To deal with this problematic and delicate issue of pointing control, we have introduced a robust, easy to implement technique to prevent the coronagraphic leaks for low IWA PMCs. We showed in simulation that with the AO residual phase as an input wavefront, the LPCS is capable of measuring tip, tilt and other low order modes with the accuracy of 2-12 nm at 1.6 μm within linear range of ± 0.1 radians. The LPCS measurement is not limited only to tip-tilt as we could also potentially measure defocus and astigmatism as shown in Fig. 3. Our next step is dedicated to simulate other phase masks such as Roddier & Roddier (Roddier et al. 1997), Vortex (Mawet et al. 2010), Eight Octant Phase Mask (Murakami et al. 2008a) and the Phase-Induced Amplitude Apodization Complex Phase Mask Coronagraph (Guyon et al. 2010) to verify performance and contrast sensitivity of the LPCS.

Regarding ELTs and space-based telescopes, the combination of PMC + LPCS promises to provide the sub mili-arcsecond level pointing stability at small IWA making it realistic to directly image the reflected light habitable planets. LPCS is indeed an appealing solution for not only ground-based but for future space missions as well.

References

1. Belikov, R., Kasdin, N. J., & Vanderbei, R. J., ApJ, 652 (2006), 833 Guyon, O., A&A, 404 (2003), 379

2. Guyon, O., ApJ, 629 (2005), 592
3. Guyon, O., Pluzhnik, E. A., Kuchner, M. J., Collins, B., & Ridgway, S. T., ApJ, 167 (2006), 81
4. Guyon, O., Matsuo, T., & Angel, R. ApJ, 693 (2009), 75
5. Guyon, O., Martinache, F., Belikov, R., & Soummer, R., ApJS, 190 (2010), 220
6. Kern, B., Guyon, O., Kuhnert, A., Niessner, A., Martinache, F., Balasubramanian, K., Proc. of SPIE, 8864 (2013), 88640R
7. Lloyd, J. P., & Sivaramakrishnan, A., ApJ, 621 (2005), 1153
8. Lagrange, A., Gratadour, D., Chauvin, G., et al., A&A, 493 (2009), L21
9. Marois, C., Macintosh, B., Barman, T., et al., Science, 322 (2008), 1348
10. Murakami, N., Uemura, R., Baba, N., Nishikawa, J., Tamura, M., Hashimoto, N., & Abe, L., PASP, 120 (2008a), 1112
11. Mawet, D., Serabyn, E., Liewer, K., et al., ApJ, 709 (2010), 53
12. Jovanovic, N., Guyon, O., Martinache, Clergeon, C., Singh, G., Vievard, S., Kudo, T., Garrel, V., Norris, B., Tuthill, P., Stewart, P., Huby, E., Perrin, G., Lacour, S., Proc. of AO4ELTs3, Paper 13396 (2013)
13. Roddier, F., Roddier, C., PASP, 109 (1997), 815
14. Rouan, D., Riaud, P., Boccaletti, A., Clenet, Y., & Labeyrie, A., PASP, 112 (2000), 1479
15. Shaklan, S. B., & Green, J. J., ApJ, 628 (2005), 474
16. Sivaramakrishnan, A., Soummer, R., Sivaramakrishnan, A. V., Lloyd, J. P., Oppenheimer, B. R., & Makidson, R. B., ApJ, 634 (2005),1416
17. Vogt, F. P. A., Martinache, F., Guyon, O., et al., PASP, 123 (2011), 1434

Appendix B

Adaptive Optics Systems IV, SPIE Astronomical Telescopes and Instrumentation (2014)

Lyot-based Low Order Wavefront Sensor: Implementation on the Subaru Coronagraphic Extreme Adaptive Optics System and its Laboratory Performance

Garima Singh[a,b], Olivier Guyon[a,d], Pierre Baudoz[b], Nemanja Jovanovic[a], Frantz Martinache[c], Tomoyuki Kudo[a], Eugene Serabyn[d], Jonas G Kuhn[d]

[a]National Astronomical Observatory of Japan, Subaru Telescope, 650 North A'Ohoku Pl, Hilo-96720, Hawaii, USA;
[b]Laboratoire d'Etudes Spatiales et d'Instrumentation en Astrophysique, Observatoire de Paris-Meudon, 5 Place Jules Janssen, F-92195 Meudon, France;
[c]Laboratoire Lagrange, UMR7293, Université de Nice Sophia-Antipolis, CNRS, Observatoire de la Côte d'Azur, Bd. de l'Observatoire, 06304 Nice, France;
[d]Jet Propulsion Laboratory, California Institute of Technology, 4800 Oak Grove Drive, Pasadena, CA 91109-8099, USA

ABSTRACT

High throughput, low inner working angle (IWA) phase masks coronagraphs are essential to directly image and characterize (via spectroscopy) earth-like planets. However, the performance of low-IWA coronagraphs is limited by residual pointing errors and other low-order modes. The extent to which wavefront aberrations upstream of the coronagraph are corrected and calibrated drives coronagraphic performance. Addressing this issue is essential for preventing coronagraphic leaks, thus we have developed a Lyot-based low order wave front sensor (LLOWFS) to control the wavefront aberrations in a coronagraph. The LLOWFS monitors the starlight rejected by the coronagraphic mask using a reflective Lyot stop in the downstream pupil plane. The early implementation of LLOWFS at LESIA, Observatoire de Paris demonstrated an open loop measurement accuracy of 0.01 λ/D for tip-tilt at 638 nm when used in conjunction with a four quadrant phase mask (FQPM) in the laboratory. To further demonstrate our concept, we have installed the reflective Lyot stops on the Subaru Coronagraphic Extreme AO (SCExAO) system at the Subaru Telescope and modified the system to support small IWA phase mask coronagraphs ($< 1\lambda$/D) on-sky such as FQPM, eight octant phase mask, vector vortex coronagraph and the phase induced amplitude apodization complex phase mask coronagraph with a goal of obtaining milli arc-second pointing accuracy. Laboratory results have shown the measurement of tip, tilt, focus, oblique and right astigmatism at 1.55 μm for the vector vortex coronagraph. Our initial on-sky result demonstrate the closed loop accuracy of < 7 x 10^{-3} λ/D at 1.6 μm for tip, tilt and focus aberrations with the vector vortex coronagraph.

Keywords: Coronagraph, High Contrast Imaging, Extreme Adaptive Optics

1. INTRODUCTION

Direct detection of exoplanets is one of the most challenging field in Astronomy today. To image an Earth around the sun from a distance of 10 pc requires a contrast of 10^{-10} in the visible and 10^{-7} in the thermal IR. Such high contrasts from ground-based telescopes are limited by many factors such as: distortion of the wavefront by the atmospheric turbulence which reduces the peak intensity of the star and creates a halo of speckles around the point spread function (PSF), the optical imperfections of the imaging instrument, the local turbulence induced due to variations in temperature and the residual quasi-static speckles.

Eight meter class telescopes equipped with high performance adaptive optics (AO) systems are capable of suppressing the speckle noise by providing typical wavefront residuals of < 200 nm rms at H band. But to achieve

Further author information: Send correspondence to Garima Singh, E-mail: singh@naoj.org, Telephone: +1 808 934 5966

Adaptive Optics Systems IV, edited by Enrico Marchetti, Laird M. Close, Jean-Pierre Véran, Proc. of SPIE Vol. 9148, 914848 · © 2014 SPIE
CCC code: 0277-786X/14/$18 · doi: 10.1117/12.2057211

a raw contrast of $\approx 10^{-4}$ and a detection contrast of at least $\approx 10^{-7}$ at small angular resolution (≈ 1 λ/D) requires high performance low inner working angle (IWA) phase mask coronagraphs (PMCs) and an extreme adaptive optic system (ExAO) to provide rms wavefront errors of < 50 nm. But how efficiently an ExAO system corrects and calibrates the wavefront aberrations occurring before the coronagraph, derives the performance of the direct imaging instruments. The lack of fine pointing control puts light in the 1 to 2 λ/D region of the focal plane, making it difficult to differentiate planet signals from the starlight leakage which has a direct impact on the sensitivity of the low IWA phase mask coronagraph.[1,2,3,4,5]

To deal with the pointing errors occurring in the phase mask coronagraphs, we have developed a Lyot-based low order wavefront sensor[6] (LLOWFS) illustrated in Figure 1. The AO-corrected beam enters the telescope pupil and encounters a phase mask at the focal plane. The phase mask diffracts the starlight outside of the geometrical pupil, which in the case of a conventional coronagraph, is absorbed by the Lyot stop in a reimaged pupil plane. With the LLOWFS approach, this unused diffracted starlight is reflected via a reflective Lyot stop (RLS) towards a reimaged focal plane. The reflected light is then sensed by the low order sensor (a detector) which measures the low order wavefront aberrations.

LLOWFS is the next generation of coronagraphic low order wave front sensor[7] (CLOWFS) which used a partially reflective focal plane mask to control pointing errors for occulting coronagraphs only. Although CLOWFS provided a high level of tip-tilt control, it was not compatible with phase mask coronagraphs as phase masks are not reflective.

In our previous work[6] we outlined the LLOWFS's principle, simulations and laboratory experiment in conjuction with a four quadrant phase mask.[8] The paper demonstrates tip/tilt measurement with an accuracy of 0.01 λ/D in a coronagraphic testbed at LESIA, Observatoire de Paris. LLOWFS is a linear wavefront reconstructor which relies on the assumption that if post AO corrected wavefront residual are < 1 radian rms then the intensity variations in the reflected light are linearly proportional to the low order aberration occurring before the focal plane phase mask.

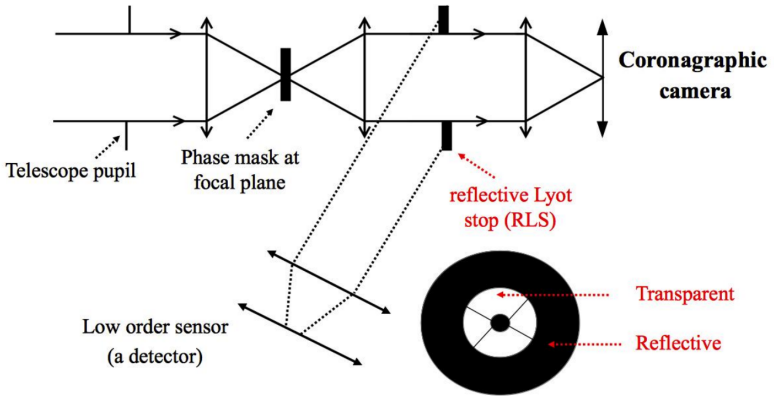

Figure 1. Basic schematic diagram of the Lyot-based low order wavefront sensor (LLOWFS). The phase mask at the focal plane diffracts starlight which is then reflected by the reflective Lyot stop (RLS) towards a reimaged focal plane. The low order sensor measures the low order aberrations. Note that the low order sensor is at a defocused position.[6,7] The defocus is introduced so that focus aberration can be detected accurately.

In this paper, we demonstrate the implementation and laboratory experiments of LLOWFS on Subaru Telescope's high contrast imaging testbed known as SCExAO,[13] the Subaru Coronagraphic Extreme Adaptive Optics system. In this body of work, we will present the LLOWFS capability of measuring the low order aberrations such as tip, tilt, focus, oblique astigmatism & right astigmatism with the vector vortex coronagraph (VVC[9]). In section 2, the SCExAO testbed is explained briefly. The integration of LLOWFS on SCExAO is illustrated in section 3. The procedure of measuring the pointing errors is defined in section 3.1. We present the laboratory

and early on-sky closed loop results with the VVC in section 4. The LLOWFS performance on SCExAO is summarized in section 5.

2. SCEXAO OVERVIEW

The Subaru Coronagraphic Extreme AO (SCExAO[12]) system is a highly flexible, high performance coronagraphic imaging system that uses intermediate remapping optics (phase induced amplitude apodization[10] (PIAA) and Inverse PIAA) and is capable of detecting exoplanets as close as 1 λ/D.

SCExAO is fed by the 188 element AO facility (AO188) of Subaru Telescope which typically provides the residual wavefront of $\approx$ 200 nm rms at H band. SCExAO has two levels: Visible upper bench which uses the light within wavelength 600 nm - 930 nm; Infrared lower bench (Figure 2) which uses the light between 950 nm - 2500 nm. SCExAO consists of numerous modules including a Pyramid wavefront sensor to measure high order aberrations in the visible at 750 nm; Lyot-based low order wavefront sensor to measure pointing errors and other low order aberrations at 1600 nm; a speckle nulling algorithm to suppress the speckle noise and a 2000 actuator MEMS Deformable Mirror (DM) to correct for high and low order aberrations. The output of SCExAO is fed to the HAWAII 2RG detector in HICIAO[11] (High contrast instrument for the Subaru Next generation AO) for deep imaging of the post coronagraphic images.

The SCExAO bench has recently been equipped with phase mask coronagraphs such as VVC, FQPM, eight octant phase mask[13] (8OPM) and the phase induced amplitude apodization complex phase mask coronagraph (PIAACMC[14]) in order to reach an IWA $<$ 1 λ/D. The corresponding reflective Lyot stops have also been installed on SCExAO. Jovanovic et al. (2014)[12] offers a detailed explanation of the SCExAO instrument.

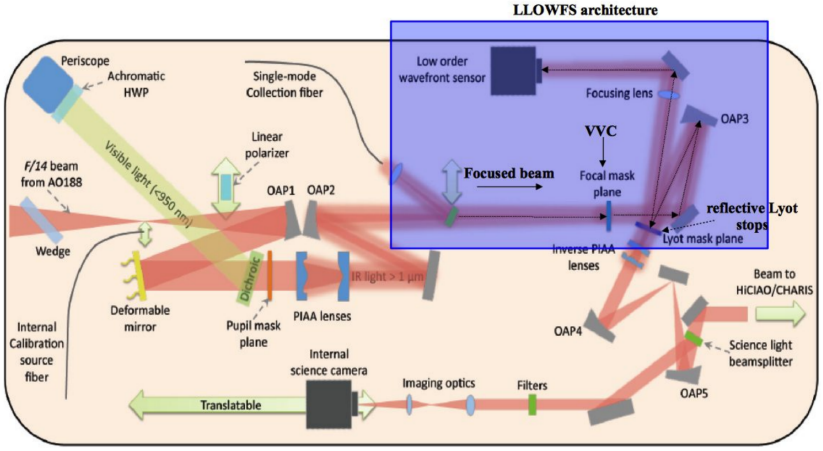

Figure 2. The schematic design of the infrared lower bench of SCExAO.[12] The highlighted area shows the configuration of LLOWFS. The f/28 focused beam encounters the VVC which is installed in one of the slots of the focal plane mask wheel. The light rejected by the VVC then encounters the Lyot mask plane wheel where the reflective Lyot stops are situated. The reflected light is directed towards the low order sensor via a focusing lens. The sensor then measures the low order aberrations.

3. LLOWFS IMPLEMENTATION ON SCEXAO

As shown in Figure 1, LLOWFS essentially requires a focal plane phase mask, a reflective Lyot stop, focusing optics and a near infrared camera. The various components of LLOWFS implemented in the laboratory on SCExAO are:

- Laser source of $\lambda =$ 1550 nm with 15 nm bandwidth

- Subaru pupil mask
- VVC (optimized at $\lambda = 1650\ nm$), mounted in a focal plane mask wheel which has degrees of freedom in the x, y and z directions. The VVC installed on SCExAO is Liquid Crystal Polymer (LCP)-based, sandwiched in A/R coated glass and is manufactured by JDSU. There is a 25 μm size metallic spot at the center of the VVC covering the central disorientation (defect) region of the vortex.
- RLS (Lyot outer pupil is 8.6 mm diameter with a reflective annulus of 25.4 mm around it) mounted in a Lyot stop wheel (degrees of freedom: x and y directions), placed at an angle of 8^o to reflect the light towards the low order sensor.

  The RLS is a fused silica disk of 1.5 mm thickness as shown in Figure 3(a). The substrate flatness is better than 5 μm. The black region is reflective chrome with 60 % reflectivity in near IR (1200 nm) while the white region is transparent
- Low-order sensor (320 x 256 pixels, InGaAs, pixel size: 30 μm, read out noise (e^-): 150, frame rate: 170 Hz). We introduced defocus in the sensor position and we estimated the value to be 5 radians rms.

Figure 2 represents the optical design of SCExAO's infrared bench. A 1500 nm diverging laser beam from the internal calibration source is incident on an off-axis parabolic mirror (OAP1) creating an 18 mm collimated beam. The reflected beam is incident on the 2000 actuator MEMS DM which is conjugated to the telescope pupil. The beam is reflected towards a fixed Subaru pupil mask (with a central obscuration and spider arms) which is positioned as close to the pupil plane as possible. The beam then encounters a dichroic which lets IR ($>$ 950 nm) to pass through the rest of the system.

There are two mask wheels immediately after the pupil mask which are also placed as close to the DM pupil as possible. These include the aspheric optics to apodize the beam for the PIAA coronagraph. The mask wheel can be moved in and out of the transmitted beam as per the coronagraph requirements. The flat mirror steers the beam onto OAP2 which focuses the beam on the focal plane mask wheel. This contains numerous phase mask coronagraphs as mentioned earlier. The VVC is situated in one of the wheel's slots. The coronagraphic beam after getting diffracted from a phase mask then encounters OAP3 which recollimates the beam to a 9 mm diameter. The collimated coronagraphic beam is incident on the Lyot stop wheel which is in a plane conjugated to the pupil. The reflective Lyot stop transmits the off axis source towards a science camera and reflects the on-axis diffracted starlight towards a focusing lens which reimages the reflective beam onto a low order sensor. We will concentrate only on LLOWFS architecture in this paper.

3.1 Procedure of measuring the aberrations

LLOWFS is a differential tip tilt sensor,[6] therefore it requires calibration prior to measuring the aberrations in the wavefront. We acquire the response matrix for tip, tilt, focus, oblique and right astigmatisms by applying known amounts of each of these aberrations to our system independently. Figure 3 (b) shows the reference image (I_0) acquired with no aberration. Figure 3 (c-f) show the calibration frame acquired by applying phasemap with 60 nm rms wavefront error to the DM for each mode as mentioned.

Considering only tip/tilt, the LLOWFS is summarized in equation:

$$I_{R(\alpha_x,\alpha_y)} - I_0 = \alpha_x S_x + \alpha_y S_y \tag{1}$$

where S_x and S_y represent the sensor's response to tip and tilt respectively. For any instant image I_R reflected by the RLS, one can identify the unknown tip-tilt (α_x, α_y), by using a least squares algorithm. Equation 1 can be modified by adding more modes and its possible to measure other low order modes more than just tip-tilt.

In the SCExAO system, we applied tip aberration between $\pm$ 85 nm rms (170 nm rms on the wavefront) with a step of 1 nm rms. This was done by sending phasemaps to the DM. For each phasemap applied to the DM, the reflected image I_R is recorded. The tip aberration for each I_R is then estimated through equation 1.

The same procedure is repeated for other modes such as tilt, focus, oblique and right astigmatisms. We discuss the response of the sensor to the aberrations applied in the next section.

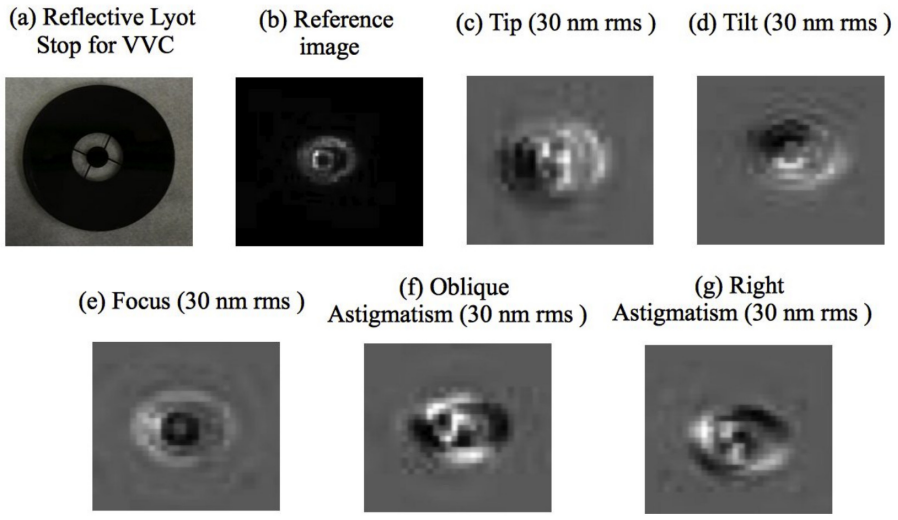

Figure 3. Images acquired on SCExAO bench in the laboratory. (a) The reflective Lyot stop for VVC. (b) Reference image with no aberration applied. The images from (*c*) to (g) are the reference subtracted calibration frames. These differential images are called as the response of the sensor to the low order modes which are obtained by sending 30 nm rms phasemap (60 nm rms on the wavefront) to the DM for (*c*) Tip mode. (d) Tilt mode. (e) Focus mode. (f) Oblique astigmatism mode. (g) Right astigmatism mode. We use these calibration frames to measure the low order aberrations in the aberrated wavefront at the entrance pupil. Note: All the calibration frames are of same brightness scale.

4. LLOWFS RESULTS

4.1 Laboratory Results

In this paper the LLOWFS's capability to measure the tip-tilt and other low order modes is presented. We intend to discuss two properties of the LLOWFS: linearity in the sensor measurement and the cross coupling between the modes. The linearity is defined as the maximum deviation of the measured aberration from the line of best fit. The fit is obtained through linear regression. The accuracy of the linear fit is calculated as the ratio of the maximum output deviation divided by the full scale output, specified as a non linearity percentage.

Figure 4, 5, 6 and 7 show the response of the sensor with respect to the aberrations applied for example: tip/tilt, focus, oblique and right astigmatisms respectively. Note that the experiment is repeated 100 times for each mode to reduce the low and high frequency noise. Each measurement is an average of 100 data points. The error bars in each graph show the noisy measurement that we have not quantified in this paper. The origin of the noise in the measurements can be DM non-linearity, photon noise, low order sensor read-out noise, drift in the reference image and local vibration of the optics.

We show that LLOWFS can measure aberrations other than just tip-tilt. LLOWFS's response to each aberration is distinguishable from other modes and there is negligible cross coupling in the measurement when each aberration is studied independently. For example, in Figure 4, the plot on the x-axis represents the tip aberration applied to the system and the y-axis represents the tip measured by the sensor. It is clear from the graph that apart from the response being linear to the tip mode, the residual in focus, oblique and right astigmatism are on average around zero, indicating little cross coupling.

However we found out that the linearity range for each aberration is different. The sensor showed a non-linearity of 4.7% over the range of $\pm$ 35 nm rms ($\pm$ 70 nm rms on the wavefront) for tip and tilt modes. Focus, oblique and right astigmatism showed a non-linearity of $< 5\%$ over the full measurement range of $\pm$ 85 nm rms ($\pm$ 170 nm rms on the wavefront). We have not studied the origin of the noise sources yet, hence we can not explain the behavior of the sensor in detail in this paper.

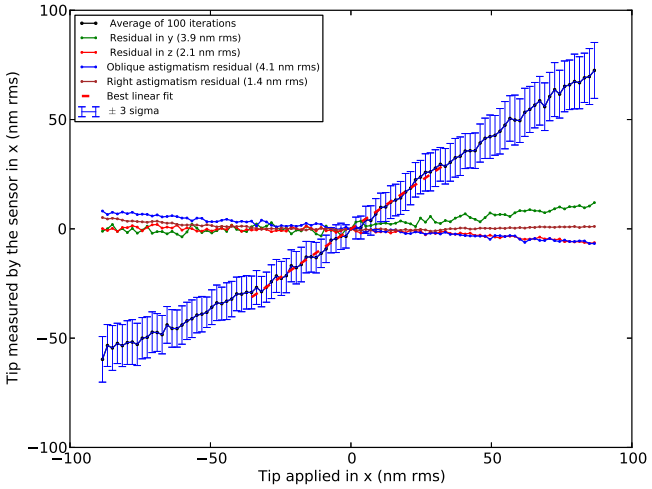

Figure 4. Linear response of the sensor to the Tip/Tilt aberration: X-axis plots the tip within ± 85 nm rms applied to the DM (± 170 nm rms on the wavefront). Y-axis plots the tip measured by the sensor. The response of the sensor is 4.7% non-linear over the range of ± 35 nm rms. The red dash line shows the best linear regression over the linear range of ± 35 nm rms. The residuals of the other low order aberrations average around zero indicating that there is no cross coupling. The experiment is repeated 100 times and the dispersion of the sensor measurements is thus shown as a ± 3σ error bar.

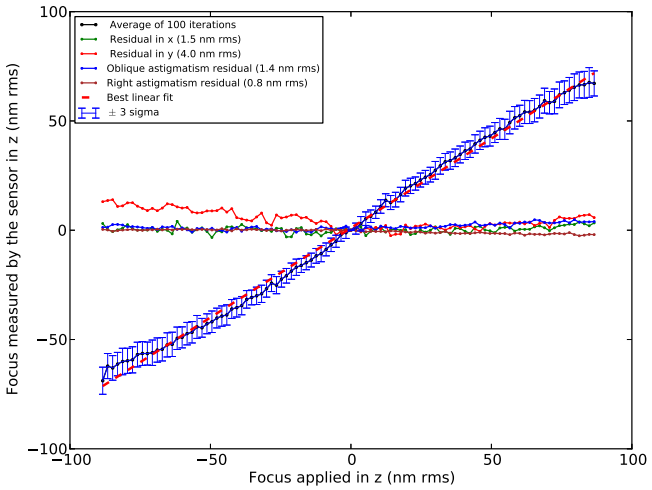

Figure 5. Linear response of the sensor to the Focus aberration: X-axis plots the focus within ± 85 nm rms applied to the DM. Y-axis plots the focus measured by the sensor. The red dash line shows the best linear fit over the full measurement range with non-linearity percentage of 3.46%. The residuals of the other low order aberrations average around zero indicating that there is negligible cross coupling. The experiment is repeated 100 times and the dispersion of the sensor measurements is thus shown as a ± 3σ error bar.

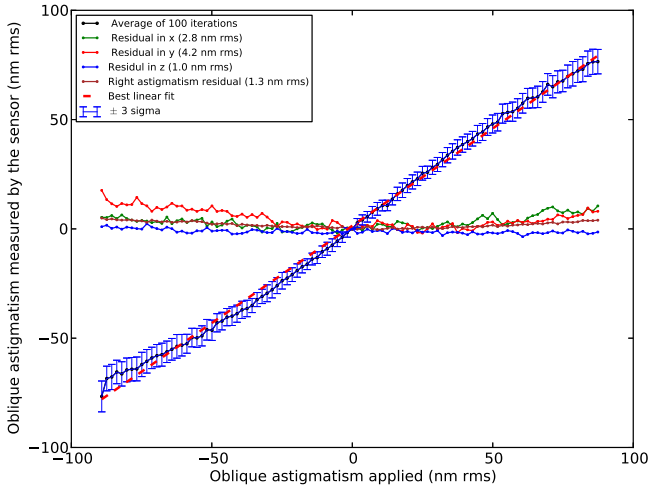

Figure 6. Linear response of the sensor to the Oblique astigmatism aberration: X-axis plots the oblique astigmatism within ± 85 nm rms applied to the DM. Y-axis plots the oblique astigmatism measured by the sensor. The red dash line shows the best linear fit over the full measurement range with non-linearity percentage of 3.1%. The residuals of the other low order aberrations average around zero indicating that there is negligible cross coupling. The experiment is repeated 100 times and the dispersion of the sensor measurements is thus shown as a ± 3σ error bar.

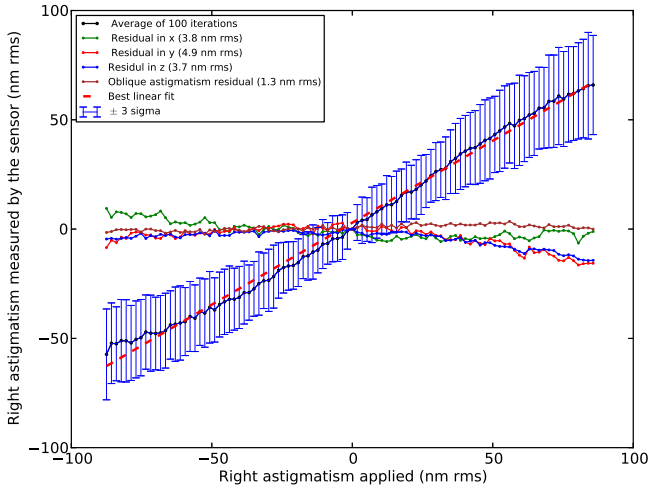

Figure 7. Linear response of the sensor to the Right astigmatism aberration: X-axis plots the right astigmatism within ± 85 nm rms applied to the DM. Y-axis plots the oblique astigmatism measured by the sensor. The red dash line shows the best linear fit over the full measurement range with non-linearity percentage of 3.58%. The residuals of the other low order aberrations average around zero indicating that there is negligible cross coupling. The experiment is repeated 100 times and the dispersion of the sensor measurements is thus shown as a ± 3σ error bar.

4.2 Early on-sky Results

We have tested the LLOWFS initial closed loop on-sky performance with the PIAA and the VVC. We report here the results with the VVC only on tip, tilt and focus. The AO188 closed the loop with a seeing of 1.3 arc seconds at H band providing strehl of $\approx$ 30 %. The LLOWFS then acquired the reference frame on-sky as shown in the Figure 8 (a). 100 nm rms phasemap of tip, tilt (0.24 λ/D angle on sky) and focus is applied on the DM individually and the response matrix for each mode is obtained as shown in Figure 8(b-d).

The LLOWFS sensed the on-sky aberrated wavefront reflected by the RLS and by using equation 1, estimated the amount of the tip, tilt and focus present in the post AO188 corrected wavefront. The control matrix was computed by the singular value decomposition method and the commands were sent to the DM to compensate for the low order aberrations. The LLOWFS successfully closed the loop on the AO188 residuals at 80 Hz on Vega at 1.6 μm. The loop kept running for $\approx$ 1 hour with a gain of 0.3. The LLOWFs loop broke temporarily when AO188's loop became unstable because of the bad seeing. In Figure 9, we obtained the closed loop residuals of 2.8 nm rms, 7.7 nm rms and 2.2 nm rms for tip, tilt and focus respectively at the time when LLOWFS loop was running.

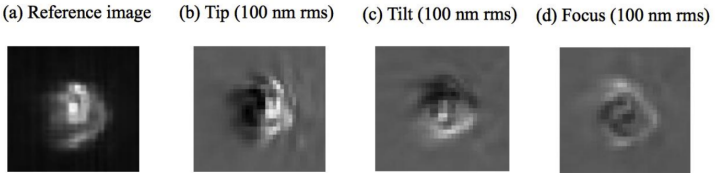

Figure 8. On-sky images: (a) Reference image. Calibration frames for (b) Tip mode. (c) Tilt mode. (d) Focus mode. All the calibration frames are obtained by applying 100 nm rms (0.24 λ/D angle on sky) phasemap to the DM for each mode individually. We used these calibration frame to close the loop on-sky. All the images are at same brightness scale.

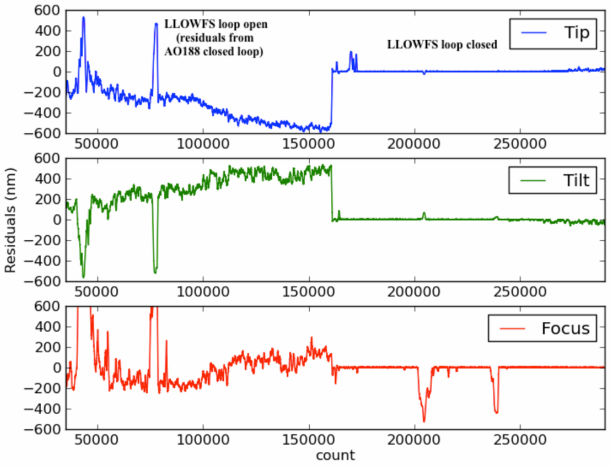

Figure 9. Initial closed loop on-sky residuals obtained with LLOWFS on SCExAO at Subaru Telescope (April 2014). The coronagraph used is the VVC. The X axis shows the data binned by 100 frames. The Y axis shows the AO188 post wavefront residuals when the LLOWFS loop is open (count from 0 to 160000) and residuals for tip, tilt and focus when LLOWFS closed the low order loop (count from 160000 and onwards). The closed loop measurement accuracy per mode is $< 7\text{x}10^{-3}$ λ/D. The dips in the residuals of focus when the LLOWFS loop is closed is because of the instability in AO188 loop.

5. CONCLUSION

We demonstrated the implementation and the initial performance of Lyot-based low order wavefront sensor (LLOWFS) on SCExAO in the laboratory as well as on-sky with the vector vortex coronagraph (VVC). The LLOWFS[6] previously measured the tip-tilt only but in this paper we showed that LLOWFS is capable of measuring other low order modes such as focus, oblique and right astigmatisms. Moreover the measurement of the low order modes are independent from each other and there is a negligible cross correlation. LLOWFS initial closed loop on-sky performance on SCExAO at Subaru Telescope demonstrated that by extracting the residual starlight at the Lyot plane, it is possible to sense and correct the low order wavefront errors without introducing non-common path errors. We closed the loop on sky on tip, tilt and focus for vector vortex coronagraph at 1.6 μm with the closed loop accuracy of $< 7\text{x}10^{-3}$ λ/D. The LLOWFS is not parametrized yet. The study of the noise sources such as read out noise, photon noise, DM non-linearity and local vibration will help to improve the performance of the sensor. SCExAO's Pyramid higher order wavefront corrections in visible will also enhance LLOWFS close loop performance in infrared by reducing the high frequency jitter. Future work includes the coupling of SCExAO's high order loop with the LLOWFS loop in order to achieve strehl ratio of $\approx$ 80 % at H band. The coupling of the control loops will introduce the differential tip tilt errors in the infrared channel which we aim to correct with LLOWFS by changing the zero point of the Pyramid wave front sensor in visible. The working and performance of LLOWFS will be tested and verified with other phase mask coronagraphs on SCExAO such as four quadrant phase mask, eight octant phase mask and PIAACMC.

REFERENCES

[1] Lloyd, J. P., & Sivaramakrishnan, A.,"Tip Tilt Error in Lyot Coronagraphy," *Astrophysical Journal*, 621, 1153 (2005)

[2] Shaklan, S. B., & Green, J. J.,"Low-Order Aberration Sensitivity of Eighth-Order Coronagraph Masks," *Astrophysical Journal*, 628, 474 (2005)

[3] Sivaramakrishnan, A., Soummer, R., Sivaramakrishnan, A. V., Lloyd, J. P., Oppenheimer, B. R., & Makidson, R. B.,"Low-Order Aberrations in Band-Limited Lyot Coronagraphs," *Astrophysical Journal*, 634, 1416 (2005)

[4] Belikov, R., Kasdin, N. J., & Vanderbei, R. J.,"Diffraction-Based Sensitivity Analysis of Apodized Pupil Mapping Systems," *Astrophysical Journal*, 652, 833 (2006)

[5] Guyon, O., Pluzhnik, E. A., Kuchner, M. J., Collins, B., Ridgway, S. T.,"Theoretical Limits on Extrasolar Terrestrial Planet Detection with Coronagraphs," *Astrophysical Journal*, 167, 81 (2006)

[6] Singh, G., Martinache, F., Baudoz, P., Guyon, O., Matsuo, T., Jovanovic N., Clergeon, C.,"Lyot-based Low Order Wavefront Sensor for Phase Mask Coronagraphs: Principle, Simulations and Laboratory Experiments," *Publications of the Astronomical Society of the Pacific* (accepted, June 2014)

[7] Guyon, O., Matsuo, T., & Angel, R., "Coronagraphic Low-Order Wave-Front Sensor: Principle and Application to a Phase-Induced Amplitude Coronagraph," *Astrophysical Journal*, 693, 75 (2009)

[8] Rouan, D., Riaud, P., Boccaletti, A., Clénet, Y., and Labeyrie, A., "The four-quadrant phase-mask coronagraph. i. principle," *Publications of the Astronomical Society of the Pacific* 112, 1479−1486 (Nov. 2000).

[9] Mawet, D., Serabyn, E., Liewer, K., et al.,"The Vector Vortex Coronagraph: Laboratory Results and First Light at Palomar Observatory," *Astrophysical Journal*, 709, 53 (2010)

[10] Guyon, O.,"Phase-induced amplitude apodization of telescope pupils for extrasolar terrestrial planet imaging," *Astronomy and Astrophysics*, 404, 379 (2003)

[11] Hodapp, K., et al.,"The HiCIAO camera for the Subaru telescope," *Society of Photo-Optical Instrumentation Engineers (SPIE) Conference Series*, 6269−142 (2006)

[12] Jovanovic. N., et. al.,"Development and recent results from the Subaru coronagraphic extreme adaptive optics system," *Society of Photo-Optical Instrumentation Engineers (SPIE) Conference Series* 9147−61 (June 2014).

[13] Murakami, N., Uemura, R., Baba, N., Nishikawa, J., Tamura, M., Hashimoto, N., & Abe, L.,"An Eight-Octant Phase-Mask Coronagraph," *Publications of the Astronomical Society of the Pacific*, 120, 1112 (2008a)

[14] Guyon, O., Martinache, F., Belikov, R., Soummer, R.,"High Performance PIAA Coronagraphy with Complex Amplitude Focal Plane Masks," *Astrophysical Journal*, 190, 220−232 (2010)